Claudio Margottini
Paolo Canuti · Kyoji Sassa
Editors

Landslide Science and Practice

Volume 5
Complex Environment

Springer

Landslide Science and Practice

Claudio Margottini • Paolo Canuti • Kyoji Sassa
Editors

Landslide Science and Practice

Volume 5: Complex Environment

Springer

Editors
Claudio Margottini
ISPRA - Italian Institute for
Environmental Protection and Research
Geological Survey of Italy
Rome, Italy

Paolo Canuti
ICL - International Consortium on Landslides
Florence, Italy

Kyoji Sassa
UNITWIN Headquarters Building
Kyoto University Uji Campus
Uji, Kyoto, Japan

Associate Editors
Filippo Catani
Department of Earth Sciences
University of Florence
Firenze, Italy

Alessandro Trigila
ISPRA - Italian Institute for
Environmental Protection and Research
Geological Survey of Italy
Rome, Italy

Additional material to Volume 1 can be downloaded from http://extras.springer.com

ISBN 978-3-642-31426-1 ISBN 978-3-642-31427-8 (eBook)
DOI 10.1007/978-3-642-31427-8
Springer Heidelberg New York Dordrecht London

Library of Congress Control Number: 2013932640

© Springer-Verlag Berlin Heidelberg 2013
This work is subject to copyright. All rights are reserved by the Publisher, whether the whole or part of the material is concerned, specifically the rights of translation, reprinting, reuse of illustrations, recitation, broadcasting, reproduction on microfilms or in any other physical way, and transmission or information storage and retrieval, electronic adaptation, computer software, or by similar or dissimilar methodology now known or hereafter developed. Exempted from this legal reservation are brief excerpts in connection with reviews or scholarly analysis or material supplied specifically for the purpose of being entered and executed on a computer system, for exclusive use by the purchaser of the work. Duplication of this publication or parts thereof is permitted only under the provisions of the Copyright Law of the Publisher's location, in its current version, and permission for use must always be obtained from Springer. Permissions for use may be obtained through RightsLink at the Copyright Clearance Center. Violations are liable to prosecution under the respective Copyright Law.
The use of general descriptive names, registered names, trademarks, service marks, etc. in this publication does not imply, even in the absence of a specific statement, that such names are exempt from the relevant protective laws and regulations and therefore free for general use.
While the advice and information in this book are believed to be true and accurate at the date of publication, neither the authors nor the editors nor the publisher can accept any legal responsibility for any errors or omissions that may be made. The publisher makes no warranty, express or implied, with respect to the material contained herein.

Printed on acid-free paper

Springer is part of Springer Science+Business Media (www.springer.com)

Preface

Landslide Science and Practice

Proceedings of the Second World Landslide Forum

The Second World Landslide Forum (**WLF**) was organized at the headquarters of the Food and Agriculture Organization of the United Nations (FAO), Rome, Italy, on 3–9 October 2011. WLF is a triennial mainstream conference of the International Programme on Landslides (**IPL**) which is jointly managed by the IPL Global Promotion Committee consisting of the International Consortium on Landslides (**ICL**), the United Nations Educational, Scientific and Cultural Organization (UNESCO), the World Meteorological Organization (WMO), the Food and Agriculture Organization of the United Nations (FAO), the United Nations International Strategy for Disaster Risk Reduction (UNISDR), the United Nations University (UNU), the International Council for Science (ICSU), and the World Federation of Engineering Organizations (WFEO).

Background to the World Landslide Forums

The International Consortium on Landslides (ICL) was established by the 2002 Kyoto Declaration "Establishment of an International Consortium on Landslides," with the Statutes adopted in January 2002. The Statutes defined the **General Assembly** of ICL: In order to report and disseminate the activities and achievements of the consortium, a General Assembly shall be convened every 3 years by inviting Members of the International Consortium on Landslides, individual members within those organizations, and all levels of cooperating organizations and individual researchers, engineers, and administrators. The General Assembly will receive reports on Consortium activities and provide a forum for open discussion and new initiatives from all participants.

The First General Assembly 2005 to the First World Landslide Forum 2008

The First General Assembly was organized at the Keck Center of the National Academy of Sciences in Washington D.C., USA, on 12–14 October 2005. At this Assembly, the first full-color book reporting consortium activities for the initial 3 years, 2002–2005, was published as "Landslides-Risk analysis and sustainable disaster management" through Springer. The 2006 Tokyo Round-Table Discussion – "Strengthening Research and Learning on Earth System Risk Analysis and Sustainable Disaster Management within UN-ISDR as Regards Landslides" – toward a dynamic global network of the International Programme on Landslides (IPL) was held at the United Nations University, Tokyo, on 18–20 January 2006. **The 2006 Tokyo**

Action Plan – *Strengthening research and learning on landslides and related earth system disasters for global risk preparedness* – was adopted. The Tokyo Action Plan established a new global International Programme on Landslides (IPL) including holding World Landslide Forums. Accordingly, the Second General Assembly 2008 was replaced by the **First World Landslide Forum** and held at the United Nations University, Tokyo, Japan, on 18–21 November 2008.

Report of the Second World Landslide Forum

The Second World Landslide Forum – *Putting Science into Practice* – was organized at the Headquarters of the Food and Agriculture Organization of the United Nations (FAO) on 3–9 October 2011. It was jointly organized by the IPL Global Promotion Committee (ICL, UNESCO, WMO, FAO, UNISDR, UNU, ICSU, WFEO) and two ICL members in Italy: the Italian Institute for Environmental Protection and Research (ISPRA) and the Earth Science Department of the University of Florence with support from the Government of Italy and many Italian landslide-related organizations.

- 864 people from 63 countries participated. Attendance was larger than expected, and twice the attendance at the First World Landslide Forum 2008 in Tokyo (430 participants: 175 from Japan and 255 from abroad).
- 25 technical sessions were held, and 465 full papers were submitted. All accepted papers were edited in 7 volumes including this volume:
  1. Landslide Inventory and Susceptibility and Hazard Zoning
  2. Early Warning, Instrumentation and Monitoring
  3. Spatial Analysis and Modeling
  4. Global Environmental Change
  5. **Complex Environment – this volume**
  6. Risk Assessment, Management and Mitigation
  7. Social and Economic Impact and Policies

Requests of Cooperation for Further Development of ICL and IPL

ICL and IPL are global multidisciplinary and cross-sectoral initiatives to promote landslide science and capacity-development to reduce landslide disasters. The core activities of ICL and IPL are ***Landslides:*** Journal of International Consortium on Landslides, World Landslide Forum, and IPL projects. Thanks to worldwide support of the journal, the Impact Factor of ***Landslides*** was 2.216 for 2011 which is the highest within 30 ISI journals in category of Engineering, Geological. The journal will develop from a quarterly journal to a bimonthly journal from Vol. 10 in 2013. The Third World Landslide Forum – Landslide risk mitigation toward a safer geo-environment – at the China National Convention Center, Beijing, China, on 2–6 June (conference) and 7–11 June (Field Trip) 2014. The ICL entered into the second decade of its activities and organized a 10th anniversary Conference on 17–20 January 2012, in Kyoto, Japan. ICL adopted the ICL Strategic Plan 2012–2021, *To create a safer geo-environment*- as an outcome of this conference.

ICL is an international nongovernmental and nonprofit scientific organization promoting landslide research and capacity-building for the benefit of society and the environment, and is the thematic landslides platform in the UNISDR Global Platform for Disaster Risk Reduction. ICL activities are supported by voluntary efforts of ICL members and supporting organizations. All people involving in landslide research and landslide disaster mitigation activities are requested to cooperate for the development of this initiative through its second decade 2012–2021. (http://www.iplhq.org/ *and* http://icl.iplhq.org/).

We are deeply appreciative of all e Second World Landslide Forum participants and of the contributions from our UNESCO, WMO, FAO, UNISDR, UNU, ICSU, WFEO partners and all of our colleagues in ICL for the development of IPL up to now. Finally we address our sincere thanks to Filippo Catani and Alessandro Trigila (the associate editors) for their extensive efforts covering the technical sessions, and reviewing and editing the papers.

Claudio Margottini
Forum Chair

Paolo Canuti
President of ICL

Paolo Canuti

Kyoji Sassa
Executive Director of ICL

Kyoji Sassa

ICL and IPL Secretariat

IPL office: UNITWIN headquarters Buildings, Kyoto University Uji Campus,
Uji, Kyoto 611-0011, Japan
ICL office: The Association for Diaster Prevention Research,
138-1 Tanaka Asukai-cho, Sakyo-ku, Kyoto 606-8226, Japan
Email: secretariat@iclhq.org
URL: http://www.iplhq.org/ and http://icl.iplhq.org/

Organizational Structure of the Second World Landslide Forum

Organizers

IPL Global Promotion Committee including:

- International Consortium on Landslides (ICL) *
- United Nations Educational, Scientific and Cultural Organization (UNESCO)
- World Meteorological Organization (WMO)
- Food and Agriculture Organization of the United Nations (FAO)
- United Nations International Strategy for Disaster Risk Reduction (UNISDR)
- United Nations University (UNU)
- International Council for Science (ICSU)
- World Federation of Engineering Organizations (WFEO)
- Italian Institute for Environmental Protection and Research (ISPRA)
  (* Members are listed in the last page of this book)

Co-sponsors

- International Union of Geological Sciences (IUGS)
- International Union of Geodesy and Geophysics (IUGG)
- International Geographical Union (IGU)
- International Flood Initiative (IFI)

Under the Auspices of

- International Association for Engineering Geology and the Environment, Italian Section (IAEG)
- Italian Association of Engineering Geologists (AIGA)
- Italian Association of Geotechnique (AGI)
- Italian Association for Mining Engineers, Environment and Territory (ANIM)
- Italian Georesources and Environment Association (GEAM)

International Organizing Board

Honorary Chairpersons

- Irina BOKOVA (UNESCO Director-General)
- Catherine BRECHIGNAC (ICSU President)
- Jacques DIOUF (FAO Director-General)

- Michel JARRAUD (WMO Secretary-General)
- Maria P. LAFFARGUE (WFEO President)
- Konrad OSTERWALDER (UNU Rector)
- Bernardo DE BERNARDINIS (ISPRA President)
- UNISDR Director

Chairpersons

- Claudio MARGOTTINI (ISPRA, Forum Chair)
- Paolo CANUTI (ICL President)
- Kyoji SASSA (ICL Executive-Director)

Deputy Chairpersons

- Peter BOBROWSKY (IUGS Secretary General)
- Deliang CHEN (ICSU Executive Director)
- Peter LYTTLE (ICL Vice President, US Geological Survey)
- Eduardo ROJAS-BRIALES (Assistant Director General of FAO)
- Badaoui ROUHBAN (Director of UNESCO's Section for Disaster Reduction)
- Yueping YIN (ICL Vice President, China Geological Survey)

Scientific Advisory Board

Representing Organisation

- Irasema ALCANTARA-AYALA (Vice President of International Geographical Union - IGU)
- Walter AMMAN (President Davos Forum)
- Michael CROZIER (President of International Association of Geomorphologists - IAG)
- Carlos DELGADO (President of International Association of Engineering Geology - IAEG)
- Luca DEMICHELI (Secretary General of EuroGeoSurveys)
- John HARDING (United Nations Secretariat to International Strategy for Disaster Reduction - UNISDR)
- Srikantha HERATH (Senior Academic Programme Officer of the United Nations University - UNU)
- Thomas HOFER (Forestry officer, Food and Agriculture Organization of the United Nations - FAO)
- Yumio ISHII (Chair of the Committee on Disaster Risk Management of The World Federation of Engineering Organizations WFEO)
- Derek MARTIN (Vice President for North America of International Society for Rock Mechanics - ISRM)
- Howard MOORE (Senior Advisor, International Council for Science - ICSU)
- Pedro SECO E PINTO (Past President of International Society for Soil Mechanics and Geotechnical Engineering - ISSMGE)
- Luciano PICARELLI (Chairperson of the Joint Technical Committee on Landslides and Engineered slopes - JTC1 of ISSMGE, ISRM, IAEG)
- Kaoru TAKARA (Vice chairperson of the Intergovernmental Council of the International Hydrological Programme of UNESCO - IHP)
- Kuniyoshi TAKEUCHI (President of GeoRisk Commission of International Union of Geodesy and Geophysics - IUGG)

Landslide Experts

- Giovanni BARLA (Politecnico di Torino, Italy)
- R.K. BHANDARI (Consultant, India)
- Christophe BONNARD (Swiss Federal Institute of Technology, Lausanne, Switzerland)
- Nicola CASAGLI (University of Florence, Italy)
- Leonardo CASCINI (University of Salerno, Italy)
- Giovanni CROSTA (University of Milano Bicocca, Milano, Italy)
- Jordi COROMINAS (Technical University of Catalonia, Barcelona, Spain)
- Dave CRUDEN (University of Alberta, Edmonton, Alberta, Canada)
- Thomas GLADE (University of Vienna, Austria)
- Jerome DE GRAFF (United States Department of Agriculture , Fresno - Ca - USA)
- Michel HERMELIN (Universidad EAFIT, Medellin, Colombia)
- Ken HO (Hong Kong Geotechnical office, Hong Kong, China)
- Jurgen KROPP (Potsdam Institute for Climate Change - PIK, Potsdam, Germany)
- Richard M. IVERSON (United States Geological Survey - Vancouver, WA , USA)
- C. F. LEE (Hong Kong University, China)
- Jacques LOCAT (University of Laval, Canada)
- Paul MARINOS (University of Athens, Greece)
- Hideaki MARUI (Niigata University, Japan)
- Hormoz MODARESSI (BRGM, Orléans, France)
- Farrouk NADIM (Norwegian Geothecnical Institute - NGI, Oslo, Norway)
- Gabriele SCARASCIA MUGNOZZA (University of Rome, Italy)
- Wang SIJING (Tsinghua University, China)
- Vern SINGHROY (Canada Centre for Remote Sensing, Ottawa, Canada)
- Alexander STROM (Institute of Geospheres Dynamics, RAS, Moscow, Russia)
- Ikuo TOWHATA (University of Tokyo, Japan)
- Keith TURNER (Emeritus Professor, Colorado School of Mines, Denver, Colorado USA)
- Keizo UGAI (Gunma University, Kiryu,Gunma, Japan)
- Roger URGELES (Institut de Ciències del Mar - CSIC, Barcelona, Spain
- Yasser el SHAYEB (Cairo University, Egypt)
- Sergio SEPULVEDA (University of Chile, Santiago)
- Mauro SOLDATI (University of Modena and Reggio Emilia, Italy)
- Pasquale VERSACE (Calabria University, Cosenza, Italy)
- Cees van WESTEN (ITC, Enschede, Netherlands)
- Kifle WOLDEAREGAY (University of Mekelle, Ethiopia)

Local Organizing Board

Forum Chairs

- Paolo CANUTI (ICL President - WLF2 Chairperson)
- Claudio MARGOTTINI (ISPRA - WLF2 Chairperson)
- Kyoji SASSA (ICL Secretary General - WLF2 Chairperson)

Scientific Programme Committee

- Luciano PICARELLI (Second University of Napoli)
- Marco AMANTI (ISPRA)
- Filippo CATANI (University of Firenze)
- Fausto GUZZETTI (CNR-IRPI)
- Javier HERVAS (JRC)

- Thomas HOFER (FAO)
- Carla IADANZA (ISPRA)
- Claudio MARGOTTINI (ISPRA - WLF2 Chairperson)
- Paolo TOMMASI (CNR-IGAG)
- Alessandro TRIGILA (ISPRA)

Editorial Committee

- Filippo CATANI (University of Firenze)
- Riccardo FANTI (University of Firenze)
- Fausto GUZZETTI (CNR-IRPI)
- Javier HERVAS (JRC)
- Irene RISCHIA (ISPRA)
- Gabriele SCARASCIA MUGNOZZA (Università di Roma "La Sapienza")
- Alessandro TRIGILA (ISPRA)

Logistic Committee

- Thomas HOFER (FAO)
- Claudio MARGOTTINI (ISPRA - WLF2 Chairperson)
- Orlando PANDOLFI (ECN)
- Luna GUBINELLI

Field Trips

- Gabriele SCARASCIA MUGNOZZA (University of Roma "La Sapienza")
- Giuseppe DELMONACO (ISPRA)
- Riccardo FANTI (University of Firenze)
- Irene RISCHIA (ISPRA)
- Daniele SPIZZICHINO (ISPRA)
- Paolo TOMMASI (CNR-IGAG)

Fund Raising and Exhibition

- Claudio MARGOTTINI (ISPRA - WLF2 Chairperson)
- Paolo FARINA (IDS SpA)
- Giorgio LOLLINO (CNR-IRPI)

Secretariat

ISPRA, Italian Institute for Environmental Protection and Research
Dept. Geological Survey of Italy, Via Vitaliano Brancati, 48-00144 Rome, Italy.

Logistics and Administration

Orlando PANDOLFI - ECN yourLIFE Foundation

Contents

Part I Submarine Landslides and Tsunamis

Introduction by Roger Urgeles, Paolo Mazzanti, and Jacques Locat

Part II Landslide in Coastal Area

Introduction by Crescenzo Violante

Part III Seismically Induced Landslides and Seismic Landslide Hazard Analysis

Introduction by Ed Harp, Hideaki Marui, and Luca Guerrieri

Part I

Submarine Landslides and Tsunamis

Introduction by Roger Urgeles[1], Paolo Mazzanti[2], and Jacques Locat[3]

1) Dept. Geologia Marina, Institut de Ciencies del Mar (CSIC), Barcelona, Spain
2) Dipartimento di Scienze della Terra, “Sapienza”, Università di Roma, Rome, Italy and Università di Roma, NHAZCA S.r.l., spin-off “Sapienza”, Rome, Italy
3) Dep. de geologie et de genie geologique, Université Laval, Québec QC, Canada

Submarine landslides are as common as their subaerial counterparts, yet they might be orders of magnitude larger. Because of the lack of direct observations and inaccessibility of the marine environment, little is known of recurrence rates, trigger mechanisms, pre- and post-failure geotechnical conditions, and the role of landslide processes in delivering sediments to deep water. Nevertheless, increasing development of seafloor-based (offshore platforms, telecommunication and energy transport facilities, . . .) and coastal infrastructures ask for better knowledge of seafloor stability conditions, submarine landslide processes and subsequent effects such as tsunamis. Session L22 at the second World Landslide Forum presented recent advances on our understanding of submarine landslides in-line with the objectives of the UNESCO-IUGS’ project IGCP585 (http://www.igcp585.org).

Modern Marine Geophysical and Mapping Techniques

The session showed how modern marine geophysical and mapping techniques might be useful in identifying the variety of features associated with offshore slope failure and associated mass transport deposits, some of them affecting areas of high ecological and environmental value such as the Great Barrier Reef (George et al. 2011). Examples from Uruguay and the NW African Margin (Krastel et al. 2011) and the Northern Sicilian margin (Sulli et al. 2012) show how changing environmental factors couple to control the styles of submarine slope failures and derived tsunami hazard. Extensive mapping efforts do not only show the distribution of previous landslides; they may also give indications on destabilizing conditions as pockmarks, steep slopes and signs of erosion. Detailed seafloor maps provide an important framework for susceptibility mapping and for further landslide hazard and risk assessment (Hansen et al. this volume). Furthermore, detailed mapping maybe the “reference level” for future monitoring of seafloor changes.

Offshore Failure Catalogues

Mapping efforts provide the base for establishing offshore failure catalogues. These are useful to understand the role of the geological structure (or setting) in controlling the patterns, frequency and magnitude of submarine slope failures. An example of catalogue for the Mediterranean Basin showed that most submarine landslides originate in water depths exceeding 2,000 m on slopes of less than 2° indicating that the continental rise, at least in this region, is a place of increased slope instability (Urgeles et al. 2011). The little constraints on ages of most events suggest that a large number of them occurred during the Holocene, indicating that climate induced stress changes (sea level and bottom temperature changes and their effect on gas hydrate and gas systems, sedimentary load,. . .) have had a major role in triggering slope failures (Urgeles et al. 2011). A second example with historical landslides from Norwegian fjords and lakes showed that in this environment landslides are often triggered by human activities (L'Heureux et al. this volume). In this setting the time of occurrence frequently corresponds with periods of unfavorable groundwater conditions (e.g. heavy rainfall, snow melt, and tidal drawdown; L'Heureux et al. this volume).

Pre-conditions and Trigger Mechanisms

The marine environment requires dedicated attention because some of the pre-conditions and trigger mechanisms are unique to this environment. In volcanic ocean islands, the physical and geomechanical characteristics of submarine hyaloclastite materials forming the base of the emerged volcanic edifices have low strength and high deformability properties (Ferrer et al. this volume). These rocks therefore play a fundamental role on the stability of the island flanks. Lafuerza et al. (2011) also showed how Quaternary sea level variations were possibly at the origin of gas exsolution, increased pore pressure and submarine slope failure initiation in gas-rich marine sediments.

Modeling the Motion of Submarine Landslides

Modeling the motion of submarine landslides is of critical importance to understand their extremely long runouts, their impact on seafloor structures and tsunami generating potential and to highlight defense interventions and remediation strategies. Results presented at the session indicate that the permeability of the matrix in subaqueous rock avalanches plays a key role in their dynamics (De Blasio this volume). Analysis of past deposits also shows that subaqueous rock avalanches are not as mobile as subaqueous debris flows (De Blasio this volume). Also the presence of larger blocks plays an important role in the dynamics of subaqueous rock avalanches. A model for the rock mass disintegration during flow in the two environments (subaerial/submerged) shows the importance of fragmentation in controlling the propagation phase of rock-avalanches (Mazzanti and De Blasio this volume). Laboratory experiments are also useful to understand the impact of submarine landslides and derived gravity flows on offshore installations such as cables and pipelines (Wang et al. this volume). The session showed numerical approaches to post-failure evolution using cellular automata (Avolio et al. this volume) and finite element modeling codes (Crosta et al. this volume) for coastal and lacustrine landslides and impact on the corresponding water bodies (Crosta et al. this volume).

Coastal/Submarine Landslides and Tsunamis

In this regard, understanding the relationship between coastal/submarine landslides and tsunamis is critical to mitigate the risks. Indeed, results presented at the session indicated that three tsunamis in eastern Sicily and southern Calabria were all chiefly initiated by earthquake induced mass failures (Billi et al. 2011). Establishing landslide scenarios is critical to understand the characteristic of the generated tsunami (i.e. travel time, periodicity, first signal polarity, wavelength) and their relation to coastal geohazard (Planinsek et al. 2011). When submarine slope failures have occurred in historical times, such as the 1888 shoreline landslide and tsunami in Trondheimsfjorden, central Norway (Glimsdal et al. this volume), they might be useful in validating models of landslide dynamics and tsunami initiation for older events or as benchmark for future scenarios.

Conclusion

The session highlighted that the threats posed by submarine landslides to human require an integrated approach taking into account all of the aspects highlighted above (Vanneste et al. this volume). In particular further research and development is needed to improve technologies for imaging the sub-surface as well as geotechnical data on high-quality soil samples. Long-term measurements that can capture pore pressure, deformation and other transients in underwater slopes are also necessary. Improved understanding of submarine landslides dynamics is required for developing numerical models that are also a key to improved tsunami modeling (Vanneste et al. this volume).

References

Avolio MV, Bozzano F, Di Gregorio S, Lupiano V, Mazzanti P (2012) Simulation of submarine landslides by cellular automata methodology. This volume

Billi A, Minelli L, Orecchio B, Presti D, Faccenna C, Neri G (2011) Historical earthquakes, landslides, and tsunamis in eastern Sicily and southern Calabria, Italy. In: Catani F, Margottini C, Triglia A, Iadanza C (eds) The Second World Landslide Forum – Abstract book. ISPRA, Rome, p 554

Crosta GB, Imposimato S, Roddeman D (2012). Interaction of landslide mass and water resulting in impulse waves. This volume

De Blasio FV (2012) Dynamics, velocity, and run-out of subaqueous rock avalanches. This volume

Ferrer M, González de Vallejo L, Seisdedos J (2012) Güímar and La Orotava mega-landslides (Tenerife) and tsunamis deposits in Canary Islands. This volume

George N, Mallace D, Webster JM, Beaman R, Abbey L (2011) Surface characterization of a large submarine landslide on the outer shelf and slope of the Great Barrier Reef, advances in the automated classification of submarine deposits. In: Catani F, Margottini C, Triglia A, Iadanza C (eds) The Second World Landslide Forum – Abstract book. ISPRA, Rome, p 558

Glimsdal S, L'Heureux J-S, Harbitz CB, Pedersen GK (2012). Modelling of the 1888 landslide tsunami, Trondheim. This volume

Hansen L, L'Heureux J-S, Longva O, Eilertsen RS, Bøe R (2012) Mapping of subaqueous landforms for near-shore landslide susceptibility assessment along Norwegian fjords. This volume

Krastel S, Winkelmann D, Hanebuth T, Strasser M, Wynn RB, Georgiopoulou A (2011) Mass wasting along Atlantic passive continental margins: a comparison between NW-Africa and the de la Plata River region (northern Argentina and Uruguay). In: Catani F, Margottini C, Triglia A, Iadanza C (eds) The Second World Landslide Forum – Abstract book. ISPRA, Rome, p 561

Lafuerza S, Sultan N, Canals M, Lastras G, Costa S, Cattaneo A, Frigola J (2011) The role of gas in triggering the Ana slide, Eivissa Channel, Western Mediterranean Sea. In: Catani F, Margottini C, Triglia A, Iadanza C (eds) The Second World Landslide Forum – Abstract book. ISPRA, Rome, p 562

L'Heureux J-S, Hansen L, Longva O, Eilertsen RS (2012) Landslides along Norwegian fjords: causes and hazard assessment. This volume

Mazzanti P, De Blasio FV (2012) The dynamics of subaqueous rock avalanches: the role of dynamic fragmentation. This volume

Planinsek P, Ceramicola S, Marson I, Zaniboni F, Tinti S, Pagnoni G, Praeg D, Forlin E, Colizza E (2011) Reconstruction of a submarine landslide and related tsunami from morpho-bathymetry and sub-bottom data on the Ionian Calabrian margin (Mediterranean Sea). In: Catani F, Margottini C, Triglia A, Iadanza C (eds) The Second World Landslide Forum – Abstract book. ISPRA, Rome, p 565

Sulli A, Agate M, Lo Iacono C, Lo Presti V, Pennino V, Polizzi V (2012) Submarine slope failures along the Northern Sicilian continental margin (Southern Tyrrhenian Sea) and possible implications for geo-hazard. This volume

Urgeles R, Camerlenghi A, Palmer F (2011) Slope failures in the continental margins of the Western Mediterranean Sea: towards understanding of environmental and geologic controls and tsunamigenic potential. In: Catani F, Margottini C, Triglia A, Iadanza C (eds) The Second World Landslide Forum – Abstract book. ISPRA, Rome, p 567

Vanneste M, Forsberg CF, Glimsdal S, Harbitz CB, Issler D, Kvalstad TJ, Løvholt F, Nadim F (2012) Submarine landslides and their consequences: what do we know, what can we do? This volume

Wang F, Sonoyama T, Honda M (2012) Model test of submarine landslide impact forces acting on cables. This volume

THE SECOND
WORLD
LANDSLIDE FORUM

Submarine Landslides and Their Consequences: What Do We Know, What Can We Do?

Maarten Vanneste, Carl Fredrik Forsberg, Sylfest Glimsdal, Carl B. Harbitz,
Dieter Issler, Tore J. Kvalstad, Finn Løvholt, and Farrokh Nadim

Abstract

The threats posed by submarine landslides to human civilization are the disappearance of valuable land near the shoreline, the destruction of seafloor installations like cables, pipelines or oil wells, and – most importantly – the devastation of coastal areas by landslide-generated tsunamis. Assessing and mitigating these hazards almost invariably implies the estimation of risk in situations where the probabilities associated with different scenarios are difficult to quantify. However, substantial progress has been made in the understanding of the geological processes and physical mechanisms operating at different stages of a submarine landslide event. This paper briefly reviews the state-of-the-art and points out why knowledge and methods from several disciplines of the physical sciences need to be combined to find solutions to the geotechnical engineering challenges from submarine landslides. A number of references to relevant case studies are also provided.

Keywords

Submarine landslides • Triggering • Flow rheology • Tsunami • Monitoring • Mitigation • Integrated geosciences

Introduction

Submarine landslides occur worldwide in a large variety of settings, including lakes, near-shore areas, fjords, active and passive continental margins/slopes (both river-fed or glacial-dominated). Slope instability is thus a potential hazard for many underwater development and construction projects. Mass movements along the seafloor will invariably create waves on the ocean surface (tsunami) that can propagate over large distances. Depending on the nature and size of the landslide as well as its location, the tsunami effects along the coast range from unnoticeable to extremely destructive. This implies that there is a general need to properly evaluate the hazard associated with submarine slope instabilities and their consequences, in order to assess and design suitable mitigation measures.

Landslides have three main phases of development, namely (a) a phase of pre-conditioning, (b) the actual triggering of the movement, and (c) finally the landslide progress or run-out (Fig. 1; e.g. Locat 2001; Canals et al. 2004). The run-out phase can often be subdivided further according to the dominant flow regime, which has implications for the run-out distance as well as the pressure exerted on seafloor infrastructure.

Tsunamis due to landslides account for 8 % of all tsunamis at the global level (NTL website), thus contributing significantly to the tsunami hazard. Important historical examples are, among others, the 1998 Papua New Guinea (Bardet et al. 2003; Tappin et al. 2008), the 1992 Flores Island (Yeh et al. 1993), the 1899 Banda Sea and the 1792 Shimabara Bay events (NGDC/WDC). Each of these tsunamis caused several thousand fatalities. Hence, these events clearly confirm that large submarine landslides are potentially catastrophic tsunami generators, although less known than tsunamis of seismic origin. A submarine landslide moves less material, but

---

M. Vanneste (✉) • C.F. Forsberg • S. Glimsdal • C.B. Harbitz •
D. Issler • T.J. Kvalstad • F. Løvholt • F. Nadim
Norwegian Geotechnical Institute and International Centre for
Geohazards, Postboks 3930 Ullevål Stadion, 0806 Oslo, Norway
e-mail: maarten.vanneste@ngi.no

C. Margottini et al. (eds.), *Landslide Science and Practice*, Vol. 5,
DOI 10.1007/978-3-642-31427-8_1, © Springer-Verlag Berlin Heidelberg 2013

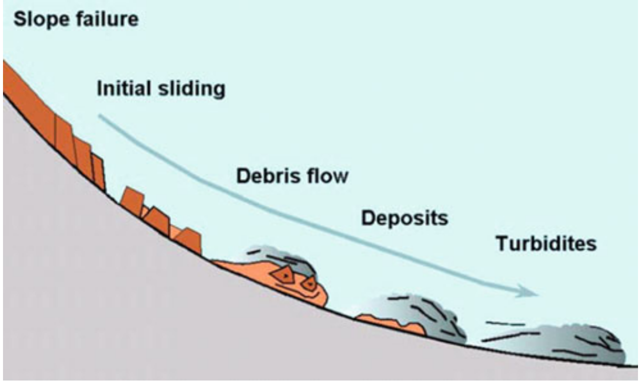

Fig. 1 Schematic representation of submarine landslide evolution. From (Bryn et al. 2005)

might move it vertically up to 100 times as much as an earthquake does, resulting in a comparable amount of tsunami energy (Okal and Synolakis 2003) and causing higher waves with shorter wavelengths. Tsunamis originating from landslides therefore propagate less efficiently in the far field compared to tsunamis due to earthquakes, but may generate high surface elevations locally. As a consequence, they exhibit a more locally constrained run-up pattern (Okal and Synolakis 2004). According to Ruff (2003), energy conversion from submarine landslides (or earthquakes) to gravity water waves can range from essentially zero to about 50 % as a practical upper bound for reasonable geological and hydrodynamic parameters.

This paper reviews our present knowledge of the salient features of the above-mentioned stages of submarine landslides in a general manner before discussing the effects on seafloor structures and possible mitigation measures. A review more oriented towards the scientific aspects of landslide dynamics can be found, e.g., in Elverhøi et al. (2005).

Preconditioning, Triggering and Back-Stepping/Retrogression

Pre-Conditioning

The preconditioning phase consists of changes over time within a sedimentary environment that drive a previously stable slope to the edge of instability. Destabilising factors reported in the literature include high sedimentation rates, unfavourable soil layering, the presence of "weak" layers providing potential slip planes, seismic or volcanic activity, steep slopes and oversteepening due to erosion, artesian pressure, fluid flow-related phenomena (e.g. diapirism, mud volcanoes), gassy soils and gas hydrate dissociation (e.g., Canals et al. 2004; Solheim et al. 2007). These factors have in common that they induce excess pore pressure and thereby reduce the effective stress and thus the frictional strength that can be activated against down-slope movement. Remarkably, pore pressure is – despite its importance – only very rarely measured offshore and thus most often assumed or modelled. Hence, a proper understanding of the geological history of a given site is of paramount importance for proper slope stability assessment. This requires combining geological and geophysical data with high-quality geotechnical data.

A typical example of preconditioning is the climate-controlled cycles that have repeatedly led to massive submarine landslides in the Storegga area between the North Sea Fan and the Vøring plateau, offshore Norway: Contourite deposits with strain-softening behaviour became sandwiched between low-permeability glacial clays as a consequence of large-scale glacial fluctuations (Bryn et al. 2005; Kvalstad et al. 2005; Solheim et al. 2007). The preconditioning factors also help explaining the areal and vertical extent of the landslide.

Particular conditions apply to coastal environments of formerly-glaciated margins like Scandinavia and Canada, where quick clays in fjord valleys are a major hazard. Quick clay deposits within the fjord may further serve as slip planes when failure happens in the fjords, as was the case, e.g., in the Finneidfjord (L'Heureux et al. 2011). Thus, onshore–offshore relationships cannot be ignored in such cases.

Triggers

The trigger required to set off a landslide depends on how far the preconditioning has progressed. Earthquakes are very often thought to play this role as they can provide ground shaking that can result in increased pore pressures and slope destabilisation (e.g. Canals et al. 2004; Solheim et al. 2007). However, seismicity is not the sole trigger for submarine landslides, and often the actual trigger is unknown, as is the case, e.g., with recent, smaller-scale failures with low mobility on the upper slope of the Vesterålen margin off Norway (Vanneste et al. in press) or the giant Hinlopen-Yermak landslide (Vanneste et al. 2006, 2011). In fact, the preconditioning process itself may continue and ultimately cause the slope to fail without a special triggering event. An example is the growth of excess pore pressure if isostatic uplifting after a glacial maximum diminishes the overburden pressure more rapidly than the pore pressure diffuses. This process may be exacerbated locally by the dissolution of gas hydrates.

In many submarine or near-coastal development projects, it is important to ascertain whether or not human intervention can be a trigger, e.g., blasting during road works in fjord areas (Finneidfjord and Trondheimfjord, Norway) (L'Heureux

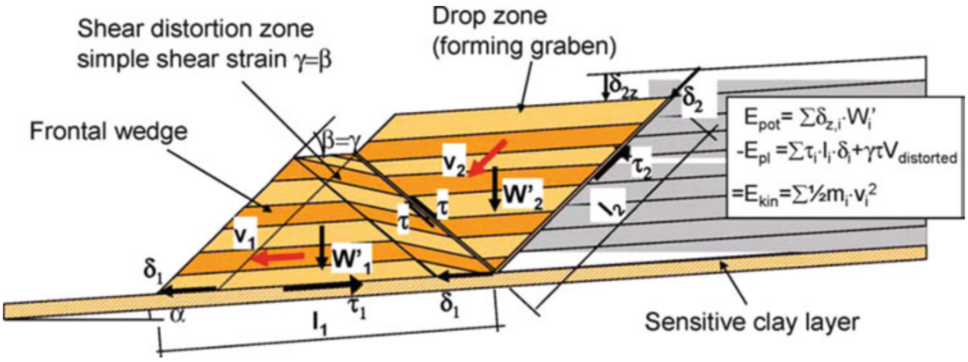

Fig. 2 Schematic representation of the dynamic wedge model. From (Kvalstad et al. 2005)

2009; L'Heureux et al. 2011) or seabed excavation related to infrastructure installations.

Retrogression

A large fraction of submarine landslides discovered appear to have developed retrogressively. Thus both the run-out and back-stepping define the area associated with the landslide and therefore the area in which mitigation measures such as relocation or rerouting have to be undertaken. Even though the impact and failures associated with run-out and back-stepping constitute the major hazards to seafloor installations from submarine landslides, the prediction of run-out and back-stepping of landslides is still a young science. It has been found, however, that the extent of back-stepping can be analysed by clever application of traditional geotechnical methods: In the potential release area, wedge-shaped pieces are sequentially removed from the downstream end and the stability of the remaining slope is reanalysed to determine the extent of the subsequent stage of failure (Fig. 2). The process comes to an end when the failure reaches more strongly consolidated soil and/or areas with a sufficiently small slope angle. A simple model met with great success when applied to the Storegga slide (Kvalstad et al. 2005). The results of this wedge model are confirmed by both detailed quasi-static finite-element simulations (Kvalstad et al. 2005) and resource-intensive, fully dynamical flow simulations using a Bingham-type constitutive law in a commercial flow solver (Fig. 3; Gauer et al. 2005).

Indirect information on the processes governing landslide release can be obtained from statistical analysis of their size distribution. A comprehensive study of the U.S. Atlantic margin (Chaytor et al. 2009) indicated an essentially linear relationship between volume, V (m^3), and area, A (m^2) – implying a preferred release thickness – and a log-normal cumulative volume distribution. In contrast, data from the Storegga Slide, a single retrogressive event with multiple phases and over 60 distinct lobes (Haflidason et al. 2004), showed a relationship $V \propto A^{3/2}$ and a power-law cumulative volume–frequency relation (Issler et al. 2005).

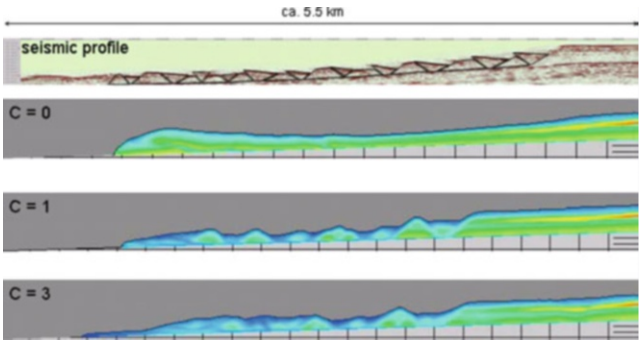

Fig. 3 Comparison of seismic profile along a lobe of the Storegga slide (top panel) and numerical simulations assuming a Bingham fluid (bottom panels). $C = 0, 1, 3$ correspond to no/ moderate/pronounced shear-induced remoulding, respectively. From (Gauer et al. 2006)

Run-Out

Substantial progress has also been achieved in the modelling of the landslide evolution. Nevertheless, major challenges remain. The first of the central problems is that the landslide material undergoes continuous transformation from a huge slab of soil to progressively smaller blocks, then to a highly viscous non-Newtonian fluid (possibly carrying clasts of different sizes) and – in many cases – to a turbidity current with fines suspended in the water by turbulence. The second issue is that these stages of flow evolution are connected to different flow regimes, which in turn require different modelling approaches. The third challenge is that the available data from real submarine landslides are essentially limited to the run-out distance and deposit distribution, whereas velocity indications are very scarce (e.g., the temporal sequence of cable breaks during the landslide triggered by the 1929 Grand Banks earthquake (Heezen and Ewing 1952)). Therefore, a great many laboratory experiments have been carried out that allow testing the modelling concepts under controlled conditions. Yet, despite their value, one encounters thorny questions of scaling when trying to apply the results to real events.

The break-up cascade from slab volumes of up to 10^{12} m^3 down to particle volumes of the order of 10^{-12} m^3 has so far not been modelled adequately, even though the run-out distance of a landslide may crucially depend on it. Back-of-the-envelope calculations show that the energy required for comminution is a moderate fraction of the potential energy released in mid-size to large landslides, but the efficiency of lateral boundaries, terrain roughness, collisions between large or small blocks and sharp local pore-pressure fluctuations needs to be investigated in more detail. The results could be used to describe the evolution of the input parameters in dynamical flow models.

Sediment composition, in particular clay content, plays a dominant role in the evolution of landslide-generated submarine mass flows (Elverhøi et al. 2010). We will briefly discuss the end members below, namely clay-rich and sand-rich flows. Intermediate soil compositions are practically important, but to the authors' knowledge, no theory successfully describing their rheology has been developed yet.

Clay-Dominated, Cohesive Soils

In the Storegga landslide complex, more than 60 separate lobes could be distinguished. The lobes have essentially equal material properties, but span some six orders of magnitude in volume and three orders of magnitude in run-out distance (Haflidason et al., 2004). Interestingly, the data show a strong power-law correlation between release volume, V (m^3), and run-out ratio $r = H/L$ (−), where H (m) is the drop height and L (m) the run-out distance, see Fig. 4 (Issler et al. 2005):

$$r = kV^{-1/3}. \tag{1}$$

Comparison with subaqueous debris flows from other areas suggests that the exponent −1/3 may be universal for clay-rich materials while the coefficient k depends on soil strength (Elverhøi et al. 2002; Issler et al. 2005). A different analysis of this data was presented by Micallef et al. (2008).

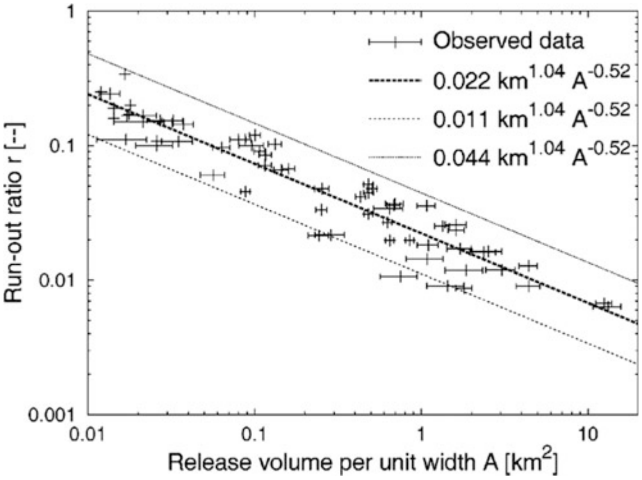

Fig. 4 Correlation between run-out ratio, r, and release volume per unit landslide width, A, for the lobes composing the Storegga Slide (Issler et al. 2005)

Correlation (1) allows inferences on the rheology of these flows, clearly ruling out Coulomb frictional behaviour for the Storegga slide. A visco-plastic rheology of the Herschel–Bulkley type,

$$\tau = \tau_y + K\dot{\gamma}^n, \tag{2}$$

where τ (Pa) is the shear stress, $\dot{\gamma}$ (s^{-1}) the shear rate, τ_y (Pa) the yield strength of the flowing material, n (−) its rheological exponent, K (kg m^{-1} s^{n-2}) its consistency (equal to the viscosity in the Bingham case $n = 1$), reproduces formula (1) well with $n = 1$ for landslide volumes up to about 0.5 km^3. The discrepancy found at larger volumes may be indicative of additional mechanisms coming into play in large flows that attain high velocities and travel long distances. No firm conclusion could be reached until now, but the main candidates are hydroplaning, progressive remoulding, and generation of excess pore pressure. Hydroplaning has been observed in the laboratory (Mohrig et al. 1998), and outrunner blocks strongly suggest that this phenomenon also commonly occurs in nature when cohesive materials are involved (Ilstad et al. 2004). Clayey materials are very sensitive to the water content so that the properties of the bottom shear layer change dramatically as the material is remoulded and incorporates ambient water or soft, water-rich seafloor sediments (De Blasio et al. 2003, 2005).

Models of different types and complexity have been developed and applied to submarine landslides. Depth-averaged one-dimensional models based on visco-plastic rheology like BING (Imran et al. 2001) can be extended to describe hydroplaning (Ilstad et al. 2004) and progressive remoulding (De Blasio et al. 2003, 2004) and to take into account the non-negligible hydrodynamic resistance. Plausible back-calculations of the different stages of the Storegga slide were obtained in this way and predictions of the run-out distance of potential future landslides with different volumes could be made, in agreement with the empirical law (1). Further developments are needed, however, to capture effects like "auto-acephalation", i.e., the formation of a thin neck and eventual detachment of the hydroplaning head from the non-hydroplaning flow body.

Sand-Rich, Low-Cohesion Soils

For dense, sand-rich low-cohesion materials, frictional effects dominate and the Herschel–Bulkley rheology (2) is not suited.

The laboratory investigations of Cassar et al. (2005) suggest that an adequate model may be obtained by modifying existing depth-averaged models for dense granular flows. Those models are characterised by an effective friction coefficient

$$\mu(I) = \mu_s + \frac{\mu_\infty - \mu_s}{I_0/I + 1} \qquad (3)$$

that depends on the so-called inertial number I (−), the ratio of the time scales associated with shearing and with overburden pressure. μ_s (−) and μ_∞ (−) are the limiting friction values under static and rapid-shear conditions, respectively, while I_0 is a reference inertial number. The main modification in the presence of an interstitial fluid concerns the time scales, i.e., I is modified while the functional form of $\mu(I)$ remains the same.

Turbidity Currents

Extensive literature exists on modelling of turbidity currents, ranging from analytically solvable box models (Dade and Huppert 1995) over one-dimensional depth-averaged formulations (Parker et al. 1986) or depth-resolved two-dimensional models with two-equation turbulence closure (Skogseth 1999) to direct numerical simulations (Necker et al. 2002). For practical applications focussing on the hazard posed by subaqueous landslides, one or two-dimensional depth-averaged models will usually be the best choice. Of particular interest are attempts to couple the turbidity current to the subaqueous debris flow from which it originated (Drago 2002), even though knowledge about the processes governing suspension of sediment from the debris flow to the turbidity current is limited (Mohrig and Marr 2003).

Consequences I: Flow Impact on Objects

The impact of a debris flow or turbidity current constitutes the major hazard to seafloor installations from submarine landslides. Damage to pipelines can also result from prolonged scour in the distal zone of a turbidity current, where the pipeline can sustain the drag force, but its support is eroded away. The most comprehensive and conclusive study of the impact of cohesive sediment flows on pipelines is reported by Zakeri (2008). For more complicated geometries, proper simulation of the flow of a non-Newtonian fluid around the object is required to determine the distribution of pressure and traction. This represents a significant effort and will not be addressed further in this paper.

A simplified description of the viscous force F (pressure drag and skin friction, in N) on objects fully surrounded by the flowing material and with an area A (m^2) exposed to the flow is given by $F = (C_D/2)\ A\ \rho\ u^2$, where the empirical drag coefficient C_D (−) is of order 1 or larger. It depends on the Reynolds number, the shape of the object and the flow direction. As the debris flow density is $\rho \approx (1\ldots2)\cdot10^3$ kg m^{-3}, high pressures result already at moderate flow velocities u (m s^{-1}). A critical question is whether there is a "water hammer" effect at first impact, which would produce very high pressures of the order of $\rho c u$, with c (m s^{-1}) the speed of sound inside the debris flow. However, Zakeri's experiments showed only peak values roughly 50 % higher than during steady flow around the pipeline and lasting for about 1 s. This mild effect is presumably due to the water and the flow having similar densities and a precursor flow of displaced ambient water building up gradually before the flow front arrives. Zakeri (2008) found that the drag coefficients for pipelines of different diameters impacted by debris flows of different compositions and velocities, but from a fixed angle, collapsed onto a single curve of the form

$$C_D(\mathrm{Re}_{nN}) = C_{D\infty} + a\mathrm{Re}_{nN}^{-b}, \qquad (4)$$

with configuration-specific asymptotic value $C_{D\infty}$, coefficient a (−) and exponent b (−). Here, the Reynolds number for a non-Newtonian fluid is defined by

$$\mathrm{Re}_{nN} = \frac{\rho u_\infty^2}{\tau}, \qquad (5)$$

where u_∞ is the free-stream velocity, τ the shear stress at the shear rate $\dot{\gamma} = u_\infty/D$ and D (m) the pipe diameter. (The modified definition (5) takes into account the variable apparent viscosity of non-Newtonian fluids.) An important point is that numerical simulations with a commercial flow solver, using the rheological parameters of the slurries determined previously in a rheometer as input, reproduced the experimental curves (4) quite closely, and thus allow further parametric studies.

This work was recently extended to look into the impact of slide blocks (kaolin clay) on submarine pipelines, using similar methods in a centrifuge testing facility, which allows much higher shear rates (Zakeri et al. 2011).

In summary, well-founded procedures for calculating the design loads for a given hazard scenario are becoming available for the cases that are most frequently encountered in practice. However, more work is needed to fine-tune impact assessment under various conditions.

Consequences II: Tsunami Formation and Propagation

Wave Generation

Tsunamis induced by landslides are less well studied compared to their seismic counterparts. Submarine landslides at large water depths are generally sub-critical, i.e. the Froude number (defined as the ratio of the landslide speed to the linear long-wave speed) is much less than one. This implies that the tsunami will normally run away from the wave-generating landslide, limiting the build-up of the wave. Critical conditions (i.e. Froude number approximately one) at water depths larger than 1,000 m require unrealistic landslide velocities around 100 m s^{-1}. The wave pattern introduced by a sub-critical landslide spreads out within a certain sector as displayed in the simulations of the Storegga Slide presented by Bondevik et al. (2005), and appears as a characteristic, symmetric sickle-shaped surface elevation followed by a surface depression (Fig. 5). For strongly sub-critical landslide motion, the maximum surface elevation generally correlates with the product of landslide volume and acceleration divided by the wave speed squared, whilst the elevated water volume correlates with the product of the landslide volume and the Froude number (Løvholt et al. 2005). However, submarine landslides in shallow water often reveal a higher Froude number as the speed of wave propagation is lower. This implies higher and sharper waves above the front of the landslide. To this end, extreme cases of tsunamigenic volcano collapses or rock slides imply large Froude number and supercritical wave generation, which is particularly evident for subaerial impact.

The landslide thickness may be simplified as a time-dependent distribution of sources and sinks causing surface displacement in the depth-averaged tsunami model. For integrating the wave build-up due to the landslide motion, the hydrodynamic surface response to an incremental change of the seafloor element should be accounted for by e.g. applying full potential hydrodynamic theory (Kajiura 1963; Pedersen 2001). Otherwise, unphysical short-wave components may be introduced. Furthermore, the interaction between the landslide and the water may be crucial for both the landslide dynamics and the generation of the tsunami (Jiang and LeBlond 1992; Harbitz 1992; Harbitz et al. 2006).

Further challenges arise with mudflows, which entrain water, producing turbulence and large vortices. In retrogressive landslide development, tsunami generation by a series of smaller slide masses may necessitate modelling beyond long-wave assumptions.

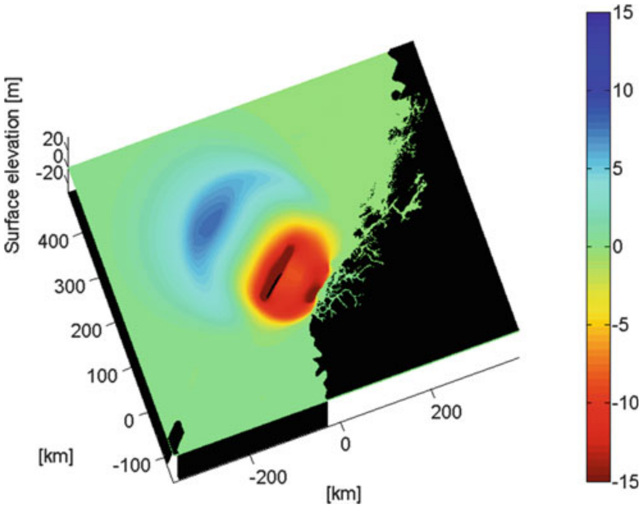

Fig. 5 Perspective view of the Storegga slide tsunami, showing colour-coded surface elevation (m) after 30 min. Modified from (Harbitz et al. 2006)

In short, a proper quantitative description of gravity mass flows and their tsunami generation requires general hydrodynamic computational tools, like Navier–Stokes-type models, but with modified rheology for the denser types of slide masses. Today, three-dimensional models of this kind are computationally demanding so that simulations with sufficient resolution are difficult to perform. One example of such a simulation demonstrated the need for large, parallel systems running for weeks or months and with a limited grid resolution for resolving solely the near-field (Gisler et al. 2006). The far-field tsunami propagation still has to be handled with some set of depth-integrated, long-wave equations, coupled with the more complex model for the source region (Løvholt et al. 2008).

Frequency Dispersion

Frequency dispersion results when the wave speed depends on the wavelength. Dispersion must be considered when the wavelength is not much larger than the water depth. The result is that the initial wave is split into its individual components. This effect is more pronounced in deeper water and over longer distances. A landslide tsunami may be much shorter than a seismic tsunami, which implies that a dispersive propagation model should be used (Lynett et al. 2003), especially for landslides with rapid acceleration or deceleration producing a large content of short-wavelength components. On the other hand, dispersion is of little importance for waves generated by large and sub-critical submarine landslides with moderate acceleration and deceleration

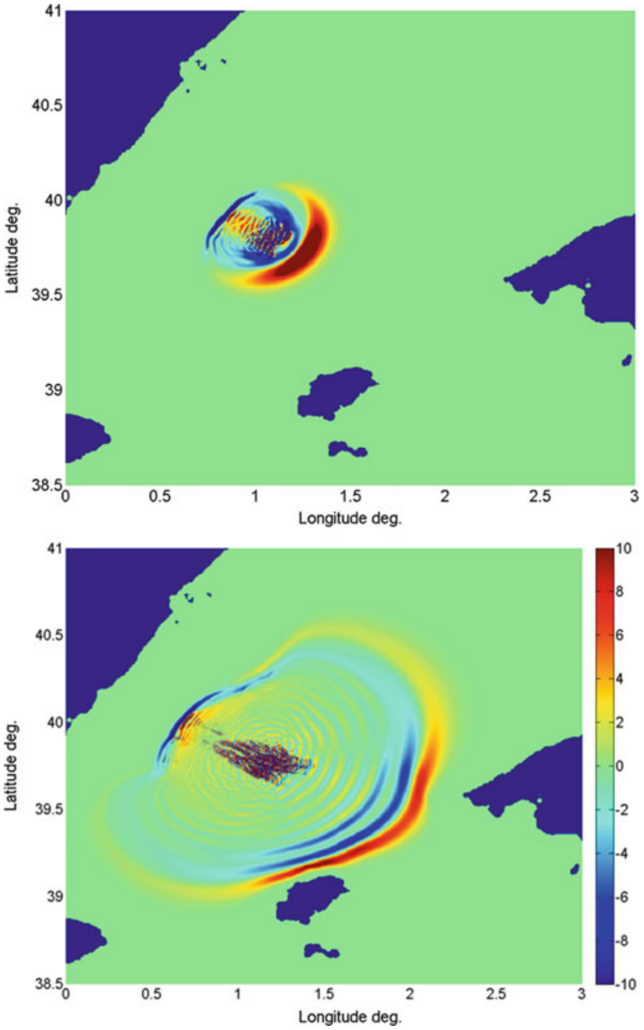

Fig. 6 Snapshots of the simulated surface elevation from the BIG'95 landslide near the source area and the Balearic Islands. *Top*: $t = 5$ min, *bottom*: $t = 15$ min

producing much longer waves than the water depth. A well-known example where dispersion proved to be important is the tsunami generated by the Papua–New Guinea landslide in 1998 (Lynett et al. 2003; Tappin et al. 2008).

To demonstrate the importance of the frequency dispersion during the generation and first stage of the propagation, we consider the BIG'95 landslide off the Ebro margin in the western Mediterranean (Urgeles et al. 2006). The evolution of the landslide is simulated along five parallel 2D transects using the BING model (Imran et al. 2001). The resulting sink–source distribution is conveyed into the tsunami model. Two snapshots of the surface elevation at 5 min and 15 min are displayed in Fig. 6. Here, the effect of dispersion is important; a hydro-static (non-dispersive) model gives a relative error of almost 50 % in the maximum surface elevation.

Detection and Mitigation

For human activity, the occurrence of a submarine landslide can be catastrophic. It is therefore of utmost importance to attempt predicting the possibility of failures and be able to plan for mitigating measures if needed in connection with projects involving seafloor installations or infrastructure. The tsunami hazard coupled to submarine landslides implies that the investigation of slope stability in near-shore areas may be warranted even if there is no infrastructure on the seafloor.

A landslide hazard evaluation typically comprises the following steps: (1) Unveiling any *previous* landsliding in the area through (geophysical) mapping, (2) analysing the *present* slope stability based on sediment sampling and in situ testing, (3) forming *landslide scenarios* (i.e., plausible release volumes) and estimating the *associated probabilities*, (4) calculating the *run-out* distances and *velocities* of those landslides based on the actual soil composition and its rheology, (5) *simulating the ensuing tsunamis and impact scenarios*, and (6) evaluating constructive and organizational *mitigation measures*.

For advanced hazard evaluations, probability calculations should be performed and the resultant risk associated with a given structure should be used to determine whether or not mitigating actions are needed. The owner of the structure may find the risk acceptable if, for example, the cost of mitigation exceeds the cost of repair.

Mapping

Geophysical methods (Figs. 7, 8, 9, and 10) are crucial to obtain insight into the regional and local sedimentary processes, and hence, landslide development. Recent landslide activity will leave scars on the seafloor. Thus seafloor morphological investigations – typically involving swath bathymetry and side-scan sonar systems – are one of the most important aspects of landslide hazard evaluations. A good horizontal resolution, preferably better than 25 m, is needed to evaluate morphological features due to both landsliding and other seafloor processes such as down-slope density flow that may contribute to the landslide hazard. To achieve the preferred resolution, multi-beam echo-sounder surveys are optimal. For investigating the morphology, however, side-scan sonar or multi-beam backscatter data are also suitable as they will allow seabed classification. In connection with hydrocarbon field developments, 3D-seismic reflection data are often available. The seafloor reflector on such data sets normally provides very good morphological information about the seafloor, and can be superior to hull-mounted swath bathymetry data (Fig. 7). For comparison, AUV's equipped with

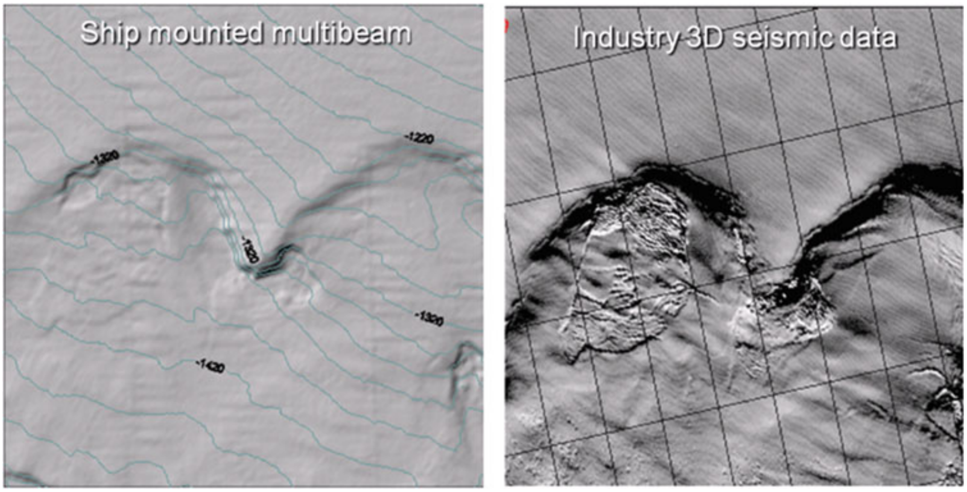

Fig. 7 Shaded relief maps of ship-mounted multi-beam data and the seafloor reflector from 3D seismic data from the deep (~1,300 m) northern margin of the Storegga Slide scar demonstrate that 3D data can provide better images of the seafloor in deep water (Mosher et al. 2006)

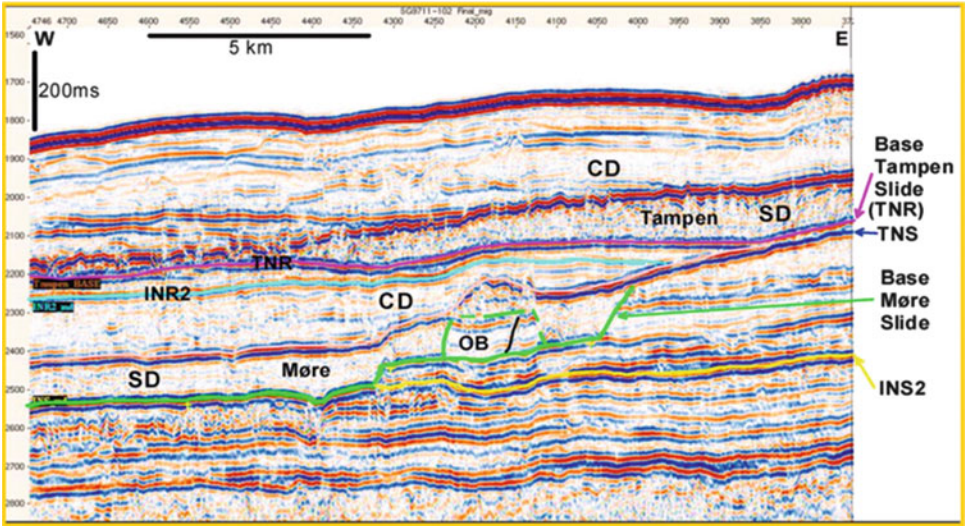

Fig. 8 Repeated sliding seen as landslide deposits (SD) in a seismic section from the Storegga area. CD: contourite deposit, OB: outlier block

multibeam echo-sounders are typically used for seabed engineering projects, in order to obtain higher spatial resolution, with bin sizes of 10 cm by 10 cm, not uncommon, e.g., for pipeline routing.

In areas with repeated or previous landsliding, older slide scars can be mapped using seismic reflection data (Fig. 9). A combination of high-resolution multi-channel 2D data and sub-bottom profiler sections is ideal. Note that, in areas with extreme sedimentation rates, relatively recent landslides may be completely buried and hence invisible from seafloor mapping (e.g., Forsberg et al. 2007). In addition, the slip planes may consist of thin intervals characterised by subtle variations in lithology compared to the surrounding soils, and may therefore be difficult to map using conventional high-resolution 2D systems. The use of very-high-resolution 3D using a chirp source, as recently performed in Finneidfjord (Norway), reveal the shallow regional slip plane – composed

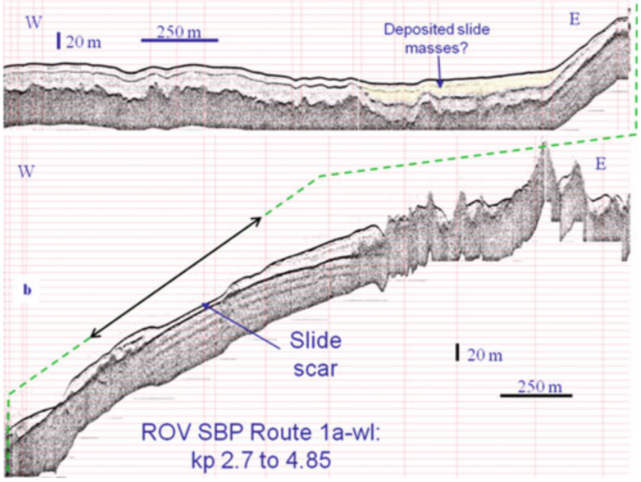

Fig. 9 Sub-bottom profiler record showing sliding in soft marine deposits laid down on top of one of the Storegga headwalls

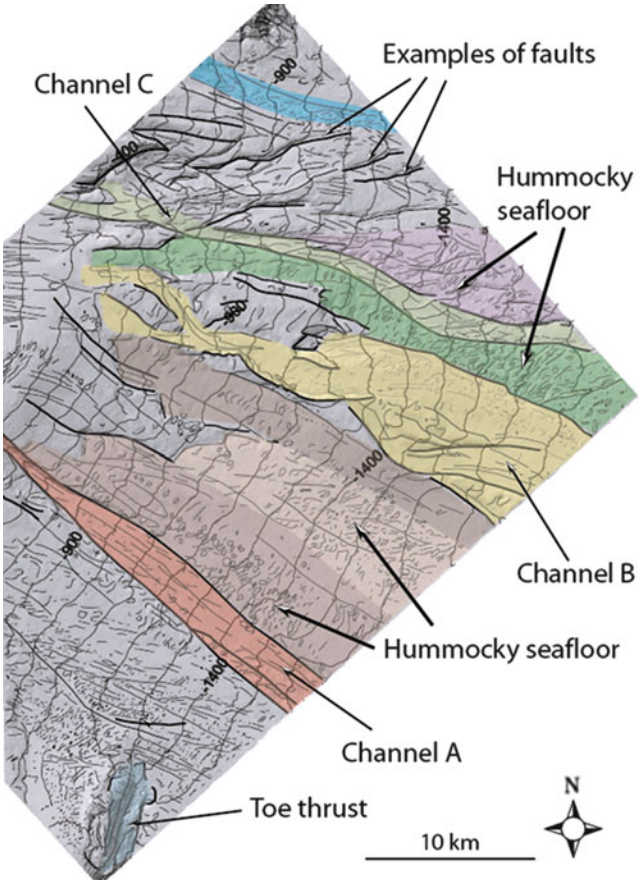

Fig. 10 Morphological map of the seafloor derived from 3D seismic data off the Krishna-Godavari Delta, East India (Forsberg et al. 2007). The data were used to help plan sediment sampling programmes and in slope stability evaluations

of a 20 cm thick turbidite sandwiched between two thin clay units – in unprecedented detail (L'Heureux et al. 2011; Vanneste et al. 2011).

An important aspect of the mapping is to relate sampling sites and sediment properties to the stratigraphy and morphology in the area. Ideally, sampling should first take place after sites and target depths have been defined based on the seismic/bathymetric investigations.

Soil Investigations

Slope stability calculations depend on geotechnical measurements whereas geological interpretations rely on sediment characteristics and ages. A sediment sampling programme is therefore needed for slope stability evaluations and to provide an understanding of previous landsliding history. The sediment analyses should aim at providing sediment strength profiles with depth, identifying layers that can act as slip planes ("weak layers"), and to provide the ages of the sediments sampled. The latter is important for modelling potential excess pore pressure in the case of rapid sedimentation and for landslide hazard evaluation in conjunction with recurrent landsliding.

Note, however, that these soil investigations do not directly determine the material properties that enter the dynamical flow models: A substantial degree of remoulding typically occurs already in the very early phase of a landslide event. Afterwards, mixing with ambient water or soft seafloor sediments will reduce the shear strength and consistency in the shear layer while dissipation of excess pore pressure has the opposite effect. Significantly more work is needed to sort these effects out and to develop reliable models of flow rheology evolution.

Monitoring, Early-Warning and Alarm Systems

Whereas offshore monitoring can be used as an early-warning system, this technology has, to the authors' knowledge, not been used for submarine mass movements. Considering the importance of excess pore pressure in submarine instabilities, pore pressure has been monitored for extended periods at only a few sites to obtain accurate measurements in advance of field development on the seabed, e.g. at Ormen Lange, offshore Norway (Strout and Tjelta 2005). In the same study, tilt metres were deployed within the Storegga slide scar to measure small-scale movements of slide blocks. No movements were detected, however.

Monitoring and early-warning/alarm systems become of paramount importance in the context of tsunami protection. Such systems are typically composed of gauge stations at the shore, GPS-equipped buoys in the open sea, a real-time transmission system, an analysis unit (usually staffed around the clock) and alarm devices (sirens, etc.). They will probably never be established specifically for a potential submarine landslide due to unknown localities, but rather for earthquake-generated tsunamis. However, they should also be effective for the former except in the near-zone of the landslide, where the coast may be hit before the first buoy or gauge station is reached.

Protection of Structures on the Seafloor and on Land

As indicated above, impact pressures from submarine mass flows on seafloor installations are typically in the range 1...1000 kPa. Dimensioning the structures for such loads is either very expensive or practically impossible. If a pipeline or cable is exposed only in a limited area, burying it in the seafloor looks like an attractive solution. However, trenches several meters deep may be required because of the erosive power of submarine mass flows (Fig. 11).

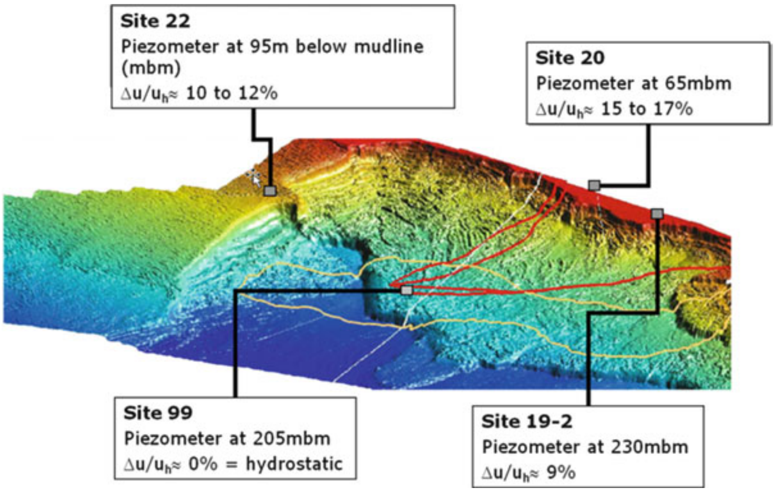

Fig. 11 Pore pressure measurements by piezometer installations in the central Storegga area. Excess pressures were measured on the flanks of the slide scar, whereas the central part (Site 99) was found to have hydrostatic pressures as is to be expected due to the unloading that occurred during the landslide (Strout and Tjelta 2005)

An alternative is to protect the structures from being hit directly by building a berm on their upstream side that leads the mass flow over the structure, which would then be protected in the berm's wake. Zakeri (2008) investigated several such configurations experimentally and concluded that this may be feasible in some cases. The berms need to be designed and dimensioned appropriately because they are exposed to substantial lift forces immediately before the arrival of the debris flow head, and to pressure and shear during the passage of the debris flow.

In densely-populated coastal areas with a significant tsunami risk (be it from earthquakes or submarine landslides), tsunami early-warning and alarm systems as well as continuous public awareness campaigns combined with tsunami shelters are necessary mitigation measures, but they are not sufficient. The most sensitive areas, such as nuclear power plants located at shorelines (e.g., Fukushima, Japan) need to be protected by sufficiently large wave breakers so that they can withstand the residual wave pressure without damage. The engineering knowledge for designing them is available, but the fundamental problem is that little is usually known about the stability of submarine slopes in seismically less active areas. Unexpected events like the 1929 tsunami generated by the Grand Banks earthquake and landslide do occur nevertheless and will inflict much more damage if they occur near densely-populated areas.

Table 1 Hazard/damage associated with some well documented submarine landslides or landslide hazards

Hazard/ Damage	Area/Event	References
Tsunami	Trondheimsfjord	Skaven-Haug 1955; L'Heureux 2009
	Storegga	Bondevik et al. 2005
	Lake Tahoe	Ichinose et al. 2000
	Nice 1979	Assier-Rzadkiewicz et al. 2000
	Grand Banks 1929	Heezen and Ewing 1952
	Lake Lucerne 1616	Schnellman et al. 2006
	Flores Island 1992	Yeh et al. 1993
Cable breaks	Martinique 1902	Pararas-Carayannis 2004
	Grand Banks 1929	Heezen and Ewing 1952; Piper et al. 1999
	Orkdalsfjord 1930	Edgers, L., 1981
Pipelines and sub-sea installations	Mississippi Delta	Bea and Aurora 1983
		Nodine et al. 2007
	Storegga	De Blasio et al. 2005
Platforms	Mad Dog, GOM	Jeanjean et al. 2003
	Atlantis, GOM	Jeanjean et al. 2003
Retrogression	Storegga	Kvalstad et al. 2005; Gauer et al. 2005
	Finneidfjord 1996	L'Hereux et al. 2011
	Nice 1979	Dan et al. 2007
	Hinlopen-Yermak	Vanneste et al. 2006; 2011

Case Studies

A large number of case studies have been conducted for authorities, in academia and for the offshore industry. Most of these studies contain proprietary information and cannot serve for illustration. However, the results from some industry studies have been published at conferences and in journals, and several research projects have been conducted in recent years (Table 1).

Outlook: Research and Development Needs

Over the course of the last decades, significant progress has been made towards understanding different aspects of submarine slope failures, yet our present-day knowledge remains limited. Further research and development is needed considering the complexities and multiple disciplines involved. It is therefore necessary to adopt a geoscientific approach to the study of submarine landsliding by integrating geology, geophysics, geochemistry, soil mechanics/geotechnics and physics to cover the entire development sequence (pre-conditioning, triggers, and landslide development) as well as their consequences (run-up, impact).

A systematic effort is ongoing to survey the continental margins with high-resolution geophysical tools (in particular swath bathymetry and to a lesser extent high-resolution seismic profiling), which will give us a better understanding of the geomorphology, frequency and spatial distribution of submarine gravity mass flows. Improved technologies for imaging the sub-surface and obtaining both qualitative and quantitative (e.g., seismic inversion, rock physical models, etc.) information of the soil properties in high resolution will be beneficial for submarine landslide studies.

There is clearly a lack of other critical and complementary data, in particular long-term pore pressure measurements and geotechnical data on high-quality soil samples, preferentially from several locations within the target area. These data would help us to better understand and identify the precursory destabilizing phenomena and landslide triggering mechanisms. It is also worth noting that the role of free gas and gas hydrate dissociation in submarine slope failures should be further investigated, as the evidence so far is circumstantial. However, laboratory testing of samples containing gas or hydrate is far from trivial, particularly for clayey soils.

Our predictive capabilities concerning the run-out distance of submarine landslide are still rudimentary. In a precious few cases, a statistical approach correlating release volume and run-out ratio is applicable, but in most situations there are not enough events with similar properties to derive a statistical correlation. When using dynamical models instead, one faces large uncertainties due to the evolving material properties in the rapidly sheared zone of the flows. Intensive research – mostly in the laboratory – will be needed to arrive at a quantitative understanding of the role and evolution of various lubrication mechanisms.

Improved modelling of the landslide dynamics is also a key to improved tsunami modelling. In general, there is still much that can be done on numerical simulations of both the landslide dynamics (e.g. improved rheologies, retrogression, extension of models to two horizontal dimensions, and water entrainment) and the resulting tsunami generation, including turbulence, vortices, and two-way landslide/tsunami interaction.

Acknowledgments The authors thank Norsk Hydro/Statoil for releasing the Ormen Lange and Storegga Slide data. We are grateful to F. V. De Blasio, A. Elverhøi, K. Høeg, J. G. Marr, G. Parker, A. Solheim, J. M. Strout and A. Zakeri for stimulating discussions and enjoyable collaboration on submarine mass flows, pore pressure measurements and submarine slope failures in general. We kindly acknowledge R. Urgeles, J. Locat and P. Mazzanti for inviting NGI and ICG to write this keynote paper, and their patience while drafting it. Writing this paper was made possible by an internal grant from NGI's publications fund. This is paper no. 361 from the International Centre for Geohazards.

References

Assier-Rzadkiewicz S, Heinrich P, Sabatier PC, Savoye B, Bourillet JF (2000) Numerical modelling of a landslide-generated tsunami: the 1979 nice event. Pure Appl Geophys 157(19):1707–1727

Bardet J-P, Synolakis C, Davis H, Imamura F, Okal E (2003) Landslide tsunamis: recent findings and research directions. Pure Appl Geophys 160:1793–1809

Bea RG, Aurora R (1983) Design of pipelines in mudslide areas. J Petrol Technol 35(11):1985–1995

Bondevik S, Løvholt F, Harbitz CB, Mangerud J, Dawson A, Svendsen JI (2005) The Storegga slide tsunami – comparing field observations with numerical simulations. Mar Petrol Geol 22(1–2):195–208

Bryn P, Berg K, Forsberg CF, Solheim A, Kvalstad TJ (2005) Explaining the Storegga slide. Mar Petrol Geol 22(1–2):11–19

Canals M, Lastras G, Urgeles R, Casamor JL, Mienert J, Cattaneo A, De Batist M, Haflidason H, Imbo Y, Laberg JS, Locat J, Long D, Longva O, Masson DG, Sultan N, Trincardi F, Bryn P (2004) Slope failure dynamics and impacts from seafloor and shallow subseafloor geophysical data: case studies from the COSTA project. Mar Geol 213(1–4):9–72

Cassar C, Nicolas M, Pouliquen O (2005) Submarine granular flows down inclined planes. Phys Fluids 17:103301

Chaytor JD, ten Brink US, Solow AR, Andrews BD (2009) Size distribution of submarine landslides along the US Atlantic margin. Mar Geol 264:16–27

Dade WB, Huppert HE (1995) A box model for non-entraining, suspension-driven gravity surges on horizontal surfaces. Sedimentology 42:453–471

Dan G, Sultan N, Savoye B (2007) The 1979 Nice harbour catastrophe revisited: trigger mechanism inferred from geotechnical measurements and numerical modelling. Mar Geol 245:40–64

De Blasio FV, Issler D, Elverhøi A, Harbitz CB, Ilstad T, Bryn P, Lien R, Løvholt F (2003) Dynamics, velocity and run-out of the giant Storegga slide. In: Locat J, Mienert J (eds) Submarine mass movements and their consequences. Kluwer, Dordrecht/Boston/London, pp 223–230

De Blasio FV, Elverhøi A, Issler D, Harbitz CB, Bryn P, Lien R (2004) Flow models of natural debris flows originating from overconsolidated clay materials. Mar Geol 213(1–4):415–438

De Blasio F, Elverhøi A, Issler D, Harbitz CB, Bryn P, Lien R (2005) On the dynamics of subaqueous clay rich gravity mass flows – the giant Storegga slide, Norway. Mar Petrol Geol 22(1–2):179–186

Drago M (2002) A coupled debris flow–turbidity current model. Ocean Eng 29(14):1769–1780

Elverhøi A, De Blasio FV, Butt FA, Issler D, Harbitz CB, Engvik L, Solheim A, Marr J (2002) Submarine mass-wasting on glacially influenced continental slopes – processes and dynamics. In:

Dowdeswell JA, Cofaigh CÓ (eds) Glacier-influenced sedimentation on high-latitude continental margins. UK, London, pp 73–88

Elverhøi A, Issler D, De Blasio FV, Ilstad T, Harbitz CB, Gauer P (2005) Emerging insights on the dynamics of submarine debris flows. Nat Hazard Earth Syst Sci 5:633–648

Elverhøi A, Breien H, De Blasio FV, Harbitz CB, Pagliardi M (2010) Submarine landslides and the importance of the initial sediment composition for run-out length and final deposit. 70th anniversary of Prof. Gjevik BN. Ocean Dynamics Special Issue. DOI 10.1007/s10236-010-0317-z

Forsberg CF, Solheim A, Kvalstad TJ, Vaidya R, Mohanty S (2007) Slope instability and mass transport deposits on the Godavari river delta, east Indian margin, from a regional geological perspective. In: Lykousis V, Sakellariou D, Locat J (eds.) Proceedings 3rd international symposium on submarine mass movements and their consequences, Santorini, Greece. Springer, Dordrecht, The Netherlands, pp 19–28

Gauer P, Elverhøi A, Issler D, De Blasio FV (2006) On numerical simulations of subaqueous slides: backcalculations of laboratory experiments of clay-rich slides. Norw J Geol 86:295–300

Gauer P, Kvalstad TJ, Forsberg CF, Bryn P, Berg K (2005) The last phase of the Storegga slide: Simulation of retrogressive slide dynamics and comparison with slide-scar morphology. Mar Petrol Geol 22(1–2):171–178

Gisler G, Weaver R, Gittings ML (2006) SAGE calculations of the tsunami threat from La Palma. Sci Tsunami Hazard 24(4):288–300

Haflidason H, Sejrup HP, Nygard A, Mienert J, Bryn P, Lien R, Forsberg CF, Berg K, Masson D (2004) The Storegga Slide: architecture, geometry and slide development. Mar Geol 213:201–234

Harbitz CB (1992) Model simulations of tsunamis generated by the Storegga Slides. Mar Geol 105:1–21

Harbitz CB, Løvholt F, Pedersen G, Masson DG (2006) Mechanisms of tsunami generation by submarine landslides: a short review. Norw J Geol 86:249–258

Heezen BC, Ewing M (1952) Turbidity currents and submarine slumps, and the 1929 Grand Banks earthquake. Am J Sci 250:849–873

Ichinose GA, Anderson JG, Satake K, Schweickert RA, Lahren MM (2000) The potential hazard from tsunami and seiche waves generated by large earthquakes within Lake Tahoe, California-Nevada. Geophys Res Lett 27(8):1203–1206

Ilstad T, De Blasio FV, Elverhøi A, Harbitz CB, Engvik L, Longva O, Marr JG (2004) On the frontal dynamics and morphology of submarine debris flows. Mar Geol 213(1–4):481–497

Imran J, Harff P, Parker G (2001) A numerical model of submarine debris flows with graphical user interface. Comput Geosci 27(6):717–729

Issler D, De Blasio FV, Elverhøi A, Bryn P, Lien R (2005) Scaling behaviour of clay-rich submarine debris flows. Mar Petrol Geol 22(1–2):187–194

Jeanjean P, Hill A, Taylor S (2003) The challenges of siting facilities along the Sigsbee Escarpment in the southern Green Canyon area of the Gulf of Mexico; framework for integrated studies. In: Proceedings of the offshore technology conference 2003, Houston, Texas. OTC No. 15156

Jiang L, LeBlond PH (1992) The coupling of a submarine slide and the surface waves which it generates. J Geophys Res 97(C8): 12731–12744

Kajiura K (1963) The leading wave of a tsunami. Bull Earthqu Res Inst Tokyo Univ 41:535–571

Kvalstad TJ, Andresen L, Forsberg CF, Berg K, Bryn P, Wangen M (2005) The Storegga Slide: evaluation of triggering sources and slide mechanics. Mar Petrol Geol 22(1–2):245–256

L'Heureux J-S (2009) A multidisciplinary study of shoreline landslides: from geological development to geohazards assessment in the Bay of Trondheim, mid Norway. Ph.D. Thesis, Norwegian University of Science and Technology, Trondheim, Norway, p 158

L'Heureux J-S, Steiner A, Longva O, Chand S, Vanneste M, Kopf A, Haflidason H, Forsberg CF, Vardy ME (2011) Identification of weak layers and their role for the stability of slopes at Finneidfjord, northern Norway. In: Proceedings of the 5th international symposium on submarine mass movements and their consequences, Kyoto (Japan), 24–26 Oct 2011

Locat J (2001) Instabilities along ocean margins: a geomorphological and geotechnical perspective. Mar Petrol Geol 18(4):503–512

Løvholt F, Harbitz CB, Haugen KB (2005) A parametric study of tsunamis generated by submarine slides in the Ormen Lange/Storegga area off western Norway. Mar Petrol Geol 22:219–231

Løvholt F, Pedersen GK, Gisler G (2008) Oceanic propagation of a potential tsunami from the La Palma Island. J Geophys Res 113:C09026

Lynett PJ, Borrero JC, Liu PL-F, Synolakis CE (2003) Field survey and numerical simulations: a review of the 1998 Papua New Guinea tsunami. Pure Appl Geophys 160:2119–2146

Micallef A, Berndt C, Masson DG, Stow DAV (2008) Scale invariant characteristics of the Storegga slide and implications for large-scale submarine mass movements. Mar Geol 247:46–60

Mohrig D, Marr JG (2003) Constraining the efficiency of turbidity current generation from submarine debris flows and slides using laboratory experiments. Mar Petrol Geol 20:883–899

Mohrig D, Whipple KX, Hondzo M, Ellis C, Parker G (1998) Hydroplaning of subaqueous debris flows. Geol Soc Am Bull 110(3):387–394

Mosher D, Bigg S, LaPierre A (2006) 3D seismic versus multibeam sonar seafloor surface renderings for geohazard assessment: case examples from central Scotian Slope. The Leading Edge 2006:1484–1494

Necker F, Härtel C, Kleiser L, Meiburg E (2002) High-resolution simulations of particle-driven gravity currents. Int J Multiphase Flow 28(2):279–300

Nodine MC, Cheon JY, Wright SG, Gilbert RB (2007) Mudslides during hurricane Ivan and an assessment of potential for future mudslides in the Gulf of Mexico. Phase II Project report to MMS. MMS Project Number 552. Texas A&M University, OTRC Library No. 10/07C185

Okal EA, Synolakis CE (2003) Field survey and numerical simulations: a theoretical comparison of tsunamis from dislocations and landslides. Pure Appl Geophys 160:2177–2188

Okal EA, Synolakis CE (2004) Source discriminants for near-field tsunamis. Geophys J Int 158:899–912

Pararas-Carayannis G (2004) Volcanic tsunami generating source mechanisms in the Eastern Caribbean region. Sci Tsunami Hazard 22(2):74–114

Parker G, Fukushima Y, Pantin HM (1986) Self-accelerating turbidity currents. J Fluid Mech 171:145–181

Pedersen, G (2001) A note on tsunami generation by earthquakes. Preprint Series in Applied Mathematics 4, Department of Mathematics, University of Oslo, Norway

Piper DJW, Cochonat P, Morrison L (1999) The sequence of events around the epicentre of the 1929 Grand Banks earthquake – initiation of debris flows and turbidity currents inferred from side scan sonar. Sedimentology 46:79–97

Ruff LJ (2003) Some aspects of energy balance and tsunami generation by earthquakes and landslides. Pure Appl Geophys 160:2155–2176

Schnellman M, Anselmetti FS, Giardini D, McKenzie J (2006) 15,000 years of mass-movement history in Lake Lucerne: implications for seismic and tsunami hazards. Eclogae Geol Helv 99(3):409–428

Skaven-Haug S (1955) Undervannsskred i Trondheim havneområde [Submarine slides in the Trondheim harbour area, in Norwegian] Teknisk ukeblad, 1955(7): 133–144. (Also published in NGI Publication no. 7., 1955, Norwegian Geotechnical Institute, Norway)

Skogseth R (1999) Turbiditetsstraumar langs eit skrått plan [Turbidity currents along an inclined plane, in Norwegian]. MSc Thesis, Geophysical Institute, University of Bergen, Bergen, Norway

Solheim A, Forsberg CF, Yang S, Kvalstad TJ, Vaidya RA, Mohanty S, Longva O, Rise L (2007) The role of geological setting and depositional history in offshore slope instability. Offshore Technology Conference 2006, Houston, Texas

Strout JM, Tjelta TI (2005) In situ pore pressures: what is their significance and how can they be reliably measured? Mar Petrol Geol 22(1–2):275–285

Tappin D, Watts P, Grilli ST (2008) The Papua New Guinea tsunami of 17 July 1998: anatomy of a catastrophic event. Nat Hazard Earth Syst Sci 8:243–266

Urgeles R, Leynaud D, Lastras G, Canals M, Mienert J (2006) Back-analysis and failure mechanisms of a large submarine slide on the Ebro slope, NW Mediterranean. Mar Geol 226(3–4):185–206

Vanneste M, Harbitz CB, De Blasio FV, Glimsdal S, Mienert J, Elverhøi A (2011) Hinlopen-Yermak landslide, Arctic Ocean – geomorphology, landslide dynamics, and tsunami simulations. In: Shipp RC, Weimer P, Posamentier H, Posamentier H (eds) Mass-transport deposits in deepwater settings, vol 96, Society of Sedimentary Geology, Special Publication. Tulsa, SEPM, pp 509–527

Vanneste M, L'Heureux J-S, Baeten N, Brendryen J, Vardy ME, Steiner A, Forsberg CF, Kvalstad TJ, Laberg JS, Chand S, Longva O, Rise L, Haflidason H, Hjelstuen BO, Forwick M, Morgan E, Lecomte I, Kopf A, Vorren TO, Reichel T (in press) Shallow landslides and their dynamics in coastal and deepwater environments, Norway. In: Proceedings of the 5th international symposium on submarine mass movements and their consequences. Kyoto, Japan, 24–26 Oct 2011

Vanneste M, Mienert J, Bünz S (2006) The Hinlopen Slide: a giant, submarine slope failure on the northern Svalbard margin, Arctic Ocean. Earth Planet Sc Lett 245(1–2):373–388

Yeh H, Imamura F, Synolakis C, Tsuji Y, Liu P, Shi S (1993) The Flores Island Tsunami. Eos, Transactions, American Geophysical Union 74(33):369–373

Zakeri A (2008) Submarine debris flow impact on pipelines. Ph.D thesis, Faculty of Mathematics and Natural Sciences, University of Oslo, Oslo, Norway. ISSN 1501–7710

Zakeri A, Chi K, Hawlader B (2011) Centrifuge modelling of glide block and out-runner block impact on submarine pipelines. In: Proceedings of the offshore technology conference 2010, Houston, Texas. OTC paper 21256

THE SECOND
WORLD
LANDSLIDE FORUM

Model Test of Submarine Landslide Impact Forces Acting on Cables

Fawu Wang, Tomokazu Sonoyama, and Mitsuki Honda

Abstract

Submarine landslides frequently damage communication cables and gas pipelines on the ocean floor, resulting in economic losses and social problems. To study the impact of submarine landslide motion on a pipeline or submarine cable, a rotatory apparatus was developed to simulate the interactions between the submarine landslide and cable. Soil and water can be put in the apparatus and a model cable is fixed in the rotatory part, so the relative motion of the landslide and cable can be measured and evaluated. In addition, shear stress gauges, a pore pressure transducer, and a normal stress sensor were installed at the bottom of the apparatus to monitor the stress change during the model slide motion. In this paper, test results of landslide impact force on the cable model are presented to demonstrate the influences of landslide motion velocity, soil type, and cable diameter on the impact forces.

Keywords

Submarine landslides • Cable • Impact force • Velocity • Soil type • Cable diameter

Introduction

Communication cables cross the oceans between continents all over the world. These cables may be damaged due to the occurrence and motion of submarine landslides, causing interruption of data transmission, and even of international communications. The economic loss is vast when cables are cut, due to the cost of cable restoration and the loss of information transmission. For instance, many communication cables were cut in the sea south of Taiwan after an earthquake in December 2006. Based on the broken time records of the cables, it was concluded that a landslide was triggered by the earthquake, and the cables were cut by landslide motion from near the coast toward deeper water (Hsu 2008). According to a report by ICPC (2009) there were 2162 cable breaks globally between 1960 and 2006. Of these at least 20 % were directly influenced by submarine landslides or turbidity currents.

Submarine landslides were initially studied for the needs of resource development in the ocean (Shanmugam 2000). For the purposes of clarifying the mechanisms of geohazards such as tsunami, many investigations and exploration have been conducted in the ocean of North Europe, especially of Norway, and of United States. Geophysical approaches have mainly been employed during field investigations, and the topographic features of the oceans have gradually been clarified. It has been found that common features of submarine landslides are that: (1) the motion influences large areas; (2) the motion can continue even at very gentle slopes, as low as 0.1° (Kokusho and Takahashi 2008). Mohrig et al. (1998) conducted model tests in the laboratory and confirmed that the mechanism of submarine landslides involves a hydroplanning phenomenon, i.e., a water layer is formed at the base of the submarine landslide during its motion. The hydroplanning phenomenon can

---

F. Wang (✉)
Department of Geoscience, Matsue, Shimane University, Nishikawatsu 1060, Shimane 690-8504, Japan
e-mail: wangfw@riko.shimane-u.ac.jp

T. Sonoyama • M. Honda
Graduate School of Geoscience, Shimane University, Matsue, Japan

C. Margottini et al. (eds.), *Landslide Science and Practice*, Vol. 5,
DOI 10.1007/978-3-642-31427-8_2,

result in low shear resistance of the submarine landslide, so that it can move for long distance even at a gentle slope.

Many features of submarine landslides and the damage they cause to communication cables are unclear, because these events occur beneath the sea's surface. Direct observation of submarine landslides would be extremely expensive, and their unpredictability makes it difficult or near-impossible. Our interest in submarine landslides lies in disaster mitigation of communication cables. In our study, we seek to understand: (1) the motion mechanism of the submarine landslide, and (2) the mechanism of submarine landslide damage on communication cables. For these purposes, an apparatus to simulate the relative motion of a submarine landslide and a communication cable was developed in laboratory, and a series experiments was conducted. Although it is difficult to simulate the flow conditions which occur in deep water, we hope the test results provide some hints for communication cable design and cable positioning in the ocean.

Submarine Landslides Apparatus

The apparatus has the shape of a car-wheel, with an axle in the centre, and a trough on its inner circumference (Fig. 1). The axle is connected to a motor so the apparatus can rotate in the vertical plane. Soil and water that are used to simulate the submarine landslide are placed in the trough. Under the action of gravity, water and soil always stay in the lower part of the apparatus. When the frame of the apparatus is rotated, the water and soil mix, and motion relative to the frame bottom occurs in a similar way to a submarine landslide or gravity flow. In this paper, we use the term "landslide" to refer to mass motion, and use the term "gravity flow" to refer to the motion of a flowing mixture, through observation.

Figure 2 is a sketch showing water and soil in the apparatus and the sensor settings. The height of the apparatus is 1.9 m, while the diameter and thickness of the rotatory part are 1.8 m and 0.4 m respectively. The maximum height of water and soil in the apparatus (lower part) is 0.3 m. Three types of sensors were set at the bottom center of the rotatory frame. These are: (1) shear stress sensors to measure the shear resistance at the bottom of the landslide model. Six main sensors were set at equal distance intervals, and three additional sensors were added in one interval; (2) Normal stress sensor. This is used to measure the normal stress generated by water and soil when the sensor comes to the lowest point; (3) Pore water pressure transducer. This is used to measure the maximum water pressure when the sensor reaches the lowest point. In point A of Fig. 2, the normal stress sensor, pore water pressure transducer, and one of the six main shear stress sensors are located along one line parallel to the axle, so that the three sensors can reach the

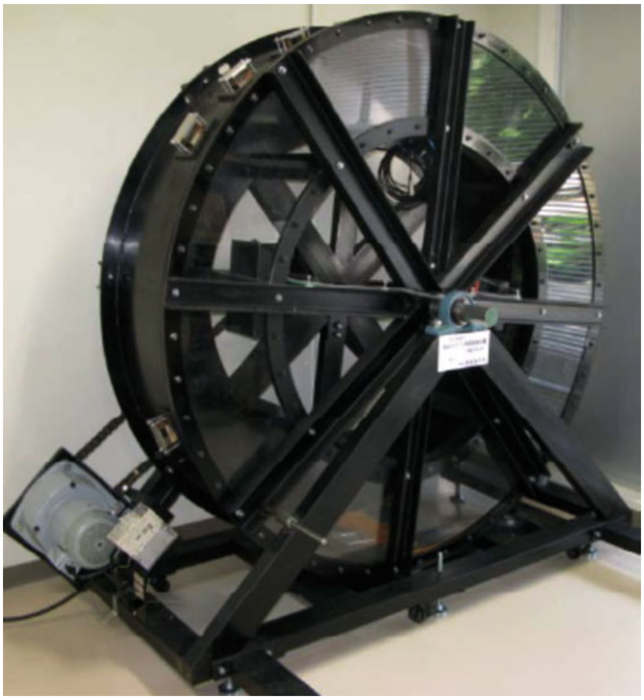

Fig. 1 Photo of the apparatus to simulate a submarine landslide and damage of a communication cable

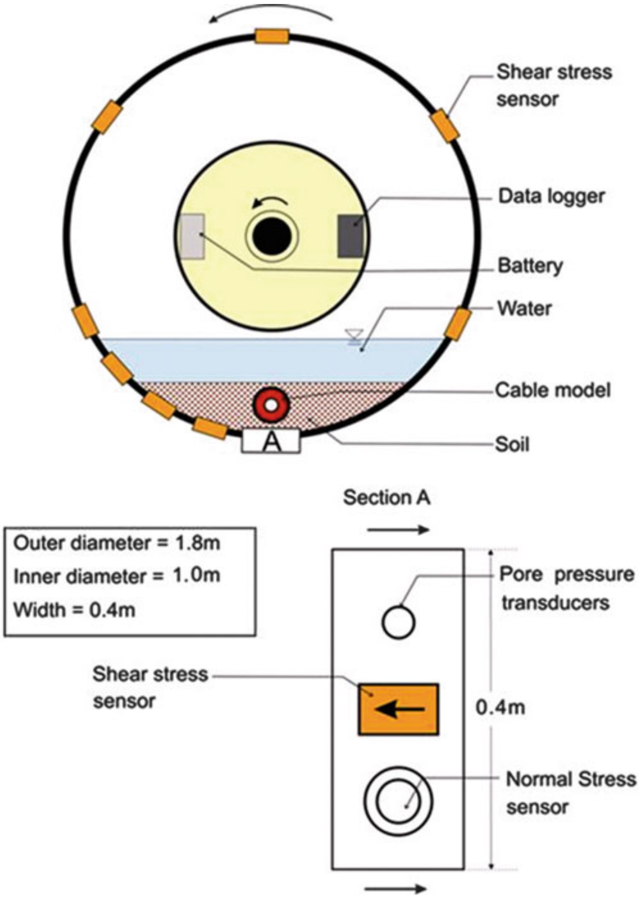

Fig. 2 Sketch showing water and soil in the apparatus and sensor setting

lowest point at the same time. Using the pore water pressure data, it is easy to find the lowest point. Using the data at the lowest point, the apparent friction coefficient during apparatus rotation can be obtained from dividing the shear resistance by normal stress. This parameter can be used to evaluate the mobility of the model landslide.

A model cable is set above point A to measure the force of impact by the mixture of water and soil. The comparison between the impact force and landslide mobility can be conducted because the cable and the set of sensors are located at the vertical line when point A comes to the lowest point. The height and diameter (size) of the cable can be changed for different tests.

Rotation speed of the rotatable part is controlled by a motor. The speed at the bottom of the rotatable part ranges from 0.013 and 0.78 m/s. A data logger and battery were fixed in the axial part of the apparatus, so that data collection is carried out in an independent unit.

The main purpose of the apparatus is to simulate the movement of a landside relative to the ocean bottom and the communication cable. In actual cases, the ocean bottom is fixed and the landslide moves. In our apparatus, the landslide body is kept in the lower part while the frame is rotated. For communication cables in actual cases, the length is always hundreds of thousands of km, and axial deformation along the cable is not permitted. In the model test, the two ends of the model cable are fixed, and the impact force from moving water and soil can be measured.

Properties of the Soil Sample Used in the Test

Silica sand no.7 and no.8 were used in this test. Silica sand is construction material for industrial use. It is made of weathered silica sand, and has a uniform grain size distribution. Grain shapes are almost all angular. It consists of 92–98 % quartz, and a small amount of feldspar. Table 1 shows the properties of the two samples.

Cable Model Used to Measure the Impact Force

Cables with different diameters are used in practice. Diameters range from 17 to 55 mm. Thick cables are used in shallow waters near coastlines to prevent damage from fish and human activity, whereas thinner cables are used in deeper waters. Most landslides occur in the deep ocean, and hence thin cables are generally those cut by such events. For example, the submarine landslides and turbidity currents that cut cables in the 2006 Taiwan earthquake were mostly generated at a depth of 2,500 m or less (Hsu 2008). In our tests, vinyl chloride cables 22 mm and 25 mm in diameter were used as models. These diameters are near those of cables used in the deep sea, and are almost the same as those cut in the Taiwan 2006 case.

Table 1 Properties of the tests soil samples

Properties	Silica sand no.7	Silica sand no.8
Specific gravity	2.64	2.64
Maximum void ratio	1.30	1.594
Minimum void ratio	0.71	0.778
Mean grain size (mm)	0.16	0.045
Effective grain size D10 (mm)	0.09	0.018
Uniformity Coefficient (Uc)	2.1	3.17

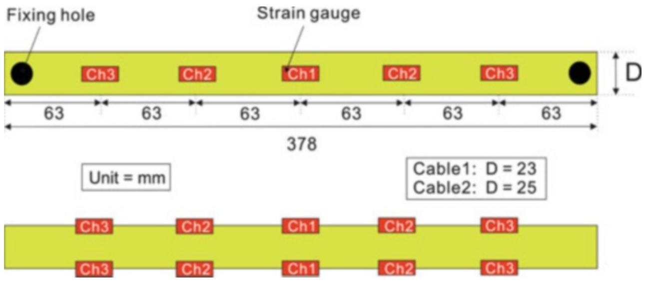

Fig. 3 Strain gauge installed cable model

The length of the model cable is 0.378 m. Two screw holes were made at both ends to fix the cable to the frame of the apparatus. To measure the impact force, strain gauges were pasted onto the model cable as shown in Fig. 3. Five strain gauges were located at equal intervals on the front and back sides of the model cable, forming three channels (ch). There were two gauges in ch1, four gauges in ch2, and four gauges in ch3, respectively. When bending caused by the impact force of the landslide model is generated in the cable, the strain gauges can measure the bending deformation. Through calibration with known load, the impact force can then be obtained.

Figure 4 shows the measurements of ch1 when the cable model was hit by the landslide model. The impact force generated on the cable increased to the maximum value when it entered the landslide, and then decreased as it exited the landslide. The peak value of the distributed load was defined as the impact force. In Fig. 4, it can be seen that the landslide entry and exit points do not have the same value. This result is caused by bending due to the deadweight of the cable itself. To eliminate the effect caused by deadweight, a line is drawn to connect the entry and exit points, and the impact force is obtained by measuring the difference between the peak value and the tie line between these points. Considering in the actual case, only sediments move on the seafloor, and sea-water keeps stable related to the seafloor, it is necessary to obtain the impacted force caused by the sediment motion only. For this purpose, the impact forces caused by water were obtained by the water-only-test at different rotating velocity with different cables. Through subtracting the impacted force caused by water only from

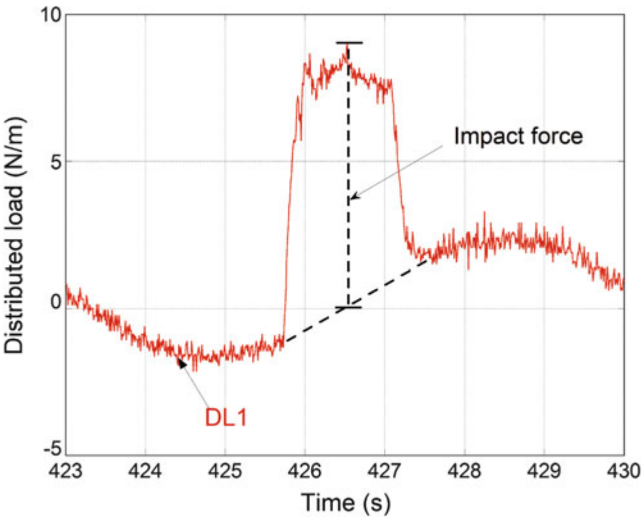

Fig. 4 The method to obtain impact force from the measured data

the measured impact force caused by the mixture of sediments and water, the impacted force caused by sediments only was obtained.

Test Results with the Cable Model

In this study, four types of tests were carried out to investigate the effect of landslide motion velocity, landslide volume, soil type of the landslide, and diameter of the cable. The details are listed below.

1. Tests were conducted at five different constant velocities, i.e., 0.26, 0.39, 0.52, 0.65, 0.78 m/s;
2. Tests were conducted at eight different constant masses, i.e., dry mass quantities of 10, 20, 30, 40, 50, 60, 70, 80 kg, respectively;
3. Two types of soils (silica sand No.7 and no.8) were used in different tests to observe the effect of soil type;
4. Two types of cable model with diameters of 0.022 m (i.e., cable-1) and 0.025 m (cable-2) were used to evaluate the effect of cable thickness.

In these tests, the cable model was set at a height of 0.08 m above the bottom of the rotatory part (point A in Fig. 2). The maximum depth of the water and soil mix was held at 0.23 m for all tests. To obtain the impact force due to water, water-only-tests were conducted at first, and the results for cable-1 and cable-2 are shown in Fig. 5.

In the true tests, dry soil of the designated mass was placed in the rotatable trough, and water was then added until the water table reached 0.23 m in height.

Test with Different Mass in Different Velocity

As an example, the results of one test are shown in Fig. 6. The soil used in the test was silica sand no.7, and the mass was 40 kg. Rotation velocity was 0.26 m/s. The peak normal stress was 3.2 kPa, and peak pore water pressure was 2.1 kPa. The peak effective stress can be calculated as 1.1 kPa. With a time lag to the peak normal stress and pore water pressure, the peak impact force was determined to be 29.6 N/m. During the test, we observed that the landslide moved as a mass, as the rotation velocity was low.

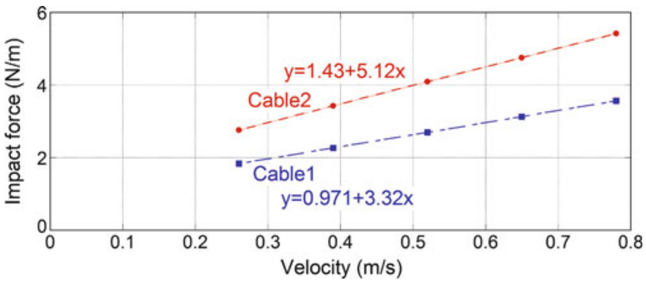

Fig. 5 Impact force due to water for cable-1 and cable-2 at different rotation velocity

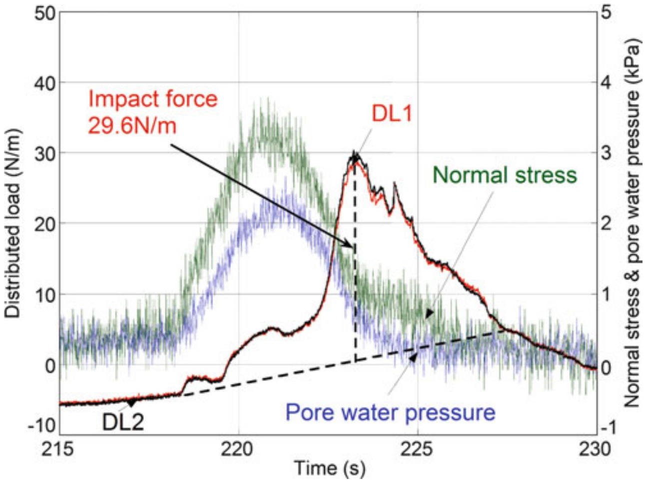

Fig. 6 Test results with silica sand no.7 (40 kg) rotated at a velocity of 0.26 m/s

Figure 7 shows the results when the rotation velocity was increased to 0.78 m/s and kept constant. Compared with the results in Fig. 6, the impact force clearly became smaller, and reached a value of 6.27 N/m. During this test, we observed that the soil and water were well mixed, and a flow formed. We describe the mixture for the test shown in Fig. 6 as a landslide, and that in Fig. 7 as a gravity flow. When the landslide mass transforms to a gravity flow, impact force is decreased considerably.

Figure 8 shows another test in which the soil mass of silica sand no.7 was increased to 60 kg, while the rotation velocity was held at 0.78 m/s. The impact force in this test increased to 11.90 N/m, showing the effect of soil mass. When the soil mass used in the tests increases, the impact force increased.

Figure 9 summarizes the test results with silica sand no.7, with masses ranging from 10 to 80 kg. Impact force was

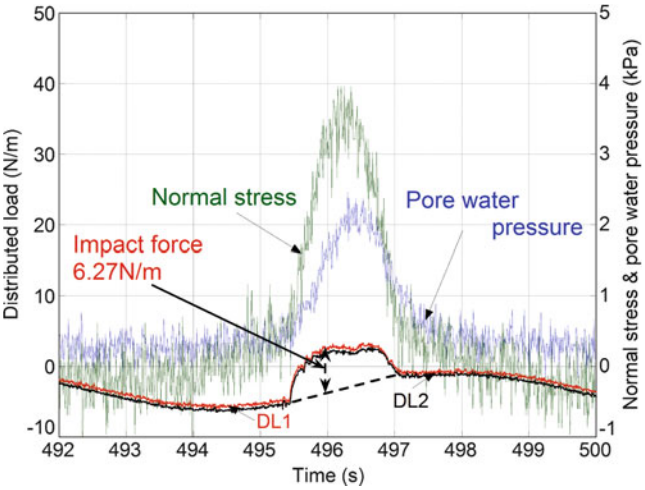

Fig. 7 Test results with silica sand no.7 (40 kg) rotated at a velocity of 0.78 m/s

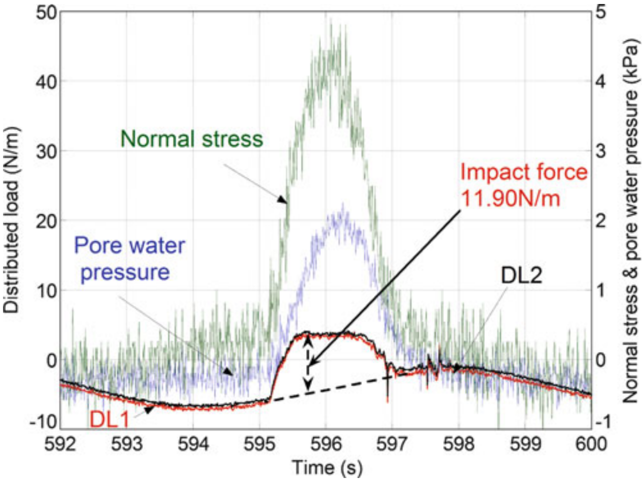

Fig. 8 Test results with silica sand no.7 (60 kg) rotated at a velocity of 0.78 m/s

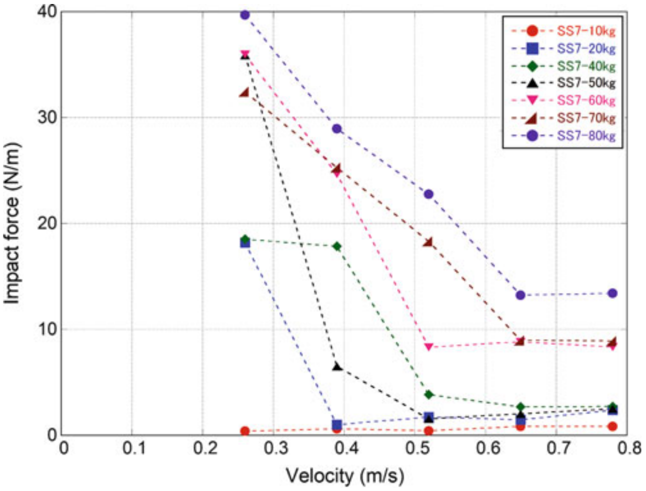

Fig. 9 The relationship between impact force and rotation velocity when using silica sand no.7 with differing masses and rotation velocities

measured for various soil masses at rotation velocities changing from 0.26 to 0.78 m/s in five steps. From this figure, it is evident that,

1. With small soil masses (such as 10 kg), the impact force is proportional to the rotation velocity;
2. With larger mass of soil, there is a turning point in the impact force curve with respect to the rotation velocity. When the rotation velocity is smaller than that at the turning point, the impact force has a negative relationship with the velocity, whereas after the turning point, the impact force increases gradually with the rotation velocity. As observed in the tests, before the turning point, the mixture of soil and water acted as a mass, whereas after the turning point it behaved as flow. From Fig. 9, it can be concluded that the mixture of water and soil changes its behaviour from landslide to gravity flow. Although the behaviour as a mass may be caused by the limited dimension of the apparatus, the results can also be used to estimate the impact force change when a landslide occurs in an actual case, i.e., the impact force is larger at the stage of landslide initiation, and then gradually decreases to lower levels when the mixture becomes a rapidly-moving gravity flow.
3. Larger masses have higher impact force.
4. The velocity at the turning point is higher for larger masses.

Test with Different Soils

The two soils used showed different tendencies. Figure 10 shows one test result, using silica sand no.8 (40 kg) as an example. At the lowest velocity of 0.26 m/s, an impact force of 6.07 N/m was obtained. This impact force is considerable smaller than that obtained from the equivalent test with silica sand no.7.

In Fig. 11, impact forces obtained from tests with silica no.7 and no.8 are plotted together for comparison. It shows that: (1) the impact forces obtained from silica no.8 are generally smaller than those of silica sand no.7; (2) Silica sand no.8 did not behave as a mass, with tests behaving as flows which had lower impact force.

Test with Cable Models with Different Diameters

Figure 12 shows test results using cable models with different diameters. Cables with diameters of 0.022 m and 0.025 m are referred to as Cable-1 and Cable-2, respectively. The mass quality used in the test is also shown in the legend.

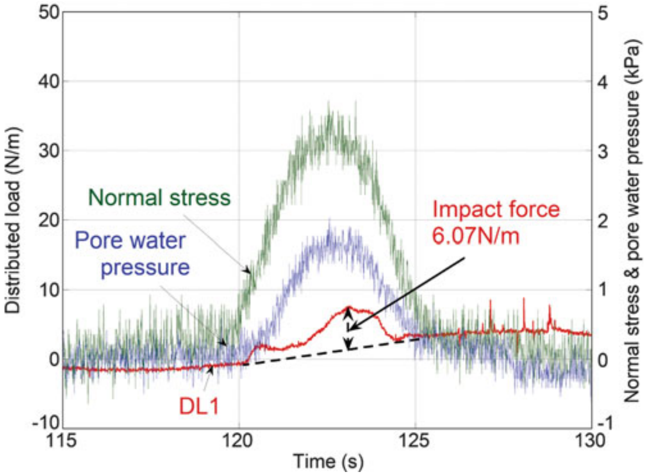

Fig. 10 Test results with silica sand no.8 (40 kg) rotated at a velocity of 0.26 m/s

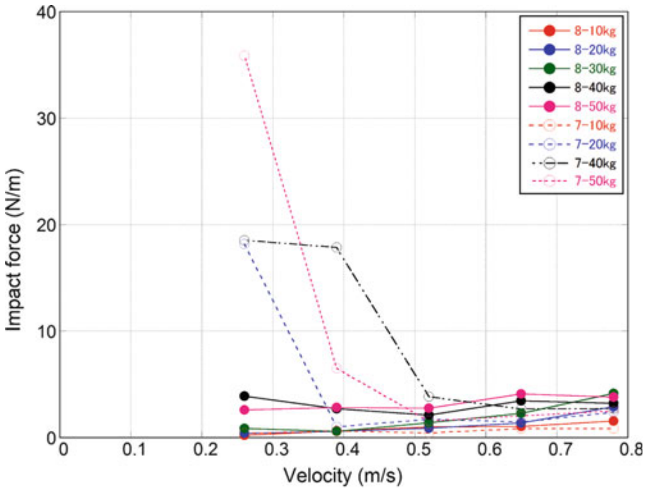

Fig. 11 Test result comparison between silica sand no.7 and no.8

Obviously, the larger diameter cable is subjected to larger impact force. Although the different in diameter is as small as 3 mm (about 14 % of the cable diameter), the impact forces in Cable-2 are almost 1.5 times to cable01 averagely (Fig. 13).

The Situation of the Mixture of Water and Soil in the Tests

It is very interesting to know the situation of the mixture of water and soil during rotation at different velocity, because the impact force changed with the rotation velocity in a non-linear way. As an example, Fig. 14 shows a set of tests when the rotation velocities were changed from 0.26 to 0.78 m/s. Silica sand no.7 (50 kg) was used in this set of tests.

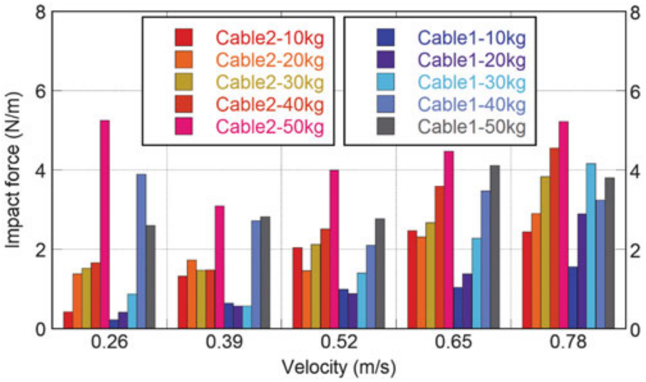

Fig. 12 Test result comparison by using Cable-1 (0.023 m diameter) and Cable-2 (0.025 m diameter)

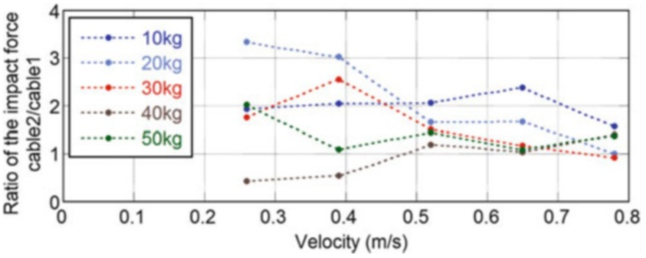

Fig. 13 Ratio of the impact force on cable-2 to cable-1

As can be seen from the front side of the apparatus, the mixture of the soil and water is divided to two layers, i.e., muddy water in the upper layer, and landslide mass or gravity flow in the lower layer. The height (indicator of the volume) of the lower layer increased with rotation velocity. Because the density of the mixture will change with the volume (height in this case), it can be estimated that the density of the lower layer became lower as the velocity increased. The decreased density in the flow compared with the landslide may be the reason for the decreased impact force on the cables, even when the velocity is much higher.

Conclusions and Future Work

Our preliminary test results have been presented in this paper. Although the dimension of the test apparatus are minute compared to actual submarine landslides and it is difficult to obtain quantitative results from these experiments, some qualitative tendencies related to the impact on cables from submarine landslides were obtained. Conclusions from the model tests and work planned for the next stage of research are given below.

1. At the same velocity, impact force increased with increased soil volume. In next stage, the height of the

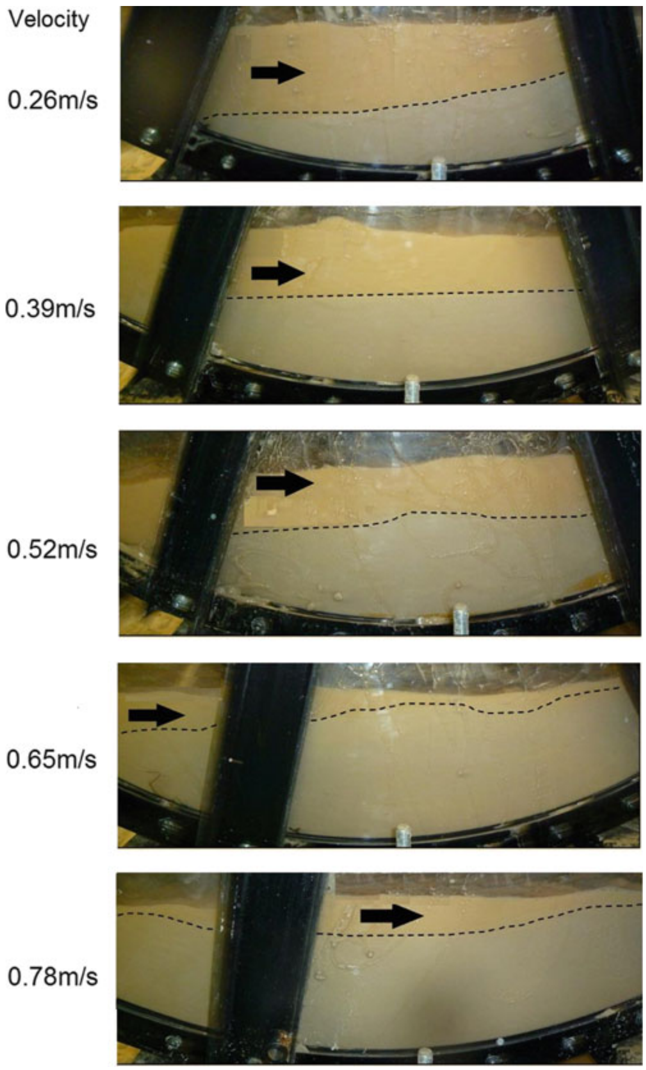

Fig. 14 Appearance of soil and water during experiment (photograph)

two layers (muddy water in the upper layer, and landslide mass or turbidity flow in the lower layer) should be measured. Method of measuring the degree of turbidity or density, method to evaluate Reynolds number and Froude number must be developed.

2. Larger cables are subjected to larger impact forces. When the diameter of the cable increased by 14 %, the impact force became to 1.5 times. Tests with much different diameter cables should be conducted to clarify the relationship between cable diameter and impact force.
3. The sliding body shows different behavior depending on the velocity. When the velocity was small, it behaved as a sliding mass, and when the velocity was high, it became a turbidity flow. The tests show that the velocity at the turning point depends on the quality of the soil mass. What factors determine the critical velocity at the turning point should be clarified in the next stage.
4. Samples with silica sand no.8 became a gravity flow at lower velocity than that of silica sand no.7. This may be due to higher buoyancy potential for finer grain size than for coarser grains.

Acknowledgments This study was conducted with the financial support by Japanese scientific research grant (No. 20310109). The authors are indebted to Associate Prof. B. Roser of Shimane University who reviewed the paper.

References

Hsu SK (2008) Turbidity currents, submarine landslides and the 2006 pingtung earthquake off SW Taiwan. Terr Atmos Ocean Sci 19(6):767–772

ICPC (2009) Submarine cables and the oceans: connecting the world. The ACM International Collegiate Programming Contest 11–25:29–53

Kokusho T, Takahashi T (2008) Earthquake-induced submarine landslides in view of void redistribution. In: Liu HL, Deng A, Chu J (eds) Geotechnical engineering for disaster mitigation and rehabilitation, Nanjing, 2008. Part 3, 177–188

Mohrig D, Whipple KX, Hondzo M, Ellis C, Parker G (1998) Hydroplaning of subaqueous debris flows. Geol Soc Am Bull 110: 387–394

Shanmugam G (2000) 50 Years of the turbidite paradigm (1950s–1990s): deep-water processes and facies models-a critical perspective. Mar Pet Geol 17:285–342

THE SECOND
WORLD
LANDSLIDE FORUM

Güímar and La Orotava Mega-Landslides (Tenerife) and Tsunamis Deposits in Canary Islands

Mercedes Ferrer, Luis González de Vallejo, Julia Seisdedos, Juan J. Coello,
J. Carlos García, Luis E. Hernández, Ramón Casillas, Candelaria Martín,
Jose A. Rodríguez, José Madeira, César Andrade, M. Conceição Freitas,
Alejandro Lomoschitz, Jorge Yepes, Joaquín Meco,
and J. Francisco Betancort

Abstract

More than 20 mega-landslides have been described in the Canary Islands affecting the flanks of the volcanic edifices. Güímar and La Orotava landslides, in Tenerife, are two exceptional cases due to their huge dimensions and outstanding geomorphological features. The estimated volume of these landslides exceed tens of cubic km. Tsunami deposits have been also identified in some of the islands of the archipelago probably associated to the large landslides of the islands flanks.

An investigation has been carried out to explain the causes of these large instability processes and their failure mechanisms. One of the main aspects investigated was the geomechanical characteristics of the volcanic rock masses, specially the hyaloclastite rocks forming the substratum underlying the emerged volcanic building. The low strength and high deformability properties of these rocks have played a fundamental role on the stability of the island flanks. The results have shown the gravitational origin of these instability processes as the main failure mechanism. Volcanic eruptions or large earthquakes could be contributing factors to the instability, but according with the data obtained in Guimar and La Orotava cases they are not necessary as triggering factors.

M. Ferrer (✉) • J.C. García
Geological Survey of Spain, Ríos Rosas 23, 28003 Madrid, Spain
e-mail: m.ferrer@igme.es

L.G. de Vallejo
Complutense University of Madrid, Madrid, Spain

J. Seisdedos
Prospección y Geotecnia, S.L. (PyG), Madrid, Spain

J.J. Coello
Consejo Insular de Tenerife, Calle Leoncio Rguez., 7 - 38003 S/C de Tenerife, Spain

L.E. Hernández
Government of the Canary Islands

R. Casillas • C. Martín • J.A. Rodríguez
University of La Laguna, Tenerife, Spain

J. Madeira • C. Andrade • M.C. Freitas
University of Lisbon, Lisbon, Portugal

A. Lomoschitz • J. Yepes • J. Meco • J.F. Betancort
University of Las Palmas de Gran Canaria, Las Palmas (The Canary Island), E-35017 Las Palmas, Spain

C. Margottini et al. (eds.), *Landslide Science and Practice*, Vol. 5,
DOI 10.1007/978-3-642-31427-8_3, © Springer-Verlag Berlin Heidelberg 2013

As a result of the field work carried out in the frame of the project, three large tsunami deposits have been identified in the islands of Lanzarote, Tenerife and Gran Canaria attributed to mega-landslides, possibly related to Guimar and La Orotava. A summary of their main features is described.

Keywords
Volcanic landslides • Tsunami deposits • Canary Islands • Tenerife

Introduction

The landslides affecting the flanks of volcanic islands are some of the largest in the world. Güímar and La Orotava valleys, in Tenerife, were formed by gigantic landslides some hundreds thousand years ago (1 and 0.6 Ma respectively). The main arguments that support this are listed below:

- The existence of landslide deposits observed inside the galleries excavated in the island.
- The identification of large volumes of landslide deposits (debris avalanches) on the ocean floor facing the valleys (Masson et al. 2002; Acosta et al. 2003).
- The similarity of morphological features with other oceanic islands in the world also affected by large flank failures.

The presence of large masses of rocks and debris avalanche deposits lying on the sea bed surrounding the island of Tenerife has been the main evidence of these large landslides. According to Acosta et al. (2003) La Orotava submarine debris avalanche deposits cover an area of 2,200 km^2 reaching as far as 75 km from the coast, and the submarine deposits from Güímar landslide occupy an area of 2,600 km^2 reaching a distance of 85 km from the coast. The volume of these debris avalanches in the ocean floor has been estimated around 120 km^3 in the case of Güímar landslide and less than 500 km^3 in La Orotava (Masson et al. 2002). In contrast the volume of these landslides deduced from the valleys sizes is much lower, and they are in the range of 30–60 km^3.

Morphological Features of Güímar and La Orotava Valleys

Güímar and La Orotava valleys are trough-shaped depressions 10–12 km wide inclined towards the sea. They present opposite orientations, ESE and NNW respectively. Their heads, partially overlapping, are located in the *Cordillera Dorsal*, a mountain chain that forms the main rift zone in the island with NE direction and maximum heights reaching between 1,700 and 2,200 m (Fig. 1).

The morphological characteristics of the valleys are singular, outstanding the symmetry and the important height of the lateral scarps (more than 500 m in some areas; Fig. 2), cut in pre-landslide volcanic materials with slope angles higher than 35°. The depressions formed by the landslides were filled with post-landslide volcanic materials, mainly lava flows coming from new volcanoes in the upper part of the valleys, with slope angles lower than 15° today.

The estimated volume of the landslide rocks from the volcanic flanks, calculated roughly from the depressions created by the rockslides, is in the order of 70–100 km^3 each.

In the submarine extension of the valleys, characteristic landslide forms have been mapped, highlighting large fan deposits with hummocky morphology.

Also in the subaerial part of the flank deposits attributed to landslides, now buried hundreds of meters deep at the bottom of the valleys are preserved; they can be seen inside the galleries excavated in the island, and consist of a sandy clay matrix with blocks of various sizes and varying composition.

The age of Güímar rockslide has been estimated approximately 1 Ma (Ferrer et al. 2008). The age of La Orotava rockslide has been estimated between 0.54 and 0.69 Ma (Cantagrel et al. 1999).

Geological and Geomechanical Conditions of the Pre-Landslide Volcanic Edifice

The materials involved in the instability processes are those which form the flanks of the volcanic edifice today in the areas not affected by landslides. They outcrop in the head and lateral scarps left by the landslides and in deep gullies carved by erosion in the pre-landslide materials. They can also be observed in the galleries excavated through the flanks of the volcanic edifice.

Geological and Geomechanical Model

One of the main aims of this investigation has been the “reconstruction” of the pre-landslide edifice, as well as to

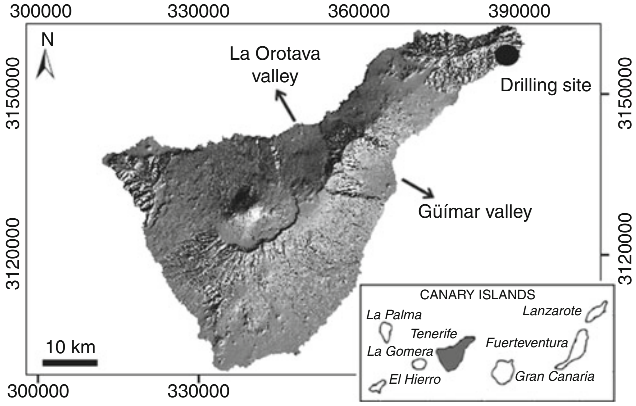

Fig. 1 Location of Güímar and La Orotava valleys and drilling site location, Tenerife (Canary Islands)

Fig. 2 View of La Orotava valley, 12 km wide, bordered by 500 m high lateral scarps. In the background El Teide volcano (3,718 m)

assign representative geomechanical properties to the different types of materials that form it. Thus, the simplified geological, geomorphological and geomechanical representative models of the pre-landslide edifice have been proposed.

The geometrical model previous to the occurrence of Güímar and La Orotava rockslides has been assessed considering paleo-morphological data obtained from the slopes and lateral scarps of the volcanic edifice not affected by landsliding processes. The morphological features of the submarine slopes have been obtained from bathymetric data analysis.

It has been assumed that the ground water conditions for the pre-failure edifice could be similar to those encountered before intensive ground water exploitation of the island aquifers had taken place. A water table at 600–700 m below surface was estimated according with ground water records. In the central part of the edifice due to the presence of a large number of dykes the ground water levels should be higher.

Geological and geotechnical data were recorded from field survey and from the extensive network of small diameter tunnels (galleries), with a total length over of 4,000 km, excavated in the subaerial island flanks for ground water supply purposes. Geotechnical properties of the volcanic materials of the emerged edifice have been also obtained from engineering geological surveys (González de Vallejo et al. 2008; Seisdedos 2008).

With respect to the geological and geomechanical data of the submarine edifice, only morphological and tectonic data are available from oceanographic surveys. In the eastern corner of the island site investigations have been carried out where submarine rocks outcrops (Fig. 1). Three boreholes have been drilled in hyaloclastites reaching one of them at 200 m depth.

Hyaloclastites and basaltic lavas have been the rock materials drilled in the three boreholes, although hyaloclastite has been the predominant lithology. In situ tests (pressuremeters) and laboratory tests have been carried out on the samples from the boreholes for the physical and mechanical characterization of the submarine materials.

The simplified geological model for the pre-failure edifice is shown in Fig. 3. The materials were grouped in those corresponding to the emerged edifice (above sea level) and the submarine edifice (below sea level). The lithological units or groups distinguished as representative for geomechanical purposes in the simplified geological model of the flanks of the island of Tenerife are described below.

Emerged Edifice Materials

On the emerged edifice the materials which form the island flanks have been distinguished from those that form the structural axis, which is the main growth area of the island. This zone is characterised by a dense network of dikes, associated with intense fracturing and alteration. There is a significant presence of pyroclasts and lava flows with scoria layers and dikes. The flanks are formed by rocks from the eruptive centres of the structural axis, mainly lava flows with scoria layers whose degree of alteration and compaction increase with depth. In the inner part of the flanks, close to the structural axis, dike intrusion is more intense. Depending on the number of dikes and the intrusion density observed in the galleries the following zones have been identified: very intense intrusion density, with more than 10 dikes per 100 m of gallery length; intense, 4–10 dikes per 100 m; low intensity, less than 4 dikes per 100 m. Some strength rock properties and alteration characteristics of the rock masses have been influenced by the hydrological processes therefore the water table depth has been considered to assess different grades of alteration.

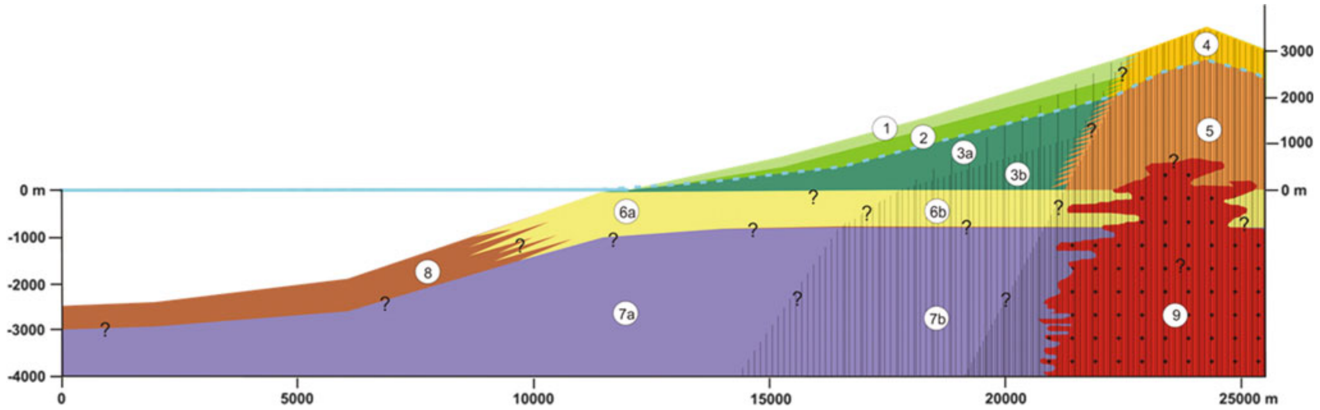

Fig. 3 Geological model representative of the pre-landslide volcanic edifice of Güímar and La Orotava landslides (*dashed blue line*: *water level*; *question marks*: uncertainties)

The lithological units, or lithological groups, that form the island flanks and the structural axis of the pre-rockslide edifice are shown in Fig. 3 and their main characteristics are:

- Unit 1: Recent lava flows with scoria layers, with a low degree of alteration, layers of loose scoria and cavities.
- Unit 2: Slightly altered lava flows with scoria layers; lower presence of cavities than Unit 1.
- Unit 3: Altered lava flows and highly compacted pyroclastic layers with intense dike intrusion. Depending on the dike intrusion density two sub-units have been differentiated (3a and 3b).
- Unit 4: Pyroclasts and lava flows with scoria, and intense dike intrusion; low degree of alteration, high grade of compaction and intense dike intrusion.
- Unit 5: Pyroclasts and altered lava flows, with very intense dike intrusion. These materials are highly compacted and fractured.

Submarine Edifice Materials

The materials which form the submerged part of the volcanic edifice represent the submarine growth phases of the island. Most of the information regarding the properties of these materials has been obtained from literature and from boreholes drilled in Tenerife island (see Fig. 1). Some of these lithological units have been subdivided depending on the dike intrusion density in the same way as in the emerged edifice. Their main characteristics are described below (see Fig. 3):

- Unit 6: Hyaloclatite rocks including the materials from subaerial flows which flow into the sea forming ‘deltas’, as well as from submarine eruptions. The thickness of this unit has been estimated as 800 m according to literature (Staudigel and Schmincke 1984; García and Davis 2001; De Paolo 2001).
- Unit 7: Pillow-lavas from submarine eruptions representing the main phase of submarine growth of the island.
- Unit 8: Gravitational deposits from gravitational slides on the submarine island flanks. These instability submarine processes occur throughout the growth of the island and produce deposits of slid materials or submarine debris avalanches.
- Unit 9: Dikes and plutonic complex. It is mainly formed by a dense dike swarm representing the feeder vents of the different island growth phases, with plutonic rocks and, to a lesser extent, submarine volcanic rocks.

Properties of the Hyaloclastites

In the eastern part of the island of Tenerife three boreholes have been drilled in hyaloclastites one of them reaching 200 m depth (Fig. 1). Hyaloclastites are composed of clastic particles of irregular shape and sizes ranging from 0.5 to 3 cm, forming a green, grey or brown coloured breccia (Fig. 4). This material is poorly consolidated and weakly cemented. Voids and vacuoles are occasionally present with sizes from 0.5 to 3 cm. Secondary minerals are observed inside them. Fracture zones and slikenside surfaces have been identified.

Pressuremeter tests inside the boreholes and laboratory tests have been carried out. The deformational properties of the hyaloclastite rock mass were obtained from 16 pressuremeter tests carried out at different depths in one of the boreholes. The values for pressuremeter moduli ranged from 50 to 3,200 MPa, with mean representative values of 560 MPa.

Table 1 shows the mean values for some physical and mechanical properties of the hyaloclastite rocks obtained from different laboratory tests on the specimens from the boreholes.

Fig. 4 Hyaloclastite rock specimens

Table 1 Hyaloclastites properties from laboratory tests

Property	Mean values
Unit weigh	2.3–2.9 g/cc
Uniaxial strength	16 MPa
Tensile strength	1.5–1.8
Young modulus	4,300 MPa
Poisson coefficient	0.27–0.31
Strength parameters c, ϕ	3–5 MPa, 43–50°

Stability Conditions of the Pre-Failure Edifice

Stability analysis has been carried out in the pre-failure edifices of Güímar and La Orotava applying limit equilibrium and stress–strain methods. A first analysis has been developed using rock mass parameters obtained from the application of Hoek-Brown failure criterion (Table 2).

Figure 5 shows the results of the analysis showing a deformational pattern affecting the whole edifice. In this case the factor of safety is SF > 1.3.

A second stability analysis has been carried out in order to obtain the "failure" values for the hyaloclastites (back-analysis). Figure 6 shows the results obtained. In this case, the strain distribution shows larger deformations affecting the hyaloclastites and defining a complex failure surface. In this analysis values of 0.1 MPa for cohesion and 16° for angle of friction are needed to reach limit equilibrium.

Although these results are still preliminary they present significant potential failure surfaces that are in accordance with the geomorphological and geological features observed in Güímar and La Orotava valleys, as well as with the geomechanical properties of the materials involved.

The importance of the hyaloclastites rocks has been also pointed out on the stability of the Hawaiian volcano flanks (Schiffman et al. 2006).

Table 2 Geomechanical properties obtained for the units of the pre-failure edifice using H-B criterion

Unit	c (MPa)	ϕ (°)	E (MPa)
1	0.9	51	6,750
2	1.7	47	8,920
3a	2.3	34	4,200
3b	3.1	25	2,780
4	0.9	33	2,300
5	2.8	22	2,050
6a	1.5	30	1,010
6b	2.5	35	1,170
7a	8.0	36	12,020
7b	11.4	34	13,180
8	1.0	20	1,000
9	13.2	33	10,230

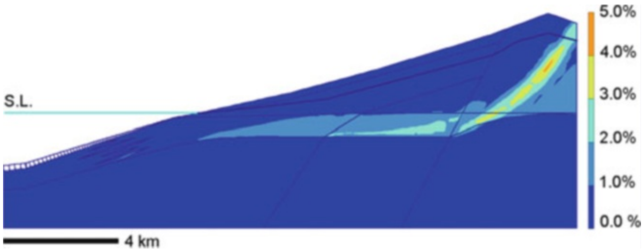

Fig. 5 Deformational model from the stability analysis using properties in Table 2. Horizontal scale = vertical scale

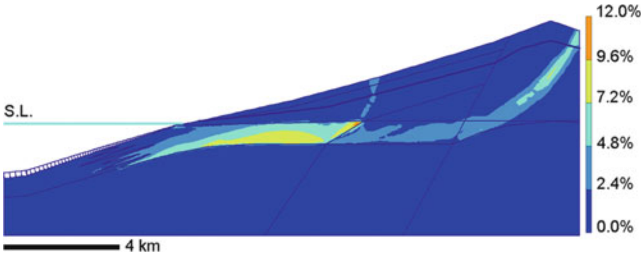

Fig. 6 Deformational model for the initiation of failure (SF = 1.0) and values for the hyaloclastite rocks: c = 0.1 MPa and ϕ = 19°. Horizontal scale = vertical scale

Tsunami Deposits

Large tsunami deposits have been identified in Teno (Tenerife), Piedra Alta (Lanzarote) and Agaete (Gran Canaria). The last one has been described by Pérez Torrado et al. (2002) and Madeira et al. (2011), and it represents at least three different tsunami events. Paleontological and paleoclimatic investigations indicate an age between 1.8 and 2.0 ma (Meco et al. 2008). Teno tsunami deposits, in Tenerife, are probably associated to the flank collapse of the Cañadas Edifice, ca 150–180 ka. Piedra Alta tsunami deposits, located in Lanzarote island, contain many

Fig. 7 Tsunami deposits in the northwest coast of Tenerife (area shown 2 m height)

Fig. 8 Tsunami deposits in the southwest coast of Lanzarote (area shown 2.5 m height)

specimens of marine fauna and an age ca 330 ka has been attributed based on paleoclimatic and paleontological criteria (Meco et al. 2008).

The characteristics of all these deposits indicate a high energy source and a high speed mechanism. Although the tsunami sources are still being investigated, a relation with the large landslides occurred in the Canary Islands during the Pleistocene, with giant rock avalanches entering into the sea is probable (Fig. 7).

The possible run-up of the largest waves of these tsunamis exceeds 50 m height at the Agaete and Teno sites, and at least 25 m height at the Piedra Alta site, as deduced from the location of the deposits today (Fig. 8).

Conclusions

The highly deformable hyaloclastite rocks can play a primary factor in the destabilization process of the flanks of Tenerife. The preliminary results obtained have shown the geometry of the potential failure surfaces of Güímar and La Orotava rockslides. These results are in accordance with the geomechanical properties of the rocks, the surface and submarine geomorphological data and the mechanisms of the geological processes involved. The results suggest that the large instability processes common of the volcanic islands flanks depend on the high deformability properties of hyaloclastites, as well as the morphological conditions of the emerged volcanic edifice, mainly the height and the slope angle of its flanks, so that they are mainly caused by gravitational disequilibrium. Other influencing or triggering factors such as dyke intrusion pressures and volcanic seismicity activity should be also considered as contributing factors. The tsunami deposits identified in three islands suggest a very rapid rock mass movement of rocks and debris entering into the see with a high energy impact. Tsunami waves have reached over 50 m height and propagated to neighboring islands at distances of many km away from the tsunami sources.

Acknowledgments This investigation has been carried out with the financial support of the Ministry of Science of Spain (CICYT – project GRANDETEN I n° CGL2004-00899 and GRANDETEN II n° CGL**2008-01423**) and the Geological Survey of Spain (IGME).

References

Acosta J, Uchupi E, Muñoz A, Herranz P, Palomo C, Ballesteros M (2003) Geologic evolution of the Canarian Islands of Lanzarote, Fuerteventura, Gran Canaria and La Gomera and comparison of landslides at these island with those at Tenerife, La Palma and El Hierro. Mar Geophys Res 24:1–40

Cantagrel JM, Arnaud NO, Ancochea E, Fuster JM, Huertas MJ (1999) Repeated debris avalanches on Tenerife and genesis of Las Cañadas caldera wall (Canary Islands). Geology 27(8):739–742

DePaolo DJ (2001) Deep drillig into a hawaiian volcano. EOS 82 (13):149, 154–155

Ferrer M, Gonzále de Vallejo LI, Seisdedos J, García JC, Coello Bravo JJ, Casillas R, Martín C, Hernández LE (2008) Large rockslides hazards in Tenerife island. Geological analysis and geomechanical modeling of instability mechanisms, IGME-CICYT CGL2004-00899 project, internal report (unpublished)

García MO, Davis MG (2001) Submarine growth and internal structure of ocean island volcanoes based on submarine observations of Mauna Loa volcano, Hawaii. Geology 29(2):163–166

González de Vallejo LI, Hijazo T, Ferrer M (2008) Engineering geological properties of the volcanic rocks and soils of the Canary Island. Soils Rocks 31:3–13

Madeira J, Ferrer M, Gonzalez de Vallejo LI, Andrade C, Freitas MC, Lomoschitz A, Hoffman D (2011) Agaete revisited: new data on the

Gran Canaria tsunamiites. Geophysical research abstracts. Vol 13, EGU2011-2292-2, EGU General Assembly 2011

Masson DG, Watts AB, Gee MJR, Urgeles R, Mitchell NC, Le Bas TP, Canals M (2002) Slope failures on the flanks of the western Canary Islands. Earth Sci Rev 57:1–35

Meco, J et al (2008) Historia geológica del clima en Canarias. http://hdl.handle.net/10553/700

Pérez Torrado F, Paris R, Cabrera MC, Carracedo JC, Schneider JL, Wassmer P, Guillou H, Gimeno D (2002) Depósitos de tsunami en el valle de Agaete, Gran Canaria (Islas Canarias). Geogaceta 32: 75–78

Seisdedos J (2008) Large paleo-rockslides of Güímar and La Orotava (Tenerife): geological analysis, instability mechanisms and geomechanical modelling. PhD Thesis (UCM), Madrid. E-prints Complutense

Schiffman P, Watters RJ, Thompson N, Walton AW (2006) Hyaloclastites and the slope stability of Hawaiian volcanoes: Insights from the Hawaiian Scientific Drilling Project´s 3-km drill core. J Volcanol Geotherm Res 151: 217–228

Staudigel H, Schmincke HU (1984) The pliocene seamount series of La Palma, Canary Islands. J Geophys Res 89(B13): 11195–11215

The Dynamics of Subaqueous Rock Avalanches: The Role of Dynamic Fragmentation

Paolo Mazzanti and Fabio Vittorio De Blasio

Abstract

Rock and debris-avalanches are catastrophic failures occurring both on land and in the subaqueous environment. The apparent friction coefficient of subaqueous rock avalanches is significantly greater than that of debris flows of the same volume. We argue that this is the consequence of the presence of large fragments in a travelling rock avalanche, which affects both the drag coefficient and the capability of hydroplaning. We suggest that the presence of water damps the fragmentation of the subaqueous rock avalanches, as indicated by the presence of much larger blocks in the deposits of subaqueous rock avalanches compared to the subaerial ones. We present simple estimates to evaluate the disintegration rates during the flow in the two different environments and we found that this is strongly reduced in water mainly due to: (1) reduction of inter-granular impact energy; (2) smoother topography in subaqueous landscape; (3) lower velocities reached due to the water resistance.

Keywords

Fragmentation • Rock avalanche • Blocks • Landslide • Dynamics • Impact • Crushing

Introduction

Rock and debris avalanches (Hungr et al. 2001) are catastrophic landslides initiating with the failure of a rock slab that disintegrates and moves rapidly as a granular flow (Hungr et al. 2001). Well-known both on land and on the seafloor, they may attain enormous volumes (maximum volumes of the order 20×10^9 m^3 on land and 3×10^{12} m^3 underwater) and long runouts (respectively 2×10^1 to 2×10^2 km) thus representing an important factor in the geomorphological evolution and reshaping of the earth surface. In the subaqueous environment, rock avalanches differ markedly from debris flows. While the former take origin from the collapse of large sectors of initially intact rocks that disintegrates when travelling, debris flows usually contain a fine matrix from the beginning so that they are characterized by cohesive properties. Aforementioned differences strongly control the dynamics of such events.

Several researchers (e.g., Scheidegger 1973; Legros 2002) have analyzed the mobility of subaerial landslides based on the graphical relationship between the apparent friction coefficient (i.e. the ratio of vertical to horizontal displacement of the landslide) and the volume and recently similar graphs have been realized for subaqueous landslides (Fig. 1). The apparent friction coefficient of subaqueous rock avalanches falls on the fit line for the subaerial ones, which indicates that subaqueous rock avalanches are not intrinsically more mobile than their subaerial counterparts. In contrast, debris flows of the same volume exhibit an apparent friction coefficient 10 times lower (De Blasio 2011).

P. Mazzanti (✉)
NHAZCA S.r.l., spin-off "Sapienza" Università di Roma, Via Cori snc, Rome 00177, Italy

CERI, Research Centre for Prevention, Prediction and Control of Geological Risks, "Sapienza" Università di Roma
e-mail: paolo.mazzanti@nhazca.com

F.V. De Blasio
NHAZCA S.r.l., spin-off "Sapienza" Università di Roma, Via Cori snc, Rome 00177, Italy

Department of Geosciences, University of Oslo, Oslo, Norway

C. Margottini et al. (eds.), *Landslide Science and Practice*, Vol. 5,
DOI 10.1007/978-3-642-31427-8_4, © Springer-Verlag Berlin Heidelberg 2013

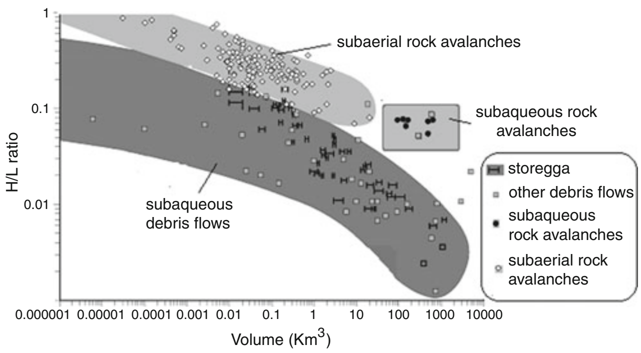

Fig. 1 Position of the subaerial and subaqueous rock avalanches and of the subaqueous debris flows on the plane H/L—volume, where H is the fall height and L is the run-out (Modified from De Blasio et al. (2006))

In order to explain these differences we developed some estimates for the dynamic fragmentation of subaerial and submarine rock avalanches thus showing why fragmentation can be seen as one of the main factors controlling the mobility of subaqueous rock avalanches.

Subaqueous Rock Avalanche Deposits

One of the most evident characteristics of subaerial rock-avalanches is the fragmentated state of the deposits (e.g. Pollet and Schneider 2004; Crosta et al. 2007). Evidently, the mechanisms of fragmentation are capable to drastically reduce the blocks size during the propagation from hundred-meter slabs down to powder-size grains (Locat et al. 2006). Davies and McSaveney (2009) found that the smallest grains are actually on the order of 10–100 nm in size. Even if the disintegration mechanisms are very powerful in a rock avalanche (Davies and McSaveney 2009), the presence of enormous blocks inside the main depositional area has been reported as well (Francis et al. 1985; Ui et al. 2000). However, they do not represent a relevant percentage of the overall debris. Differently, enormous blocks (10^3–10^9 m^3) often represent a significant fraction of the deposit of subaqueous rock avalanches. These blocks may reside within the disintegrated matrix even if occasionally they appear detached from the rest of the deposit. In addition, blocks size distributions do not exhibit any evident correlation with distance.

Deposits of subaqueous rock or debris avalanches exhibiting these characteristics can be found at different scales in many regions of the world such as volcanic islands (e.g. Deplus et al. 2001; Masson 1996; Masson et al. 2002, Lipman et al. 1988; Mitchell et al. 2002; Hildenbrand et al. 2006; Satake and Kato, 2001; Chiocci and de Alteriis 2006), non volcanic areas (e.g. Lewis and Collot, 2001; Bohannon and Gardner 2004; Normark et al. 2004) and also in closed or semi-closed basins (e.g. Lee et al. 2006; Gardner et al. 2000). Similar features can be find also in coastal rock avalanches that start in a subaerial environment (Mazzanti and Bozzano 2011).

Two examples will suffice to illustrate the huge size of subaqueous blocks:

- The Hawaiian deposits blocks reach the incredible height of 500 m and a width of 10 km, even with a fall height well over 5 km (Moore et al. 1994);
- The Canary rock avalanches reveal intact blocks of some hundreds metres to 1–2 km in size (Urgeles et al. 1997, 1999; Masson et al. 2002).

Grain to Grain Impact Disintegration

At present, the role of impact fragmentation in the dynamic fragmentation of a rock avalanche is unclear. Whereas some authors deny that particle-particle impacts plays any role during disintegration (Davies and McSaveney 2009), numerical simulation with molecular dynamics indicate that energetic impacts between grains might play a role at least at the beginning of the landslide motion especially for the top layer of the rock avalanche where the confining pressure is lower. To estimate the rates of impact disintegration, we consider a simple model of an ensemble of grains in a box. Grains are assumed as spheres of mass m and radius R, and the coefficient of restitution ε is constant and independent to the velocity. The box is assumed to move rigidly along with the body of the rock avalanche. Hence, in our model the energy is supplied by the shaking due to the high speed combined to roughness in the ground, and it is dissipated due to inelastic particle-particle impacts.

In the absence of a fluid, the energy per unit particle (e) evolves in time according to a modified version of the Haff's equation (Haff 1983) in:

$$\frac{de}{dt} = -\left(\frac{2}{3}\right)^{\frac{5}{2}} \cdot C \cdot \left(1-\varepsilon^2\right) \cdot n \cdot R^2 \cdot e^{\frac{3}{2}} + \dot{e}_{sh} \tag{1}$$

where

$$C = 4\pi \cdot \left(\frac{3}{m}\right)^{\frac{1}{2}} \tag{2}$$

and n is the number of grains per unit volume.

Following the topographic roughness assumed of sinusoidal form, the material moves vertically as

$$y = A \cdot \sin\left(\frac{2\pi U t}{\lambda}\right) \tag{3}$$

where t is time, U is the landslide velocity, A and λ are respectively the amplitude and wavelength.

The average energy (e_{sh}) input per particle and unit time is then

$$\dot{e}_{sh} = \frac{m \cdot \pi^2 \cdot A^2 \cdot U^3}{\lambda^3} \tag{4}$$

Otherwise, in the presence of a fluid, an extra effect of energy dissipation (e_{drag}) arises due to the drag force exerted by the medium on the particles. In a simple model we take

$$\dot{e}_{drag} \approx -F_{drag} \cdot v = -\frac{1}{2}\pi \cdot R^2 \cdot C_D \cdot \rho_w \cdot v^3 \tag{5}$$

where F_{drag}, v, C_D and ρ_w are respectively the drag force on a particle, the mean square root velocity of a particle against the medium, the drag coefficient, and the water density.

Assuming for simplicity constant velocity for the landslide and setting $de/dt = 0$ the equilibrium energy per particle (e_{eq}) can be obtained by combining (1), (2), (4) and (5):

$$\dot{e}_{eq} = (\pi \cdot A)^{\frac{4}{3}} \cdot \left(\frac{U}{\lambda}\right) \cdot K^{-\frac{2}{3}} \cdot m^{\frac{2}{3}} \tag{6}$$

where we define:

$$K \approx \left(\frac{R^2}{m^{\frac{1}{2}}}\right) \cdot \left[7.89 \cdot (1 - \varepsilon^2) \cdot n + \frac{4.4 \cdot \rho_w \cdot C_D}{m}\right] \tag{7}$$

and the particle number density is written as

$$n = \frac{D}{R^3} \tag{8}$$

where D is a geometrical constant.

For example, the collision energies per unit mass obtained assuming $D = 0.01$, $\lambda = 5$ m, $A = 1$ m $R = 1$ cm, m = 11.3 g, $C_D = 0.6$, ε = 0.4, U = 25 m/s are 32.52 J/kg and 11.92 J/kg for the subaerial and the subaqueous cases, respectively. Thus, the values of e_{eq} are lower in the subaqueous case. Analysing more calculations, we conclude than the water reduces significantly the efficiency of the fragmentation mechanism even when the subaqueous and subaerial topographic properties and landslide velocities are the same; moreover, the reduction is higher with low values of packing density (more realistic in the upper part of the moving mass). Values suggested by King (2001) for the disintegration of large particles are: $e_{rupture} \approx$ *114.2 J/kg and 43.4 J/kg* for limestone and quartz respectively. So far, we have compared the specific energy between the subaerial and the subaqueous case with the same topography and landslide velocity. However this is an extremely conservative view since velocities of underwater avalanches are lower for subaerial counterparts due to opposing forces like drag and buoyancy. Furthermore, subaqueous morphology is much smoother than on land due to depositional mechanisms (like the dispersal of sand and silt from rivers that tend to fill the gaps in the subaqueous terrain) and more quiet geomorphic agents. Therefore, subaqueous environments are likely characterized by lower values of A and higher values of λ compared to the subaerial ones.

We conclude that the impact energy between grains or blocks in the subaqueous environment is significantly reduced by both the presence of water and the more regular pathway.

Crushing

Studies of granular materials under confined pressure show that the stress is unevenly distributed among the grains; in fact it spreads through the medium along force chains where the stress becomes particularly intense (Duran 1999).

With increasing pressure P_N, the force chains tend to merge in a more continuum-like distribution. As a consequence, the distribution $P(f)$ of forces f acting on the grains acquires a Gaussian form (Makse et al. 2000)

$$P(f) = \exp\left[-\left(\frac{f}{\langle f \rangle} - 1\right)^2\right] \tag{9}$$

considering

$$f = \frac{kR^2\sigma}{2} \tag{10}$$

and

$$\langle f \rangle = kP_N R^2 \tag{11}$$

where $\langle f \rangle$ is the average force, R is the particle radius and k a geometrical constant and σ the vertical stress acting on the particle.

Crushing occurs when

$$\sigma = \frac{2f}{kR^2} > \sigma_F \tag{12}$$

where $\sigma_F = \beta R^b$ is the maximum stress that a spherical particle can withstand before rupturing (and is related to the tensile strength) whereas β and $b < 0$ are materials constants (McDowell and Bolton 1998).

Table 1 Results for crushing from 5, 6 and 7, using the following sets of values: $\sigma_{F,W} = \sigma_{F,A} = 2$ MPa; H = 10 m; $\rho = 2700$ kg/m^3

Case	U_w	U_A	λ_w	λ_A	A_W	A_A	T_W	T_A	α
1	5	5	20	20	2	2	1.88	2.31	0.25
2	10	10	20	20	2	2	0.811	0.751	0.88
3	20	20	20	20	2	2	0.225	0.221	0.976
4	20	20	50	50	2	2	1.177	1.055	0.766
5	10	30	5	5	1	1	0.013	0.114	0.11
6	10	30	20	5	1	1	1.429	0.013	0.003
7	10	10	20	5	1	1	1.429	0.114	0.024
8	10	30	20	5	1	2	1.429	0.007	0.001
9	40	40	20	5	1	2	0.115	0.004	0.031
10	20	40	20	5	1	2	0.435	0.004	0.007

As an example, the data for oolitic limestone presented by McDowell and Bolton (1998) give $\beta = 5.67$ MPa and b $= -0.343$ with R expressed in mm, which means that for example a stress of about 1 MPa particle will break a particle of radius 5 cm, but 5 MPa are needed for a particle of 2 mm. Higher stress values will be required for example for quartz. Notice that crushing requires the presence of oriented stresses: the experiments of McDowell and Bolton (1998) were indeed performed by stressing the specimens between flat platens.

By the explicit formulation of (9) (obtained by the combination with (10) and (11)), the fraction of grains that are subjected to a stress larger than the critical stress can be computed as follows

$$\eta(\sigma{>}\sigma_F) \propto \frac{\int_{\sigma_F}^{\infty} \exp\left[-\left(\frac{\sigma}{2P_N}-1\right)^2\right] d\sigma}{\int_{0}^{\infty} \exp\left[-\left(\frac{\sigma}{2P_N}-1\right)^2\right] d\sigma} = \frac{\left[1-erf\left(\frac{\sigma_F}{2P_N}-1\right)\right]}{1+erf(1)} \tag{13}$$

Similarly to the case of impact breakage examined earlier, dynamic stresses caused by the fast movement on an irregular terrain may result in a strong additional force. Approximating again the irregular topography with a sinusoid of amplitude A and wavelength λ, the effective gravity field averaged over the path length amounts to:

$$g' = \frac{\Delta\rho}{\rho_{solid}} g + \frac{8\pi^2 AU}{\lambda^2} \tag{14}$$

Using (13), we find that ratio of the fraction of broken particles between the subaqueous and the subaerial situation goes like

$$\alpha = \frac{\eta_w(\sigma{>}\sigma_F)}{\eta_A(\sigma{>}\sigma_F)} = \frac{T_A \cdot \sigma_{F,W}}{T_W \cdot \sigma_{F,A}} \cdot \frac{1-erf[T_W-1]}{1-erf[T_A-1]} \tag{15}$$

where:

$$T_W = \frac{\sigma_{F,W}}{2H\left(\Delta\rho g + \frac{8\pi^2 A_W {U_W}^2 \rho_{solid}}{{\lambda_W}^2}\right)} \tag{16}$$

$$T_A = \frac{\sigma_{F,A}}{2H\left(\rho_{solid} g + \frac{8\pi^2 A_A {U_A}^2 \rho_{solid}}{{\lambda_A}^2}\right)} \tag{17}$$

The indices "A" and "W" refer to the subaerial "air" and subaqueous "water" situations. It is clear that the combination

$$\rho g + \frac{8\pi^2 AU^2 \rho_{solid}}{(\lambda^2)} \tag{18}$$

at the denominator of both T_W and T_A is much greater for the subaerial than for the subaqueous case. This is because the three parameters involved in the numerator ρ, A, U are larger for the subaerial case, whereas the term in the denominator λ is smaller. Evidently, many parameters contribute to the values of T_W and T_A. As an illustrative example, we show in Table 1 the predicted values of T_W, T_A and α.

When the topographic features and the velocities are the same for the subaerial and the subaqueous cases, the values of α ranges from ~1 ($T_W \cong T_A$) to 0.25. A strong difference appears when the disparity in velocity and topography between subaerial and submerged case are introduced in the model. Cases 5–10 of Table 1 show that the ratio α becomes very low (of the order of 10^{-3}) signifying that the disintegration process is strongly damped in the subaqueous environment.

In short, we find that also the fragmentation due to the crushing mechanism is reduced by the presence of water (even when the subaerial and subaqueous topographic features are the same) but the discrepancy between the two cases becomes extreme if we consider also a lower velocity and smoother pathway in the submerged case.

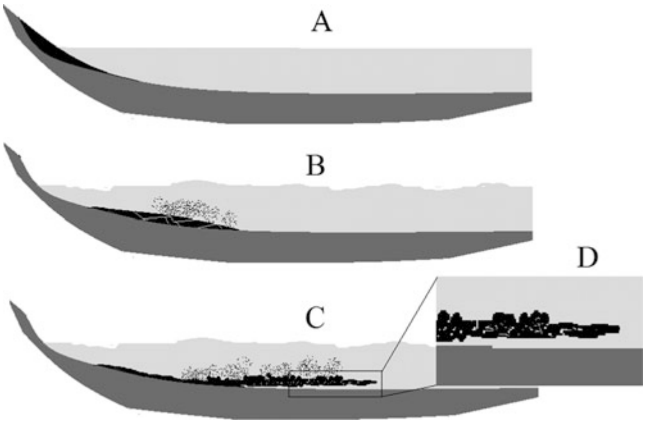

Fig. 2 Hypothetical model for the evolution of a subaqueous rock avalanche

Final Remarks

A significant reduction of the fragmentation occurs in submerged rock and debris avalanches compared to the subaerial ones. The efficiency of both disintegration and crushing is reduced in the subaqueous environment by the presence of drag force and is strongly affected by the landslide velocity and travel path roughness, two parameters which are significantly lower in the submarine environment. Thus, the average grain size in a subaqueous rock avalanches is predicted to be much greater than for a subaerial rock avalanches.

Except for a few specific examples (Crosta et al. 2007; Locat et al. 2006), the spectra of particle size distribution in subaerial deposits are poorly known; for subaqueous deposits the uncertainties are even greater. The measurement of the grain size spectrum for a subaqueous rock avalanche is an important issue for future offshore studies in order to better understand the dynamic behaviour.

Lower fragmentation leads to a lower percentage of fine material and the presence of larger blocks. The resulting matrix will be more permeable than for subaerial rock avalanches and even more than for subaqueous debris flows. Higher permeability reduces the efficacy of the hydroplaning effect (Mohrig et al. 1998) which has been suggested as an explanation for the high mobility of subaqueous landslides. In order to reach hydroplaning regime, the sediment needs to have low permeability; else, the water layer beneath the landslide mass will not be maintained.

Hence, we can conclude that the reduced fragmentation of subaqueous rock avalanches reduce the efficacy of hydroplaning, thus increasing the basal friction coefficient. Figure 2 shows schematically the suggested dynamics of a subaqueous rock avalanche.

The failure (A) and disintegration (B) leads to partial hydroplaning of the rock avalanche (C) in which the water layer (inset D) is partially diminished due to the matrix permeability. This scenario could perhaps explain why the effective friction coefficient for subaqueous rock avalanches is greater than that of subaqueous debris flows (Fig. 1).

The model presented above is far from exhaustive in explaining the overall dynamic of subaqueous rock avalanches. Nevertheless, it clearly indicates the importance of dynamic fragmentation in controlling the behaviour of subaqueous rock avalanches.

Acknowledgements We acknowledge financial support from the CERI, Research Centre for Hydrogeological Risks, University of Rome "Sapienza".

References

Bohannon RG, Gardner JV (2004) Submarine landslides of San Pedro Escarpment, southwest of Long Beach, California. Mar Geol 203:261–268

Chiocci FL, de Alteriis G (2006) The Ischia debris avalanche: first clear submarine evidence in the mediterranean of a volcanic island prehistorical collapse. Terra Nova 18:202–209

Crosta GB, Frattini P, Fusi N (2007) Fragmentation in the Val Pola rock avalanche, Italian Alps. J Geophys Res 112. doi:10.1029/2005JF000455

Davies TR, McSaveney MJ (2009) The role of rock fragmentation in the motion of large landslides. Eng Geol 109(1–2):67–79

De Blasio FV, Elverhøi A, Engvik L, Issler D, Gauer P, Harbitz C (2006) Understanding the high mobility of subaqueous debris flows. Nor J Geol, special issue on "Submarine mass movements and their consequences" 86:275–284

De Blasio FV (2011) Introduction to the physics of landslides: lecture notes on the dynamics of mass wasting. Springer, Netherlands. doi:10.1007/978-94-007-1122-8

Duran J (1999) Sands, powders, and grains: an introduction to the physics of granular materials. Springer, Berlin

Deplus C, Le Friant A, Boudon G, Komorowski JC, Villemant B, Harford C, Segoufin J, Cheminée JL (2001) Submarine evidence for large scale debris avalanches in the Lesser Antilles Arc. Earth Planet Sci Lett 192:145–157

Francis PW, Gardeweg M, O'Callaghan LJ, Ramirez CF, Rothery DA (1985) Catastrophic debris avalanche deposit of Socampa volcano, north Chile. Geology 13:600–603

Gardner JV, Mayer LA, Hughs Clarke JE (2000) Morphology and processes in Lake Tahoe (California-Nevada). GSA Bull 112(5):736–746

Haff PK (1983) Grain flow as a fluid-mechanical problem. J Fluid Mech 134:401–430

Hildenbrand A, Gillot PY, Bonneville A (2006) Offshore evidence for a huge landslide of the northern flank of Tahiti-Nui (French Polynesia). Geochem Geophys Geosyst (G3) 7(3):Q03006. doi:10.1029/2005GC001003

Hungr O, Evans SG, Bovis MV, Hutchinson JN (2001) A review of the classification of landslides of the flow type. Environ Eng Geosci 7(3):221–238

King RP (2001) Modeling and simulation of mineral processing systems. Butterworth Heinemann, Boston

Lee H, Ryan H, Kayen RE, Haeussler PJ, Dartnell P, Hampton MA (2006) Varieties of submarine failure morphologies of seismically-induced landslides in Alaskan fjords. Nor J Geol 86:221–230

Lewis K, Collot JY (2001) Giant submarine avalanche: was this “Deep Impact” New Zealand style? Water Atmos 9:26–27

Lipman PW, Normark WR, Moore JG, Wilson JB, Gutmacher CE (1988) The giant submarine Alika debris slide, Mauna Loa, Hawaai. J Geophys Res 93:4279–4299

Legros F (2002) The mobility of long runout landslides. Eng Geol 63:301–331

Locat P, Couture R, Leroueil S, Locat J, Jaboyedoff M (2006) Fragmentation energy in rock avalanches. Can Geotech J 43(8):830–851

Makse HA, Johnson DL, Schwartz LM (2000) Packing of compressible granular materials. Phys Rev Lett 84:4160–4163

Masson DG (1996) Catastrophic collapse of the volcanic island of Hierro 15 ka ago and the history of landslides in the Canary islands. Geology 24:231–234

Masson DG, Watts AB, Gee MJR, Urgeles R, Mitchell NC, Le Bas TP, Canals M (2002) Slope failures on the flanks of the western Canary Islands. Earth Sci Rev 57:1–35

Mazzanti P, Bozzano F (2011) Revisiting the February 6th 1783 Scilla (Calabria, Italy) landslide and tsunami by numerical simulation. Mar Geophys Res. doi:10.1007/s11001-011-9117-1

Mcdowell GR, Bolton MD (1998) On the micromechanics of crushable aggregates. Geotechnique 48:667–679

Mitchell NC, Douglas G, Masson DG, Watts AB, Gee MJR, Urgeles R (2002) The morphology of the submarine flanks of volcanic ocean islands: a comparative study of the Canary and Hawaiian hotspot islands. J Volcanol Geotherm Res 115:83–107

Mohrig D, Whipple KX, Hondzo M, Ellis C, Parker G (1998) Hydroplaning of subaqueous debris flows. Geol Soc Am Bull 110: 387–394

Moore JG, Normark WR, Holcomb RT (1994) Giant Hawaiian Landslides. Ann Rev Earth Planet Sci 22:119–144

Normark WR, McGann M, Sliter R (2004) Age of Palos Verdes submarine debris avalanche, southern California. Mar Geol 203: 247–259

Pollet N, Schneider JLM (2004) Dynamic disintegration processes accompanying transport of the Holocene flims sturzstrom (Swiss Alps). Earth Planet Sci Lett 221:433–448

Satake K, Kato Y (2001) The 1741 Oshima-Oshima eruption: extent and volume of submarine debris avalanche. Geophys Res Lett 28: 427–430

Scheidegger A (1973) On the prediction of the reach and velocity of catastrophic landslides. Rock Mech 5:231–236

Ui T, Takarada S, Yoshimoto M (2000) Debris Avalanches. In: Sigurdsson H (ed) Encyclopedia of volcanology. Academic, San Diego

Urgeles R, Canals M, Baraza J, Alonso B, Masson DG (1997) The last major megalandslides in the Canary Islands: the El Golfo debris avalanche and the Canary debris flow, west Hierro Island. J Geophys Res 102:20305–20323

Urgeles R, Masson DG, Canals M, Watts AB, Le Bas T (1999) Recurrent giant landslides on the west flank of La Palma, Canary Islands. J Geophys Res 104:25331–25348

THE SECOND WORLD LANDSLIDE FORUM

Submarine Slope Failures Along the Northern Sicilian Continental Margin (Southern Tyrrhenian Sea) and Possible Implications for Geo-Hazard

Attilio Sulli, Mauro Agate, Claudio Lo Iacono, Valeria Lo Presti,
Valentina Pennino, and Sabrina Polizzi

Abstract

In this study we present an overview of the mass wasting features (e.g.: submarine canyons, landslides, debris flows) and downslope movements that have contributed to shape the northern Sicily continental margin (southern Tyrrhenian Sea) since the Late Quaternary. The study is based on Multibeam data and high-resolution seismic reflection profiles, which allowed to define the morphology and the stratigraphy of the mass transport deposits and related failures of the area. We distinguished slope failures related to different mechanisms. In the Palermo Gulf and in the eastern sector of the northern Sicily margin tectonic activity, fluid escaping and oversteepening triggered downslope turbiditic currents and concurrent up-slope retrogressive mass failures. In the Ustica offshore gravitational collapse of volcanic edifices is mainly linked to neotectonic activity and volcanism. These data allow us to understand geological features and processes which may represent a threat for coastal areas of the northern Sicily margin.

Keywords

Slope failures • Swath bathymetry • Geo-hazard • Southern Tyrrhenian

Introduction

Since the early stages of modern exploration of the ocean various-scale features due to seafloor instability were recognized typically at the shelf break, where slopes are steeper, and in areas of high sedimentation rates. Mass failures consist of the movement of a volume of generally consolidated material along a slipping surface and represent one of the main processes for long distance sediment transport along continental margins (Haflidason et al. 2004). Repeated events of mass movement can remove a significant amount of submarine slope sediment strongly affecting slope morphology (Canals et al. 2004).

The classification of Mulder and Cochonat (1996) divided the processes involving submarine failed deposits into slides or slumps, plastic flows and turbidity currents. They are distinguished on the base of their style of movement, the shape of their failure surfaces, and the architecture of the resulting deposit. Multiple retrogressive failures propagating upslope are among the most common types. Although major slope failures tend to lower the regional slope angle, failure scars result in locally over-steepened slopes that require further morphological evolution before stabilization. The present-day morphology provides insights into the cumulative effects of failures and post-failure processes.

The triggering mechanisms and the predisposing factors favouring mass wasting are still not totally understood, even if it's well known that the type and frequency of mass failure processes are controlled by the interplay of different elements. The mechanical behaviour of sediments and

A. Sulli (✉) • M. Agate • V.L. Presti •
V. Pennino • S. Polizzi
Dipartimento di Scienze della Terra e del Mare, Università di Palermo,
via Archirafi 22, Palermo, Italy
e-mail: attsu@unipa.it

C.L. Iacono
CSIC, Unidad de Tecnología Marina, Paseo Maritimo de la Barceloneta
37-49, Barcelona, Spain

C. Margottini et al. (eds.), *Landslide Science and Practice*, Vol. 5,
DOI 10.1007/978-3-642-31427-8_5, © Springer-Verlag Berlin Heidelberg 2013

slope geometry exert key roles in failure development and also have a high impact on the mass movement transport mechanisms, which can occur either in a cohesive or disintegrative fashion (McAdoo et al. 2000).

Sediment overloading and slope oversteepening represent the most common predisposing factors, whereas tectonic and volcanic activity, gas and fluid escape (Greene et al. 2002) and slope undercutting (Baztan et al. 2005) are commonly invoked as the trigger for instabilities. Dynamic processes along continental shelves and earthquake shaking are also common processes that instigate seafloor failures. These processes decrease the shear strength of the sediment down to a failure threshold by increasing the interstitial fluid pore pressure. Moreover, earthquakes generate ground accelerations in addition to the gravitational force (Almagor and Wisenam 1977). These causes make slope failures in submarine environments a common process that occurs also on gently dipping slopes (Lewis 1971).

Recent studies carried out on the Hawaii, Canary and Marianne Islands edifices have revealed considerable variability in flank morphology of the submarine volcanoes, indicating that they are affected by tectonic lineaments, minor volcanic apparatus and a range of mass wasting processes. The latter range from debris avalanches (Siebert et al. 1987), to slumps, slide scars generated by small-scale sliding (Chiocci et al. 2008), and flows of volcanogenic sediment (Urgeles et al. 1997). Submarine slope failures represent an important hazard to the coastal community as well as the offshore activities for exploitation of marine resources. Thus, the interpretation of the physical processes that regulate mass failures constitutes the basis for the assessment and monitoring of the geo-hazard potential in coastal regions.

Evidences from many regions all over the world demonstrated that submarine failures are capable of generating even destructive tsunamis (Ward 2001). Historical records report that Greece and southern Italy are the most affected regions in the Mediterranean, interested by many destructive events in the past, mainly related to tsunamigenic earthquakes and slides (Chiocci et al. 2008; Mazzanti and Bozzano 2011). Most of the major tsunami occurred along the Sicilian-Calabrian coasts. After various events occurred during the last 300 years along the northern Sicily coasts, the most destructive tsunami occurred in the Messina Strait owing to the 1908 earthquake and landslide (Billi et al. 2008) while the more recent was generated at Stromboli in 2002, in the Aeolian Islands, by submarine and subaerial sliding of volcanic material (Chiocci et al. 2008).

In this paper, we analyse in details the seafloor morphology along the northern Sicily continental margin, located between the Tyrrhenian back-arc basin and the Sicilian chain (central Mediterranean). Evidences of several mass-movement types have arisen from swath-bathymetry and high-resolution seismic collected along this active margin slope, affected by widespread volcanism and seismicity.

The aims of this study are: (1) to outline the morphology of the mass failure features mapped in the northern Sicily continental margin, (2) to describe the mass-movement types, run out distances and transport mechanisms, (3) to recognize the main geological processes that control the mass failure processes of the area and (4) to highlight their potential implications for the geo-hazard of the northern Sicily offshore.

Bathymetric data (MultiBeam Echo Sounder) and seismic reflection profiles used for this study were mainly collected during several cruises in the frame of marine geological mapping (CARG) and geohazard assessment (MAGIC) Italian projects.

Geological Setting

The northern Sicily continental margin (Fig. 1) is located in the southern Tyrrhenian Sea, from the north Sicily continental shelf to the Marsili Abyssal Plain, in the transitional area between the Sicilian-Maghrebian chain to the south and the Tyrrhenian Basin to the north. This continental margin is composed of: (1) a narrow (<8 km) and moderately steep (1°–2°) continental shelf, (2) a very steep (7°–8°) upper continental slope ranging in depth from 150 to 1,000 m, (3) a flat intra-slope basin plain at a depth of 1,500 m, (4) a lower continental slope that is wider and gentler than the upper slope and (5) a bathyal plain from a depth of 3,000 m.

The opening of the southern Tyrrhenian back-arc basin led to the subsidence of the northern Sicilian margin since the Late Tortonian (Sedimentari 1980). During the Pleistocene, E-W- to NE-SW-trending normal faults exerted a control on the morphology of the present day shelf and coastal areas.

Along the margin, intra-slope basins, termed peri-Tyrrhenian basins by Selli (1970), originated as a consequence of crustal thinning, compressional events and strike-slip faulting (Agate et al. 2000). The peri-Tyrrhenian basins have been filled with Late Neogene to Quaternary evaporitic, hemipelagic, siliciclastic and volcaniclastic deposits, up to 1,200 m thick (Sedimentari 1980).

Along the shelf and the upper slope regions, the Quaternary deposits consist of seawards dipping clastic and terrigenous deposits coming from the northern Sicilian margin (Pepe et al. 2003; Agate et al. 2005), whereas in the basinal areas hemipelagic sediments are found, locally intercalated with volcanoclastic sediments (Sedimentari 1980).

In the continental shelf, the Pleistocene deposits are truncated by an erosional surface formed during the last glacio-eustatic oscillation. Local uplift caused the systematic non-preservation

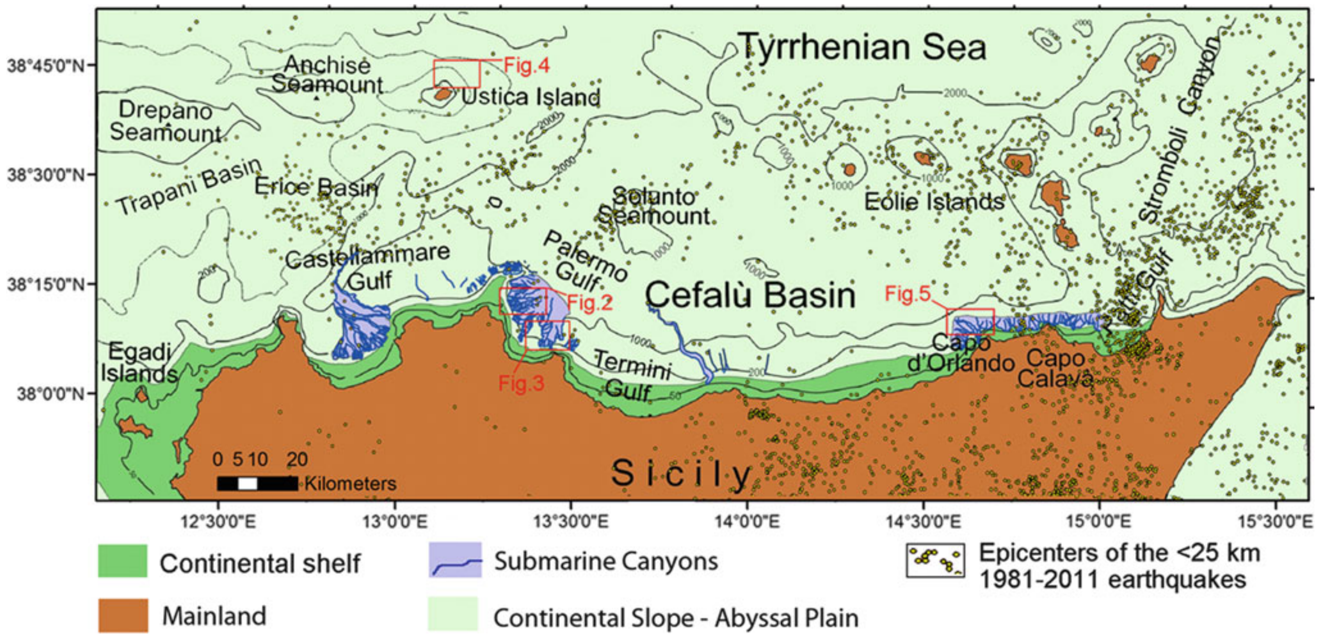

Fig. 1 Simplified physiographic setting of northern Sicily offshore and distribution of epicentres related to the upper crustal seismic activity. Location of the studied instabilities is also shown

of portions of the oldest sequences (Pepe et al. 2003). Prograding sedimentary wedges of coastal deposits formed during the Last Glacial Maximum (about 18 kA) are present along the shelf margin. The prograding wedges are absent where the heads of the canyons or failure scars have indented the outer shelf (Lo Iacono et al. 2011).

Tectonic activity persists today with the occurrence of shallow (<25 km) seismic events of low to moderate magnitude (max Md 5.6 on September 2002; www.ingv.it) along an E-W trending belt located northward of the study area (Fig. 1). The focal mechanisms related to the main seismic shocks are in agreement with a dominant NE-SW fault trend coupled with a NW-SE compressive offset direction (Agate et al. 2000; Giunta et al. 2009).

Submarine Survey

The morphology of the area has been studied by means of MultiBeam Echo Sounder (MBES) data, acquired in three different oceanographic cruises in 2001, 2004 (CARG cruises) and 2009 (MaGIC cruise), by using both the Reson SeaBat 8111, with depth range of 35–800 m, and the Reson SeaBat 8160, with depth range of 30–3,000 m.

Post-processing of MultiBeam data included the graphic removal of erroneous beams, noise filtering, processing of navigation data and correction for sound velocity. Once cleaned, gridding of the filtered soundings was carried out to obtain the final DTM, which provided high resolution 3D views of the sea-floor, shaded relief maps, slope maps and bathymetric cross sections.

Various sets of CHIRP and multi- and single-channel seismic profiles provided high resolution to high penetration data of the Plio-Quaternary sedimentary succession. The seismic lines interpreted using seismic facies analysis, which allowed depositional units, characterized by different seismic attributes, to be distinguished.

Landslide volume was estimated by subtracting a pre-slide bathymetry from the actual bathymetry. The pre-slide bathymetric model was reconstructed by interpolating bathymetric nodes along the scar edges.

Results

Several examples of slope failures were analysed along the northern Sicily continental margin, whose morphological characters appear to be associated to different processes and related to a number of triggering and predisposing factors.

The Palermo Gulf

In the Palermo Gulf submarine canyon valleys deeply scour the upper slope or indent the shelf-edge, entering the Palermo intraslope basin at a depth of around 1,300 m (Lo Iacono et al. 2011). The canyons evolved through concurrent top-down

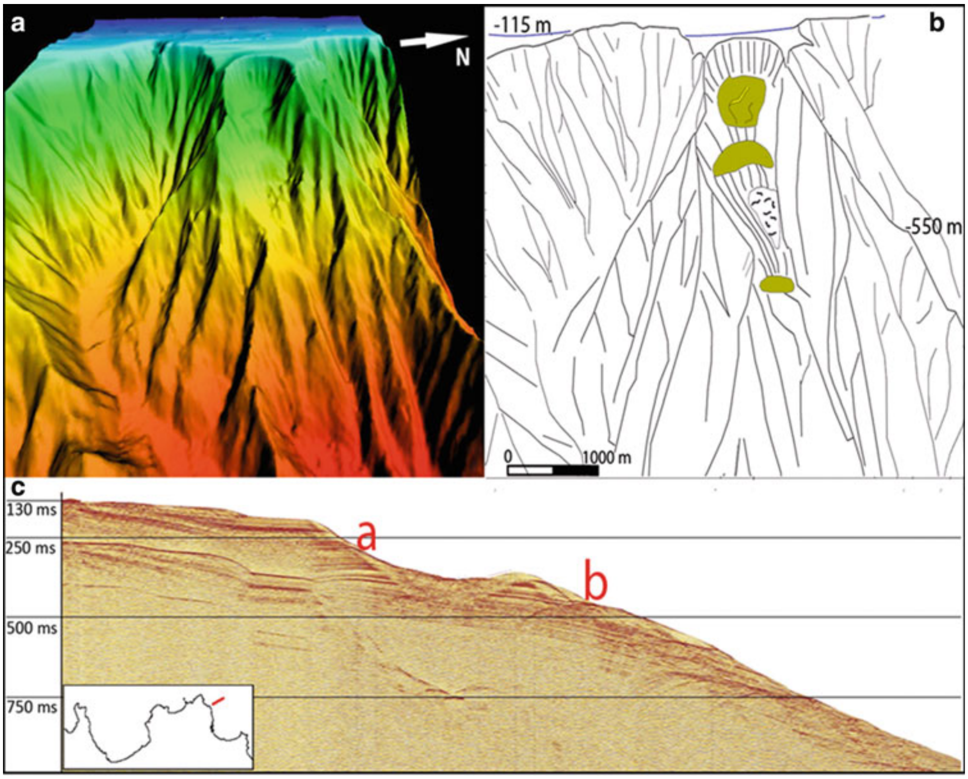

Fig. 2 (**a**) 3D shaded relief model (vertical exaggeration is ×3) derived from swath bathymetry data showing the Priola Scar. (**b**) Interpretative drawing showing the slide scar and related landslide deposits. (**c**) High resolution seismic profile imaging the Priola Scar truncating the Upper Quaternary deposits (*a*); chaotic facies on the right (*b*) corresponds to the slide deposits

turbiditic processes and bottom-up retrogressive mass failures. Most of the mass failure of the area are related to canyon shaping processes. Headward erosion processes are the main controlling factor in shaping the western sector of the Palermo Gulf, due to the occurring of a highly dissected substrate along the slope, which shows steep to very steep gradients that appear to favour a retrogressive evolution of the canyons. On the contrary, in the central-eastern sector, NNE trending canyons breaching the shelf break develop in connection with the Oreto and Eleuterio rivers that cross the coastal plain (Lo Iacono et al. 2011).

Many slope failures are present along the flanks of all the canyons. The only large slope failure feature that is not confined inside a canyon valley is the Priola Scar, along the western side of the Gulf (Fig. 2). The Priola scar displays a well preserved, semicircular shape with an upward concave failure plan; the headwall, that lies 3.5 km from the coastline at a depth of 145 m, is about 900 m wide and 100 m high. The failure displacement surface extends as far as 3 km across the upper slope; it displays sharp slope breaks that highlight few secondary scars that can be up to 70 m high. Chaotic slide blocks, has been observed at a depth of about 475 m. The Priola Slide is a complex slide made up of a slip plane with rotational displacement downslope evolving to a translation component. Total volume of the slide has been estimated to about 0.049 km^3. No drapes by younger sediments have been imaged on high resolution seismic profiles, therefore we hypothesize a recent age of the failure. In this case slope oversteepening and the local tectonic setting appear to be the main predisposing factors.

The occurrence of pockmarks and small carbonate outcrops (illustrated in Lo Iacono et al. 2011) also suggests the probable role that fluid seeps play in the mass wasting processes of the area. A cluster of slides has been detected in the central sector of the Palermo Gulf (Fig. 3) where the continental shelf is wider (up to 4.750 m) and the adjacent upper slope shows a lower gradient (about 3°) than others sectors in the Gulf. A train of pockmarks, on average 15 m deep, has also been detected in this area (Fig. 3) at a depth of 250–450 m, with a diameter of 100–250 m. Failure scars occur just below the pockmarks, so we hypothesize a genetic link between the latter and slope failure features, as consequence of gas charging that reduces the sediment strength.

The Ustica Offshore

Here we present an example of slope failure features in the volcanic edifices of the central Mediterranean coming from the NE offshore of Ustica Island, a Quaternary dormant volcano (Fig. 4), where a field of minor volcanic cones and mass wasting morphologies have been imaged during a recent bathymetric survey. Two kilometres far from the Ustica coastline, at a depth of 400 m, two small volcanic cones up to 100 m wide, built inside and older crater, 550 m wide and 270 m high. The eastern flank of the older crater

Fig. 3 (**a**) 3D shaded relief model (vertical exaggeration is ×3) derived from swath bathymetry data showing the slide scars and the pockmark field in the southern sector of the Gulf of Palermo slope. (**b**) Interpretative drawing of A where location of bathymetric profiles illustrated in (**c**) and (**d**) is shown

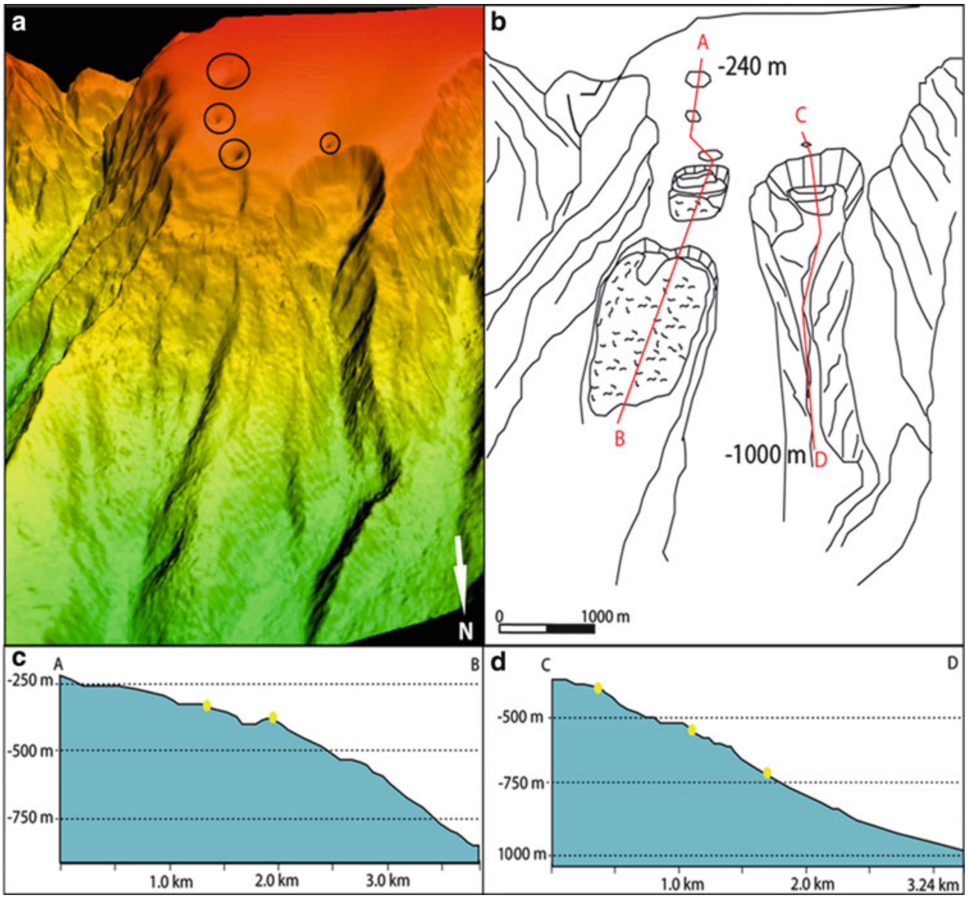

Fig. 4 (**a**) 3D shaded relief model (vertical exaggeration is ×3) derived from swath bathymetry data showing the volcanic apparatus detected in the NE Ustica offshore. (**b**) Interpretative drawing of slope failure and related landslide deposits; (**c**) single channel seismic profile crossing the landslide deposits

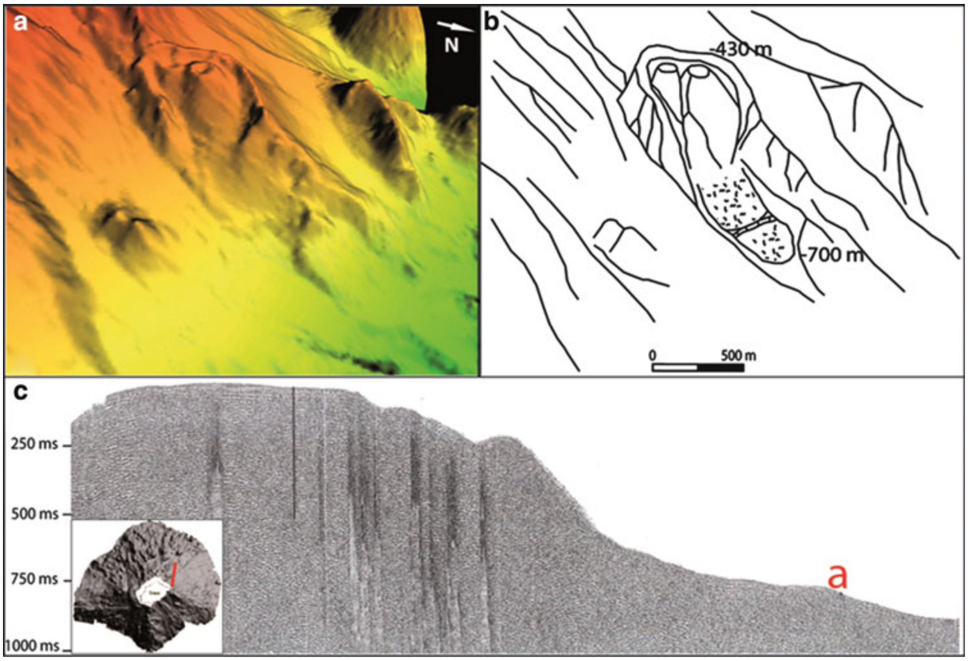

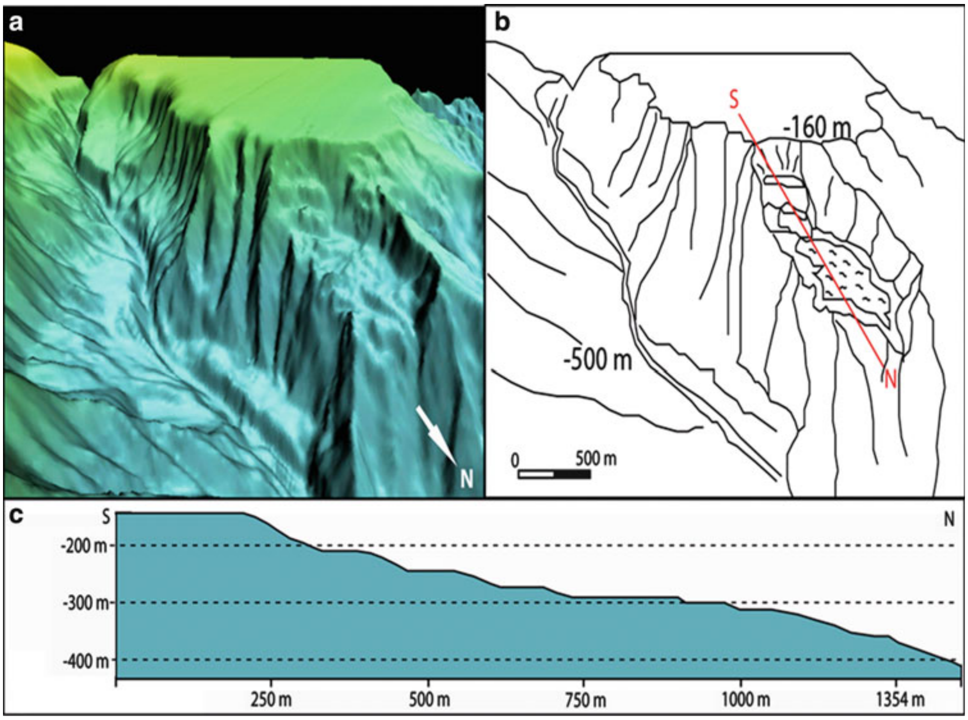

Fig. 5 (**a**) 3D shaded relief model (vertical exaggeration is ×3) derived from swath bathymetry data showing the slide recognized along the western flank of the submarine canyon off Capo Calavà. (**b**) Interpretative drawing of A where location of bathymetric profile illustrated in (**c**) is shown. Note the staircase pattern of the seabottom profile and the hummocky seabed topography where chaotic slide deposits accumulated

collapsed, probably during the build-up of the new cones. A chaotic mass transport about 14 × 10^{-6} km^3, lies 1,000 m south-eastward from the crater and accumulated inside a SW-NE trending structural depression, 700 m deep, bounded by others minor volcanic cones.

The Eastern Sector of the Northern Sicily Margin

Along the offshore sector between Capo d'Orlando and Capo Calavà (Fig. 1) an extensive network of submarine canyons (Fig. 5) scour a narrow continental shelf, no wider than 4.5 km up to a depth of 15 m. Unlike the western sector of the northern Sicily margin, here the canyon heads are very close to the coastline, up to around 300 m in front of Capo Calavà, and form deep incised valley across the continental shelf. The flanks of these valleys host mass failure features.

The largest submarine landslide of the northeastern Sicily offshore has been observed along the western flank of a canyon located west of Capo d'Orlando. The canyon headscarp is at a water depth of 18 m and is characterized by two small incisions that merge together in a major submarine channel, oriented along a N-S direction along the shelf and a SE-NW direction along the slope. Along the canyon, sediment instability induced the gravitational collapse of a sector of the western flank. The slide headwalls is 150–170 m deep and show a semi-circular shape. The collapsed deposits accumulated over a surface of 0.12 km^2, at a depth of 350 m. A few secondary scars have been observed producing a staircase bathymetric profile (Fig. 5). The landslide body consists of many, heterogeneous blocks accumulated in a chaotic pattern determining a typical hummocky sea floor surface. The slide is hanging 150–200 m above the canyon thalweg. Its total length is about 1 km and a total volume of 0.012 km^3 has been estimated. Many others minor landslides are presents along the upper slope close to the major that has been here illustrated.

Discussion

Morphobathymetric and stratigraphic features suggest that a concurrence of processes contribute to the origin and the evolution of the slope failures in the northern Sicily continental margin.

The axial incision observed along the thalweg in most of the canyons demonstrates that active or recent downslope sedimentary fluxes occur along the slope (Baztan et al. 2005). Thus undercutting by turbidity currents and other erosive flows could have been responsible for gravity instability, contributing to the evolution of the submarine canyons.

In others cases sediment failures such as slumps, sliding or debris flows along the canyon walls suggest retrogressive mass failure events (Nelson and Maldonado 1988; Greene et al. 2002) that facilitate the upslope propagation of embryonic canyons towards the shelf margin (Mitchell 2005). So, shelf-indenting canyons may represent an evolutionary stage that is more mature than that of the juvenile canyons which are still confined to the slope. Once the landward migrating canyons indent the shelf-edge, they may intercept new sediment sources such as fluvial or along-shore transported sediments. During the evolution of the canyons, the retrogressive mass failures probably trigger turbidity currents, creating incisions along the thalweg. Axial incision would provoke undercutting, oversteepening and consequent instability of the canyon flanks, leading to further slumpings during a complex scenario of concurrent top-down and bottom-up erosional mechanisms (Pratson and Coakley 1996).

In general, the mass failure features that occur on the canyon walls are relatively small and confined. They therefore do not pose a significant hazard to offshore infrastructures and do not constitute a possible threat of tsunamis along the coast (Driscoll et al. 2000). Nonetheless, some headscarps not confined to canyons could be potentially dangerous. Based on the morphometric analysis, the Priola Scar is the feature that deserves most attention. Mass failures with similar characteristics (3.5 km from the coast, 24–28 × 10^6 m^3, 150 m depth) may constitute a potential of tsunami inundation at local scale (Dan et al. 2007).

Based on the available data, the main pre-conditioning geomorphological factor which could have induced sediment instability is the steep gradient of the slope. The average slope gradient of 20° registered on the canyon walls and canyon heads may have favoured the occurrence of frequent mass failure events. The steep slopes of some of the canyon axes could have provoked a deep undercutting of the canyon heads and bring about headward migration by mass failure inside the narrow shelf. Most of the observed mass failure features were probably generated or were more active during the glacial periods when the coastline was closer to the slope and when the shelf margin constituted a shallow and more dynamic setting (Burger et al. 2003). The structural setting could also have contributed to the evolution of the submarine canyons and the mass failure processes. Some evidence of this control was found in the faults and folded structures.

Furthermore, the occurrence of pockmarks and highs that probably consist of authigenic carbonates above faulted and folded strata suggests a local relationship between structural control, fluid escape and mass failure. Some of the tectonic features could have represented a preferential escape route for fluids as evidenced by the pockmarks. Pockmarks may in turn trigger mass failures as evidenced by the headscarps observed below them. The structural features are possibly associated with the recent tectonics mapped on-land as well as the widespread seismicity of the margin.

Volcanic islands are the geological setting where submarine failures are very common as well as being among the largest slope failures on the seafloor. Impressive examples come from Hawaiian and Canary Islands (Masson et al. 1998; Urgeles et al. 1999).

In the Ustica offshore volcanism related features (gravitational collapse of volcanic edifices, debris avalanche and debris flows) are mainly linked to neotectonic activity and volcanism that tend to build, load and steepen the submarine slopes with time.

One important aim of future researches could be to ascertain whether these features are active and whether they pose a risk today. This would entail the identification of the main triggering mechanisms and the evaluation of the threat to coastal populations.

This study represents a first step in the understanding of those geological features and processes which may represent a threat for coastal areas of the northern Sicily margin. Further information, such as rate, recurrence period, released energy of the processes are necessary to evaluate the likelihood of occurrence to assess the geohazard of the study area related to mass failure. Future studies will become crucial to establish standard procedures for managing risks related to geological processes, considering also exposure and susceptibility (vulnerability) to losses.

Conclusions

Morphobathymetric and seismostratigraphic data revealed the presence of mass failure features in the northern Sicily continental margin (Southern Mediterranean). The morphologies suggest that downslope turbiditic currents and concurrent up-slope retrogressive mass failures contribute to the shaping of the slope. Some canyons seem to be more controlled by turbiditic currents whereas the canyons of the steeper slopes are more dominated by retrogressive mass failure events.

The most prominent pre-conditioning factor in controlling the evolution of the mass failures is the steep gradient of the seafloor, especially along some sectors of the slope. The tectonic and volcanic setting of the area and punctual fluid escape processes may have contributed to slope instability.

In the light of our findings, most of the mass failures are small and enclosed in canyon systems, representing on the whole a low geo-hazard. The obtained results constitutes a reliable base for evaluating the geo-hazard potential related to slope failures in the area. Higher resolution morphobathymetric data, geotechnical test, monitoring of potential areas prone to mass failure and modelling landslides consequences along coastal areas would produce valuable informations for geohazard assessment and mitigation strategies.

References

Agate M, Beranzoli L, Braun T, Catalano R, Favali P, Frugoni F, Pepe F, Smriglio G, Sulli A (2000) The 1998 offshore NW Sicily earthquakes in the tectonic framework of the southern border of the Tyrrhenian Sea. Mem Soc Geol It 55:103–114

Agate M, Mancuso M, Lo Cicero G (2005) Late Quaternary sedimentary evolution of the Castellammare Gulf (North-Western Sicily offshore). Boll Soc Geol It 124:21–40

Almagor G, Wisenam GH (1977) Analysis of submarine slumping in the continental slope of the southern coast of Israël. Mar Geotech 2:349–380

Baztan J, Bernè S, Olivet JL, Rabineau M, Aslanian D, Gaudin M, Rehault JP, Canals M (2005) Axial incision: the key to understand submarine canyon evolution (in the western Gulf of Lion). Mar Pet Geol 22:805–826

Billi A, Funiciello R, Minelli L, Faccenna C, Neri G, Orecchio B, Presti D (2008) On the cause of the 1908 Messina tsunami, southern Italy. Geophys Res Lett. doi:10.1029/2008GL033251

Burger RL, Fulthorpe CS, Austin JA (2003) Effects of triple junction migration and glacioeustatic cyclicity on evolution of upper slope morphologies, offshore eel river basin, northern California. Mar Geol 199:307–336

Canals M, Lastras G, Urgeles R, Casamor JL, Mienert J, Cattaneo A, De Batist M, Haflidason H, Imbo Y, Laberg JS, Locat J, Long D, Longva O, Masson DG, Sultan N, Trincardi F, Bryn P (2004) Slope failure dynamics and impacts from seafloor and shallow subseafloor geophysical data: case studies from the COSTA project. Mar Geol 213(1–4):9–72

Chiocci FL, Romagnoli C, Tommasi P, Bosman A (2008) The Stromboli 2002 tsunamigenic submarine slide: Characteristics and possible failure mechanisms. J Geophys Res 113:B10

Dan G, Sultan N, Savoye B (2007) The 1979 Nice harbor catastrophe revisited: trigger mechanism inferred from geotechnical measurements and numerical modelling. Mar Geo 245:40–64

Driscoll NW, Weissel JK, Goff JA (2000) Potential for large-scale submarine slope failure and tsunami generation along the US mid-Atlantic coast. Geology 28:407–410

Giunta G, Luzio D, Agosta F, Calò M, Di Trapani F, Giorgianni A, Oliveri E, Orioli S, Perniciaro M, Vitale M, Chiodi M, Adelfio G (2009) An integrated approach to investigate the seismotectonics of northern Sicily and southern Tyrrhenian. Tectonophysics 476:13–21

Greene HG, Maher NM, Paull CK (2002) Physiography of the Monterey bay national marine sanctuary and implications about continental margin development. Mar Geol 181:55–82

Haflidason H, Sejrup HP, Nygard A, Mienert J, Bryn P, Lien R, Forsberg CF, Berg K, Masson D (2004) The Storegga Slide: architecture, geometry and slide development. Mar Geol 213:201–234

Lewis KB (1971) Slumping on a continental slope inclined at 1°–4°. Sedimentology 16:97–110

Lo Iacono C, Sulli A, Agate M, Lo Presti V, Pepe F, Catalano R (2011) Submarine canyon morphologies in the Gulf of Palermo (Southern Tyrrhenian Sea) and possible implications for geo-hazard. Mar Geophys Res. doi:10.1007/s11001-011-9118-0

Masson DG, Canalis M, Alonso B, Urgeles R, Huhnerbach V (1998) The Canary Debris Flow: source area, morphology and failure mechanism. Sedimentology 45:411–432

Mazzanti P, Bozzano F (2011) Revisiting the February 6th 1783 Scilla (Calabria, Italy) landslide and tsunami by numerical simulation. Mar Geophys Res. doi:10.1007/s11001-011-9117-1

McAdoo B, Pratson G, Orange LF (2000) Submarine Landslide Geomorphology, U.S. Continental Slope. Mar Geol 169: 103–136

Mitchell NC (2005) Interpreting long-profiles of canyons in the USA Atlantic continental slope. Mar Geol 214:75–99

Mulder T, Cochonat P (1996) Classification of offshore mass movements. J Sediment Res 66:43–57

Nelson CH, Maldonado A (1988) Factors controlling depositional patterns of Ebro turbidite systems, mediterranean sea. AAPG Bull 72:698–716

Pepe F, Sulli A, Agate M, Di Maio D, Kok A, Lo Iacono C, Catalano R (2003) Plio-Pleistocene geological evolution of the northern Sicily continental margin (southern Tyrrhenian Sea): new insights from high resolution, multi-electrode sparker profiles. Geo Mar Lett 23:53–63

Pratson LF, Coakley BJ (1996) A model for the headward erosion of submarine canyons induced by downslope-eroding sediment flows. GSA Bull 108(2):225–234

Sedimentari B (1980) Dati geologici preliminari sul bacino di Cefalu' (Mar Tirreno). Ateneo Parmense Acta Nat 16:3–18

Selli R (1970) Cenni morfologici generali sul Mar Tirreno. G Geol 37:5–24

Siebert L, Glicken H, Ui T (1987) Volcanic hazards from Bezymiannyand Bandai-type eruptions. Bull Volcanol 49:435–459

Urgeles R, Canals M, Baraza J, Alonso B, Masson DG (1997) The most recent megaslides on the Canary Islands: the El Golfo Debris Avalanche and the Canary Debris Flow, west El Hierro Island. J Geophys Res 102:20305–20323

Urgeles R, Masson DG, Canals M, Watts AB, Le Bas T (1999) Recurrent giant landslides on the west flank of La Palma, Canary Islands. J Geophys Res 104:25331–25348

Ward SN (2001) Landslide tsunami. J Geophys Res 106:11201–11215

THE SECOND
WORLD
LANDSLIDE FORUM

Interaction of Landslide Mass and Water Resulting in Impulse Waves

Giovanni B. Crosta, Silvia Imposimato, and Dennis Roddeman

Abstract

Landslides can occur in different environments and can interact with water basins of different characteristics. The transition from subaerial to subaqueous conditions can strongly control the landslide evolution and the generation of impulse waves, and therefore the final hazard zonation. Modelling the landslide spreading, the impact with the water surface and the generation of the impulse wave is a challenging work. We verify the capabilities of a fully 2D FEM approach to perform such a modelling and to analyse near-field evolution. To this aim we simulate the Vajont rockslide and the consequent impulse wave, and some laboratory tests available in the literature.

Keywords

Rock avalanches • Impulse wave • Tsunami • Modeling • FEM • Granular flow

Introduction

Large fast moving landslides can be originated along slopes in mountainous terrains with natural and artificial lakes, or fjords at the slope foot. Extremely large fast moving landslides can also occur as a consequence of a volcano flank or edifice collapse. Rock and debris avalanches can reach extremely high speed along subaerial slopes and the impact can involve a variably steep landslide snout and an immobile mass of water. As a consequence, the spreading of large landslide masses can be at the origin of large waves. Landslide generated impulse waves (landslide tsunami) can be subdivided in three different steps: initiation, propagation and, finally, runup. The type of phenomena can be strongly controlled by the landslide initial position (high on a slope, partially submerged or completely submerged), the landslide speed, the type of material, the slope inclination and its geometry, both subaerial and subaqueous, the relative size of the landslide mass with respect to the depth of water. These phenomena are highly destructive, even if associated to relatively small volumes, and can be characterised by a high recurrence frequency at sites susceptible to landsliding.

Extreme landslide tsunami events occurred as a consequence of subaerial landslides at very different sites, for example: the 1963 Vajont rockslide (Italy, about 2,900 casualties) characterised by an extremely low water depth to landslide thickness ratio; the 1958 Lituya Bay event (Alaska, Miller 1960, site of multiple historical slope failures and tsunami: 1853–1854, 1936, 1958), the 1934 Tafjord event (Norway, Blikra et al. 2005), the Loen events (Norway); up to some catastrophic volcano collapses in deep ocean waters (Hawaii and Canary islands, Keating and McGuire 2000; Ward and Day 2003). Many other events are associated to subaqueous landslides of very different sizes and triggering.

Landslide impulse waves and tsunamis are generally characterized by larger heights in the near field, by rapid decay, high turbulence, flow separation and subsequent reattachment, strong mixing of air and water.

Various researchers completed a systematic experimental work on 2D and 3D wave generation and propagation

---

G.B. Crosta (✉)
Dipartimento di Scienze Geologiche e Geotecnologie, Università degli Studi di Milano-Bicocca, Milan, Italy
e-mail: giovannibattista.crosta@unimib.it

S. Imposimato • D. Roddeman
FEAT, Maaierhof 27, 6418, JL Heerlen, The Netherlands

C. Margottini et al. (eds.), *Landslide Science and Practice*, Vol. 5,
DOI 10.1007/978-3-642-31427-8_6, © Springer-Verlag Berlin Heidelberg 2013

(Kamphuis and Bowering 1970; Huber 1980; Müller 1995; Huber and Hager 1997; Fritz 2002; Zweifel 2004; Panizzo et al. 2005; Heller 2007; Heller and Kinnear 2010; Sælevik et al. 2009), using both rigid blocks and deformable granular" masses, and their data can be used to calibrate and validate numerical modelling tools.

Analytical and numerical methods, have been developed and applied to simulate landslide induced tsunamis. In most of this studies the subaerial movement has been analysed in a simplified way (Harbitz 1992; Jiang and LeBlond 1993; Grilli et al. 2002; Grilli and Watts 2005; Lynett and Liu 2005; Tinti et al. 2006; Abadie et al. 2010) whereas simplified rheologies (viscous rheologies) have been considered for subaqueous spreading.

We pose our attention on the simulation of the initiation or generation by the rapid movement and impact of a landslide mass. In particular, we are interested in the simulation of a landslide mass, considered as a continuous deformable material, spreading along a slope, both under subaerial and submerged conditions, and its interaction with the water body.

We simulated some of the 2D experimental tests performed by Fritz (2002) and Sælevik et al. (2009) considering deformable masses or rigid blocks, to demonstrate the performance of the model. Furthermore, we present the 2D simulation of the Vajont rockslide and of the consequent wave along a well documented cross section (Rossi and Semenza 1965).

Materials and Methods

Numerical Model

We use a FEM code (Roddeman 2008; Crosta et al. 2006, 2009) adopting an Eulerian–Lagrangian method which guarantees accurate calculation results also for large deformations (see Crosta et al, in this proceedings volume). The numerical model uses isoparametric finite elements for space discretisation. We typically apply three-noded triangles in 2D, and eight-noded hexahedrals in 3D. For the 2D calculations we used 40,000–150,000 triangular three-node elements to discretize the 2D space with a mean element size ranging between 0.004 and 0.01 m. An implicit Euler time stepping, with automatic time step adjustment is adopted. The material is considered as a fully deformable elasto-plastic continuum. This makes a difference with the more commonly used approach adopting solution of the Navier–Stokes equation.

In the literature, water has been generally modelled using the Navier–Stokes equations, considering water either fully incompressible or nearly incompressible (Quecedo et al. 2004). The viscous contribution in these equations is relevant for small Reynolds numbers, whereas for large Reynolds numbers inertia and pressure dominate over viscosity. In the present study the velocity of soil and rock slides/avalanches impacting on the water surface tend to be quite high, so that we neglect viscosity. For the compressible part we apply a nearly incompressible penalty formulation:

$$\dot{p} = \lambda v_{i,i} \tag{1}$$

where $p^{\cdot}$ is the water pressure rate, $v_{i,i}$ denotes water velocity v_i gradient along the spatial x_i direction. A large value is chosen for the penalty factor, λ, so that the water behaves as a nearly incompressible fluid. On the other hand, the values should not be excessively high in order to prevent numerical problems with ill-conditioned system matrices or very small time steps needed to capture extremely fast pressure changes.

Then the equations adopted for the water domain are:

$$\rho \dot{v}_i = \sigma_{ij,j} + g_i \tag{2}$$

where ρ is the water density, v_i the water velocity along spatial x_i direction, σij is the water stress matrix which contains only a diagonal part $\sigma_{11} = \sigma_{22} = \sigma_{33} = p$, and finally g_i is the gravity force on the water.

Vajont Rock Slide

The October 9, 1963 Vaiont landslide (Semenza 1965; Semenza and Ghirotti 2000) is one of the most studied or analysed landslide case study (e.g. Broili 1967; Ciabatti 1964; Semenza and Ghirotti 2000; Hendron and Patton 1985; Müller 1964; Sitar et al. 2005; Vardoulakis 2000) because of its unusual nature, the catastrophic consequences and the unexpected effects, the availability of pre- and post-failure observations. The sliding mass (ca 275 million m^3 covering about 2 km^2) moved laterally some 360 m, and 140 m upward on the opposite valley flank, at an estimated average velocity of 20–30 m s^{-1}. The failure lasted about 50 s (Ciabatti 1964) and produced seismic shocks with a total duration of up to 97 s, inclusive of the signal generated by the water wave.

The water of the reservoir, which was filled to about two-thirds (ca 115 Mm^3, mean depth: 100 m), was completely displaced by the rockslide reaching 935 m a.s.l (235 m above the reservoir level). The wave swept across the dam reaching over 100 m above its crest.

On the basis of this data it is possible to compute a rough value of the slide Froude number ($Fr = v/(gh)^{1/2}$; v = slide velocity, h = reservoir water depth) ranging between 0.26 and 0.75. We performed both fully 2D and 3D slope stability and runout modeling (Crosta et al. 2007). Here we present

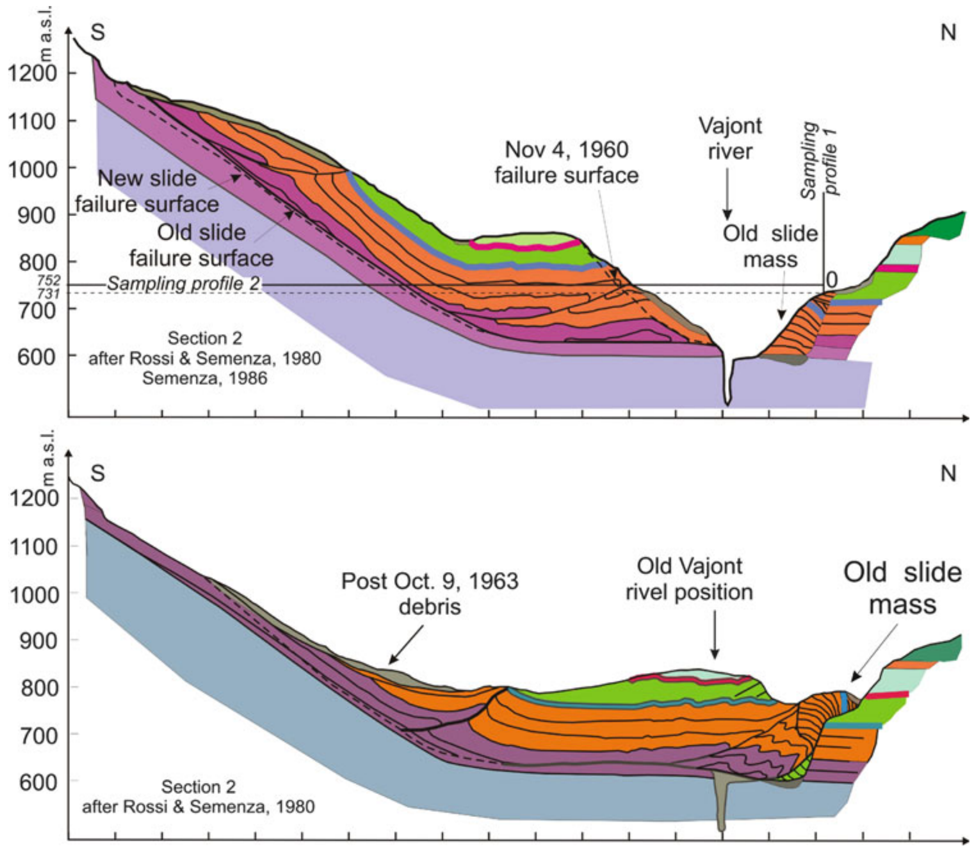

Fig. 1 Pre and post failure geologic cross sections corresponding to Sect. 2 by Rossi and Semenza (1965). Two sampling profiles used to sample velocities in the numerical model (see Fig. 3) are shown in the upper pre-failure cross section

a fully 2D modeling of the runout and impulse wave computed along the geologic cross section #2 (Figs. 1 and 2) by Rossi and Semenza (1965).

We use 71800 triangular elements with an average size of 4 m, of which 15,500 for the landslide, 1000 for the old landslide material and about 1800 for the water reservoir. We consider a Mohr-Coulomb material for the landslide ($\rho = 24$ kN/m^3; $\nu = 0.23$, $\phi = 17°$, $c = 300$ kPa) and along the basal plane ($\phi = 7.5°$, $c = 10$ kPa; see Skempton 1966; Hendron and Patton 1985; Tika and Hutchinson 1999), and lower properties for the old landslide material located on the opposite valley flank ($\phi = 13$–$7.5°$, $c = 100$ kPa to 10 kPa reduced according to a plastic strain softening model).

The landslide motion lasts about 30 s and water motion starts after 6–8 s from landslide onset. The water is progressively pushed upward against the opposite valley flank and reaches a maximum elevation of about 850 m a.s.l. after approximately 30 s since the initial movement. After that the water flows back and start oscillating till complete rest. This second phase does not correspond to the real event because most of the water was expelled laterally. In any case the water is not able to erode or drag the more superficial parts of the landslide material. The material slides along the failure surface with an internal deformation which results in a final arrangement very similar to the representation given by Rossi and Semenza (1965; see Fig. 1).

During the movement the upslope sector compact and partially step over the lower sector. On the other hand, the old landslide material is deformed and pushed slightly upward along the opposite valley flank. The water velocity sampled along the vertical and horizontal profiles (1 and 2 in Fig. 1) is plotted in Fig. 3 and allows a more detailed analyses (time steps = 2 s). Along the vertical sampling profile the velocity wave propagates upward for about 25 s and then it is followed by a progressive decrease up to 32 s. The maximum elevation (ca. 845 m a.s.l.) is reached after 38 s.

Along the horizontal sampling profile (#2), it is observed that the water close to the opposite valley side is still at rest till 20 s, when the wave motion induces the maximum velocity (ca 21 m s^{-1}). The peak velocity decreases progressively up to 30 s and it is followed by a progressive slowdown.

Fritz's Water Tank Tests

Among the tests performed by Fritz (2002) releasing granular landslides in a 7.5 m long water tank, we chose the case

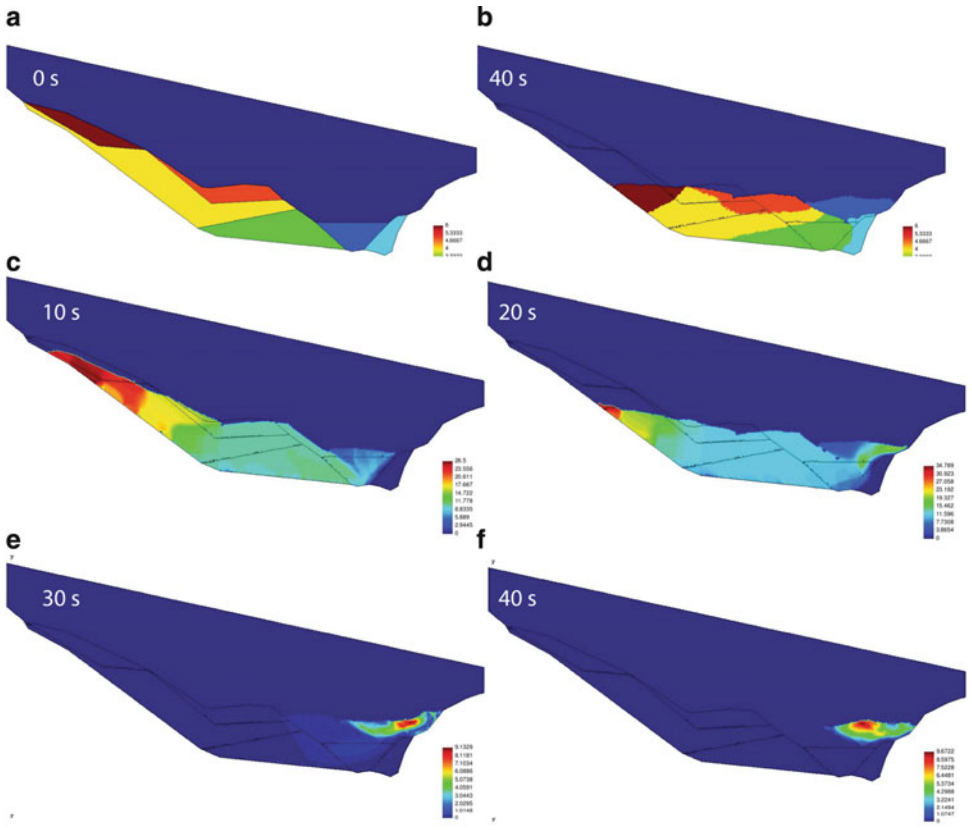

Fig. 2 (**a**) and (**b**) Material geometry for the numerical model of the Vajont rockslide at 0 s and 40 s along same section of Fig. 1. (**c–f**) Landslide and water velocity (m s^{-1}) at four different time steps (10, 20, 30 and 40 s). Colour legends are differently scaled to evidence velocity distribution

of an outward collapsing impact crater. In the experimental setup the slope inclination is 45°, the water depth 0.3 m, the granular slide 0.6 m long and 0.118 m thick with an initial velocity of 5.2 m s^{-1}.

The adopted properties for the granular landslide are $\rho = 18$ kN/m^3; $\nu = 0.23$, $E = 10^4$ kPa, $\phi = 43°$, whereas along the basal surface $\phi = 24°$, and water bulk compressibility modulus equal to 10^4 kPa. We use 76,200 linear-triangular elements, with an average length of 0.02 m, of which 370 elements to discretize the landslide and 12,800 for the water. The soil material impact on the water occurs after 0.13 s. The velocity at the impact is 5.4 m/s (experimental: 5.49 m s^{-1}), the length of the material "box" is 0.68 m (exp.: 0.764 m), the thickness is 0.118 m (exp.: 0.093), and the calculated Froude number is 3.15 (exp.: 3.2). Figure 4 clearly shows the impact of the granular material, the deformation of the front transforming in curved and steep snout, the flow separation and the successive rising of the wave.

The evolution of the slide material is more discernible in Fig. 5. The slide tends to elongate and thin along the initial subaerial slope and after the impact gets a little bit shorter and starts developing a pronounced snout front. The front is steep and convex whereas the back progressively thin till the end of motion when the landslide tail stops just beyond/at the submerged slope toe.

At 0.24 s the frontal part of the slide is torn off by the water action and starts to develop a sort of backward tilted plume that rejoin the upper slide material before 0.7 s.

The collapse of the crater on the upper part of the landslide occurs when the landslide has already reached the bottom of the tank. After about 0.84 s a small part of the flow flows back towards the sloping bed, while a large part of the flow moves towards the right generating a primary wave. This wave moving along the tank is shown passing through a vertical cross section located at 3.3 m from the slope toe (Fig. 6). The symmetry of the primary wave appears clearly from the similarity of the velocity profiles during the transit of the ascending and descending flanks. Furthermore, we observe that the velocity is almost constant along the entire profile excepted when reaches the peak.

Aknes Rockslide: Sælevik's et al.

A series of wave tank experiments were preformed by Sælevik's et al. (2009) to model the landslide tsunami that could occur because of the Aknes rockslide (Norway, Blikra et al. 2005) rapid collapse. The water depth was 0.6 m and a smooth transition connected the 35° slide plane with the tank bottom. The slide was represented by means of a series of

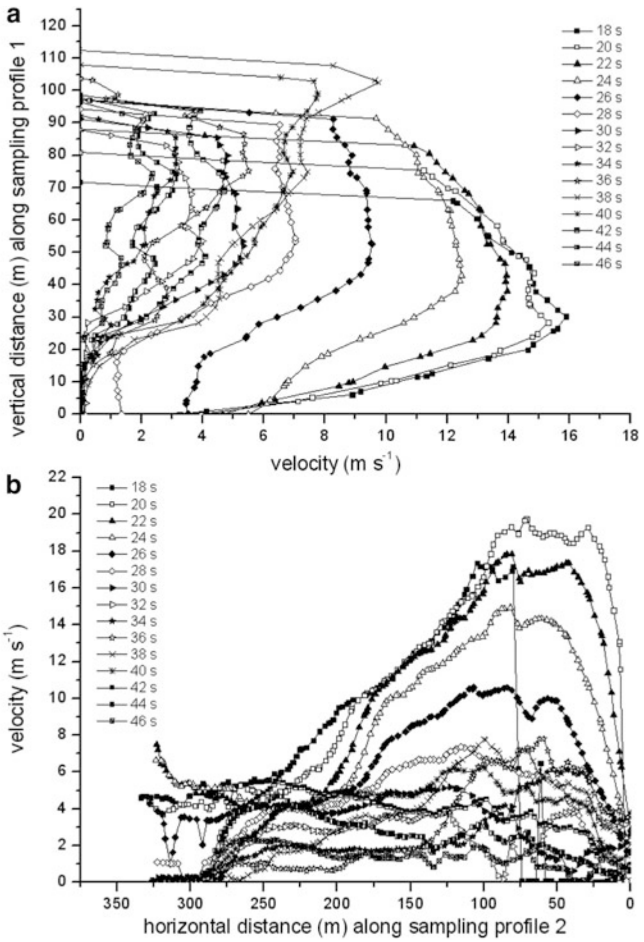

Fig. 3 Water velocity computed at different time steps along (**a**) a vertical profile and (**b**) an horizontal profile (shown in Fig. 1) for the 2D modelling of the Vajont rockslide

rigid box modules with a front angle of 45° (0.5 and 0.6 m in length, 0.12 and 0.16 m in height, and 45 cm wide) amounting to a total length of 1, 1.6 and 2 m. Initial velocity was controlled by means of a conveyor belt.

We chose the scenario # 2 by Saelevick et al., with a 0.16 m box height and a total length of 1 m, an initial velocity of 3.38 m s^{-1}, and a Froude number equal to 1.4. We used 63,500 triangular elements with an average size of 0.02 m, 840 for the boxes and 32,500 for the water in a 9.14 m long tank. The boxes have been considered deformable ($\rho = 18$ kN/m^3; $\nu = 0.23$, $E = 10^5$ kPa, $\phi = 43°$, $c = 0$ kPa) to avoid impact of the front wedge-shaped block with the bottom of the tank. For the basal plane we adopted a basal friction angle $\phi = 24°$.

We assigned a bulk compressibility modulus to the water equal to 10^4 kPa. This experiment is an example of a backward collapsing crater.

Figure 7 shows the backward collapse occurring after the formation of the water crater. The crater closes progressively over the surface partially by collapsing and by backward flow over the back of the slide material and finally it originates a splash rising along the sloping ground.

At this moment the flow diverges and this becomes at 0.50 s when a clear rounded crest develops with a small part of the water flowing backward and the primary wave moving to the right.

The propagation of the primary wave is well represented by the horizontal velocity profiles sampled along a vertical profile located 3 m from the slope toe (see Fig. 8). As in the previous case, the velocity remains almost constant along

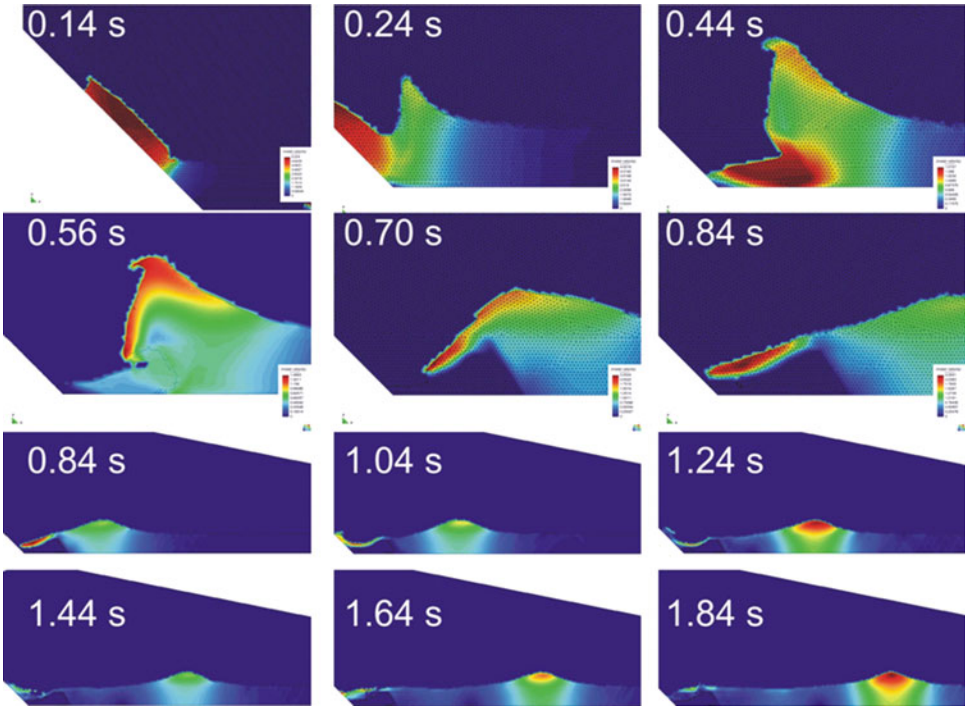

Fig. 4 Velocity field (m s^{-1}) computed for an impact velocity of 5.4 m s^{-1} of a 0.118 thick granular slide, Fr = 3.15 showing an outward collapsing impact crater

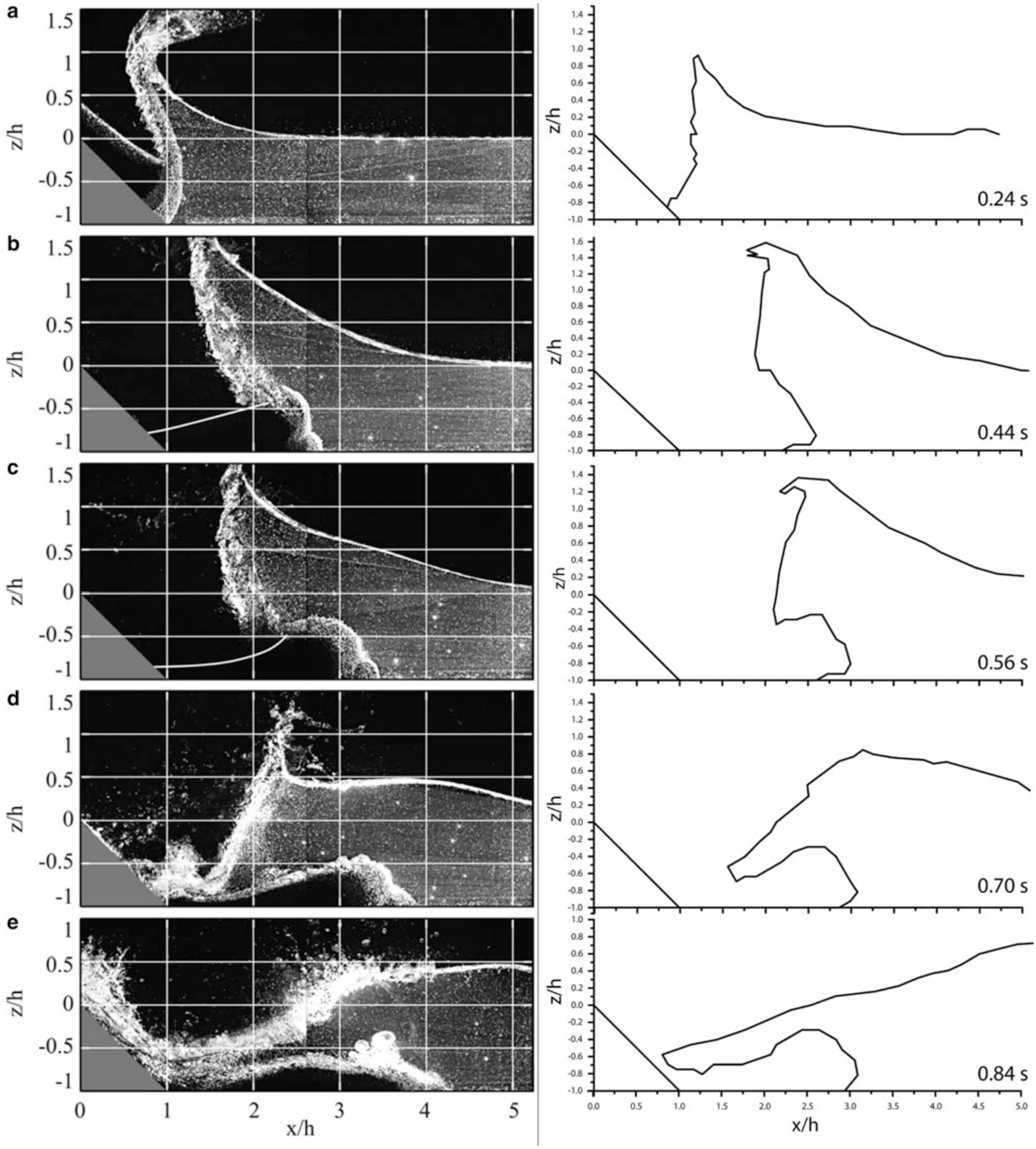

Fig. 5 Comparison of the observed (Fritz 2002, on the *left*) and computed wave profiles (on the *right*) for the same times. Slight differences could derive by small initial differences in impact velocity, material deformability and exact timing

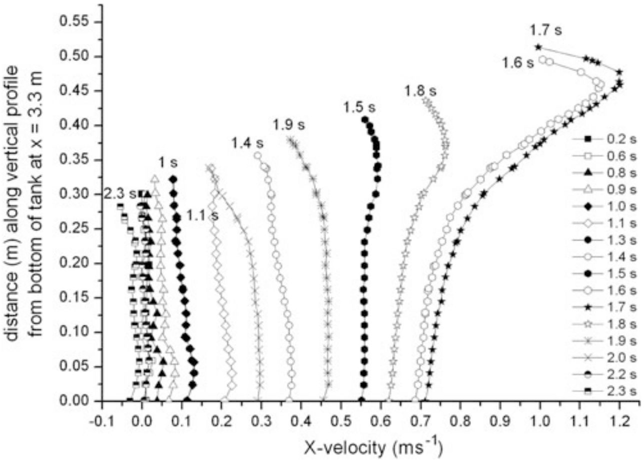

Fig. 6 X-velocity component at different time steps computed along a vertical profile positioned at 3.3 m from the slope toe. The constant velocity value along the profile at different time steps is evident

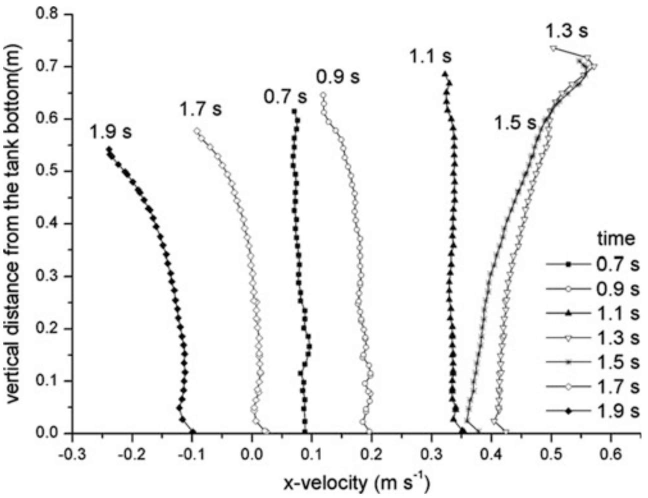

Fig. 8 X-Velocity component computed at different time steps along a vertical profile, located at x = 3 m, for the 2D modelling of Aknes rockslide-Sælevik's et al. (2009) experiment

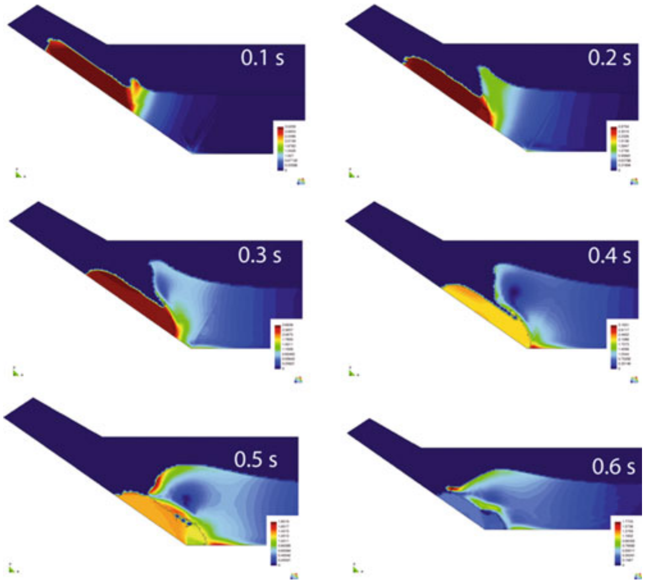

Fig. 7 2D modelling of Aknes rockslide – Sælevik's et al. (2009) experiment. The velocity field (m s^{-1}) computed for an impact velocity of 3.38 m s^{-1} of a 1 m long "deformable" granular slide (Fr = 1.4) is presented. A backward collapsing impact crater develops during the modeling. Original experiments have been completed by using an underfomable block

the entire profile suggesting an intermediate-shallow water character (Heller 2007).

Discussion

Various authors have suggested, observed and evaluated the relevance of material properties, deformability, landslide length, profile and front shape, landslide velocity and duration, on the generation of impulse wave both in the near- and in the far-field, and as a consequence also on the tsunami hazard assessment. Nevertheless, very few studies have tried and succeeded at simulating these ensemble of elements. On the contrary, some studies consider only an instantaneous change in properties at the transition from subaerial to subaqueous conditions but completely omit the impact at the water surface and the effects on the landslide.

By using a FEM code (Roddeman 2008) we have performed a set of simulations to verify its modeling capabilities. Three different examples have been modeled, characterized by different geometries and slide Froude number: 0.25–0.9, 3.15 and 1.4. The Vajont case study is an extreme case where the water reservoir is much smaller than the slide and due to the slide the reservoir bottom is raised during the motion. In all the cases the main features have been simulated in 2 dimensions, but the code capabilities have been demonstrated also at simulating 3D events (see Crosta et al., these proceedings). Impulse wave characteristics will be probably very different in 3D conditions, because of the radial energy dissipation and the combined effects of slide thickness and breadth. We are currently performing some 3D modeling to evaluate model capabilities and sensitivity.

In the present set of simulations no water seepage is considered but its role cannot be excluded in controlling the propagation and final geometry of the landslide and could be a further step in the development of the approach. At the same time the models considers only the presence of one fluid (water) and exclude the possible effects related to the presence of air. This could play a certain role during the impact crater collapse and the successive slowing of the landslide by the release of air from the granular mass and the progressive water saturation.

Acknowledgments This study has been partially funded by the EC Safeland Project, GA No.: 226479, Living with landslide risk in Europe: Assessment, effects of global change, and risk management strategies.

References

Abadie S, Morichon D, Grilli S, Glockner S (2010) Numerical simulation of waves generated by landslides using a multiple-fluid-Navier–Stokes model. Coastal Eng 57:779–794

Blikra L, Longva O, Harbitz C, Løvholt F (2005) Quantification of rock-avalanche and tsunami hazard in storfjorden, western norway. In: Senneset K, Flaate K, Larsen JO (eds) Landslides and Avalanches, ICFL 2005 Norway. Taylor & Francis, London, pp 57–64

Broili L (1967) New knowledge on the geomorphology of the Vaiont Slide slip surfaces. Rock Mech Eng Geol J Int Soc Rock Mech V (1):38–88

Ciabatti M (1964) La dinamica della frana del Vaiont. Giornale di Geologia XXXII(I):139–154

Crosta GB, Imposimato S, Roddeman DG (2006) Continuum numerical modelling of flow-like landslides. In Evans SG, Mugnozza GS, Strom A, Hermanns RL (eds) NATO ARW, landslides from massive rock slope failure. NATO science series, Earth Environ Sci 49:211–232

Crosta GB, Frattini P, Imposimato S, Roddeman D (2007) 2D and 3D numerical modeling of long runout landslides – the Vajont case study. In: Crosta GB, Frattini P (eds) Landslides: from mapping to loss and risk estimation. IUSS Press, Pavia, pp 15–24

Crosta GB, Imposimato S, Roddeman D (2009) Numerical modeling of 2-D granular step collapse on erodible and nonerodible surface. J Geophys Res 114:F03020

Fritz HM (2002) Initial phase of landslide generated impulse waves. Thesis Versuchsanstalt für Wasserbau, Hydrologie und Glaziologie, ETH Zürich, Swiss ETH No. 14'871. Swiss Federal Inst. Techn., Zürich, ISSN 0374–0056

Grilli ST, Watts P (2005) Tsunami generation by submarine mass failure part I: modeling, experimental validation, and sensitivity analysis. J Waterw Port Coast Ocean Eng 131(6):283–297

Grilli ST, Vogelmann S, Watts P (2002) Development of a 3D numerical wave tank for modeling tsunami generation by underwater landslides. Eng Anal Bound Elem 26(4):301–313

Harbitz CB (1992) Model simulations of tsunamis generated by the Storegga slides. Mar Geol 105:1–21

Heller V (2007) Landslide generated impulse waves: prediction of near field characteristics. Thesis, ETH Zürich, Swiss ETH No. 17531. Swiss Federal Inst. Techn., Zürich

Heller V, Kinnear RD (2010) Discussion of "experimental investigation of impact generated tsunami; related to a potential rock slide, Western Norway" by Sælevik G, Jensen A, Pedersen G [Coastal Eng. 56 (2009) 897–906]. Coastal Eng 57:773–777

Hendron AJ, Patton FD (1985) The Vaiont slide, a geotechnical analysis based on new geological observations of the failure surface. Tech Rep GL-85–5, 2 vols. Department of the Army, US Corps of Engineers, Washington, DC

Huber A (1980) Schwallwellen in seen als floge von felssturzen (reservoir impulse waves caused by rockfall), technical report mitteilung 47, Lab. hydraulics, hydrology and glaciology, ETH

Huber A, Hager WH (1997) Forecasting impulse waves in reservoirs, Comminsion Internationale des Grands Barrages, 19 Congres des Grand Barrages. Florence 1997:993–1005

Jiang L, LeBlond PH (1993) Numerical modeling of an underwater Bingham plastic mudslide and the wave which it generates. J Geophys Res 98:304–317

Kamphuis JW, Bowering RJ (1970) Impulse waves generated by landslide. In: Proceedings of 12th coastal engineering conference, pp 575–588

Keating BH, McGuire WJ (2000) Island edifice failures and associated tsunami hazards. Pure Appl Geophys 157:899–955

Lynett P, Liu PL-F (2005) A numerical study of the run-up generated by three-dimensional landslides. J Geophys Res 110:C03006, 16 pp., doi: 10.1029/2004JC002443

Miller D (1960) Giant waves in Lituya Bay Alaska. USGS Prof Paper 354-C:51–83

Müller L (1964) The rock slide in the Vaiont valley. Rock Mech Eng Geol 2(3/4):148–212

Müller D (1995) Auflaufen und uberschwappen von impulswellen an talsperren (run-up and overtopping of impulse waves at dams), technical report mitteilung 137, Lab. of hydraulics, hydrology and glaciology, ETH

Panizzo A, De Girolamo P, Di Risio M, Maistri A, Petaccia A (2005) Great landslide events in Italian artificial reservoirs. Nat Hazard Earth Syst Sci 5:733–740

Quecedo M, Pastor M, Herreros MI (2004) Numerical modelling of impulse wave generated by fast landslides. Int J Numer Methods Eng 59:1633–1656

Roddeman DG (2008) TOCHNOG user's manual. FEAT, 255 pp., www.feat.nl/manuals/user/user.html

Rossi D, Semenza E (1965) Carte geologiche del versante settentrionale del M. Toc e zone limitrofe, prima e dopo il fenomeno di scivolamento del 9 ottobre 1963, Scala 1:5000, Ist. Geologia Universit'a di Ferrara, 2 Maps

Sælevik G, Jensen A, Pedersen G (2009) Experimental investigation of impact generated tsunami; related to a potential rock slide, Western Norway. Coastal Eng 56(9):897–906

Semenza E (1965) Sintesi degli studi geologici sulla frana del Vaiont dal 1959 al 1964. Mem Mus Trident Sci Nat A XXIX–XXX (16):1–51

Semenza E, Ghirotti M (2000) History of 1963 Vaiont Slide. The importance of the geological factors to recognise the ancient landslide. Bull Eng Geol Environ 59:87–97

Sitar N, MacLaughlin MM, Doolin DM (2005) Influence of kinematics on landslide mobility and failure mode. J Geotech Geoenviron Eng 131(6):716–728

Skempton AW (1966) Bedding-plane slip, residual strength and the Vaiont landslide. Géotechnique XV(1):82–84

Tika Th E, Hutchinson JN (1999) Ring shear tests on soil from the Vaiont landslide slip surface. Geotechnique 49(1):59–74

Tinti S, Pagnoni G, Zaniboni F (2006) The landslides and tsunamis of the 30th of December 2002 in Stromboli analyzed through numerical simulations. Bull Volcanol 68:462–470

Vardoulakis I (2000) Catastrophic landslides due to frictional heating of the failure plane. Mech Coh Frict Mat 5:443–467

Ward SN, Day S (2003) Ritter Island Volcano—lateral collapse and the tsunami of 1888. Geophys J Int 154:891–902

Zweifel, A. (2004). Impulswellen: Effekte der Rutschdichte und der Wassertiefe. Ph.D thesis, ETH Zurich, Zurich

Dynamics, Velocity, and Run-Out of Subaqueous Rock Avalanches

Fabio Vittorio De Blasio

Abstract

Two models are introduced for the rheology and dynamics of subaqueous rock avalanches. Both models stem from the premise that the initial rock slab is rapidly transformed into a fragmented medium. The first model is based on hydroplaning; however, if hydroplaning occurs, it can start only after sufficient fragmentation, and with a permeable matrix. In a second model, the fragmenting rock absorbs water in its matrix, thus changing into a non-hydroplaning cohesive flow that progressively loses strength. Numerical simulations and theoretical considerations show that both processes are theoretically possible.

Keywords

Fragmentation • Subaqueous rock-avalanche • Landslide dynamics

Introduction

The dynamics of subaqueous landslides is still poorly known. Recently, increased availability of field data and computational tools, growing interest for offshore petroleum exploration, and awareness of tsunami hazards represented by landslides, has led to improved interest in the dynamics of submarine mass movements. While some (termed generically “debris flows”) originate from clastic material, rock avalanches on land as well as in water environment derive from the failure or huge rock portions. Most subaqueous rock avalanches have occurred at the flanks of hotspot islands such as the Canary or the Hawaii, but also the Lesser Antilles (Urgeles et al. 2003; Hildenbrand et al. 2006; Lipman et al. 1988; Mitchell et al. 2002; Masson et al. 2002; Deplus et al. 2001).

Some researchers have analyzed the mobility of subaerial landslides on an H/R-volume plot where the volume for a large number of events is reported in abscissa, and the ratio between the fall height H and the run-out R are reported on the ordinate scale. Data for both debris flows and rock avalanches (Fig. 1) exhibit a marked decrease of the **ratio** H/R as a function of the volume, implying an increase of mobility with the volume. While this “volume effect” is understandable for debris flows, the frictional rheology of dry granular flows would predict a constant ratio H/R as a function of the volume.

When similar graphs are realized for *subaqueous* landslides, something even more puzzling becomes apparent (De Blasio et al. 2006a). In Fig. 1, the data for subaqueous landslides have been divided into three groups: subaqueous debris flows, subaqueous rock avalanches, and isolated blocks. The ratio H/R of subaqueous rock avalanches falls approximately on the same fit line of the subaerial rock avalanches, which indicates that subaqueous rock avalanches are not intrinsically more mobile than their subaerial counterparts. In contrast, debris flows of the same volume exhibit an apparent friction coefficient some 10 times lower.

F.V. De Blasio (✉)
Department of Geosciences, University of Oslo, Oslo, Norway

NHAZCA S.r.l., spin-off “Sapienza” Università di Roma,
Via Cori snc, Rome 00177, Italy
e-mail: fvblasio@geologi.uio.no

C. Margottini et al. (eds.), *Landslide Science and Practice*, Vol. 5,
DOI 10.1007/978-3-642-31427-8_7, © Springer-Verlag Berlin Heidelberg 2013

Subaqueous Debris Flows

Although this contribution deals with subaqueous rock avalanches, it is useful to start the discussion with subaqueous debris flows, which are perhaps better studied.

The glacial clay-rich Bear Island mudflows (Barents sea) appear as parallel lobes, which exhibit long run-out (>150 km) despite an average slope of only 0.7°, which corresponds to $H/R = 0.012$ (De Blasio et al. 2006a). Mudflow lobes are about 30 m thick and 10 km wide. The neat tongue-like appearance of lobes has been preserved during such long travel (Elverhøi et al. 2002). This tends to exclude sediment dilution of the clay-rich material as viable explanation of the high mobility. The lack of granular fraction should in principle ensure a relatively “simple” rheology for the mudflow. Yet it is very difficult to explain the observed runout with shear strengths greater than a fraction of kPa, corresponding to a diluted slurry rather than a mudflow with well defined outline.

Researchers have run experiments in the laboratory with small-scale subaqueous debris flows (Mohrig et al. 1998; Ilstad et al. 2004; Breien et al. 2007), in which an artificial slurry is prepared by mixing clay, sand, and water. The material is then released either along a flume with confining walls, or in open pool. Lubrication of clay-rich slurries by a water layer intruded underneath, named hydroplaning, has been identified in such experiments (Mohrig et al. 1998). Based on the laboratory results, hydroplaning has been invoked to explain the long run-out observed in nature for mudflows and debris flows rich in cohesive component.

Hydroplaning is controlled by a balance between the dynamic pressure at the front of the debris flow (Mohrig et al. 1998).

$$P_F \approx \frac{1}{2}\rho_W U_F^2 \tag{1}$$

and the overburden pressure at the base

$$P_{BASE} \approx \Delta\rho\, g\, D\;\cos\beta \tag{2}$$

where U_F is the front velocity, ρ_W is the density of ambient water, D is the debris flow thickness, ρ is the density of the debris flow, β is the slope angle, g is gravity acceleration, and $\Delta\rho = \rho - \rho_F$. When $P_F > P_{BASE}$, the front of the debris flow rises slightly, facilitating the formation of a lubricating water corridor underneath. The condition for hydroplaning can be conveniently written as

$$U > Fr_C\sqrt{\frac{2\,\Delta\rho\, g\, D\;\cos\beta}{\rho_W}} \tag{3}$$

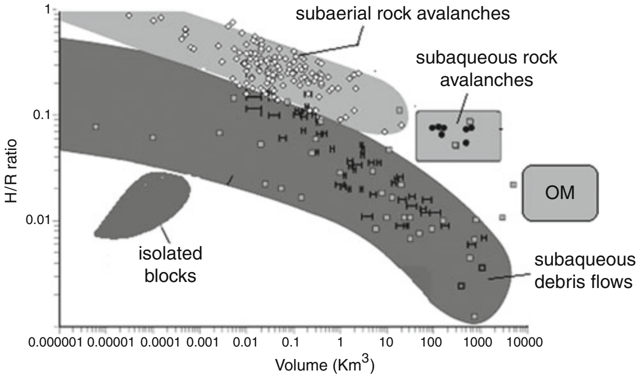

Fig. 1 Position of the subaerial and subaqueous rock avalanches and of the subaqueous debris flows on the plane H/R – volume, where H is the fall height and R is the run-out. From De Blasio et al. (2006a), modified. While rock avalanches take origin from the collapse and fragmentation of large sectors of initially intact rocks, debris flows are cohesive from start as they normally contain a fine matrix. In analyzing data with this kind of plot, it is necessary to remember that the H/R ratio also depends on the geometry of failure. On land, landslides are usually more mobile when travelling along channels rather than unconstrained. However, the majority of submarine landslides travel unconstrained. “Isolated blocks” are rigid blocks that outrun the front of submarine landslides. The area “OM” refers to the landslides of the Olympus Mons on Mars (see further)

where $Fr_C \approx 0.3$ is the critical densimetric Froude number in correspondence of which hydroplaning starts. For example, a debris flow of density of 1.7 $Kg\ m^{-3}$ and thickness 10 m could start hydroplaning at a speed of the order 3–4 m/s. In an equivalent description, one can introduce a lift coefficient C_L and cast the condition for hydroplaning in the form $U > \sqrt{2\rho\, g\, D/(C_L \rho_W)}$. The coefficient is difficult to determine because of its dependence on the shape of the debris flow snout.

The lifting up of the debris flow results in diminished contact with the bed. Shear resistance becomes reduced from a value of the order of the shear strength τ_y to $\approx \mu_W U/D_W$ where $U,\ \mu_W,\ D_W$ are respectively the debris flow velocity, the water viscosity, and the water layer depth.

Even though hydroplaning has been unambiguously observed in the laboratory, it has never been seen to take place also in natural debris flows. It appears, however, as a natural process occurring under general conditions. It is interesting that hydroplaning may occur spontaneously in simple systems such as cleaning liquid poured in water. A simple test shows debris flows lobes similar, albeit to a much smaller scale, as those of the Bear Island fan (Appendix A).

Concerning isolated blocks (see Fig. 1), hydroplaning is the sole plausible explanation for their extraordinary runout up to some tens of Km along nearly flat areas. Such blocks were pulled up from the terrain by the lift force. They “floated” on top of a water layer avoiding friction with the terrain (De Blasio et al. 2006b), as demonstrated by small-scale experiments (Engvik et al., private communication).

We now turn our attention to the main topic of this contribution: subaqueous rock avalanches.

Subaqueous Rock Avalanche Deposits

On land, rock avalanches (called also “sturzstroms” when massive) are catastrophic landslides initiating with the failure of a rock slab that disintegrates and moves rapidly as a granular flow (Hungr et al. 2001). They may attain enormous volumes (maximum recorded volumes of the order $2 \times 10^{10}\, m^3$ and long runouts up to 20 km) and are an important factor in the geomorphological evolution and reshaping of the earth surface. In the subaqueous environment, rock avalanches reach volumes of the order $3 \times 10^{12}\, m^3$.

One of the most evident characteristics of subaerial rock-avalanches is the fragmented state of the deposits (e.g. Pollet and Schneider 2004; Crosta et al. 2007 Locat et al. 2006). Evidently, the mechanisms of fragmentation are capable to drastically reduce the blocks size during the flow from hundred-meter slabs down to powder-size grains. The smallest grains may be of the order 10–100 nm in size. The fragmentation processes are likely to be less powerful in subaqueous rock avalanches, as testified by the presence of huge blocks in the deposits. This is probably a consequence of the buffering effect of water in rock crushing and also to the more regular slope path (Mazzanti and De Blasio, this volume and references therein).

Concerning the Canary rock avalanches, blocks of some hundreds metres to 1–2 km across have been reported (Urgeles et al. 2003). The Canary Islands are considered in more detail in the present study, and in particular a large rock avalanche in the island of El Hierro. The scarp, partly above sea level, merges with a 200 m thick submerged deposit which widens in the ocean bottom developing a broad fan. The slide is about 70 km long and has volume of $150 - 180 km^3$.

A Simple Estimate of Velocity, Run-Out, and Effective Friction of Subaqueous Rock Avalanches

As a starting point, it is interesting to estimate the coefficient of friction that would be necessary to recover the run-out of a rock avalanche with the geometrical properties and volume of the El Hierro. In a simple approach, here called the “rigid block model”, the landslide is modelled like a slab of width 25 km, height of 200 m and length 30 km for a total volume of 150 km^3. Coulomb-frictional resistance acts at the base of the slab in contact with the sea floor. Ambient water exerts a drag force on the slab. The equation of motion for the slab is solved with the drag coefficients and added mass as explained in De Blasio (2011a). The drag force influences dramatically the motion of subaqueous rock avalanches. While for subaerial rock avalanches the friction coefficient in the Coulomb frictional resistance is equal to the ratio H/R for the centre of mass, the drag force breaks this simple rule in a subaqueous rock avalanche. Hence, the ratio H/R must be determined solving numerically the equation of motion with a realistic slope path. The presence of blocks carried on top of the rock avalanche as those observed in the deposits offer more resistance to flow than a smooth surface. The skin friction coefficient is estimated from Schlichting’s formula of the order $0.0167 < C_F < 0.0433$ where the extremes are found with a roughness of 100 m and 1 km respectively, and the characteristic length is taken of the order 10 km. A value $C_F = 0.02$is used in the calculations.

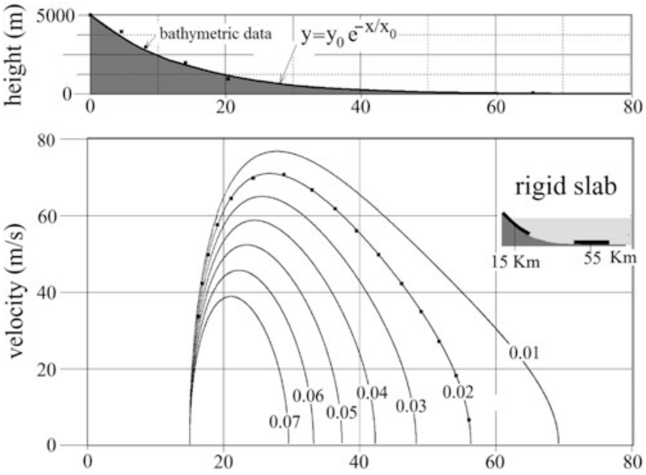

Fig. 2 Simulation of a block sliding on the ocean floor with characteristics and slope path compatible to El Hierro subaqueous rock avalanche. The synthetic slope path of the exponential form (as indicated) with characteristic length of 14 km appears as a good approximation to the bathimetric data (squares). The height, width, and length used in the simulation are respectively 200 m, 25 km, and 30 km

The velocity of the slab as a function of the distance of the centre of mass is shown in Fig. 2 for different values of the friction coefficient. The friction coefficient that reproduces the data best is 0.02, giving a final position of the centre of mass at 55 Km, and the avalanche front at the maximum run-out observed of 70 Km. The maximum velocity reached by the rock avalanche is of the order 70 m/s, or 250 Km/h. This is a quite high value compared to the best measured velocity (28 m/s) of the Canadian Grand Banks slide of 1929. The maximum velocity of 28 m/s was observed at a slope angle of only 0.33°, far lower than the 15–20° at the top of the El Hierro chute. The remarkable difference between the simulated velocity of El Hierro and that observed for the Grand Banks is likely due to the much gentler slope offshore

Newfoundland compared to the Canary Islands. Because the Grand Banks landslide created a significant tsunami up to 9 m high that killed several people some hundred Km from the epicentre, it is apparent that a rock avalanche of high velocity as the one of the El Hierro would be highly destructive. How to explain a coefficient of the order of 0.02 for El Hierro?

Consider the following result: repeating the calculation with one thousandth of the volume considered in Fig. 2 (i.e., 0.15 km^3), the distance would be only 18 km. In other words, for a fixed friction coefficient the simulation indicates that mobility increases with size. This is because the gravity increases with the volume of the rock avalanche, while the drag force increases with the surface area. This implies that single isolated blocks will travel to shorter distance than large ones (the issue is more complicated because also the lift force increases with the surface area; we neglect these complications for a moment). Thus, we cannot envisage subaqueous rock avalanches as single blocks travelling independently. It is likely that despite the fragmented state, rock avalanches travel as a whole.

The figure below shows the velocity as a function of the position of the middle of the slab (the centre of mass). The numbers indicate the coefficient of friction. The simulation that fits the run-out best is highlighted with dots; it returns peak velocities of the order 70 m/s. Note how the friction coefficient should be considerably low (of the order 0.02) for the slab centre of mass to reach the observed distance of about 55 Km and the front the distance of 70 km.

Model 1: Hydroplaning in a Fragmenting Rock Avalanche

A first model for subaqueous rock avalanche flow invokes hydroplaning. Compared to subaqueous debris flows, there is one more complication due to the fact that a rock avalanche has to fragment thoroughly before hydroplaning can set in.

The fall of a rock avalanche on land is accompanied by a tremendous fragmentation ending up with an ensemble of grains that range from sub-millimetric size to huge blocks (Crosta et al. 2007). Hydraulic conducivities measured for the fragmented material of the Val Pola rock avalanche give permeability between $10^{-9} - 10^{-14}\,m^2$. Water buffers dramatically the fragmentation effect in a subaqueous rock avalanche (Mazzanti and De Blasio, this book). Added to the effect of gentler slope path compared to land, this leads to the qualitative prediction that subaqueous rock avalanches are more coarse-grained than subaerial rock avalanches.

Hydroplaning necessitates a low permeability of the subaqueous rock avalanche, else the water underneath the slab will penetrate from the basal region at high pressure through the bulk of the rock avalanche and so dissipate the water layer. Let us model the granular permeable medium as an ensemble of spherical blocks of diameter ϕ in a regular cubic lattice of spacing a. The voidage ratio (volume fraction of voids) is $\varepsilon = 1 - (\pi/6)(\phi/a)^3$. The velocity u of water through the granular medium is given by the Ergun relation (Rhodes 2008)

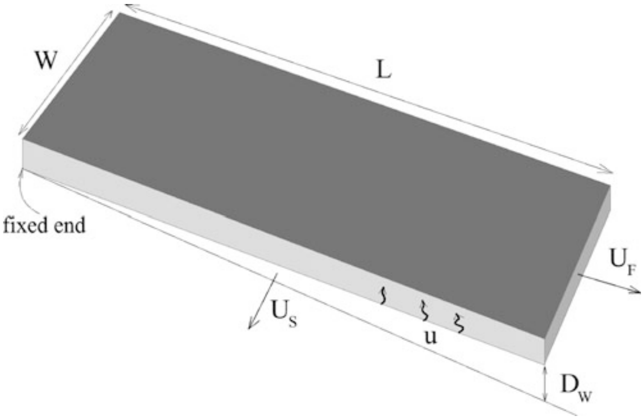

Fig. 3 For the analysis of a porous hydroplaning slab as a model for hydroplaning rock avalanche

$$\left|\frac{\partial P}{\partial y}\right| \approx 150\frac{\mu\,u}{\phi^2}\frac{(1-\varepsilon)^2}{\varepsilon^3} + 1.75\frac{1-\varepsilon}{\varepsilon^3}\frac{\rho_F\,u}{\phi} \tag{4}$$

where ρ_F is the fluid density, ρ is the density of the medium, μ is the water viscosity. The first and second addenda on the right hand side of (4) represent respectively the contribution of the laminar and turbulent flow throughout the granular medium. If the rock avalanche hydroplanes, the pressure gradient is of the order $\partial P/\partial x \approx \Delta\rho\, g$. The average thickness of the water layer δ during hydroplaning changes like

$$\frac{d\delta}{dt} \approx U_F\frac{D_W}{L} - U_S\frac{D_W}{W} - u \tag{5}$$

where U_S is the average velocity of water escaping at the sides, D_W is the thickness of the water layer at the snout, W and L are respectively the rock avalanche width and length, which may change during the flow. The first and second terms on the right hand side of (5) are the water intake at the front and water loss at the sides (Fig. 3). For a geometry like that in Fig. 3, evidently $\delta \approx D_W/2$. Note that according to (5), while a widening of the rock avalanche will promote increase of the water layer thickness, stretching will decrease it. If the water intake at the front is comparable to that exiting at the sides, then the value of u becomes determinant for the persistance of the water layer. For hydroplaning to be sustained, $u \ll u_{CRIT} = \delta/T$ where $T \approx 10^3\ s$ is the typical travel duration of the rock avalanche. The critical velocity u_{CRIT} of water in the granular medium turns out to be $u_{CRIT} \approx 1 - 10\ mm/s$. Equation 4 gives $u \approx 0.4\ mm/s,\ 34\,mm/s,\ 0.3\ m/s$ for particle diameters $\phi = 0.1\,mm$, $1\,mm$, $10\,mm$ respectively. So in order to ensure the persistence of hydroplaning, there should be a matrix of particles some fraction of mm across. Whether this fine component forms during the flow of a rock avalanche, is an open question.

Model 2: Water Assimilation in the Fragmenting Rock Avalanche

Model 2 is based on the idea that fragmentation and water assimilation in the pores will progressively decrease the material strength. Weathered basaltic rock starts with a shear strength of $\tau_{y,0} = 5$ MPa, a value representative for the flanks of Hawaii (Schiffmann et al. 2005) and is assumed to lose strength as

$$\tau_y = \tau_{y,\infty} + \left(\tau_{y,0} - \tau_{y,\infty}\right)\exp(-\gamma(t)\,\Gamma) \tag{6}$$

where Γ is a constant, $\tau_{y,\infty}$ is the final value of the shear strength, and

$$\gamma(t) = \int_0^t \left|\frac{\partial U}{\partial y}\right|_{y=0} dt \tag{7}$$

is the total shear at the base of the rock avalanche. The framework to calculate the rock avalanche shape and velocity is a modified version of the BING model (Imran et al. 2001). Different calculations have been performed. Figure 4 shows the results of the simulation that reproduced the data best with a residual shear strength of 60 kPa. According to the relations presented by Locat and Lee (2001), this residual strength would correspond to a mass fraction of water about 50 % for a clay-silt slurry corresponding to a volume fraction of 73 % of water, which gives an idea of the amount of water ingested. The panels in A show four snapshots of the landslide profile. B and C show respectively the front velocity as a function of the position and of time. Note that the peak velocity (65 m/s) is comparable to the one calculated with the slab model of Fig. 2.

Subaqueous Rock Avalanches on Mars?

Understanding the dynamics of subaqueous rock avalanches on Earth may also provide some hint on the climatic evolution of Mars. With its 24 km above the average level and some 500–600 Km in diameter, the Olympus Mons on Mars is the highest and one of the largest volcanoes on Mars and in the whole solar system (Fig. 5). Around the main edifice, there appear several gingantic semicircular halos surrounding the volcano some hundred km from the caldera. The composite deposit has been termed the “aureole”, a name deriving from the expression for “golden” in Latin. Strictly speaking, the aureole is the mysterious haze surrounding the holy personages in sacred icons and paintings; its adoption to denote the structures around Olympus Mons seems appropriate, considering its awesome magnificence accompanied to the riddle of its formation. Among the morphological intepretations of these astounding structures, the landslides hypotesis is the one fitting the observations best (see e.g. literature cited in De Blasio 2011b). But how to explain the run-out of the order of 600 km or more on an area sloping a mere 0.2°?

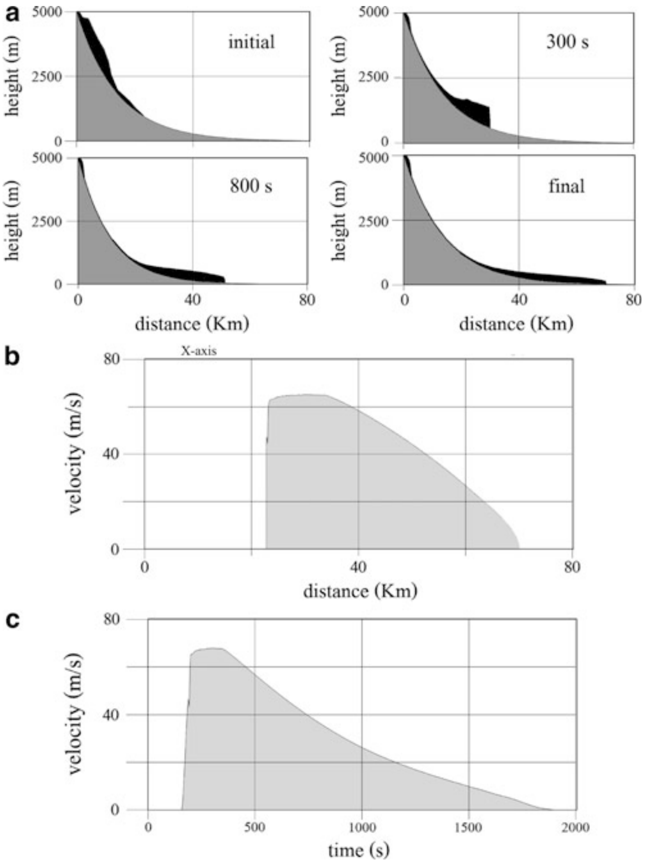

Fig. 4 Evolution of a rock avalanche described as a Bingham fluid with progressive loss of shear strength. The avalanche starts with a shear strength of 5 MPa and ends with a strength of 60 kPa. (**a**) four snapshots from the initial to the final configuration, including the rock avalanche outline at 300 and 800 s. (**b**) The velocity as a function of the front position. (**c**) the velocity as a function of time. The values of $\Gamma = 0.0002$; $\tau_{y,0} = 4\,MPa$; $\tau_{y,\infty} = 60\,kPa$. The viscosity is 10 Pa s. The density is 2,700 $Kg\ m^{-3}$

There are about ten distinct lobes composing the aureole, each being probably the remains of a different rock avalanche. Figure 1 shows with “OM” the area on the H/R ratio-to volume for the aureoles. The data points fall between the extension of the fit line for terrestrial rock avalanche data and the region of submarine debris flows.Thus the aureoles appear to be more mobile than subaqueous rock avalanches on Earth, but less mobile than debris flows.

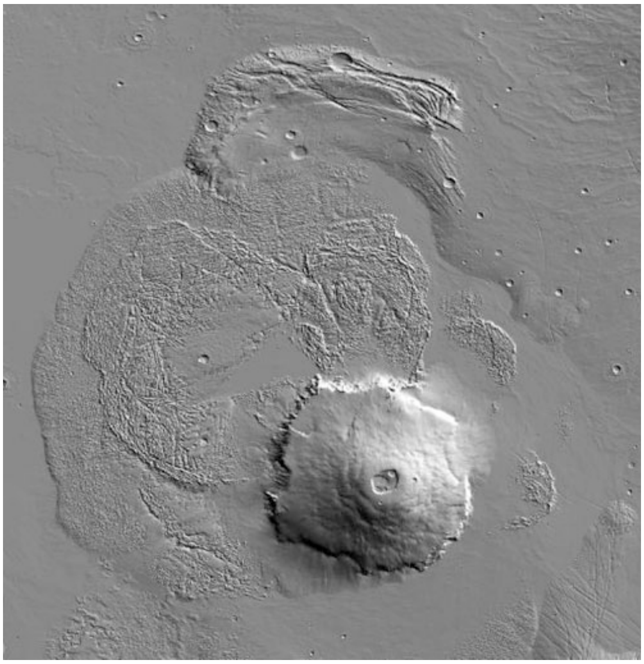

Fig. 5 The Olympus Mons on Mars as from the MOLA laser altimeter data. The composite "aureole" deposit comprises several units that depart from the main volcano edifice. Horizontal length approximately 1,750 km. Courtesy NASA/JPL

The presence of an Oceanus Borealis in the northerrn lowlands of Mars has been suggested based on the dichotomic division of altimetric levels, reminescent of the ocean-continents divisions on Earth (Parker et al. 1993). The difference between the Earth and Mars is that the alleged Martian oceanic basins are mostly concentrated in the northern hemisphere. Ancient costlines, however, are difficult to ascertain. Because the Olympus Mons stems from the base of the northern basin, could it be that it was partially submerged during part of its history? In this case, is the aureole the product of ancient gigantic subaqueus rather than subaerial landslides? If one could substantiate the subaqueous character of the Olympus Mons landslides from the detailed imagery available and numerical modelling, the implications for the existance of the Oceanus Borealis could be strengthened. Perhaps Olympus Mons was similar, albeit to a much larger scale, to the basaltic volcanic islands like El Hierro. In this case, however, it is unlikely that the ocean was reaching to the highest cliffs of Olympus Mons (8 km), because this would imply a huge amount of water to get rid of. The analysis of landslides on other planets, and especially on Mars, may be instrumental in reconstructing the past climate even billions years ago.

Final Remarks

Two models have been suggested for the dynamics of subaqueous rock avalanches. In the hydroplaning model, the rock avalanche travels like a porous hydroplaning debris flow. In a second model, the fragmented rock avalanche ingests water in the pores, diminishing considerably the shear strength. Both models show the importance of water and of fragmentation.

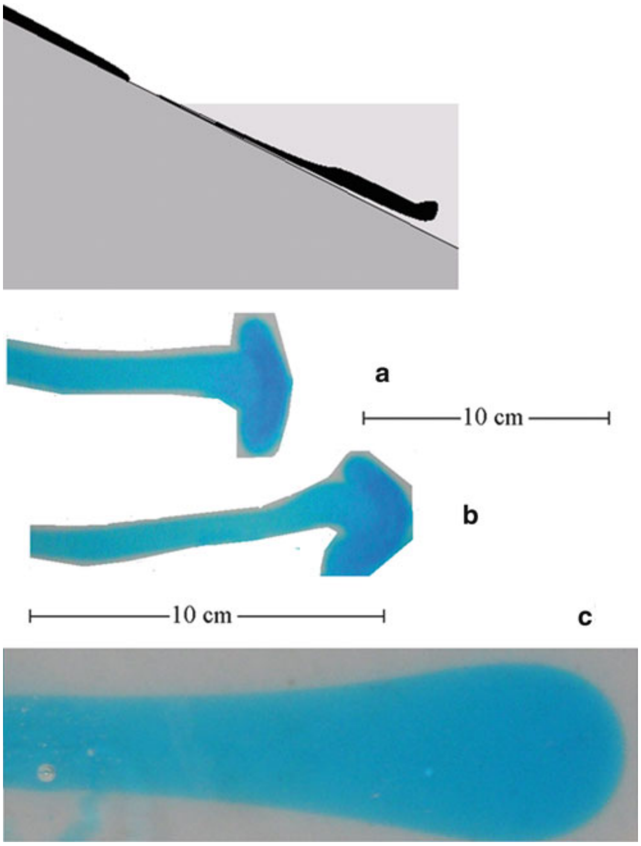

Fig. 6 Probably the simplest way to observe hydroplaning in an artificial gravity mass flow is by pouring cleaning liquid along an inclined plane immersed in water (*top*). (**a**, **b**) Two successive snapshots of the same experiment. At high speed, the head of the "debris flow" opens up like an umbrella due to the effect of the front drag force. The liquid in the front is often observed to "flip back". (**c**) At lower speed, the liquid travels acquiring a tongue-like shape

Appendix: Simple Analogical Experiment of Hydroplaning

It is possible to replicate hydroplaning with extremely simple tools. Direct visual observation of hydroplaning has its didactical value in classroom demonstrations and can be inspiring in understanding the forces at play.

The experiment consists in pouring a small amount (100 ml) of chlorine-based cleaning liquid onto a flat sloping surface submerged at one end (Fig. 6). When reaching the water, the liquid may hydroplane travelling detached from the base. It may develop umbrella-like shapes (A and B of Fig. 6) at high speed (e.g. 10 cm/s) as a consequence of the drag force. Flip back may also occur. At lower speeds, tongue-like shapes are more common, resembling the Bear Islands debris flows (Fig. 6 C).

References

Breien H, Pagliardi M, Elverhøi A, De Blasio FV, Issler D (2007) Experimental studies of subaqueous vs. Subaerial debris flows-velocity characteristics as a function of the ambient fluid. In: Lykousis V, Sakellariou D, Locat J (eds) Submarine mass movements and their consequences. Springer, Berlin

Crosta GB, Frattini P, Fusi N (2007) Fragmentation in the Val Pola rock avalanche, Italian Alps. J Geophys Res 112. doi:10.1029/2005JF000455

De Blasio (2011b) Submitted to earth and planetary science letters

De Blasio FV (2011) Introduction to the physics of landslides. Springer, Berlin

De Blasio FV, Elverhøi A, Engvik L, Issler D, Gauer P, Harbitz C (2006a) Understanding the high mobility of subaqueous debris flows. Nor J Geol, special issue on "Submarine mass movements and their consequences". 86:275–284

De Blasio FV, Engvik LE, Elverhøi A (2006b) Sliding of outrunner blocks from submarine landslides. Geophys Res Lett 33:L06614. doi:10.1029/2005GL025165

Deplus C, Le Friant A, Boudon G, Komorowski JC, Villemant B, Harford C, Segoufin J, Cheminee JL (2001) Submarine evidence for large scale debris avalanches in the Lesser Antilles Arc. Earth Planet Sci Lett 192:145–157

Elverhøi A, De Blasio FV, Butt FA, Issler D, Harbitz C, Engvik L, Solheim A, Marr J (2002) Submarine mass wasting on glacially influenced continental slopes-processes and dynamics. In: Glacier-influenced sedimentation in high-latitude continental margins, Geological Society. London, Special Publications 203, 73

Hildenbrand A, Gillot PY, Bonneville A (2006) Offshore evidence for a huge landslide of the northern flank of Tahiti-Nui (French Polynesia). Geochem Geophys Geosyst (G3) 7(3):Q03006, doi:10.1029/2005GC001003

Hungr O, Evans SG, Bovis MV, Hutchinson JN (2001) A review of the classification of landslides of the flow type. Environ Eng Geosci 7 (3):221–238

Ilstad T, Marr J, Elverhøi A, Issler D, Harbitz C (2004) Laboratory studies of subaqueous debris flow by measurements of pore-fluid pressure and total stress. Mar Geol 213:403–414

Imran J, Harff P, Parker G (2001) A numerical model of submarine debris flows with graphical user interface. Comput Geosci 27 (6):721–733

Lipman PW, Normark WR, Moore JG, Wilson JB, Gutmacher CE (1988) The giant submarine Alika debris slide, Mauna Loa, Hawaai. J Geophys Res 93:4279–4299

Locat J, Lee HJ (2001) Submarine landslides: advances and challenges. Can Geotech J 39:193–212

Locat P, Couture R, Leroueil S, Locat J, Jaboyedoff M (2006) Fragmentation energy in rock avalanches. Can Geotech J 43(8):830–851

Masson DG (1996) Catastrophic collapse of the volcanic island of Hierro 15 ka ago and the history of landslides in the Canary islands. Geology 24:231–234

Masson DG, Watts AB, Gee MJR, Urgeles R, Mitchell NC, Le Bas TP, Canals M (2002) Slope failures on the flanks of the western Canary Islands. Earth Sci Rev 57:1–35

Mazzanti P and De Blasio FV (2011) The dynamics of subaqueous rock avalanches: the role of dynamic fragmentation. This book

McSaveney M and Davies T (2006) Rapid rock-mass flow with dynamic fragmentation, In: Scarascia Mugnozza G, Strom A, Hermanns RL (eds) NATO science series. Springer, Berlin (2006)

Mitchell NC, Douglas G, Masson DG, Watts AB, Gee MJR, Urgeles R (2002) The morphology of the submarine flanks of volcanic ocean islands: a comparative study of the Canary and Hawaiian hotspot islands. J Volcanol Geotherm Res 115:83–107

Mohrig D, Whipple KX, Hondzo M, Ellis C, Parker G (1998) Hydroplaning of subaqueous debris flow. Geol Soc Am Bull 110 (3):387–394

Normark WR, McGann M, Sliter R (2004) Age of Palos Verdes submarine debris avalanche, southern California. Mar Geol 203: 247–259

Parker TJ, Gorsline DS, Saunders RS, Pieri D, Schneeberger DM (1993) Coastal geomorphology of the martian northern plains. J Geophys Res 98:11061–11078

Pollet N, Schneider JLM (2004) Dynamic disintegration processes accompanying transport of the Holocene Flims sturzstrom (Swiss Alps). Earth Planet Sci Lett 221:433–448

Rhodes M (2008) Introduction to particle technology. Wiley, Chichester

Satake K, Kato Y (2001) The 1741 Oshima-Oshima eruption: extent and volume of submarine debris avalanche. Geophys Res Lett 28:427–430

Schiffmann P, Watters RJ, Thompson N, Walton AW (2005) Hyaloclastites and the slope stability of Hawaiian volcanoes: Insights from the Hawaiian Scientific drilling project's 3-km drill core. J Volcanol Geoth Res 151:217–228

Ui T, Takarada S, Yoshimoto M (2000) Debris avalanches. In: Sigurdsson H (ed) Encyclopedia of volcanology. Academic, San Diego

Urgeles R, Canals M, Masson DG, Gee MJR (2003) El Hierro: shaping of an Oceanic Island by mass wasting. In: Mienert J, Weaver P (eds) European margin sediment dynamics. Springer, Berlin

Simulation of Submarine Landslides by Cellular Automata Methodology

V. Avolio Maria, Bozzano Francesca, Di Gregorio Salvatore, Lupiano Valeria, and Mazzanti Paolo

Abstract

Numerical modelling is a powerful tool for assessing risk related to submarine landslides and their possible consequences (i.e. impact on structures, induced tsunamis, etc.). To this aim, the simulation of the propagation phase of flow-like landslides is particularly important. A new model (named SCIDDICA-SS2), which is based on the Macroscopic Cellular Automata computational paradigm, has been specifically designed for the simulation of coastal and underwater landslides. SCIDDICA-SS2 is a fully 3D model based on the equivalent fluid approach. It accounts for the most important mechanism controlling the propagation of an underwater landslide as well as peculiar mechanisms like erosion of the seabed, hydroplaning and air to water impact (in the case of coastal landslides). The 1997 debris flow (subaerial–submerged landslide) at Lake Albano (Italy), the 2008 submarine debris flow at Bagnara Calabra (Italy) and the 1888 submarine debris flow at Trondheim (Norway) have been simulated by SCIDDICA-SS2, showing its high performances in simulating submarine landslides.

Keywords

Cellular automata • Flow-like landslides • Modelling • Propagation • SCIDDICA

Introduction

Landslides are common events on the earth's surface and their impact on the community is quite evident. However, several landslides occur even underwater and sometimes can be particularly dangerous (Hampton et al. 1996). Underwater landslides may cause serious damage to gas and oil platforms as well as to transmission lines. Furthermore, they can generate tsunamis with a strong impact on coastal communities (Hampton and Locat 1996).

Catastrophic events occurred in the last decades highlight the risk related to tsunamis in coastal areas especially if the increasing population living in coastal regions is considered.

However, the investigation and analysis of submarine regions is very difficult, therefore numerical modeling may be considered an important support for studying underwater landslides and assessing the induced risk (De Blasio 2011).

Underwater landslides are ruled by similar mechanics to that of their subaerial counterparts. However, in coping with the modelling of submarine mass movements, several important differences due to the different medium (water instead of air) must be accounted for (Mazzanti 2008).

In this paper we focus on flow-like landslides (Hungr et al. 2001), i.e. landslides characterized by a fluid-dynamical behaviour after failure. These landslides, such as debris-flows and debris-avalanches are among the most

---

V.A. Maria • D.G. Salvatore (✉)
University Of Calabria, Department of Mathematics, Rende, Italy
e-mail: dig@unical.it

B. Francesca • M. Paolo
Dipartimento di Scienze della Terra, "Sapienza", Università di Roma, Rome, Italy

NHAZCA S.r.l., spin-off "Sapienza", Università di Roma, Rome, Italy

L. Valeria
University Of Calabria, Department of Earth Sciences, Rende, Italy

C. Margottini et al. (eds.), *Landslide Science and Practice*, Vol. 5,
DOI 10.1007/978-3-642-31427-8_8, © Springer-Verlag Berlin Heidelberg 2013

dangerous events both in the subaerial and in the submarine environment.

These landslides may attain enormous distances, especially underwater, and can reach very high speed (De Blasio 2011). Furthermore, they are the events that most frequently trigger tsunamis.

However, the mechanics ruling subaerial and even more subaqueous flow like landslides are complex, involving properties similar to those employed in fluid, particle, and soil mechanics. Frictional interaction between grains, viscous and cohesional behavior of clays, and collisional dampening by pore-water all rule the transfer of momentum within such a type of landslides. Furthermore, additional particular mechanisms like hydroplaning seem to play a relevant role in the dynamics of submarine flow-like landslides (Mohrig et al. 1998; De Blasio et al. 2004).

Modelling such a system particle-by-particle inevitably is computationally cumbersome. Hence, the most used models are based on the equivalent fluid approach, which assumes simplified rheological models to approximate the flow behaviour of a flow like landslide. For example, on the basis of Herschel–Bulkley, Bingham and bilinear rheologies, Jeffrey G. Marr and co-authors (Maar et al. 2002) developed the numerical code BING for the simulation of submarine debris/mud flows. This numerical model is based on explicit finite differences. BING can be considered as the first numerical model specifically developed for submarine landslides. However, it is affected by several limitations since it does not account for the 3D geometry of the seabed, erosion, entrainment of water and so on.

On the other side, complex models based on a 3D framework have been developed, especially for subaerial landslides using the equivalent fluid approach and different rheological models (Hungr 1995; McDougall and Hungr 2004 Denlinger and Iverson 2001; Pirulli and Marco 2010, amongst others).

Some methods have been also recently developed to extend the application of these models to submarine and coastal landslides (Mazzanti and Bozzano 2009).

A different approach to simulate submarine flow-like landslides (Avolio et al. 2008, 2009, 2010; Mazzanti et al. 2009) has been recently proposed, based on the framework of Macroscopic Cellular Automata (MCA).

In this paper the SCIDDICA-SS2 model will be presented together with its application to some real cases of submarine landslides.

Cellular Automata (CA) Approach

CA were introduced for the first time by John von Neumann (von Neumann 1966). The methodology adopted in CA models is generally empirical-inductive, i.e. trying to identify the basic mechanisms that control the overall behaviour of an observed phenomenon and attempting to find simple laws that determine the interaction mechanisms among the basic components. Subsequently, one defines a model that translates in formal terms the identified laws and adopts a verification phase prior to a monitoring one, necessary to evaluate the reliability of the model in relation to the real phenomenon.

A CA is a mathematical representation of a physical system, whose space (1/2/3 dimensions) is divided into simple, regular, uniform size parts called cells. Each cell embeds an elementary, identical, computation unit *fe* (a finite automata), whose states identify the properties of the portion of space corresponding to the cell which are considered "significant" for the evolution of the phenomenon. The *fe* input of a cell c is given by the states of m neighbouring cells, including the cell c. The neighbourhood conditions are determined by a pattern which is invariant in time and constant over the cells.

At step 0, all *fe* are in arbitrary states, describing the initial conditions of the system; then, the CA evolves changing the state of all cells simultaneously at discrete times (CA step), according to the rules operated by what is called the *transition function*: $\tau{:}S^m \rightarrow S$. Complex macroscopic phenomena, like debris flow (DF), need an extension of the original CA definition (MCA) (Di Gregorio and Serra 1999) in order to fit the modelling requirements of many macroscopic phenomena. In MCA, major novelties regard the *state* of a cell, which is decomposed in "*sub-states*", each one representing a particular feature (e.g. lava temperature, debris amount, etc) of the phenomenon to be modelled, and precisely, the state values of a cell is defined at the centroid of the cell, are assumed as representative of the entire cell. In addition, in MCA some "parameters" are generally considered, which allow to "tune" the model for reproducing different dynamic behaviours of the phenomenon of interest (e.g., thresholds concerning minimum possible outflows from a cell toward a neighbour one). Moreover, even the state transition function is split in "elementary processes", each one describing a particular aspect of the considered phenomenon (e.g., detrital cover mobilization).

The model here adopted (and described herein) to simulate complex macroscopic phenomena, as in other models for simulating lava flows, landslides, etc. (Avolio et al. 2003), is two-dimensional in order to keep the model as simple as possible. Furthermore, cell features concerning the third dimension (i.e., the height), e.g., "cell average altitude", "debris thickness in the cell", "debris kinetic head" etc, are defined as sub-states (Di Gregorio and Serra 1999), specified better in the following, and thus the third dimension varying features are enclosed in the states of the cells or may be introduced (e.g. vertical variation in debris density may be approximated in the cell by sub-states "layers", that may be expressed as a variable thickness, related to a fixed range of density values). For these reasons, the model can be considered fully 3D.

In fact, another peculiarity of this type of MCA model is that it is possible to consider characteristics of the *cell* (i.e. *sub-states*), typically expressed in terms of volume (e.g. debris volume), in terms of thickness. This simple assumption permits to adopt an efficacious strategy that computes *incoming* and *outgoing* flows of a physical quantity (that is, in case of SCIDDICA-SS2, landslide material) from the central cell to the neighbouring ones, by leading to variations of its height, in order to minimize the non-equilibrium conditions. This equilibrium state is attained by considering interactions between each cell and its surrounding neighbours. By applying this idea to every neighborhood in the lattice, the whole system is driven to the most stable configuration by the *Minimization of Differences* algorithm (Di Gregorio and Serra 1999).

MCA were proposed for the first time in 1982 to model the dynamics of macroscopic spatially extended systems, and firstly applied to the simulation of basaltic lava flows (Crisci et al. 1982). Since then, MCA were adopted for the simulation of diverse natural phenomena: pyroclastic flows (Avolio et al. 2006), snow avalanches (Barpi et al. 2007; Avolio et al. 2010b), density currents (Salles et al. 2007) and, in particular, both subaerial–submarine flow type landslides by our research group (for an extended bibliography see Avolio et al. 2010a) and others (Segre and Deangeli 1995, Clerici and Perego 2000).

Among existing Macroscopic Cellular Automata models, we will focus on SCIDDICA, a family of deterministic MCA models, specifically developed for simulating DF. This model has been developed according to an incremental strategy, permitted by the underlying CA properties, that allow to build a model by the composition of "*elementary processes*". This permits to consider first models of the family for less complex case studies. Subsequently, new versions are generated step by step by introducing other "*elementary processes*" in order to model more complex real cases.

A general description of the model SCIDDICA-SS2 will be given in next sections, together with the results of some applications to real cases of only submarine and both subaerial – submarine landslides.

SCIDDICA-SS2 Model: General Framework

SCIDDICA is a family of deterministic MCA models, specifically developed for simulating flow like landslides. The latest version, SCIDDICA-SS2, introduces new features, with respect to previous versions of SCIDDICA (Avolio et al. 2008), (Avolio et al. 2010). This release is an extension to combined subaerial-subaqueous flow-type landslides, with a new flows characterization according to the position and velocity of the centre of mass (Avolio et al. 2008, 2009). Hence, SCIDDICA-SS2 can be considered as the only "global model" for landslides, able to simulate both subaerial, submarine and mixed landslides. Furthermore, a new release of SCIDDICA for extra-terrestrial landslides has been recently designed.

Constitutive features of the equivalent fluid, which are expressed by some SCIDDICA-SS2 parameters, cannot be sometime measured in laboratory when they represent fictitious statistical properties, and are determined by back analyses of real cases.

SCIDDICA-SS2 is a two-dimensional MCA with hexagonal *cells*. Formally, SCIDDICA-SS2 can be defined as follows:

$$\mathrm{SCIDDICA} - \mathrm{SS}_2 = <R, X, S, P, \tau>$$

where:

- R identifies the cells, covering the finite region, where the phenomenon evolves;
- X is the cell neighbourhood relation, that includes the cell itself and its adjacent cells;
- S is the finite set of states of the *fe*, embedded in the cell; it is equal to the Cartesian product of the sets of the following *sub-states*: S_a(cell altitude, in meters); S_{th} (thickness of landslide debris, in meters); S_x and S_y (coordinates of the debris barycentre with reference to the cell centre, in meters); S_d (maximum depth of detrital cover that can be transformed by erosion in landslide debris, in meters); S_E (total energy of landslide debris, in joule), S_{kh} (debris kinetic head, in meters); ${S_{oi}}^6$ and ${S_{oe}}^6$ (debris outflows toward the six adjacent cells: internal part that remains inside the central cell, external part that penetrates the adjacent cell, normalised to a thickness, in meters); ${S_{ex}}^6$, ${S_{ey}}^6$, ${S_{ix}}^6$ and ${S_{iy}}^6$ (barycentre coordinates of the debris external and internal outflows with reference to the cell centre, in meters);
- P is the finite set of parameters which account for the general frame of the model and the physical characteristics of the phenomenon (e.g the size s of the cell specified by the cell side or the apothem and the time correspondence to a MCA step t);
- τ is the MCA deterministic transition function that is applied, step by step, to all the cells in R, the MCA configuration changes obtaining the evolution of the simulation.

Initial conditions are specified by primary values of *sub-states*: S_{th} is zero everywhere except for the detachment area, where the thickness of landslide mass is specified. S_a and S_d

are the morphological height and the initial depth of detrital cover, respectively. S_E at step 0 represents only the potential energy, related to debris mass. All the values related to the remaining *sub-states* are zero.

In the following, a sketch of the main local elementary processes of the transition function of SCIDDICA-SS2 will be given.

Altitude, kinetic head and debris thickness vary by detrital cover mobilization. When the kinetic head value overcomes an opportune threshold p_m, a mobilisation of the debris cover occurs, which is proportional to the quantity overcoming p_m; variation, Δ, of involved *sub-states* is computed as:

$$\Delta S_D = \Delta S_A = \Delta S_{TH} = p_e(S_{KH} - p_m)$$

where p_e is an empirical parameter, which quantifies the progressive erosion.

Debris outflows (thickness, barycentre co-ordinates, kinetic head) are blocks whose bulk is determined by the minimization algorithm, that accounts also for energy. Their barycentre shift (*sh*) towards a neighbourhood cell is computed according to the following motion equation in the subaqueous context:

$$sh = \left(\frac{1 - e^{-\alpha t}}{\alpha}\right)\left(v_0 - \frac{g'(\sin\theta - \mu\cos\theta)}{\alpha}\right) + \left(\frac{g'(\sin\theta - \mu\cos\theta)}{\alpha}\right)t$$

This shift formula for subaqueous debris considers the slope θ between the central cell and its adjacent, the initial velocity $v_0 = \sqrt{2g'S_{KH}}$, the coefficient of friction μ and considers also the water resistance, using modified Stokes equations with a form factor, α, proportional to mass and $g' < g$ (g the acceleration of gravity), where g' accounts for buoyancy and is dependent on the density of the material of the landslide (Avolio et al. 2008).

Composition of debris inside the cell (remaining debris more inflows) and determination of new thickness, barycentre co-ordinates and total energy is calculated considering internal and external flows and computing all *sub-states* in terms of weighted average formulae, and new thickness of debris and its kinetic and potential energy are so updated.

The effect of turbulence is modeled by a proportional kinetic head loss:

$$-\Delta S_{KH} = p_{td} S_{KH}$$

where p_{td} is energy dissipation parameter by turbulence.

SCIDDICA-SS2: Submarine Landslides Case Histories

The SCIDDICA-SS2 model has been applied over the last years to the simulation of several subaerial, submarine and coastal landslides. In what follows, we will show the results achieved by back-simulating one coastal and two completely underwater flow-like landslides:

- The 1997 coastal debris flow at Lake Albano (Rome zone, Italy);
- The 2008 submarine debris flow in the nearshore of Bagnara Calabra (South Italy);
- The 1888 submarine debris flow in the nearshore of the Trondheim harbour(Norway).

Detailed bathymetric data derived by sonar multibeam surveys as well as geological data derived from geophysical and geological surveys were available for the three sites thus allowing a strong control on the achieved results. Note that hydroplaning was not applied in the studied real events, because not relevant (for the considered approximation degree) for their overall phenomenological behaviour.

A quantitative evaluation of simulations results were also performed according to a fitness function based on the areal comparison of real and simulated event (Iovine et al. 2005). The used function is $e = \sqrt{((R \cap S)/(R \cup S))}$, where R is the set of cells involved in the real event and S the set of cells involved in the simulated event. Note that e can range from 0 (total failure) to 1 (perfect simulation).

Lake Albano

The 1997 Lake Albano (Rome, Italy) event (Fig. 1) is a rare case of well constrained combined subaerial-subaqueous debris flow (Mazzanti et al. 2007; Bozzano et al. 2009). This event occurred in the eastern slope of the Lake Albano on the 7th November 1997 after an intense rainfall (128 *mm* in 24 h), and began as a soil slide, mobilizing about 300 m^3 of eluvial material. The mobilized mass was channelled within a steeply dipping impluvium (about 40°) entraining a large amount of debris material along the bottom of the channel and thus reaching an estimated volume of some thousands of m^3 at the coastline. A few amount of material was deposited at the coastline, while a greater quantity entered in water generating a little tsunami wave. Numerical Simulation by SCIDDICA-SS2 model was performed by using a 1 m resolution DTLM (Digital Terrain and Lacustrine Model) derived from an aerial LiDAR survey and a sonar multibeam bathymetric survey. Geomorphological

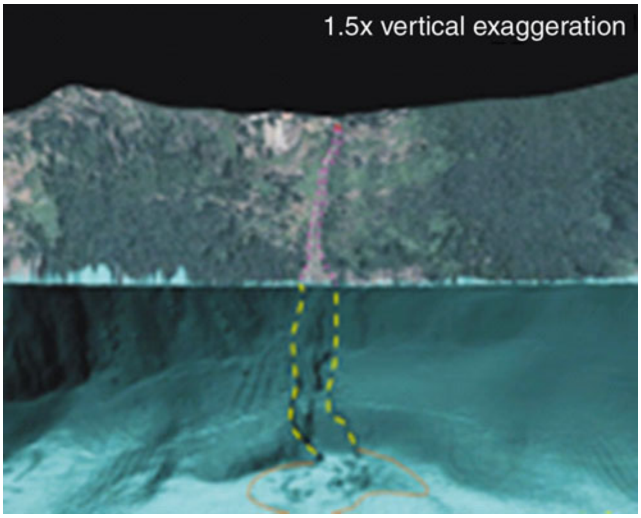

Fig. 1 The 1997 Albano lake subaerial-subaqueous debris flow

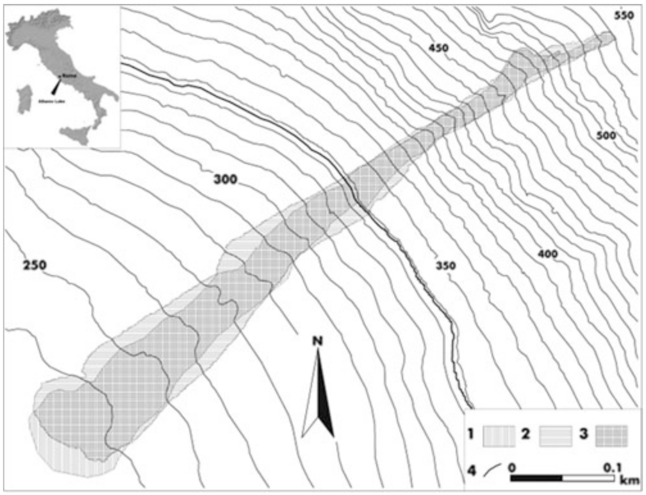

Fig. 2 The 1997 Albano lake subaerial-subaqueous debris flow as simulated by the SCIDDICA-SS2 model. Key: (*1*) real event, (*2*) simulated event, (*3*) intersection between real and simulated event, (*4*) water level

interpretation of the real event was performed by using multi-temporal aerial photos for the subaerial part of the slope and high resolution bathymetry for the submerged part. Geological and geotechnical parameters were also determined by dedicated field surveys.

Subsequently, the real event was back analysed by the SCIDDICA-SS2 model thus achieving a quite satisfactory result in terms of fitness function (Fig. 2). A value of *e* of 0.85 was obtained for the aerial path (Avolio et al. 2008). Furthermore, results show a good agreement also in terms of erosion and deposits on both subaerial and subaqueous parts. Landslide velocities ranging from 0 to 15 *m/s* were found with a peak at the coastline. Values lower than 12–13 m/s were recorded in the submerged part (Fig. 3).

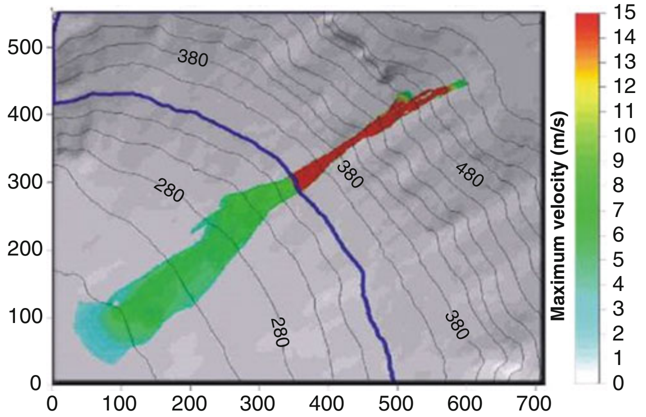

Fig. 3 Maximum velocity computed during the entire simulation of the Albano landslide

The 1997 debris flow at Lake Albano has been recently simulated also by the DAN3D model (McDougall and Hungr 2004) using the EFEM approach (Mazzanti and Bozzano 2009).

Achieved results are very similar to those obtained by SCIDDICA-SS2. Furthermore, SCIDDICA demonstrated to be more efficient in some respects like:

- Simulation of two or more niches along the path;
- Seabed erosion directly computed by the model (and not imposed at the beginning like in DAN3D);
- Better management of the air to water transition.

Further details can be found in Mazzanti et al. 2009.

Bagnara Calabra

A completely submarine landslide was detected in the near-shore of Bagnara Calabra (Italy) by comparing detailed bathymetries coming from two sonar multibeam surveys carried out in November 2007 and in September 2008. Landslide detachment area was located between 10 and 20 *m* b.s.l., about 100 *m* far from the coastline. Initial landslide volume was also estimated at about 16,000 m^3 with a maximum thickness of 9 *m*. Erosion up to 4 *m* has been recorded along the pathway between 20 and 60 *m* b.s.l.. Final deposits are partly distributed between 60 and 90 *m* b.s.l. and partly below 100 *m* with a maximum thickness of 5 *m*.

The landslide was simulated by the SCIDDICA-SS2 model and a fitness value of 0.85 was achieved (Avolio et al. 2009). Furthermore, deposit and erosion locations in the simulation agree very satisfactorily with the real event; moreover, deposit thickness and erosion depth values do not differ substantially (Fig. 4). The detachment area was completely emptied after about 1 min and the flow propagated until its final position in few minutes. Landslide velocity was up to 6 m/s in the upper part of the slope, immediately after the mass release, and dropping below

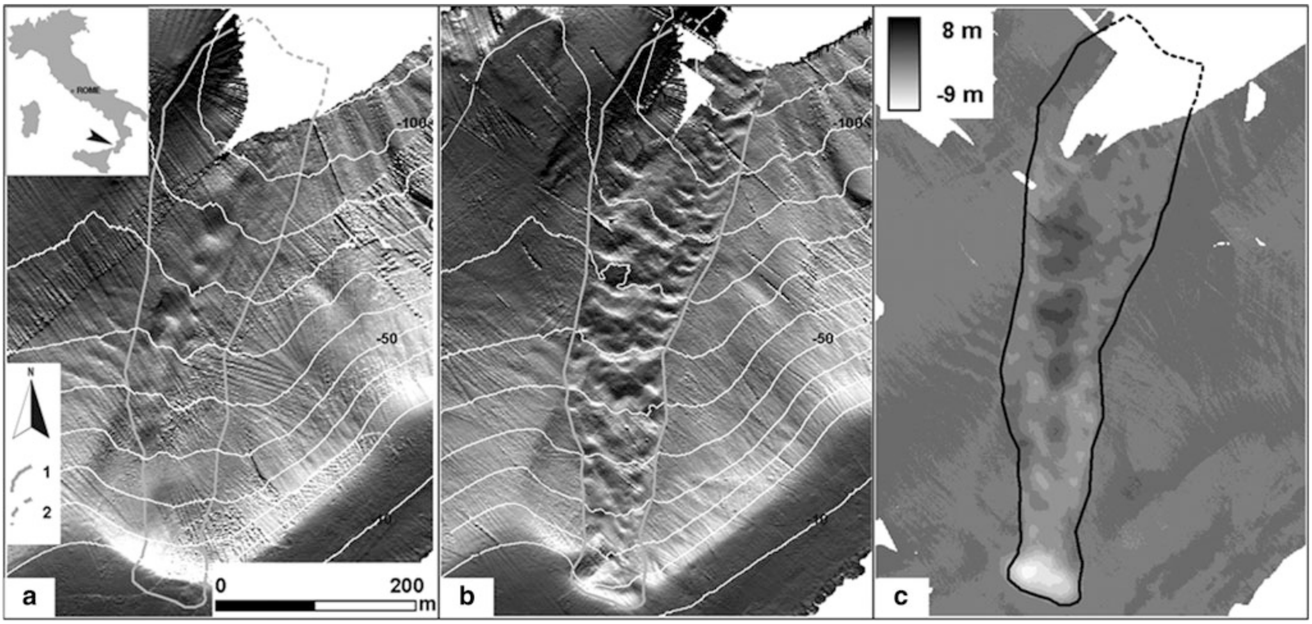

Fig. 4 (**a**) Shaded relief of the pre-landslide bathymetry; (**b**) shaded relief of the post- landslide bathymetry; (**c**) residual between the pre- and the post- landslide bathymetry (missing data areas are in *white*); lines superimposed to contours identify: (*1*) perimeter of real event, (*2*) probable real event perimeter in missing data area

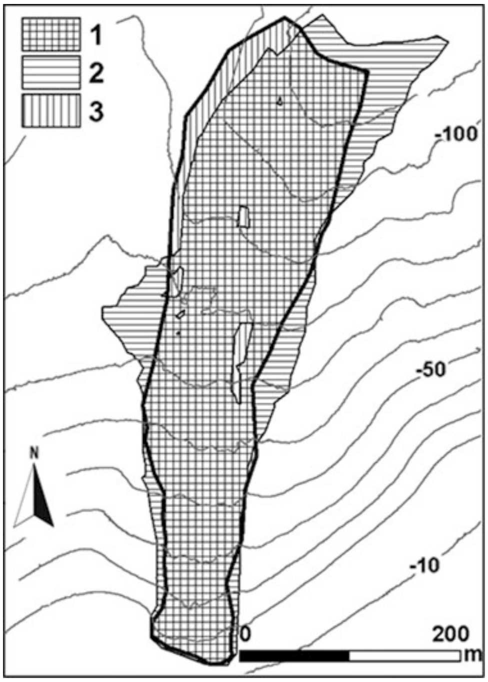

Fig. 5 Simulation of Bagnara subaqueous landslide. Intersection between real and simulated event: (*1*) intersection; (*2*) only simulated (*3*) only real

4 m/s in the following stages. Such values of velocity may be considered reasonable according to analyses of main characteristics of the event (type and volume of landslide, slope gradient up to 12°, etc.) and indicative results of subsequent approximate calculations (De Blasio 2011).

Figure 5 shows the simulation of Bagnara subaqueous landslide obtained by SCIDDICA-SS2.

Trondheim

Nearshore landslides in the bay of Trondheim have been recorded since the XIX century, such as the 1888 landslide and tsunami. The most dangerous landslide occurred on April 23rd, 1888, and was accompanied by a 5–7 m high tsunami, that killed one person and caused major damage to port facilities (L'Heureux et al. 2010 and references therein).

Recent studies provide detailed information about the morphology of the seafloor and landslide mechanisms (L'Heureux et al. 2010). Geomorphological data suggest an offshore detachment along a weak clayey sediment layer and consequent retrogression across the shoreline. Due to the deltaic nature of sediments involved, the landslide transformed rapidly into a DF, that propagated along the Nidelva channel reaching a distance of about 3–4 km from the coastline at a water depth of about 400 m. Seabed erosion along the pathway triggered slope failures on the flanks of the channel, thus increasing the total amount of involved material. Following L'Heureux et al. 2010, the largest landslide along the flanks of the Nidelva channel (named W-landslide) was triggered 2 km off-shore at a water depth of 80–160 *m*.; its total volume can be estimated to ~1.45×10^6 m^3.

Aiming at better understanding the complex behaviour of this landslide, preliminary numerical simulation using SCIDICASS2 has been performed. The landslide was simulated by accounting for an initial progressive failure of the scar (trying to simulate the retrogressive behaviour of the landslide) and then propagating as a debris-flow. In the simulation W-landslide has been triggered by the transit and erosion at the toe. The simulated path of the landslide was compared with the one suggested by L'Heureux et al. 2010, thus obtaining a fitness function value close to 0.73.

Conclusions

SCIDDICA-SS2 is a powerful model for simulating submarine landslides. Several peculiar features make it suitable for the simulation of events characterized by different features. First of all submarine landslides initiated in a subaerial slope can be simulated in a rigorous way. Furthermore, the management of secondary landslides triggered along the path allows to properly simulate events like the 1997 Lake Albano and 1888 Trondheim debris-flows. Moreover, SCIDDICA-SS2 showed its effectiveness in simulating flow-like landslides both on open slopes and on narrow and complex channels. Several outputs can be obtained by SCIDDICA-SS2 such as the area affected by the landslides, the erosion along the path, the thickness of the mass and velocity. These data can be very useful in back analysing past landslides and their induced effects (i.e. tsunamis); however, if a suitable calibration is carried out, different scenarios based on the analysis for future events can also be performed. Hence, SCIDDICA-SS2 can be used for assessing the risk related to future events and for designing possible countermeasures.

References

Avolio MV, Crisci GM, D'Ambrosio D, Di Gregorio S, Iovine G, Rongo R, Spataro W (2003) An extended notion of cellular automata for surface flows modelling. WSEAS Trans Comput 4 (2):1080–1085

Avolio MV, Crisci GM, Di Gregorio S, Rongo R, Spataro W, D'Ambrosio D (2006) Pyroclastic flows modelling using cellular automata. Comput Geosci 32:897–911

Avolio MV, Lupiano V, Mazzanti P, Di Gregorio S (2008) Modelling combined subaerial-subaqueous flow-like landslides by cellular automata. LNCS 5191. In: Proceedings of ACRI 2008, Yokohama, pp 329–336, 23–26 Sept 2008

Avolio MV, Lupiano V, Mazzanti P, Di Gregorio S (2009) An advanced cellular model for flow-type landslide with simulations of subaerial and subaqueous cases. In: Proceedings of the 23rd international conference on informatics for environmental protection, 1, Berlin, pp 131–140, 9–11 Sept 2009

Avolio MV, Di Gregorio S, Lupiano V, Mazzanti P, Spataro W (2010) Application context of the SCIDDICA model family for simulations of flow-like landslides. In: Proceedings of the 2010 international conference on scientific computing, Las Vegas, pp 40–46, 12–15 July 2010

Avolio MV, Errera A, Lupiano V, Mazzanti P, Di Gregorio S (2010) Development and calibration of a preliminary cellular automata model for snow avalanches. In: LNCS 6350, proceedings of ACRI 2010, Ascoli, pp 329–336, 21–24 Sept 2010

Barpi F, Borri-Brunetto M, Delli VL (2007) Cellular-automata model for dense-snow avalanches. J Cold Reg Eng 21 (4):121–140

Bozzano F, Mazzanti P, Anzidei M, Bianchi Fasani G, Esposito C, Esposito A, Floris M (2009) Slope dynamics of lake Albano (Rome, Italy): insights from the high resolution bathymetry. Earth Surf Process Landf 34:1469–1486

Clerici A, Perego S (2000) Simulation of the parma river blockage by the Corniglio landslide (Northern Italy). Geomorphology 33:1–23

Crisci GM, Di Gregorio S, Ranieri GA (1982) A cellular space model of basaltic lava flow. In: Proceedings of AMSE conference modelling & simulation, Paris-Sud, pp 65–67, 1–3 July 1982

De Blasio FV (2011) Introduction to the physics of landslides. Lecture notes on the dynamics of mass wasting. Springer, Heidelberg (ISBN 978-94-007-1121-1) 408p

De Blasio FV, Engvik LE, Harbitz CB, Elverhøi A (2004) Hydroplaning and submarine debris flows. J Geophys Res 109 (C01002):1–16

Denlinger RP, Iverson RM (2001) Flow of variably fluidized granular masses across three-dimensional terrain: 2. Numerical predictions and experimental tests. J Geophys Res 106 (B1):553–566

Di Gregorio S, Serra R (1999) An empirical method for modelling and simulating some complex macroscopic phenomena by cellular automata. Future Gener Comput Syst 16:259–271

Hampton MA, Lee HJ, Locat J (1996) Submarine landslides. Rev Geophys 34(1):33–59

Hungr O (1995) A model for the runout analysis of rapid flow slides, debris flows, and avalanches. Can Geotech J 32:610–623

Hungr O, Evans SG, Bovis MJ, Hutchinson JN (2001) A review of the classification of landslides in the flow type. Environ Eng Geosci 7 (3):221–228

Iovine G, D'Ambrosio D, Di Gregorio S (2005) Applying genetic algorithms for calibrating a hexagonal cellular automata model for the simulation of debris flows characterised by strong inertial effects. Geomorphology 66:287–303

L'Heureux JS, Glimsdal S, Longva O, Hansen L, Harbitz CB (2010) The 1888 shoreline landslide and tsunami in Trondheimsfjorden, central Norway. Mar Geophys Res 32:313–329

Marr JG, Elverhøi A, Harbitz C, Imran J, Harff P (2002) Numerical simulation of mud-rich subaqueous debris flows on the glacially active margins of the Svalbard Barents sea. Mar Geol 188:351–364

Mazzanti P (2008) Analysis and modelling of coastal landslides and induced tsunamis. Ph.D. thesis, Department of Earth Sciences, "Sapienza" University of Rome, Rome

Mazzanti P, Bozzano F (2009) An equivalent fluid/equivalent medium approach for the numerical simulation of coastal landslide's propagation: theory and case studies. Nat Hazard Earth Syst Sci 9:1941–1952

Mazzanti P, Bozzano F, Esposito C (2007) Submerged landslides morphologies in the Albano lake (Rome, Italy). In: Lykousis V, Sakellariou D, Locat J (eds) Submarine mass movements and their consequences, advances in natural and technological hazards series 27. Springer, Heidelberg, (ISBN 9781 4020 6511 8) 424p

Mazzanti P, Bozzano F, Avolio MV, Lupiano V, Di Gregorio S (2009) 3D numerical modelling of submerged and coastal landslides propagation. In: Mosher DC, Shipp C, Moscardelli L, Chaytor J, Baxter C, Lee H, Urgeles R (eds) Submarine mass movements and their consequences IV, advances in natural and technological hazards series, 28. Springer, Heidelberg (ISBN: 9048130700) p 786

McDougall S, Hungr O (2004) A model for the analysis of rapid landslide run out motion across three dimensional terrain. Can Geotech J 41(6):1084–1097

Mohrig D, Whipple K, Ellis C, Parker G (1998) Hydroplaning of subaqueous debris flows. Geol Soc Am Bull 110:387–394

Pirulli M, Marco F (2010) Description and numerical modelling of the October 2000 Nora debris flow, Northwestern Italian Alps. Can Geotech J 47:135–146

Salles T, Lopez S, Cacas MC, Mulder T (2007) Cellular automata model of density currents. Geomorphology 88:1–20

Segre E, Deangeli C (1995) Cellular automaton for realistic modelling of landslides. Nonlinear Processes Geophys 2(1):1–15

von Neumann J (1966) Theory of self reproducing automata. University of Illinois Press, Urbana (ISBN 0598377980) 388p

Modelling of the 1888 Landslide Tsunami, Trondheim, Norway

Sylfest Glimsdal, Jean-Sebastien L'Heureux, Carl B. Harbitz, and Geir K. Pedersen

Abstract

The modelling of the tsunami generated by the 1888 landslide close to the Trondheim harbour, Norway is revised. Results for the tsunami generation, propagation, and inundation are shown. Improvements for the modelling are made for the generation phase. A special filter for the sea-surface response from the landslide is applied. In this manner the generated waves are more realistic, and spurious trailing waves due to too sharp gradients on the surface are effectively damped. Further, the landslide in the numerical model follows the most likely track for the 1888 event, and not only a straight line as in previous studies.

Keywords

Harbour • Fjord • Submarine landslide • Tsunami • Numerical modelling • Trondheim

Introduction

Submarine landslides are widely recognized as a potential hazard to offshore development and coastal infrastructures (e.g. Locat and Lee 2002), as well as a source for destructive tsunamis (e.g. Tappin 2009). In fjords, these natural hazards frequently occur and pose a constant threat to coastal communities. L'Heureux et al. (this volume) show that 45 % of the historical near-shore landslides in unconsolidated sediments along Norwegian fjords led to tsunamis with registered run-up heights of 1–7 m. With the population and industrial development continuously increasing along Norwegian fjords, there is a need for a better understanding of these natural hazards for land use planning and design of mitigation measures.

The bay of Trondheim, central Norway, is well suited for the study of near-shore mass wasting processes and their consequences. Here, landslides have occurred repeatedly during the last century causing damages to port facilities as well as loss of life (Bjerrum 1971; L'Heureux et al.. 2007, 2010a, b). The most devastating submarine landslide in this fjord deltaic setting occurred April 23rd, 1888, and was accompanied by a 5–7 m high tsunami (L'Heureux et al. 2010a). The characteristics of the 1888 event in Trondheim is similar to other historical submarine landslide events, which showed a sequence of offshore initiation, retrogression close to, or across, the shoreline, and generation of waves [e.g. the 1975 Kitimat event in British Columbia (Prior et al. 1982) and the 1979 Nice catastrophe in France (Dan et al. 2007)]. For many of these events it has been difficult to pinpoint the causes for slope failures and the generation of tsunamis.

In the present paper, the generation, propagation, and inundation of the 1888 tsunami in Trondheim are studied. A special filter to model the hydrodynamic response of the water surface during the generation phase is implemented and is applied in the simulations. In addition, the landslide follows the most likely track and not only a straight line as in

---

S. Glimsdal (✉) • C.B. Harbitz
Norwegian Geotechnical Institute, P.O.Box 3930, Ullevål Stadion, 0806, Oslo, Norway

International Centre for Geohazards, Oslo, Norway
e-mail: sgl@ngi.no

J.-S. L'Heureux
Geological Survey of Norway, Trondheim, Norway

International Centre for Geohazards, Oslo, Norway

G.K. Pedersen
Dept. of Mathematics, University of Oslo, Oslo, Norway

International Centre for Geohazards, Oslo, Norway

C. Margottini et al. (eds.), *Landslide Science and Practice*, Vol. 5,
DOI 10.1007/978-3-642-31427-8_9, © Springer-Verlag Berlin Heidelberg 2013

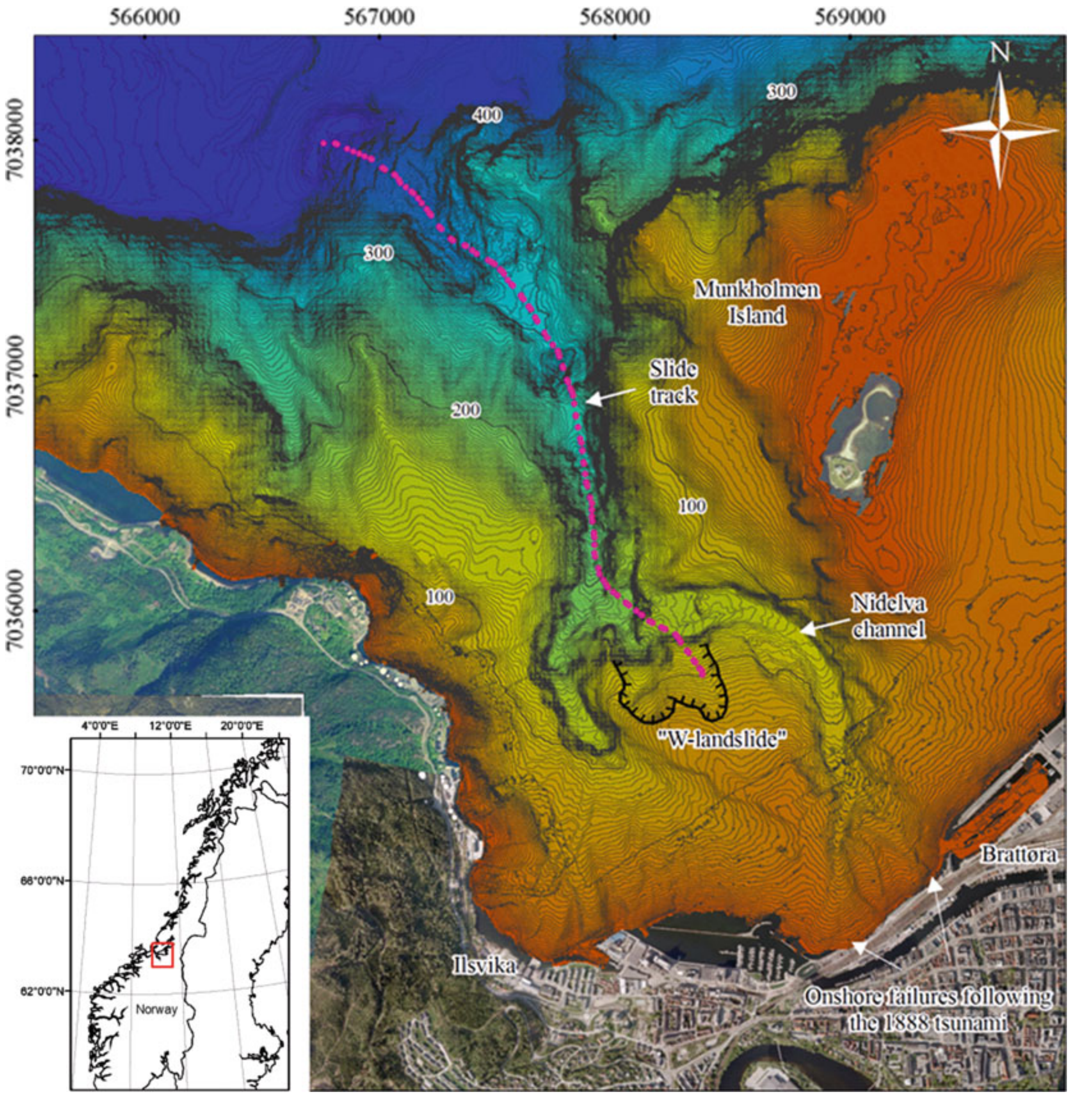

Fig. 1 Location of the study area with bathymetric contours and shaded relief image from the bay of Trondheim in central Norway. The locations of places mentioned in the text are shown together with the location of the "W-landslide". The applied landslide track is indicated with dashed pink line

the previous studies, L'Heureux et al. (2009) and L'Heureux et al. (2010a).

Background and Study Area

From the testimony of 20 eye witnesses (Skaven-Haug 1955), it is known that a flood wave suddenly appeared halfway between the island of Munkholmen and Ilsvika located along the shore line in the bay of Trondheim on 23rd April 1888 (Fig. 1). Records indicate that the wave propagated towards the shoreline and first struck the shore line at Ilsvika (Fig. 1). Some minutes later another wave climbed over a 5–7 m high embankment fill at Brattøra and, just as it receded, a 170 m long portion of the railway station slumped into the fjord. Three railway tracks were washed away and one man perished in the event.

Based on an integrated dataset of cores, cone penetration tests (CPTU), high resolution bathymetry, and slope stability analyses, L'Heureux et al. (2010a, b) showed that the 1888 sequence of events likely started with an initial underwater landslide in front of the harbour and near Brattøra (Fig. 1). The landslide transformed rapidly into a debris flow and subsequently triggered slope failures along a deep underwater channel (i.e. the Nidelva channel, Fig. 1) by undercutting the flanks. One of the landslides mapped along the submarine channel (i.e. the "W-landslide", Fig. 1) mobilised 1.45×10^6 m^3 of sediment and, due to its age, volume and location, was associated with the 1888 tsunami (L'Heureux et al. 2010a, b).

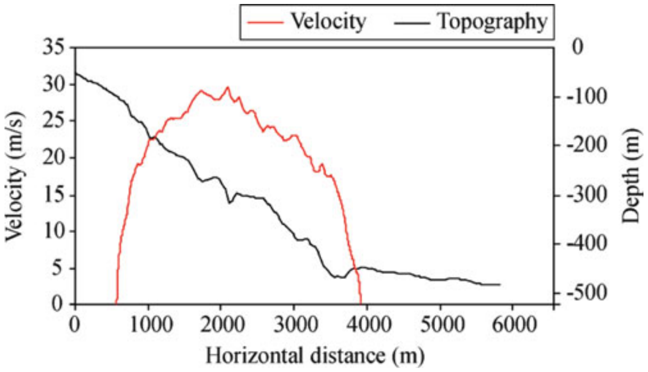

Fig. 2 2D bathymetric profile of the Nidelva Channel (from the location of the "W-landslide" to the deep fjord basin) and frontal flow velocity from the 2D-BING model (from L'Heureux et al. 2009). The track of the 2D profile is indicated in Fig. 1

Modelling

The interpretation of the W-landslide as the cause for the 1888 tsunami in the bay of Trondheim is here investigated by numerical simulations. First, the volume and the run-out distance of the "W-landslide" are prescribed inputs from the observations. There are of course no observations of the acceleration, the velocity, or the general landslide behaviour. Hence, the failed mass is modelled as a deformable visco-plastic Bingham fluid (where no deformation takes place until a certain yield strength is exceeded and the flow starts to move as a Newtonian fluid) applying the two-dimensional BING model (Imran et al. 2001). In other words, the landslide moves as a plug flow riding on top of a shear layer with a thickness determined by flow height and yield stress of the material. The two-dimensional (2D) model assumes that the sediments disintegrate and liquefy instantly upon failure. The landslide body is initially given a height of 8 m and a length of 320 m based on the morphological data. The yield strength is set to 50 Pa (L'Heureux et al. 2009). In Fig. 2 the frontal flow velocity of the landslide is shown. The applied rheological parameter (i.e. yield strength of 50 Pa) might be too low (the value is enforced to get the landslide started in the BING model), and as a result the maximum velocities might be too high (Marr et al. 2002). However, the volume and the initial acceleration are often more important than the velocity for the resulting tsunami (Løvholt et al. 2005).

In the tsunami model, the landslide is simplified as a flexible box with a prescribed velocity progression deduced from the BING model landslide simulations (cf. Fig. 2). The maximum velocity of the front (about 30 m/s) is reached after a travel distance of 1,400 m (about 2,000 m horizontal distance along the track), and the landslide has come to rest after a distance of about 3,200 m. The "box-slide" is rounded to represent a more realistic landslide, with a volume of 1.32 × width (430 m) × height (8 m) × length (320 m) or approximately 1.45 × 10^6 m^3. A factor of 1.32 comes from the applied rounding of the landslide. In the tsunami model, landslide propagation follows the most likely track of the 1888 landslide, (L'Heureux et al. 2010a) (track is found in Fig. 1). In light of the overall uncertainty (landslide parameters, etc.), these models give reasonable results for tsunami propagation. For further details on landslide representation we refer to Harbitz (1992) and Løvholt et al. (2005).

Tsunami Generation

The landslide motion will cause a time dependent bottom which may be represented as a sink/source distribution. In most tsunami models the distribution is copied directly onto the sea surface, which often leads to sharp gradients and steep features in the generated wave. The artificial short wave components may amplify too much in shallower water causing an overestimation of the run-up heights. However, in reality a bottom source is spread in a 3D fashion and yields a surface response extending a horizontal distance of a few water depths, at least (Kajiura 1963; Pedersen 2001). Hence, the water will act as a kind of low-pass filter.

From Kajiura (1963) we adopt the Green function for surface response from a point source in unitary depth on the form

$$G(r) = R(r^2) = \frac{1}{\pi}\sum_{n=2}^{\infty}\frac{(-1)^n(2n+1)}{\{(2n+1)^2+r^2\}\{(2n+1)^2+r^2\}^{\frac{3}{2}}}.$$

This series converges rapidly and is used to tabulate the function R with high accuracy and resolution. At each time step we have a discrete distribution of the bottom source, $D_{i,j}$, where i,j denotes a grid point. The contribution from a $\Delta x \times \Delta y$ domain centered at this point is represented as a point source of strength $\Delta x \Delta y D_{i,j}$. When the depth, h, is taken into account this gives contribution to the elevation rate at another grid point, k,l, corresponding to

$$\eta_{ij,kl} = \sigma\frac{\Delta x\Delta y}{h^2}D_{ij}R\left(\frac{|\boldsymbol{r}_{kl}-\boldsymbol{r}_{ij}|^2}{h^2}\right).$$

The function R decays rapidly and the contributions are neglected when the distance is larger than 5 depths. To preserve volume the factor σ is determined such that the sum of the nonzero contributions equals the strength of the discrete point source. For grid increments up to one depth, say, the grid resolves the distribution of each point source well and σ remains close to unity. Gradients in the

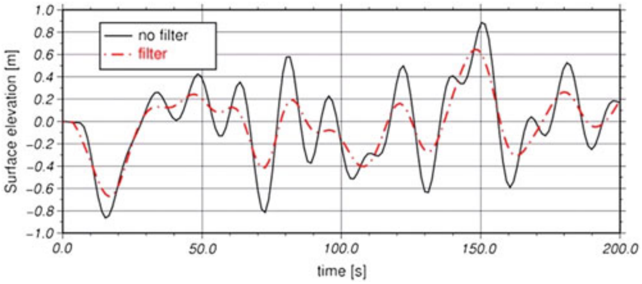

Fig. 3 Comparison of the time-history of the surface elevation at gauge 1 (Fig. 4) for dispersive solutions with and without filtering

source distribution, as in the front of a landslide, will then be redistributed over a distance of a few depths. For grid increments much larger than the depth this is not possible. The inclusion of the factor σ then essentially assures that the bottom source distribution is copied onto the surface, without volume loss. For a landslide filtered contributions are added to the surface at each time level. Figure 3 shows a comparison of the time history of the surface elevation of solutions with and without filtering the source distribution. The largest effects are on the shorter wave components (spurious waves) that follow the longer leading ones.

Tsunami Propagation

Most tsunami simulations are accomplished in two horizontal dimensions (2HD) for sea-surface elevation and depth-averaged horizontal wave current speed, by solving the linear and non-dispersive (hydrostatic) shallow-water (LSW) equations for conservation of mass and momentum (Mei 1989). However, in our case we see that the waves generated by the “W”-landslide are influenced by frequency dispersion, i.e. the waves propagate with a speed dependent on the wavelength; longer waves propagate faster than shorter ones. Non-linearity (the effect that leads to steepening of the wave fronts when entering shallower water) is only slightly changing the waveforms. The tsunami model is based on the Boussinesq equations, see Pedersen and Løvholt (2008) and references therein.

In Figs. 4 and 5, the surface elevation of the tsunami generated by the “W-landslide” is shown after 1 and 3 min, respectively. The maximum surface elevation during the simulation period is shown in Fig. 6. Inside and close to the area of the sliding masses the surface elevations are more than 10 m, and attenuate down to below 1 m in the central part of Trondhjemsfjorden. Close to the shoreline on the northern side of the fjord, the waves amplify from less than 1 m up to about 2 m. The amplification here is due to shoaling. The filter described in the latter section is applied with a typical depth of 100 m.

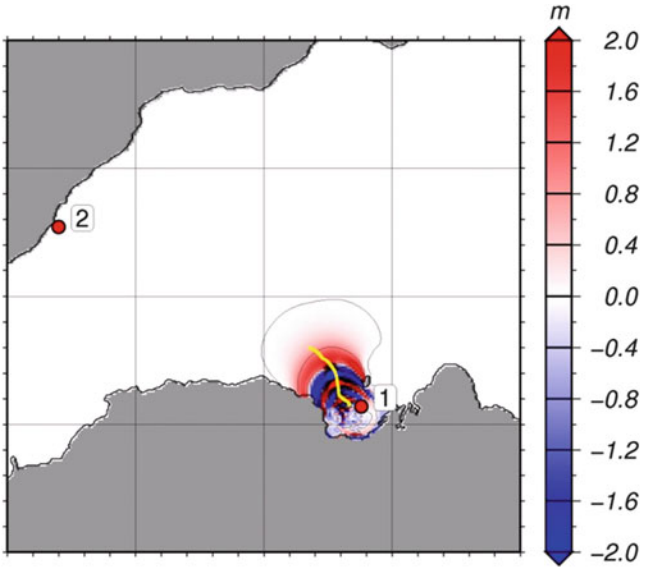

Fig. 4 Results from the tsunami simulation showing the surface elevation after 1 min. The locations of the gauges 1–2 are shown and the applied landslide track is indicated by a yellow line

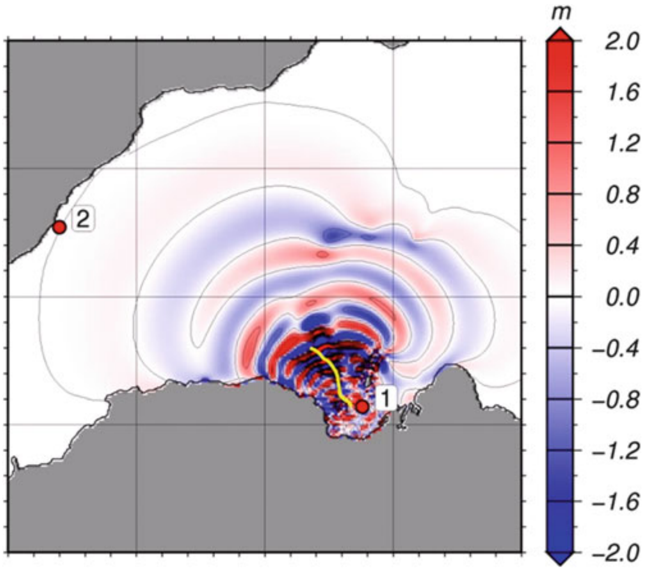

Fig. 5 Results from the tsunami simulation showing the surface elevation after 3 min, see also Fig. 4

To discuss the effects of dispersion and non-linearity, we compared time series of the surface elevation at synthetic gauges at two locations in the fjord (see Fig. 4 for the locations). Figure 7 reveals the results for gauges located outside Brattøra (gauge 1) and at Rørvika (gauge 2). At Brattøra the first wave is a depression formed by the infill of water at the tail of the landslide prior to the arrival of the wave peak formed above the front of the landslide. The effect of dispersion is here more or less absent for the leading waves due to short travel time for influence of

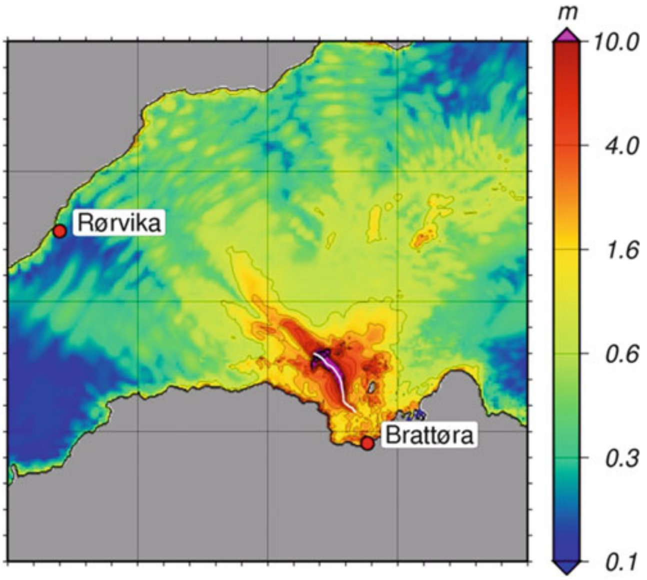

Fig. 6 Results from tsunami simulation showing the maximum surface elevation during the total simulation time. The white line shows the applied landslide track

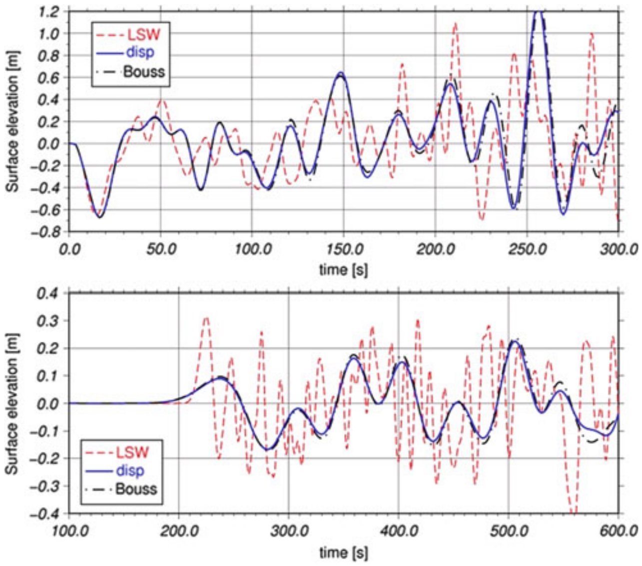

Fig. 7 Time history results of surface elevations outside Brattøra (gauge 1; *upper panel*) and Rørvika (gauge 2; *lower panel*) for different mathematical descriptions as explained in the text. The legends "LSW", "disp", and "Bouss" reflect the linear hydrostatic (or the linear non-dispersive), the linear dispersive, and the full Boussinesq descriptions (including both dispersion and non-linearity), respectively

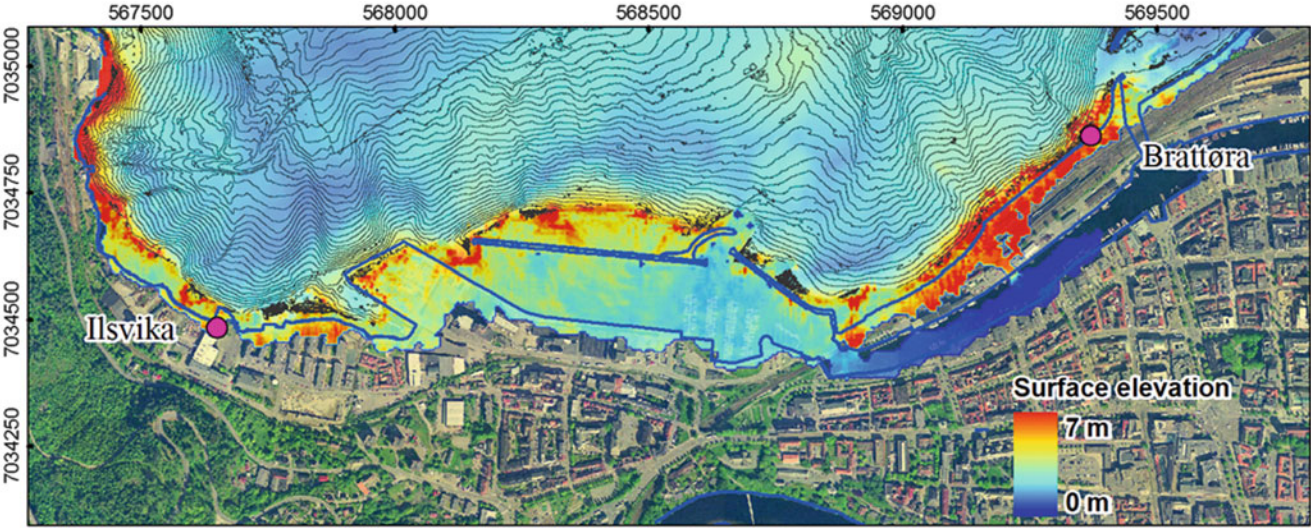

Fig. 8 From the tsunami inundation simulations, showing the maximum surface elevation off shore and maximum water levels on-shore (in meters). The time history of the water levels at the two marked locations on land is presented in Fig. 9

dispersion and shallower water. In addition, there is no significant effect of non-linearity. However, as we will see below, non-linear effects are important during inundation. On the other hand, when the waves have propagated a longer distance, to Rørvika, dispersion is clearly seen to give a lower and longer leading crest than in the LSW solution (Fig. 7). This is the typical characteristic of a dispersive wave front (Mei 1989; Løvholt et al. 2008). Also in the following wave train the dispersive solution is smoother since short components are left behind.

Tsunami Inundation

The tsunami inundation is calculated using the standard model ComMIT/MOST (ComMIT 2011; Løvholt et al. 2010). The surface elevation and velocity components from the tsunami propagation (linear dispersive description) above are given as input to the inundation model. The maximum surface elevations (offshore) and inundation heights (onshore) are shown in Fig. 8. Outside the shoreline

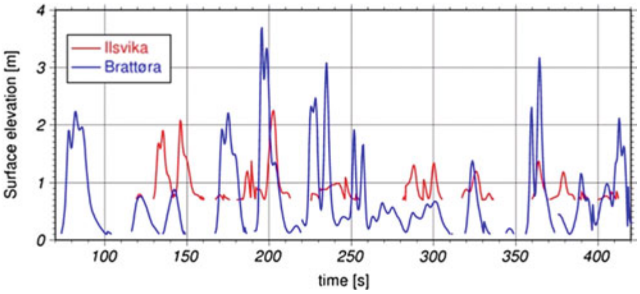

Fig. 9 The time history of the water levels (in meters) at the locations indicated in Fig. 8

the waves are breaking due to non-linear effects, leading to a reduction of the surface elevation. On land the maximum inundation heights are in the range of 2–7 m.a.s.l. Time history of the water level at two selected locations (onshore and close to the shoreline, Fig. 8) is presented in Fig. 9. The numerical simulations show that the waves arrives Ilsvika slightly before Brattøra. The simulated wave caused an inundation height of up to about 7 m along the shoreline at Brattøra, which compares well with the run-up height of 5–7 m observed in 1888 (Bjerrum 1971). Beyond the fact that the eyewitnesses described a wave approaching the shore from mid fjord, this confirms that the 1888 tsunami was generated by the "W"-landslide.

The water exposure onshore at Brattøra lasts up to 20–30 s for the impact of the first and fifth wave (Fig. 9). In this area, the stability of the near-shore slopes and embankment fill was greatly reduced following the initial landslide (c.f. L'Heureux et al. 2010a). As the wave receded, part of the railway station slumped into the fjord. It remains to be shown whether the lowering of the water level associated with the tsunami (i.e. increase in deviatoric stresses) and duration of the inundation were sufficient to trigger the observed final near-shore landslides / debris flows from the upper part, or whether they possibly developed retrogressively from below the sea surface.

Conclusion

The study of the tsunami generated by the 1888 landslide close to the Trondheim harbour, Norway is revised. The simulations are improved by introducing a special filter modelling the hydrodynamic response of the water surface during the generation phase. Further, the most likely landslide track (winding) is applied, as opposed to the straight line applied in previous studies. The filter reduces spurious waves in the generation area giving a more realistic wave pattern. The winding landslide track increases the inundation at Brattøra, due to better representation of the landslide position during the run-out (especially the first phase close to land). On the other hand, the filtering of the hydrodynamic response reduces the water levels, and in combination with the winding landslide the run-up is slightly higher compared to previous study (run-up only reported in L'Heureux 2010a). The modelling results are comparable to the one observed back in 1888.

Acknowledgements The authors are indebted to the International Centre for Geohazards (ICG) and the Norwegian Geotechnical Institute (NGI) for financing the writing of the present paper. The paper is ICG publication no. 366. Finn Løvholt is acknowledged for his contribution to this paper.

References

Bjerrum L (1971) Subaqueous slope failures in Norwegian fjords. Norwegian Geotechnical Institute, Publ. No. 88

ComMIT (2011) Software and documentation, http://nctr.pmel.noaa.gov/ComMIT/index.html, 2011-05-27

Dan G, Sultan N, Savoye B (2007) The 1979 nice harbour catastrophe revisited: trigger mechanism inferred from geotechnical measurements and numerical modelling. Mar Geol 245:40–64

Harbitz CB (1992) Model simulations of tsunamis generated by the storegga slide. Mar Geol 105:1–21

Imran J, Harff P, Parker G (2001) A numerical model of submarine debris flow with graphical user interface. Comput Geosci 27:717–729

Kajiura A (1963) The leading wave of a tsunami. Bull Earthq Res Inst 41:535–571

L'Heureux J-S, Longva O, Hansen L, Vingerhagen G (2007) The 1990 submarine slide outside the Nidelva River mouth, Trondheim, Norway. In: Lykousis V, Sakellariou D, Locat J (eds) Submarine mass movements and their consequences. Kluwer Series on Advances in Natural and Technological Hazards Research 27:259–267

L'Heureux JS, Longva O, Glimsdal S, Hansen L, Harbitz CB, Gauer P (2009) Causes for the 1888 shoreline landslide and tsunami in Trondheimsfjorden, Mid-Norway. In: Proceedings of the 1st international conference on seafloor mapping for geohazard assessment, Ischia Island, 11–13 May 2009

L'Heureux JS, Glimsdal S, Longva O, Hansen L, Harbitz CB (2010) The 1888 shoreline landslide and tsunami in Trondheimsfjorden, central Norway. Special Issue of Marine Geophysical Researches on Seafloor Mapping for Geohazard Assessment. DOI 10.1007/s11001-010-9103-z

L'Heureux JS, Hansen L, Longva O, Emdal A, Grande L (2010b) A multidisciplinary study of submarine landslides at the Nidelva fjord delta, central Norway – Implications for geohazards assessments. Norw J Geol 90:1–20

L'Heureux JS, Hansen L, Longva O, Eilertsen RS (this volume) Landslide along Norwegian fjords: characteristics, triggers and hazard assessment. In: Proceedings of the second world landslide forum, Rome

Locat J, Lee HJ (2002) Submarine landslides: advances and challenges. Can Geotech J 39:193–212

Løvholt F, Harbitz CB, Haugen KB (2005) A parametric study of tsunamis generated by submarine slides in the Ormen Lange/Storegga area off western Norway. Mar Pet Geol 22:219–231

Løvholt F, Pedersen G, Gisler G (2008) Oceanic propagation of a potential tsunami from the La Palma Island. J Geophys Res 113: C09026. doi:10.1029/2007JC004603

Løvholt F, Pedersen G, Glimsdal S (2010) Coupling of dispersive tsunami propagation and shallow water coastal response. In: Accepted for publication in Zahibo N, Pelinovsky E, Yalciner A, Titov V (eds) Proceedings of the "Caribbean Waves 2008" workshop in Guadeloupe Dec 2008. The Open Oceanography Journal 4:71–82

Marr JG, Elverhøi A, Harbitz CB, Imran J, Harff P (2002) Numerical simulation of mud-rich subaqueous debris flows on the glacially active margins of the Svalbard-Barents sea. Mar Geol 188:351–364

Mei CC (1989) The applied dynamics of ocean surface waves: advanced series on ocean engineering. World Scientific, Singapore, 760 p

Pedersen G (2001) A note on tsunami generation by earthquakes. Mech Appl Math 4:1–8

Pedersen G, Løvholt F (2008) Documentation of a global Boussinesq solver. Department of Mathematics, University of Oslo, Norway. http://urn.nb.no/URN:NBN:no-27775

Prior DB, Coleman JM, Bornhold BD (1982) Results of a known instability event. Geo-Mar Lett 2:117–122

Skaven-Haug S (1955) Undervannsskred i Trondheim havneomraade. Teknisk Ukeblad vol 102(7) (also in publ. 7, Norwegian Geotechnical Institute, Oslo, p 133–144)

Tappin DR (2009) Mass transport events and their tsunami hazard. In: Mosher DC, Shipp RC, Moscardelli L, Chaytor JD, Baxter CDP, Lee HL, Urgeles R (eds) Submarine mass movements and their consequences, advances in natural and technological hazards research, vol 28. Springer, Dordrecht, pp 667–684

THE SECOND
WORLD
LANDSLIDE FORUM

Landslides Along Norwegian Fjords: Causes and Hazard Assessment

Jean-Sebastien L'Heureux, Louise Hansen, Oddvar Longva,
and Raymond S. Eilertsen

Abstract

A collection of 28 well-known historical and near-shore landslide data is analysed in order to better understand the key factors governing mass-wasting processes along Norwegian fjords. The distribution of near-shore slope failures in Norway is linked to the occurrence of thick marine deposits. Compared to those found along deltas and on the steep side-walls of fjords, slope failures in bays and inlets have more often endangered coastal populations and infrastructures due to their extensive retrogression. Factors such as the presence of a weak layer, unfavourable groundwater conditions and stream erosion are found to often contribute to the failure of slopes. However, the dataset shows that more than 60 % of historical failures along Norwegian fjords are related to human activity. This enhances the need for a methodology integrating both on- and off-shore data for mapping the hazard and risks associated to such natural processes in Norway.

Keywords

Landslide • Near-shore • Fjords • Pre-conditioning factors • Trigger mechanisms • Norway

Introduction

Landslides along Norwegian fjords occur periodically and pose a constant threat to coastal communities. At several occasions, a relatively small underwater landslide cut back across the shoreline resulting in the loss of lives and severe damages (e.g. Longva et al. 2003). There are also examples of destructives landslide-triggered tsunami along Norwegian fjords (e.g. L'Heureux et al. 2010). The increasing societal awareness, together with a continuously growing coastal population and industrial development, calls for a better understanding of such natural hazards for planning and protection purposes.

Analysis of past landslide events can lead to important information regarding the factors contributing to failure, the mechanisms of sliding, and the links between mass-wasting processes and their tsunamigenic potential. With the aim to better understand the causes of slope failures along Norwegian fjords, a compilation of information about historical landslides was undertaken. This includes their distribution in relation to the geological settings. The acquired knowledge has important implications for the assessment of coastal hazards and their consequences in Norway.

Data and Limitations

This study compiles data from 28 historical landslides in the last 175 years in unconsolidated sediments along Norwegian fjords. The selected landslides have either initiated onshore at the shoreline or, started offshore and encroached on land. The landslides were selected based on available geomorphological, geological and geotechnical data found in the literature or in geotechnical reports.

J.-S. L'Heureux (✉) • L. Hansen • O. Longva
Geological Survey of Norway (NGU), 7491 Trondheim, Leiv Eirikssons vei 39, Norway
e-mail: jean.lheureux@ngu.no

R.S. Eilertsen
Geological Survey of Norway (NGU), Tromsø, Norway

C. Margottini et al. (eds.), *Landslide Science and Practice*, Vol. 5,
DOI 10.1007/978-3-642-31427-8_10, © Springer-Verlag Berlin Heidelberg 2013

High resolution bathymetric data and seismic data were used for morphological analysis where available. In other cases, coarse bathymetric data from the Norwegian hydrographic service were used. For most of the landslides, the data allowed volume estimations based on a given length, width and thickness of the failed areas. The data also allowed for estimation of maximum slope angle in the source area, slope angle in the deposition area, run-out length and length of retrogression onshore. Information regarding each landslide was catalogued in a geographically referenced framework.

One should bear in mind that the data presented in this study only gives a partial representation of mass wasting processes acting along Norwegian fjords. The coverage of slope failures is not necessarily representative as some areas have been investigated in greater details than others, e.g. due to economic interest or human activities. For example, failures that disturbed human activities are more thoroughly registered than events that occurred far from any human settlements. Another important asset is that the database, at this moment, only contains historical events. Numerous Holocene mass wasting deposits have been documented from several fjords in Norway and these should be incorporated to the catalogue in the future (e.g. Aarseth et al. 1989; Bøe et al. 2003).

Distribution of Landslides Along Norwegian Fjords

The distribution of the 28 historical landslides along Norwegian fjords is shown in Fig. 1. Events are concentrated from the middle of Norway and northwards, and in south-eastern Norway. Here, glacio-isostatic rebound and rapid fall of relative sea-level resulted in the emergence of thick, glacimarine and marine deposits. Subsequent leaching, by fresh groundwater during the Holocene, resulted in the development of very sensitive clays or quick clays (Rosenqvist 1953). Landslides along fjords are frequently associated with quick clays.

The registered slope failures have been divided based on the type of near-shore environment in which they occurred, i.e. along fjord deltas, in bays/inlets, or along steep sidewalls. Most of the registered near-shore landslides seem to occur in bays or inlets (65 %) where thickest deposits of clayey marine and glacimarine deposits are usually encountered (Fig. 2). Gravitational movements and slope processes are also frequent in the active deltaic environment of fjords (e.g. Prior et al. 1982; L'Heureux et al. 2007), but few are known to have encroached far onshore, or disturbed areas close to the shoreline (only 15 %). Landslide events along the steep sidewalls slopes count for 20 % of all failures. However, the boundary

Fig. 1 Distribution of historical near-shore landslides in sediment along Norwegian fjords

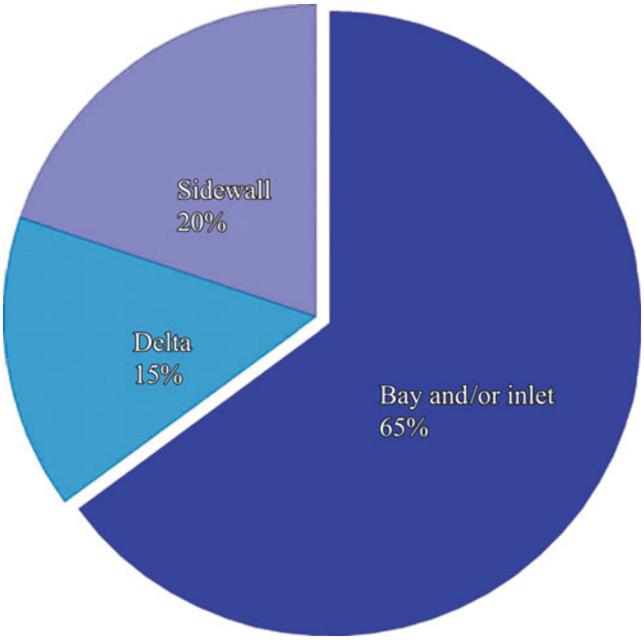

Fig. 2 Historical landslide distribution in the different types of fjord environments in Norway

between these environments is often difficult to assess. For example the bays and the steep sidewalls of a fjord are often affected by sedimentary processes from the river deltas.

The occurrence and distribution of landslides along fjord shorelines seems to be, at least to some extent, controlled by slope gradients. The average slope gradient in the source area is 17° with a range from 12° to 21° (Fig. 3a). These results are different than those presented by Hühnerbach et al. (2004) for Norwegian and Canadian fjords. This may be attributed to the quality and limited dataset presented by these authors, but also to the fact that our study only focuses on landslides that occurred in the vicinity of the shoreline.

Landslide Characteristics and Morphology

High resolution bathymetry data shows that landslides along Norwegian fjords often have distinct morphologies (see also Hansen et al. this volume). Similarly to other geological environments in the submarine realm (e.g. O'Leary 1991; Lastras et al. 2004; Bryn et al. 2005), fjord-marine deposits are seldom uniform and slope movement commonly follows inhomogeneities or specific layers in the stratigraphy. This results in flake-shaped or translational landslide (e.g. 1930 landslide in Orkdalsfjorden; Fig. 4). The scar area for such landslides shows a smooth and planar surface devoid of debris and is usually bordered by a distinct scarp, a few meters to tens of meters high. The planar surface often correlates to a distinct reflection on high resolution seismic data also interpreted as weak layers (e.g. Longva et al. 2003). Recent studies have shown that the weak layers in fjord settings often correlate to distinct event beds consisting of clays with thin seams of sand (L'Heureux et al. 2010b, c, 2011a). These stratified event beds have been linked to turbidity currents/flows generated in the fjord following terrestrial landslides in the emerging marine clays (Hansen et al. 2011a). Comparable event beds are documented from Canadian fjords (e.g. St-Onge et al. 2004).

Bowl-shaped landslides are also found at a few locations along fjords and inlets (e.g. Hansen et al. this volume; L'Heureux et al. 2011b). For these, the surface of rupture is usually curved and concave in profile. Because rotational landslides occur in relatively homogenous deposits, their incidence in man-made fills along fjord shoreline is much higher than for other types of movement. Such movement is also often observed in the cases where very sensitive clays or quick clay have been destabilised (by either natural or man-made factors). When sensitive clays are encountered in near-shore areas, the initial rotational landslide may lead to a retrogressive process propagating normally to the main slide axis. This results often in bottle-neck type of slides. Such features have been described for terrestrial quick clay landslides (e.g. Ter-Stepanian 2000).

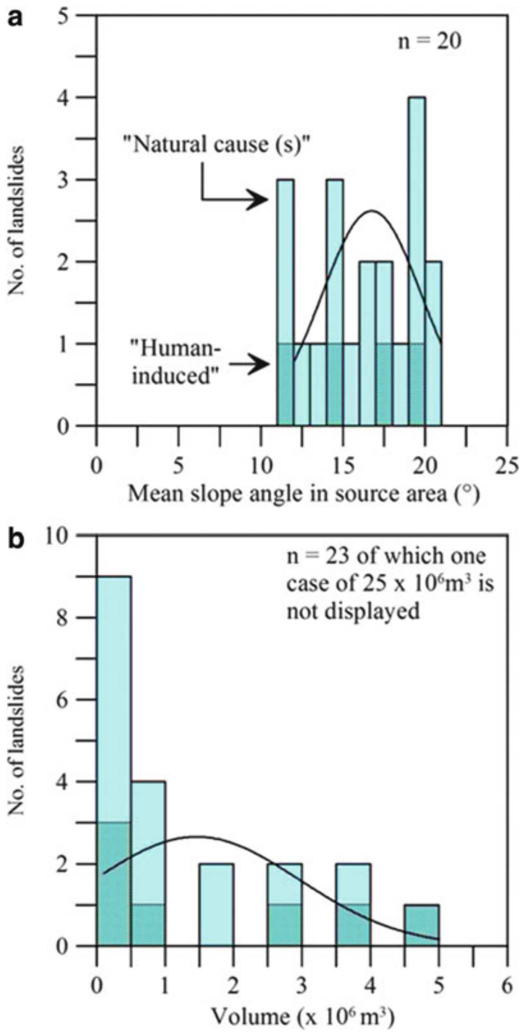

Fig. 3 Histograms showing the mean slope angle in the source area (**a**) and the volume (**b**) for historical landslides along Norwegian fjords. The solid black lines represent normal distributions for the parameters presented in each histogram

Landslides are important sedimentological processes along fjords and landslide debris often cover large portions of the fjord basins (Fig. 4). The historical database shows that the average mobilised volume of sediment is in the order of 1.5×10^6 m^3 (Fig. 3b). The dimensions of the landslides vary greatly and are usually limited by the morphology and geometry of the fjord (Syvitski et al. 1987), but also on the regional extent of failure-prone beds (L'Heureux et al. 2010b).

Causes and Failure Mechanisms

The registered near-shore landslides are not evenly distributed along Norwegian fjords. They tend to occur where there are thick bodies of fjord marine sediments,

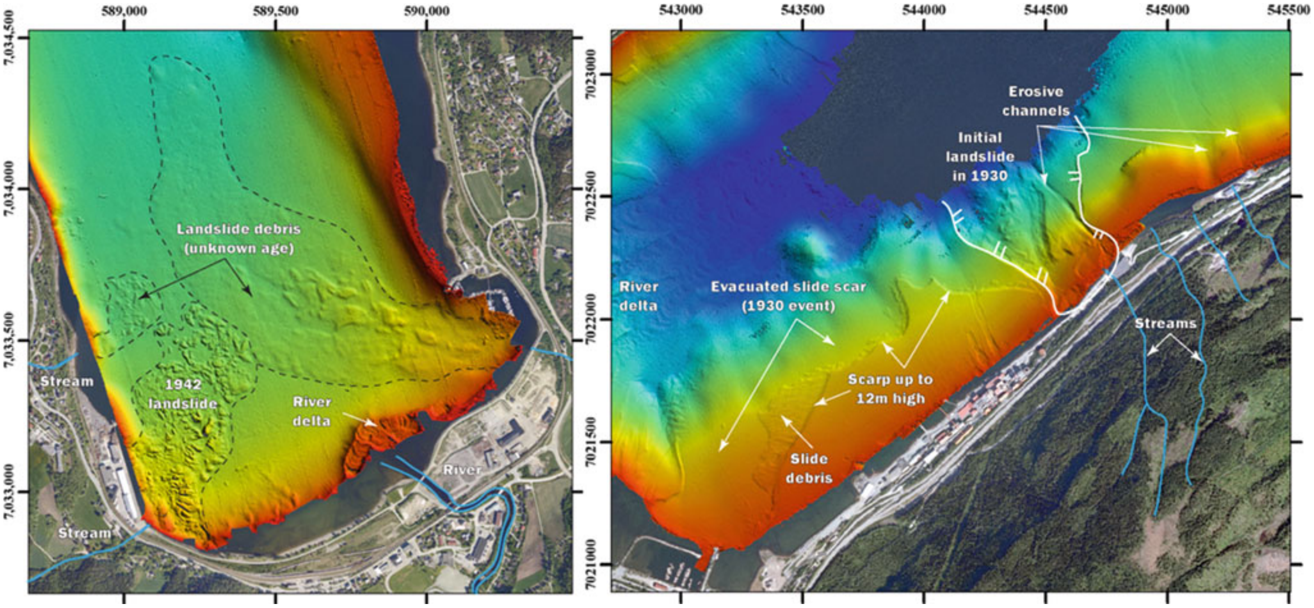

Fig. 4 Example of historical near shore landslides in Hommelvika (*left*) and Orkdalsfjorden (*right*). Note the presence of small streams debouching near the landslide locations

where the slopes are steep (Fig. 3a). Many factors are known to contribute to the initiation of landslides along fjords (Hampton et al. 1996; Locat and Lee 2002) and one of the major triggering mechanisms is often attributed to human activity. Out of the 28 landslides registered in this study, 17 (i.e. 60 %) can be attributed to the placement of fill or rock blasting during (or immediately after) construction work along the shore. As an example, rock blasting is responsible for at least three historical landslides along the shores of Sørfjorden/Finneidfjord (i.e. 1978, 1996 and 2006) (L'Heureux et al. 2010c). A similar mechanism has recently caused a large catastrophic failure along the shores of Kattmarka, near the town of Namsos, in 2009 (Nordal et al. 2009). The influence of human activity is further exemplified in Fig. 5 where during periods of nationwide public holidays in the summer (i.e. July), no landslides have been registered. Climatic reasons could also be invoked here as July is usually the driest month of the year in Norway.

There are most of the time natural predisposing factors needed for a landslide to be initiated, even for those triggered by human activity. Previous studies have shown that near-shore landslides frequently occur during periods of low tide through a mechanism similar to that of the rapid drawdown condition in earth dams. (i.e., the pore pressure in the sub-aerial part of the deposits does not have time to reach steady state conditions for the groundwater flow; Kramer 1988). The regional groundwater regime in the near-shore sediments also seems to play an important role in the predisposing of failure. Indeed, a great majority of the landslides occur during the thawing season in the spring and during the rainy season in the fall (Fig. 5a). This is similar with the timing of other coastal landslides elsewhere (e.g. Nice airport, Dan et al. 2007).

On land, stream erosion is generally accepted as a major cause of landslide initiation (e.g. Karlsrud et al. 1985). Active and erosive channel systems are also often found in areas where rivers and streams debouch into the fjord (e.g. Bøe et al. 2003; L'Heureux et al. 2009; Hansen et al. this volume). More than 55 % of the 28 historical landslides catalogued in this study initiated in areas where stream erosion might have played an important role in the predisposing and triggering of initial slope failure (e.g. Fig. 4).

Subaqueous and near-shore slope failures are often associated to earthquake loading (e.g. Lee et al. 2007). Along Norwegian fjords however, very few landslides can be linked to earthquakes in the historical record as the seismicity of Scandinavia is generally low. Such triggering mechanism was certainly more important in the early stages of the Holocene due to the higher rates of post-glacial rebound (e.g. Bøe et al. 2003).

Shallow gas is often found in fjord-marine sediments (e.g. L'Heureux et al. 2011a) and this may significantly alter the sediment's geotechnical properties, primarily by increasing the compressibility and reducing the undrained shear strength (e.g. Sills and Wheeler 1992). There is however, very little indication of mass movements in the vicinity of a prominent gas front in Sørfjorden/Finneidfjord (Vanneste et al. 2011). This could be related to local, smaller slope angles and/or regional variation in sediment properties. This calls for further investigations on the actual role of free gas in submarine mass movements (c.f. Vanneste et al. 2011).

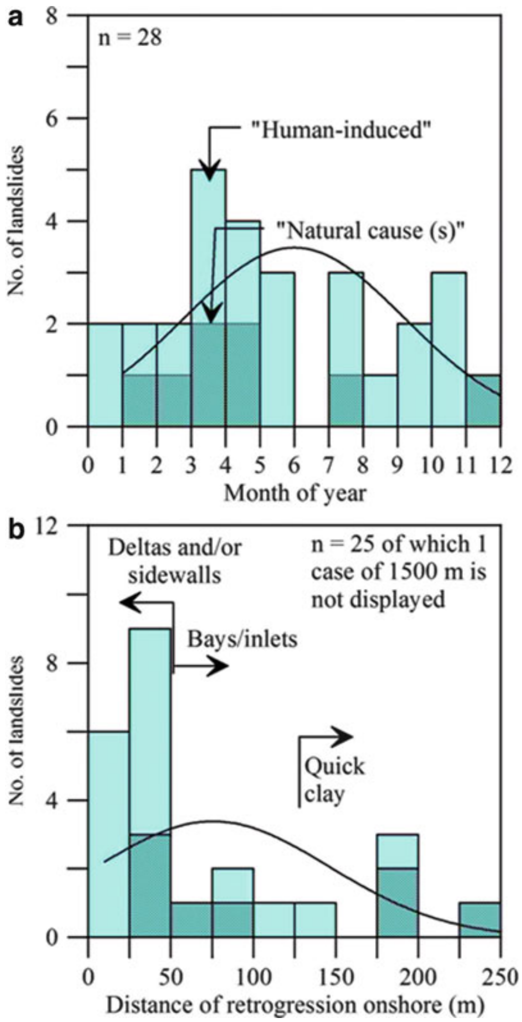

Fig. 5 (**a**) Frequency distribution of historical near-shore landslides along Norwegian fjords, and (**b**) histogram showing the magnitude of onshore retrogression for 25 historical near-shore landslides. The solid black lines represent normal distributions as the parameters presented in each histogram

Rapid deposition of sediment, such as in a fjord delta environment, can often outpace the expulsion of pore water and cause a state of underconsolidation and consequent low static shear strength (Hampton et al. 1996). There is however little knowledge on the influence of sedimentation rate on the stability of slopes along Norwegian fjords. Many of the larger Norwegian rivers are affected by human infrastructures (e.g. dams and retaining walls) and this likely influences sedimentation rates. The main factors affecting slope stability in deltas is rather attributed to slope over-steepening, erosional processes and to the accumulation/overloading of stratified deposits with contrasting geotechnical properties. Recent studies have shown that the presence of a weak layer is often necessary for the occurrence of a landslide (Longva et al. 2003; L'Heureux et al. 2010b, c, 2011a). These failure-prone layers tend to show a higher water content, lower shear strength, higher sensitivity, greater plasticity and lower permeability than the surrounding fjord-marine sediments. The regional extent and low-permeability of these beds may also allow for the formation of artesian groundwater pressure at different stratigraphic levels. This causes a lowering of effective stresses in the surrounding deposit and undermining slope stability.

Once triggered, an initial landslide may develop retrogressively. The magnitude of landslide retrogression is governed to a large extent by the capacity of the remoulded slide debris to flow out of the slide crater (Tavenas et al. 1983). Factors affecting this outflow will therefore play an important role in the development of retrogression (e.g. sensitivity of the deposit and morphology of the slide scar). In deltaic environments, the distance of onshore retrogression is usually less than 50 m (Fig. 5b) and this may be attributed to the presence of coarser material at the shoreline (e.g. L'Heureux et al. 2010b). For bays and inlets, the distance of retrogression is usually greater than 50 m and, in the case where quick clay is present in the vicinity of the shoreline, the distance of retrogression is usually more than 125 m (Fig. 5b). The marine and glacimarine deposits present along the steep sidewalls of a fjord also favours retrogression, but often the deposits in this environment are thin and do not extend far inland.

When assessing the hazard potential from near-shore landslides, not only the process leading to failure is of concern, but also the post-failure behaviour of the displaced mass. As seen in many fjords systems, a single slope failure can develop into an erosive sediment gravity flow affecting large areas and even trigger tsunamis. According to the present data set, up to 45 % of the 28 registered near-shore landslides have triggered tsunamis. Run-up heights were registered in 26 % of the cases with values from 1 to 7 m. The links between landslides and their potential to generate tsunamis is however not always clear. In the Trondheim harbour, for example, only one out of three large historical failures during the last century caused a tsunami wave (i.e. the 1888 event). The reason for this has been attributed to the seabed morphology surrounding the area of the 1888 landslide (i.e. along the flank of a deep underwater channel) and which led to an increased acceleration potential and a restricted evacuation path for the debris (L'Heureux et al. 2010a). The transition from failure to post-failure processes is crucial and has a direct influence on the acceleration and volume involved in the tsunami generation (e.g. Tinti et al. 2006; L'Heureux et al. 2011c).

Summary and Implications for Hazard Assessment

Key predisposing factors contribute to slope instability in near-shore areas of fjords. These are associated to the morphology of the slopes, the groundwater regime and the geological and geotechnical properties of the deposits. In many cases, landslides occur along given weak layers and the properties of these layers are similar in several fjords. A prerequisite for the occurrence of the weaker beds is the presence of prehistoric clay-slide activity in the catchment and a low to moderately dipping fjord margin on which the event beds are able to accumulate (Hansen et al. 2011). As sensitive, glacimarine sediments and clay-slides are common in uplifted fjord valleys of Canada and Scandinavia, and to a lesser extent in Alaska, beds with a similar origin as to those described here could play an important role for the stability of other near-shore areas (e.g. Saguenay fjord; Perret et al. 1995). Detecting these slide-prone beds is therefore of great importance for geohazards assessment. Such slide-prone beds have successfully been detected in Norwegian fjords using high-resolution seismic data in combination with in-situ geotechnical measurements (e.g. Longva et al. 2003; L'Heureux et al. 2010a; L'Heureux et al. 2011b).

The present database shows unequivocally that large landslides are frequent along Norwegian fjords and that this natural hazard poses a constant threat to the coastal communities. Such landslides have often been triggered by human activity. This unfortunately shows that there is a general lack of knowledge and/or data regarding the mechanism of slope failures in near-shore areas. During the last two decades, researchers have shown the great potential of combining multi-beam bathymetric surveys, high resolution seismic methods and more traditional geotechnical sounding techniques for studying landslides processes in the submarine environment (e.g. Locat and Lee 2009). Such methods can also be coupled to onshore mapping in order to fully understand processes acting in near shore areas (e.g. L'Heureux et al. 2010b; Cauchon-Voyer et al. 2011). Future mapping of the hazard and risk posed by mass wasting processes in near-shore areas should therefore combine on- and off-shore data (e.g. Hansen et al. this volume). The data set presented in this study shows that mapping should concentrate in areas where thick deposits of fjord-marine sediments are present and where streams, rivers and creeks debouch into the fjords.

Acknowledgments This is contribution no. 362 from the International Centre for geohazards.

References

Aarseth I, Lønne Ø, Giskeødegaard O (1989) Submarine slides in glaciomarine sediments in some western Norwegian fjords. Mar Geol 888:1–21

Bøe R, Rise L, Blikra LH, Longva O, Eide A (2003) Holocene mass movements process in Trondheimsfjorden, Central Norway. Norw J Geol 83:3–22

Bryn P, Berg K, Forsberg CF, Solheim A, Kvalstad TJ (2005) Explaining the Storegga slide. Mar Pet Geol 22:11–19

Cauchon-Voyer G, Locat J, Leroueil S, St-Onge G, Demers D (2011) Large-scale subaerial and submarine Holocene and recent mass movements in the Betsiamites area, Quebec, Canada. Eng Geol. doi:10.1016/j.enggeo.2011.04.011

Dan G, Sultan N, Savoye B (2007) The 1979 nice harbour catastrophe revisited: trigger mechanism inferred from geotechnical measurements and numerical modelling. Mar Geol 245:40–64

Hampton MA, Lee HJ, Locat J (1996) Submarine landslides. Rev Geophys 34:33–59

Hansen L, L'Heureux JS, Longva O (2011a) Turbiditic, clay-rich event beds in fjord-marine deposits caused by landslides in emerging clay deposits – palaeoenvironmental interpretation and role for submarine mass-wasting. Sedimentology 58:890–915

Hansen L, L'Heureux JS, Longva O, Eilertsen RS (2011) Undersjøiske landformer og skredprosesser langs strandsonen i Drammensfjorden. NGU rapport 2011.003

Hansen L, L'Heureux JS, Longva O, Eilertsen RS (this volume) Mapping of subaqueous landforms for near-shore landslide susceptibility assessment along Norwegian fjords. In: Proceedings of the 2nd world landslide forum, Rome

Hühnerbach V, Masson DG, and COSTA project partners (2004) Landslides in the north Atlantic and its adjacent seas: an analysis of their morphology, setting and behaviour. Mar Geol 213:343–362

Karlsrud K, Aas G, Gregersen G (1985) Can we predict landslide hazard in soft sensitive clays? Summary of Norwegian practice and experiences, vol 158. Norwegian Geotechnical Institute, Oslo, pp 1–24

Kramer SL (1988) Triggering of liquefaction flow slides in coastal soil deposits. Eng Geol 26:17–31

L'Heureux JS, Longva O, Hansen L, Vingerhagen G (2007) The 1990 submarine slide outside the Nidelva river mouth, Trondheim, Norway. In: Lykousis V, Sakellariou D, Locat J (eds) Submarine mass movements and their consequences, Kluwer Series on Advances in Natural and Technological Hazards Research 27:259–267

L'Heureux JS, Hansen L, Longva O (2009) Development of the submarine channel at the mouth of the Nidelva River, Trondheimsfjorden, Norway. Mar Geol 260:30–44

L'Heureux JS, Glimsdal S, Longva O, Hansen L, Harbitz CB (2010) The 1888 shoreline landslide and tsunami in Trondheimsfjorden, central Norway. Special Issue of Marine Geophysical Researches on Seafloor Mapping for Geohazard Assessment

L'Heureux JS, Hansen L, Longva O, Emdal A, Grande L (2010b) A multidisciplinary study of submarine landslides at the Nidelva fjord delta, Central Norway – Implications for geohazards assessments. Norw J Geol 90:1–20

L'Heureux JS, Longva O, Hansen L (2010) Mechanism for near-shore landslides along Norwegian fjords: examples from Trondheimsfjorden and Sørfjorden in Hemnes (In Norwegian). In: Kristiansen J, Gjelsvik V, Olsson R, Engen S (eds) Fjellsprengningsteknikk/Bergmekanikk/Geoteknikk 2010

L'Heureux JS, Longva O, Steiner A, Hansen L, Vardy ME, Vanneste M, Haflidason H, Brendryen J, Kvalstad TJ, Forsberg CF, Chand S, Kopf A (2011) Identification of weak layers and their role for the stability of slopes at Finneidfjord, northern Norway. In: Proceedings of the 5th international symposium on submarine mass movements and their consequences, Kyoto, Oct 2011

L'Heureux JS, Eilertsen RS, Hansen L, Sletten K (2011) Morphology and landslide mapping in lake Botnen at Rissa, Sør Trøndelag. (In Norwegian) NGU rapport 2011.037

L'Heureux JS, Eilertsen RS, Glimstad S, Issler D, Solberg IL, Harbitz CB (2011) The 1978 quick clay landslide at Rissa, mid-Norway: subaqueous morphology and tsunami simulations. In: Proceedings of the 5th international symposium on submarine mass movements and their consequences, Kyoto, Oct 2011

Lastras G, Canals M, Urgeles R, Hughes-Clarke JE, Acosta J (2004) Shallow slides and pockmark swarms in the Eivissa Channel, western Mediterranean sea. Sedimentology 51:1–14

Lee HJ, Ryan H, Haeussler PJ, Kayen RE, Hampton MA, Locat J, Suleimani E, Alexander C (2007) Reassessment of seismically induced tsunamigenic submarine slope failures in Port Valdez, Alaska, USA. In: Lykousis V, Sakellariou D, Locat J (eds) Submarine mass movements and their consequences. Springer, Dordrecht, pp 357–365

Locat J, Lee HJ (2002) Submarine landslides: advances and challenges. Can Geotech J 39:193–212

Locat J, Lee HJ (2009) Submarine mass movements and their consequences: an overview. In: Sassa K, Canuti P (eds) Landslides – disaster risk reduction. Springer, Berlin/Heidelberg, pp 115–142

Longva O, Janbu N, Blikra LH, Boe R (2003) The 1996 Finneidfjord slide: seafloor failure and slide dynamics. In: Locat J, Mienert J (eds) Submarine mass movements and their consequences, 531–538. Kluwer, Dordrecht

Nordal S, Alén C, Emdal A, Jendeby L, Lyche E, Madshus C (2009) Skredet i Kattmarkvegen i Namsos 13. mars 2009 – Rapport fra undersøkelsesgruppe satt ned av Samferdselsdepartementet. Tapir Uttrykk, Trondheim

O'Leary DW (1991) Structure and morphology of submarine slab slides: clues to origin and behaviour. Mar Geotech 10:53–69

Perret D, Locat J, Leroueil S (1995) Strength development with burial in fine-grained sediments from the Saguenay Fjord, Quebec. Can Geotech J 32:247–262

Prior DB, Coleman JM, Bornhold BD (1982) Results of a known instability event. Geo-Mar Lett 2:117–122

Rosenqvist IT (1953) Considerations on the sensitivity of Norwegian clays. Géotechnique 3:195–200

Sills GC, Wheeler SJ (1992) The significance of gas for offshore operations. Cont Shelf Res 10:1239–1250

St-Onge G, Mulder T, Piper DJW, Hillaire-Marcel C, Stoner JS (2004) Earthquake and flood-induced turbidites in the Saguenay Fjord (Québec): a Holocene paleoseismicity record. Quartern Sci Rev 23:283–294

Syvitski JPM, Burrell DC, Skei JM (1987) Fjords – processes and products. Springer, New York, p 379

Tavenas F, Flon P, Leroueil S, Lebuis J (1983) Remoulding energy and risk of slide retrogression in sensitive clays. In: Symposium on slopes on soft clays, Linköping, Swedish Geotechnical Institute, report no. 17, pp 423–454

Ter-Stepanian G (2000) Quick clay landslides: their enigmatic features and mechanism. Bull Eng Geol Environ 59:47–57

Tinti S, Pagnonil G, Zaniboni F (2006) The landslides and tsunamis of the 30th of December 2002 in Stromboli analysed through numerical simulations. Bull Volcanol 68:462–479

Vanneste M, L'Heureux JS, Baeten N, Brendryen J, Vardy ME, Steiner A, Forsberg CF, Kvalstad TJ, Laberg JS, Chand S, Longva O, Rise L, Haflidason, H, Hjelstuen, BO, Forwick, M, Morgan, E, Lecomte I, Kopf A, Vorren TO, Reichel T (2011) Shallow landslides and their dynamics in coastal and deepwater environments, Norway. In: Proceedings of the 5th international symposium on submarine mass movements and their consequences, Kyoto, Oct 2011

Mapping of Subaqueous Landforms for Near-Shore Landslide Susceptibility Assessment Along Norwegian Fjords

Louise Hansen, Jean-Sebastien L'Heureux, Oddvar Longva,
Raymond S. Eilertsen, and Reidulv Bøe

Abstract

Landslides in unconsolidated sediments along the shoreline of Norwegian fjords are recurrent phenomena and can have large consequences. With high-resolution bathymetric mapping it is possible to get a quick overview over regional patterns of subaqueous, near- shore conditions. Test programs at the Geological Survey of Norway have mapped submarine near shore areas along selected Norwegian fjords. Subaqueous features were identified and classified to obtain a comprehensive overview over near-shore processes and deposits. The focus was identification of mass-wasting processes and features of relevance for the stability of fjord sediments. The mapping shows that traces of, for example, mass-wasting processes are more widespread than previously known. The maps can be combined with terrestrial data and used for near-shore landslide susceptibility assessment and hazard mapping, but are also considered as relevant for other purposes.

Keywords

Landslides • Mapping • Susceptibility • Fjord • Shoreline • Subaqueous landforms

Introduction

Landslides along fjords occur due to a variety of natural factors such as erosion, rapid sedimentation, earthquake shaking, tidal variations or wave action, and are also often linked to human activity. L'Heureux et al. (this volume) show that more than 60 % of the shoreline mass failures in Norway during the last 175 years are related to human activity. This has resulted in loss of human life and large damage to infrastructures. There is, therefore, a need for mapping areas susceptible to shoreline hazards for planning and protection purposes.

Landslide types along fjord shorelines vary and depend on the morphology of the fjord, the type of sediment involved and the triggering mechanism. The more severe mass-wasting events are often associated with sensitive clay or quick clay (e.g. Longva et al. 2003; L'Heureux et al. this volume). Quick clay occurs in marine deposits due to leaching processes (Rosenqvist 1953) and such deposits are widespread along Norwegian fjords. Quick clays have also been registered up to 100 m from the shoreline into the fjord (Sleipnes 1997, 1998). Following the 1978 landslide at Rissa, a programme for quick-clay hazard mapping was undertaken in Norway. The main goal of the programme was to map areas susceptible to large landslides based on topographical, geological, geotechnical and hydrological criteria. The programme has, however, focused only on quick clay hazard on land and areas off the shoreline have not been evaluated.

Modern swath bathymetric data provides important information on the morphology and sedimentary processes in deep water and also in near-shore environments. Although there are several detailed examples of high-resolution bathymetric

---

L. Hansen (✉) • J.-S. L'Heureux • O. Longva • R. Bøe
Geological Survey of Norway (NGU), Leiv Eirikssons vei 39,
N-7491 Trondheim, Norway
e-mail: louise.hansen@ngu.no

R.S. Eilertsen
Geological Survey of Norway (NGU), Polarmiljøsenteret,
N-9296 Tromsø, Norway

C. Margottini et al. (eds.), *Landslide Science and Practice*, Vol. 5,
DOI 10.1007/978-3-642-31427-8_11, © Springer-Verlag Berlin Heidelberg 2013

mapping in fjords and other near-shore areas (e.g. Bøe et al. 2003, 2004; Longva et al. 2003; Lyså et al. 2008; L'Heureux et al. 2010; Cauchon-Voyer et al. 2011), there has been little focus on mapping near-shore areas at a regional scale for geohazard purposes. During various test projects at the Geological Survey of Norway (NGU), high resolution bathymetric mapping has been carried out along more than 100 km of Norwegian fjords (Longva et al. 1999; Hansen et al. 2005; Hansen et al. 2011). With high resolution maps of underwater landforms it is possible to recognize areas subjected to erosion and instability (e.g. Locat and Lee 2009). This paper presents a first landform classification scheme covering the range of subaqueous processes typically affecting near-shore deposits. The purpose of the paper is to summarize the subaqueous landform types and to show their relevance for landslide susceptibility mapping. The purpose is also to show how land data and sea data can be combined as a basis for hazard and risk assessment along the shoreline.

Norwegian Mapping Procedures

The development and production of susceptibility, hazard and risk maps require several types of basic data such as maps showing Quaternary geology, geomorphology and topography.

Quaternary Mapping

According to Norwegian standards, Quaternary maps on land are produced mainly on the basis of air photo interpretation and extensive fieldwork. The maps display genetic deposit types as polygons with different colours, landforms as line signatures, general grain size information and several additional features. Mapping is carried out at various scales (typically 1:50,000 or 1:20,000). The maps have been produced over several decades and are used for a broad range of purposes such as mapping of natural resources, environmental conditions and as a basis for understanding the general landscape history. Subaqueous conditions are generally not included in standard Quaternary maps. Exceptions are some maps at 1:50,000, where general deposit types in the central parts of fjords are included but with little information along the shoreline. NGU has recently started to publish digital "Marine Base Maps" from the coastal zone. These maps can be compared to other digital seabed maps published by the MAREANO Programme in the offshore areas (www.mareano.no) and are intended to represent a first step towards systematic marine geological map production in the coastal zone.

Landslide Susceptibility and Hazard Mapping

In Norway, terrestrial landslide susceptibility maps for some landslide types are available to the public via the web (www.skrednett.no). Here, hazard and risk maps for quick-clay landslides on land are available. Hazard maps for quick-clay landslides are based on the distribution of unconsolidated marine deposits that have emerged above sea level due to glacioisostatic rebound. The hazard mapping requires, in addition, topographical information of appropriate resolution and test drillings. Signs of active erosion and the distribution of landforms such as landslide scars and ravines are taken into account. This information can be extracted from the Quaternary maps, topographical data and field surveys. Mapping procedures are described by Gregersen (2008). It should be stated that the onshore maps are not hazard maps sensu stricto since probability is not considered, but they could be regarded as susceptibility maps pointing out areas where larger landslides can potentially occur.

Seafloor Mapping

In Norway there are several institutions that perform bathymetric mapping, including the Hydrographic Service and the Defence Research Institute. Still, large parts of the coast lack coverage of high resolution maps. NGU has developed methods for mapping near shore instabilities and bathymetric data are collected using a 125 kHz and 250 kHz GeoSwath interferometric sidescan sonar from GeoAcoustics (e.g. Lyså et al. 2008; Lepland et al. 2009). Depths from near sea level down to between 80 and 200 m can be mapped. Two types of data are recorded: bathymetric and backscatter data. The former gives high-resolution depth information, while the latter gives information about the seafloor character (e.g. grain size, bedrock, roughness). The accuracy of depth measurements during data acquisition is in centimetre–decimetre scale. The high-resolution bathymetry data can be combined with the onshore Quaternary maps, using GIS. Such combination gives the opportunity to map several types of subaqueous landforms and see how they relate to potentially unstable deposits onshore.

Classification of Subaqueous, Near-Shore Landforms

Below is a generalized summary of typical landforms that have been observed from high-resolution bathymetric information in near-shore areas of selected Norwegian fjords.

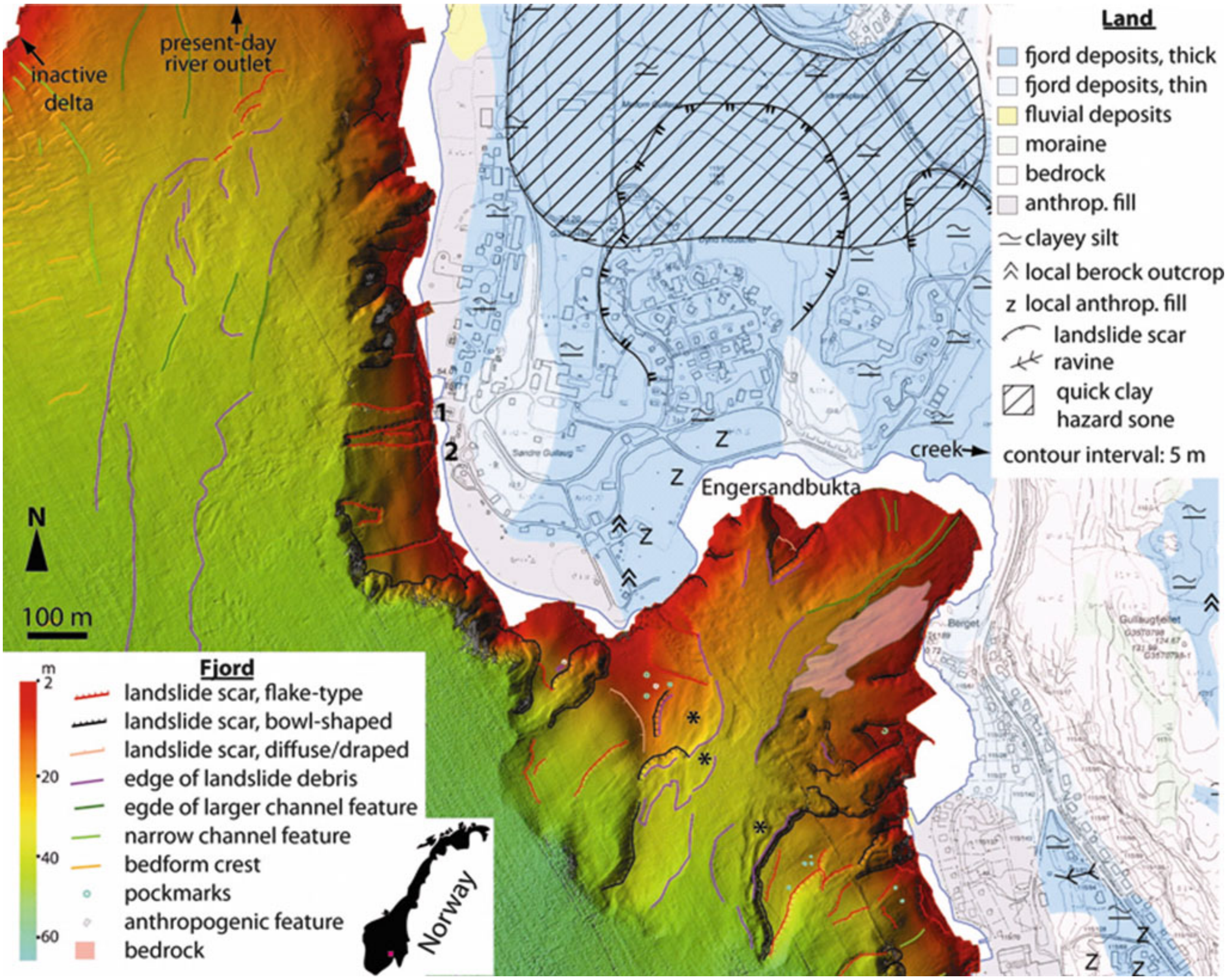

Fig. 1 Example of map combining information from land and interpreted high-resolution bathymetric data from Drammensfjorden, southern Norway (from Hansen et al. 2011). A landslide following land filling occurred at 2 in 1974 south of the existing pier at 1. Flake-type landslide scars are interpreted as associated to this event. Areas marked with asterisk show areas with signs of undercutting at the base of subaqueous slopes at the mouth of the embayment at Engersandbukta

Several landforms are interpreted to have impact on near shore stability. Larger landforms such as deltas and major moraines are also included. The landforms are divided into nine main classes some of which are further subdivided into types. The landforms are in different scales and some forms are superimposed on larger forms. Examples of landforms are illustrated in Fig. 1.

1. Landslide scars. Two types of landslide scars occur frequently. These are flake-shaped and bowl-shaped scars (e.g. Hansen et al. 2005; Lyså et al. 2008; Hansen et al. 2011). The flake-type scars have planar centres and a back scarp typically a few metres high (Fig. 1). The debris is often evacuated from the scar (e.g. Bøe et al. 2003). The areal extent can be several hundred square metres and gradients are typically down to around 5° as recorded in Drammensfjorden. Locally, scars with lower gradients have been recorded (Lyså et al. 2008). The bowl-shaped scars are deeper than the flake-type scars. These scars are either singular features or are composed of several smaller coalescing scars (Fig. 1). A few scars show similarities with bottle-neck shaped, onshore quick-clay landslide scars (Hansen et al. 2011). Large landslide events can leave complex morphologies with several scars and landslide debris (e.g. L'Heureux et al. 2007; L'Heureux et al. 2009). A third variation comprises scars that are draped by sediment to the degree that they appear diffuse and are not easily assigned to the two other types (Fig. 1).
2. Landslide debris. Landslide debris is recognized by an irregular and rugged fjord bottom and consists of blocks and flakes of partially intact deposits and/or lobes/fans of more remoulded debris and diluted flows

(e.g. Longva et al. 2003; Lyså et al. 2008; Hansen et al. 2011). The debris is present on near-shore slopes where it is commonly accumulated in landslide scars and in depressions sloping towards the central fjord. Debris is also commonly found on the flat, central fjord basin floor along the foot of marginal slopes (e.g. Fig. 1). Debris is also common at the mouth of channel-like features and embayments. Previous studies show that debris can travel several kilometres along the fjord bottom. This is confirmed by bathymetric data (e.g. Hansen et al. 2011).

3. Channel features. There are several types of channel features. Some are narrow and linear extending from shallow water, for example as the extension of an onshore stream, and into deeper parts of the fjord. Chute-channels can be identified on the slope of delta bodies. Others are wider with a more planar base, locally with debris (e.g. L'Heureux et al. 2009). Deeply incised V-shaped features are comparable to onshore ravines. Several channel-like features are partially or entirely limited by bedrock outcrops. Some channel-like features locally represent the tracks from out-runner blocks from rock failures or landslides in unconsolidated sediments (e.g. Longva et al. 2003).
4. Plunge pools. Plunge pools are found on the fjord floor and are either linear and parallel to the slopes or are more circular. The more circular types are found in the extension of channel features and/or landslide scars on the fjord marginal slopes. Craters up to 2 m deep are common (e.g. Hansen et al. 2011) but features over 10 m deep have been recorded (L'Heureux et al. 2009).
5. Pockmarks. Pockmarks are circular features on the fjord floor where water or gas have escaped. Pockmarks are found in shallow water as well as on the deep floor bottom. There are two main types. The more common type is a circular depression with typically a diameter of 4–12 m and a depth from a few decimetres to over a few metres (Hansen et al. 2005; Hansen et al. 2011). A few are over 30 m in diameter with a depth up to 9 m as, for example, registered along the base of a slope in Drammensfjorden. Even larger features have been registered in a Norwegian lake (L'Heureux et al. 2011). Ring-shaped features with a small protuberance in the middle represent another type of pockmark and are typically 10–40 m in diameter and with a relief on the decimetre scale (e.g. Lyså et al. 2008).
6. Bedforms. Dunes have been recorded where currents are, or have been, active. They occur on deltas, where undercurrents are occasionally active, and in shallow areas along the shoreline where long-shore currents prevail (e.g. Hansen et al. 2005; Lyså et al. 2008; Hansen et al. 2011).
7. Deltas and cones. These are shown as protuberances in the bathymetry in the extension of streams on land. Smaller features such as landslide scars or bedforms and channels (chutes) are often superimposed (e.g. see upper left corner in Fig. 1).
8. Glacigenic features. Some features are of glacigenic origin such as partially buried moraine ridges (e.g. Hansen et al. 2011). Smaller features, such as landslide scars, are often superimposed and can help to distinguish moraines from, for example, bedrock outcrops.
9. Bedrock. Bedrock is identified as irregular features on the sea bottom (e.g. Fig. 1).
10. Anthropogenic features. Anthropogenic activities have left many traces in the investigated fjords such as land fill, anchor marks, ship wrecks and dumped material (e.g. Hansen et al. 2011).

Identification of most of the above features requires high resolution bathymetric data. The larger features such as deltas and moraines can be identified on low resolution maps but they will often lack important details. The above classification will likely be adjusted as experience increases. Only morphological information is included here and the addition of backscatter information can also lead to some adjustments.

One advantage of the high resolution information is that the causal relationship between various landform types can be assessed. As an example, slopes in one area in an embayment that show signs of undercutting can be assigned to erosive flows generated in another part of the same embayment. An example of this is shown in Fig. 1 at the mouth of the embayment at Engersandbukta (see asterisk). Also, relative ages can be assessed roughly as diffuse landforms draped by sediments are older than well-defined forms with distinct outlines.

The subaqueous datasets give a general overview of sedimentary processes along the shoreline through time. Some stretches of the shoreline display little signs of mass-wasting and erosion whereas others seem to have more activity. The maps generally show that traces of various near-shore processes are more widespread than previously known (e.g. Fig. 1).

Integration of On- and Off-Shore Data for Landslide Susceptibility Assessment Along Norwegian Fjords

The combination of terrestrial and marine near-shore datasets indicate where erosional processes can affect areas across the shoreline. The terrestrial Quaternary maps show the distribution of deposits that could potentially be affected by an underwater landslide through onshore retrogression.

The detailed information on near-shore landforms is comparable to the type of information used for the ongoing, onshore quick clay hazard-mapping programme. For this programme, the hazard level is calculated as the sum of scores on various factors such as height of slope, signs of ongoing erosion, distribution of old landslide scars, and pore pressure conditions. (Gregersen 2008). In this way the detailed subaqueous information can supplement the onshore data.

As for the onshore maps, high resolution bathymetry data will accurately give indication of slope heights and gradients. Signs of earlier landslide activity and erosion processes (e.g. channels) can be mapped. Of special importance are indications of undercutting of slopes. Such information cannot be extracted from low resolution bathymetric information or air photos. Unfavourable groundwater conditions are important to map for hazard assessment. Here, some qualitative information about the pore pressure conditions can be extracted from seabed imagery through the mapping of pockmarks. Such features show areas that, at least temporarily, could be exposed to high pore pressures. Stabilizing features such as bedrock or moraines can be extracted. The bathymetric information is also valuable for tsunami modelling.

Although there are several similarities of the types of information that can be extracted from on- and offshore datasets, important differences also exist. Onshore areas are only locally exposed to natural sedimentation. Here erosion prevails, for example along rivers or in ravines. In contrast, subaqueous areas are subjected to a combination of deposition and erosion which is a primary factor for changes in stability over time.

Studies by, for example, L'Heureux et al. (2010) and Cauchon-Voyer et al. (2011) show the importance of integrating on- and off-shore data sets for understanding near-shore mass-wasting processes. On a regional scale, the classification scheme presented above provides important information on subaqueous landforms and mass-wasting processes that can be used for landslide susceptibility mapping. As a first step, stretches along the shoreline that display high activity of near-shore processes with regard to erosion and groundwater or gas seeps could be regarded highly susceptible to near-shore landslides (e.g. Hansen et al. 2005). On the other side, stretches of the shoreline with few signs of activity could be regarded as low susceptibility zones.

Priorities for Mapping

L'Heureux et al. (this volume) demonstrate the need for more systematic mapping of near shore hazard in Norway. There have been previous suggestions on how hazard mapping could be extended into the fjord (Emdal et al. 1997; Longva et al. 1999; Gregersen 1999; L'Heureux 2009). However, the Norwegian shoreline is c. 83,000 km long (regional scale including islands; no.wikipedia.org) and several stretches are dominated by bedrock and/or have little or no population. Careful planning and priorities are therefore needed to perform the most beneficial and cost-effective mapping of near-shore areas. At present there is no defined plan for such mapping in Norway. Several factors, besides the density of the population, can be used as a basis for choosing areas for near-shore mapping. The occurrence of previous shoreline landslides or onshore quick clay landslides is one factor (L'Heureux et al. this volume). Other factors are the percentage of stretches along the fjord with exposed marine and other unconsolidated deposits versus, for example, stretches with bedrock. Embayments, where numerous historic landslide events have been recorded (L'Heureux et al. this volume), should be given priority. In addition, areas with expected high sedimentation rates (e.g. near river outlets) could be weighed. Areas susceptible to other geohazards such as rock fall events or unstable rock slopes could also be considered. Additional factors for priority could be the need for subaqueous mapping for other purposes such as marine habitats, Quaternary geology or marine resources. The most beneficial would be an integrated regional marine mapping program including both near-shore areas and deeper areas. Airborne surveys of the near-shore bathymetry could potentially give important subaqueous information over vast areas relatively fast (e.g. Wozencraft 2001). However, further development of the techniques is needed to increase penetration and obtain data of sufficient resolution.

Some prioritized areas can be surveyed repeatedly over many years in order to monitor potential changes in morphology which may have consequences for hazard assessment. Although near-shore mapping using swath bathymetry is relatively efficient it will take time before the important areas have been mapped. However, databases on high-resolution, near-shore, bathymetric data from the fjords are growing. Once the data sets are available, no matter the original reasons for mapping, the data should be used for landslide susceptibility assessment and hazard mapping.

Conclusions

High-resolution, near-shore bathymetric maps not only show the distribution of previous landslide events; they also indicate the presence of potentially destabilizing conditions in the fjord such as pockmarks, steep slopes, signs of erosion and other features. The maps give information on the interplay between the various processes and show which areas undergo changes, such as progressive undercutting of subaqueous slopes. The high-resolution data helps to point out areas that are more active over time and more susceptible to slope failure. Such information cannot be extracted from the available near-shore bathymetric information of low resolution. The improved bathymetric information also allows for more confident local stability assessments. All together, the data provide a valuable framework for further landslide hazard and risk assessment along the shorelines of Norwegian fjords. The high-resolution maps also provide a step towards extending detailed, onshore Quaternary maps into the fjord to link on- and offshore landscape development. Priorities for mapping should be coordinated with other mapping activities. An additional advantage of the interpreted, high-resolution images is that they increase public awareness concerning stability along the shoreline.

Acknowledgements A recent project on method development for mapping of areas susceptible to shoreline landslides was financed by the Norwegian Water Resources and Energy Directorate (NVE).

References

Bøe R, Rise L, Blikra LH, Longva O, Eide A (2003) Holocene mass movements i Trondheimsfjorden, Central Norway. Nor J Geol 83:3–22

Bøe R, Longva O, Lepland A, Blikra LH, Sønstegaard E, Haflidason H, Bryn P, Lien R (2004) Postglacial mass movements and their causes in fjords and lakes in western Norway. Nor J Geol 84:35–55

Cauchon-Voyer G, Locat J, Leroueil S, St-Onge G, Demers D (2011) Large-scale subaerial and submarine Holocene and recent mass movements in the Betsiamites area, Quebec, Canada. Eng Geol 121(1–2):28–45

Emdal A, Nordahl S, Janbu N (1997) Videreføring av kartlegging av fare for løsmasseskred i Norge. Høringsutkast. Norwegian University of Science and Technology (NTNU) report O.97.03-1. 33p. In Norwegian

Gregersen O (1999) Testprosjekt Tromsø. Kartlegging av skredfare. Kartblad M711 1534 III. Norwegian Geotechnical Institute (NGI) report 980074–1. 22p. In Norwegian

Gregersen O (2008) Program for økt sikkerhet mot leirskred – Metode for kartlegging og klassifisering avfaresoner, kvikkleire. Norwegian Geotechnical Institute (NGI) report 20001008–2 (3rd revision). 24p. In Norwegian

Hansen L, Eilertsen R, Longva O (2005): Skredkartlegging langs kystsonen i Trondheimsområdet, Datagrunnlag og morfologi. Geological survey of Norway. NGU rapport 2005.054. 25p. In Norwegian

Hansen L, L'Heureux J-S, Longva O, Eilertsen RS (2011) Undersjøiske former og skredprosesser langs strandsonen i drammensfjorden. Geological survey of Norway. NGU rapport 2011.003. 34p. In Norwegian

L'Heureux J-S (2009) A multidisciplinary study of shoreline landslides: from geological development to geohazard assessment in the bay of Trondheim, Mid-Norway. Ph.D. thesis. Norwegian University of Science and Technology (NTNU). 158p

L'Heureux J-S, Hansen L, Longva O, Vingerhagen G (2007) The 1990 submarine slide souside the Nidelva river mouth, Trondheim, Norway. In: Lykousis D, Sakellariou D, Locat J (eds) Submarine mass movements and their consequences. Kluwer Series on Advances in Natural and Technological Hazards Research 27:259–267

L'Heureux J-S, Hansen L, Longva O (2009) Development of the submarine channel at the mouth of the Nidelva river, Trondheimsfjorden, Norway. Mar Geol 260:30–44

L'Heureux J-S, Hansen L, Longva O, Emdal A, Grande L (2010) A multidisciplinary study of submarine landslides at the Nidelva fjord delta, Central Norway – Implications for geohazards assessments. Nor J Geol 90:1–20

L'Heureux J-S, Eilertsen RS, Hansen L, Sletten K (2011) Morfologi og skredkartlegging i Botn, Rissa, Sør-Trøndelag. 25p. NGU rapport 2011.037. In Norwegian

L'Heureux J-S, Hansen L, Longva O, Eilertsen RS (2011) Landslides along Norwegian fjords: causes and hazard assessment. In: Proceedings of the second world landslide forum, Rome. This volume

Lepland A, Bøe R, Lepland A, Totland O (2009) Tracking the volume and lateral spread of disposed sediments by acoustic methods, Oslo Harbour, Norway. J Environ Manage 90:3589–3598

Locat J, Lee H (2009) Submarine mass movements and their consequences: an overview. In: Sassa K, Canuti P (eds) landslides-disaster risk reduction. Springer, Berlin/Heidelberg, pp 115–141

Longva O, Blikra LH, Mauring E, Thorsnes T, Reither E (1999) Testprosjekt Finneidfjord; Integrert skredfarekartlegging – metodevurdering. NGU report 99.051. 62p

Longva O, Janbu N, Blikra LH, Boe R (2003) The 1996 Finneidfjord slide; seafloor failure and slide dynamics. In: Locat J, Mienert J (eds) Submarine mass movements and their consequences. Kluwer, Dordrecht, pp 531–538

Lyså A, Hansen L, Christensen O, L'Heureux JS, Longva O, Olsen HA, Sveian H (2008) Landscape evolution and slide processes in a glacioisostatic rebound area; a combined marine and terrestrial approach. Mar Geol 248:53–73

Rosenqvist IT (1953) Considerations on the sensitivity of Norwegian clays. Géotechnique 3:195–200

Sleipnes A (1997). Ground investigation and data report: Wh-07.07.8 – RV808-01: Finneidfjord E6 – Hemnesberget. Ras ved Finneidfjord. Statens Vegvesen. Supplerende undersøkelser. In Norwegian

Sleipnes A (1998). Ground investigation and data report: Wh-07.07.11 – RV808-01: Finneidfjord E6 – Hemnesberget. Ras ved Finneidfjord. Sikring med kalk-sementpeler. Erfaringsrapport. Statens Vegvesen. In Norwegian

Wozencraft JM (2001) The coastal zone revealed through SHOALS LIDAR data. In: Proceedings, Hydrographical Society of America (THSOA). http://www.thsoa.org/hy01/9_1.pdf

Part II

Landslide in Coastal Area

Introduction by Crescenzo Violante

CNR, Istituto per l'Ambiente Marino e Costiero, Naples, Italy

Coastal areas are potentially subject to mass-wasting events over a range of magnitude and period of recurrence that account for active cliff recession, lateral collapse of coastal slopes, and sudden increase in sediment load in short coastal rivers (flash floods). These phenomena deliver significant amount of materials in the sea at intermittent time interval in the form of cliff debris, landslide accumulations, coarse-grained delta and as turbiditic flows. The resulting deposits are transient trough the shore zone and mostly redeposited at great depth, exposing the coast to wave action and ultimately to an irreversible loss of land over a human-scale periods.

Retreat of coastal slope is both produced by wave and weathering action. Although basal erosion is a critical factor for slope instability, precipitation and infiltration of waters resulting from rainfalls and groundwater can act in the upper part of the slope significantly contributing to coastal failure. The importance of wave action as eroding factor and of coastal seas as a sink for displaced materials, highlight the role of marine geological investigations for coastal landslide hazard assessment. Furthermore, the use of historical data is an important task in this matter particularly for assessing damage to property and infrastructures.

This session received eight papers dealing with different aspect of coastal landslides that occurred under the influence of both marine and terrestrial processes. Slope failure, mass wasting and floods are described in terms of physical changes, and on the basis of geologic, hydrologic and geotechnical features. Tools and methodologies are proposed to model and recognize landsliding features and occurrence.

Aringoli et al. hypothesize a mutual control of sea-level oscillations and tectonic uplift on a large landslide along the Adriatic coast with a deep sliding surface, encompassing the coastal and marine areas. The paper by Berov et al. illustrate the state of the art along the North Bulgarian Black sea coast whose features indicate a strong control by seismic activity, also confirmed by historical sources. Hydro-meteorological trigger on a French coastal landslide was identified by Bogaard et al. who proposed a conceptual water balance approach to show a link between landslide re-activations and oscillations in the rainfall-groundwater system. Physical modelling for landslide hazard mapping and statistical sea cliff susceptibility assessment are proposed by Olivier et al. and Marques et al. respectively, which indicate tools and methodologies for the management of coastal instability. Hazard-related seafloor features including large debris avalanches off Ischia island and Somma Vesuvius, and flood dominated fan-deltas off the Costiera Amalfitana, are illustrated by Violante that uses sea-land correlation to assess the stability of Napoli and Salerno coastal areas. Underwater geologic features are reported also by Pennetta and Lo Russo that indicate the occurrence of shore platforms as a main control on sea cliff erosion at Capri island. Finally, historical data have been used by Porfido et al., to reconstruct and classify, in terms of typology and magnitude, more than 100 flood events occurred along the Sorrento peninsula in the last five centuries.

State of the Art for Landslides Along the North Bulgarian Black Sea Coast

Boyko Berov, Plamen Ivanov, Nikolai Dobrev, Rosen Nankin, and Miroslav Krastanov

Abstract

The Northern Bulgarian Black Sea coast is about 100 km strip that almost along its entire length is affected by landslides. hese landslides are irregularly distributed in four landslide areas. Most of the landslides are complex and deep-seated. The present article analyses the old and recent sliding phenomena along the coastal zone in this part of Bulgaria. The analysis of the structures of the landslides along the Northern Bulgarian Black Sea coast gives the reason to considerate the earthquakes as one of the main factors that activate their creation and their periodical reactivation. The other factors are the slow tectonic movements, the fluctuation of groundwater level during rainfalls or snow melting, the abrasion and different types of man-made impacts that contribute to decreasing of slope stability along the coast line.

Keywords

Seismicity • Landslides • Coastal area

Introduction

The territory of the Bulgarian Black Sea coast (especially the northern part) has a high degree of landslide hazard in economic loss, social and environmental consequences. In areas along the Black Sea coast, more than 120 landslide events have been registered until now. 80 % of landslides in the districts of Varna and Dobrich affect the coast line. Most are active landslides in the northern Black Sea coast of Varna to Kavarna (between the resorts of St. St. Constantine and Elena, Zlatni Pyasatsi, Albena, and the Balchik area). These are old and recent, deep-seated and complex type landslides. The depth of the main slip surface is usually up to 50–60 m or more (reaching more than 100 m at some places). The slopes, on which they are developed, are in a state close to equilibrium and the activation of landslides could be provoked by sufficiently small additional destabilizing factors - abrasion, erosion, prolonged rainfalls, seismic and man-made impact (Evstatiev and Rizzo 1984; Konstantinov 1991; Frangov et al. 1997; Varbanov et al. 1997, and others). Many of slope phenomena (including rock deformations) that are depicted in the World classification of Varnes (1978) of slope movements can be found here: rockfall, earth fall, earth slump, earth block slide, rock lateral spread and rapid earth flow.

Depending on the depth range, geological and tectonical structure, and the engineering geological properties of the geological units, the Bulgarian Black Sea coast can be divided into three landslide zones: Northern zone, Middle zone and Southern zone. The attention is focussed on the Northern landslide zone (Fig. 1).

Iliev (1974) gives five main characteristics of seismally induced landslides in Bulgaria. The first is the presence of weakly inclined (2–3°) to almost horizontal sliding surfaces. The second characteristic is the large horizontal component of displacements than the vertical one. The third feature is the clear activation of landslides during or immediately after the earthquake. It should be noted and the so-called

---

B. Berov (✉) • P. Ivanov • N. Dobrev • R. Nankin • M. Krastanov
Bulgarian Academy of Sciences, Department of Geohazards, Geological Institute, G. Bonchev Str., Blok 24, Sofia 1113, Bulgaria
e-mail: b_berov@geology.bas.bg

C. Margottini et al. (eds.), *Landslide Science and Practice*, Vol. 5,
DOI 10.1007/978-3-642-31427-8_12, © Springer-Verlag Berlin Heidelberg 2013

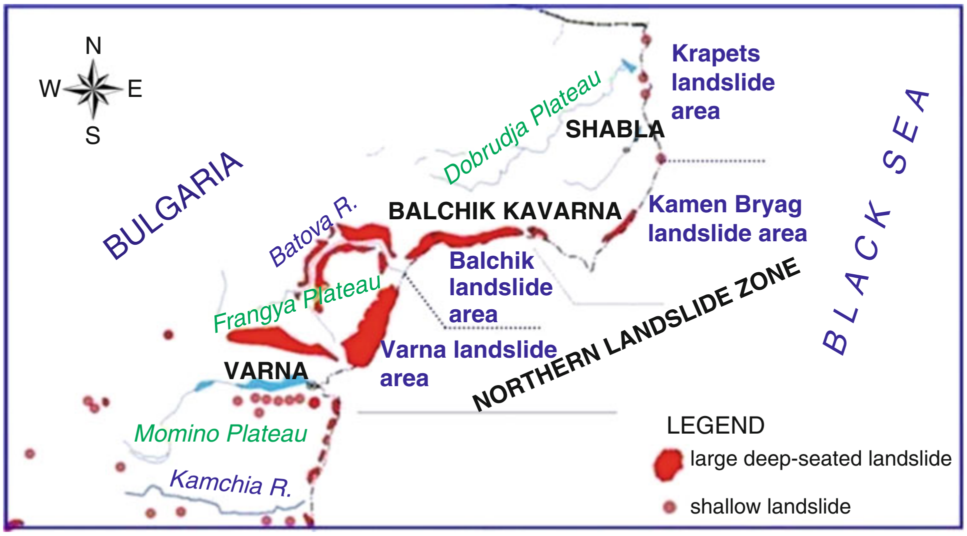

Fig. 1 Simple sketch of landslide areas along the North Bulgarian Black Sea coast

"effect of the delay" of the active landslide phase, which is sometimes observed. The fourth feature of the seismically induced landslides is the involvement of significant volumes of rock or soil masses. And the fifth feature is a common complex building of landslides.

Such characteristics of the landslide sites are observed along the North Bulgarian Black Sea coast. The characteristics of landslides triggered by earthquakes exist clearly north of the Batova River to the town of Kavarna. Here the coast is almost continuous landslide zone of ancient and recent landslides. We will stop our attention on the larger landslides in this area: Karamanlii, Momchil, Balchik, Tuzlata, Ikantalaka, Balaklar, and Kalkantepe. Two deep landslides of lateral spread type – Taukliman and Yaylata are situated northward of the town of Kavarna. Deep-seated landslides also occur south from Batova River forming four large semi-circular scarps from the Frangya Plateau. These landslides are Zlatni Pyasatsi (Golden Sands), Aladjamanastir, Vinitsa and Varna.

Relief and Geological Features

The Northern Black Sea coast is characterized by plateaus relief, slight to steeply sloping, almost horizontal layers (up a slight slope of 3–5°E) and sedimentary rocks of Paleogene and Neogene age. The coast can be divided into two sub-zones: the low plateau's and the high plateau's.

The low plateau's sub-zone covers the strip part of Dobrudja Plateau to the north and west of Kavarna town, including Kaliakra Cape and continuing to northward (to Bulgarian-Romanian border in the frames of Bulgarian territory). The plateau's edge is up to 140 m above the sea level at the town of Kavarna, up to 70 m at the Kaliakra Cape and several meters at the region of Shabla town. The landslides here are concentrated in two areas: Krapets area and Kamen Bryag area.

The high plateau's sub-zone includes Frangya Plateau and the southern part of Dobrudja Plateau. The plateau's edge is up to 300 m above the sea level at the Varna City, up to 200 m at the sea-side resort of Albena and up to 140 m at the town of Kavarna.

The scarp of the plateaux is high about 20–30 m up to 40 m. The slopes below the plateaux are built by sliding and falling materials. In many places the big rock blocks are separated from the plateaux and slowly creep down toward the sea. In this manner are formed landslides of lateral spreading and complex block type landslides.

Four main geological formations with Sarmatian age can be distinguished along the North Bulgarian Black Sea coast. They are called: Odartsi, Euxinograd, Topola and Karvuna (Popov and Kojumdjieva 1987). The Odartsi Formation is built by different types of limestones with slim intercalations of sands or clays. Its thickness is from a few to 50 m. It reveals along the edge of the Frangya plateau and in the region near to Taukliman and Yaylata. The Euxinograd Formation is built mainly by grey and ochre sandy and clayey aleurolites, and aleurolite clays containing Diatomaceae and silicate sponges (Koleva-Rekalova et al. 1996). Its thickness is 100–110 m. The dip of strata is 1–3º NE (Kamenov et al. 1972). It reveals well between the Golden Sands Resort, Kranevo village, Albena Resort, the town of Balchik to the Topola village. The Topola Formation is built mainly by white unconsolidated aragonite sediments called aragonitites – chemical precipitates of magnesium carbonate (Koleva-Rekalova 1992). Its thickness is from 45 to 80 m. It follows the upper part of slopes above the sea from Kranevo village to the west of Kaliakra Cape. The Karvuna Formation is built mainly by molluscan limestones. Its thickness is from 25 to 50 m. This Formation is revealed NE of Varna city, mainly in the region of Balchik sea coast.

Seismicity

The territory of Bulgaria as a part of the Alpine-Himalayas seismic belt is characterised by a relatively high seismicity. The area of the Northern Bulgarian Black Sea coast belongs to the seismically active zone, called Shabla seismic zone, with possible magnitude of earthquakes more than 7. On the map of shakeability and the expected influences for the period of 1,000 years this area situated in the north of Varna City could expect the earthquakes with the intensity more than 9 MSK. The epicentral distribution of the seismic events is usually situated along the fault with NE-SW orientation in the Black Sea.

The historical data about strong earthquakes in the Shabla seismic zone are known since I century BC and after that in 543, 1444, and 1901 (Grigorova and Palieva 1963). These facts give reason to suppose that in the near geological time strong earthquakes have also occurred. Some of these seismic events are directly connected with the new rockfall and landslide occurrences with considerable volumes. In the past 20th century the seismic zone of Shabla manifested more than 100 earthquakes but only few of them were with intensity equal or more than 7 (MSK scale). The most powerful earthquake since 1900 is the one that happened on 31.03.1901, M7.2, intensity $I = 10$ MSK, with an epicentre in the Black Sea, E of Shabla town and with a depth of 8 km. It was followed by a series of weaker earthquakes in 10 years after. Also significant earthquake (M5.5, depth 2 km) occurred on 30.06.1956. The epicenter was near the 1901 event. Most of the coastal strip within the landslide area falls under the influence of earthquakes with intensity level of 8–9 MSK. The latest Vrancea earthquakes of 1977, 1986 and 1990 caused rock falls in the rocky cliffs and rapid slips along the deepest slip surfaces.

Historical Data of Landslides

Landslides have surrounded the development of the coast in antiquity and flourishing cities were destroyed. One of them, the Greek colony Bizon, located in the eastern part of Chirakman Cape (near Kavarna town) was destroyed during an earthquake in the second half of I century BC (Fig. 2). Then, most of the colony sank into the sea. Chaotic mixing of rock and cultural layers shows that the process of destruction has passed very quickly including a manifestation of mudflow (Iliev 1973; Koleva-Rekalova et al. 1996).

Fig. 2 A view of Chirakman cape

In recent times, the landslide at the Momchil Village (3.5 km W of Balchik town) has been triggered as a result of 31 March 1901, M7.2 earthquake. The landslide affected an area of 300 dka. On the edge of the Dobrudja plateau bearing here the name Momchilski Rid large rock block broke a vertical slope and joined the sliding masses. Significant changes occurred in the field - appeared cracks, small hills, falling and slipping masses entered into the sea. All these changes occurred in a short time. There was no landslide in the region, until the earthquake. However the cracks were observed in the slope, which probably was close to its limit equilibrium. Landslides have been continued in later years usually after the snow melt and rains. Gradually landslide processes have covered and adjacent areas of the coast (Iliev 1973). From the same earthquake Sivri Tepe hill in Balchik town sunk by 3 m. In the town, vertical scarps collapsed and wide opened cracks in the ground appeared. The town is located in a vast old landslide with the depth of sliding surface more than 100 m (Kamenov et al. 1973).

Landslide Areas

Krapets Landslide Area

This area covers the Black Sea coast between the Bulgarian-Romanian border and Shabla Cape. The coast is high, steep and often with vertical slopes. It is composed by 10–20 m thick loess complex that is deposited on shellfish karst Sarmatian limestone (Karvuna Formation), which reveals at the level of the sea. Landslides occurred in the loess deposits. Landslides are shallow and rare, because they are rapidly destroyed by the abrasion action of the sea.

Kamen Bryag Landslide Area

This region is characterized with landslides and rockfalls. On both sides of Kaliakra Cape are formed vertical cliffs, with a 50–60 m height, with apparent influence of abrasion, weathering processes and rockfalls (occurred by seismic and abrasion action). Two landslides are revealed here: Yaylata and Taukliman. Their sizes are: width respectively 3,500 m and 1,300 m, and average length - 275 m and 200 m. Landslides are of lateral spread type. Limestone blocks of Odartsi Formation are separated from the plateau and sink into the plastic clay layer of Oligocene age towards the sea. Relics of the old limestone steps can be seen hundreds of meters into the sea (such as small islands). It is supposed that the formation of large sliding steps (up to 7) has been supported by the occurrence of earthquakes with intensity up to 9 MSK (Kamenov et al. 1973). The remains of Thracian walls (3,000 years old) are found in the forehead parts of the landslides. This is the evidence that the sliding process is very old and slow.

During the strong Vrancea earthquake of 4 March 1977 M7.4, the area near the Taukliman and Yaylata landslides reacts with intensity of 7 MSK. The inspection in the days after the earthquake (Brankov 1983) established that the top step of the landslide Taukliman has been cracked across in a few blocks that have been engaged on independent movements. The cracks have had a width of about 30 cm. The new longitudinal cracks have been created also at the top step of the landslide. In many places on the individual steps of the landslide occurred small rockfalls. The monitoring of slow movements shows a creep to the sea with rate of 1.0–1.2 mm/a (Avramova-Tacheva et al. 1998).

Balchik Landslide Area

The Black Sea coast, northeast of Batova River to the town of Kavarna, is covered by old and recent landslides. The most spectacular hazardous phenomena along the Bulgarian shoreline are situated here (Frangov et al. 1997; Varbanov et al. 1997, and others). The Balchik coast occupies a narrow strip of south-eastern part of the Dobrudja plateau. The relief has typical landslide morphology (Fig. 3). The landslide strip has an average width of 400–600 m. The plateau scarp is rocky, steep, and sometimes vertical, with a height of 40–50 m. In the southwest it is cut across by deep creeks.

Lithologically, the sediments of Euxinograd Formation are at the bottom of the section. It is represented by diatomaceous clays. Its thickness at Balchik area is less than 50–60 m (Fig. 4). The Topola Formation lies above Euxinograd Formation. It is represented by alternating layers of limestones and aragonite clays, called as aragonitites (Koleva-Rekalova 1992, 1994, 1997; Koleva-Rekalova et al. 1996). The thickness of Topola Formation is up to 140 m. Plateau parts of the coastal strip are built by the sediments of Karvuna Formation – organic and cavernous limestones with thickness up to 20–25 m. In northeast direction limestones significantly increase its thickness. The landslides in this area are deepest and most active. They are of a complex type, often the upper parts of them trigger suddenly. Along the deepest slip surface, the landslides move slowly huge blocks towards the sea. The deepest landslide surface continues under the sea. At a depth of 125–153 m a zone of creep deformations is delimited (Kamenov et al. 1973). The vertical fissures in the overlying rock masses are formed and the separation of big sliding blocks is manifested. The sliding process is aided by the sea erosion and the earthquakes in the past.

Fig. 3 Kalkantepe landslide, between Balchik town and Kavarna town

In this landslide area from the Batova River to the town of Kavarna the follow large landslides are situated: West Karamanlii, Momchilski Rid, Balchik, East Karamanlii, Tuzlata, Ikantalaka, Balaklar and Kalkantepe. All these landslides are ancient with recent activations in some parts of theme. Their average dimensions are given in (Table 1).

The huge rock blocks have preserved their internal stratification but they are inclined at different degree toward the sea. Somewhere these blocks are turned aside or sunk into the plastic substratum. There are also the blocks with disturbed layers that have not so deep (up to 30 m) slide surfaces. In this way landslides of second order are formed (Kamenov et al. 1973). The delluvial (mainly aragonitic sediments) and decomposed materials of limestone are situated between the sliding blocks. These deposits create conditions for occurrences of earthflows. The manifested earthflows are shallow and rapid. Sometimes they start suddenly. More of themes have a width of 40–60 m, a length of 100–300 m and a depth up to 5 m (Koleva-Rekalova et al. 1996). There exist also earthflows with impressive sizes. The Ikantalaka landslide is an example. It represents ancient earthflow starting from the plateau edge at an altitude of 160 m with almost vertical main slop 50 m height. This earthflow is long 1,200 m and has a different depth varying from 15 m in his lower end to 55 m at his higher parts (Evstatiev and Evlogiev 2007).

Rockfalls are also manifested along the scarp of plateau zone. Their volumes are small and the falling materials rapidly degraded. The mechanism of these large and complex block-type landslides has been discussed from many authors (Pašek and Rybář 1969; Kamenov et al. 1972, 1973;

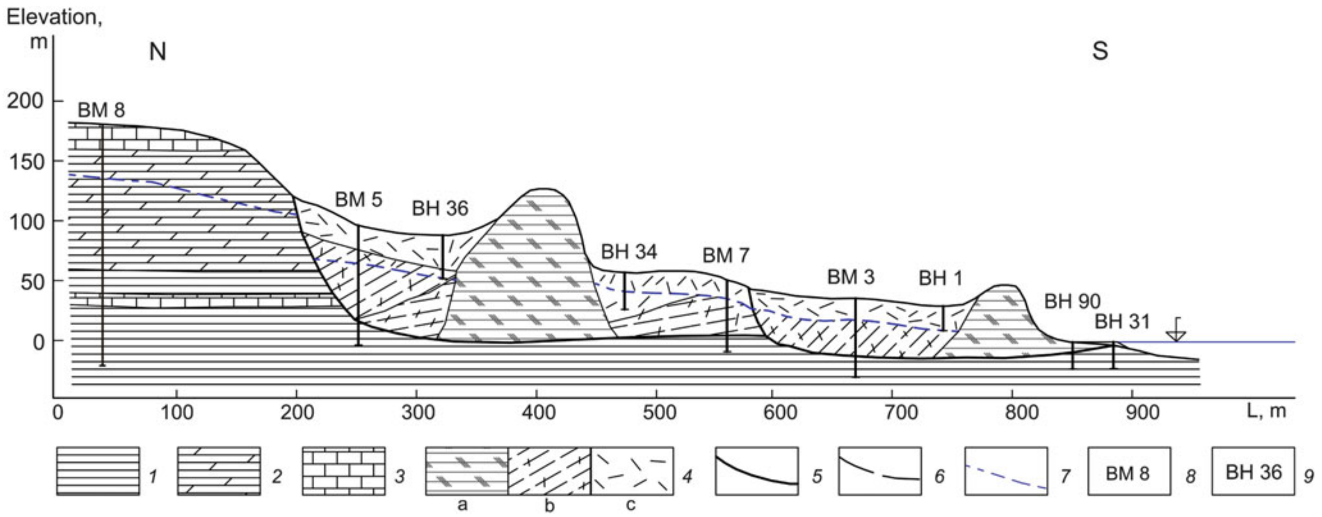

Fig. 4 Typical profiles of landslide slopes along the Northern Black Sea coast at town of Balchik (by Kamenov et al., 1972 with supplements): (*1*) – clays with sandy interbeds; (*2*) – calcareous and diatomite clays; (*3*) – limestones; (*4*) – landslide materials (Qdp): (*a*) packets with preserved horizontal layer raw; (*b*) packets with altered layer raw; (*c*) mixed sandy-clayey sediments with marly and calcareous pieces; (*5*) – the deepest landslide surface; (*6*) – recent active landslide surface; (*7*) – ground water level; (*8*) – underground bench-mark; (*9*) – borehole

Table 1 Average dimensions of the landslides in the Balchik landslide area

Name of landslide	Maximal length (m)	Width (m)	Altitude of plateau edge (m)	Altitude of highest sliding block (m)
West Karamanlii	600	1,650	200	118
Momchilski Rid	650	1,000	200	130
Balchik	700	1,250	200	123
East Karamanlii	800	2,100	190	115
Tuzlata	900	1,600	190	115
Ikantalaka	1150	1,750	170	125
Balaklar	650	650	160	100
Kalkantepe	700	1,850	150	70

Evstatiev and Rizzo 1984; Hamamdshiev et al. 1992; Evstatiev and Evlogiev 2007 and others). The mechanism is not entirely clarified but all investigators accept the idea of seismic influences over the landslide occurrences.

Varna Landslide Area

Varna landslide area includes the coast of Varna City to the Valley of Batova River at the Kranevo village. In the morphological structure this line refers to the north-eastern edge of Frangya Plateau. The formation of deep-seated landslides in this area is mainly a result of the marine abrasion. Lithological composition of rocks, morphological characteristics and hydrogeological conditions have had a big impact.

The length of the coastal zone affected by these landslides reaches 20 km. Maximum width of a profile line is about 5 km (at the village of Vinitsa). Large circular scarps at the plateau edge are formed. Downslope, the masses pass into gradually mixing, as a flow. Lowest parts of landslides periodically activate due to impacts of sea erosion and rainfalls. The velocity of landslide movements to the sea is estimated as 0.5 mm/a using the 3D monitoring system (Dobrev and Avramova-Tacheva 1997; Avramova-Tacheva et al. 1998).

Typical landslide activation due to raising of the level of groundwater occurred. Small landslides are activated in the frame of ancient landslides. Three landslides have been activated in this region due to extraordinary high precipitation and the saturation of the terrains by failing of the water supply tubes during the period of April 1996 to April 1997. Their volumes vary between 0.2 and 1.0 million cubic meters (Varbanov et al. 1997). As a result the road Varna-Zlatni Pyasatsi has been interrupted in several places and dozens houses and villas have been destroyed.

Landslide to restaurant Tryphon Zarezan near Varna was activated in March 2005. The panoramic road to Zlatni Pyasatsi resort was damaged and closed for cars. Until today Tryphon Zarezan Landslide continues to be going every day and collapsing slowly to the sea. Landslide slopes are formed of several meters. The restaurant Tryphon Zarezan was destroyed. The landslide area covers about 50 dka as well as about 30 below sea level.

There is a real danger of isolation of the resorts Zlatni Pyasatsi and St. St. Constantine and Elena, as a result of landslide activity in the region of Trakata in Varna. The big problem is that this road has a tourist importance and it is the main communication to the resorts of Zlatni Pyasatsi and St. St. Constantine and Elena.

In the summer of 2010 is activated landslide at Briz locality, Varna. There is a danger for the water supply line Varna-Zlatni Pyasatsi, which is located less than a hundred meters from the landslide.

Conclusions

The analysis of the structures of the landslides along the northern Bulgarian Black Sea coast gives the reason to considerate the earthquakes as one of the main factors that activate their creation and their periodical reactivation. The separation of the huge blocks to the plateau edge is most probably a direct result of strong seismic events. The seismicity with the other factors as the slow tectonic movements, the fluctuation of groundwater level during the precipitations or snow melting, the sea erosion and different types of man-made factors contribute to decreasing of slope stability along the entire coast line. The problem of assessing the impacts of earthquakes on the stability of slopes and rocky cliffs still remains under studying. There is a connection between the slope movements and the seismicity in the region from local seismic source zones at sea (Shabla zone) and also from more distant foci such Strazhitsa and Vrancea. Several Vrancea earthquakes of 1977, 1986 and 1990 caused rockfalls in the rocky cliffs and rapid slips along the deepest slip surfaces. Rockfalls had been identified during the last earthquake at Kamen Bryag, 5 Aug. 2009, M = 5.0. Landslide studies have so far only a descriptive meaning. They depict the landslide occurrences, their type and geomorphological forms with different purposes - mainly for various types of construction. Specialized research concerning the probability of slide triggering, susceptibility mapping, modelling, risk assessment and impacts of various destabilizing factors (seismic foci located in different places, for example) have not been made.

References

Avramova-Tacheva E, Kostak B, Dobrev N (1998) Present dynamics of a landslide process in the Black Sea coast region north of Varna (Bulgaria). Acta Montana, IRSM AS CR, Prague. Series A, 12(107):5–15

Brankov G (eds) (1983) Vrancea Earthquake in 1977. Its after-effects in Bulgaria. Publ. House of the Bulgarian Academy of Sciences, Sofia, 427p. (in Bulgarian)

Dobrev N, Avramova-Tacheva E (1997) Analysis and prognostication of monitored rock deformations. In: Proceedings of IAEG conference, Athens 1997. Balkema, Rotterdam, pp 613–618

Evstatiev D, Evlogiev Y (2007) On the origin of the "Ikantalaka" landslide – the Balchik coast. Geologica Balcanica 36(3–4):25–30

Evstatiev D, Rizzo V (1984) Sull, origine ed evoluzione delle frane nella zonna di Balchik, sul mar nero (Bulgaria). Geologia applicata e idrogeologia. Bari XIX: 289–305

Frangov G, Varbanov R, Yordanova J, Stakev M (1997) Contemporary activity of the landslides along the Varna and Balchik coast line. Coll.: coastal fortification along the Bulgarian Black Sea. Bulgarian Academy of Sciences, Bulgarian, pp 20–29

Grigorova E, Palieva K (1963) Seismicity of the Black Sea coast at Balchik and Blatnitsa. Bulletin of the Geophysical Institute. Bulgarian Academy of Sciences, Bulgarian, vol IV, pp 253–268

Hamamdshiev K, Stakev M, Chitarlieva T, Frangov G (1992) Stabilisation of landslides in Bulgaria. Stab Landslides Eur IV:1–21

Iliev I (1973) Effect of earthquakes on the appearance and activation of landslides along the Dobroudja Black Sea coast. Rev Bulg Geol Soc 34(1):75–85 (in Bulgarian)

Iliev L (1974) Features of Landslides caused by earthquakes. Series engineering geology and hydrogeology. Bulletin of the Geological Institute of Bulgarian Academy of Sciences, Bulgarian, vol XXIII, pp 161–166

Kamenov B, Demirev A, Vutkov V, Tsvetkov S, Avramova E, Iliev I, Simeonova G, Ilieva L, Milev G (1972) The landslides along the Black Sea coast near the town of Balchik. Series engineering geology and hydrogeology. Bulletin of the Geological Institute of Bulgarian Academy of Sciences, Bulgarian, vol IX–XX, pp 5–32

Kamenov B, Iliev I, Tsvetkov S, Avramova E, Simeonova G (1973) Influence of the geological structure on the occurrence of different types of landslides along the Bulgarian Black Sea coast. In: Proceedings of the IRPI (CNR) Conference on Geologia Applicata I Idrogeologia, vol VIII, part 1, Naples-Cosenza, pp 209–220

Koleva-Rekalova E (1992) Unconsolidated aragonite sediments of Sarmatian age in Northeastern Bulgaria. Compt Rend Bulg Acad Sci 45(9):73–76

Koleva-Rekalova E (1994) Sarmatian aragonite sediments in North-eastern Bulgaria – origin and diagenesis. Geologica Balcanica 24(5):47–64

Koleva-Rekalova E (1997) Sedimentological characteristics of the Sarmatian rocks in the Balchik area, Northeastern Bulgaria. Rev Bulg Geol Soc 58(1):31–42 (in Bulgarian with English abstract)

Koleva-Rekalova E, Dobrev N, Ivanov P (1996) Earthflows in the Baltchik landslide area, North-eastern Bulgaria. In: Proceedings of the 7th international symposium on landslides, Trondheim, pp 473–478

Konstantinov B (1991) Probable secondary seismic deformations along the Bulgarian Black Sea coast. Ann Min Geol Univ 37(3): 67–78 (in Bulgarian)

Pašek J, Rybář J (1969) Analysis of the slope movements on the Black Sea coast in Bulgaria. Časopis pro mineralogii a geologii 14(3–4):273–284, Prague. (in Czech)

Popov N, Kojumdjieva E (1987) The Miocene in Northeast Bulgaria (lithostratigraphic division and geological development). J Bulg Geol Soc 48(3):15–33 (in Bulgarian)

Varbanov R, Frangov G, Evstatiev D (1997) New destructive landslides northward from the town of Varna. J Minno Delo i Geologia 5:6–12 (in Bulgarian)

Varnes DJ (1978) Slope movement types and processes. In: Schuster RL, Krizek RJ (eds) Landslides, analysis and control. Special Report 176. Washington

Flood Historical Data for Flood Risk Estimation in Coastal Areas, Eastern Tyrrhenian Sea, Italy

Sabina Porfido, Eliana Esposito, Flavia Molisso, Marco Sacchi,
and Crescenzo Violante

Abstract

A reconstruction of historical floods occurred along the Amalfi coast, during the last five centuries is presented. The analysis of historical sources allowed to achieve a chronological reconstruction of more than 100 floods, four of which classified as catastrophic events. In this task, the level of information was decisive to carry out space–time identification, estimate the affected area and define the type of damage to the structures, and the environment (e.g. mud flow, debris flow, rock falls, shoreline progradation, fan deltas), which may be relevant for the recognition of similar events within the geologic record. The magnitude of the events was finally estimated, taking into account the size of the areas affected by flooding as well as the type of effects induced on the urban and physical environment and the recurrence intervals.

Keywords

Historical floods • Tyrrhenian sea • Amalfi coast • 1954 flood event

Introduction

The Salerno rocky coast (Campania, Southern Italy) is particularly subject to the hydrogeologic risk (landslides and flooding), which represents a threat to the natural environment and a persistent menace to urban areas, in terms of human lives, socio-economic costs and modification of the landscape.

A reliable time frequency of the flood recurrence is the most useful tool for flood risk assessment and it requires long time series obtained mostly from historical data. The coast of Salerno province experienced numerous flooding events after heavy thunderstorm, that triggered a series of associated phenomena like intense landslides, inundations, denudation, shoreline progradation, etc.. In this study historical floods since the sixteenth century were analysed in detail to provide a sound basis for reliable risk assessment and a confident land planning on flood-prone areas.

Geological Setting of the Sorrento Peninsula

The study area is located on the southern slope of the Sorrento Peninsula (Amalfi coast). The peninsula is a major Quaternary morpho-structural unit of the western flank of Southern Apennines and forms a narrow and elevated mountain range (up to 1,444 m) that separates two major embayments of the eastern Tyrrhenian margin, namely the Naples and Salerno Bays (Fig. 1). It is mostly formed by a pile of Mesozoic carbonate rocks, covered by Tertiary to Quaternary siliciclastic and pyroclastic units and is deeply cut by a network of bedrock rivers and channels characterized by relatively small catchment areas and pronounced disequilibrium of the stream profiles. These rivers display flow regimes with a distinct seasonality and a torrential behaviour (Esposito et al. 2004a, b; Budillon et al. 2005; Liquete et al. 2005; Sacchi et al. 2009; Violante et al. 2009). Their source is very high relative to the base level, so that

S. Porfido (✉) • E. Esposito • F. Molisso • M. Sacchi • C. Violante
Istituto per l'Ambiente Marino e Costiero, CNR,
Calata Porta di Massa - 80133, Naples, ITALY
e-mail: sabina.porfido@iamc.cnr.it

C. Margottini et al. (eds.), *Landslide Science and Practice*, Vol. 5,
DOI 10.1007/978-3-642-31427-8_13, © Springer-Verlag Berlin Heidelberg 2013

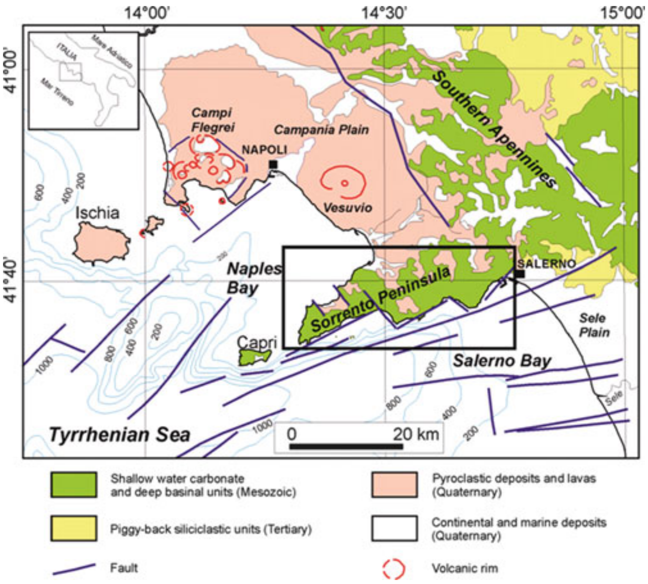

Fig. 1 Tectonic sketch-map of the Campania Apennines and location of the Amalfi coast of the Sorrento Peninsula

erosion processes proceed relatively rapidly, and tipically create a rugged morphology (Reineck and Singh 1975; Einsele 2000).

Being a horst-like structure in a half-graben basin setting the Sorrento peninsula displays a remarkable asymmetry in the morphology of the two flanks, the southern one (Amalfi coast) being steeper and narrower than the northern one (Sorrento coast). The asymmetry can be also observed offshore, where the narrow continental shelf on the Amalfi side contrasts with a definitely wider shelf in the southern part of the Naples Bay. As a consequence the Amalfi flank of the peninsula is characterized by tectonically uplifted rocky and steep backdrops, deeply incised gorges, and coastal cliffs (Brancaccio et al. 1991).

Coarse-grained coastal alluvial fans confined by narrow valleys at the mouth of the major streams are relatively common in this setting. They are formed by deposition from flash floods, during heavy rain falls.

Methods

Historical records are an important source for the evaluation of flooding episodes caused by torrential or prolonged rainfall and become indispensable to define the quality and completeness of the information needed to outline the trends climatic oscillations and the frequency of extreme events (Agasse 2003; Bayliss and Reed 2001; Barriendos et al. 2003, Porfido et al. 2009, Esposito et al. 2011).

Rich of history, the study area reached its maximum opulence during the Middle Ages, when Amalfi became the first of the Italian Repubbliche Marinare with commercial activities all over the Mediterranean basin and acquired remarkable political influence and military power. A priceless documentary heritage is available for this area, found at the State Archives, municipal and ecclesiastical Libraries, public and private cultural associations, local or regional historiography, since the XVI century.

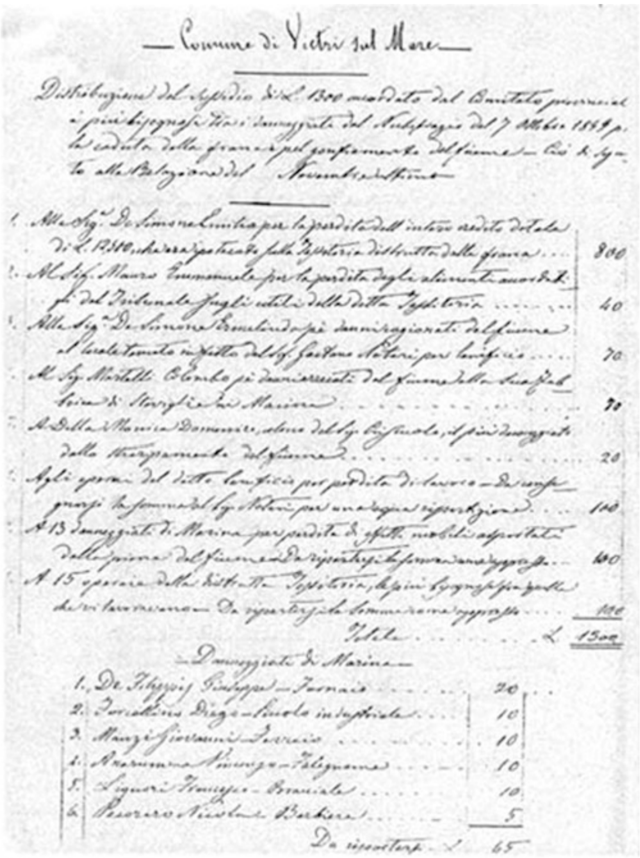

Fig. 2 Archival sources. 7th, October 1899 flooding and government subsidy to the Vietri sul Mare homeless (Prefettura, I Serie, 1899)

Selected documental sources were collected, including: (1) Administrative documents, consisting of collections written by central/local authorities such as the interior Ministry, the Major, engineering, technical etc. (Fig. 2); (2) Notarial documents, mostly represented by purchase-sale acts, reporting relevant details on pertinent facts and accurate descriptions of localities and events; (Fig. 3); (3) Ecclesial documents, consisting in rich collections of letters, memoirs, chronicles, written by the local ecclesial authorities; (4) Private collections, including letters, memoirs, chronicles, written by noble families, historians, scientists, etc; (5) Bibliographic sources, consisting of texts written by eyewitnesses and specific studies, such as scientific literature and national/local newspapers articles written during or after the event. New sources of information have been identified by analyzing photographs, particularly for the twentieth century, postcards, prints, drawings and art reproductions.

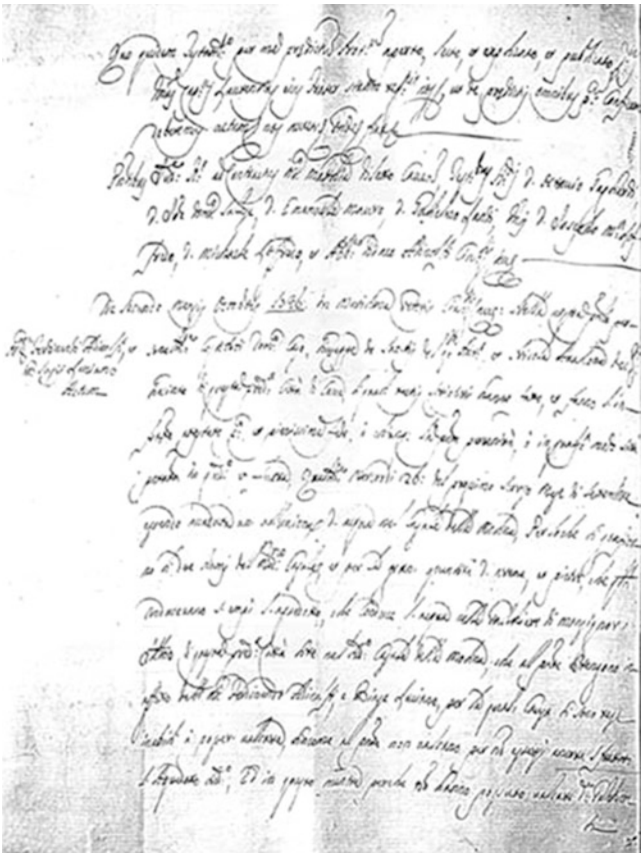

Fig. 3 Archival sources. 25th, January 1736 flooding and destruction along the Bonea Stream in Molina di Vietri sul Mare (Protocolli Notarili, 1736)

The selected sources were grouped on the basis of the document's intrinsic quality, strictly connected with: (a) source chronologically contemporary with the event; (b) reliability of the writer.

Particularly, three types of sources were distinguish as follows:

- Type 1 (highest quality of reference): documentary or bibliographic sources, chronologically contemporary with the event, written by a local or regional administrator, lawyer, historian, parish priest, journalist, scientist, academician or technician.
- Type 2 (medium–high quality of reference): documentary or bibliographic sources, subsequent to the event (from 5 to 50 years), written by a local historian, parish priest, journalist, or scientist or technician.
- Type 3 (medium quality of reference): bibliographic sources, subsequent to the event (over 50 years), written essentially by local literary figures and journalists.

The information obtained from the selected documentary sources were also grouped into three categories taking into account the level of detail of the description:

- Detailed. This category (from technical reports, projects, etc.) gives the precise location of the event, the extent of the flooded area, and the type of flood-induced damage. Occasionally, drawings or photographs of the flood-induced geological effects are also available.
- General. This category gives information on the event type, sometimes the size, and the location of the event.
- Scarce. This category gives very poor information regarding prevalently the flooding date into a generic area of occurrence.

Applying these criteria on the documentary series we were able to classify three different levels of flooding:

1. Minor flood: restricted area of flooding, minor damage to buildings locate adjacent to the river and no serious damage to the population.
2. Intermediate flood: large area of flooding, severe damage and partial destruction to buildings located adjacent to or along the river. Infrastructures are destroyed along several hundred metres.
3. Major or catastrophic flood: large flooded area, severe damage or complete destruction of infrastructures close to the river, and stretches of roadways eventually swept away.

The informations obtained from the selected documentary sources provide useful information on the dates of meteorological events, flooding duration, river location, description of flood impact on manmade structures and population.

Data Treatment

The systematic search of about 3,500 documents has led to the identification and classification of 136 floods, which affected the whole province of Salerno, specifically the Amalfi coast. Once the analysis of the historical content has been carried out, the towns most frequently hit by floods were identified. Starting from 1581 to 2010 Salerno, Vietri sul mare, Cava de' Tirreni, Amalfi, Majori, Minori, and Atrani were the most damaged. The most intense flooding events occurring along the Amalfi coast which caused extensive inundation, landslides, debris flows and flash floods, shoreline progradation and deaths (Esposito et al. 2002; Esposito et al. 2004b; Porfido et al. 2009; Violante 2009).

The flooding phenomena hit areas spanning from a few km^2 to several hundred km^2, mainly located along rocky coasts and subordinately in the inner part of the Appenines. The inventory of historical flood allowed the definition of the major events that occurred on the Amalfi cioast during last five centuries, including a detailed information of the number of casualties. As regards the sixteenth and seventeenth century, the available data set allowed the identification of five events, among these, the 30th September, 1581

Fig. 4 1954 Flood event: destruction in the Marina di Vietri, at the Bonea stream mouth (Foto Parisio 1954, Col. EPT, Salerno)

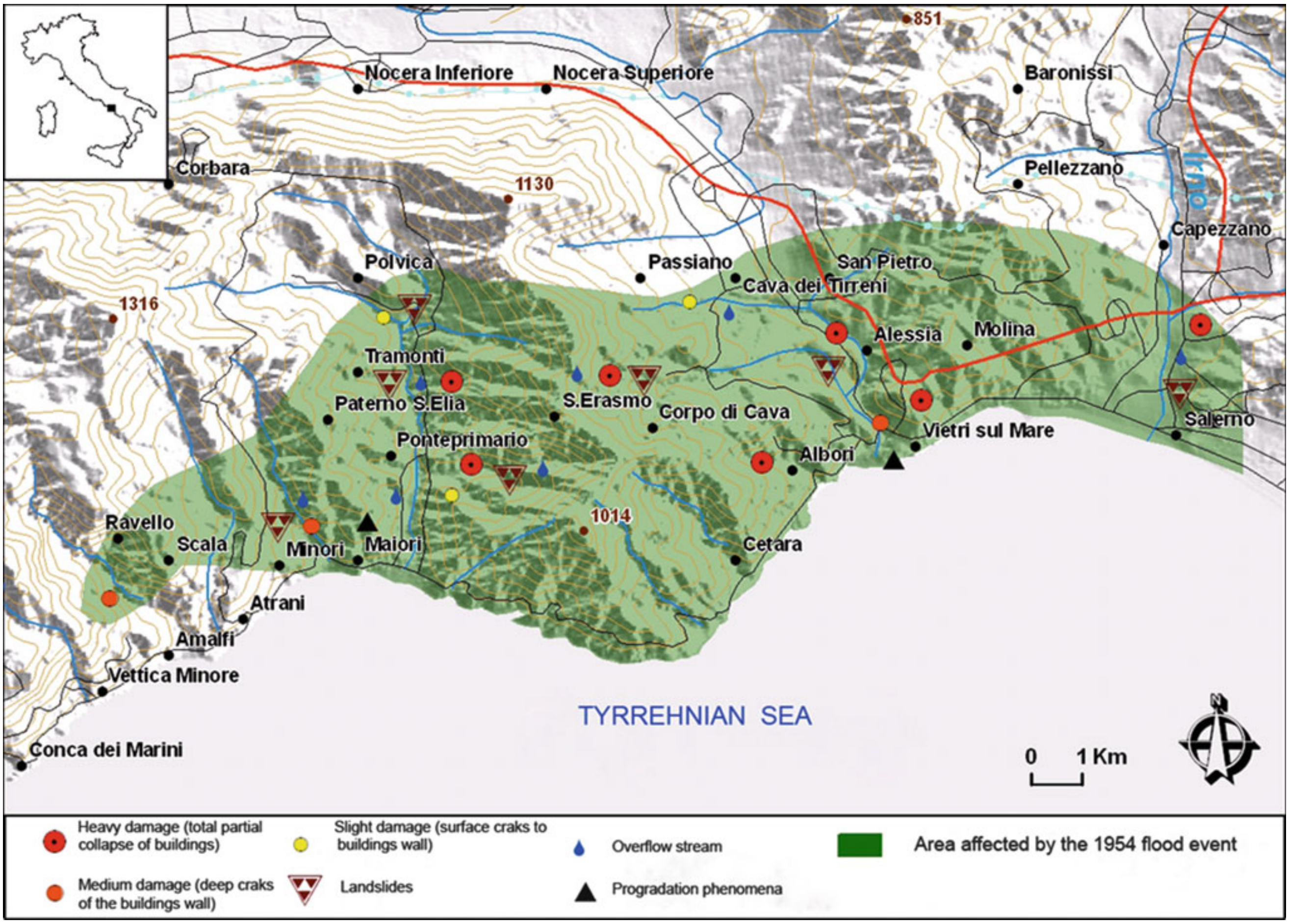

Fig. 5 Damage pattern and geological effects induced by the 1954 flood event between Salerno and Ravello (Salerno province). A catastrophic flood affected 46 villages, causing the collapse of houses. Stream flow and landslides occurred over a wide area extent. Twenty three localities lying along river banks suffered more severe damage (318 victims)

and the 31 August, 1588 has been classified as catastrophic, the first for the extensive damage produced in several localities distributed both on the inland and coast and for extensive inundation (300 victims), high landslide activity and shoreline progradation in Salerno, the second induced severe damage to the public and private property and fan delta in the Atrani village.

The eighteenth century was accompanied by 17 events. Among these the 23rd November 1750 has been classified as intermediate flood. The most destructive event occurred on

Fig. 6 1954 Flood event: the mouth of the Bonea stream, a few days after the flooding (Foto Parisio 1954, Col. EPT, Salerno)

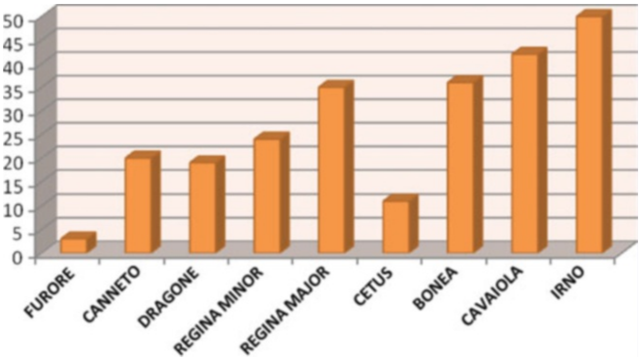

Fig. 7 Floods distribution in the Stream/River basins along the Amalfi coast during the last five centuries

11 November 1773, classified as a catastrophic on the bases of extensive inundation, high landslides activity and diffuse shoreline progradation (400–450). The nineteenth century was characterized by 44 flood events. The 7th,October 1899 flood event produced a widerspread pattern of destruction in almost 23 localities (Fumanti et al. 2001), causing massive destruction of thousands of houses, hydraulic mills, aqueducts, main and secondary roads, bridges as well as railways, with 86 deaths.

On the 70 floods recorded in the twentieth century the most significant occurred in the year, 1924, 1954 and 1966.

The major flooding event was certainly the one that stroke the Amalfi coast on 25 and 26 October 1954 and resulted in more than 300 casualties, 350 injured and 10,000 homeless.

Rainfall lasted about 12 h with a total value of 504 mm and maximum intensity of 150 mm per hour. The most heavily damaged areas included the Bonea torrent (Fig. 4) and Irno river respectively in Vietri sul Mare and Salerno; the Regina Major stream caused also many damages to the village of Maiori. The damage, including destruction of buildings and industries, road, railways and aqueducts. It was estimated in about 35–40 billions of Lira (550 M Euro).

This rainfall event, though of limited extension (Fig. 5), was well recorded because the rain gauge network resolution at that time was quite adequate.

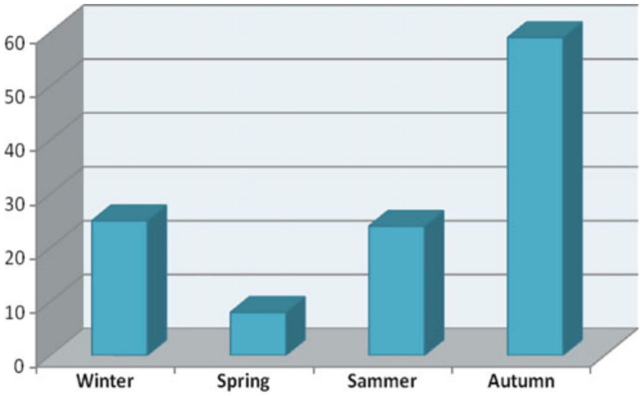

Fig. 8 Seasonal floods distribution along the Amalfi coast (Salerno province)

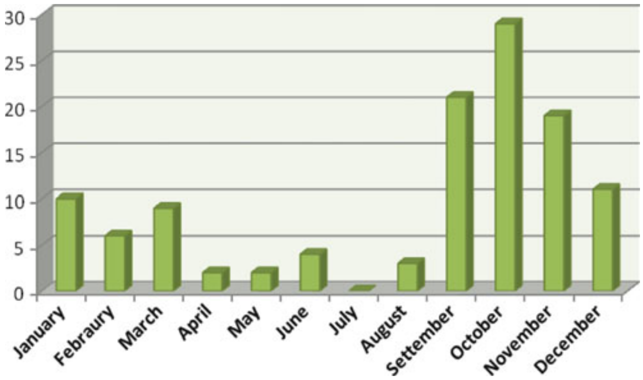

Fig. 9 Monthly floods distribution along the Amalfi coast (Salerno province)

Temporary dams developed at points where the course of the streams narrowed. Marina di Vietri suffered a major flooding that caused a shoreline shift of about 150 m, associated with the formation of a fan-delta at the stream mouth (Fig. 6).

The orographic left of Bonea stream, where both railway and main roads are located, was also affected by severe damage.

Several erosional phenomena including debris flows, solifluction, and denutation occurred along the western side of the S. Liberatore hill, burying and sweeping away large part of communication line. Solifluction and debris flows phenomena were also observed downhill Tresaro, Dragonea and Tresare. These processes released large amounts of material straight into Bonea river bed, reinforcing the overflowing phenomena.

The extreme sensitivity of the Amalfi coast to severe and chatastrophic floodings originates from its peculiar geological and geomorphologic setting and it is clearly evidenced by the high frequency in the recurrence of such events over the last five centuries.

Preliminary analysis indicates that the Irno stream with its 50 events is the river basin with the highest flooding records of the region, followed by the Cavaiola river, 42 events, Bonea, 36 events, Regina Major, 35 events, Regina minor, 24 events, Canneto, 20 events and Dragone with 19 events (Fig. 7).

In particular the Dragone stream basin was the site of the last tragic flood that hit the village of Atrani and caused the death of a young women, on the 10th of September 2010.

These events are mostly concentrated in autumn and winter, with the highest number of floods 59 (51 %) and 25 (21 %) cases respectively (Fig. 8).

Figure 9 shows the number of flood cases occurred monthly: October, with the highest number of events, 29, followed by September with 21 events (18 %) and November with 19 events (16 %) on a total number of 100 flood events considered.

Conclusion

This study shows that historical sources can be an important contribute to improve and evaluation of natural hazards. In particular, this research permitted the recognition of 136 flooding phenomena in the Amalfi Coast, one of the most beautiful coastal location in the world, included in the UNESCO world heritage list since 1997. In this context the level of information is decisive, in fact has been possible to carry out space-time distribution, estimate the affected area and the type of damage to public and private structures, and the geological effects induced.

The Amalfi Coast experienced cartastrophic events both in terms of human and economic losses in 1581 (Castiglione di Giffoni), 1588 (Atrani), 1773 (Cava de' Tirreni), 1899 (Castiglione di Giffoni), 1910 (Cetara), 1924 (Amalfi) and 1954 (Vietri sul Mare - Salerno).

Each of these reported events was triggered by a few days of steady rain followed by several hours of heavy rain. The effects included extensive landslides, significant floods along the streams axes and modifications of the coastline at the mouth of several strams (Irno, Bonea, Dragone etc.).

Such information combined with hydraulic/hydrogeological and economic data may be used for the assessment and reduction of hydrogeological risk in the context of management of coastal area.

References

Agasse E (2003) Flooding from the 17th to 20th centuries in Normandy (western France) methodology and use of historical data. In: Thorndycraft VR, Benito G, Barriendos M, Llasat MC (eds) Paleofloods, historical floods and climatic variability: applications in flood risk assessment, PHEPRA workshop, Barcelona, pp 99–105. (ISBS 84-921958-2-7) 380p

Barriendos M, Coeur D, Lang M, Llasat MC, Naulet R, Lemaitre F, Barrera A (2003) Stationarity analysis of historical flood series in France and Spain (14th–20th centuries).NHESS 3:583–592

Bayliss AC, Reed W (2001) The use of historical data in flood frequency estimation. Report to MAFF, CEH. World Wide Web Address www.nwl.ac.uk/feh/historical_floods_report.pdf

Brancaccio L, Cinque A, Romano P, Russo F, Santangelo N, Santo A (1991) Geomorphology and neotectonic evolution of a sector of the Tyrrhenian flank of the southern Apennines (Region of Naples, Italy). Z Geomorphol 82:47–58

Budillon F, Violante C, Conforti A, Esposito E, Insinga D, Iorio M, Porfido S (2005) Event beds in the recent prodelta stratigraphic record of the small flood-prone Bonea Stream (Amalfi Coast, Southern Italy). Mar Geol 222–223:419–441

Einsele G (2000) Sedimentary basin: evolution, facies and sedimentary budget. Springer, Berlin/Heidelberg, 792 p

Esposito E, Porfido S, Violante C, Alaia F (2002) Disaster induced by historical flood in a selected coastal area (Southern Italy). PHEFRA (Palaeofloods, historical data & climatic variability: application in flood risk assessment), pp 143–148. ISBN-84-921958-2-7

Esposito E, Porfido S, Violante C, Alaia F (2003) Disaster induced by historical floods in a selected coastal area (southern Italy). In: Thorndycraft VR, Benito G, Barriendos M, Llasat MC (eds) Paleofloods, historical floods and climatic variability: applications in flood risk assessment, PHEPRA workshop, Barcelona, (ISBS 84-921958-2-7), 380p

Esposito E, Porfido S, Violante C (eds) (2004a) Il Nubifragio dell'Ottobre 1954 a Vietri sul Mare, Costa d'Amalfi, Salerno. Scenario ed effetti di una piena fluviale catastrofica in un'area di costa rocciosa. GNDCI, n. 2870. (ISBS 88-88885-03-X) 380p

Esposito E, Porfido S, Violante C, Biscarini C, Alaia F, Esposito G (2004b) Water events and historical flood recurrences in the Vietri sul Mare coastal area (Costiera Amalfitana, southern Italy). In: Rodda G, Ubertini L (eds) The basis of civilization – water science?, vol 286. International Association of Hydrological Sciences Publication, Wallingford, pp 1–12

Esposito E, Porfido S, Violante, Molisso F, Sacchi M, Santoro G (2011) Flood risk estimation through document sources analysis: the case of the Amalfi rocky coast. Marine reSEArch@CNR.it (in press)

Fumanti F, Rischia I, Serva L, Trigila A, Violante C (2001) Effetti sul territorio dell'evento meteorico del 7–8 Ottobre 1899 nel salernitano. Accademia Naz. Dei Lincei, 181, 395–410 (ISBN: 88-218-0878-5) p 540

Liquete C, Arnau P, Canals M, Colas S (2005) Mediterranean river systems of Andalusia, southern Spain, and associated deltas: a source to sink approach. Mar Geol 222–223:471–495

Porfido S, Esposito E, Alaia F, Molisso F, Sacchi M (2009) The use of documentary sources for reconstructing flood chronologies on the Amalfi rocky coast (southern Italy). In:Violante C (ed) Geohazard in rocky coastal areas. GS, London, Sp. Publ.322, 173–187. (ISBS 978-1-86239-282-3), 210p

Reineck HE, Singh IB (1975) Depositional sedimentary environments, XVIth edn. Springer-Verlag, New York, 439 S

Sacchi M, Molisso F, Violante C, Esposito E, Insinga D, Lubritto C, Porfido S, Toth T (2009) Insights into flood dominated fan deltas: very high-resolution seismic examples off the Amalfi cliffed coasts, eastern Tyrrhenian Sea. In: Violante C (ed) Geohazard in rocky coastal areas. G.S. L Publ., 322, 33–72. (ISBS 978-1-86239-282-3). 210p

Violante C (2009) Rocky coast: geological constraints for hazard assessment. In: Violante C (ed) Geohazard in rocky coastal areas. G.S.L Publ., 322, 1–31. (ISBS 978-1-86239-282-3). 210 p

Violante C, Biscarini C, Esposito E, Molisso F, Porfido S, Sacchi M (2009) The consequences of hydrological events on steep coastal watersheds: the Costa d'Amalfi, eastern Tyrrenian Sea. In: The Role of hydrology in Water Resources Management, vol 327. IAHSE, pp 102–113. ISBN:978-1-901502-94-7. http://iahs.info/redbooks/327.htm

THE SECOND
WORLD
LANDSLIDE FORUM

Contribution of Physical Modelling to Landslide Hazard Mapping: Case of the French Basque Coast

Marc Olivier, Olivier Sedan, and Bernard Monod

Abstract

In the frame of the DO-SMS project (created within the European SUDOE partnership), a new landslide hazard mapping method is experimented on the French “Pays Basque” coast. Based on a physical landslide modelling and integrated into a software named *ALICE*®, its aim is to propose a quantitative classification of landslide hazard by calculating a probability of occurrence of landslides on each point of the studied area. The method highlights a useful tool to gain time and efficiency in hazard mapping.

Keywords

Physical modelling • Probabilistic approach • Landslide hazard • Landslide zoning • Pays Basque coast

Introduction

Mechanical approaches represent a solution for quantitative landslide susceptibility and hazard modelling. These methods consist in, (1) generalizing at regional scale geometrical and geotechnical parameters which contribute to slope stability regarding two types of landslide (i.e. rotational and translational), (2) applying triggering factors to the studied area (water table level and/or seismic stress for example), and (3) calculating a safety factor for each point of the area.

However, as the quantity and the quality of data are generally very heterogeneous at a regional scale, it is necessary to take into account the uncertainty in the analysis. In this perspective, a new hazard modelling method, using a probabilistic approach, is developed and integrated in a software called *ALICE*®.

This method is experimented for landslide hazard mapping on the French Basque coast. Situated in the South West of France, this region presents high human and economic stakes. Indeed, the Pays Basque littoral has a population density of 504 people/km, whereas it is of 81 people/km in average in the South West littoral of France (Mouhali 2005). Numerous instability problems affect the 42 km long Basque coast and contribute for a great part to the littoral erosion (Mallet et al. 2005). Landslides are concentrated in a 12 km long coastal zone between Biarritz and Saint-Jean-De-Luz (Fig. 1) while the rest of the coast is more subject to rock fall phenomenon.

A ground movement (landslides and rock falls) hazard map at a scale of 1/20,000 already exists on the Basque coast (Nédellec et al. 2005), made by an “expertise” analysis. The works presented in this paper aim at designing a more precise landslide hazard map (1/10,000) with a more objective method.

This paper provides a short presentation of the method, developed through the software *ALICE*® and the different steps which led to a new landslide hazard map of the French Basque coast area.

M. Olivier • B. Monod (✉)
SGR/MPY, BRGM, Toulouse, France
e-mail: m.olivier@brgm.fr; b.monod@brgm.fr

O. Sedan
RNSC, BRGM, Orleans, France

C. Margottini et al. (eds.), *Landslide Science and Practice*, Vol. 5,
DOI 10.1007/978-3-642-31427-8_14, © Springer-Verlag Berlin Heidelberg 2013

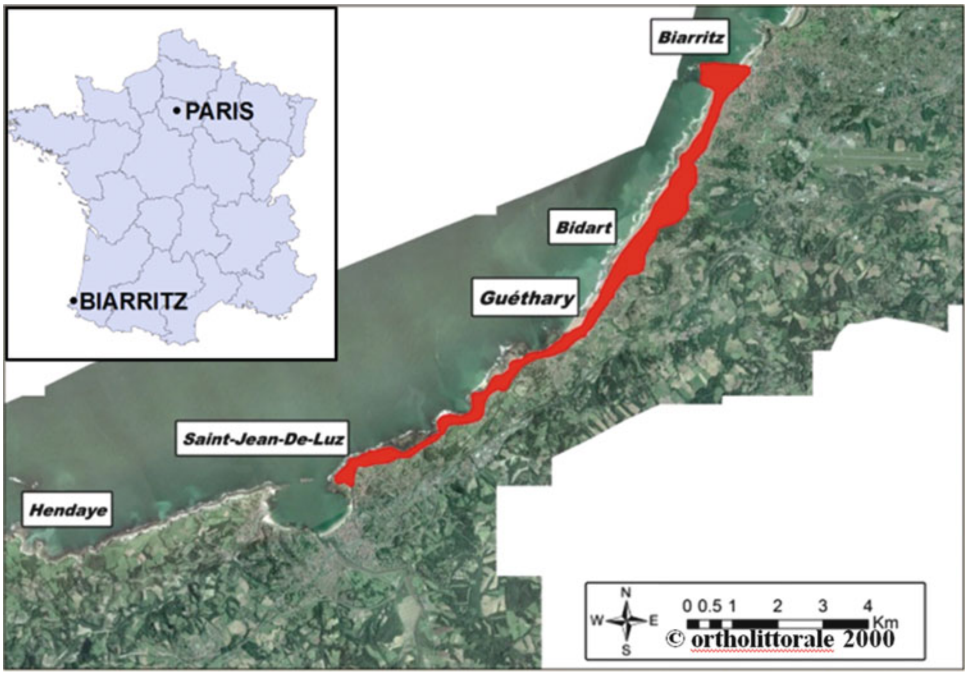

Fig. 1 Situation of the studied area (in *red*) which represents the portion of the coast the most affected by landslide phenomena

A New Landslide Physical Modelling Software: *ALICE*®

Principle

ALICE®, which stands for Assessment of Landslides Induced by Climatic Events, is a software designed to support landslide hazard mapping (Sedan 2011).

The model is based on a mechanical and geotechnical approach for which the main physical characteristics of the medium are quantified and used by a mathematical model calculating a safety factor (Aleotti and Chowdhury 1999). In these models, the spatial variability of the parameters (e.g. mechanical characteristics) has to be known and is handled through GIS software.

The probabilistic approach used in the software allows to take into account uncertainties by giving probabilistic distributions to some of the model parameters (Stillwater 2007).

Modelling

The software uses the Morgenstern and Price method (1965, 1967), which is a finite slope stability model based on the equilibrium calculation between slices subdividing the landslide volume. This method is used on regularly spaced topographic 2D profiles which cover the whole studied area. These profiles are automatically generated by the software using four input raster maps: a Digital Elevation Model (DEM), a slope map, a flow direction map and a flow accumulation map.

Pedological and geological characteristics are taken into account thanks to the altitude maps of the interfaces between each soil layer, the highest limit corresponding to the topographic surface (DEM).

Variability and uncertainty of the geotechnical parameters are introduced in the software by means of probabilistic distributions (normal, uniform, triangular or trapezoid). A distribution is attributed to each soil characteristic (cohesion (c), angle of friction (ϕ) and unit weight (γ)) and for each soil layer.

The safety factor calculation also needs the landslide type (rotational or translational) and its length. These parameters are defined for the whole studied area.

Water table level is set by determining two piezometric maps: one for the maximal water table level and the other for the minimal. The water table is then automatically generated between these piezometric levels by setting a filling ratio.

Software Output

On each profile of the studied area, the software calculates safety factors for several landslide positions (Fig. 2).

The probability of having the safety factor below than one represents the probability of occurrence of the landslide for a given triggering scenario (i.e. landslide geometry and water table level). The dispersion of the distribution gives the uncertainty of the result.

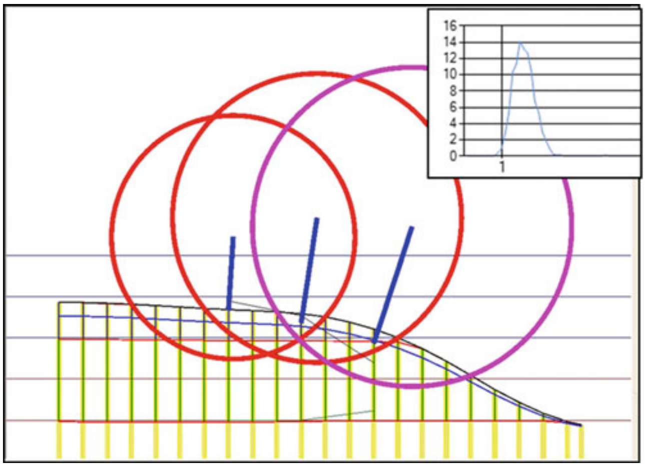

Fig. 2 Illustration of the way the software calculates safety factors for several landslide positions (*red* circles) along a topographic profile on the Basque coast. The *pink* circle represents the landslide position with the highest probability of occurrence along the profile. The graph in the *top right* hand corner shows the distribution of calculated safety factors for the pink landslide. (For a detailed description of the cross section, see Fig. 11)

The calculated probability of occurrence is then attributed to all the pixels of the result raster located on the profile and intersecting the landslide geometry. Thus a pixel receives as many probabilities as landslide positions it is included in. Finally, a map is created, displaying the highest calculated probability of occurrence for each pixel of the studied area.

Application to the Basque Coast

General Context

Geology

The French Basque coast displays folded rock units that regionally dip towards the north. Thus, from north-east near Biarritz to south-west near Saint-Jean-de-Luz, geological formations are mainly composed of tertiary sandstone, marly-calcareous and marl formations until Bidart city, and cretaceous flysch with flint, calcareous flysch until Saint-jean-de-Luz city (Fig. 3).

A major fault zone is located north of Bidart city, at the base of the tertiary strata. It is responsible for the outcropping of triassic gypsiferous shale and the grinding of rocks around.

The bedrock displays two facies along the coastal cliff: fresh rocks at the base and weathered rocks, called alterite, to the top (few meters from the surface). The alterites are well developed over the eocene units and over the santonian-coniacian flysches.

Plio-quaternary Onesse and Arengosse formations, together with sand formations were deposited over the eocene alterites. Alluvium and colluvium deposits fill in the troughs and the valleys.

The coastal instabilities are concentrated into the alterites and the plio-quaternary formations which present poor mechanical characteristics.

A simplified geological model has been developed, grouping together the coast formations into three "geotechnical units": Plio-quaternary, Alterites and Bedrock (Peter-Borie 2008, Fig. 3). Hundreds of borehole reports were gathered and interpreted in order to interpolate the altitude of each interface, allowing the creation of maps for the base and the top of each unit.

Hydrogeology

Water circulations are very complex within the Basque coast reliefs and suffer from a lack of information and studies (Winckel et al. 2004). However, some punctual studies showed that water level was close to the surface at the time of various landslide triggering (Capedeville et al. 1982; Peter-Borie 2008).

Geotechnical Parameters

Despite the numerous geotechnical studies carried out on Basque coast instabilities, few laboratory tests were made on the materials. Thus some of them had to be determined thanks to expert statements. Ranges of values were then established for each parameter and for each soil unit (right columns, Fig. 3). For the safety factor calculations, triangular distributions of these values, which can be compared to discretized Gaussian functions, were chosen because this type of simple distribution is well adapted when few data are available.

First Modelling Scenario

Based on the documents available on the studied area and on a short field visit, a first triggering scenario is established: a constant 2 m deep water table and 25 m long landslides are used as input parameters in the software.

The results of this first scenario are presented for the Arretgia beach area (Fig. 4a). A high probability means that the landslide will occur if the triggering scenario is achieved, even if the material has the highest values within the geotechnical characteristic distributions. On the other hand, low probabilities point out stable areas, even for materials with very poor characteristics.

This result map can be used directly in order to evaluate quantitatively the landslide hazard. For a wider accessibility, to integrate public policy documents for example, a "classical" zoning map, with hazard levels (low, moderate, high), is recommended.

Thus a preliminary zoning of the studied area is realised, based on the software results, satellite images and 5 m spaced contour lines created from the DEM (Fig. 4b). Four hazard levels are defined from the probabilities of

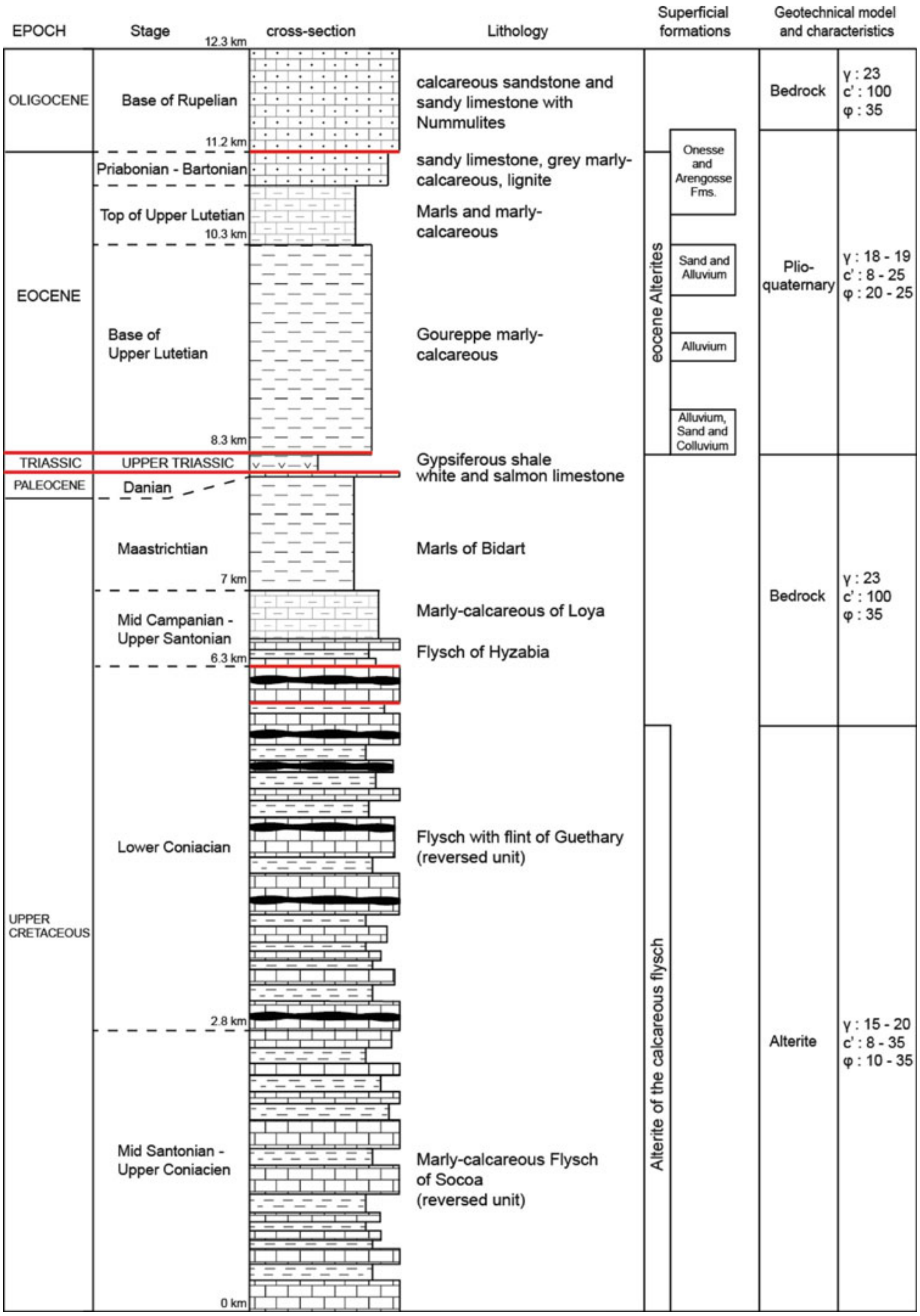

Fig. 3 Vertical representation of the geological formations out cropping along the Basque coast and geo-mechanical model associated. The north-dipping rock units are represented in the same order as they are exposed along the coast, from the SW (*bottom*) to the NE (*top*). The thickness of the formations represented is proportional to the outcropping thickness along the coast. Main faults are represented in red. Units for the geotechnical parameters are: γ: kN.m^{-3}; c:kPa; ϕ:°

occurrence: Very Low (0 %); Low (<10 %); Moderate (10–30 %); High (>30 %).

Field Checking

A second field visit was carried out in order to face the modelling results and the hazard zoning with the ground truth. The whole studied area was observed and commented. In general, a good correlation exists between the modelling results and the reality. However, several areas seem to be under-evaluated by the modelling regarding the existing instability evidences. In some areas, the modelling does not correspond at all to the field observations.

Three sample areas are detailed in this paper: (1) the Erromardie beach presents several zones with various probabilities of occurrence which correspond to the stability context of the area, (2) the Parlementia sector presents some instability evidences which don't fit with the modelling low probabilities and (3) the "Côte des Basques" modelling

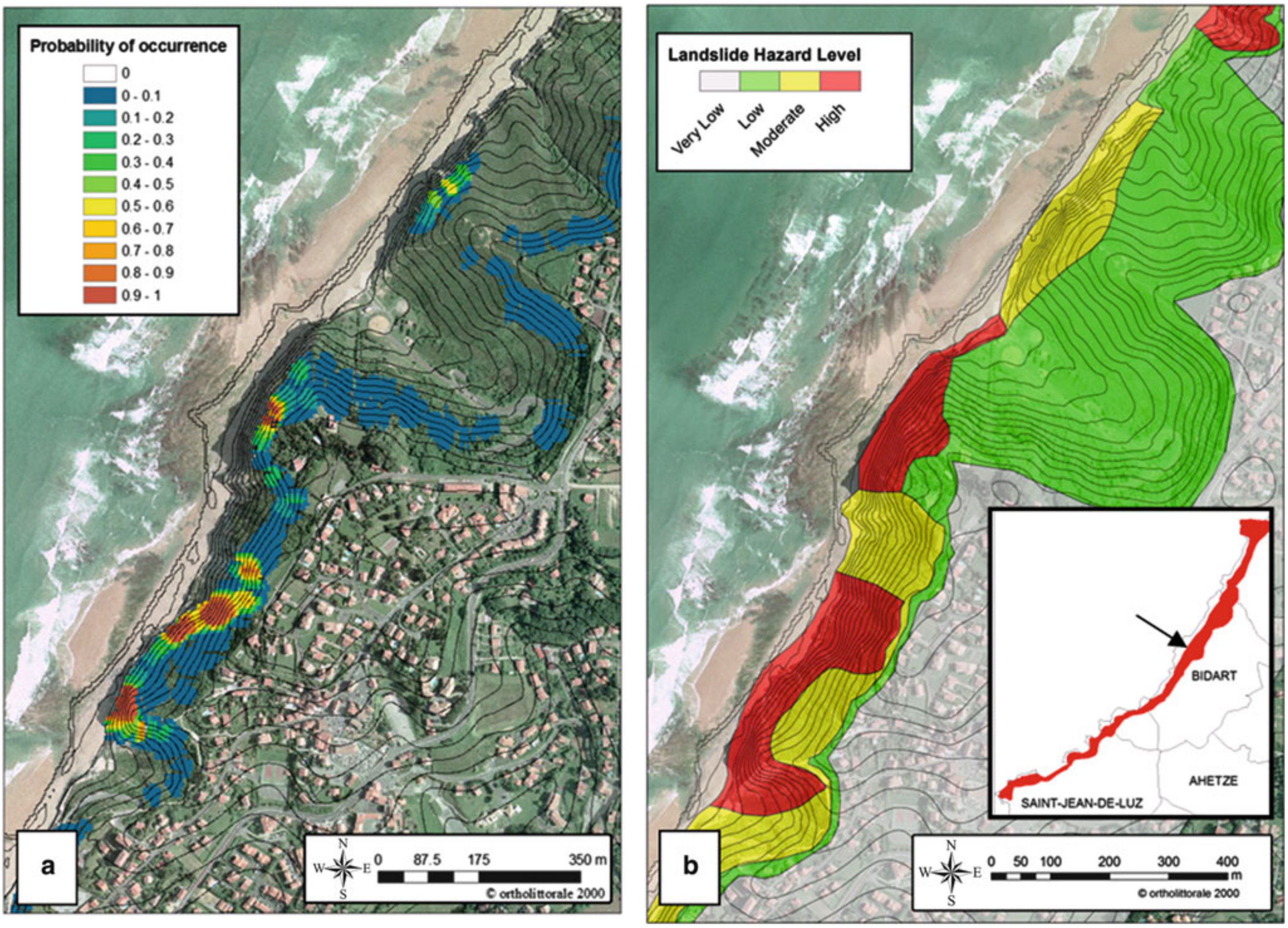

Fig. 4 Results of the first modelling scenario on the Erretgia Beach area (**a**) and corresponding preliminary hazard zoning (**b**)

shows no landslide hazard whereas instabilities are visible nearly all along the area. Erromardie and Parlementia instabilities take place into the alterites of the flysches whereas the Côte des Basques ones are located into marly-calcareous formations.

Erromardie

Erromardie beach, situated in the city of Saint-Jean-De-Luz, presents many instabilities, from 10 to 40 m long. The result of the modelling shows many zones with high probabilities of landslide occurrence but also some with lower values (Fig. 5) and this lateral variation is well observed on the field.

The high probabilities correspond to the sea bank showing either recurrent instabilities (Fig. 6b), or recent landslides (Fig. 6a, c) while the low values match with zones without bank (the main sand beach), where the bank slope is less steep or where the bedrock is closer to the surface. Thus the preliminary hazard zoning designed from the modelling results is validated by the ground truth.

Parlementia

In this area, the modelling gives a low probability of landslide occurrence (Fig. 7) which resulted in a low hazard zone for the zoning map.

However on the field, the sea bank showed signs of instabilities such as tension cracks on the road or on the materials of the bank. Moreover, the slopes situated under the coast houses are comforted by geotextiles and draining blanket in order to avoid infiltration of water within the soil. One of the draining blankets was in construction at the time of the visit (Fig. 8). The need for such soil protections implies a history of instabilities threatening the houses on this site. Here, the preliminary zoning is wrong and have to be modified.

This difference between modelling and reality was encountered several times along the coast. A hypothesis for the bad modelling of these areas is that the landslide size of 25 m chosen in input is too short. Indeed, many landslides encountered along the coast were longer than 35 m.

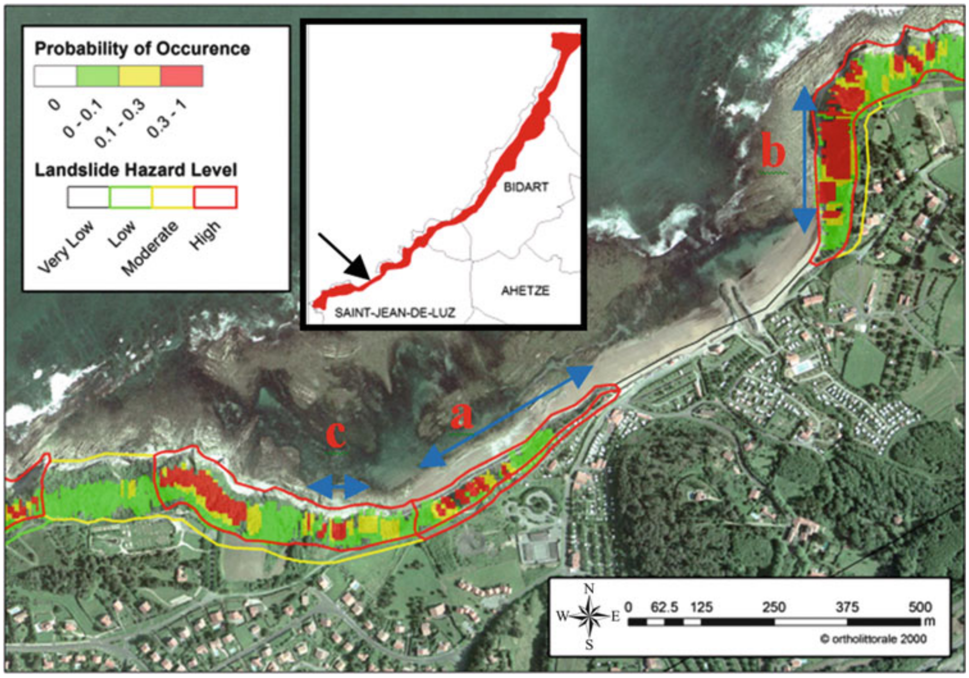

Fig. 5 Results of the modelling (probabilities of occurrence) and preliminary hazard zoning map on the Erromardie beach area. The *blue arrows* show the locations of the photographed banks of Fig. 6

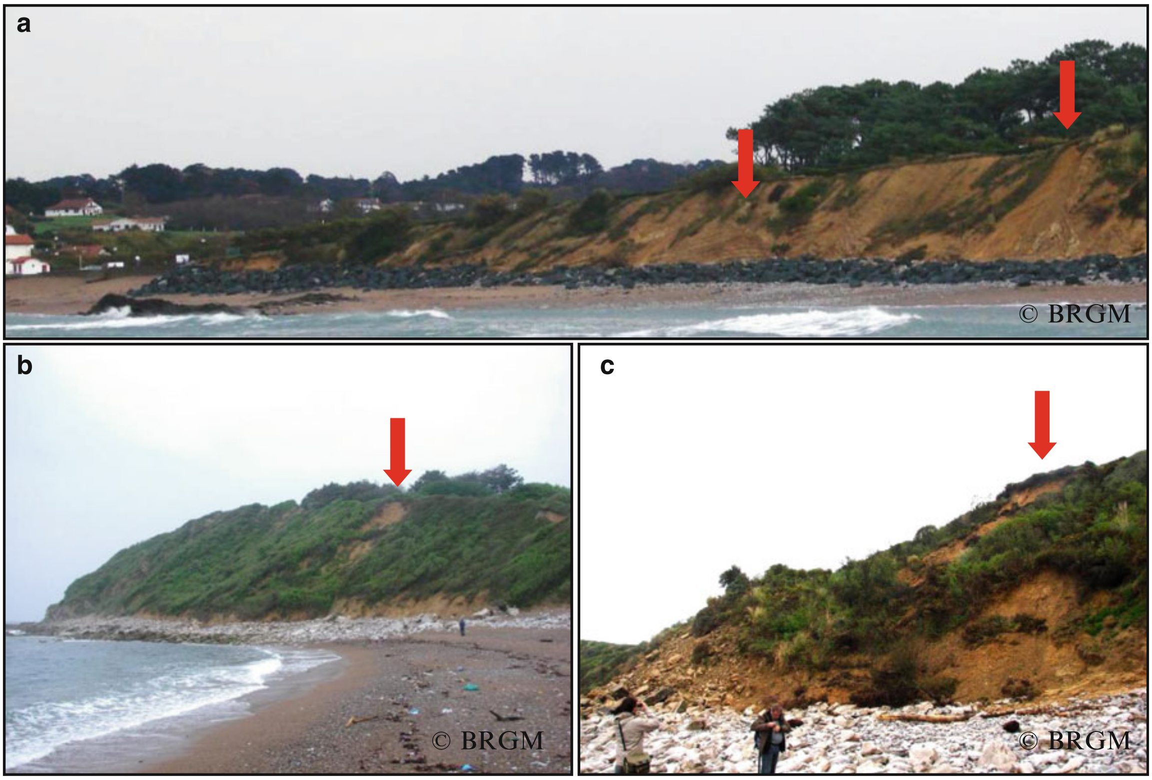

Fig. 6 Different instability areas on Erromardie beach. The *red arrows* point at recent landslides

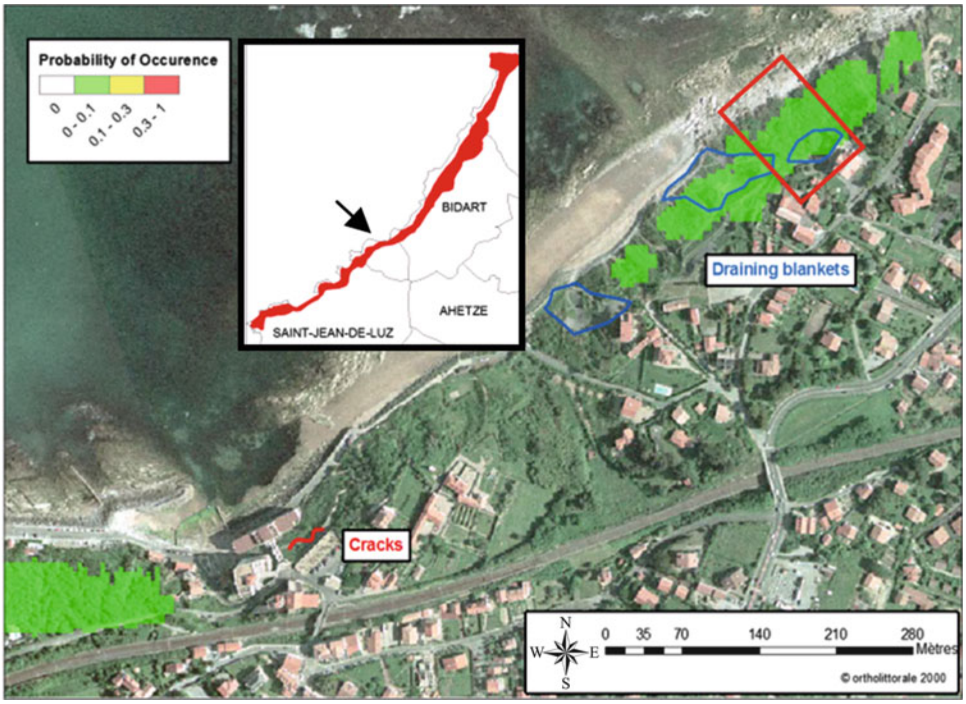

Fig. 7 Results of the modelling on the Parlementia area and locations of movement evidences and soil protections observed. The red rectangle represents the localisation of Fig. 8

Fig. 8 Construction of a draining blanket over slid materials

Fig. 9 Forbidden area due to frequent landslide occurrence on the South of the Côte des Basques (see localisation on Fig. 10)

Côte des Basques

The cliffs of the Côte des Basques area are well known for their frequent instability problems and many studies and stabilization works have already been carried out to secure them. Levelling works are still in progress on a part of this area, and the access of the beach underneath is forbidden (Fig. 9). However, the modelling only shows a few low probability areas which are not even matching with the most active landslide zone (Fig. 10).

The problem was identified as coming from the simplified geological model used with the software. Indeed, in this model, the Marly-calcareous rocks of the Cote des Basques cliffs are classified as Bedrock unit. Thus, strong mechanical characteristics are assigned to this formation for the software stability calculations (Fig. 3). However, a decompression fringe corresponding to the first meters of rock below the surface displays highly weathered materials (Capedeville et al. 1982). Geotechnical tests on these materials gave much lower characteristics. Thus the modelling is widely overestimating the stability of this area.

Moreover, as the banks are at least 50 m long, the input landslide size is not adapted to this area.

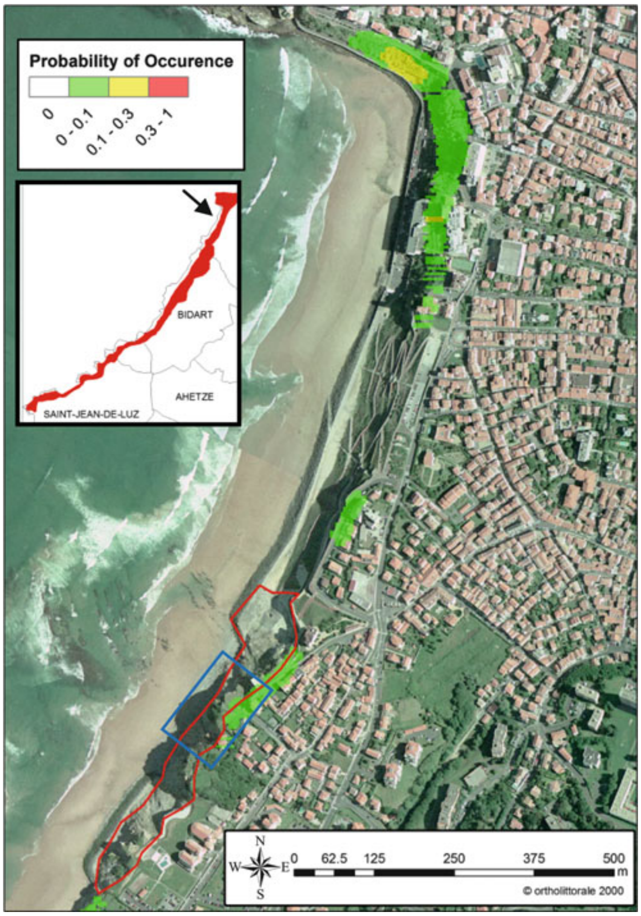

Fig. 10 Results of the modelling on the Côte des Basques cliffs. The most active area is highlighted by the red lining. The *blue rectangle* represents the localisation of Fig. 9

Second Modelling Scenario

Following the field visit and the observations made, a second modelling scenario was established in order to get closer to the reality:

- Input landslide size is raised up to 40 m to be more representative of the instabilities existing in the studied area.
- Water table level is created using a filling ratio of 90 % between the topographic and the sea levels (Fig. 11). Doing so, the water gets closer to the surface while reaching the bottom of the sea bank. This behaviour is close to the ground truth as many smalls water springs were observed in the bottom part of the sea banks.

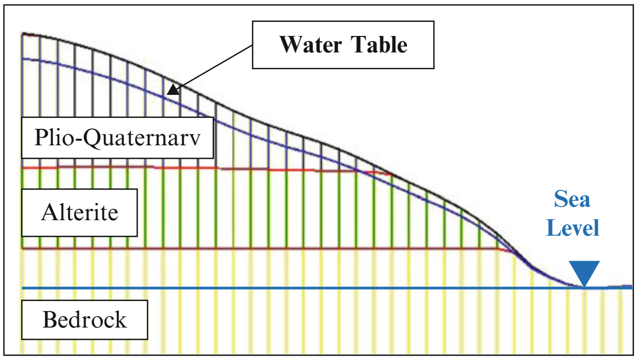

Fig. 11 Cross section along the Basque coast showing the topographic surface, the geological model, sea and water table levels. In this example, water table depth is determined as being 10 % of the difference between the topographic and the sea levels

- The Côte des Basques sector is treated separately from the rest of the coast. The mechanical characteristic values of the Marly-calcareous formations are lowered, corresponding to weathered rock characteristics. For the stability calculation a landslide depth limit of 10 m is defined based on the estimated thickness of the decompression fringe.

The results of this second modelling are much more representative of the actual instabilities of the Basque coast than the first, as it can be seen on the Parlementia and Côte des Basques areas (Fig. 12). However, some localized sectors still do not match the field observations. It happens mainly in high geological heterogeneities areas (e.g. major fault disturbances, Fig. 3) which are not taken into account in the simplified geological model.

Final Landslide Hazard Zoning

Based on the new modelling and the field observations, the preliminary landslide hazard map is modified to represent accurately the hazard level on the French Basque coast. In the zones where the modelling is not relevant, a classical expertise approach is used. The final map for the city of Bidart is presented (Fig. 13)

A "Very High" hazard level is added for the zoning. It corresponds to zones showing recurent landslide events and can be associated to sectors where the triggering scenario is regularly achieved.

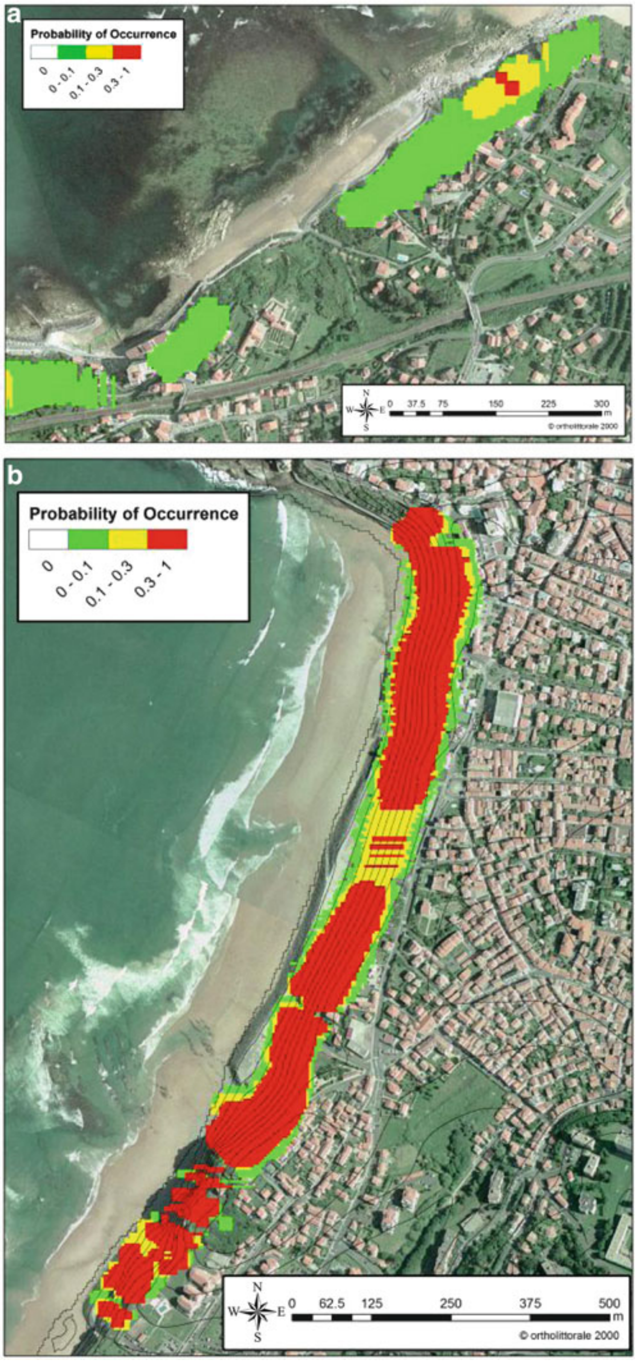

Fig. 12 Results of the second modelling for (**a**) the Parlementia beach and (**b**) the Côte des Basques cliffs. The displayed probabilities of occurrence correspond much better to the field observations compared to Figs. 7 and 10

Finally, a regression zone of 20 m in average is delimited behind the sea bank. The mapping of these areas is based on the results of the software and the study of the historical coast erosion (Peter-Borie, 2008).

As the map was designed at a scale of 1/5,000, it has to be used at a maximal scale of 1/10,000.

Conclusions and Perspectives

A landslide hazard map has been designed on the French Basque coast, based mainly on the results of a physical modelling software.

The *ALICE*® software provides a useful tool for landslide hazard zoning. It creates a probability of occurrence map for given landslide type and water table level. This map allows a fast spotting of the most sensible areas and a hazard quantification of these areas. However, it still cannot be dissociated from a ground truth approach as shown in the example of the French Basque coast. The main purpose of developing such method is to be able to combine quantitative hazard data with quantitative vulnerability data in order to have a quantitative assessment of the landslide risk.

The difficulties which could be encountered when using this method will probably come from the quantity and quality of data needed. Very few areas are endowed with a 3D geological model and enough geotechnical characteristics values.

For future works on the Basque coast landslide hazard map, the hydrological modelling should be improved. It could be done using the *GARDENIA*® rain/flow model (Thiéry 2003) which simulates the water cycle from rain on a watershed to a phreatic level at a given point or a flow at an exit point. This model involves periodic rainfall and piezometric measurements as well as weather data (e.g. temperature and moisture of the air) in order to highlight the periodic variations of the water table in the coast reliefs.

For the software perspectives, it is planned to generalized the probabilistic approach on other parameters than geotechnical characteristics, like landslide geometry, soil layer thickness or water table level. *ALICE*® should also be combined with a landslide material propagation software in order to create a complete landslide modelling tool.

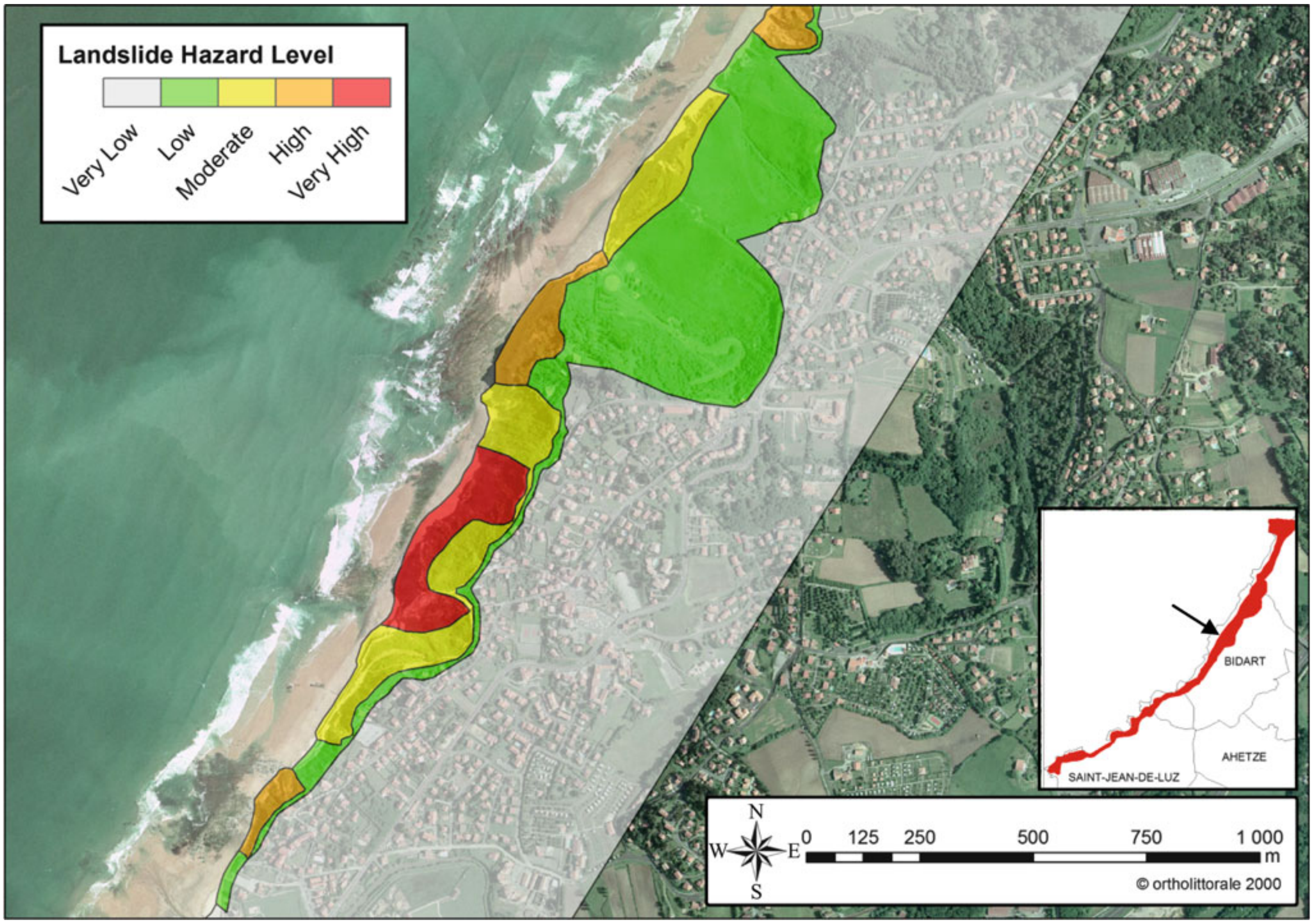

Fig. 13 Final landslide hazard map on the city of Bidart

Acknowledgments The authors would like to thank Christian Mathon who accepted to share is strong knowledge on the French Basque coast and who provided many useful advices all along the study. We express our gratitude to José Darrozes for both leading the DO-SMS project and reviewing this article providing very useful suggestions. We also wish to thank Sandrine Aubie for accompanying us on our first field visit on the Basque coast and Anais Hoareau for her precious help in the handling of the numerical data. Finally, the authors express their gratitude to all the partners of the DO-SMS project who showed their interest in our work and shared their point of view and experience on difficult parts of our researches.

The DO-SMS project is financially supported by the STC SUDOE through the Interreg IV B funding.

The geological model and some other numerical data on the French Basque coast were provided by the OCA organisation.

References

Aleotti P, Chowdhury R (1999) Landslide hazard assessment: summary review and new perspectives. Bull Eng Geol Env 58:21–44

Capedeville JP, Combe M, Dubreuilh J, Teissier JL (1982) – Géologie et hydrogéologie de la falaise de la côte des basques et de son arrière-pays. Schéma de principe pour le drainage. 82 SGN 562 AQI, 36p

Mallet C, collaboration Aubié S, Capdeville JP, Dubreuilh J, Genna A, Lamarque C, Nédellec JL, Mathon C, (2005) – Synthèse des études réalisées sur les instabilités de la côte basque entre 2001 et 2005. BRGM/RP-54012-FR, 32p

Morgenstern NR, Price VE (1967) A numerical method for solving the equations of stability of general slip surfaces. Computer Journal 9:388–393

Morgenstern NR, Price VE (1965) The analysis of the stability of general slip surfaces. Geotechnique 15(1):79–93

Mouhali K (2005) Littoral aquitain, diagnostic de territoire. INSEE Aquitaine, 45p

Nédellec JL, Zornette N, Mathon C, collaboration Aubie S. et Imbault MH (2005) Evaluation et cartographie de l'aléa mouvements de terrain sur la côte basque. – Observatoire de la Côte Aquitaine – BRGM/RP-52783-FR rapport final, 41p

Peter-Borie M (2008) – Les massifs rocheux du Crétacé supérieur du Labourd occidental: processus d'altération et instabilités littorales. Thèse de doctorat, Université Bordeaux 1, 342p

Sedan O (2011) – Logiciel ALICE version 7 – Guide Utilisateur. BRGM/RP-60004-FR, 32p

Stillwater Sciences (2007) Landslide Hazard in the Elk River Basin, Humboldt County, California. Final report. Prepared by Stillwater Sciences, Arcata, California for the North Coast Regional Water Quality Control Board

Thiéry D (2003) Logiciel GARDÉNIA version 6.0 – Guide d'utilisation, In French (GARDÉNIA software release 6.0 User's guide), BRGM/RP-52832-FR

Winckel A, Petitjean J, Borie M, Mallet C, Aubié S (2004) – Etat des connaissances hydrologiques et hydrogéologiques de la côte basque. BRGM/RP-53372-FR, 113p

THE SECOND
WORLD
LANDSLIDE FORUM

Landslides in Sea Cliffs Area Along the Capri Coast (Gulf of Naples, Italy)

Micla Pennetta and Elio Lo Russo

Abstract

Capri island is located in the Tyrrhenian Sea, on the south side of the Gulf of Naples, Italy. The island is almost completely bordered by high and steep rocky coasts (coastal cliffs) of structural control, often articulated in a succession of prominent headlands and embayments.

The sea cliffs affected by landslide processes are evident in the eastern coastal area resulting in a high degree of hazard in this stretch. The morphology of the coastal system consists in a cliff with sloping shore platform at the base of the cliff. The presence of the shore platform, which controls the erosional and shaping activities by wave motion of the cliff, play an important role and represent the main hazard factor. The other main erosional processes on rocky coast represent subordinated hazard factors. Namely, structural and stratigraphic features (hard limestone, above clastic less resistant rocks, involved in rock falls caused by basal mechanical wave erosion; the rock strata dipping seaward; presence of NW-SE trending fault), high and very steep cliffs, limestone features.

Instead, the western sector of the island of Capri is present a limestone coast with a plunging cliff; the water depth at the base of the cliff is greater than the breaker depth. The waves are reflected from the cliff face and the mechanical wave erosion and subsequent mass movements do not occur; weathering and bio-erosion processes are the major erosive mechanisms. As a result the coastal hazard for the western sector is very low.

Keywords

Coastal cliffs • Shore platform morphology • Morphological evolution • Landslides • Hazard factors • Capri Island

Introduction

The Capri island is almost completely bordered by rocky high and steep coastal cliffs of structural control, often articulated in a succession of prominent headlands and bays.

In the eastern coastal area there are obvious effects of a parallel retreat of coastal cliffs and landslide processes, that confers a high hazard in this section.

In the central-west coast of Capri island, instead, a stable coast is diffused thank to a rather negligible erosive action by the waves; these elements allow to indicate, for this area, a low coastal hazards.

Marine erosive action over coasts produces high cliffs, coastal forms represented by rocky steep slopes in contact with the sea. The retreat of a cliff and its morphological evolution, which determines and influences the degree of hazard in high coasts, is mainly related to the activity of marine abrasion. This is a determining factor, acting at the

---

M. Pennetta (✉)
Dipartimento di Scienze della Terra, Università degli Studi di Napoli “Federico II”, Largo S. Marcellino, 10. 80138, Naples, Italy
e-mail: pennetta@unina.it

E.L. Russo
c/o Dipartimento di Scienze della Terra, Università degli Studi di Napoli “Federico II”, Largo S. Marcellino, 10. 80138, Naples, Italy

C. Margottini et al. (eds.), *Landslide Science and Practice*, Vol. 5,
DOI 10.1007/978-3-642-31427-8_15, © Springer-Verlag Berlin Heidelberg 2013

mean sea level, which creates an eroded notch; the constant increasing of the notch, prepares the upper rock to collapse and then to fall taking to the increase of hazard conditions.

The aim of this study is to focus the role of the morphology of submerged areas near the cliffs to evaluate hazard in the high coasts.

Geological and Geomorphological Features

Capri island is the morphostructural extension of Sorrento Peninsula ridge (Figs. 1 and 2); it forms together with Lattari Mounts an elongated ridge to SW in the Tyrrhenian Sea.

Carbonate cliffs are sometimes affected by eroded notches derived from Last Interglacial (~125 ky BP), located at a height coinciding with the eustatic one (6 m +/−3 m above current sea level), linked to the sea erosion during the transgressive peak. This height, detected in other Italian coastal with known neotectonic behavior, allowed us to derive a substantial tectonic stability of the island in the last 125 Ky (Brancaccio et al. 1968; Brancaccio et al. 1991; Romano 1992). However, recent detailed measures of its height show higher values in the SE area of the island, that decrease from N to W. They can be attributed to small tectonic dislocations (Ferranti and Antonioli 2007).

It gradually lowers westward until resurgence with Capri island, from which it differs for the facies of carbonate units (Lias – Paleogene). They are constituted by limestone, rudites with corals and Ellipsactinie (Fig. 3), (Barattolo and Pugliese 1987; Barattolo et al. 1992; Brancaccio et al. 1988; Autorità di Bacino di Sarno 2003; D'Argenio et al. 2004).

In Capri island are evident effects of Miocene tectonic compression that has structured the Apennines; (Patacca et al. 1990) it produced in the island the overlap of the Meso-Cenozoic carbonate units over Miocenic flysch. The two superimposed tectonic slices together are dislocated by transcurrent faults (2 Myr BP), oriented EW and NE-SW (geological section in Fig. 3), (Ferranti and Antonioli 2007). The overlap is evident at the base of cliffs in the north-eastern sector of the island, constituting the main hazard factors which affect this coastal tract.

In the island profile there are two main carbonate blocks, Monte Solaro in the West and Il Capo in the East (Fig. 3), separated by a median saddle consisting of the Miocene flysch buried by pleistocenic deposits (Barattolo et al. 1992). Here the morphology of the island shows maximum thinning related to less rock's resistance to erosion (Fig. 1). The steep structural carbonate cliffs give way to a coastal landscape less steep, in which there are the two largest harbors: the main *Caterola Marina (Marina Grande)* in the North (Figs. 1 and 3), and the minor *Marina Piccola* in the South (Fig. 3).

Fig. 1 Capri island seen from the West. In the foreground, on the *left*, *Marina Grande* harbour; *left* background, *Sorrento* Peninsula separated from the isthmus of *Bocca Piccola*. On the *left*, after the harbor, is evident the north-eastern part of the coastal cliff (Punta Caterola, La Fossa: see Figs. 6 and 8); there are residuals of marine terraces on the *top*

During the last glaciation (18 ky BP) the sea level falls at the current depth of 120 m (Marani et al. 1988; Pirazzoli 1993). The isthmus of *Bocca Piccola* (Figs. 1 and 2), between *Sorrento* Peninsula and the Capri island, actually within the 85 m depth, at that time emerged, leading to a peninsular condition of Capri which also permitted the migration of terrestrial vertebrates from the Sorrento Peninsula. During this glacial period, the abandoned cliff is subjected to periglacial conditions and becomes mantled by weathered material, producing large amounts of debris accumulated at the base of the slopes, remodeled with sea levels rise during the Holocene. The sea levels rising after the last glaciation, with alternated phases ends about 6,000 years B.P. reaching the level of about +2 m (Holocene transgression) during the climatic optimum; the activity of sea erosion in this period (Brunn 1962) models the erosional cliffs along the coasts of Capri island. The alluvial fan phase during the transgression created the conditions for the development of the beaches at the streams mouth.

From the climatic Optimum, the island coasts looks similar to the present, characterized by small gravels beaches.

Study Methods

Geomorphological observations along coast, bathymetric profiles, and underwater inspections performed allowed to delineate the main morphological features of the studied coastal system in its emerged portion to a depth of about −20/−30 m from sea level (Pennetta 2004; Pennetta et al. 2003).

The studied coastal area was subjected by a detailed geologic field activity study united to detection of aerial photos and satellite images; characters found were mapped at 1:5,000 scale maps (Carta Tecnica della Regione Campania 1987).

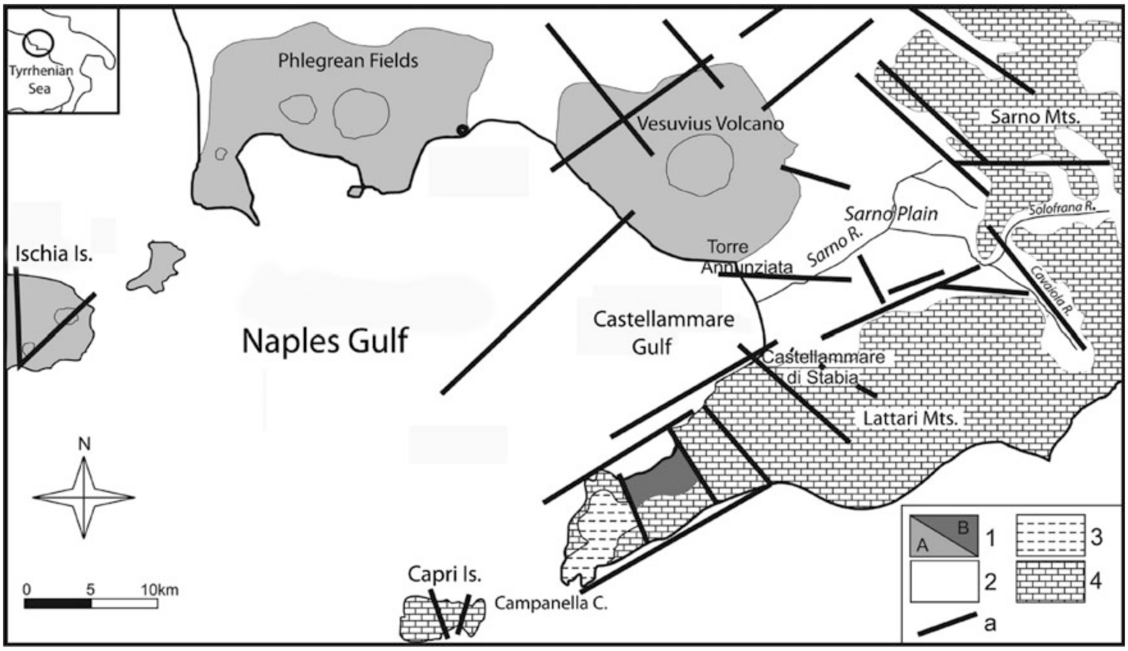

Fig. 2 Schematic geological structure of the Capri island, *Sorrento* Peninsula (*Lattari Mts.*) and Naples Gulf. (*1*) – lava and pyroclastic products of the main volcanic systems: (*A*) lava and pyroclastic of late Pleistocene-Holocene (*B*) Campanian Ignimbrite; (*2*) – Quaternary coastal, lagoons, alluvial and volcanoclastic deposits; (*3*) – Miocene flysch deposits; (*4*) – Mesozoic carbonate rocks; a – main normal faults

The morphology of the seabed was derived from bathymetry in 1:5,000 scale (Fig. 4) acquired thank to bathymetric survey.

These ones were made using GPS differential with Sky Station and a continuous ultrasound record; GPS and ultrasonograph were connected in real time to a registration station through acquisition-navigation software with acquisition of Coordinate System *UTM WGS84* and the depth of 15 points per second. The measurements were carried out along transects perpendicular to the coast of Capri at wheelbase between 150 and 300 m. Beyond measurements along transects, bathymetric measurements were carried out parallel to the shoreline from the depth of 0.5 m.

Every measurement requested the calibration of the ultrasound signal through automated calculation of the depth, of the unit of sound pulse to the surface of the sea and the speed of sound as a function of water characteristics (salinity, density, temperature). One million records were acquired, then subjected to quality control, using a form of acquisition-navigation software. Bathymetry has been developed by a dedicated software and geo-referenced using GIS system according *UTM WGS 84* System.

Geomorphological Analysis

Detailed analysis of emerged and submerged coastal system (Fig. 4) allowed to define the rocky coast morphology and morphological evolution and to identify mass movements can occur on rocky coasts of Capri island.

The entire island is rimmed by steep cliffs (Fig. 4) of structural setting (about 2 Myr), often articulated in alternating headlands and embayments, sometimes with small pocket beaches at the base. These are generally set at the intersection structural weakness, or are related to the fall of tectono-karst cavities developed along the cliffs.

In the submerged area, the cliffs are bordered by sloping shore platforms, that from the sea level are inclined seaward (type A – sloping shore platform: Sunamura 1992). A further analysis (De Pippo et al. 2007) has permitted to divide the type A in two morphologies: A1 (sloping shore platform: wideness maximum 200 m and sloping 3–10 %) and A2 (narrow sloping shore platform: wideness maximum 100 m and sloping 10–30 %).

In detail, in the central and eastern sector of Capri island, low-gradient sloping shore platform (A1) characterizes the coast with a cliff from *Punta Sbruffo* to *La Fossa* (Figs. 4 and 5); the presence of the shore platform, which determines the genesis of breaking waves can erode and shape the cliff, has a predisposing essential role for the morphological evolution of the cliffs.

On the platform the submerged gravel-sandy beach is presented, rarely it emerged to form the pocket beaches, which extends within the 8–10 m depth. The depth of the sea at the base of the cliffs is zero everywhere except in rare parts affected by the presence of small pocket beaches. Furthermore, this coastal area is characterized by stratigraphic and structural disposition schematized in *Punta Caterola* (Figs. 6 and 7) and *La Fossa* (Fig. 8) geological sections.

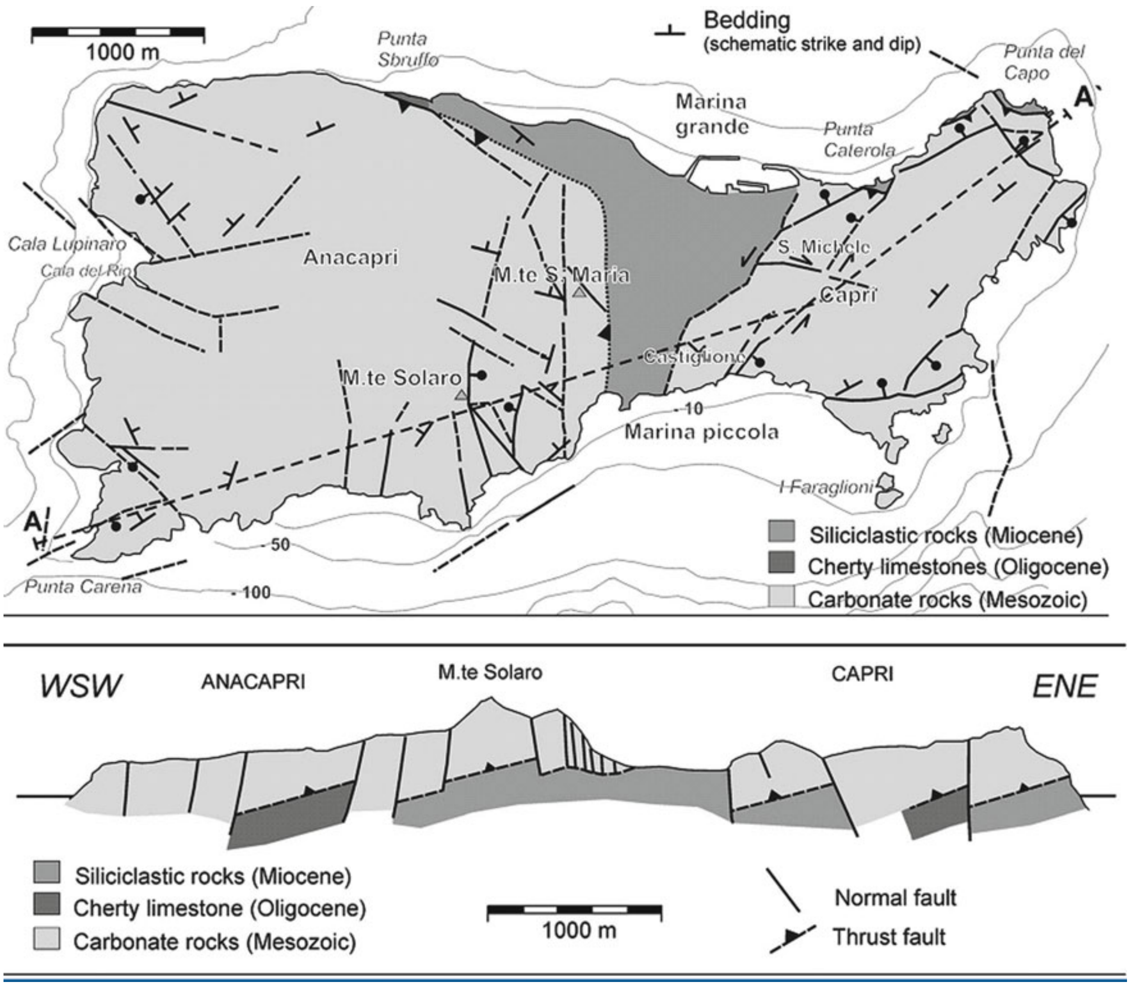

Fig. 3 Geological Map (*up*) and schematic geological section (*down*), (by Barattolo et al. 1992; Ferranti and Antonioli 2007. Faults, layers giacitures by D'Argenio et al. 2004)

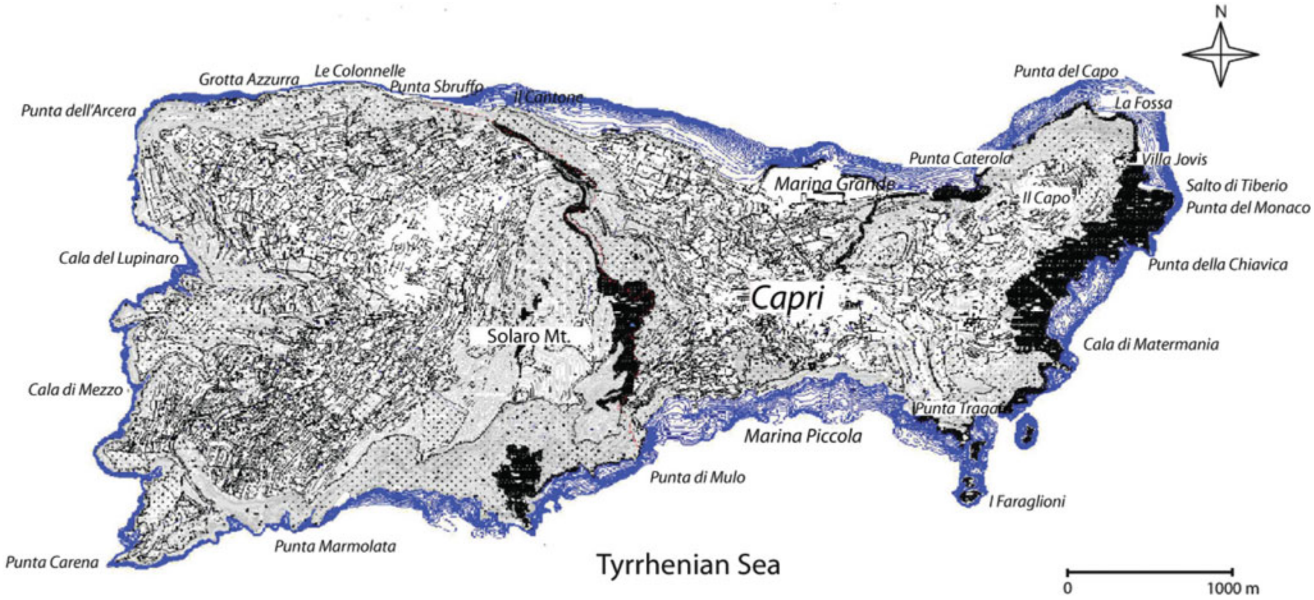

Fig. 4 Bathymetric and topographic map of Capri island (isobaths coloured blue with 1 m equidistance). Island western sector is characterized by emerged steep coastal cliffs with height of about 30 m; isobath densification indicates a coast with a plunging cliff. Island eastern sector is characterized by a coastal cliff morphologies constituted by high steep cliffs bordered by sloping shore platform (A1 and A2 types)

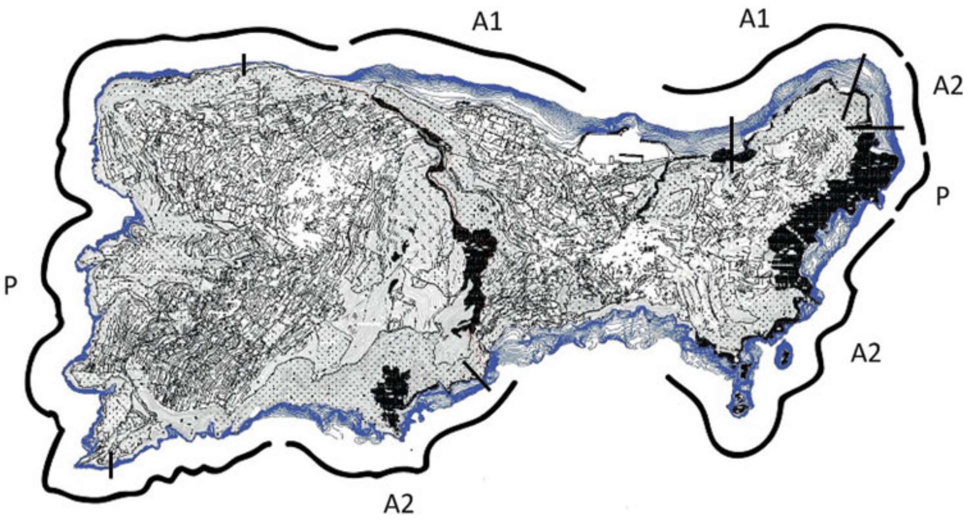

Fig. 5 Capri island coastal cliff morphologies: profiles line of the schematic geological sections of the coastal system. A1 – sloping shore platform – wideness maximum 200 m and sloping 3–10 %. A2 – sloping shore platform – wideness maximum 100 m and sloping 10–30 %. P – Plunging cliff

Fig. 6 Schematic geological section (see Figs. 1, 4 and 5) of the coastal tract near *Punta Caterola*

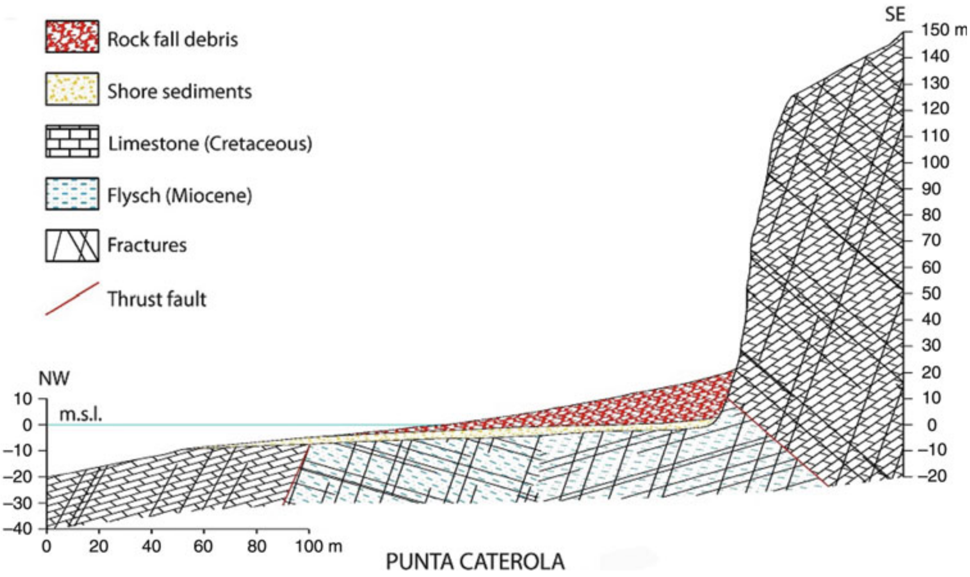

Fig. 7 Limestone cliff of *Marina di Caterola*, at the Est of the *Marina Grande* harbour, characterized by the thrust of carbonate rocks over miocenic flysch: a less resistant rock overlain by a resistant rock. At the base of the steep cliff is evident the debris from the rock fall of the 1973; on the left of landslide debris is evident yellowish flysch. Seaward, there is a wide and gently sloping shore platform (see Fig. 6)

The cliffs have spectacular heights between 120 and 200 m and are modeled in weaknesses limestone breccias tectonically superimposed, with SSW immersion thrust surface, to arenaceous – clay succession (Fig. 7).

This arrangement encourages the wave action at the base of the cliff against the Miocenic flysch deposits less resistant overlain by resistant rocks. These factors determinate mass movements of carbonate deposits and a parallel retreat of cliff; they confer a high level of hazard in this section.

The A2 morphotype characterizes the coast from *La Fossa* to *Punta Marmolata* (Figs. 4 and 5). One exception is the sector between *Punta del Monaco* and *Punta della Chiavica* (plunging cliff morphotype) and in the less high coastal tract at *Marina Piccola*. In the coastal tract characterized by A2 morphotype, the cliffs are modeled in weaknesses Cretaceous carbonate breccias and dolomites, with a predominant horizontal layers. They are characterized by spectacular sub-vertical growth with heights between

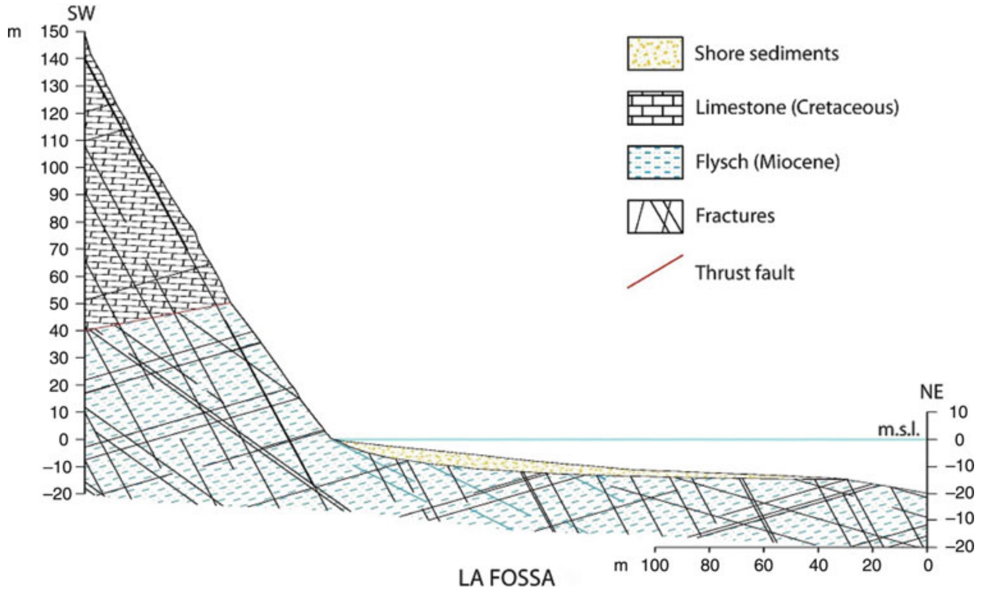

Fig. 8 Schematic geological section of the coastal tract at *La Fossa* (see Figs. 4 and 5), characterized by A1 morphotype

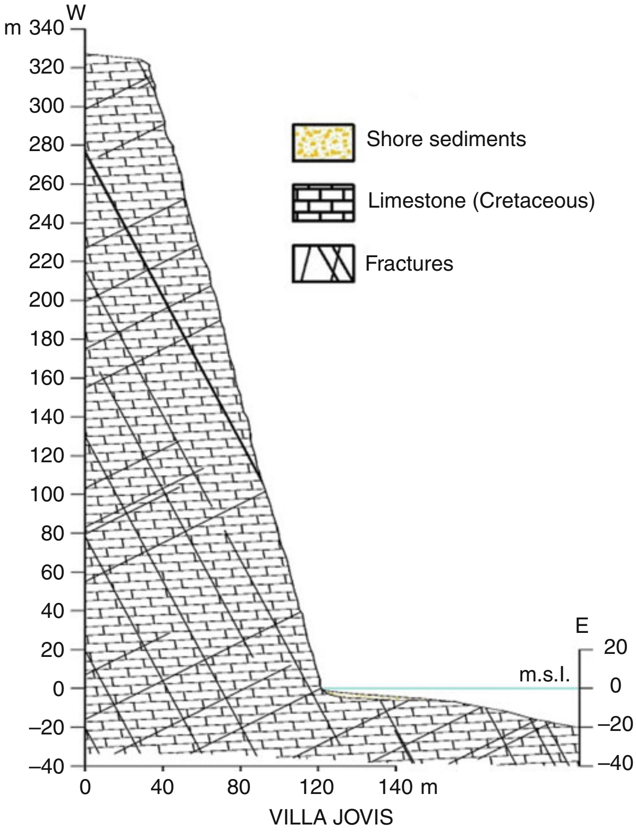

Fig. 9 Schematic geological section of the coastal tract at *Villa Jovis* (see Figs. 4 and 5), characterized by A2 morphotype

100 m (*Punta Tragara)* and 350 m (*Cala Ventroso*) or 320 m (*Salto di Tiberio*).

The presence of the narrow shore platform, sloping 15–25 %, determines also for this morphotype exposure to

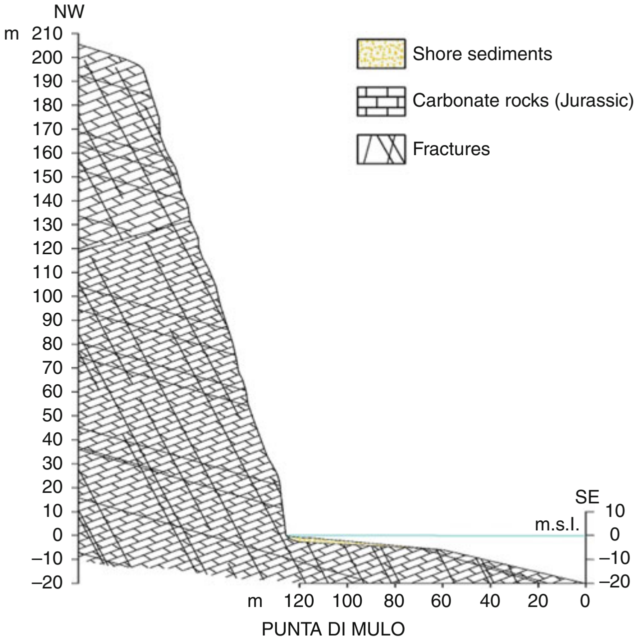

Fig. 10 Morphotype A2: schematic geological section of coastal tract of *Punta di Mulo* (see Figs. 4 and 5)

marine erosion that occurs with cliff retreat caused by rocky fall facilitated by a preparatory weathering processes that make the rocks surface unstable.

The eastern coastal area is schematized in the section of *Villa Jovis* (Fig. 9); in the southern section of *Punta Mulo* (Fig. 10) the high cliffs with sub-vertical growth are modeled in layered Jurassic marlstones dolomite.

In the western sector of the island, and in few stretches of east coast, the vertical cliffs continue underwater environment to depths often exceeding 20 m, sometimes down to

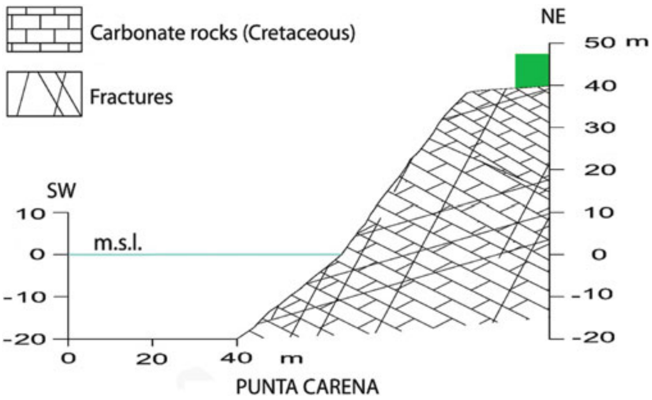

Fig. 11 Schematic geological section of the cliff at *Punta Carena* (see Figs. 4 and 5), representative of the coastal morphotype *plunging cliff*, which characterizes the western sector of Capri island

Fig. 12 SW-NE view of *Punta Carena*. Tectonized and fractured carbonate cliff (see Fig. 11) which extends deep with a similar sloping (plunging cliff). The incident waves erosive action on the cliff is practically zero, while subaerials processes can lead to the collapse of masses in correspondence of weakness area

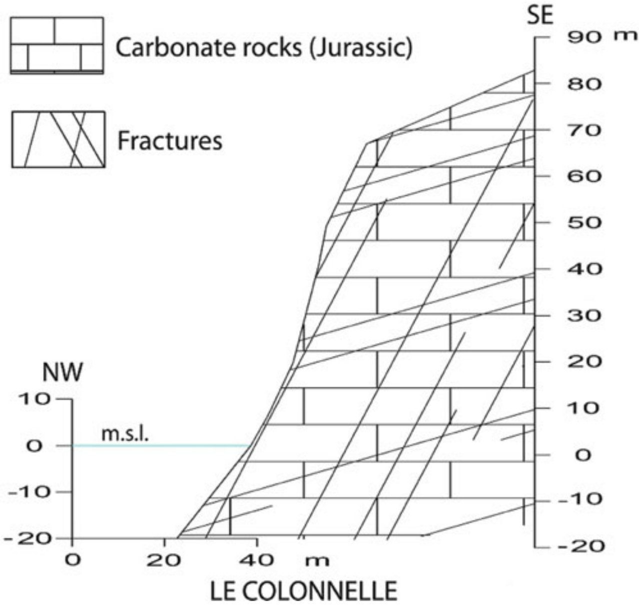

Fig. 13 Plunging cliff morphotype: schematic geological section of the cliff at *Le Colonnelle* (see Figs. 4 and 5), in the west sector of the cliff where the *Grotta Azzurra* is incised. The section is representative of the coastal morphotype that characterizes the western sector of Capri island

Fig. 14 Coastal tract that characterizes the northwestern sector of Capri island. It 's evident a calcareous cliff where the karst cave of *Grotta Azzurra* is incised; the cliff is affected by subvertical fractures and incisions and it is covered by a detritic calcareous-pyroclastic blanket partly terraced and stabilized by vegetation. The coastal morphotype present in this section and in the west coast of the island consists of a plunging cliff (see Fig. 13), with a very low rate of recession and a reduced hazard degree

−50 m (plunging cliff: Sunamura 1992). Plunging cliffs, with structural control, characterize island sector from *Punta Marmolata* to *Punta Sbruffo* (Figs. 4 and 5). The bathymetric profiles, e.g. Fig. 11 (*Punta Carena*, in the south) and 11 *(Le Colonnelle*, in the northern stretch), follows almost the subvertical cliff (Figs. 12 and 14) in deep water. The water depth at the base of the cliff is greater than the breaker depth; incident waves do not break, but are reflected from the cliff face, resulting in standing waves. So the erosional processes, determined by mechanical wave erosion, drastically decrease; this area it can be considered generally stable and characterized by a reduced hazard degree.

Siliciclastic miocenic rocks at the base of the carbonate rocks are an impermeable substrate which supports the water table, where underground extensive karst have developed, whose shapes (including for example the famous geological site of *Grotta Azzurra*) today are totally or partially submerged. In particular, the cliff with moderate height (Fig. 14), where the Grotta Azzurra is incised, is vertical plunging cliff (see section in Fig. 13 that represents also the submerged area). It is not affected by erosion activity from the impact exercited by the waves. It is therefore a stable system and the hazard level is insignificant; only on the cliff there are the conditions for the genesis of physical degradation (north-facing versant) and biochemistry of rock mainly in weakness zones which then lead to the fall of debris.

Conclusions

Cliffs retreat and their morphological evolution, that determines the hazard degree, are associated to a set of predisposing and determinants factors. Among them the main and indispensable predisposing role is the presence of the shore platform at the base of the high rocky coast which allows cliffs mechanical wave erosion. A narrow shore platform in the shallow water depths determines the genesis of wave breaking which corresponds to an erosion activity by the waves. The erosional processes of the waves are more effective in the narrow area that extends slightly below the level of quiet water until the wave crest; they decrease rapidly below the water surface.

The input of debris occurred during the Last Glacial Maximum (25 kyr B.P.) when sea level falls to the current depth range of 120 m, it provided debris materials accumulating at the base of the cliffs as depositional talus. The availability of material was higher in the highest cliffs in the eastern sector of the island of Capri; it is to correlate also to other intrinsic factors e. g. hardness of rock, rock structure, litology, orizzontal rock strata or dip seaward, the structural setting, juxtaposition of lithologies with different resistance to erosion. Rocky coasts are affected by a range of processes including mechanical wave erosion, physical and chemical weathering, bio-erosion and mass movements.

When the sea level rises again the following interglacial, renewed wave attach shapes depositional talus in a shore platform. Morphodynamic system of the cliffs is the result of their erosional processes and the presence or absence of material at their base; this material may constitute, in its first setting, especially when it emerges from the sea, a defense to the foot of the cliff. With time, to response to multiple cycles of erosion and a stable sea level, the modeling of this depositional body and its modification in the shore platform determines the activation of erosional processes by the waves motion.

The effects of these processes are evident in the high cliffs of the eastern sector of Capri island; there are also, particularly intense in the outcrop at sea level, highly erodible flysch deposits (in the NE and E section).

The height of the cliffs influences the rate of erosion; for high cliffs greater is material that accumulates when the base is eroded by the waves and the slope is affected by weathering. The supply of debris exceeds the capacity of removal at the base of the cliff due to marine processes, so the rate of retreating clearly decreases. The shore platforms appear to be the result of the combined action carried out by wave erosion and the effects caused by the activity of weathering.

These environmental features, closely connected between them, determine a high degree geomorphological hazard in a well-known coastal zone for touristic purposes.

The predisposing conditions to the erosion of the cliffs are much less incisive in those sections where the coastal morphotype is plunging cliff. The water depth at the base of the cliffs is greater than the breaker depth. Incident waves do not break, but are reflected from the cliff face, resulting in standing waves, which corresponds to an insignificant erosive action of waves. In this case, all other intrinsic and/or predisposing factors won't be able to provide any assistance to coastal hazard.

These depth values recorded in the west coastal area of the island, can be attributed to the relatively low height of the cliffs in emersion (about 30 m) and to the high resistance to erosion of the rock outcropping that have produced small amounts of debris eroded during the last glaciation in combination with the absence of coastal abrasion platform.

Along this coastal tract the conditions are practically of very low hazard; erosional processes occurs only with collapses in that the areas affected by particular structural weakness.

Ultimately, predisposing conditions similar to each other, can lead, for different morphological submerged structures, to different morphological evolution models and different conditions of coastal hazards. If in Capri island the tectonic contact between flysch and limestone, that is a predisposing factor to a rapid morphological evolution, was located in the western sector of the island characterized by a plunging cliff, the coastal hazard tends to be practically zero.

References

Barattolo F, Pugliese A (1987) Il Mesozoico dell'isola di Capri. Quaderni dell'Accademia Pontoniana 8:1–172

Barattolo F, Cinque A, D'Alessandro E, Guida M, Romano P, Russo Ermolli E (1992) Geomorfologia ed Evoluzione Tettonica Quaternaria dell'isola di Capri. Studi Geologici Camerti vol Spec 221–229

Brancaccio L (1968) Caratteri e Genesi delle Forme Costiere nella Penisola Sorrentina. Boll Soc Nat Napoli 77:247–274

Brancaccio L, Pescatore T, Russo F (1988) Periplo del Golfo Di Napoli. 74° Congresso Nazionale S.G.I., Sorrento

Brancaccio L, Cinque A, Romano P, Rosskopf C, Russo F, Santangelo N, Santo A (1991) geomorphology and neotectonic evolution of a sector of the Thyrrhenian flank of the southern appenines (Region of Naples, Italy)- Zeitscrift Fur Geomorfologie, N.F., Suppl. Bd., 82:47–58

Brunn P (1962) Sea level rise as a cause of shore erosion. J Waterw Harb Div Asce 88:117–130

Carta tecnica della Regione Campania (1987) Sportello cartografico, catasto incendi, reti geodetiche

D'argenio B, Violante C, Sacchi M, Budillon F, Pappone G, Casciello E, Cesarano M (2004) Capri, *Bocca Piccola* and Punta Campanella. Marine and land on – land geology compared. In: Pasquare G, Venturini C, Groppelli G (eds) Mapping geology in Italy. Apat Dipartimento Difesa Suolo, Servizio Geologico D'italia, Selca, Firenze

De Pippo T, Pennetta M, Valente A, Terlizzi F (2007) Principali Tipi di Falesia nella Penisola Sorrentina e nell'isola di Capri: Caratteri e Lineamenti Morfoevolutivi. Boll Soc Geol It 126:181–189

Autorità di Bacino del Fiume Sarno (2003) Cartografia Geologica – 1:10.000- Progetto Carg. Carta Geologica D'Italia, 1:50.000

Ferranti L, Antonioli F (2007) Misure del Solco Tirreniano (Mis 5.5) nell'isola di Capri: Valutazione di Attività Tettonica Durante il Pleistocene Superiore. Il Quaternario 20(2):125–136

Marani M, Taviani M, Trincardi F, Argnani A, Borsetti AM, Zitellini N (1988) Pleistocene Progradation and Postglacial Events of the Tyrrhenian Continental Platform between the Tiber River Delta and Capo Circeo. Memorie Società Geologica Italiana 36:67–89

Patacca E, Sartori R, Scandone P (1990) Tyrrhenian Basin and Appenninic Arc: Kinematic Relations Since Late Tortonian Times. Mem Soc Geol It 45:425–451

Pennetta M (2004) Studio dei Fattori di Pericolosità per la Valutazione del Rischio Costiero lungo il Litorale Compreso tra Punta Campanella e Napoli – S. Giovanni A Teduccio. (Emissario Depuratore di Napoli Est). – Attività di Ricerca del Dipartimento di Scienze della Terra- Università di Napoli Federico II- Responsabile Scientifico Prof. Micla Pennetta – Autorità di Bacino Del F. Sarno (Regione Campania)

Pennetta M, Pace L, Baistrocchi F (2003) Protocollo delle Indagini Geologiche e Geognostiche da Eseguire per gli Studi di Compatibilità Idrogeologica e per la Riperimetrazione delle Aree a Rischio di Frana (Piano Stralcio per l'assetto Idrogeologico). Geologia Tecnica & Ambientale, Rassegna Legislativa Regionale, Inserto Redazionale, 4:1–7

Pirazzoli PA (1993) Global sea-level changes and their measurement, vol 8, Global and planetary change. Elsevier Sc. Publ. B. V, Amsterdam, pp 135–148

Romano P (1992) La Distribuzione dei Depositi Marini Pleistocenici lungo le Coste della Campania. Stato Delle Conoscenze e Prospettive di Ricerca. Studi Geologici Camerti vol Spec 265–269

Sunamura T (1992) Geomorphology of Rocky Coasts. Wiley, New York

Large Landslides in Sea-Cliff Areas of the Central Adriatic Coast (Italy)

Domenico Aringoli, Marcello Buccolini, Marco Materazzi, Bernardino Gentili, Gilberto Pambianchi, and Nicola Sciarra

Abstract

The present work deals on an example of large landslide at Marina di Altidona, along the central Italy Adriatic coast, representative of many situations observed along the sea-cliff areas of the Marche and the Abruzzo regions; all these phenomena are located in areas which correspond to the most uplifted sectors during the Quaternary. The data collected, allow to hypothesize a past activation of a huge mass movement along a deep sliding surface, presently submarine. It was related to the high relief connected to the strong tectonic uplift of the middle-upper Pleistocene, to which a probable high seismicity was also associated. The validation of the geomorphological model has been carried out by applying a Finite Difference Numerical Code (FLAC_2D) to a huge gravitational movement and, in particular, by characterizing the dynamic evolution along significant transects.

Keywords

Mass movement • Sea-cliffs • Tectonic uplift • FLAC_2D • Central Italy

General Setting

The Adriatic coast of central Italy is characterised by rather wide gravelly-sandy low beaches. In a backward position, along the watersheds, medially inclined slopes and inactive cliffs alternate. These are modelled in marine sediments whose age range between late Miocene and early Pleistocene made up of marly clays at the base and conglomerates on the top, often placed in a bland monoclinal setting (Bigi et al. 1995).

The active cliffs of Mount Conero, SE of Ancona, and of San Bartolo, SE of Pesaro (Fig. 1), are instead made up, respectively, of limestones and marly limestones and of arenaceous turbidites. Their genesis is connected to the compressive tectonic phase, still active as the frequent earthquakes prove (Dramis et al. 1995). Tectonic alignments with Apennine and anti Apennine direction work as extensive elements placed at different depth and interfere, in certain cases, with the compressive structures below. This is demonstrated by the seismic profiles of the coast carried out for oil exploration, and also by the lower Pleistocene sediments that dip down to the sea with scarps and benches aligned according to the Apennine direction (Riguzzi et al. 1989).

Evolutionary Model of Coastal Landslides Along the Central Adriatic Coast

Different mass movements have been recognised in the active and inactive cliffs of the sector in question (Dramis and Sorriso-Valvo 1994; Aringoli et al. 2010). The studies analysed single phenomena whose still active movement, recent or historical, was certain.

D. Aringoli • M. Materazzi (✉) • G. Pambianchi
University of Camerino (Italy), School of Environmental Sciences, Camerino, Via Gentile III da Varano, Italy
e-mail: marco.materazzi@unicam.it

M. Buccolini • N. Sciarra
Department of Geotechnologies for the Environment and the Territory, University of Chieti (Italy), Chieti, Italy

B. Gentili
University of Camerino (Italy), School of Architecture and Design “Edoardo Vittoria”, Ascoli Piceno, Italy

C. Margottini et al. (eds.), *Landslide Science and Practice*, Vol. 5,
DOI 10.1007/978-3-642-31427-8_16, © Springer-Verlag Berlin Heidelberg 2013

Fig. 1 Geological sketch of the study area. (*1*)– Quaternary continental deposits; (*2*)– sandy-clayey-conglomeratic bedrock (Pliocene-Pleistocene); (*3*)– mainly arenaceous bedrock (Miocene); (*4*)– mainly calcareous bedrock (Trias-middle Eocene); (*5*)– main normal faults; (*6*)– main thrusts; (*7*)– location of main phenomena (in *red* the study case described in this work)

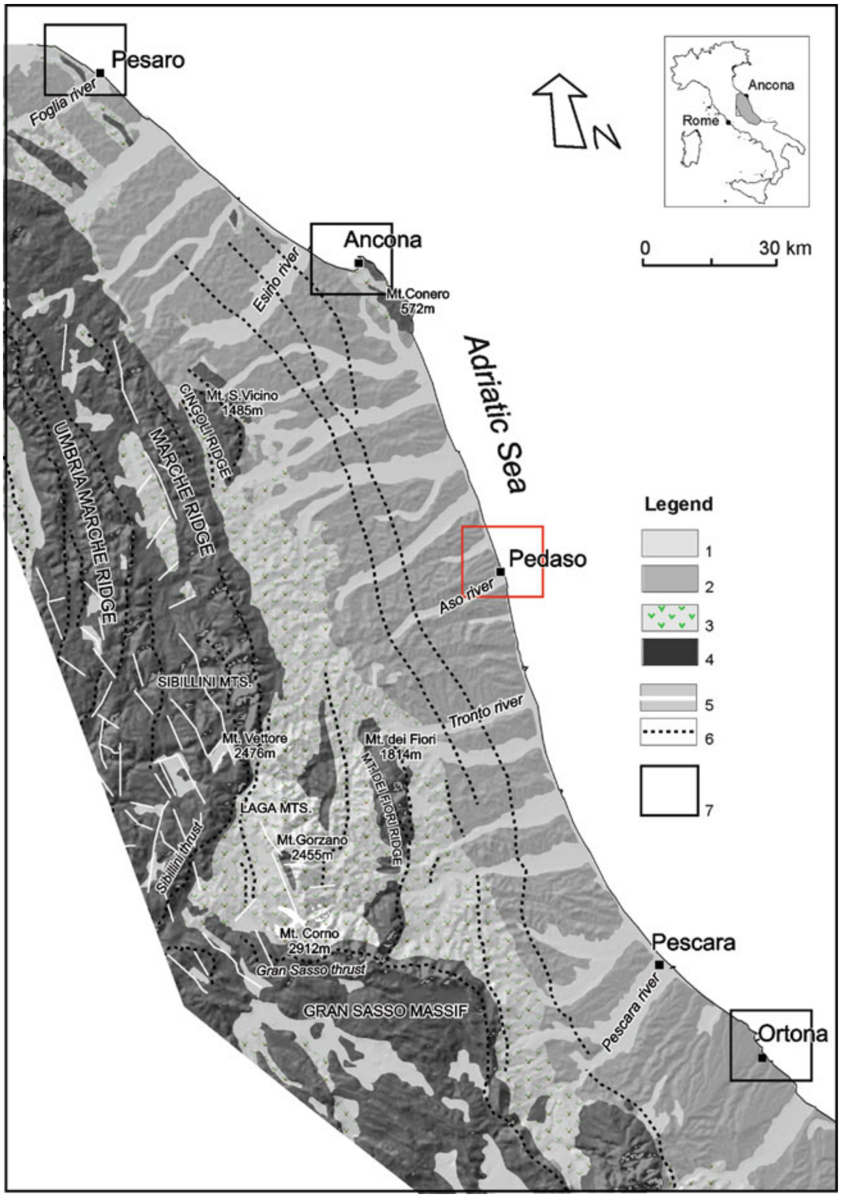

Exclusively referring to the present morphological setting of the emerged and submerged coast they identified the following control factors: extreme climatic conditions, seismic activity, stratigraphic-structural and tectonic setting of bedrock (D'Alessandro et al. 2003). A more recent study allowed us to hypothesise on the basis of geomorphological elements and numerical models, deep mass movements, probably correlated to the Pleistocene-Holocene sea level oscillation (Aringoli et al. 2002).

In depth and systematic geomorphological analyses, extended to the entire coastal sector, evidenced the almost systematic recurrence of valleys roughly parallel to the coast line in correspondence to the major inactive cliffs, whose dimensions can be even a few kilometres in length, 500 m in width and 100 m in depth. Another significant geomorphological element is the presence, east of the first, of suspended valleys on the coast that dissect the erosive summit surface modelled in the Quaternary deposits (Fig. 2). These belong to an ancient and primordial hydrographic network that flowed out roughly perpendicular to the shoreline. They are even a few hundred metres wide and they open and deepen rapidly towards the interior.

The geomorphological elements described seem to be in definite contrast with the normal evolution of the hydrographic network; nevertheless they can be associated to a deep-seated gravitational slope deformation, activated in a context of rapid tectonic uplifting, to which a great increase of the relief, the genesis of faults and fractures and frequent earthquakes are associated.

Concerning faults evolution, the genesis of listric-type ones with Apennine direction is particularly important. This is favoured by the morphostructural setting of the coast and by

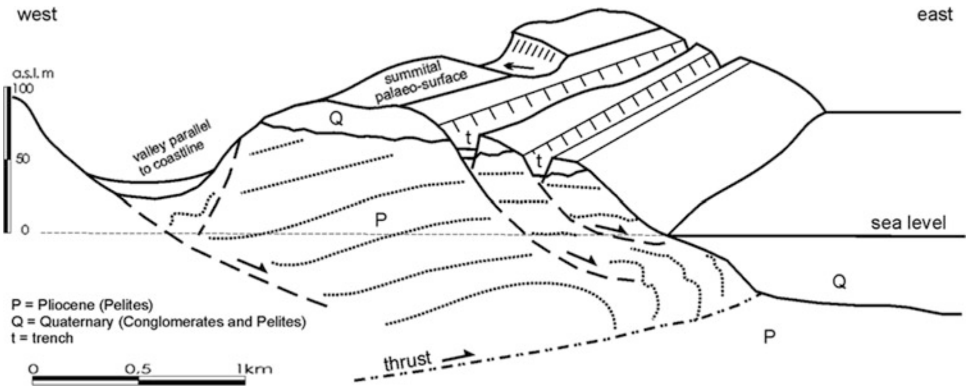

Fig. 2 Block diagram showing the evolutionary model hypothesized

the presence, in depth, of a huge clayey body deformed by the compressive tectonics. These faults have constituted a sure predisposing factor for the following action of gravity.

In this context, however, an important decisive role could has played by the late-Pleistocene sea level oscillations, according to the following mechanism: (1) in agreement with other authors, the sea level rising up to the present height, in a coast with ongoing uplifting, modified the slope geometry previously regularised by the long emersion occurred during the glacial phase of the upper Pleistocene when the sea level was around 100 m lower than present (Pirazzoli 1997; Lambeck et al. 2004); (2) the rising of the sea level also produced a general decay of the mechanical characteristics of bedrock, due to the reduction of the pore pressures; (3) this setting favoured the activation or the reactivation of great mass movements (as well as superficial phenomena whose accumulations have been eroded by the sea), of which only traces in the high sectors of the cliffs remain (Fig. 2); (4) the alignments connected to the gravitational dislocations guided the setting up and the development of the hydrographic network, that has underlined the alignments themselves; as a result, it activated the genesis of the cliff, in agreement with what observed in other areas.

Study Case: The Marina di Altidona Landslide

Geological and Geomorphological Setting

The study area is located in the southeastern sector of the outer Marchean basin (Fig. 1), characterized by a terrigenous sedimentation that closed the Plio-Pleistocene marine cycle, and it is made up of mainly sandy-conglomeratic deposits (Sicilian-Crotonian), overlying the Emilian clayey bedrock.

The overall morphological setting is marked by an inactive trending NNW-SSE cliff, whose modeling was probably driven by normal faults consequently to the above described tectonic uplift. The reliefs are distinguished by sub-planar summits and steep slopes (up to 30° and more), facing to the east, where they run parallel to the coast; moreover, some deviations are evident in the minor hydrographic network (Fig. 3).

Concerning mass movements, phenomena of different typology and extent are present: minor landslides attributable to the deepening of the minor hydrographic network, and more extensive slope deformations revealed by trenches that can be noted in the upper portions of the reliefs (Figs. 3 and 4).

All the elements above have been conditioned by the tectonic fracturing.

Numerical Modeling

The geological-geomorphological model of the Marina di Altidona landslides, have been subsequently analyzed in depth by means of a numerical simulation. The code used (FLAC_2D) is a two-dimensional method of numerical analysis of finite differences for calculations of mechanics of continua FLAC_2D (2000). FLAC code is based on a “lagrangian” calculation scheme which is very adaptable in the modeling of large-scale deformations and collapse of materials.

Using this code in seismic situations two particular behavior patterns of the model in different conditions of sea level were analyzed.

The former simulation, considered the sea level in the same position as present while the latter hypothesize the sea-level much lower, such as during the end of Pleistocene (absence of water table in the model). The geotechnical parameters of each lithological unit, whose data come from laboratory and in situ tests, are summarized in Table 1.

The general analysis carried out, as imposed by the code, consists in an overall re-equilibrium of the system and therefore in the study of failure conditions. The analysis of the process of global re-equilibrium is divided into three phases.

The first phase analyses the filtration within the model in order to identify, once the hydraulic equilibrium has been

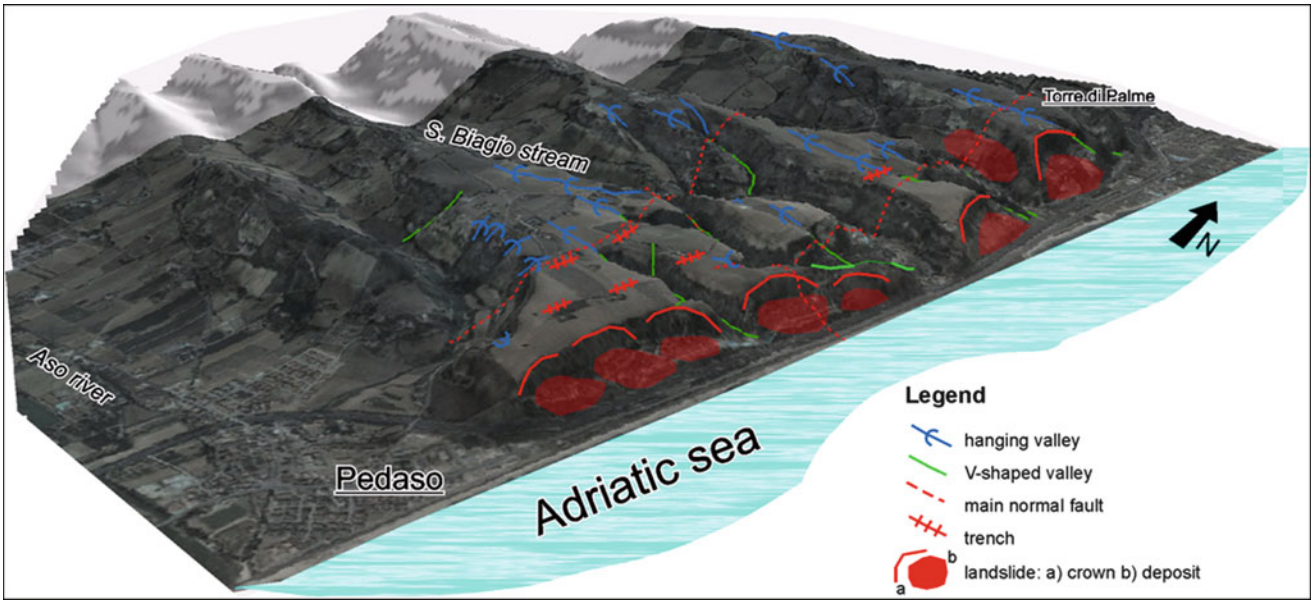

Fig. 3 Schematic geomorphological block diagram of the study area

Fig. 4 Panoramic view (from south) of the cliff; the trenches (in *yellow*) and the trend of minor and suspended valleys (in *cyan*) are evidenced

Table 1 Bedrock parameters used for model implementation

	γ	c′	ϕ	E	
Lithological unit	Unit weight (KNm^{-3})	Cohesion (kPa)	Friction angle	Young modulus	σ'_{max} $c'/tg\phi'$
Sandstone, conglomerates	20.1	20	30	7.5 (GPa)	35 (kPa)
Pelites	19.5	10	23	600 (kPa)	23 (kPa)

reached, the negative pressure distribution irrespective of any mechanical effect.

In the second phase, the model operates a mechanical adjustment using the values of neutral pressure obtained from the first phase and imposing as zero the compressibility module of the water (any variations of the negative pressures is avoided).

In the third phase there is contemporary analysis of the process of filtration and the relative mechanical adjustment. At the end of the process of global equilibrium it is possible to represent the vectors of movement. In this way it is possible to observe the behavior of the system being studied.

Figure 5 shows the results of the simulation and, in particular, the different responses connected to models, also checking the sea level influence and the role of seismicity on global system behavior, can be observed.

The case studied demonstrates how the present sea level standing plays an important role on the deformation condition, particularly with an higher development of shear stress concentrated zones. The presence of a water table confirms a general weakening of the model, theorizing a general translational movement toward right. The mechanism is that typical of a lateral spread. It is also observable the generation of failure planes producing trenches on the topographic surface.

We can conclude that the geomorphologic peculiarities of the surveyed areas, interpreted like a natural geological evolution due to the gravity, are confirmed by the numerical

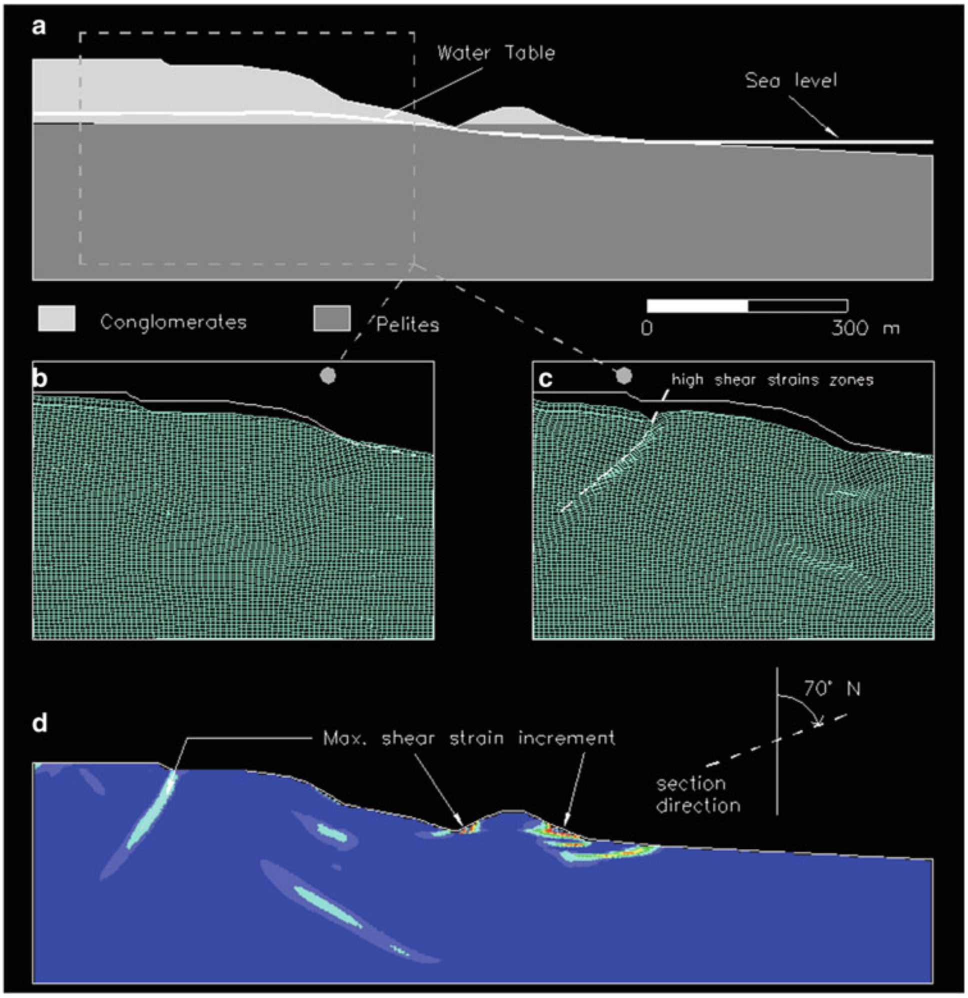

Fig. 5 Modeling of a cross section along the study area (see Fig. 2): (**a**) geological model; (**b**) meshes deformation in dry conditions; (**c**) meshes deformation introducing the water table; (**d**) representation of the shear strain increments

modeling carried out. Therefore the Pleistocene sea level variation, associated to seismic conditions, have had a fundamental role on the real morphological settings of the study area.

Acknowledgments The authors wish to thank the anonymous reviewers for their critical review.

References

Aringoli D, Calista M, Crescenti U, Gentili B, Pambianchi G, Sciarra N (2002) Modelling of two complex gravitational phenomena in Marchean coastal areas (Central Italy). In: McInnes RG, Jakeways J (eds) Instability – planning and management. Thomas Telford, London, pp 195–202

Aringoli D, Gentili B, Materazzi M, Pambianchi G (2010) Mass movements in the adriatic central Italy: activation and evolutive control factors. In: Werner ED et al (ed) "Landslides: causes, types and effects". Nova Science/Nova Science, New York/London, pp 1–71

Bigi S, Cantalamessa G, Centamore E, Didaskalou P, Dramis F, Farabollini P, Gentili B, Invernizzi C, Micarelli A, Nisio S, Pambianchi G, Potetti M (1995) La fascia periadriatica marchigiano-abruzzese dal Pliocene medio ai tempi attuali: evoluzione tettonico-sedimentaria e geomorfologia. Studi Geologici Camerti vol Spec 1995/1:37–49

D'Alessandro L, Berti D, Buccolini M, Miccadei E, Piacentini T, Urbani A (2003) Relationship between the geological-structural framework and landslide types in Abruzzi (central Apennine). In: Atti 1° Congresso Nazionale AIGA, 19–20 febbraio 2003, Chieti, 255–275, Rendina Editori Roma ISBN-88-86698-40-2

Dramis F, Farabollini P, Gentili B, Pambianchi G (1995) Neotectonics and large-scale gravitational phenomena in the Umbria-Marche Apennines, Italy. In: Slaymaker O (ed) Steepland geomorphology. Wiley, Chichester, pp 199–217

Dramis F, Sorriso-Valvo M (1994) Deep-seated gravitational slope deformations, related landslides and large-scale rock avalanches. Eng Geol 38(3–4):231–243

FLAC_2D (2000) Fast Lagrangian Analysis of Continua. Release 4.0. Itasca Consulting Group, Minneapolis

Lambeck K, Antonioli F, Purcell A, Silenzi S (2004) Sea-level change along the Italian coast for the past 10,000 yr. Quat Sci Rev 23: 1567–1598

Pirazzoli PA (1997) Sea –level changes: the last 20 000 years. Wiley, Chichester, 211pp

Riguzzi F, Tertulliani AZ, Gasparini C (1989) Study of seismic sequence of Porto San Giorgio (Marche) – 3 July 1987. Il Nuovo Cimento della Soc It di Fisica 12(4): 452–466

THE SECOND WORLD LANDSLIDE FORUM

Coupling On-Land and Marine Investigations to Assess Coastal Instability in the Napoli and Salerno Bays (Campania, Southern Italy)

Crescenzo Violante

Abstract

The Napoli and Salerno coast is a densely urbanized area mostly composed of a volcanic range, including the Campi Flegrei, Procida and Ischia islands, and the Somma-Vesuvio district where documented human activities have been developing for more than 2,000 years. Along the coast massive transport of rock, regolith, sedimentary cover and soil has occurred episodically, accounting for cliff recession, sudden increase in solid load in short coastal rivers, and flank collapse of volcanic structures. In many cases erosion and transport of material is strictly associated with volcanic activity and exposes coastal communities to hazard with potential damage to property and infrastructure, and loss of life.

In this paper it is stressed that proper comprehension of mass wasting hazard on the coasts has to include investigations of nearby marine areas: the main delivery area for coastal landslide events.

Keywords

Coastal area • Landslide • Marine geology • Sea-land correlations

Introduction

The 55 % of the Campania coastal area is rocky and predisposed to failures over a range of magnitude and period of recurrence (Table 1). In these area episodes of slope instabilities are significantly driven by volcano-tectonic activity and is associated with rapid deposition of pyroclastic fall-out deposits following explosive eruptions (Cinque et al. 2000; Cinque and Robustelli 2009; Violante et al. 2006, 2008, 2009; Zanchetta et al. 2004). Cliff erosion produced by both wave and weathering action occurs in different lithologies including volcanic coastal structures, Mesozoic carbonates and Miocene flysch (Budetta et al. 2008; Di Crescenzo and Santo 2007). Large coastal slope failures have been documented at Ischia volcanic island and Somma-Vesuvius whilst flash floods typically characterize the small watersheds of the Amalfi Coast (Fig. 1; Chiocci and de Alteriis 2006; de Alteriis and Violante 2009; Milia et al. 2003; Esposito et al. 2004a; Sacchi et al. 2009; Violante 2009b; Violante et al. 2009).

Coastal seas preserves reliable sedimentary records of past coastal slope instability, and seafloor investigations can enhance significantly the assessment of the coastal geohazard. Material eroded from rocky coasts is mostly delivered in the marine environment at intermittent time intervals in the form of cliff debris, landslide accumulations, coarse-grained deltas and ultimately as fluvial turbiditic flows (hyperpycnal flows). As a result of high-gradient seafloor topography and often a narrow or nonexistent shelf along rocky coasts, the eroded deposits often go straight to the open sea and less frequently, as a wider shelf develops, can be trapped at shallow depth as sandy lobes. Consequently persistence of the displaced material in the littoral environment as a natural armour for wave action is significantly low. This exposes rocky coasts to an irreversible loss of land over human-scale periods.

C. Violante (✉)
Institute for Coastal Marine Environment (IAMC), National Research Council (CNR), Naples, Calata Porta di Massa, Italy
e-mail: crescenzo.violante@iamc.cnr.it

C. Margottini et al. (eds.), *Landslide Science and Practice*, Vol. 5,
DOI 10.1007/978-3-642-31427-8_17, © Springer-Verlag Berlin Heidelberg 2013

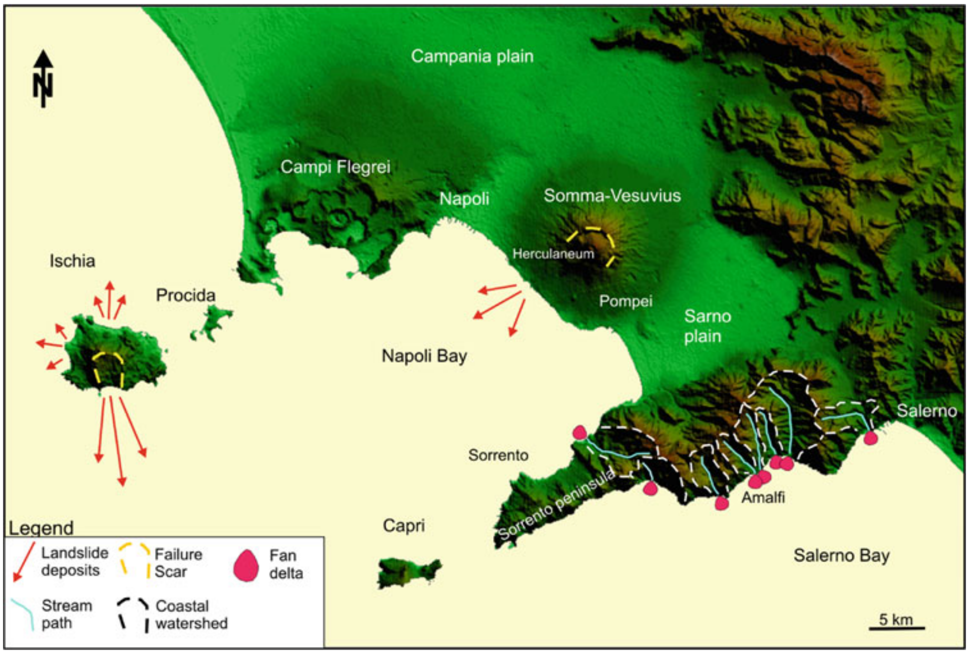

Fig. 1 The study area and location of the discussed landslide phenomena

Table 1 Processes, factors and forms associated with coastal instability in the Napoli and Salerno Bay (Modified from Violante 2009b)

	Cliff recession	Flash flood	Large slope failure
Geological processes	Rock fall	Shallow landslide	Debris avalanche
	Topple	Debris flow	Debris flow
	Rotational slump	Slope-to-stream delivery	Turbidity current
Promoting and triggering factors	Wave action	Localized burst of waters	Volcanic eruption
	Storm surge	Volcanic watershed disturbance	Volcano-tectonic uplift
	Weathering		Tectonic stress
	Unloading of cliff toe	Small/medium, steep/high watersheds	
	Water seepage		
Associated forms and phenomena	Debris toe	Temporary dam	Tsunami
	Shore platform	Flood wave	Hummocky topography
		Fan-delta	Amphitheatre scarp

This paper focuses on the importance of sea-land correlations for studying coastal slope instability. Processes of hazardous sediment transfer and accumulation at rocky coasts are discussed in the frame of large slope failures and flash floods occurred on Ischia island and Somma-Vesuvius, and Costiera Amalfitana respectively. The reported landslide features include large aprons of avalanche deposits and steep sedimentary progradations at mouth of bedrock streams and small rivers detected by marine geophysical investigations.

Overview of the Study Area

The study area (Fig. 1) is an integral part of a large Quaternary extensional basin located between the western flank of southern Italy and the eastern Tyrrhenian margin. It includes the Campania plain, the Napoli and Salerno Bays, the Sorrento peninsula and among the most active volcanoes, namely Somma-Vesuvius, Campi Flegrei, Ischia, and Procida. These latter bound the Napoli Bay to the North and to the East whilst Mesozoic carbonate rocks of the Sorrento mountain range develop on the southern side.

The Neapolitan volcanoes played a major rule on coastal instability with significant hazard-related geomorphic implications. Coastal slopes has been repeatedly mantled during the last millennia by the pyroclastic products from explosive eruptions. Particularly, the AD 79 Plinian event have accumulated loose pyroclastic material over large areas of the Campania region (Sirgudsson et al. 1985), thus creating favourable conditions for volcaniclastic debris to generate mass flows and flash floods in concomitance with rainy periods.

On the Amalfi Coast volcanic watershed disturbance caused conditions of increased geomorphic instability over the last 2,000 years as testified by maritime Roman villas buried by stream-flood deposits. The Amalfi catchments are smalls and very high relative to the base level with main delivery areas into the adjacent marine shelf. They show a distinct seasonality and torrential behaviour (Esposito et al. 2004a, b; Sacchi et al. 2009; Violante et al. 2009). The steep topographic gradients and emplacement of large amount of pyroclastic fall-out material coupled with rainfall events produced recurrent stream-flows, often with catastrophic implications for people living at stream mouths. Indeed, on the Costiera Amalfitana low relief alluvial fan surfaces occurring at mouth of the of bedrock rivers and channels are heavily urbanized putting local communities at high risk during intense rainfall able to trigger flash floods.

The study of historical sources allowed the identification and classification of 106 floods occurring during the last five centuries on the Amalfi coast, confirming the severe impact produced by flash floods throughout the centuries (Porfido et al. 2009; Esposito et al. 2004a). In more recent times, heavy damage was produced by at least four catastrophic events, documented both in the historical and environmental records. Geological and hydrological data point to elevated fluvial bed load transport strictly associated with sediment delivery from slope to streams in conjunction with heavy rainfalls (Schumm 1977; Benda 1990; Anthony and Julian 1999; Esposito et al. 2004b; Violante 2009b; Violante et al. 2009).

On Ischia island volcano-tectonic ground uplift (Orsi et al. 1991; Tibaldi and Vezzoli 1998), coupled with intense hydrothermal weathering and seismic shaking, has strongly favoured recurrent landsliding over the subaerial flanks of Mt. Epomeo, the major relief of the island. These landslides, in the form of debris slides, debris flows or mud flows, and their effects on humans have been frequently reported in historical chronicles from the Middle Ages to the present (see Guadagno and Mele 1995; Mele and Del Prete 1998). Landslide deposits have been discovered in coastal and deep water as well, providing examples of mass-transport deposits related to volcanic flank collapses in prehistoric times (Chiocci et al. 1998; Violante et al. 2004; Chiocci and de Alteriis 2006; de Alteriis and Violante 2009).

These studies have revealed the importance of gravity-driven processes leading to the development of catastrophic landslides along the Ischia coast. Underwater deposits are one or more orders of magnitude greater than the on-land landslides but they are all related to the volcano-tectonic uplift of Mt. Epomeo. As suggested by bio-stratigraphic data (Barra et al. 1992) the central block of the island has risen to at least 800 m above sea level (a.s.l.) in the past c. 30 ka, at an average rate of 20 mm a^{-1}, putting the Epomeo flanks under a significant volcano-tectonic stress. High vertical accretion and the resulting seismic activity produced slope collapse at any scale, from small rock falls and debris flows of some hundred to a few thousand cubic metres to debris avalanches that involve up to 3 km^3 of material.

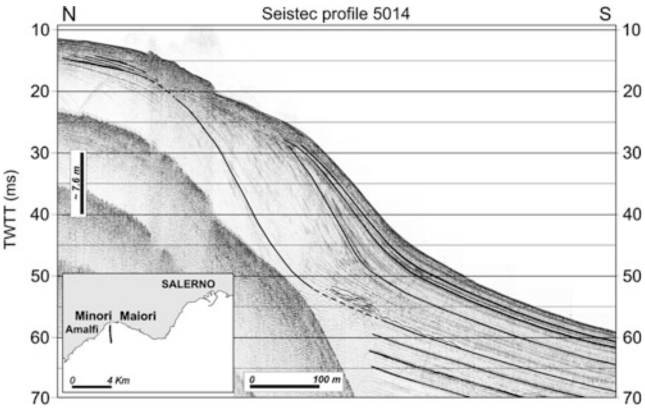

Fig. 2 High-resolution seismic profiles off Amalfi Coast showing prograding clinoforms (*black* lines) at mouth of the stream Regina Minor (inset map in the lower *left* corner)

Flash Floods on the Amalfi Coastal Range

On the Amalfi and Sorrento rocky coasts severe alluvial crisis induced by volcanic watershed disturbance following the AD 79 Somma- Vesuvio fall-out event, deposited a large amount of pyroclastics in the form of fan deltas and coarse clinoforms at the mouth of major coastal streams. Catastrophic stream-flows occurred soon after the Pompei eruption buryed the Roman maritime villas of Positano, Amalfi and Marina di Equa with a significant costal progradation of some hundred meters (Cinque and robustelli 2009; Sacchi et al. 2009; Violante 2009b; Violante et al. 2009).

Fan deltas have been imaged by high resolution seismic investigations (Fig. 2) and swath bathymetry coupled with sedimentologic analysis (Violante et al. 2006; Sacchi et al. 2009). The individual deltaic bodies are about 1 km^2 wide and a few tens of meters thick. They display a generally conical morphology with a delta front slope of approx. 20° and foresets inclination ranging from 15° to 30°. On the whole, the fan-deltas produced a pronounced step in the coastal sea-bed morphology that exerts a ‘damming effect’ and protects the modern sea-cliff from erosion by storm activity.

The pattern of seismic reflectors indicates that the stratigraphic architecture of the deltaic wedge is characterized by an average increase coupled with significant variations of progradation rates in the delta foresets. The seismic record also shows evidences of gravity-driven instability at various stratigraphic levels in the front of the delta system, particularly at the base of the prograding foresets. Gravity flows locally form debris-flow units and/or turbidite lobes with a thickness of a few meters and width of a few tens of meters. Fine-grained turbidites are found above the AD 79 tephra layer, as suggested by the internal seismic facies and the external geometry of the deposits.

The prominent gravity-driven instability and deformation of sediments detected at various stratigraphic levels within the delta slopes suggest that the stratal geometry of the fan deltas was dominantly dictated by the effective transfer of sediments by hyperpicnal (e.g. inertia, turbidity) flows directly fed by river floods. This implies a primary control by stream-flow episodes that have provided conspicuous sediment yields to the coastal area, concomitant with the famous AD 79 Somma-Vesuvius eruption.

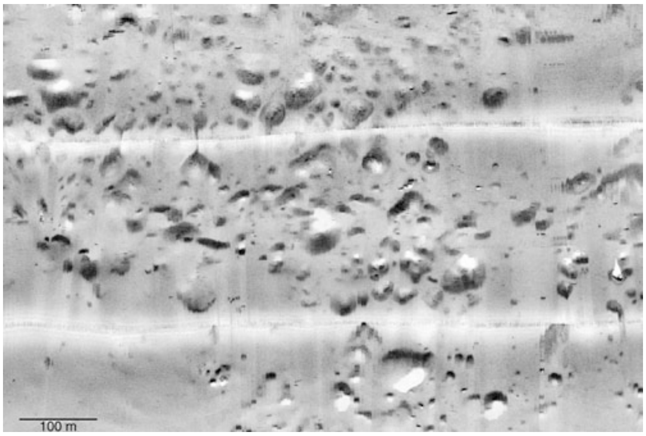

Fig. 3 Seafloor acoustic image off Ischia island characterized by hummocky topography. Blocks with different size are covered by pelitic sediments

Instability and Failure at Ischia Island and Somma-Vesuvius

High resolution geophysical surveys carried out off the Ischia volcanic island and Somma-Vesuvius revealed a complex seafloor topography controlled by hummocky features (Fig. 3) typically indicative of debris avalanche deposits (Chiocci et al. 1998; Milia et al. 2003; Violante et al. 2004; Chiocci and de Alteriis 2006; de Alteriis and Violante 2009). These deposits partly associate with underwater failure areas, but the occurrence of a subaerial amphitheatre scarps clearly suggest a terrestrial initiation of the landslide phenomena.

At Ischia island landslide deposits radiate out from Mt. Epomeo and spread over the southern continental slope, and over the western and northern shelf areas. The southern undersea section of the island consists of a very steep upper slope, which shows a 4 km wide trapezoidal scar. A similar anphitheater scar develops onland along the southern flank of the Epomeo structure. The debris avalanche appears as an elongated field of blocks covering an area of about 150 km^2 reaching a distance of 40–45 km from the source area (Chiocci et al. 1998; Chiocci and de Alteriis 2006; de Alteriis and Violante 2009). It forms elongated lobes from -800 to $-1{,}000$ m with heights of 15–20 m above the surrounding sea floor. A secondary debris tongue, which possibly originated from an eastern scar, travelled downslope towards the SSE, climbing a 70 m submarine high. Post-avalanche seabottom features include incipient creep with concave failure patterns, comet marks and abundant minor slope instabilities, mostly in the form of debris chutes along the upper slope. Estimates of the volume of the landslide deposit range from 1.5 to 3 Km^3.

West of the Ischia island landslide deposits spreads over an area of c. 11 km^2 with hummocky topography extending from about -30 m to the shelf break at -150 m. In contrast to what is observed to the south, here the radial pattern suggests spreading of the avalanche deposits in an overall fan shape. Most of the hummocky facies is represented by circular mounds that range in size from a few metres to some 30 m across and are a few metres to some 20 m above the surrounding sea floor. The avalanche deposit is thicker in its central section, attaining 35 m at about 1.5 km from the coastline, and creates, on the whole, a positive topography in the form of a fan-shaped apron. Estimates of the volume of the landslide deposit based on seismic reflection profiling and swath bathymetric data range from 0.2 to 0.5 Km^3.

In contrast to the western and southern debris avalanches, the northern landslide deposits are characterized by an overall major topographic relief and a particularly uneven morphology. They extend for a total length of 12 km and have a variable width ranging from 5 to 8 km; blocks are found from a few metres to 140 m bsl. The overall shape of the hummocky terrain is that of a tongue slightly verging to the west and downslope to the shelf edge. The most evident morphological feature off northern Ischia is a fan-shaped proximal area lying in a 15–20 m depression and constrained between erosional and depositional levees. High resolution seismic investigations show an average thickness of 50–60 m at around 2 km from the coastline and 3 km from the toe of Mt. Epomeo, in an area where blocks rise some 30–40 from the sea floor. Based on these data the incised fan-shaped valley is likely to be related to the emplacement of a very recent landslide event that has chiefly eroded the basal deposit leaving a channel like scar and an associated depositional levee to the west. Estimates of the volume of the landslide deposit range from 0.2 to 0.6 Km^3.

Hammocky deposits associated with volcanic debris avalanches have been found off the Somma-Vesuvius as well (Milia et al. 2003). These structures develop down to a depth of 100 m over an area of about 30 km^2 and are mostly buried by shelf deposits suggesting an earlier emplacement. Moreover wavy seafloor structures induced by pyroclastic current derived deposits associated with the AD 79 eruption occur off the Herculaneum archaeological site (Milia et al. 2008). Wavy facies correspond to dunes showing smaller size and dimension in the distal area of the subaqueous density flow suggesting a gradual decrease in grain size toward the sea.

Conclusions

Sea-land correlations and marine geophysical investigations clearly indicate the influence of volcanic activity on the stability of Napoli and Salerno coastal geomorphic systems. In these areas episodes of coastal instabilities are mainly driven by volcano-tectonic activity and associate with rapid deposition of pyroclastic fall-out deposits following explosive eruptions.

Instability and failure at Ischia island and Somma-Vesuvius are testified by conspicuous debris avalanches deposits found offshore. These are mega-slides with significant catastrophic implications that involve volume of materials ranging from 0.2 to 3 Km^3. Triggering mechanisms imply volcano-tectonic uplift at Ischia island whilst explosive eruptions and possibly volcanic lateral blasts are likely responsible for Somma-Vesuvius debris avalanches. Landslide deposits partly associate with underwater failure areas, but the occurrence of subaerial amphitheatre scarps clearly suggest a terrestrial initiation of the landslide phenomena.

Recent marine investigations in the Costiera Amalfitana have found evidence of coarse fan deltas at mouth of main streams indicative of recurrent flood events associated with explosive eruptions. In particular early mobilization from steep coastal slopes of the air-fall deposits of the Vesuvius eruption of AD 79 induced a significant alluvial crisis lasting some decades in early Imperial age. In historical times, volcanocalstic streamflows induced a number of catastrophic flash floods causing serious damage and casualties. Such events are associated with sediment supply from side slopes through a variety of mass-wasting phenomena that deliver sediment to streams during heavy rainfalls.

References

Anthony EJ, Julian M (1999) Source-to-sink sediment transfers, environmental engineering and hazard mitigation in the steep Var River catchment, French Riviera, southeastern France. Geomorphology 31:337–354

Barra AD, Cinque A, Italiano A, Scorziello R (1992) Il Pleistocene superiore marino di Ischia: paleoecologia e rapporti con l'evoluzione tettonica recente. Studi Geologici Camerti 1992:231–243

Benda L (1990) The influence of debris flows on channels and valley floors in the Oregon coast range, USA. Earth Surf Processes Landf 15:457–466

Budetta P, Santo A, Vivenzio F (2008) Landslide hazard mapping along the coastline of the Cilento region (Italy) by means of a GIS-based parameter rating approach. Geomorphology 94:340–352

Chiocci FL, de Alteriis G (2006) The Ischia debris avalanche. First, clear submarine evidence in the Mediterranean of a volcanic island pre-historic collapse. Terra Nova 18:202–209

Chiocci FL, Martorelli E, Sposato A, Tivoli Research Group (1998) Prime immagini TOBI dei fondali del Tirreno centromeridionale (settore orientale). Geologica Romana 34:207–222

Cinque A, Robustelli G (2009) Alluvial and coastal hazards caused by long-range effects of Plinian eruptions: the case of the Lattari Mts. After the AD 79 eruption of Vesuvius. In: Violante C (ed) Geohazard in Rocky Coastal Areas. Geological Society, London, Special Publications, 322: 155–171

Cinque A, Robustelli G, Scariglia F, Terribile F (2000) The dramatic cluster of pyroclastic debris flows ccurred on 5–6 May 1998 on the Sarno mountains (Vesuvius regions, southern Italy): a geomorphological perspective. In: Bromhead E, Dixon N, Ibsen MC (eds) Landslides in research, theory and practice, vol I. Thomas Telford, London, pp 273–278

de Alteriis G, Violante C (2009) Catastrophic landslides off Ischia volcanic island (Italy) during pre-history. Special Publication, Geological Society of London 322:73–104

Di Crescenzo G, Santo A (2007) High-resolution mapping of rock fall instability through the integration of photogrammetric, geomorphological and engineering–geological surveys. Quat Int 171–172:118–130

Esposito E, Porfid, S, Violante C (eds) (2004a) Il nubifragio dell'Ottobre 1954 a Vietri sul mare-Costa di Amalfi, Salerno. Scenario ed effetti di una piena fluviale catastrofica in un'area di costa rocciosa. Pubblicazione CNR-GNDCI n. 2870, ISBN_88-88885-03-X, 381 p

Esposito E, Porfido S, Violante C, Biscarini C, Alai F, Esposito G (2004b) Water events and historical flood recurrences in the Vietri sul Mare coastal area (Costiera Amalfitana, southern Italy). In: Rodda JC, Ubertini L (eds) The basis of civilization – water science? Proceedings of the UNESCO/IAHS/IWHA symposium, IAHS Publ., Rome, 286:1–12

Guadagno FM, Mele R (1995) La fragile isola d'Ischia. Geologia Applicata e Idrogeologia 30:177–187

Mele R, Del Prete S (1998) Fenomeni di instabilita'dei versanti in Tufo Verde del Monte Epomeo (Isola d'Ischia, Campania). Bollettino della Societa' Geologica Italiana 117:93–112

Milia A, Torrente MM, Zuppetta A (2003) Offshore debris avalanches at Somma-Vesuvius volcano (Italy): implications for hazard evaluation. J Geol Soc Lon 160:309–317

Milia A, Molisso F, Raspini A, Sacchi M, Torrente M (2008) Syneruptive features and sedimentary processes associated with pyroclastic currents entering the sea: the AD 79 eruption of Vesuvius, Bay of Naples, Italy. J Geol Soc Lon 165:839–848

Orsi G, Gallo G, Zanchi A (1991) Simple shearing block-resurgence in caldera depression. A model from Pantelleria and Ischia. J Volcanol Geotherm Res 47:1–11

Porfido S, Esposito E, Alaia F, Molisso F, Sacchi M (2009) The use of documentary sources for reconstructing flood chronologies on the Amalfi rocky coast (southern Italy). In: Violante C (ed) Geohazard in rocky coastal areas. Geological Society, Special Publications, London 322:173–187

Sacchi M, Molisso F, Violante C, Esposito E, Insinga D, Lubritto C, Porfido S, Tóth T (2009) Insight into flood dominated, mixed sliciclastic-volcanoclastic fan deltas: very high-resolution seismic examples off the Amalfi cliffed coast, Eastern Tyrrhenian Sea. In: Violante C (ed) Geohazard in rocky coastal areas. Geological Society. Special Publications, London 322:32–72

Schumm SA (1977) The fluvial system. Wiley, New York, 245p

Sirgudsson H, Carey S, Cornell W, Pescatore T (1985) The eruption of vesuvius in AD 79. Natl Geogr Res 1(3):332–387

Tibaldi A, Vezzoli L (1998) The space problem of caldera resurgence: an example from Ischia island, Italy. Geol Rundschau, Springer, Berlino 87:53–66

Violante C (ed) (2009a) Geohazard in rocky coastal areas, Special Publication, Geological Society of London, 322. ISBN_978-1-86239-282-3. 208p

Violante C (2009b) Rocky coast: geological constraints for hazard assessment. In: Violante C (eds) Geohazard in ocky coastal areas, Special Publication, Geological Society of London 322:1–31

Violante C, Budillon F, Esposito E, Porfido S, Vittori E (2004) Submerged hummocky topographies and relations with landslides on the northwestern flank of Ischia island, southern Italy. In: Picarelli G (ed) Proceedings of 'Occurrence and mechanisms of flow-like landslides in natural slopes and earthfills', Sorrento, 14–16 May 2003. Associazione Geotecnica Italiana, Bologna, pp 309–315

Violante C, Biscarini C, Esposito E, Molisso F, Porfido S, Sacchi M (2009) The consequences of hydrologic events on steep coastal watersheds: the Costa d'Amalfi, eastern Tyrrhenian sea. In: Liebsher HJ et al (eds) IAHS Publ., Red Book, 327:102–113

Violante C, de Alteriis G, Esposito E (2006) Seafloor base maps, geological features and hazard assessment in marine coastal areas. Example from the Bay of Naples, Campania, Southern Italy. In: Proceedings of the 5th European congress on geoscientific cartography and information systems. Institute of Geology Catalunia, Barcelona 1:534–537

Violante C, de Alteriis G, Sacchi M (2008) Marine geohazards in the Bays of Napoli and Salerno, eastern Tyrrhenian sea. In: Rendiconti della Società Geologica Italiana Sassari, 15–17 settembre, ROMA: Società Geologica Italiana, 3:777–778

Zanchetta G, Sulpizio R, Di Vito MA (2004) The role of volcanic activity and climate in alluvial fan growth at volcanic areas: an example from southern Campania (Italy). Sediment Geol 168:249–280

Identification of Hydro-Meteorological Triggers for Villerville Coastal Landslide

Thom Bogaard, Laxmi Devi Maharjan, Olivier Maquaire, Candide Lissak,
and Jean-Philippe Malet

Abstract

The Villerville–Cricqueboeuf landslide (Normandy, France) is an example of a very well monitored coastal landslide. The long time series goes back to the 1980s initiated after the January 1982 major re-activation of the landslide complex. The combination of translational movement of large blocks of chalk and sandstone and the rotational movement at the cliff's toe results in a very complex hydrological system. Earlier research showed a qualitative connection of displacement or re-activation with meteorological forcing and inland hydrological circumstances.

This study aims to analyse the hydrological processes within the larger landslide area and quantifies the hydro-meteorological triggering thresholds. Long-term continuous single point time series and shorter more spatially distributed information were used for the analysis. A conceptual water balance approach on monthly time scale was used to model the regional groundwater system showing a clear non-linear response at higher groundwater levels. An empirical rainfall threshold for landslide re-activation was proposed using rainfall and inland groundwater level as proxy for antecedent conditions.

Keywords

Hydrology • Threshold • Landslide

Introduction

Coastal landslides combine toe erosion through wave actions with hydrological triggering through local infiltration or regional groundwater flow from a often large hinterland. The densely populated coastal areas, key infrastructure and important economic activity, like tourism in these regions, make coastal landslides a major natural risk. However, not so many long-term multi-technique monitoring programs seem to exist in coastal landslides. Furthermore, the attention seems to be mostly directed to slope deformation and displacement monitoring and less research attention focuses on the local and regional hydrology. This is understandable as undercutting, and thus slope steepening, is often the main cause for the instability in steep coastal landscapes. However, the real on set of movement (the trigger) could well be the hydro-meteorological conditions. Additionally, slow-moving rainfall triggered coastal landslides exist which are

T. Bogaard (✉)
Water resources section, Delft University of Technology,
PO Box 5048, 2600, GA Delft, The Netherlands

UNESCO-IHE Institute for Water Education, Westvest 7, 2601,
DA Delft, Netherlands
e-mail: t.a.bogaard@tudelft.nl

L.D. Maharjan
UNESCO-IHE Institute for Water Education, Westvest 7, 2601,
DA Delft, Netherlands

O. Maquaire • C. Lissak
UMR 6554 CNRS, LEGT- Geophen, University of Caen Basse-Normandie, Caen, France

J.-P. Malet
Institut de Physique du Globe de Strasbourg, CNRS UMR 7516,
Université de Strasbourg, Ecole et Observatoire des Sciences de la
Terre, 5 rue Descartes, F-67084 Strasbourg, France

C. Margottini et al. (eds.), *Landslide Science and Practice*, Vol. 5,
DOI 10.1007/978-3-642-31427-8_18,

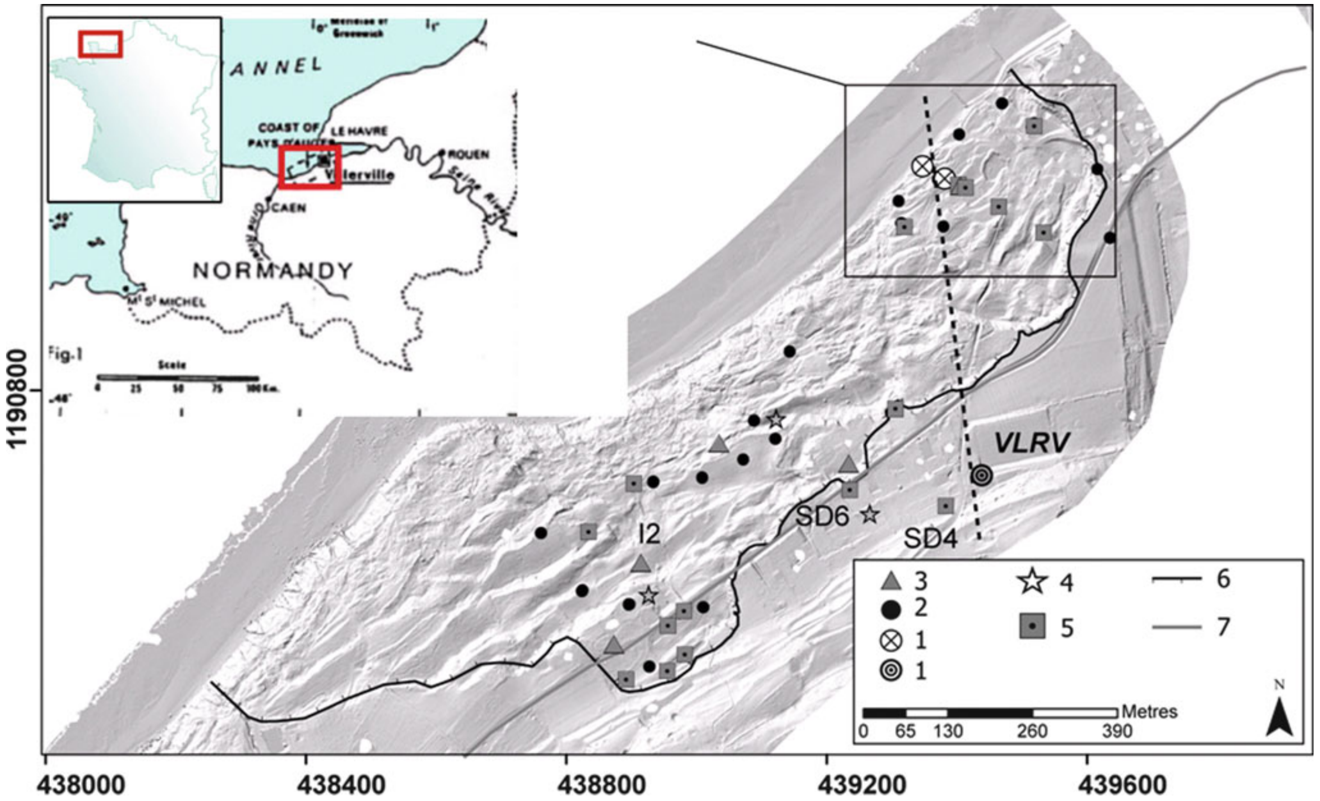

Fig. 1 Monitoring network for the 'Cirque des Graves' landslide: (*1*) GPS receivers, (*2*) Topographic benchmarks, (*3*) Inclinometers, (*4*) Pore water pressure sensor, (*5*) Piezometers, (*6*) Limits of the active zone, (*7*) Main road RD 513

fed by very large regional groundwater systems. Unravelling the hydrological triggering, being it local infiltrated rainwater or that a larger groundwater catchment has to be taken into account can be quite cumbersome.

This study analyses the hydrological processes within the Villerville landslide, the surrounding slopes and the adjacent inland plateau and quantifies the hydro-meteorological triggering thresholds for the onset of displacement.

Research Area and Hydro-Meteorological Monitoring

The Villerville–Cricqueboeuf landslide is located north of Trouville-sur-Mer, at the south bank of the Seine estuary in Normandy, France. The study area Cirque de Graves is located at the high cliffs of the Pays d'Auge plateau. The heterogeneous geology consists of Cenomanian chalk and Albian sandstone on top of a thick layer of easily weathered Kimmeridgian marls (Flageollet and Helluin 1986; Maquaire 1990). The cliff coast is retreating by slow-moving, translational and rotational sliding Cenomanian chalk blocks. This landslide area is an example of a very well monitored coastal landslide. The long time series goes back to the 1980's initiated after the January 1982 major crisis of the landslide complex. Multi-technique permanent monitoring (Lissak et al. 2010) showed slow, permanent movement, spatial differences and clear re-activations. The Villerville landslide monitoring network is constituted of 18 cemented benchmarks to evaluate surface displacements, 3 inclinometers, 10 piezometers and 21 wells to analyze landslide kinematic and groundwater level variations (Fig. 1). Climatic data comes from the Saint-Gatien-des-Bois meteorological station which is 5 km southeast of the landslide and rainfall is also measured at the landslide using a standard tipping bucket.

The depth of the piezometers ranges between 6 and 22 m below surface. All piezometers are measured manually except for four (SD4, SD6, Pz1 and I2, see Fig. 1) which are equipped with automatic pore pressure devices. From 2005 onwards irregular monitoring was performed. Starting 2008 monthly observations and the four continuous logging piezometers are available. Furthermore, daily groundwater level data is available from 1974 onwards for 3 piezometers being part of the regional BRGM groundwater monitoring network. These are located on the plateau around the 10-20 km away from the landslide area. Lastly, since June 2010 four permanent Geobeads (Alert Solution) multi-sensors (installed at −1 till −5.8 m below surface) were installed consisting of vertical tilt sensors, pore pressure devices and

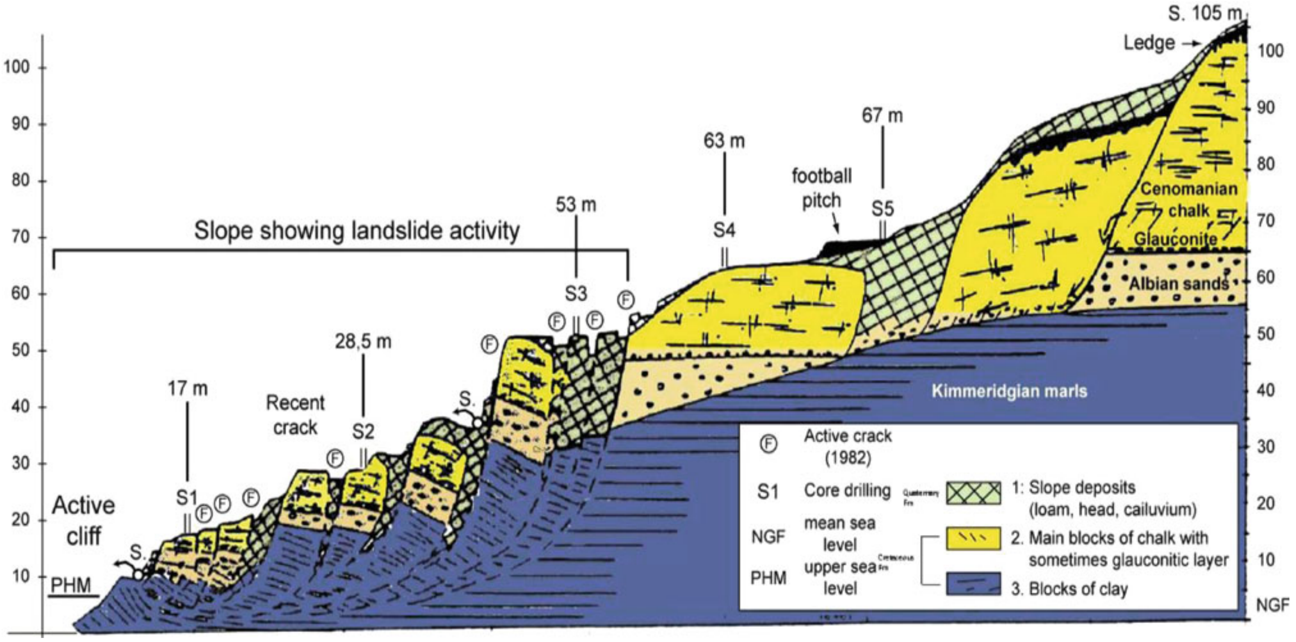

Fig. 2 Geological cross-section of the Cirque des Graves' landslide. Altitude is in meters above sea level

temperature measurements. These are designed as early warning system network (Peters et al. 2010) (Fig. 2).

The landslide combines translational movement of large blocks of chalk underlain by sandstone and marls in the upper part with more rotational movement at the cliff's toe which results in a complex hydrological system. The water quality within the landslide body shows a calcium-carbonate type of water indicating water flows mainly through Cenomanian chalk (Lafenêtre 2010). Lissak et al. (2009) showed a correlation between rainfall, groundwater level in the Pays d'Auge hinterland and the four major reactivations. However, a difference of more than 1.5 m water level height exists in the hinterland groundwater levels at the moment of the four reactivations. This suggests the hydrology of the region and its relation with the reactivations is quite complex and non-linear

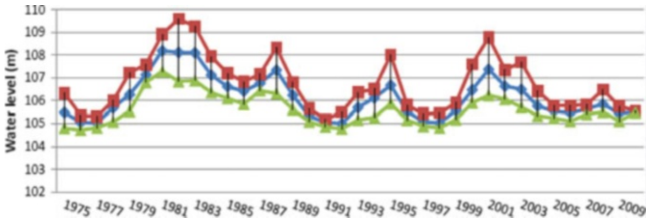

Fig. 3 Annual average (*blue* squares point down), maximum (*red* squares) and minimum (*green* triangles) water levels of the Danestal well. The re-activations of the Villerville landslide took place in Jan 1982, Feb 1988, Jan 1995 and Mar 2001

Hydrological Analyses of the Villerville Landslide

Overall, the groundwater pattern within the landslide area does not change between dry and wet season, is quite close to the surface but clear difference exists throughout the landslide area in annual amplitude of the groundwater levels ranging from several decimetres to 3 m. Seasonal trends of the water level on the landslide were analysed for 4 piezometers having 2 year of continuous data. Using a harmonic analysis the periodicity of the groundwater system can be determined. The analysis shows a clear seasonal trend, high groundwater levels in spring (April/May) and the lowest values around September. Superimposed to the seasonal trend a signal is obvious corresponding to shorter time scale precipitation events. Cross correlation analysis of rainfall versus the groundwater level dynamics shows a 1–2 day time lag. The groundwater levels at plateau are well represented by the Danestal piezometer (Lissak et al. 2009; Maquaire 2000).

Figure 3 shows the annual average groundwater levels together with the maximum and minimum values. There is also a strong relationship between the annual groundwater level amplitude and the average height of the groundwater. Also a groundwater recession analysis showed that there exists a strong relationship between recession constant and average groundwater level. This means that when the average water level is rising also the groundwater dynamics are increasing.

A further hydrological analysis was performed with a tentative hydrological modelling using monthly effective

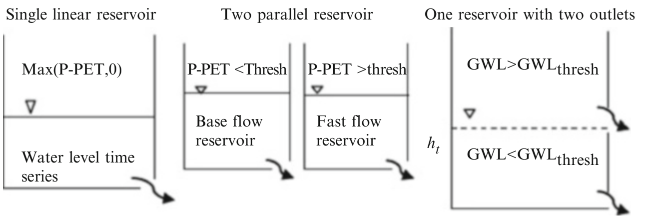

Fig. 4 Three conceptual linear reservoir systems to model the Danestal groundwater dynamics

precipitation (P-PET) and groundwater level (h_t) data. The monthly groundwater level was modelled based on:

$$h_t = h_{t-1}e^{-\frac{dt}{k}} + f \cdot ([\max[(P - PET), 0]) \cdot (1 - e^{-\frac{dt}{k}}) \qquad (1)$$

for which h is the groundwater level, k the depletion constant, P-PET the effective rainfall and f denotes the rainfall multiplication factor in which also the effective porosity is included. Three different conceptual models were used (Fig. 4). The first is a standard linear reservoir, the second consists of two linear reservoirs with a rainfall threshold (a dual porosity system which become active when a rainfall threshold is passed) and the third is a linear reservoir with dual outlet, basically mimicking a groundwater system that accelerates when a groundwater threshold is passed (higher groundwater level taps a faster responding part of the subsurface).

Standard optimisation technique was used based on the RMSE and explained variance (R^2) between observed and modelled groundwater level to obtain the best fit conceptual model.

The simple linear reservoir was not able to mimic the more flashy behaviour at higher groundwater levels. The second conceptual model envisages a system where a precipitation threshold has to be surpassed to activate faster responses within the subsurface. This improved the model results. Using two outlets a regional groundwater system is mimicked that consists of a lower reservoir that behaves relatively modest and a top reservoir that simulates the faster responses. The best fit (lowest RMSE) and best correlation between measured and modelled groundwater levels showed the groundwater threshold for Danestal around 107 m (Fig. 5).

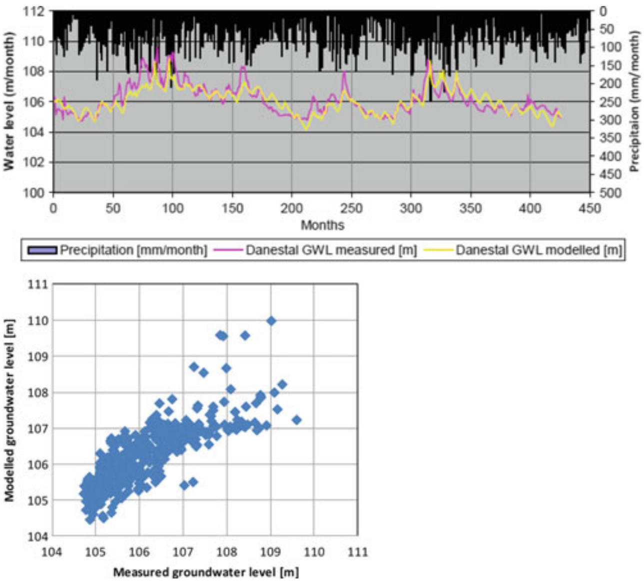

Fig. 5 Model results for the dual outlet model using a threshold of 107 m. (**a**) time series starting 1974 and (**b**) the scatter plot

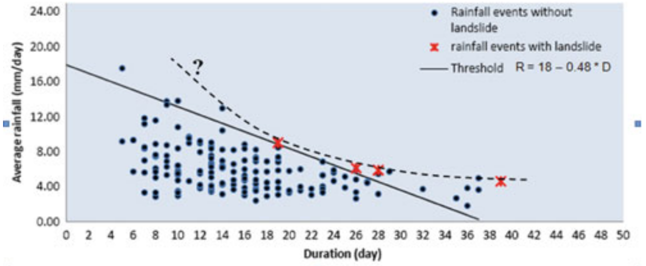

Fig. 6 Empirical rainfall-duration threshold for Villerville landslide area. The empirical threshold equation is given by: R = 18–0.48 * D, with R is the average daily rainfall intensity in [mm/day] and D the duration in [days]. Dashed line is indicates possible curved envelope threshold

Hydro-Meteorological Threshold for Reactivation of the Villerville Landslide Area

Guzzetti et al. (2007) define a threshold for rainfall induced landslide as “the rainfall, soil moisture or hydrological condition that, when reached or exceeded, is likely to trigger landslides”. Following Guzzetti et al. (2007) here (1) the empirical rainfall threshold was determined and (2) the antecedent condition threshold using the Danestal groundwater information. The local empirical threshold was established on the basis of cumulative rainfall, duration or their combination. The daily rainfall data of St Gatien station was checked thoroughly to count the number of days having continuous rainfall. Continuous rainfall is here defined as a series of consecutive rainy days with maximum one dry day in-between. Similarly, the cumulative effective rainfalls of those rainfall events of the landslide area were also analyzed.

As only four landslide re-activations are known, also the rainfall events without landslide activity are plotted. Two thresholds are plotted: a linear threshold and a sketched curved envelope. This gives an indicative rainfall-duration threshold for one landslide area. The limited re-activation events make it impossible to argue in favour of the linear threshold or the curved envelope which are indicated in Fig. 6. More data of especially landslide re-activations are needed for that.

Instead of using only rainfall information we analyzed also the relation between groundwater level as proxy for

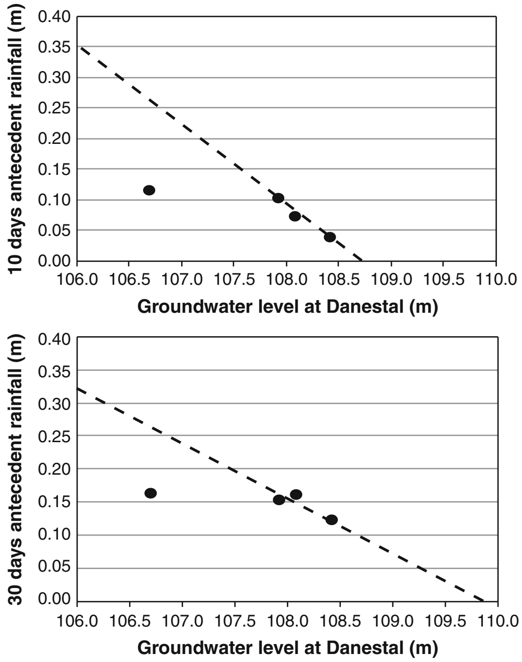

Fig. 7 Empirical 10- and 30-days cumulative rainfall – groundwater level thresholds for the Villerville landslide area

antecedent moisture condition, cumulative rainfall and landslide re-activation. Considered were 3-days, 5-days, 10-days and 30-days cumulative antecedent rainfall. For groundwater we used the Danestal piezometer time series. Figure 7 shows the relationships for 10-days cumulative and 30-days cumulative rainfall versus average monthly groundwater level before the re-activation.

It is clear from Fig. 7 that three reactivations followed basically the same hydro-meteorological threshold whereas the 1995 event with an initial monthly averaged groundwater level below the 107 m cannot be explained by the same threshold.

Conclusions

The hydrological analysis of the Villerville landslide shows that the landslide re-activations are linked to hydro-meteorological circumstances at the landslide and in its hinterland. Long-term continuous time series and shorter more spatially distributed information were used for the analysis. Both the on-site observations and the analysis of the groundwater levels in the plateau region show seasonal and event based responses.

A conceptual water balance approach was used to model the rainfall-groundwater system showing a clear non-linear response The Villerville groundwater system responds relatively modest when the overall groundwater levels are average or low. When the regional groundwater system increases also the dynamics of the hydrological responds accelerates. For the Danestal piezometer the threshold groundwater level is estimated to be around 107 m above sea level.

The empirical hydrological triggering threshold of the Villerville landslide was assessed while only four re-activations were known using rainfall intensity and rainfall duration and using cumulative antecedent rainfall and regional groundwater level as proxy for antecedent moisture conditions. The new Geobeads monitoring system (Peters et al. 2010) is installed to give more detailed registration of slope movement and hydrological conditions. This will lead to improved insight in the hydrological on set of movement on the landslide it self. Then also the relationship between regional and local groundwater system can be assessed.

Acknowledgments This research was funded through the ANR Risk-Nat project '*SISCA: Système intégré de Surveillance de Crises de glissements de terrain argileux*' (2009–2011).

References

Flageollet JC, Helluin E (1986) Morphological investigations in the sliding areas along the coast of Pays d'Auge, near Villerville, Normandy, france. Int Geomorphol 1:447–486

Guzzetti F, Peruccacci S, Rossi M, Stark CP (2007) Rainfall thresholds for the initiation of landslides in central and southern Europe. Meteorolog Atmos Phys 98:239–267

Lafenêtre S (2010) Etude hydrogéologique d'un versant instable : Cas des glissements de terrain de Villerville-Cricqueboeuf (Calvados, Basse-Normandie). Unpublished MSc thesis, Université d'Avignon

Lissak C, Maquaire O, Malet J-P (2009) Role of hydrological process in landslide occurrence: Villerville-Cricqueboeuf landslides (Normandy coast, France). In: Proceedings of the international conference on landslide processes: from geomorphologic mapping to dynamic modelling, Strasbourg, CERG Editions, pp 175–180, Feb 2009

Lissak C, Maquaire O, Malet J-P, Déprez A, Masson F, Ulrich P, Peters ET (2010) Multi-technique permanent monitoring of a slow-moving coastal landslide in Normandy. In: Proceedings of the international conference: mountain risks: bringing science to society, Florence 2010. pp 267–274, Nov 2010

Maquaire O (1990) Les mouvements de terrain de la côte du calvados, recherche et prévention. Document BRGM no.197, Eds BRGM: 431

Maquaire O (2000) Effects of groundwater on the Villerville-Cricqueboeuf landslide. Sixteen years of survey (Calvados, France). In: Proceedings of the 8th international symposium of landslides, landslides in research, theory and practice, Cardiff, pp 1005–1010

Peters ET, Malet J-P, Bogaard TA (2010) Multi-sensor monitoring network for real-time landslide forecasts in early warning systems. In: Proceeding conference on mountain risks: bringing science to society, Florence, pp 335–340, Nov 2010

THE SECOND
WORLD
LANDSLIDE FORUM

Statistically Based Sea Cliff Instability Susceptibility Assessment at Regional Scale, at the Burgau-Lagos Coastal Section (Algarve, Portugal)

Fernando Marques, Rita Matildes, and Paula Redweik

Abstract

Mass movements of different types and sizes are the dominant process of sea cliff evolution, being a considerable source of natural hazard. To assess the spatial component of sea cliff hazard assessment with implications on planning, i.e. the susceptibility of a given cliff section to be affected by instabilities causing retreat of the cliff top, a statistically based study was carried out along the top of the sea cliffs of Burgau-Lagos coast (Southwest Algarve, Portugal), using the bivariate information value and the multi-variate logistic regression methods applied to a set of predisposing factors related with geology and geomorphology, which were correlated with a photogrammetry based inventory of past cliff failures. The two susceptibility models provided promising results, validated against the inventory data using ROC curves, which indicate that these methods are adequate to assess cliff instability susceptibility at regional scale.

Keywords

Sea cliffs • Susceptibility • Information value • Logistic regression

Introduction

Slope mass movements, including rock falls and different types of landslides, are the dominant process of sea cliff retreat (Trenhaile 1987; Sunamura 1992), and an important source of natural hazard and a constraint for human activities in coastal areas (Moore and Griggs 2002). There is an increasing social and economic importance of this problem in the context of the general growth of occupation of cliffed coastal areas, where the economic value of land tends to be very high, as a result of increasing demand for exceptional location building areas for houses and beach and leisure resorts.

High retreat rate sea cliffs processes and evolution studies are the most commonly covered in the literature, with low retreat rate cliffs receiving much less attention, partly due to the difficulties in monitoring an episodic, comparatively low frequency event based process, located in highly irregular and frequently inaccessible locations. In fact, most sea cliffs correspond to steep slope surfaces, poorly represented in aerial photographs and maps, making its accurate monitoring an arduous and difficult task.

Some attempts have been performed to provide conceptual frameworks for evolution predictions, but restricted to fast retreating cliffs (Lee et al. 2001, 2002; Hall et al. 2002; Milheiro-Oliveira 2007). For low retreat rate cliffs hazard assessment, the published work is very scarce and may be grouped in expert based classification of indicators of near future instability (e.g. De Pippo et al. 2008), or attempts to

---

F. Marques (✉) • R. Matildes
Faculty of Sciences, Department of Geology, Centre of Geology, University of Lisbon, Ed. C2, 3rd, Campo Grande, 1749-016 Lisbon, Portugal
e-mail: fsmarques@fc.ul.pt

P. Redweik
Faculty of Sciences, Department of Geology, Centre of Geology, University of Lisbon, Ed. C2, 3rd, Campo Grande, 1749-016 Lisbon, Portugal

Faculty of Sciences, Department of Geographic Engineering, Geophysics and Energy and Centre of Geology, University of Lisbon, Lisbon, Portugal

C. Margottini et al. (eds.), *Landslide Science and Practice*, Vol. 5,
DOI 10.1007/978-3-642-31427-8_19, © Springer-Verlag Berlin Heidelberg 2013

characterize the role of sets of conditioning factors weighted according local experience (Del Río and Gracia 2008; Nunes et al. 2009). However in these attempts there is no objective assessment of the weight assigned to the conditioning factors and the results were not object of validation using standard methods.

In non coastal area landslides, a complete hazard assessment includes the space, time (Varnes 1984) and magnitude components (Guzzetti et al. 2005), with the susceptibility being the less difficult and the one which is more frequently assessed. By analogy with the landslides studies, the susceptibility of occurrence of cliff failures corresponds to the propensity of a given area to be affected by these phenomena, based solely on terrain conditions (Soeters and Van Westen 1996), without any implication of the time component, i.e. time frequency or recurrence periods. The terrain conditions correspond to a set of predisposing factors which statistically correlate with the occurrence of landslides, with the correlations being assessed using various bi-variate or multivariate techniques (Guzzetti et al. 2005).

To assess the spatial component of sea cliff hazard, i.e. the susceptibility of a given sector of cliffs being affected by failures causing cliff top retreat, a statistically based study was applied to the cliffed coastline section Burgau-Lagos, located in southern Algarve, Portugal, using an aerial photogrammetry based inventory of cliff retreat events covering a 60 year period (1947–2007), and a set of predisposing factors. The results obtained are validated using standard statistical methods, and also analyzed and discussed.

Setting

The 13 km long Burgau-Lagos coastal section is located in SW Algarve (Portugal) and is composed of a 10.5 km WSW-ENE, W-E and WNW-ESE trending section exposed to SW and SE main directions of storms, and a 2.5 km N-S section which is more sheltered and only affected by SE storm waves.

The cliffs in the studied coastal section have a widely variable morphology, expressed in cliff height, cross profile and plan contour variations, and also lithological composition. The geology and geomorphology of the cliffs is described in detail in Marques (1997), together with a systematic inventory of cliff failures for the period 1947–1991, compiled using aerial photo based simplified methods (Marques 2006). This inventory was validated and completed by a digital photogrammetry based study covering the period 1947–2007 (Redweik et al. 2008, 2009).

From west to east, the cliffs sections are composed by (Rocha et al. 1983): (a) Barremian marls, alternating marls and marly limestones; (b) Aptian sandstones, marls, a late Mesozoic basaltic pipe and marly limestones alternating with marls; (c) Miocene weak calcarenites with karst features filled with Plio-Pleistocene silty sands. The cliff height varies between 20 m and more than 100 m, and corresponds mainly to irregular cross profile slopes, with a general dip of 60–80° in the Cretaceous rocks, and near vertical with frequent overhanging sections in the Miocene rocks.

Methods

To assess the possibility of occurrence of future failures affecting areas located along the top of the sea cliffs of Burgau-Lagos coast (Southwest Algarve, Portugal), a cliff instability hazard assessment was performed, based on the application of the bi-variate Information Value Method (Yin and Yan 1988), and the multi-variate logistic regression method, to a set of predisposing factors, mainly related with geology and geomorphology, which were correlated with a systematic photogrammetry based inventory of past cliff failures (1947–2007).

The predisposing factors were selected to provide a complete description of geological and geomorphological constrains which are usually considered as relevant in conditioning the occurrence of sea cliff failures and, simultaneously, could be obtained with an acceptable level of work at a regional scale. The factors selected included geological and geomorphological aspects (major lithological units; geological structure, i.e., bedding dip in relation with the cliff faces; presence of faults; presence and type of cliff toe protection) and morphometric aspects derived from a 2 m grid DTM (cliff height; mean cliff slope angle; maximum cliff slope angle; aspect, plan curvature; profile curvature).

The results of the application of the statistical methods were validated using standard Receiver Operator Curves.

Susceptibility Assessment

The susceptibility assessment was performed using a simple statistical method of Bayesian inspiration, the bi-variate Information Value Method (Yin and Yan 1988), which has been applied successfully for landslide susceptibility assessment (Yin and Yan 1988; Wu et al. 2000; Zêzere 2002).

The use of this method requires that each factor is divided in classes, with each one corresponding to a variable. The information value Ii of each variable Xi is (Yin and Yan 1988):

$$I_i = log \frac{S_i/N_i}{S/N} \quad (1)$$

Where S_i is the number of terrain units with cliff failures of a given type in the units with the variable X_i, N_i is the number of terrain units with the variable X_i, S is the total number of terrain units with cliff failures of the same type, and N is the total number of terrain units in the study area. The I_i positive values indicate that the variable is positively correlated with the possibility of occurrence of cliff failures, the negative ones indicate that the variable (or property) is associated with low susceptibility. The near zero values indicate that the variable is not significant in terms of susceptibility ranking.

The total information value I_j for a given terrain unit j is:

$$I_j = \sum\nolimits_{i=1}^{m} X_{ji} I_i \tag{2}$$

where m is the number of variables, X_{ji} is 0 if the variable is not present in the terrain unit j, or 1 if the variable is present.

This method enables an objective assessment of the susceptibility, based only on the spatial distribution of the predisposing factors classes (variables) and on the presence or absence of cliff failures in each terrain unit. The main limitation of this method results from its bi-variate character, i.e., it does not take into account correlations that may exist between variables.

The susceptibility assessment was also performed using the multi-variate logistic regression method that has also been successfully used for landslide hazard assessment (Guzzetti el al. 2005).

This method consists of the regression of a dichotomic dependent variable (ex. 0 without instabilities, 1 with instabilities) with a set of explanatory independent variables which may be continuous, categorical or dichotomic. The relation between instability occurrence in a given terrain unit and the set of explanatory variables is:

$$S = \frac{1}{(1 + e^{-\Psi})} \quad 0 \le S \le 1 \tag{3}$$

where S (from 0 to 1) is the probability of a given terrain being in the group of the units affected by instabilities. Ψ is the logit, which is linearly related with the independent variables

$$\begin{aligned}\Psi &= log\left(\frac{p}{1-p}\right)\\ &= \beta_0 + \beta_1 v_1(r) + \beta_2 v_2(r) + \ldots + \beta_m v_m(r) + \varepsilon\end{aligned} \tag{4}$$

where b_0, b_1, …, b_m are the unknown parameters of the Logistic Regression, n_0, n_1, … n_m are the independent variables in each terrain unit and ε is the error associated to model fitting.

Inventory of Cliff Failures

A substantially complete inventory of past cliff failures was produced by multi-temporal aerial photo based studies, using digital photogrammetric methods (Redweik et al. 2008, 2009) which involved several aerotriangulation steps, generation of pseudo-camera data for the older aerial photos without camera calibration information, stereo plotting of the cliff top, ridges and toe, and automatic generation of digital terrain models (Redweik et al. 2009). The results were validated by systematic stereo photo interpretation, helped by oblique aerial photos and field surveys.

This study enabled the detection and characterization of 137 cliff failures occurred between 1947 and 2007 along the 13 km long cliffs, causing the loss of 10,234 m^2 of horizontal area at the cliffs top. The cliff failures correspond to steeply sloping failure plane planar slides (58%) mainly in Cretaceous alternating limestone and marls, toppling failures (17%) mainly in Miocene calcarenites, slumps (15%) in Plio-pleistocene silty sands, and the remaining 10% correspond to complex movements, rockfalls and not determined cases.

The space distribution of cliff failures is quite irregular but enables the objective separation of sub sections with homogeneous retreat behaviour, with computed mean retreat rates varying from 5×10^{-3} m/year in strong sandstones to 5×10^{-2} m/year in Miocene calcarenites with frequent karst sinkholes filled with Plio-pleistocene silty sands (Redweik et al. 2009). The maximum cliff top local retreat was 33 m, with more frequent values in the range of 2–6 m.

Susceptibility Predisposing Factors

The factors considered were those which could be related with the cliff failure occurrence and which could be obtained with acceptable level of work and detail at regional scale of analysis. The geological and geomorphological factors considered were: (a) major lithological units; (b) geological structure (bedding dip relations with the cliff faces); (c) Presence of faults; (d) Presence and type of cliff toe protection (plunging cliffs, cliff toe protection by fallen debris, sandy or boulder beaches, wave cut platforms). The characterization and mapping of these factors was based on field surveys in accessible sections of the cliffs, completed by oblique and vertical aerial photo interpretation.

The factors related with the cliffs morphometry include: (e) cliff height; (f) mean cliff slope angle; (g) maximum cliff slope angle; (h) aspect (direction of cliff face exposure) (i) mean plan curvature of the cliff faces; (j) mean cross profile curvature of the cliff faces.

These morphometry related factors were derived from a 2 m grid DTM obtained from a 1:2.000 aerophotogrammetric survey by the water national authority (INAG), with source data (aerial photographs) obtained between 2001 and 2003. The maps in vector format were object of systematic checking and correction of errors in order to enable the production of an accurate DTM. The cliff top line and toe were obtained by stereoplotting using PCI Geomatica software and hardware for 3D visualization of large scale (1:8.000) aerial photographs.

One fundamental aspect not included in this study is any form of mapping of wave action along the coastline, which is due to the unavailability of a reliable database on wave regime for the study area. However, when such database is available, the results of this study can be easily updated and improved.

One important aspect for this type of studies is the definition of the terrain units to consider for application of the statistical methods. In fact, a pixel based approach is affected by several drawbacks: some predisposing factors mapping (e.g. toe protection) cannot be extended to all unit cells that cover a given cliff face; the cliff stability is dependent of the predisposing factors present along the entire cliff face and not in an pixel per pixel basis; grid cells located landwards of the cliff top but with limits very close to it would produce low susceptibility values due to very small values of slopes and other morphometric derived factors, but this result will be misleading because its susceptibility is mainly dependent on the adjacent cliff top cells values. Considering these problems a terrain unit approach was selected.

The mapping and analysis of the factors was made in ArcGIS 9.3, using terrain units defined along 25 m long sections of the cliff top line, smoothed with a 25 m radius of tolerance. At the ends of each segment, the lateral limits of terrain units were drawn in directions approximately perpendicular to the cliff contour lines. The lower limit of the terrain units corresponds to the stereoplotted cliff toe line.

To get a complete sampling of the morphometric properties of each terrain unit, 1 m buffers were created along the cliff top an toe lines, and the areas limited by the buffers were added to the cliff terrain units. The study cliffs were divided in 547 terrain units containing 25 m long sections of cliff top line.

Data Processing and Results

The shape of most cliff failures in the study area corresponds to the detachment of relatively thin and high slabs of rocks or soils, separated by steeply dipping failure surfaces of planar, slump or toppling failures, the analysis of the inventory data was made including all events recorded, and thus the dependent variable is composed of terrain units with cliff failures (187) in a total number of 547 terrain units. The data processing for the production of the mapping and distribution of variables in all terrain units was performed in ArcGIS 9.3.

The factors were classified according with the distribution of inherent categories, as in lithology, or in classes with near homogeneous data distribution in each class. The number of classes considered for all factors was large (62), distributed as follows: lithology (11); structure (5); mean slope (6); height (7); aspect (8); toe protection (5); maximum slope (6); plan curvature (6); faults (2); profile curvature (6). The maximum Ii value was recorded in lithology, variable “marly limestones, marls, calcarenites”, with 0.466, and the lowest, of −0.358 for structure, with beds dip against the cliff face. These classes were used for the application of the information value and logistic regression methods.

The logistic regression computation was made using SPSS v17.

Results, Validation and Discussion

The results obtained with the two statistical methods are comparable, and for each variable were divided in classes with a homogeneous distribution of terrain units number in each class. The information value results were presented in Marques et al. (2011), and the logistic regression model results are compared with the inventory data in Fig. 1. Analysis of the results suggests that lithology, geological structure, mean slope angle, cliff height, aspect, toe protection and maximum slope angle were the more important susceptibility predisposing factors.

The results of the models were validated using success rate curves (Fig. 2), which corresponds to a plot of the areas in decreasing order of susceptibility ranking against the percentage of terrain units with failures captured by a given model in the total number of terrain units. The global results are analyzed better using the computed area under the curve (AUC) that, using all the variables of the information value model, provided a value of 0.64, and the logistic regression with all variables provided a value of 0.66, which are low in absolute terms (Table 1). However, as there is a large proportion of terrain units with movements (34%) an “ideal” model, one that could predict only terrain units with cliff failures in the higher susceptibility values, would only provide a AUC value of 0.83, making the results of the model much more meaningful. It should also be noted that the models do not incorporate any factor representing wave action along the studied coastline, which may be able to enhance the models results.

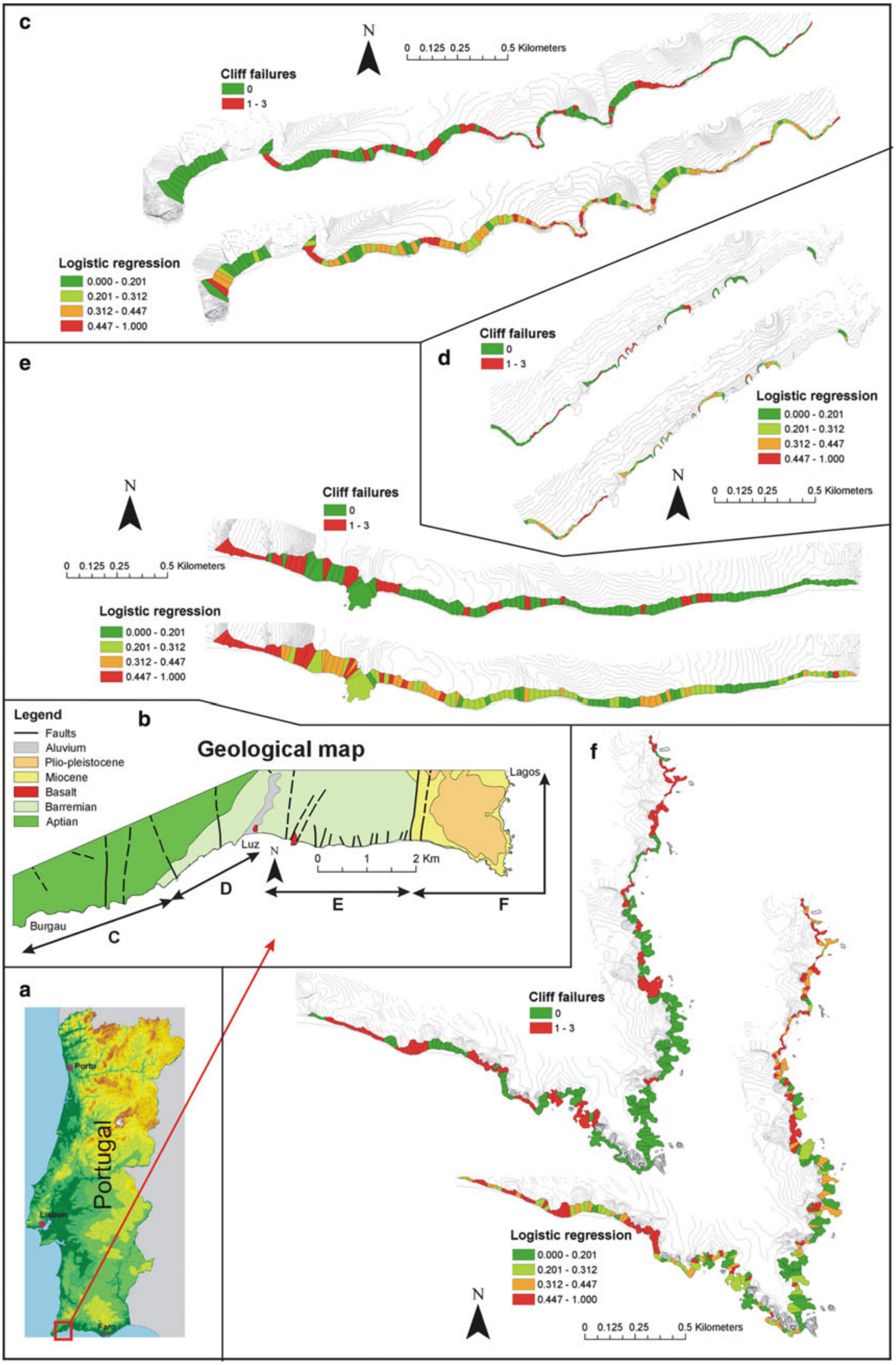

Fig. 1 **a** – Localization of study area. **b** – Geological map with indication of extent of cliff sections *c, d, e* and *f*. **c**, **d**, **e** and **f** – Comparison of cliff failures inventory with the logistic regression susceptibility model results

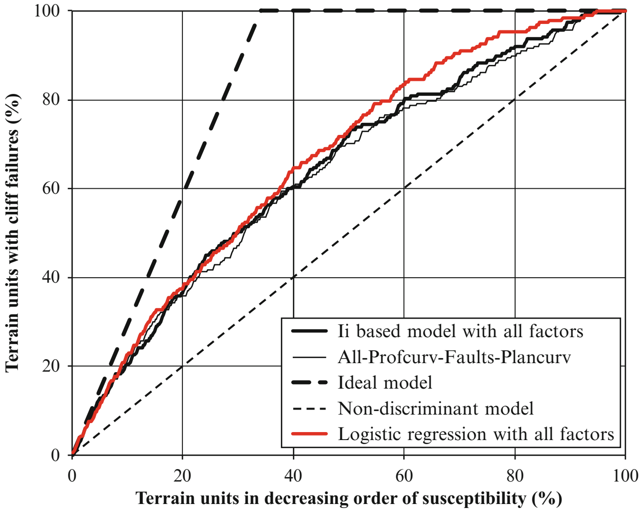

Fig. 2 Success rate curves for the susceptibility models with all factors, and information value with all factors minus curvatures (plan and profile, and faults), the maximum curve for an "ideal model", and the diagonal line for a non-discriminant (random) model

Table 1 Area under the curve (AUC) for different susceptibility model success rate

Susceptibility model	AUC
Maximum ROC curve for this situation	0.829
Logistic regression with all factors	0.666
Ii based model with all factors	0.644
All -Profcurv	0.641
All -Profcurv-Faults	0.640
All -Profcurv-Faults-Plancurv	0.635
All -Profcurv-Faults-Plancurv-slopemax	0.626
All -Profcurv-Faults-Plancurv-slopemax-toe	0.615
All -Profcurv-Faults-Plancurv-slopemax-toe-aspect	0.606
All-Profcurv-Fault-Plancurv-slopemax-toe-asp-height	0.604

Conclusions

The statistical information value and the logistic regression methods provide an objective way of assessing a susceptibility of cliff failure ranking using a set of predisposing factors, which are compatible with a regional scale of analysis.

The standard success rate curve is also an objective way of validating the results of susceptibility models, but the significance of the area under de curve (AUC) must take into account the proportion of terrain units with failures in relation with the total terrain units of the study area.

The results obtained with these statistically based methods, validated with the inventory of cliff failures occurred in a 60 years period were promising, indicating that the study methods presented in this paper may be very useful for complete cliff instability hazard assessment, in combination with appropriate models for magnitude and time components.

This study also suggests that further research is needed in various aspects, mainly on: (1) improvement of methods for the definition of terrain units; (2) to improve the resolution of each of the predisposing factors of cliff instability used in this study and also the inclusion of others that may prove useful to increase susceptibility model reliability; (3) to obtain reliable wave action data at the toe of the cliffs, with methods compatible with a regional scale of analysis.

Acknowledgments Are due to ARH do Algarve for financial support of this research and to IGP for the supply of part of the aerial photographs used under the program FIGIEE.

References

De Pippo T, Donadio C, Pennetta M, Petrosino C, Terlizzi F, Valente A (2008) Coastal hazard assessment and mapping in Northern Campania, Italy. Geomorphology 97:451–466

Del Río L, Gracia FJ (2008) Erosion risk assessment of active coastal cliffs in temperate environments. Geomorphology 112:82–95

Guzzetti F, Reichenbach P, Cardinali M, Galli M, Ardizzone F (2005) Probabilistic landslide hazard assessment at the basin scale. Geomorphology 72:272–299

Hall JW, Meadowcroft IC, Lee EM, van Gelder PHAJM (2002) Stochastic simulation of episodic soft coastal cliff recession. Coast Eng 46:159–174

Lee EM, Hall JW, Meadowcroft IC (2001) Coastal cliff recession: the use of probabilistic prediction methods. Geomorphology 40:253–269

Lee EM, Meadowcroft IC, Hall JW, Walkden M (2002) Coastal landslide activity: a probabilistic simulation model. B Eng Geol Environ 61:347–355

Marques FMSF (1997) The sea cliffs of the coast of Algarve. Dynamics, processes and mechanisms. University of Lisbon, Ph.D. thesis, 556p (in portuguese)

Marques FMSF (2006) A simple method for the measurement of cliff retreat from aerial photographs. Zeitschrift für Geomorphologie—Supplementbände 144:39–59

Marques FMSF, Matildes R, Redweik P (2011) Statistically based sea cliff instability hazard assessment of Burgau-Lagos coastal section (Algarve, Portugal). J Coastal Res SI 64:927–931

Milheiro-Oliveira P (2007) Bayesian statistical methods for modeling and prediction of major landslides in coastal areas. Coastal Eng J 49 (1):45–61

Moore LJ, Griggs GB (2002) Long-term cliff retreat and erosion hotspots along the central shores of the monterey bay national marine sanctuary. Mar Geol 181:265–283

Nunes M, Ferreira Ó, Schaefer M, Clifton J, Baily B, Moura D, Loureiro C (2009) Hazard assessment in rock cliffs at Central Algarve (Portugal): a tool for coastal management. Ocean Coast Manage 52(10):506–515

Redweik P, Marques F, Matildes R (2008) A strategy for detection and measurement of the cliff retreat in the coast of Algarve (Portugal) by photogrammetry. EARSeL eProceedings 7(2):92–104

Redweik P, Matildes R, Marques FMSF, Santos L (2009) Photogrammetric methods for monitoring cliffs with low retreat rate. J Coast Res SI 56:1577–1581

Rocha RB, Ramalho MM, Antunes MT, Coelho AVP (1983) Carta Geológica de Portugal na escala 1: 50 000 e Notícia Explicativa da Folha 52-A, Portimão. Serviços Geológicos de Portugal, Lisboa

Soeters R, Van Westen CJ (1996) Slope instability recognition, analysis and zonation. In: Turner AK, Schuster RL (eds) Landslides. Investigation and mitigation, transportation research board, Special report 247, National Academy Press, Washington, DC, pp 129–177

Sunamura T (1992) Geomorphology of rocky coasts. Wiley, New York, 302pp

Trenhaile AS (1987) Geomorphology of rock coasts. Clarendon, Oxford, 384pp

Varnes DJ (1984) Landslide Hazard Zonation: a review of principles and practice. UNESCO Press, Paris, 63p

Wu Y, Yin K, Liu Y (2000) Information analysis system for landslide hazard zonation. In: Bromhead E, Dixon N, Ibsen M-L (eds) Landslides in research, vol 3, Theory and practice. Thomas Telford, London, pp 1593–1598

Yin KL, Yan TZ (1988) Statistical prediction models for slope instability of metamorphosed rocks. In: Bonnard C (ed) Landslides, proceeding fifth international symposium on Landslides, vol 2. Balkema, Rotterdam, pp 1269–1272

Zêzere JL (2002) Landslide susceptibility assessment considering landslide typology. A case study in the area north of Lisbon (Portugal). Nat Hazards Earth Syst Sci 2:73–82

Part III

Seismically Induced Landslides and Seismic Landslide Hazard Analysis

Introduction by Ed Harp[1], Hideaki Marui[2], and Luca Guerrieri[3]

1) U.S. Geological Survey, Golden, USA
2) Niigata University, Research Institute For Natural Hazards And Disaster Recovery, Japan
3) ISPRA, Italian Institute For Environmental Protection And Research, Italy

With 46 presentations, both oral and poster, session L25 included a broad spectrum of studies ranging from finite-element and other displacement modeling to case studies of earthquake-triggered landslides. Presentations included the latest developments in seismic landslide hazard and risk analysis and mapping as well as novel theories of the mechanisms of landslide triggering. In addition to the variety of topical papers with a focus on seismically triggered landslides, an equally wide range of settings were featured from pre Himalaya slopes in Pakistan to the Denali Range in Alaska. Similarly, a large range of triggering events were covered, from small to moderate earthquakes in Greece and Spain to large magnitude events in Japan and China.

New seismic monitoring techniques have resulted in the discovery of directional amplification of ambient seismicity suggesting that triggering ground motions may have been directionally enhanced in the direction of landslide movement in past earthquakes. Studies using both finite-element and Newmark (both single and multi-block) methods of modeling landslide displacement have allowed comparisons and evaluations of the relative merits of these methods. The use of GIS (Geographic Information Systems) tools in modeling seismic landslide susceptibility, hazard, and risk was featured in numerous presentations of the session. Also, GIS analyses were employed to visualize the relationship between the earthquake-triggered landslide distribution and fault-slip modeling based on teleseismic records and coseismic GPS (Global Positioning Satellite) displacements. These and many other new methods of monitoring, recording, and displaying landslide data have made it clear that we are now able to analyze and interpret seismically triggered landslides in new ways and understand their occurrence in the context of a greater quantity and variety of data than ever before. An important message arising from the presentations in this session is that the completeness and precision of landslide inventories is paramount in allowing scientists to analyze the landslides and other spatial parameters in order to reach greater understanding of landslide processes and the hazard and risk created by them.

The Effect of Complex Fault Rupture on the Distribution of Landslides Triggered by the 12 January 2010, Haiti Earthquake

Edwin L. Harp, Randall W. Jibson, and Richard L. Dart

Abstract

The M_W 7.0, 12 January 2010, Haiti earthquake triggered more than 7,000 landslides in the mountainous terrain south of Port-au-Prince over an area that extends approximately 50 km to the east and west from the epicenter and to the southern coast. Most of the triggered landslides were rock and soil slides from 25°–65° slopes within heavily fractured limestone and deeply weathered basalt and basaltic breccia. Landslide volumes ranged from tens of cubic meters to several thousand cubic meters. Rock slides in limestone typically were 2–5 m thick; slides within soils and weathered basalt typically were less than 1 m thick. Twenty to thirty larger landslides having volumes greater than 10,000 m^3 were triggered by the earthquake; these included block slides and rotational slumps in limestone bedrock. Only a few landslides larger than 5,000 m^3 occurred in the weathered basalt. The distribution of landslides is asymmetric with respect to the fault source and epicenter. Relatively few landslides were triggered north of the fault source on the hanging wall. The densest landslide concentrations lie south of the fault source and the Enriquillo-Plantain-Garden fault zone on the footwall. Numerous landslides also occurred along the south coast west of Jacmél. This asymmetric distribution of landsliding with respect to the fault source is unusual given the modeled displacement of the fault source as mainly thrust motion to the south on a plane dipping to the north at approximately 55°; landslide concentrations in other documented thrust earthquakes generally have been greatest on the hanging wall. This apparent inconsistency of the landslide distribution with respect to the fault model remains poorly understood given the lack of any strong-motion instruments within Haiti during the earthquake.

Keywords

Earthquake-triggered landslide • Haiti • Fault modelling

Introduction

The M_W 7.0, 12 January 2010, Haiti earthquake triggered more than 7,000 landslides in an asymmetric pattern to the south of the modelled fault source (Hayes, et al. 2010; Fig. 1). Most of the landslides were rock and soil slides from limestone and weathered basalt on 25°–65° slopes. Volumes ranged from tens of cubic meters to several thousand cubic meters; 20–30 landslides had volumes greater than 10,000 m^3. The densest landslide concentrations were south of the fault source, which parallels the Enriquillo-Plantain-Garden fault zone (EPGFZ). Both here and in an area about 15 km northwest of Jacmél landslides in limestone blocked drainages and created small lakes that were soon breached with little impact on population or infrastructure.

The asymmetry of the landslide distribution with respect to the epicenter and modelled fault source on which most of the fault displacement took place (Hayes et al. 2010) is unusual in that relatively few of the triggered landslides were triggered

---

E.L. Harp (✉) • R.W. Jibson • R.L. Dart
U.S. Geological Survey, Denver Federal Center, Box 25046, MS 966, Denver, CO 80225, USA
e-mail: harp@usgs.gov

C. Margottini et al. (eds.), *Landslide Science and Practice*, Vol. 5,
DOI 10.1007/978-3-642-31427-8_20, © Springer-Verlag Berlin Heidelberg 2013

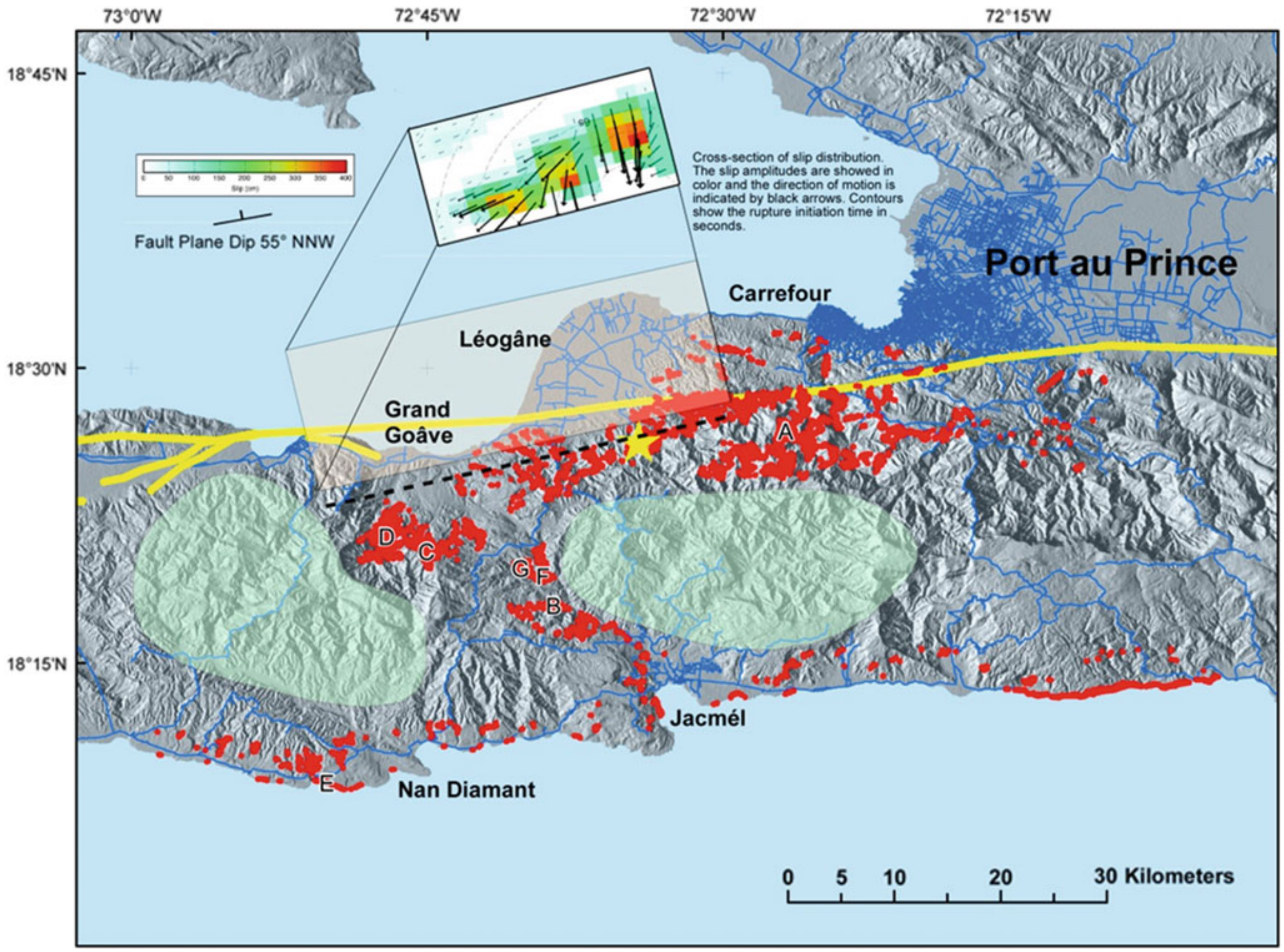

Fig. 1 Location of study area in Haiti showing patterns of earthquake-triggered landslides (*red dots*), earthquake epicenter (*yellow star*), modelled slip on blind thrust responsible for 80 % of moment release, the projected surface intersection of modelled fault plane (*black dashed line*), areas of sampled landslide concentrations (*A–G*), areas of scattered landslides which have not yet been systematically mapped (*light green polygons*), and roads (*blue*)

on the hanging wall of the blind thrust fault. Most landslides occurred to the south and west of the fault plane on the footwall. This pattern contrasts with landslide distributions from other thrust earthquakes, where most landslides were concentrated on the hanging wall. With no strong-motion instruments in Haiti at the time of the earthquake, the only shaking information upon which to base an explanation for this skewed pattern comes from teleseismic stations.

Landslides Triggered by the Earthquake

Landslide Types

Most of the landslides triggered by the earthquake were disrupted rock falls and rock slides in limestone and weathered basalt, which are the predominant rock types in the region surrounding the EPGFZ (landslide terminology after Varnes 1978). The landslides consist of disrupted masses of rock that form on steep slopes of deeply incised river valleys and coastal bluffs. Failures in the limestone consist of falls and slides of cobble- to boulder-sized fragments that have failed along pre-existing fractures (Fig. 2). Failures in the weathered basalt are predominantly falls and slides of weathered basalt regolith and colluvium (Fig. 3) with fragments ranging in size from gravel to small boulders. Lateral spreads (horizontal movement of blocks of soil on nearly level ground) occurred at some port facilities in Port-au-Prince and along coastal areas to the west (Fig. 4).

Numbers and Distribution

We acquired imagery after the earthquake from a variety of sources, including Google Earth, Digital Globe's Quickbird, Geoeye, and Worldview 2, and National Oceanographic and

Fig. 2 Rock fall comprised of limestone boulders that have failed along preexisting fractures

Fig. 3 Shallow soil slides in weathered basaltic regolith within the EPGFZ

Fig. 4 Lateral-spread cracks along coast west of Port-au-Prince near Léogâne

Atmospheric Administration (NOAA) aerial photography; the resolution for all sources is 60–100 cm. The imagery was used to map landslides as polygons in Arc Map or as kmz files generated within Google Earth. These files were then converted to shape files and imported into Arc Map. More than 7,000 landslides have been mapped, and the work is still in progress (Fig. 1).

As of June 2011, we have mapped approximately 70 % of the area covered by imagery. Figure 1 shows enlarged landslide centroids and thus indicates general areas of densest concentrations. The number of landslides mapped to date is in the high end of the range indicated by worldwide studies relating number of earthquake-triggered landslides to earthquake magnitude (Keefer 2002).

The area affected by landslides extends about 53 km to the southeast and 30 km to the southwest from the fault source, and from the foothills south of Port-au-Prince south across the entire peninsula to the coast (Fig. 1). Keefer (1984) maximum distance limit for a M 7.0 earthquake is about 200 km, which suggests that the shaking produced by this earthquake is well below the maximum of similar historical earthquakes worldwide. The concentration of landslides triggered by the earthquake is not uniform within the area affected and is related to slope, lithology, and regional variations in ground motion as defined by analysis of teleseismic records, InSAR, and field work used to construct the fault-source model for the earthquake (Hayes, et al. 2010).

Because the landslide inventory is not yet complete, a systematic analysis of landslide concentration has not yet been undertaken, however a number of areas of landslide concentrations at varying distances from the fault source have been sampled (see Fig. 1, letters, A-G). One of the areas of densest landslide concentration is southeast of the fault source and the EPGFZ (**a** in Figs. 1 and 5). These steep slopes consist mostly of limestone bedrock, with some slopes underlain by weathered basalt. Concentrations of landslides here, 4.9 km from thenearest edge of a surface projection of the fault source, reach area percentages of almost 19 %. At 15.4 km from the fault source (**b**, Fig. 1) the landslide concentration is 5.7 %. Areas C and D, at 6.3 and 4.7 km respectively, have concentrations of 4 and 6.8% respectively. Along the south coast, west of Jacmél at 28.7 km from the fault source, the concentration is almost 11% (**e**, Fig. 1). Figure 6 shows a plot of landslide concentration versus fault-source distance.

Figures 1 and 6 show that landslide concentration does not decrease in a simple manner as a function of distance from the fault source. With no strong-motion records from the near field in this earthquake, there is no local information on the variation of shaking to compare with the landslide distribution. However, a comparison of this distribution with the modeled fault source and attendant slip is useful to gain

Fig. 5 Dense concentration of landslides in limestone near the EPGFZ about 10 km south-southwest of Carrefour

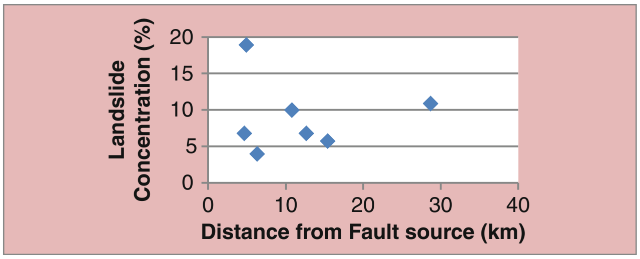

Fig. 6 Landslide concentration versus fault-source distance

some general understanding of fault movement and landslide patterns based on teleseimic records, interferometric synthetic aperture radar, and geologic field observations (Hayes, et al. 2010).

Landslide Dams

Numerous landslides blocked stream drainages and impounded lakes. The greatest concentration of these landslide dams was about 15 km northwest of Jacmél (Fig. 7). Most of these lakes had been breached within a month of the earthquake but were not large enough to pose significant threats to local populations or infrastructure. Despite being breached, some of the lakes are only partially drained and still have small impounded bodies of water.

Ongoing Landslide Hazards

The earthquake shaking created many partially detached landslide masses (Fig. 8). These masses may be precarious, and renewed movement could occur in future earthquakes and has already occurred during rainy periods. Many landslides at the tops of slopes have related cracks behind the main scarp. These cracks indicate a potential for continued landsliding during future earthquakes or rainy periods which could enlarge the slides. The earthquake-triggered landslides have moved large amounts of sediment into stream drainages; additional material has been detached from slopes but has not slide all the way to the valley bottoms. During future rainy periods, this sediment will move, and has already moved to some extent, into the the river systems and create significant increases in sedimentation downstream.

Fig. 7 Small lakes impounded by landslide dams along a 600-m length of stream northwest of Jacmél

Fig. 8 Detached landslide blocks (*arrows*) about 15 km northwest of Jacmél that could move in future earthquakes or rain storms

Fault Slip Compared to Landslide Distribution

The fault-rupture model for the Haiti earthquake developed by Hayes et al. (2010) is based on a joint inversion of InSAR, measurements of uplifted coral, and teleseismic body-wave data. This complex model suggests that rupture began first on a plane striking N83°E that has an average orientation similar to the EPGF, which dips 70° to the south. Movement was then transferred to a 55°–N-dipping blind thrust fault, called the Léogâne Fault by Hayes et al. (2010, Fig. 1). This fault was responsible for 80 % of the moment released during the event (Hayes et al. 2010, p. 801). The last part of surface motion is best modelled by a 45°-S-dipping fault having right-lateral displacement (Hayes et al. 2010). Because the second of these faults accounts for most of the moment released in the earthquake, we focus on this fault plane for a comparison of its modelled slip and the landslide distribution triggered by the shaking.

A comparison of the spatial distribution of landslides and the fault-slip distribution as shown on the modeled blind thrust (Fig. 1) reveals several relationships between the landslides and the fault motion. First, the majority of landslides are located on the footwall of the blind thrust; relatively few are on the hanging wall. This is unusual as compared to other earthquakes such as the 1994 Northridge, California earthquake (Harp and Jibson 1996) and the 1999 Chi-Chi, Taiwan earthquake (Liao and Lee 2000), where most of the landslides occurred on the hanging walls of the faults. The landslides triggered by the Haiti earthquake show quite the opposite pattern and indicate that shaking on the hanging wall of the fault might not have been as severe as that to the south (the direction of fault slip as shown in Fig. 1). Differences in susceptibility of slopes due to lithology and/or morphology do not seem to play a significant a role in this asymmetric distribution as there are similar variations in these factors both to the north and south of the fault source.

Figure 1 also shows that one of the areas of maximum landslide concentration (**a** in Fig. 1) is closest (within 10 km as compared to 30 km for the next closest area) to the area of maximum slip on the fault plane. If the area of maximum slip also generated the strongest surface ground motion, then it seems reasonable that the densest landslide concentration would occur there, as well. More broadly, the large majority of the landslides lie south of the fault zone; this suggests the possibility that southward thrusting on this fault plane generated southward-directed strongest shaking, which triggered more landslides to the south (on the footwall), than to the north (on the hanging wall). Unfortunately, the lack of local strong-motion records leaves us with no way to corroborate this.

Summary and Conclusion

The 12 January 2010 Haiti earthquake (M_w 7.0) triggered more than 7,000 landslides consisting mainly of disrupted slides and falls in limestone and highly weathered basalt. The distance limits of the triggered landslides suggest that the shaking levels of the earthquake were well below the maximum levels that could be expected for a M_w 7.0 earthquake. It is therefore very probable that a future earthquake of equal or greater magnitude could trigger more landslides and higher concentrations of landslides over a broader area than did the January 2010 earthquake.

The distribution of landslides triggered by the earthquake is highly asymmetric with respect to the modeled blind-thrust fault source (Hayes et al. 2010). Most of the landslides lie south of the fault on the footwall. Relatively few landslides are located on the hanging wall. Thus, most of the landslides are located in the direction of fault rupture (to the south), which suggests that fault slip from the earthquake could have caused the strongest shaking to be directed southward. Areas of highest landslide concentration lie closest to the zone of maximum modelled fault slip as shown in Fig. 1. This relationship between the pattern of landslides triggered by the earthquake and the results of fault modelling from teleseismic records and geodetic and geologic observations indicates that much can be learned from closely comparing the landslide distributions triggered by earthquakes and the variations in shaking produced by the earthquake even when near field strong-motion records are non-existent.

References

Harp EL, Jibson RW (1996) Landslides triggered by the 1994 Northridge, California, earthquake. Bull Seismol Soc Am 86(1B):S319–S332

Hayes GP, Briggs RW, Sladen A, Fielding EJ, Prentice C, Hudnut K, Mann P, Taylo FW, Crone AJ, Gold R, Ito T, Simon M (2010) Complex rupture during the 12 January 2010 Haiti earthquake. Nat Geosci 3:800–805

Keefer DK (2002) Investigating landslides caused by earthquakes–A historical review. Surv Geophys 23:473–510

Keefer DK (1984) Landslides caused by earthquakes. Geol Soc Am Bull 95:406–420

Liao HW, Lee CT (2000) Landslides triggered by the Chi-Chi earthquake. In: Proceedings of the 21st asian conference on remote sensing, Taipei, pp 383–388

Varnes DJ (1978) Slope movement types and processes. In: Schuster RL, Krizek RJ (eds) Landslides analysis and control. National Academy of Sciences, Washington, pp 11–33, 234

THE SECOND
WORLD
LANDSLIDE FORUM

Numerical Analysis of Two Wooden House Damages Induced by Dune Liquefaction during the 2007 Niigata Chuetsu-Offshore Earthquake

Fei Cai, Keizo Ugai, Akihiko Wakai, Seiichiro Kuroda, Atsuo Onoue,
and Kunihiro Higuchi

Abstract

Many wooden houses near a dune at Kariwa Village, Kashiwazaki City, Niigata Prefecture were damaged because of the liquefaction of the dune during the 2007 Niigata Chuetsu-offshore Earthquake, Mw = 6.8. This paper performs fully coupled dynamic finite element analysis to reproduce the ground liquefaction of two wooden houses. Here, wooden house A of which the ground was improved only using horizontal drainage pipes was fully damaged; however, wooden house B of which the ground was improved by horizontal drainage system to lower the ground water level, surface ground improvement, and steel-pipe piles was slightly deformed. For wooden house B, it was found, based on the numerical results, that steel-pipe piles were more effective liquefaction mitigation measure.

Keywords

Dune • Liquefaction • Numerical analysis

Introduction

Most wooden houses at Kariwa Village, Kashiwazaki City, Niigata Prefecture, were damaged because of the liquefaction of the dune during the 2007 Niigata Chuetsu-offshore Earthquake, Mw = 6.8. Such houses were rebuilt because they had been damaged also by the dune liquefaction induced by the 2004 Niigata Chuetsu Earthquake, Mw = 6.8, and various techniques were used for various houses to mitigate the potential effects of liquefaction. Wooden house A of which the ground was improved only using horizontal drainage pipes was fully damaged; however, wooden house B of which the ground was improved by horizontal drainage system to lower the groundwater level (GWL), surface ground improvement, and steel-pipe piles was slightly deformed.

This paper performs fully coupled dynamic finite element analysis to reproduce the ground liquefaction of the above-mentioned two wooden houses, and to clarify the mechanisms of the wooden house damages. For wooden house B, it was checked, based on the numerical results, which of the liquefaction mitigation measures was more effective.

House Damages in the Inaba District in Kariwa Village

The Inaba district in Kariwa Village locates at the eastern foot of a dune which separates the Japan Sea from the of Kariwa plain. Most wooden houses from house A to house B in Fig. 1, built at the eastern foot of the dune were intensively damaged because of the liquefaction of the dune during the 2007 Niigata Chuetsu-offshore Earthquake. Many wooden houses in the same district had been damaged because of the liquefaction of the dune during the 2004 Niigata Chuetsu

---

F. Cai (✉) • K. Ugai • A. Wakai
Gunma University, Department of Civil and Environmental Engineering, Kiryu, Gunma 376-8515, Japan
e-mail: feicai@gunma-u.ac.jp

S. Kuroda
National Agriculture & Food Research Organization, Tsukuba, Japan

A. Onoue
Nagaoka College of Technology, Department of Civil Engineering, Nagaoka, Japan

K. Higuchi
Kuroiwa Survey Design Office Co, Ltd, Maebashi, Japan

C. Margottini et al. (eds.), *Landslide Science and Practice*, Vol. 5,
DOI 10.1007/978-3-642-31427-8_21,

Fig. 1 Schematic map of the Inaba district in Kariwa Vallage, Kashiwazaki City, Niigata prefecture (Marked by the red ellipse above, and Google aerial photo below)

Fig. 2 Fully damaged wooden house A (*above*) and slightly damaged wooden house B (*below*)

Earthquake. As shown in Fig. 2, the rebuilt wooden house A, of which the ground was improved only using horizontal drainage pipes, displaced horizontally 130 cm, and vertically 120 cm upward, and inclined forward about 9°˜. The ground deformed significantly and the house was fully damaged. However, the rebuilt wooden house B, of which the ground was improved by horizontal drainage system to lower the GWL, surface ground improvement, and steel-pipe piles was slightly settled 12 cm. The details of such house damages have been reported by Isobe et al. (2008), Inotsume et al. (2008), and Yamada et al. (2008).

As liquefaction mitigation measures of the wooden house B, the horizontal drainage system to lower the GWL, surface ground improvement, and steel-pipe piles were constructed. Underdrainage had a standard cross section 50 cm wide and 40 cm high, which was constructed wrapping gravel with mat and had a sand filter. Pouros concrete pipe 100 mm in diameter was buried in the gravel, and Netlon pipe 75 mm in diameter was used as a reserve pipe. The underdrainage was buried around the wooden house B with a bottom depth of 1.7–2.4 m, as shown in Fig. 3. The groundwater from the western dune and the neighbood houses was also shut out, and the underdrainage was connected with a side ditch of the road.

Surface ground improvement of the house B used 10 t cement, and mixed 1 m of the surface ground. The average uniaxial compression strength was 545 kN/m^2 of three samples. Figure 4 shows the construction of the surface ground improvement.

Total of 88 steel pipe piles 6 m long and 114 mm in outer diameter were installed.

Fully Coupled Dynamic Effective Stress Analysis

A fully coupled dynamic effective stress analysis software UWLC (Forum 8 Co. Ltd. 2005) was used, which consists of three parts: (1) a program used to determine the parameters of constitutive laws by simulating the laboratory tests, (2) a program to calculate the initial stress before the

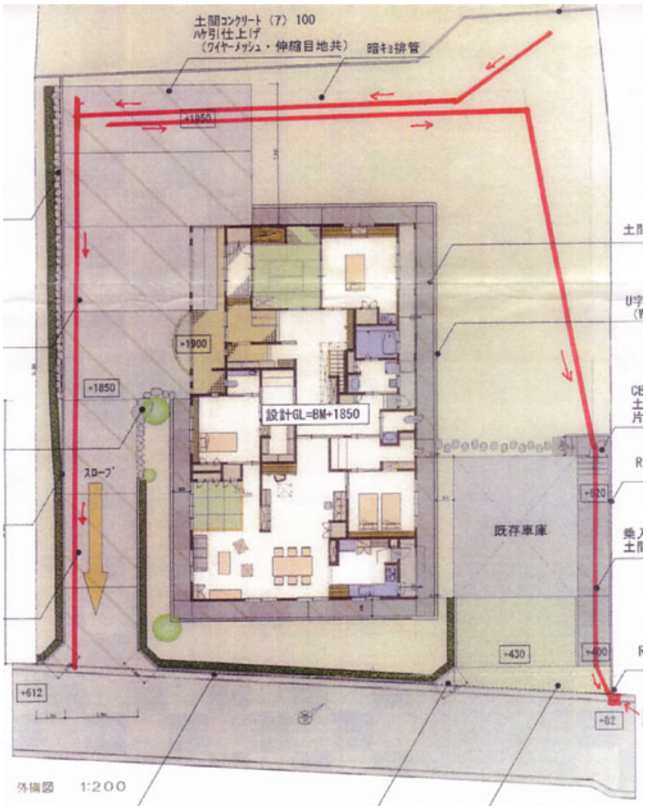

Fig. 3 Underdrainage (*red line*) for house B

Fig. 4 Construction of surface ground improvement for house B, total of 10 t cement was mixed into the ground

earthquake, and (3) a fully coupled dynamic effective stress analysis program to calculate the seismic response.

The fully coupled dynamic effective stress analysis program uses the u-p formulation. Based on Biot's theory, the dynamic governing equation is given by

$$\mathbf{M}\ddot{\mathbf{u}} + \mathbf{C}\dot{\mathbf{u}} + \mathbf{K}\mathbf{u} - \mathbf{Q}\mathbf{p} = \mathbf{f}^u \tag{1}$$

where **M** is mass matrix, **C** is damping matrix, **K** is stiffness matrix, **Q** is coupled matrix, **u** is displacement vector, $\mathbf{f}^u$ is external load vector, and **p** is excess pore water pressure vector.

The governing equation for the pore water pressure is given by

$$\mathbf{Q}^{\mathrm{T}}\dot{\mathbf{u}} + \mathbf{H}\mathbf{p} + \mathbf{S}\dot{\mathbf{p}} = \mathbf{f}^p \tag{2}$$

where **H** is seepage matrix, **S** is compression matrix, $\mathbf{f}^p$ is external load vector for the pore water.

Dynamic governing equation is integrated in time domain using Newmark's method of direct integration. Using the acceleration, velocity, and displacement, excess pore water pressure rate, and excess pore water pressure at time step n, those at time step $n + 1$ can be given by

$$\ddot{\mathbf{u}}_{n+1} = \ddot{\mathbf{u}}_n + \Delta\ddot{\mathbf{u}}_n \tag{3}$$

$$\dot{\mathbf{u}}_{n+1} = \dot{\mathbf{u}}_n + \ddot{\mathbf{u}}_n\Delta t + \theta_1\Delta\ddot{\mathbf{u}}_n\Delta t \tag{4}$$

$$\mathbf{u}_{n+1} = \mathbf{u}_n + \dot{\mathbf{u}}_n\Delta t + \frac{1}{2}\ddot{\mathbf{u}}_n\Delta t^2 + \frac{\theta_2}{2}\Delta\ddot{\mathbf{u}}_n\Delta t^2 \tag{5}$$

$$\dot{\mathbf{p}}_{n+1} = \dot{\mathbf{p}}_n + \Delta\dot{\mathbf{p}}_n \tag{6}$$

$$\mathbf{p}_{n+1} = \mathbf{p}_n + \dot{\mathbf{p}}_n\Delta t + \theta\Delta\dot{\mathbf{p}}_n\Delta t \tag{7}$$

where θ_1, θ_2, and θ are integration coefficients. For numerical stability, $\theta_1 = \theta_2 = 0.5$, and $\theta = 0.5$ was used. Inserting (3)–(7) into (1) and (2), the following equation can be obtained.

$$\begin{bmatrix} \mathbf{M} + \theta_1\Delta t\mathbf{C} + \frac{\theta_2}{2}\Delta t^2\mathbf{K} & -\theta\Delta t\mathbf{Q} \\ -\theta\Delta t\mathbf{Q}^{\mathrm{T}} & -\frac{\theta}{\theta_1}(\theta\Delta t\mathbf{H} - \mathbf{S}) \end{bmatrix} \begin{Bmatrix} \Delta\ddot{\mathbf{u}}_n \\ \Delta\dot{\mathbf{p}}_n \end{Bmatrix} = \begin{Bmatrix} \psi^u_{n+1} \\ \psi^p_{n+1} \end{Bmatrix} \tag{8}$$

where ψ^u_{n+1} and ψ^p_{n+1} are residual vectors, and given by

$$\psi^u_{n+1} = \mathbf{f}^u_{n+1} - \mathbf{M}_{n+1}\ddot{\mathbf{u}}_{n+1} - \mathbf{C}_{n+1}\dot{\mathbf{u}}_{n+1} - \int_\Omega \mathbf{B}^{\mathrm{T}}\boldsymbol{\sigma}' d\Omega + \mathbf{Q}_{n+1}\mathbf{p}_{n+1} \tag{9}$$

$$\psi^p_{n+1} = -\frac{\theta}{\theta_1}\left(\mathbf{f}^p_{n+1} - \mathbf{Q}_{n+1}\dot{\mathbf{u}}_{n+1} - \mathbf{H}_{n+1}\mathbf{p}_{n+1} + \mathbf{S}_{n+1}\mathbf{p}_{n+1}\right) \tag{10}$$

Inital stiffness method was used to solve (8). Rayleigh damping with a damping coefficient of 0.02 was also introduced. The time increment of 0.001 s was used.

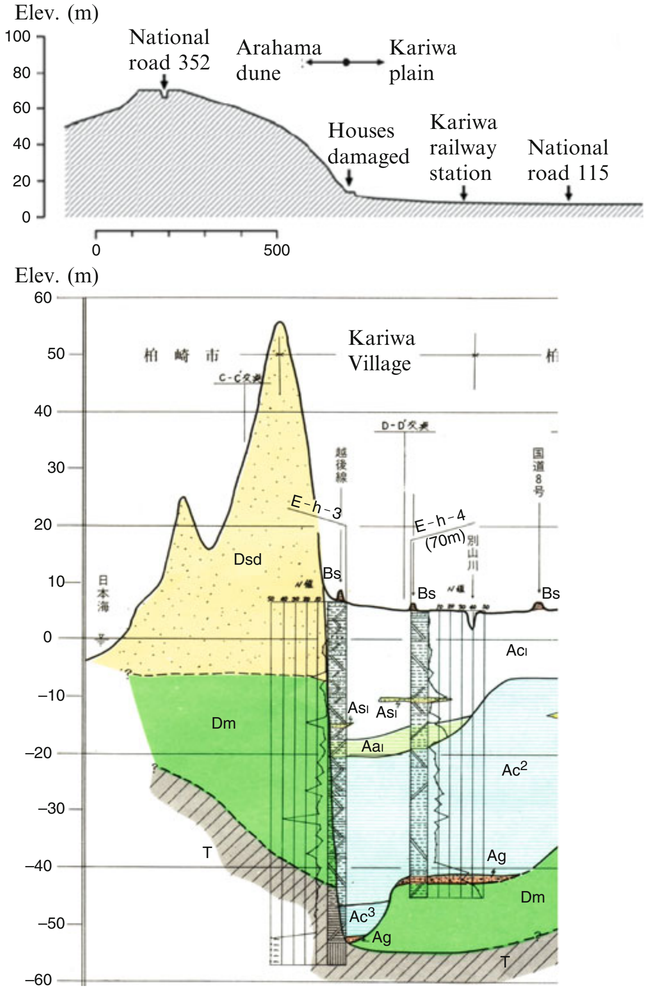

Fig. 5 Topography at the Inaba district in Kariwa Village (*above*) and a geological cross section 2 km from the Inaba district (see *red line* in Fig. 1). Bs: fills, Asd: younger dune sand, Ap: humus soil, Ac1: clayey soil, Dsd: older dune sand, As1: sand

Cross Section Analyzed and Input Motion

Topography of the Inaba district in Kariwa Village and a cross section at about 2 km from the Inaba district are shown in Fig. 5. Vertical array for strong motion was instrumented at the service hall of Kashiwazaki-Kariwa Nuclear Power Plant (KK-NPP) at the top of the dune. The reported soil layers and their elastic wave velocity are by Tikimatsu et al. (2008). Cross section was determined based on Fig. 5, and sewer system map made in 2005, and investigation after the Chuetsu-offshore Earthquake. The soil layers was simplified as three layers: (1) younger dune sand, (2) older dune sand, and (3) alluvial clayey soil, based the site investigations after the earthquake (Isobe et al. 2008; Inotsume et al. 2008).

Cross sections used in the finite element analysis for the wooden house A and B were shown in Fig. 6. Because there is a clayey soil layer at the left side of the analyzed extent, a short extent of this side was selected. The boundary of the right side was set at the service hall of KK-NPP, where seismic motions were recorded. The bottom was set at the older dune sand layer. The younger dune sand layer above the older dune sand layer had a thickness not changed with position. The GWL near the houses was measured (Inotsume et al. 2008), and it at the service hall of KK-NPP was determined by the depth at which Poisson's ratio, calculated using the S- and P-wave velocity, changed significantly. Additionally, only the younger dune sand below the GWL was considered as a material potentially liquefied.

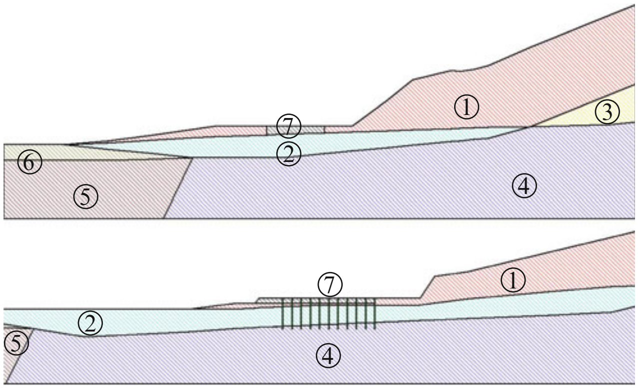

Fig. 6 Cross section analyzed, (*above*) wooden house A, and (*below*) wooden house B. *1*: younger dune sand above the GWL, *2*: younger dune sand below the GWL, *3*: older dune sand above the GWL, *4*: older dune sand below the GWL, *5*: upper clayey soil, *6*: lower clayey soil, *7*: soil just-under the house, *8*: improved ground, *9*: steel pipe piles

In this paper, the generalized plasticity for sand developed by Pastor et al. (1990) and modified in some aspects (Cai et al. 2002) was used for the younger dune sand below the GWL, and Ramberg-Osgood model was used for other ground materials. After the earthquake, sampling of the younger dune sand was conducted, and static triaxial drained compression tests and cyclic triaxial compression tests were performed. Such laborlatory test results were used to identify the parameters of the generalized plasticity model for the younger dune sand. The simulated liquefaction strength of the younger dune sand using the identified parameters was consistent with the labortory results, as shown in Fig. 7. The parameters of Ramberg-Osgood model for other soil materials were determined referred to the nonlinear material characteristics (Tikimatsu et al. 2008) estimated using the accelergrams of the vertical array at the service hall of KK-NPP.

The input seismic motion was determined using the accelergram recorded at the service hall of KK-NPP. First, the seismic motion at the bottom of the older dune sand layer in NW and EW was calculated using the recorded accelerogram at the service hall of KK-NPP. Second, the seismic motion at the bottom of the older dune sand layer in the direction of the cross section analyzed was calculated.

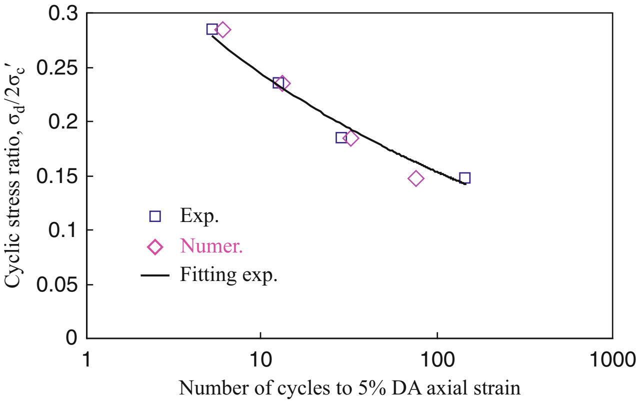

Fig. 7 Liquefaction strength of younger dune sand

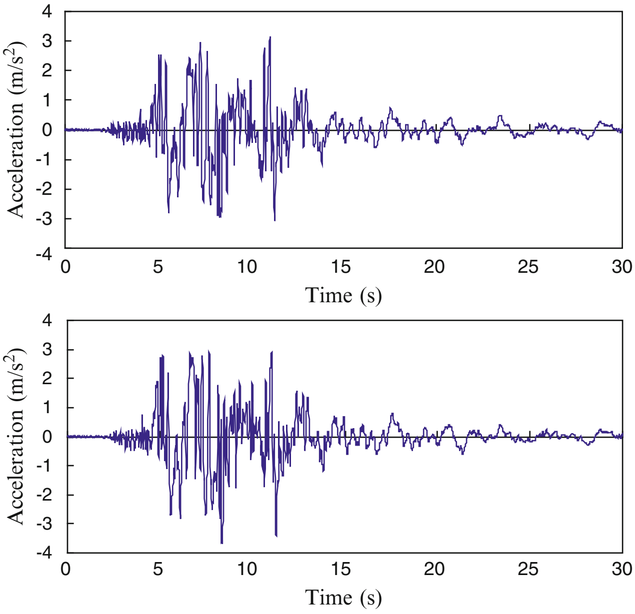

Fig. 8 Input seismic motions at the bottom of older dune sand layer for house A (*above*) and B (*below*)

Because the directions of the cross section for the houses A and B were different, the seismic motions for the houses A and B had also some differences, as shown in Fig. 8. Because the distance between the service hall of KK-NPP and the houses A and B was about 400 m, the influence of the distance from the epicenter on the seismic motions was not considered in this paper.

Numerical Results

Numerical Results for Wooden House A

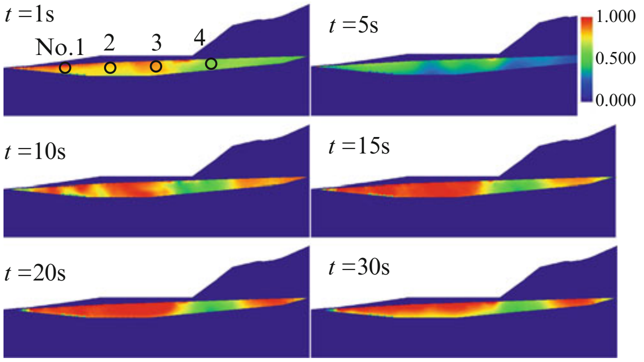

Fig. 9 Ration of excess pore water pressure to initial vertical stress at various times for the house A

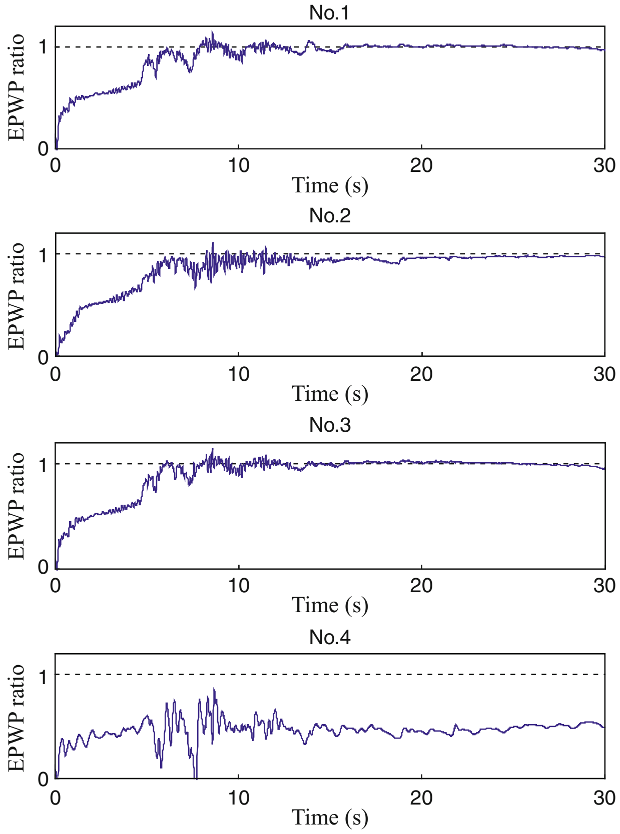

Fig. 10 Histogram of ratio of excess pore water pressure (EPWP) at No. 1–4 points for house A

The ratio of the excess pore water pressure to the initial vertical stress at various times is shown in Fig. 9 for the house A, and Fig. 11 shows the histogram of the ratio of the excess pore water pressure to the initial vertical stress at typical points as shown in Fig. 10. Figures 9 and 10 show that the excess pore water pressure increased slowly before 5 s because the seismic motion was not so strong, and after that it increased rapidly due to strong seismic motion. The ratios of excess pore water pressure at No. 1–3 points except No. 4 point reached 1.0. This shows that effective stress of the ground of the house A became zero, and liquefaction occurred.

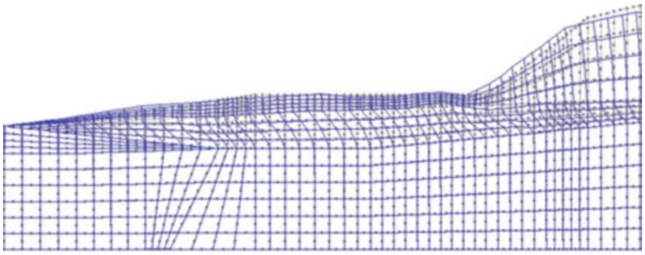

Fig. 11 Finite element meshes near the house A before and after earthquake

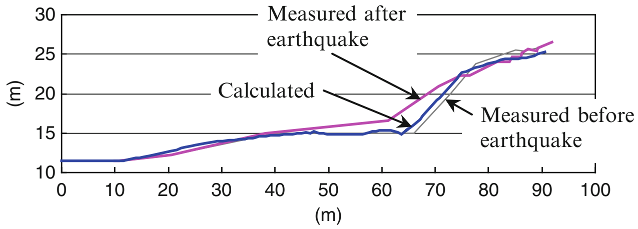

Fig. 12 Deformation of the ground surface for house A

Figure 11 shows deformed finite element mesh. Comparing the mesh before and after earthquake, the deformation induced by the earthquake can be obtained. Figure 11 shows that large spreading of the younger dune sand layer below the GWL occurred because of its liquefaction. Figure 12 shows the ground surface measured before and after the earthquake. Measured lateral spreading of the house A was about 2.3 m and the ground in the rear of the house A rose up. Figure 12 shows that calculated and measured deformations were generally consistent with one another though there were some differences. The difference between the measured and calculated deformation of the younger dune sand layer above the GWL was some significant. One of the main reasons for this was because the finite element analysis cannot satisfactorily simulate the cracks and sliding deformation occurred. Another was because the limit of Ramberg-Osgood model had.

Numerical Results for Wooden House B

The ratio of the excess pore water pressure to the initial vertical stress at various times is shown in Fig. 13 for the house B, and Fig. 14 shows the histogram of the ratio of the excess pore water pressure to the initial vertical stress at typical points as shown in Fig. 13. Figures 13 and 14 show that the excess pore water pressure increased slowly before 5 s because the seismic motion was not strong, and after that it increased rapidly due to strong seismic motion. The ratios of excess pore water pressure at No. 2 and 3 points reached 1.0 but it did not at No. 1 and 4 points. This shows that liquefied region for house B was smaller than that for house A.

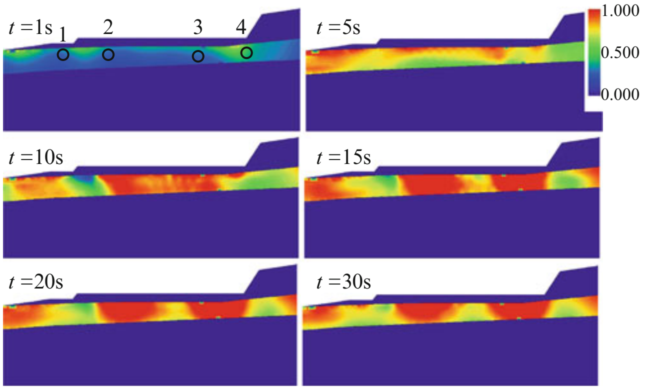

Fig. 13 Ration of excess pore water pressure to initial vertical stress at various times for house B

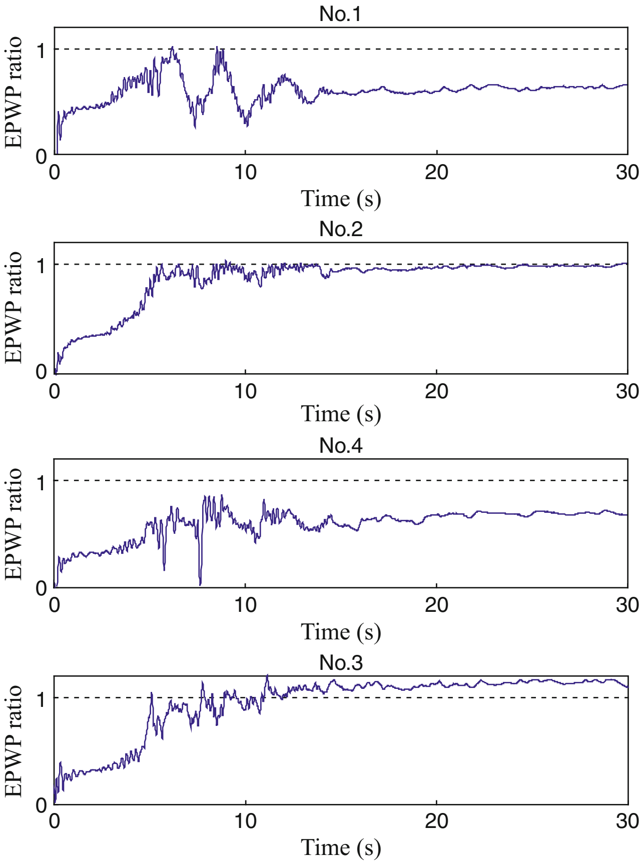

Fig. 14 Histogram of ratio of excess pore water pressure (EPWP) at No. 1–4 points for house B

The deformation for the house B in Figs. 15 and 16 shows that 1.5 m lateral spreading of the younger dune sand layer below GWL was calculated although steel-pipe piles were installed. However, calculated vertical settlement 7 cm was consistent with the observed.

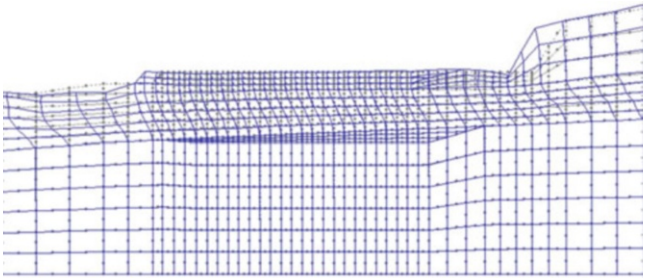

Fig. 15 Finite element meshes near the house B before and after earthquake

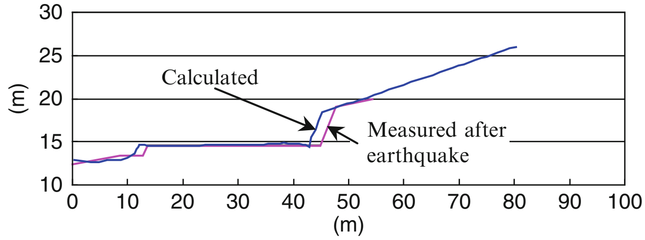

Fig. 16 Deformation of the ground surface for house B

Numerical Analyses of Various Liquefaction Mitigation Measures for Wooden House B

Figure 17 shows histograms of deformation if only one of the three liquefaction mitigation measures, which had been used for house B actually, was constructed for house B. Numerical results show that the ground surface improvement had almost not influence on the lateral spreading and vertical settlement. The lateral spreading for the case of three liquefaction mitigation measures constructed was almost the same as that for the case of only steel pipe piles installed. The effectiveness for vertical settlement was ordered as three liquefaction mitigation measures constructed, only steel pipe piles installed, and lowering the GWL.

Conclusions

Fully coupled dynamic finite element analysis of wooden houses A and B shows that the lateral spreading were induced by the liquefaction of the younger dune sand layer below the GWL. The liquefaction also occurred in the ground of house B; however, the deformation was small because of the effect of the liquefaction mitigation measures.

Finite element analysis for various liquefaction mitigation measure shows that the most effective liquefaction mitigation measure was steel pipe piles. The analysis process reported in this paper can be used to select cost-effective liquefaction mitigation measure for various civil structures and housings.

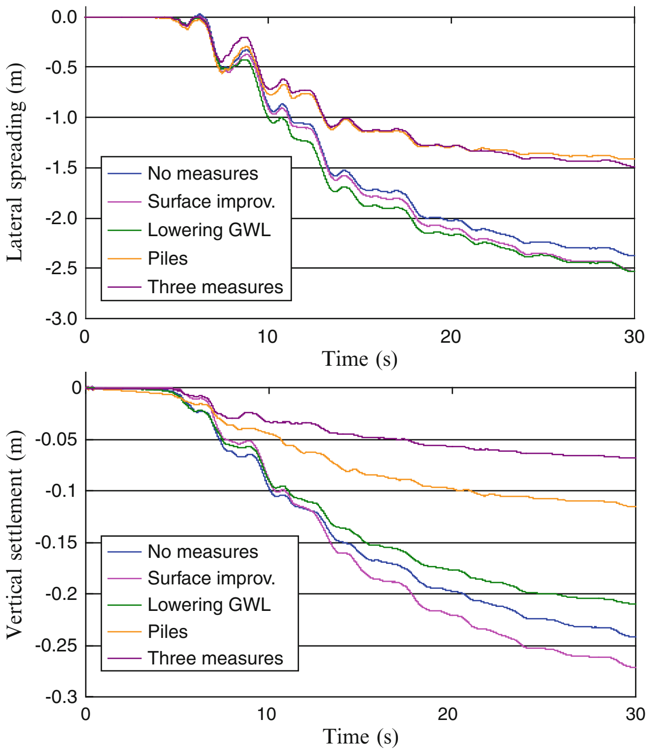

Fig. 17 Histogram of deformation of the ground for house B

References

Cai F, Hagiwara T, Imamura S, Ugai K (2002) 2D Fully coupled liquefaction analysis of sand ground under tank. In: Proceedings of the 11th Japan earthquake engineering symposium, pp 819–824 (in Japanese)

Forum 8 Co. Ltd (2005) Finite element fully coupled dynamic effective stress analysis program (UWLC), Electrical Manual, http://www.forum8.co.jp

Inotsume T, Onoue A, Tsuchida K, Ohzawa H, Ugai K, Wakai A, Cai F, Higuchi K, Kuroda S (2008) An example of ground deformation difference induced by the existence or no liquefaction mitigation measures. In: Proceedings of the 25th annual conference of Niigata civil engineering society, pp 152–155 (in Japanese)

Isobe K, Ohtsuka S, Hirade T, Hayashi K, Sugimura S (2008) Seismic damage of residential area by 2007 Niigataken Chuetsu-oki Earthquake (Part4 Kariwa village). In: Proceedings of the 20th Japan national conference on geotechnical engineering, pp 1749–1750 (in Japanese)

Pastor M, Zienkiewicz OC, Chan AHC (1990) Generalized plasticity and the modeling of soil behavior. Int J Numer Anal Meth Geomech 14:151–190

Tikimatsu K, Arai H, Minowa K (2008) Soil nonlinearity and bedrock strong motions estimated from downhole array records at Kashiwazaki-Kariwa nuclear power plant during the 2007 Niigata-ken Chuetsu-oki earthquake. J Struct Constr Eng Trans AIJ 73 (630):1273–1280 (in Japanese)

Yamada S, Towhata I, Ezoe A, Olivahal B, Tanaka R (2008) Liquefaction of the residential land ground due to the Niigata Chuetsu Oki Earthquake-Inaba, Kariwa-. In: Proceedings of the 20th Japan National conference on geotechnical engineering, pp 1775–1776 (in Japanese)

THE SECOND
WORLD
LANDSLIDE FORUM

The Recent Activities in the Earthquake-Induced Landslides Research Project Carried Out by the Japan Landslide Society: The Interim Report

Akihiko Wakai, Keizo Ugai, and Committee Members of ELRP

Abstract

The Japan Landslide Society has established a task force to carry out the special research project entitled “Development of a methodology for risk assessment of the earthquake-induced landslides”. Altogether 8 Working Groups, which are carrying out concrete investigations and analyses on individual items, were organized to cover all the objectives of the task force. In this report, a few of the essential research items treated in them are described in detail.

Keywords

Mechanism of landslides • Risk assessment • Risk management • Secondary disasters • Countermeasures • Design procedures • Warning and evacuation • Monitoring • Review of past events

Introduction

For developing the technical guidelines for risk assessment of the earthquake-induced landslides, as one of the most important missions our activities in The Japan Landslide Society, we have established a task force to carry out the special research project entitled “Development of a methodology for risk assessment of the earthquake-induced landslides”. Altogether 8 Working Groups, which are carrying out concrete investigations and analyses on individual items, were organized to cover the all objectives of the task force. The individual research items of the each Working Group are the followings:

WG 1: Mechanism of the earthquake-induced landslides
WG 2: Methodology for risk assessment and risk management
WG 3: Secondary disasters
WG 4: Countermeasures and design procedures
WG 5: Warning and evacuation/Monitoring
WG 6: Historical analyses of the past events
WG 7: Review of the overseas events
WG 8: Review of the recent events in Japan

Here two typical examples in their activities are introduced briefly.

Database for Past Earthquake-Induced Landslides in Japan

The first one is the study performed by WG 6 (Historical analyses of the past events), making up database which covers all types of earthquake-induced landslides during pre-historical and historical age in Japan (Fig. 1; after Doshida (2012)). The database describes geomorphological, geological and geotechnical features of ca.100 former landslides. It will be useful for making clear characteristics of former earthquake-induced landslides.

A. Wakai (✉) • K. Ugai
Department of Civil and Environmental Engineering, Gunma University, Gunma 376-8515, Kiryu, Japan
e-mail: wakai@ce.gunma-u.ac.jp

Committee Members of ELRP
The Earthquake-induced Landslides Research Project, The Japan Landslide Society, Tokyo, Japan

C. Margottini et al. (eds.), *Landslide Science and Practice*, Vol. 5,
DOI 10.1007/978-3-642-31427-8_22, © Springer-Verlag Berlin Heidelberg 2013

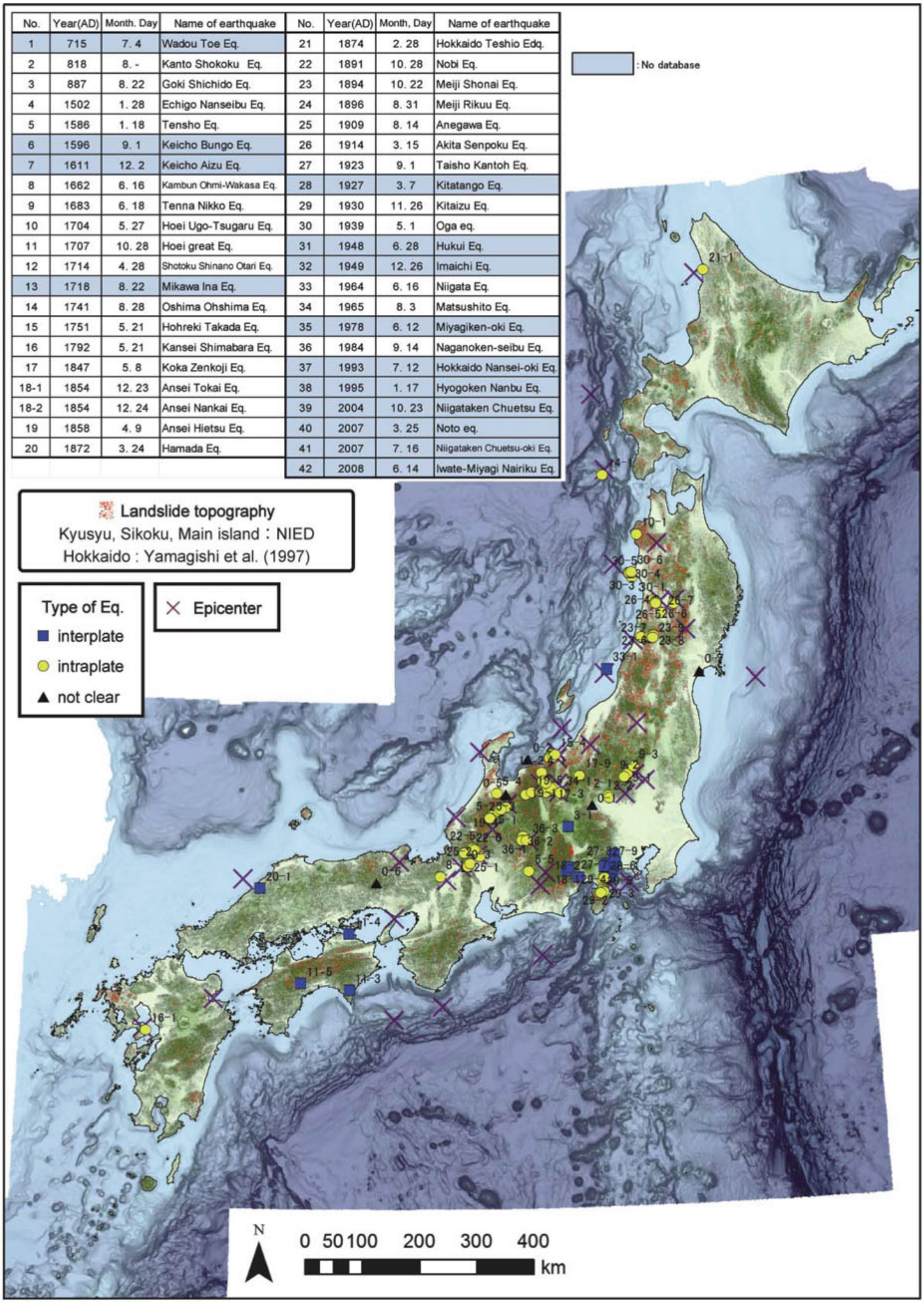

No.	Year(AD)	Month. Day	Name of earthquake
1	715	7. 4	Wadou Toe Eq.
2	818	8. -	Kanto Shokoku Eq.
3	887	8. 22	Goki Shichido Eq.
4	1502	1. 28	Echigo Nanseibu Eq.
5	1586	1. 18	Tensho Eq.
6	1596	9. 1	Keicho Bungo Eq.
7	1611	12. 2	Keicho Aizu Eq.
8	1662	6. 16	Kambun Ohmi-Wakasa Eq.
9	1683	6. 18	Tenna Nikko Eq.
10	1704	5. 27	Hoei Ugo-Tsugaru Eq.
11	1707	10. 28	Hoei great Eq.
12	1714	4. 28	Shotoku Shinano Otari Eq.
13	1718	8. 22	Mikawa Ina Eq.
14	1741	8. 28	Oshima Ohshima Eq.
15	1751	5. 21	Hohreki Takada Eq.
16	1792	5. 21	Kansei Shimabara Eq.
17	1847	5. 8	Koka Zenkoji Eq.
18-1	1854	12. 23	Ansei Tokai Eq.
18-2	1854	12. 24	Ansei Nankai Eq.
19	1858	4. 9	Ansei Hietsu Eq.
20	1872	3. 24	Hamada Eq.
21	1874	2. 28	Hokkaido Teshio Edq.
22	1891	10. 28	Nobi Eq.
23	1894	10. 22	Meiji Shonai Eq.
24	1896	8. 31	Meiji Rikuu Eq.
25	1909	8. 14	Anegawa Eq.
26	1914	3. 15	Akita Senpoku Eq.
27	1923	9. 1	Taisho Kantoh Eq.
28	1927	3. 7	Kitatango Eq.
29	1930	11. 26	Kitaizu Eq.
30	1939	5. 1	Oga eq.
31	1948	6. 28	Hukui Eq.
32	1949	12. 26	Imaichi Eq.
33	1964	6. 16	Niigata Eq.
34	1965	8. 3	Matsushito Eq.
35	1978	6. 12	Miyagiken-oki Eq.
36	1984	9. 14	Naganoken-seibu Eq.
37	1993	7. 12	Hokkaido Nansei-oki Eq.
38	1995	1. 17	Hyogoken Nanbu Eq.
39	2004	10. 23	Niigataken Chuetsu Eq.
40	2007	3. 25	Noto eq.
41	2007	7. 16	Niigataken Chuetsu-oki Eq.
42	2008	6. 14	Iwate-Miyagi Nairiku Eq.

Fig. 1 Distribution of recent earthquake-induced landslides in Japan before 2008 (after Doshida 2012)

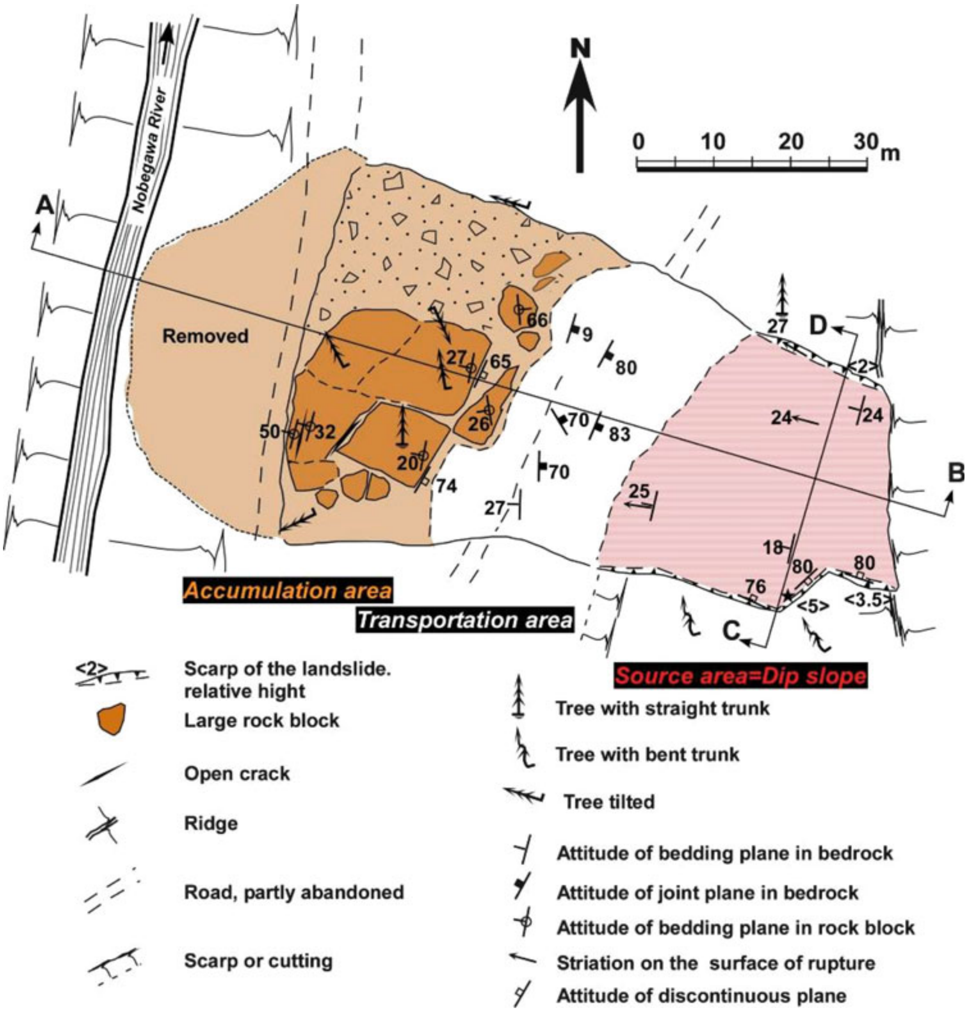

Fig. 2 Schematic plan view of the Yokowatashi landslide occurred at the time of The 2004 Mid Niigata Prefecture Earthquake in Japan (Nagata and Nozaki 2007)

Classification of Past Earthquake-Induced Landslides

The other example demonstrated here is the study performed by WG 8 (Review of the recent events in Japan). They have reviewed the recent typical earthquake-induced landslides occurred in Japan. It is very important to classify the features of each landslide for analysing their failure mechanism, which is also related to the works done by WG 1 & WG 4. Figure 2 is one of the examples in reviewed landslides, a landslide occurred at Yokowatashi district in Ojiya city, at the time of The 2004 Mid Niigata Prefecture Earthquake in Japan. It will be reported in detail in the following chapters.

Other Activities

Furthermore, a few actions have been performed as a spin-off from the above activities. These are mostly related to field investigations for the recent earthquake disasters including international cooperation as follows:

- The Iwate-Miyagi Inland Earthquake in Japan
- The Wenchuan Earthquake in China, jointly with Chengdu University of Technology
- The various types of landslides in Gansu Province in China including the disasters affected by the Wenchuan Earthquake, supported with the Gansu Society on Landslides and Debris Flows.

Fig. 3 Photos for the Yokowatashi landslide occurred at the time of The 2004 Mid Niigata Prefecture Earthquake in Japan (Point B in the right photo indicates the soil sampling point)

Each of the above activities is too wide to be comprehensively described in here. Therefore, only the case of the typical research items related to WG 1 (Mechanism of the earthquake-induced landslides), a numerical modeling of the earthquake-induced landslides occurs in a dip slope, is summarized briefly in the following chapters.

A Numerical Modelling of Dip Slope Failure Induced by Earthquake (From one of the Research Activities Related to the WG1) (Wakai et al. 2010)

Case of a Typical Dip-Slope Landslide, the Yokowatashi Landslide

Typical earthquake-induced catastrophic landslides often occur at dip slopes, where the directions of the bedding planes and the surface inclinations are approximately parallel. In this report, a typical case of a dip-slope landslide, the Yokowatashi Landslide (Figs. 2 and 3), is reported in detail. As shown in Fig. 3, part of the upper Shiroiwa layer and the surface earth with tall trees remained intact, at the far end. Here, the side face of the remaining upper Shiroiwa layer of soft silt rock is exposed. The other part of the upper Shiroiwa layer, which makes up the opposite side of the slide area is visible on site. The portion of the upper Shiroiwa layer between these parts covered the planer tectonic dip surface, which can be clearly seen in the photograph, and this part has slid more than 70 m to the west, toward the Shinano River.

The inclination of the bedding plane is approximately 22°. The thickness of the slide block of the upper Shiroiwa layer at the end is approximately 4 m, and the thickness of the earth on this block ranges from 0.2 m to 1 m. The height of the upper Shiroiwa layer remaining at the other side is approximately 2.5 m, with a 0.6 m-thick earth cover near the ridge of the slope.

Elasto-Plastic Strain-Softening Model with Total Stress Formulations

In this study, the total stress formulations will be adopted, because the bedding plane lost its strength due to structural damage to the sandwiched tuff seam. The basic concept of the newly proposed model with strain softening is the same as the simple cyclic loading model originally proposed by Wakai and Ugai (2004). In these models, the undrained shear strength τ_f with Mohr-Coulomb's c and ϕ is specified as the upper asymptote of the hyperbolic stress–strain curve.

In addition, in the new model, the shear strength value τ_f has been modified as a simply decreasing function of the accumulated plastic octahedral shear strain γ^p. Thus, the shear strength value τ_f during an earthquake is given as follows:

$$\tau_f = \tau_{f0} + \frac{\tau_{fr} - \tau_{f0}}{A + \gamma^p}\gamma^p \tag{1}$$

where τ_{fr} is the residual shear strength after large shear deformation, which is usually much smaller than the initial shear strength τ_{f0}. A is a parameter to be determined based on experimental data. The equation (1) can be modified as the equation (2), for simulating strain-softening materials with a very thin configuration as in this case.

$$\tau_f = \tau_{f0} + \frac{\tau_{fr} - \tau_{f0}}{B + \delta^p}\delta^p \tag{2}$$

where δ^p is the sliding component of the relative displacement at the thin plastic zone. The parameter B is equal to $t \cdot A$, where t is the thickness of the thin plastic element. B controls the speed of softening, which corresponds to the plastic shear

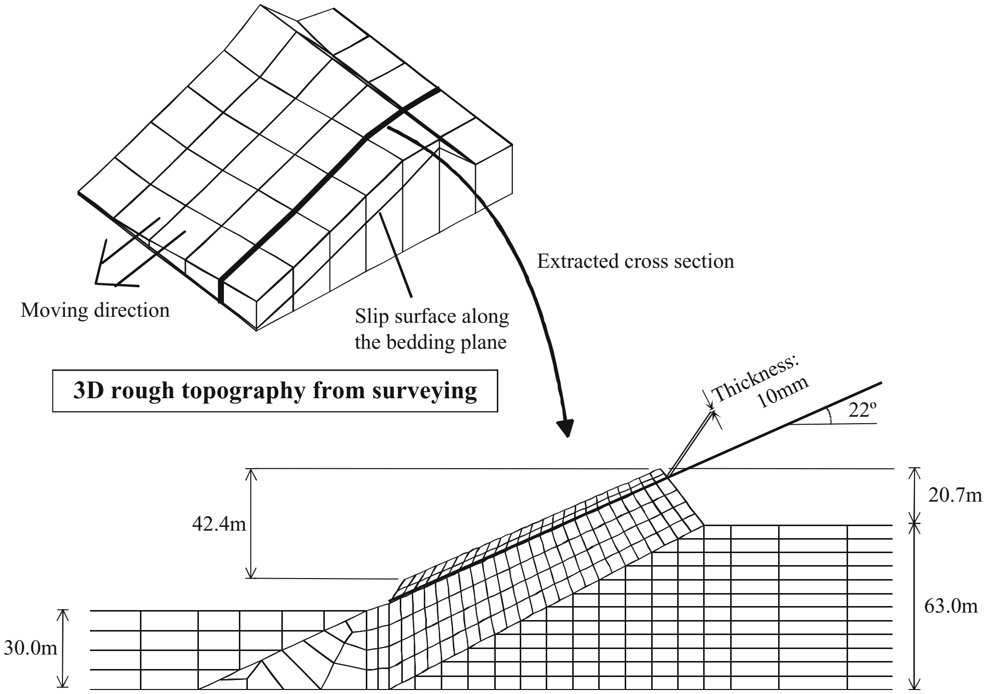

Fig. 4 Two-dimensional finite element meshes for the simulation (Wakai et al. 2010)

displacement value δ^p at the moment when the apparent shear strength τ_f becomes equal to the average of τ_{f0} and τ_{fr}. Other elasto-plastic formulations are the same as the original model, which were reported in detail by Wakai and Ugai (2004).

Finite Element Modeling for Dynamic Response Analysis

Figure 4 shows the finite element meshes with eight-nodes elements used for the simulation of the Yokowatashi Landslide. The fineness of such a mesh descretization corresponds to the maximum frequency of about 15–20 Hz, which can be thought as sufficiently high, in engineering point of view. The upper and lower soft rock layers were assumed to be elastic materials, and the sandwiched tuff seam was assumed to be an elasto-plastic material having a thickness of 10 mm, taking strain-softening characteristics into consideration. The equation (1) was adopted as the softening function for the tuff seam elements, while the equation (2) will be used for the comparisons with the laboratory test results. The surface soil at the foot of the slope was sand and gravel spreading down to the Shinano River, which was modeled as an elasto-plastic material with no strain softening.

Simulation of the Laboratory Test Results

Figure 5 shows a specimen consisting of the upper and lower Shiroiwa layers and the tuff seam between these layers, which has been used for a cyclic direct shear test under a constant-volume condition. Idealized specimens with very slight disturbance have been prepared by the careful control of a diamond cutter. The specimen was placed such that the position of the seam should be in accordance with the level of the shearing plane between the shear boxes. Repeated loading was applied in one direction from the neutral point (loading from zero to a certain value, unloading, reloading and so on).

Fig. 5 Test specimen consisting of upper and lower silt rocks with tuff seam in between (This photo was taken after the test)

Figure 6 compares the simulated hysteretic loops obtained by the proposed model to the hysteretic loops measured during the cyclic direct shear tests. The parameters used in here will be also used in the simulation of the Yokowatashi Landslide. As shown in this figure, the

Fig. 6 Observed and simulated hysteretic loops under cyclic loading

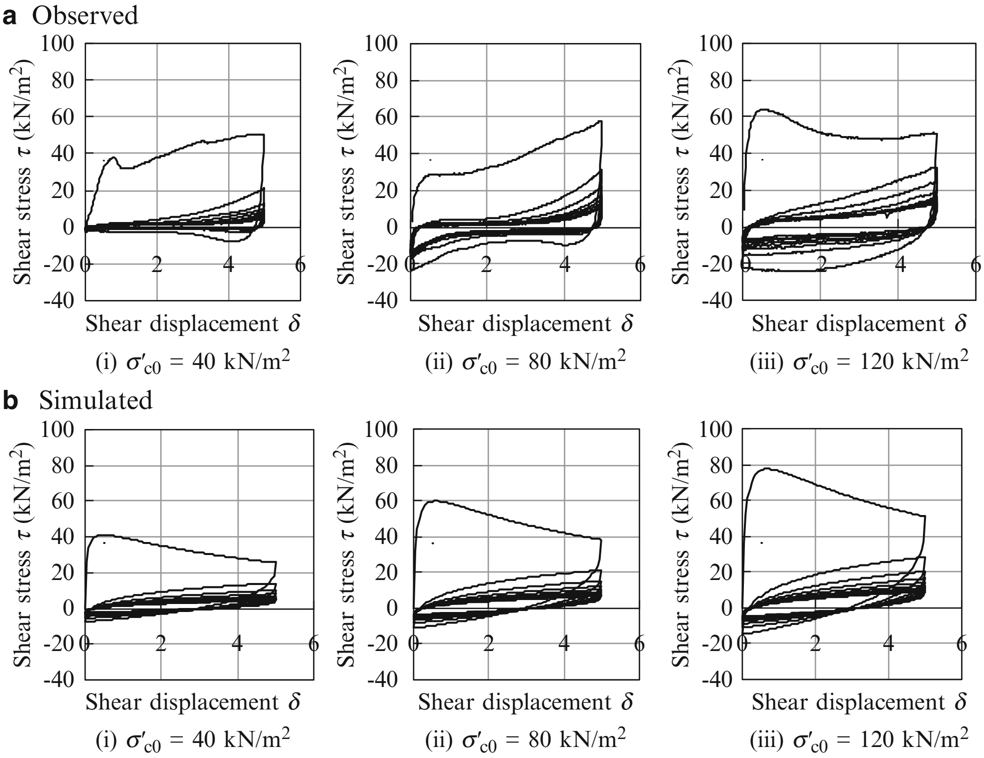

observed shear stress during the second loading cycle was only slightly mobilized, whereas the shear stress during the first cycle was fully mobilized to nearly the peak strength value. The increase in the number of cycles gradually decreases the mobilized shear stress during cyclic loading. Although the simulated result doesn't perfectly agree to the observed result, it is sufficiently similar to it in various confining pressures.

Simulation of the Yokowatashi Landslide by the Dynamic Elasto-Plastic FEM

The material parameters used in the landslide analysis are described in Wakai et al. (2010). The strength parameters and the softening parameters of the tuff seam filling the bedding plane were determined based on the results of a laboratory test, as described in the previous section. The parameters $b\gamma_{G_0}$ and n for hysteretic damping were determined as the analytical $h - \gamma$ curves fit with common measurements in undrained cyclic triaxial compression tests of sandy soils based on trial and error. The undrained conditions with the total stress formulations were assumed, and the von Mises-type plastic potential was adopted. Therefore, the dilatancy angle ψ could be maintained as zero during the earthquake.

The amplitude of the input waves at the base has been adjusted so that the EW component of the observed records at Takezawa in Old Yamakoshi Village should be realized at the ground level in the finite element meshes shown in Fig. 4. The time history of the input horizontal acceleration is shown in Fig. 7. Unfortunately, the wave propagation from the seismic center and the geological and topographical difference between Takezawa and Yokowatashi ground profiles were not considered appropriately in the preparations of these input motions. More precise consideration of actual input motion, including the effect of vertical component will provide us a better answer from numerical simulations.

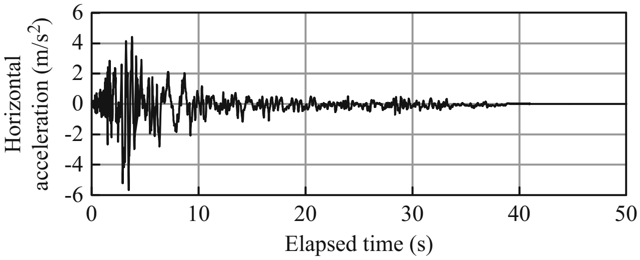

Fig. 7 Input horizontal acceleration at the base

The residual deformations at 0, 20, 40, and 50 s after the beginning of the seismic motion are shown in Fig. 8. The long-distance movement of the upper Shiroiwa block along the bedding plane is evident. This result is in agreement with the actual phenomenon. Note, however, that the predicted velocity of the sliding mass may not have sufficient accuracy. In order to simulate precisely the sliding behavior after having started such high-speed motion, it would be better to improve

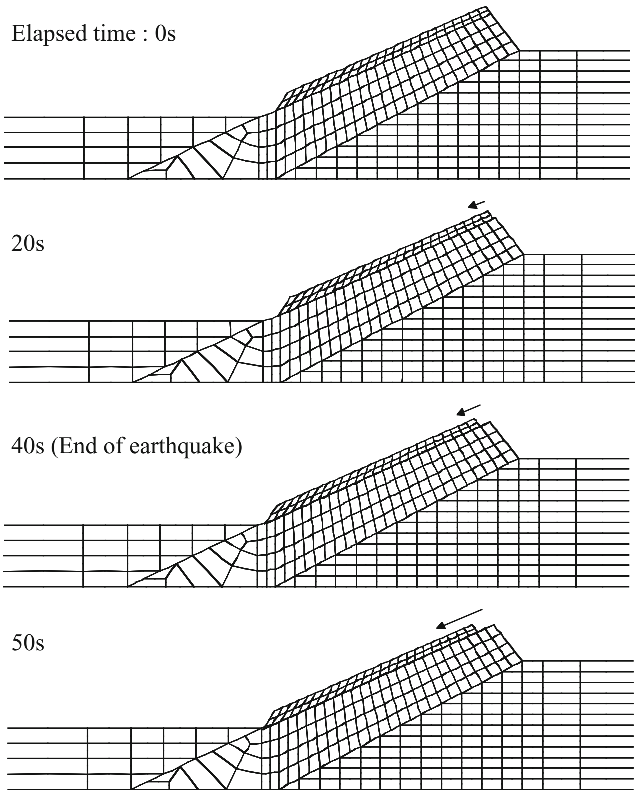

Fig. 8 Movement of the sliding rock on the bedding plane (Wakai et al. 2010)

the numerical model for the friction and damping at the bedding plane, which will be a subject for future investigation. Although an exact simulation of the high-speed movement cannot be obtained, this analysis provides information for judging the occurrence of such a catastrophic failure.

Conclusions and Social Impact

As mentioned in the first part of this report, for developing the technical guidelines for risk assessment of the earthquake-induced landslides, as one of the most important missions in our activities, we have established a task force to carry out the special research project entitled "Development of a methodology for risk assessment of the earthquake-induced landslides". Altogether 8 Working Groups, which are carrying out concrete investigations and analyses on individual items, were organized to cover the all objectives of the task force.

Whole investigation results by individual 8 Working Groups will be combined, and finally the appropriate technical guidelines for risk assessment of the earthquake-induced landslides will be made up, based on the comprehensive analyses of all collected data. It will have been all completed until April 2012.

The results of the activities will be finally reported in the organized session during a newly planned international symposium on the earthquake-induced landslides held on 7–9 November 2012, in the Kiryu City, Gunma Prefecture, Japan. The conference will be designed to provide a valuable opportunity for exchange of opinions with landslide hazards and their management. We have just started a new working group in preparation for the holding of the conference.

Acknowledgments A part of the present study was conducted as the IPL Project #154. The authors would like to thank for the support.

References

Doshida et al (2012) Section 1.2, Features of past earthquakes around Japan, Earthquake-induced landslides – summary of research in the Japan Landslide Society Earthquake-induced Landslides Research Project, pp 5–7

Nagata, Nozaki (2007) Slope disasters in mountainous area, The investigation report on the 2004 Mid Niigata prefecture earthquake by The Japan Landslide Society, pp 16–172

Wakai A, Ugai K (2004) A simple constitutive model for the seismic analysis of slopes and its applications. Soils Found 44 (4):83–97

Wakai A, Ugai K, Onoue A, Kuroda S, Higuchi K (2010) Numerical modeling of an earthquake-induced landslide considering the strain-softening characteristics at the bedding plane. Soils Found 50 (4):515–527

Environmental Impact of the Landslides Caused by the 12 May 2008, Wenchuan, China Earthquake

Lynn Highland and Ping Sun

Abstract

The magnitude 7.9 (M_w) Wenchuan, China, earthquake of May 12, 2008 caused at least 88,000 deaths of which one third are estimated to be due to the more than 56,000 earthquake-induced landslides. The affected area is mountainous, featuring densely-vegetated, steep slopes through which narrowly confined rivers and streams flow. Numerous types of landslides occurred in the area, including rock avalanches, rock falls, translational and rotational slides, lateral spreads and debris flows. Some landslides mobilized hundreds of million cubic meters of material, often resulting in the damming of rivers and streams, impacting river ecosystems and morphology. Through an extensive search of both Chinese- and English-language publications we provide a summary of pertinent research on environmental effects, emphasizing key findings. Environmental effects caused by landslides include the alteration of agriculture, changes to natural ecosystems, changes in river morphology due to landslide dams and other effects such as sedimentation and flooding. Damage by landslides to the giant panda reserve infrastructure and habitat, was severe, threatening the survival of one of the world's rarest species. The Panda reserves are of national significance to China, and to the vital tourism economy of the region. One of the major impacts to both the natural and built environment is the complete relocation of some human populations and infrastructure to new areas, resulting in the abandonment of towns and other areas that were damaged by the earthquake and landslides. The landslide effects have affected the biodiversity of the affected area, and it has been hypothesized that strict forest preservation measures taken in the years preceding the earthquake resulted in a reduction of the environmental damage to the area.

Keywords

Earthquake-triggered landslides • Environmental effects • Wenchuan • China

Introduction

Mass movements affect the following elements of the environment: (1) the topography of the earth's surface, particularly the morphologies of mountain and valley systems, both on the continents and the ocean floors; (2) the character/quality of rivers and streams and groundwater flow; (3) the forests that cover much of the earth's subaerial surface; and (4) the habitats of natural wildlife that exist on the earth's surface, including rivers, lakes and oceans (Schuster

---

L. Highland (✉)
U.S. Geological Survey, MS 966, Denver, CO, USA 80225
e-mail: highland@usgs.gov

P. Sun
Institute of Geomechanics, Chinese Academy of Geological Sciences, Beijing 100081 China

C. Margottini et al. (eds.), *Landslide Science and Practice*, Vol. 5,
DOI 10.1007/978-3-642-31427-8_23,

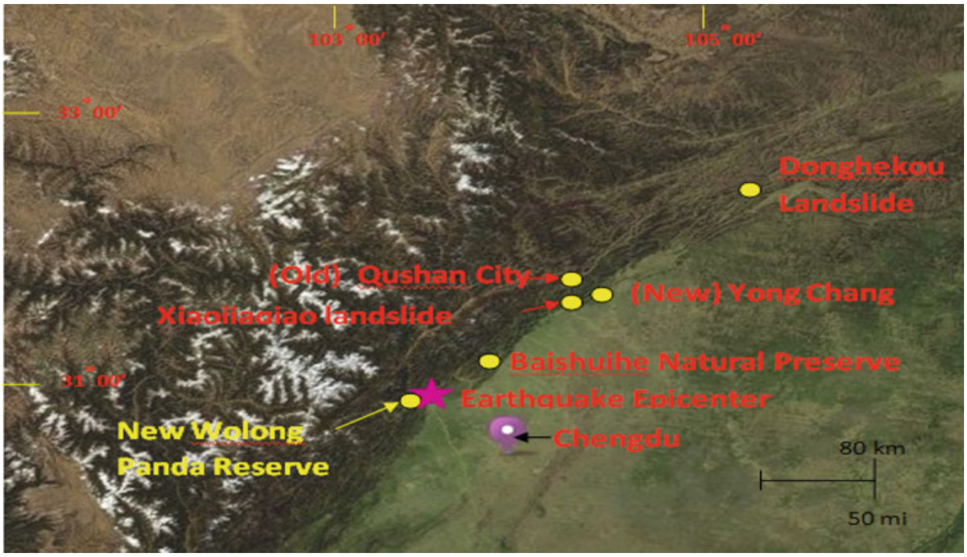

Fig. 1 This map shows the locations of the cities, landslides and the reserve and preserve discussed in the paper

and Highland 2007). The landslides resulting from the Wenchuan earthquake resulted in profound effects to the natural and built environment; and many of these effects have been negative. We have examined 36 reports published in English and Chinese languages that represent many scientific disciplines, which document the environmental effects of the earthquake-triggered landslides. In what follows, we present a summary of some of these findings. Cheng et al. (2008) cite studies published previously on some of the environmental effects from landslides caused by worldwide strong earthquake events that include similar affects to those caused by the Wenchuan earthquake-triggered landslides. Some of these effects cited in other events are, for example: long-term changes that occur to soil temperature, chemistry and soil microbiology; plant succession disturbances on bare slopes; loss of root strength that occurs through disturbance and denudation of slopes; change in animal habitat; increases in forest canopy gaps that change the understory environment. The following sections summarize some of the key findings by researchers on environmental effects.

The Wenchuan Earthquake and Landslide Overview

The Wenchuan Earthquake occurred May 12, 2008 with a USGS moment magnitude of 7.9, Maximum Modified Mercalli Intensity XI–XII (Yin et al. 2009). The epicenter (shown in Fig. 1) was on the Longmenshan fault system in a steep, mountainous area of Sichuan County, China.

There are estimated to have been 56,000 landslides during this quake and its aftershocks documented by field investigations and information acquired from satellite data (Cui et al. 2009; Dai et al. 2011; Sato and Harp 2009; Yin et al. 2009). There were landslides, rock avalanches, rock falls, debris flows initiated within landslides, and lateral spreads. There were many instances of reactivation of old landslide at some sites, and the creation of 256 landslide dams on streams and rivers (Yin et al. 2010, Wang et al. 2008, Chigara et al. 2010).

After the earthquake, teams of scientists from the Chinese government, various universities, and other researchers throughout the word, were in the field studying the earthquake and landslide effects on ecosystems, agriculture, soils, wildlife, soil and water chemistry, stream and river hydrology, and geomorphological effects. In what follows we summarize some of their results.

Geographic/Geomorphic Character of the Area

The earthquake and landslides affected several provinces, primarily Sichuan Province. The land expanse of the area affected by the earthquake is mostly mountainous. The relief of the area is greater in the northwest and lower in the southeast, with the highest elevation being 4,769 m and the lowest, 540 m. The area has some of the highest releif in the world. The affected area, features densely-vegetated, steep slopes through which narrowly confined rivers and streams flow. Hillsides are typically densely-vegetated and abundant rainfall feeds rivers and streams that flow through narrow, steep-walled valleys. Hillslope gradients within the deeply-dissected topography are steep, with many slopes commonly exceeding 30°. Landslides have been identified as a dominant erosion process throughout this region prior to the earthquake, and many landslide dams have periodically blocked drainages throughout the evolution of the incised river gorges, (Quimet 2010).

There are many wildlife, forest, and other types of nature reserves, parks and open-spaces in the area, as well as UNESCO cultural and natural heritage sites. The local economies benefit greatly from the tourists who visit the area to experience the impressive natural environment, and preservation activities.

Landslide Effects on Mountain-Valley Morphology

Landslide dams act as a primary control on river morphology and longitudinal bed profiles, inhibiting incision and further preventing the complete adjustment of rivers to regional tectonic and climatic occurrences (Korup 2006). Often, by construction of channel spillways or outlet tunnels, human remedial efforts affect the longevity of landslide dams and their impoundments, and thus influence the long-term effects of these natural features on mountain-valley morphology. Landslide-related changes in soil properties and surface exposure may also contribute to changes in the hydrology and sediment transport regimes of the area. In addition, the combination of the increased supply of unconsolidated landslide debris and denuded slopes increased the frequency and magnitude of deadly post-event debris flows in the affected areas (Fan et al. 2009; Tang et al. 2009; Liu and Sun 2009).

Inventories compiled from satellite-imagery recorded the formation of at least 256 landslide dams, contributing to drastic changes in drainage network characteristics and channel morphology, loss of aquatic wetland and riparian habitat, and reduction in water quality (Fan et al. 2009; Xu, L. et al. 2009; Xu, Q. et al. 2009). Figure 2 shows one of the largest landslide dams which was formed by the Xiaojiaqiao landslide in Anxian County. Researchers have used satellite imagery to assess the amount of material displaced by landslides following the earthquake, and found that it was two to seven times greater than the mass displacement due to uplift caused by the fault motion. They conclude that, even if only a fraction of the debris from the landslides is removed by erosion, it will still result in a net loss of material from the region (Parker et al. 2011).

Fig. 2 The Xiaojiaqiao landslide which formed the second largest landslide dam on the Chaping River, in Anxian County. An artificial spillway was blasted and dug through the landslide dam to allow the river to resume its flow. The dead tree-line marks the elevation of the maximum level of the water, which was building up behind the dam, before the spillway was dug (Photo taken July 6, 2008, by Lynn Highland, U.S. Geological Survey)

Landslide dams can influence mountain-valley morphology significantly in the vicinity of the dam sites, as well as upstream and downstream. The effects are: (1) impoundment of lakes that results in changes in stream gradients, (2) deposition of lacustrine and deltaic sediments in these impoundments that causes changes in surficial morphology and geologic materials upstream from the dams, (3) diversion of stream channels at and near the dam sites, (4) formation of avulsively-shifting channels downstream from the dams by the introduction of high sediment loads from erosion of landslide deposits or sediments in the landslide-dammed lakes, and (5) secondary landslide activity along the shores of the impounded lakes due to rapid drawdown when the dams fail. Often, by construction of channel spillways or outlet tunnels, remedial efforts by humans affect the longevity of landslide dams and their impoundments, and thus influence the long-term effects of these natural features on mountain-valley morphology. Deposition of lacustrine and deltaic sediments in lakes impounded by dams result in changes of stream gradient, surface morphology and surficial geology upstream from the blockages. There is the formation of shifting channels downstream from the dams by the introduction of high sediment loads from the erosion of the landslide deposits. There can be secondary landsliding along the shores of the impounded lakes because of reservoir filling or rapid drawdown of the natural dams, or when they fail suddenly (Korup 2006; Schuster and Highland 2007). Most lakes formed by landslide dams are short-lived because most landslide dams fail. However, a few become permanent geomorphic features. Sudden breaching can cause rapid flooding downstream. There were at least 33 of the total landslide dams that were major threats and which were mitigated by engineering measures (Fan et al. 2009; Liang 2009).

Landslide Impact on Ecosystems and Habitat

The earthquake was centered in the Minshan-Hengduan Mountains, a key area of biodiversity conservation that is ecologically very sensitive and rich in species: 12 national first-class protected animals and 24 state-level rare and endangered plants have habitats there. Like the situation with the bamboo habitat, possible invasion of alien plant species is possible, interfering with natural plant succession on denuded slopes (Li et al. 2008). The red pandas and golden monkeys of the area may also have been affected (Wang et al. 2008). The landslides resulted in the alteration of 67,018 ha (hectares) of natural ecosystems, which includes forests, shrubs, grassland, and wetlands, and have caused the permanent loss of an estimated 400,000 ha of crop land affected in terms of changes to habitat or habitat destruction – studies are ongoing (Wang and others 2008).

Surficial changes that occurred in the Minushan-Hengduan Mountain region severely damaged one of the world's most biodiverse temperate forests and an important carbon sink in China. The combination of the vegetation loss and decomposition has the potential to increase atmospheric CO_2 emissions and reduce the rate of carbon sequestration in the area (Ouyang et al. 2008). It has been estimated that due to landslides, the burial of approximately 235 million tons of carbon in the form of vegetation from Longmenshan's forest ecosystem may have future effects in the form of methane production and possible release into the atmosphere (Ren et al. 2009). Viña et al. (2009) estimate that 192.6 square km of forest were lost in Wenchuan County, representing just under 11 % of the forest cover that was mapped in 2007. These authors present the hypothesis that strict forest preservation measures taken in the years preceding the earthquake had an impact in reducing the total forest area lost from landslides, although studies of this idea are ongoing.

Landslide Impact on Forested Areas

In addition to the mountain slopes that were denuded of trees and other plants, there are other changes to the forest ecosystem related to landslides in the earthquake-affected area occurred. The mobilization of debris flows has increased, although the rate of increase has not been documented as of this writing. Vittoz et al. (2001) stated that along with the direct effects of forest removal, many trees eventually die of pathogenic attacks, soil drought or disturbances of root system development in the decades that follow the debris flows. Natural rates of erosion will, for at least a number of years, be accelerated. As previously mentioned, changes in plant succession on bare slopes may change the nature of the eventual re-growth of the forest. In addition to the panda's food, mature bamboo and other types of forests also provide food and shelter for a number of animal species, which may be affected by the removal of the forest cover.

Landslide Impact on Giant Panda Reserves

There are 49 giant panda nature reserves in 43 counties most of which are located in Sichuan, with a few in Gansu and Shaanxi Provinces (Deng et al. 2010). There are estimates of between 2 and 3,000 Pandas in the wild, and 53 % of the panda habitat was affected by the landslides (Deng et al. 2010). At the Wolong Reserve, about 30 km from the epicenter (and a popular tourist destination) almost all panda facilities were destroyed in the earthquake and about 6,117 ha out of a total of 203, 601 ha of habitat in the Wolong Reserve was destroyed by earthquake (Deng et al. 2010). It is not expected that pandas will move elsewhere, because they exist within a very narrow range of elevation, climate, and subsist only where bamboo grows.

A total forest area of 48,180 ha was damaged by the earthquake (Deng et al. 2010) and researchers have found that large habitat areas have been fragmented into smaller, disconnected patches. This fragmentation may be just as harmful as habitat destruction, because it isolates pandas from each other resulting in disturbance of group reproduction and communication behaviors (Xu, L. et al. 2009). There is also a danger of alien species intruding on denuded slopes, formerly covered by bamboo (Li et al. 2008). A new center is being located in the Shenshuping area of Gengda Township (shown on Fig. 1 as New Wolong Panda Reserve), some 22 km northeast of its previous location, because it is thought to be a safer site, by many researchers. Figure 3 shows before and after photos illustrating the damage to the Panda's habitat at Sichuan Baishuihe Natural Preserve.

Landslide Impact on Agriculture and Livestock

Sichuan is a major agricultural province in China, with the highest rice yield in the nation. Agricultural products occupy an important position in the region's economy, but the agricultural system has been severely damaged and is still threatened by the earthquake and landslide effects. According to the National Economic Prosperity Monitor Center of China, in the six worst affected counties at least 365 million pigs died, and approximately 27 million ha of food crops were damaged (Deng et al. 2009). The earthquake not only caused crop loss, but rock- and mudslides have caused an estimated 400,000 ha of arable land to be permanently lost. Iirrigation systems have also been damaged and will require lengthy repairs. According to a United Nations report, $6 billion in damage occurred to the province's agricultural sector (United Nations FAO report 2008). In addition, agricultural land is vulnerable as reconstruction begins, since this land may be taken over by temporary settlements or used for rebuilding towns, such as the case

Fig. 3 The Sichuan Baishuihe Natural Preserve, 30 km from Chengdu, showing a general area in the preserve before (*top*) and a general photograph (in a different location) after the landslides occurred (*bottom*). This preserve's giant panda habitat was badly damaged with vegetation loss of 3,300 ha. Photograph and information: http://www.panda.org.cn/english/News/news_view.asp?newsid=219

of Yong Chang town, which is being constructed in a new area, replacing the devastated Qushan town.

Impact of Population Relocation Away from Hazardous Areas

The Town of Qushan, in the County seat of Beichuan in the epicentral area, was devastated from earthquake shaking, earthquake-triggered landslides, and subsequent debris flows. The county town, which prior to the earthquake had a population of 20,000, has been transformed into a memorial park. The town will not be rebuilt as the site is too vulnerable to geologic hazards. As a result, it is thought that the area around the park will return to a somewhat natural state. The new Beichuan county seat, Yong Chang, is being built 23 km away, in a location deemed to have a lower susceptibility to earthquake shaking and landslides (Huang et al. 2009). The old location of Qushan town and the new town, Yong Chang are shown in Fig. 1. Many survivors of the earthquake have been relocated to the newly-built city. It has been built on the banks of the Anchang River and surrounded by green open space and parks (Beijing Review 2011). The Chinese government is providing new farmland in close proximity to the new town, as well as new housing, cultural amenities and greenbelts for the displaced population, thereby drastically transforming the former environment of the new town site.

Fig. 4 Two photographs of the Donghekou landslide. The top photo shows the landslide in July, 2008, two months after the earthquake. The landslide buried Donghekou Village and killed at least 300 people. Donghekou Village will not be rebuilt and is now a memorial to the victims. The bottom photo shows the memorial park that was built on top of the landslide. The top photograph is by Lynn Highland, USGS, and the bottom photograph was taken by Dr. Fawu Wang, Shimane University, Japan, in August, 2010

Another example of the environmental changes from landslides is the site of the Donghekou landslide (location shown in Fig. 1). This extremely large landslide buried at least 300 people, and destroyed Donghekou Village. Figure 4 shows two photos of the Donghekou area; one photo shows this area two months after the earthquake and landslides occurred, and the other photo, taken in 2010, shows the current state of the site. The site has become a permanent memorial park and the Donghekou Village will not be rebuilt.

Conclusion

The Wenchuan earthquake can be considered to be one of the best examples showcasing a wide variety of landslide effects on both the built and natural environments. Fortunately, this earthquake and its landslide effects will be widely studied by scientists in a variety of disciplines, and the composite results should be extremely informative. Also, the geographic distribution and the documented effects of these landslides will give planners, government officials and the public, valuable information for the improvement of landslide hazard mitigation.

References

Beijing Review (2011) From rebirth to revival, http://www.bjreview.com.cn/Cover_Stories_Series_2011/2011-05/11/content_357027_2.htm

Cheng S, Kong J, Song H (2008) Wenchuan 5/12 earthquake and Giant Panda Habitat in Wolong, China: a review of strong earthquake effects. J Mt Sci 26(A1):65–69

Chigira M, Wu X, Inokuchi T, Wang G (2010) Landslides induced by the 2008 Wenchuan erthquake, Sichuan, China. Geomorphology Elsevier 118:225–238

Cui P, Chen XQ, Zhu YY, Su FH, Wei FQ, Han YS, Liu HJ, Zhuang JQ (2009) The Wenchuan earthquake (May 12, 2008) Sichuan Province, China, and resulting Geohazards. Natural Hazards, Springer, 56(1):19–36

Dai FC, Xu C, Yao X, Xu L, Tu XB, Gong QM (2011) Spatial distribution of landslides triggered by the 2008 Ms 8.0 Wenchuan earthquake, China. J Asian Earth Sci 40(4):883–895

Deng X, Ge Q, Xu Z, Wang S, Jiang Q, Lin Y (2009) Immediate impacts of the Wenchuan earthquake on the prices and productions of grain and pork products. Front Earth Sci China 8

Deng, Xiangzheng, Qunou, Jiang, Ge, Quangsheng, Yang, Linsheng (2010) Impacts of the Wenchuan Earthquake on the Giant Panda Nature Reserves in China. J Mt Sci 7 (2): June, 7(2):197–206

Fan X, Gorum T, van Westen CJ, Xu Q, Tang C, Huang R (2009) Distribution of Large Landslides and Landslide Dams triggered by the Wnechuan earthquake, Sichuan, China. Geophys Res Abstr 11: EGU2009–2863

Huang RQ, Li YS, Li WL (2009) Engineering geological evaluation of reconstruction sites following the Wenchuan earthquake. Bull Eng Geol Environ 68:449–458

Korup O (2006) Rock-slope failure and the river long profile. Geology 34:45–48

Li W, Fan QA, Zhang F (2008) Potential effect of Wenchuan earthquake, in invasion Alien species and management strategies. Acta Ecologica Sinica 28(12):5871–5875

Liang J (2009) Fluvial process influenced by earthquqke lakes and restoration of mountain rivers. J Sichuan Univ (Eng Sci Edition) 41(6):13–17

Liu Z, Sun S (2009) The disaster of May 12th Wenchuan earthquake and its influence on debris flows. J Geogr Geol 1(1):26–30

Ouyang AY, Xu WH, Wang XZ, Wang WJ, Dong RC, Zheng H, Lid H, Liz HQ, Ahang HF, Zhuang CW (2008) Impact assessment of Wenchuan earthquake on ecosystems. Acta Ecol Sin 28 (12):5801–5809

Parker RN, Densmore AL, Rosser NJ, de Michele M, Li Y, Huang R, Whadcoat S, Petley DN (2011) Mass wasting triggered by the 2008 Wenchuan earthquake is greater than orogenic growth. Nat Geosci 4:449–452. doi:10.1038/ngeo1154

Quimet WB (2010) Landslides associated with the May 12, 2008 Wenchuan earthquake: implications for the Erosion and Tectonic evolution of the Longmen Shan. Tectonophysics 491:244–252

Ren D, Wang J, Fu R, Karoly DJ, Hong Y, Leslie LM, Fu C, Huang G (2009) Mudslide-caused ecosystem degradation following the Wenchuan earthquake 2008. Geophys Res Lett Am Geophys Un 36. doi:10.1029/2008GL036702

Sato HP, Harp EL (2009) Interpretation of earthquake-induced landslides triggered by the 12 May 2008, M 7.9 Wenchuan earthquake in th Beichuan area, Sichuan Province, China, using satellite imagery and Google Earth. Landslides 6:153–159, Springer

Schuster RL, Highland LM (2007) Overview of the effects of mass wasting on the natural environment. Environ Eng Geosci Geol Soc Am XIII(1):25–44

Tang C, Zhu J, Li WL, Liang JT (2009) Rainfall-triggered Debris flows following the Wenchuan earthquake. Bull Eng Geol Environ 68 (2):187–194, Springer Verlag

United nations food and agriculture organisation (FAO) News (2008) http://www.un.org/apps/news/story.asp?NewsID=27211&Cr=sichuan&Cr1

Viña A, Chen X, McConnell W, Liu W, Xu W, Ouyang Z, Zhang H, Liu J (2010) Effects of natural disasters on conservation policies: the case of the 2008 Wenchuan earthquake, China. AMBIO A J Hum Environ 40(3):274–284. doi:10.1007/s13280-010-0098-0

Vittoz P, Stewart GH, Duncan RP (2001) Earthquake impacts in old-growth *Nothofagus* forests in New Zealand. J Veg Sci 12:417–426

Wang, Gonghui, Kamai, Hirotaka, Chigira, Masahiro, Wu, Xiyong (2008) Some catastrophic landslides triggered by the May 12, 2008 Sichuan earthquake. In: Casagli, Nicola, Fanti, Riccardo, Tofani, Veronica (eds) Proceedings of the first world landslide forum, Nov, 2008, Tokyo, Japan, parallel sessions. http://www.iclhq.org/WLFweb/WebProceedings_Index.htm

Wang D, Li S, Sun S, Wang H, Chen A, Li S, Li J, Lu Z (2008b) Turning earthquake disaster into long-term benefits for the Panda. Conserv Biol Soc Conserv Biol 22(5):1356–1360

Xu L, Dai F, Tu X, Wang M (2009) Morphological and hydrological effects of Wenchuan earthquake on modern rivers. Geol J China Univ 15(3):365–370

Xu Q, Fan XM, Huan RQ, Van Westen C (2009) Landslide dams triggered by the Wenchuan earthquake, Sichuan Province, South West China. Bull Eng Geol Environ 68:373–386

Yin Y, Wang F, Sun P (2009) Landslide Hazards triggered by the 2008 Wenchuan earthquake, Sichuan, China. Landslides 6(2):139–152

Yin J, Chen J, Xu X, Wang X, Zheng Y (2010) The characteristics of the landslides triggered by the Wenchuan M_s 8.0 earthquake from Anxian to Beichuan. J Asian Earth Sci 37(5–6):452–459

Mechanism of Landslide Composed of Strongly Weathered Mudstone Induced by the 2004 Mid-Niigata Earthquake

Keizo Ugai, Akihiko Wakai, Fei Cai, and Seiichiro Kuroda

Abstract

This paper reports the mechanism of a landslide composed of strongly weathered mudstone induced by the 2004 Mid-Niigata Earthquake. The size of the landslide is 250 m long, 150 m wide and 15 ~ 20 m deep. Undisturbed soil samples of strongly weathered mudstone were obtained from the soil layer near the assumed sliding surface by boring. Cyclic undrained triaxial tests performed on the undisturbed soil specimens revealed the possibility of the landslide mechanism that the excess pore water pressure was induced in the soils near the sliding surface by the cyclic earthquake shaking and the safety factor of the slope became fairly less than 1.0, which led to the long-distance sliding of the landslide.

Keywords

Earthquake-induced landslide • Geotechnical testing • Landslide mechanism • Weathered mudstone

Introduction

A large-scale landslide occurred during the 2004 Mid-Niigata Earthquake (M 6.8) (Onoue et al. 2006; Wakai et al. 2010). The geological constitution of the slope was strongly weathered mudstone that has the history of about five million years. Photo 1 shows the overview of the landslide, the size of which is 250 m long, 150 m wide and 15 ~ 20 m deep.

The sliding distance was estimated as 30 ~ 40 m. Figure 1 is the central section view of the landslide, showing the slope shapes before and after failure and boring locations set up after the landslide. After the landslide deep wells were constructed at the landslide site to collect the ground water and lower the water level. Figure 2 shows acceleration records observed at the station 8 km away from the landslide site.

From Fig. 2 it is seen that the strong motion continued more than 10 s and the acceleration records exceeded 500 gal at several moments during the earthquake shaking.

Properties of Weathered Mudstone

Figure 3 shows a particle size distribution curve of the weathered mudstone obtained from the soil layer near the assumed sliding surface by boring. It is found that this soil is classified into sandy clay. The density of soil particle was 2.71 g/cm^3, the unit weight of the undisturbed soil was 1.95 g/cm^3, the liquid limit was 65.8 and the plasticity index was 41.8.

Undisturbed soil sampling was done from two locations, that is, the lower surface of the slope (Photo 2) and the soil layer near the assumed sliding surface whose location is indicated in Fig. 1. Undisturbed soil samples from the above two locations were subject to the consolidated undrained triaxial tests and the cyclic undrained triaxial tests in a laboratory. Both samples from these two locations showed similar test results. The test results of the undisturbed soil samples obtained from the soil layer near the assumed sliding surface are show below.

K. Ugai (✉) • A. Wakai • F. Cai
Civil Engineering, Kiryu, Gunma University, Gunma 376-8515, Japan
e-mail: ugai@ce.gunma-u.ac.jp

S. Kuroda
National Institute for Rural Engineering, Tsukuba, Japan

C. Margottini et al. (eds.), *Landslide Science and Practice*, Vol. 5,
DOI 10.1007/978-3-642-31427-8_24,

Photo 1 Overview of the landslide site

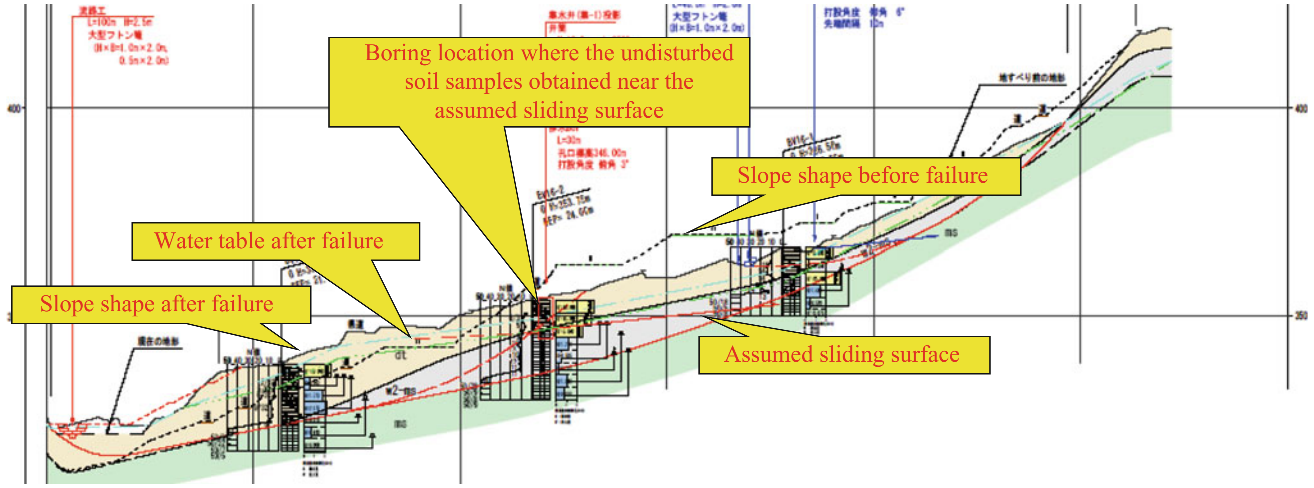

Fig. 1 Central section view of the landslide

Consolidated Undrained (CU) Triaxial Test Results

Static tests: CU tests for the undisturbed soils were done under the initial confining pressures of 80, 160, 320 kN/m^2. Figure 4a shows relations of the principal stress difference and the excess pore water pressure with the axial strain. Figure 4b shows the effective stress paths during the tests. From Fig. 4a, b it is found that the positive excess pore water pressure arises due to loading and the soil specimens show undrained shear behaviour similar to lightly over-consolidated clays. From Fig. 4b the effective cohesion and the effective friction angle are calculated as 8.5 kN/m^2 and 34.8°, respectively. The undrained shear strength of the specimens indicated by small circles in Fig. 4b is summarized in Table 1. From this Table the average ratio of the undrained shear strength and the initial confining pressure is calculated as 0.9.

Cyclic Undrained Triaxial Test Results

Dynamic tests: Cyclic undrained triaxial tests for the undisturbed soils were done under the initial confining pressure of 170 kN/m^2 which corresponds to the mean effective principal stress at the sampling depth. Test results are shown in Fig. 5a, b, c where relations of the difference of axial and lateral stresses, the axial strain and the excess pore water pressure ratio, respectively, with loading cycles are seen. Figure 5c reveals that the positive excess pore water pressure arose and increased steadily due to the undrained cyclic loading. It is noticed that the relatively high positive excess pore water pressure remained after the loading cycles ended. From these phenomena it is expected that the pore water pressure near the sliding surface of the landslide increased during the earthquake and the high pore water pressure remained after the earthquake, which led the soils near the sliding surface to the weak strength condition and considerably lowered the safety factor of the landslide slope, having triggered the occurrence of the landslide.

Figure 6 shows the relation between the stress ratio $(\sigma^d/2\sigma_c)$ and the number of loading cycles, where $\sigma^d/2$ is the maximum shear stress and σ_c is the confining pressure. The liquefaction resistance ratio R_L is defined as the value of $(\sigma^d/2\sigma_c)$ where the double amplitude of the axial strain reaches 5 % at the 20th loading cycle. From Fig. 6, R_L of the undisturbed soils is 0.473. For reference, R_L of the undisturbed soils obtained from the lower surface of the slope (Photo 2) was 0.32. This means that the soils near the lower surface of the slope is more disturbed compared to the soils near the assumed sliding surface.

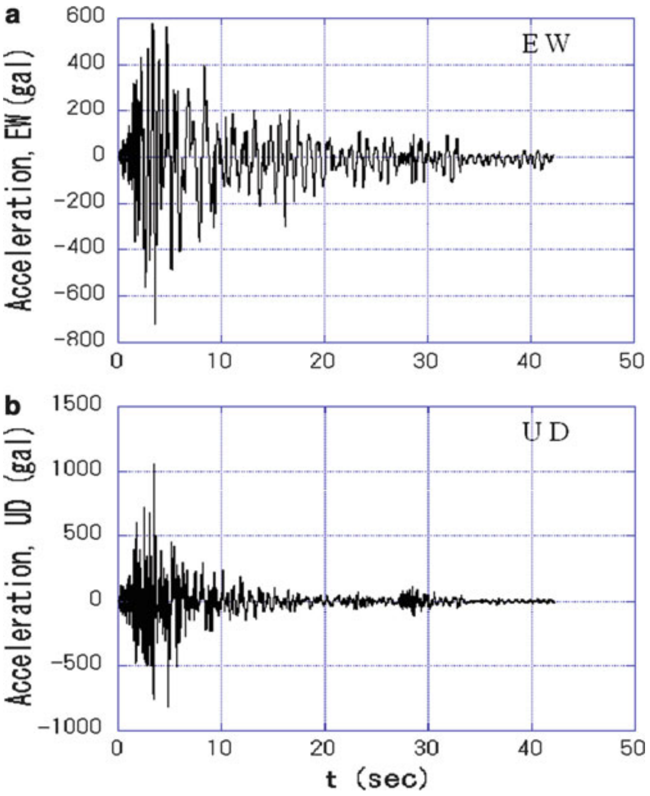

Fig. 2 Acceleration records observed at the station 8 km away from the landslide site

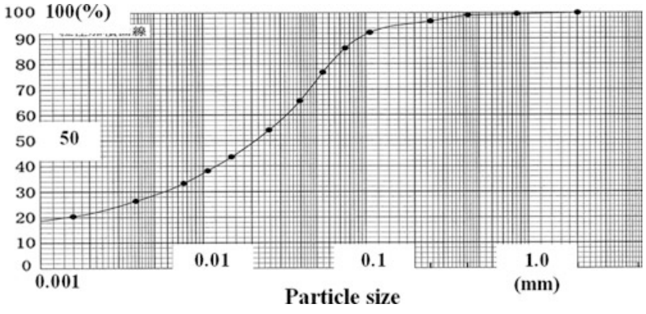

Fig. 3 Particle size distribution curve of weathered mudstone obtained from the soil layer near the assumed sliding surface

Discussions on the Mechanism of the Landslide

Based on the test results the mechanism of the landslide is discussed as follows. To make the discussions simple the slope before failure is assumed as an infinite slope with the sliding surface of 18 m depth, that was estimated from Fig. 1. The angle of the sliding surface and the depth of the ground water table are assumed 20° and 5 m from the slope surface, respectively. Figure 7 shows a block with 1 m width which is a part of the slope above the sliding surface. Forces acting on this block are shown in Fig. 7. Lateral forces acting on both sides of the block were assumed balanced each other.

Photo 2 Undisturbed soil sampling at the lower surface of the slope

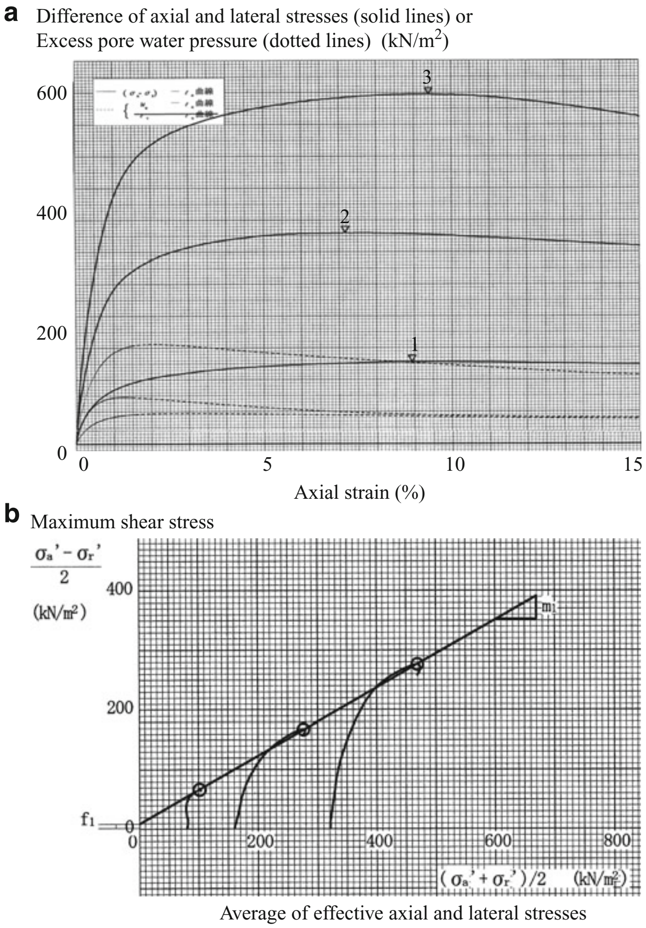

Fig. 4 (**a**) Relations of the principal stress difference and the excess pore water pressure with the axial strain during CU tests, (**b**) Effective stress paths during CU tests

The weight of the block is 351 kN (as $\rho_{sat} = 1.95\ g/cm^3$) and its effective weight is 224 kN, from which the effective normal force on the sliding surface is taken as 210 kN (=224 × cos20°). Assume the acceleration of 500 ~ 600 gal acting on the block which is estimated from the peak values of the acceleration records shown in Fig. 2.

Table 1 Ratio of the undrained shear strength and the initial confining pressure obtained by CU tests

Initial confining pressure (A) kN/m^2	Undrained shear strength (B) kN/m^2	B/A	Average of B/A
80	65	0.81	0.9
160	165	1.03	
320	274	0.86	

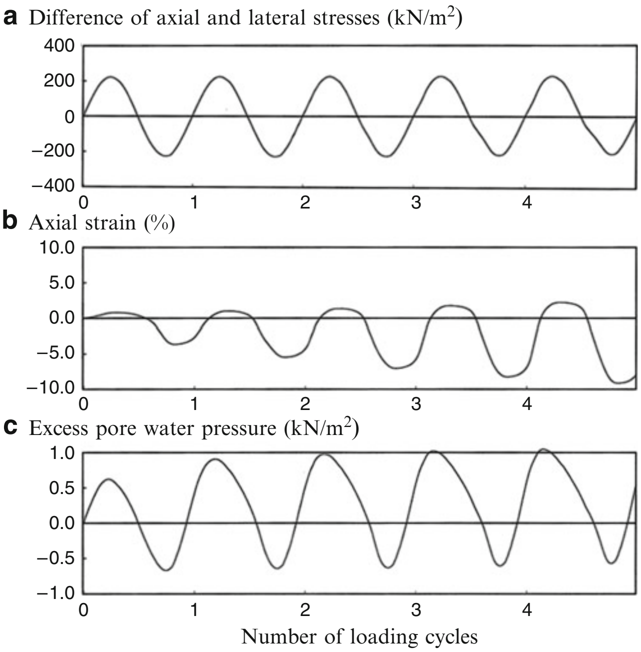

Fig. 5 (**a**) Relation of difference of axial and lateral stresses with number of loading cycles, (**b**) Relation of axial strain with number of loading cycles, (**c**) Relation of excess water pressure with number of loading cycles

Then the shear forces corresponding to these accelerations become 176 ~ 211 kN. Therefore, the ratio of the shear force and the effective normal force on the sliding surface is calculated as 0.84 ~ 1.00. This result may show that the shear force estimated from the earthquake records overcomes the static shear strength (resistance force) of the soils shown in Table 1. However, this occasion is only a few moments during the earthquake. So it is difficult to conclude the mechanism of the long distance sliding behaviour of the landslide based on the above discussions.

On the other hand when we consider the deterioration of the strength of soils due to cyclic loading during the earthquake which was shown in Fig. 6, it is not difficult to assume the mechanism of the landslide. That is because R_L of the undisturbed soils (=0.473) is much smaller than the ratio of the shear force and the effective normal force on the sliding surface (=0.84 ~ 1.00).

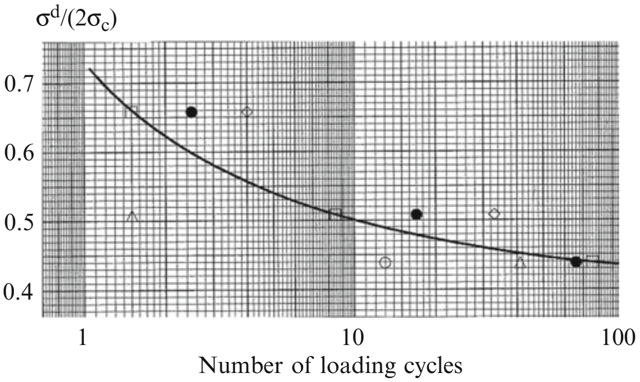

Fig. 6 Relation between $\sigma^d/(2\sigma_c)$ and number of loading cycles

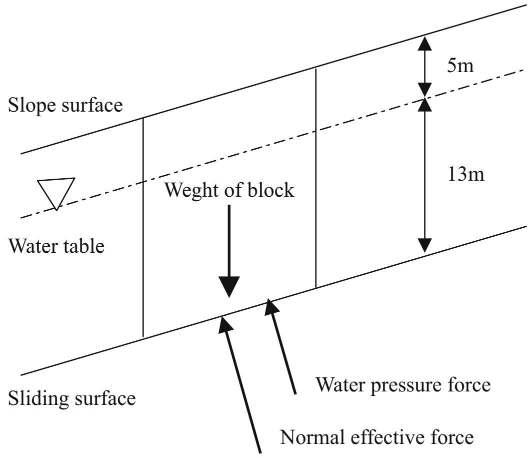

Fig. 7 Forces acting on a block with 1 m width

Moreover, the mechanism of the landslide is reasonably considered from the view point of the effective stress. From Fig. 6 after the end of the 5th loading cycle the excess pore water pressure ratio of 0.5 is remaining. By use of this value the effective normal force on the sliding surface is estimated as 110 kN (=220–220 × 0.5) after the end of the earthquake shaking. The static shear force along the sliding surface is assumed as 120 kN (=351 × sin20°). Then the static shear resistance force is calculated as 86.9 kN (=112 × tan34.8° + 8.5kN/cos20°). Therefore, the safety factor of the slope just after the end of the earthquake shaking is 0.72 (=86.9/120) which is much smaller than 1.00. This discussion reveals that the considerable amount of excess water pressure arose and increased during the earthquake, which remained in the slope after the earthquake, having resulted in the safety factor much smaller than 1.00, which led the slope to the long distance travelling failure.

Conclusions

The mechanism of a landslide composed of strongly weathered mudstone induced by the 2004 Mid Niigata Prefecture Earthquake was studied in this paper. From the discussions based on the results of the cyclic undrained triaxial tests of the undisturbed soils taken from the soil layer near the assumed sliding surface, it was concluded that the considerable amount of excess water pressure arose and increased along the sliding surface during the earthquake, which remained in the slope after the earthquake, having resulted in the safety factor much smaller than 1.00, which led the slope to the long distance travelling landslide.

Acknowledgments The present study was conducted as a “Research project for utilizing advanced technologies in agriculture, forestry and fisheries” with support from the Ministry of Agriculture, Forestry and Fisheries of Japan.

References

Onoue A, Wakai A, Ugai K, Higuchi K, Fukutake K, Hotta H, Kuroda S (2006) Slope failures at Yokowatashi and Nagaoka college of technology due to the 2004 Niigata-ken Chuetsu earthquake and their analytical considerations. Soils Found 46(6):751–764

Wakai A, Ugai K, Onoue A, Kuroda S, Higuchi K (2010) Numerical modeling of an earthquake-induced landslide considering the strain-softening characteristics at the bedding plane. Soils Found 50(4):533–545

THE SECOND
WORLD
LANDSLIDE FORUM

Tien-Shan Landslides Triggered by Earthquakes in Pamir-Hindukush Zone

Isakbek Torgoev, Rustam Niyazov, and Hans-Balder Havenith

Abstract

Sudden landslides cause big problems all over the world. These landslides often take place in the fault areas marked by a high seismic activity. Here, we study the impact of teleseismic events, located in the Pamir-Hindukush source zone, on the stability of the landslide-prone slopes in Tien-Shan. The Pamir-Hindukush zone is a unique seismic region of the Earth, where the strongest earthquakes occur at depths of 200–250 km. Some of those earthquakes have a magnitude of $M > 7$. Overall, 89 perceptible earthquakes ($M > 5$) occurred from 1991 to 2010 (according to the available data) with 35% of them occurring in springtime. In the mountainous regions of the Tien-Shan, such earthquakes cause liquefaction on water saturated slopes with accompanying slumping and cracking. This paper describes mechanisms of sudden landslide movement using the example of Sary-Bulak landslide which failed in 1976 after the earthquake in the Pamir-Hindukush zone.

Keywords

Landslides • Earthquakes • Tien-Shan • Pamir and Hindukush mountains

Introduction

The Pamir – Tien-Shan mountainous area in Central Asia is an active zone of collision between Eurasian and Indian tectonic platforms (Fig. 1a), which started in late Cainozoic. As the result of long-term tectonic and geodynamic activity marked by folding and ground uplift in Pamir – Tien-Shan area there are a lot of earthquakes and mass movements in shape of rockfalls and landslides taking place in this area (Havenith and Bourdeau 2010). The most hazardous events are landslides triggered by strong earthquakes, especially, those occurring in Pamir-Hindukush zone (Niyazov and Nurtaev 2009).

Here, we will show statistic analyses of correlation between occurrence of sensible earthquakes ($M > 4.5$) in the Pamir-Hindukush zone and the formation of large landslides in the Kyrgyz and Uzbek parts of the Tien-Shan between 1969 and 2010. It was found out that the majority of landslides out of 80 were triggered by liquefaction, then there are reactivated landslides and, finally, there are seismogenic block slides in the vicinity of active faults existing in target area.

Owing to the USGS earthquake catalogue (NEIC) there were more than 1,500 seismic events with $M > 4.5$ registered in Hindukush during the last 40 years (1969–2010). 655 seismic events out of all happened in springtime, and there were 89 seismic events with $M > 5$ registered in the target area. These events are expressed in shape of low frequency, long-lasting seismic vibrations which in springtime can cause liquefaction of water-saturated loess material followed by failure of material travelling over long distances.

I. Torgoev (✉)
Scientific-Engineering Center GEOPRIBOR, Academia of Sciences of Kyrgyz Republic, Institute of Geomechanics and Development of Subsoil, Mederova street, 98, Bishkek 720035, Kyrgyzstan
e-mail: isakbektor@hotmail.com

R. Niyazov
HYDROENGEO, Institute of Hydrogeology and Engineering Geology, Khodjibaev street, 64, Tashkent 100041, Uzbekistan

H.-B. Havenith
Department of Geology, University of Liege, B-18, 4000, Liege, Belgium

C. Margottini et al. (eds.), *Landslide Science and Practice*, Vol. 5,
DOI 10.1007/978-3-642-31427-8_25, © Springer-Verlag Berlin Heidelberg 2013

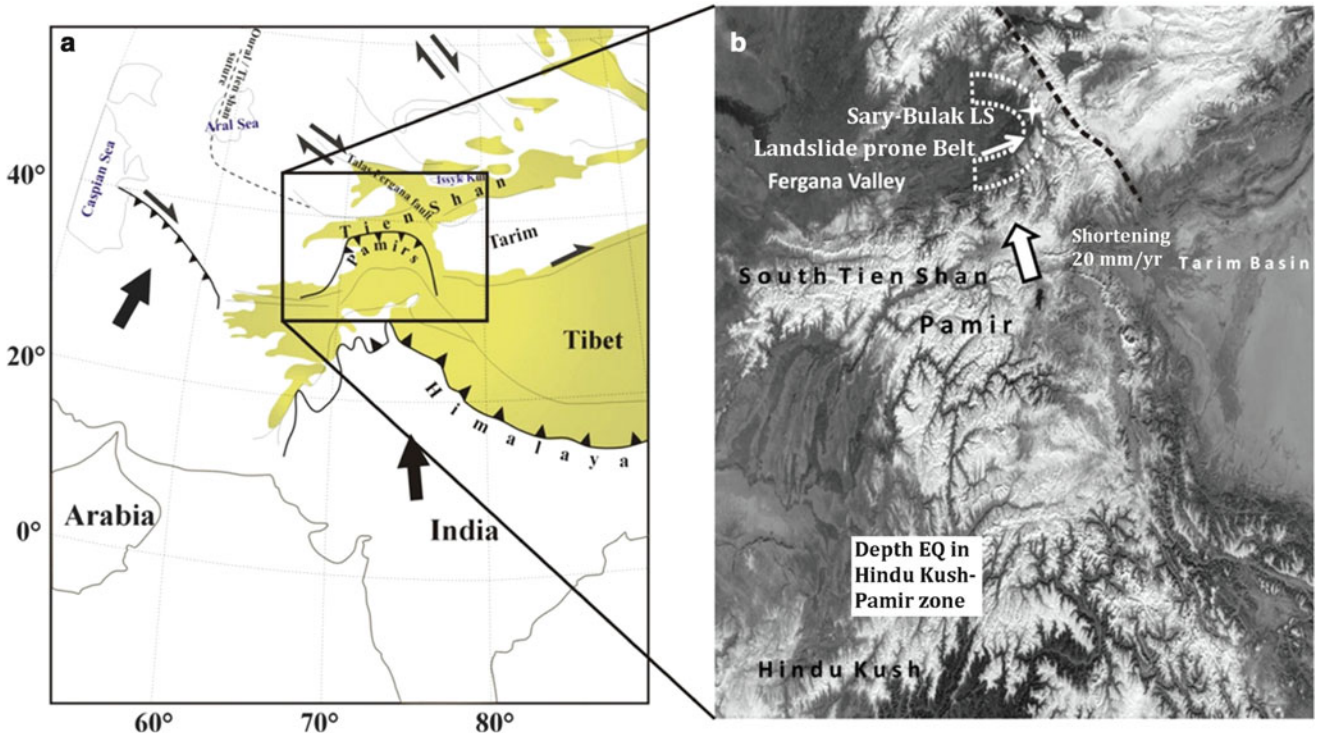

Fig. 1 (**a**) Schematic tectonic map of Tien-Shan – Pamir – Hindukush (elevation of *shaded areas* is above 2000 m, *arrows* show current motion of Iran and India towards Asia); (**b**) Deep Earthquake in the Pamir-Hindukush zone; *TFF* Talas-Fergana fault; (*dotted line* is landslide prone area in the eastern part of Fergana valley)

Such kind of landslides and flows triggered by Hindukush earthquakes are extremely hazardous because of their unexpectedness. These mass movements usually result in big death toll and significant economical losses because of high destructive energy and high speed of failed material. In connection with that there is a strong need to provide regional scale studies of the Hindukush earthquakes impact on slope stability in landslide prone areas of the Tien-Shan for reliable landslide and seismic risk estimations. The current report presents the results of studies provided on different types of large Tien-Shan landslides triggered by Hindukush earthquakes.

Correlation Between Hindukush Earthquakes and Tien-Shan Landslides

Pamir-Hindukush epicentral zone (Fig. 1a) is one of the most seismically active continental areas. Earthquakes are registered almost everywhere from crust down to upper mantle. The distribution of the deep seated Hindukush earthquakes can be described as follows: the highest concentration of earthquakes with $M > 4.9$ is found at depths of 80–150 and 180–260 km, the strongest seismic events (besides crust events) occur at the depths of 80–120 and 180-230 km. The deepest earthquakes are concentrated in the area 70–71°E and 35.5–36.5°N (Fig. 1b). Crust seismic events and those located at the depth interval 80–150 km are upthrust, shear and downthrust types, while those from the depth interval 180–260 km are basically upthrust type.

The average annual number of deap-seated earthquakes in the target area with energy class $K \geq 11$ ($M \geq 4$) and hypocenter depth 70–320 km is more than 120.

There is a high seismic activity in the higher energy level – maximal energy class can reach $K = 17$ ($M \approx 7.5$). Some of the Hindukush earthquakes have $M = 7.5$ and more, while the intensity of seismic events in the territory of Afaganistan can reach 9 balls. Shaking intensity in Kyrgyzstan and Uzbekistan, located 350–500 km far from the Pamir-Hindukush epicentral zone, is not more than 4–5 balls, but vibrations have low frequency and long duration – 2 min and more. There is some hazard related to the set of relatively weak ($M = 3.8$–4.5) Hindukush earthquakes ocuuring several days in springtime, like it was in 2002, 2003, 2008.

It is well known, that the impact of seismic vibrations on non-stable rocks is evaluated through three parametres: amplitude of vibrations, prevailing period (or frequency) and duration of these vibrations. The type and level of impact on the slope also depends on seismogeological position of this slope, its orientation with respect to hypocenter. The slope is particularly susceptible to failure when the seismic waves

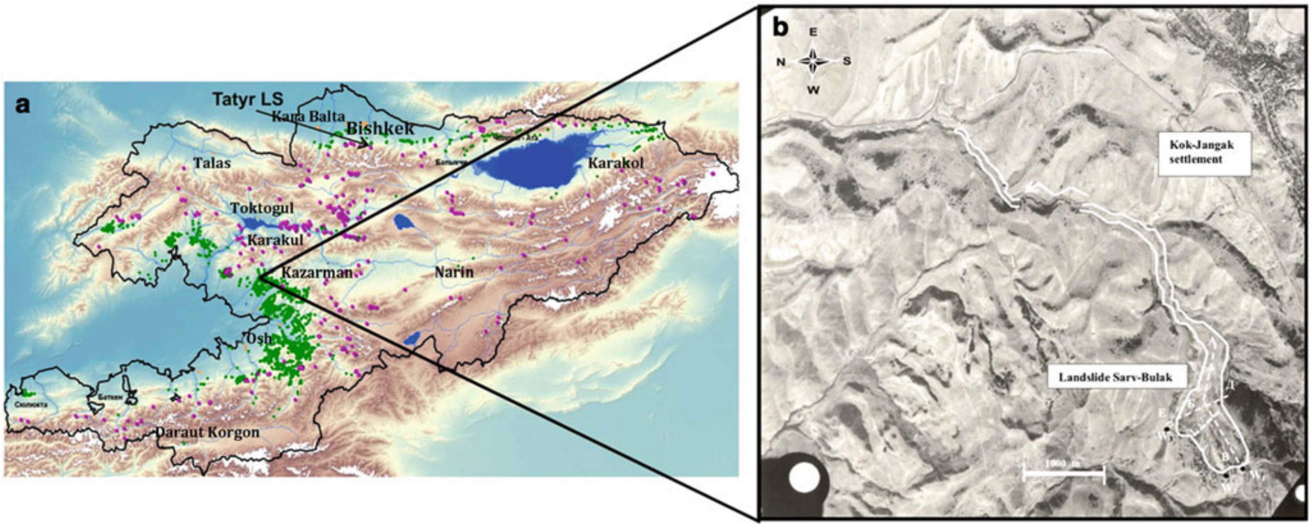

Fig. 2 (**a**) Landslides in the territory of Kyrgyzstan (*green dots* – landslides in Mesozoic-Cainozoic sediments, *red dots* – rockslides and landslides in Palaeozoic rocks); (**b**) Sary-Bulak landslide in the vicinity of Kok-Jangak settlement

propogate in the direction of the possible mass movement. In this respect, Hindukush earthquakes are mainly deap seated sources of vibrations which are propogating upwards and pushing non-stable slopes from below.

The biggest portion of seismically triggered landslides are registered in springtime (March-May), when there is high water saturation of the slopes resulting from intense snow melting and precipitation. It was especially true for the spring periods 2002–2003 when extreme atmospheric precipitation was combined with high seismic activity in Pamir-Hindukush zone. The highest number of seismic events was registered in spring, 2002, when during the March-May period there were 30 registered seismic events with $M > 4.0$ in the Pamir-Hindukush zone. The strongest seismic events occured on March, 3 2002: first, at 12:08 am the foreshock with $M = 6.3$ was registered on the depth 209 km, then 12 s later another seismic event with $M = 7.4$ was registered at a depth 256 km. Intense seismic vibrations were felt in Afganistan, Pakistan, India and over vast territory of Central Asia. On March 3, 2002 as a result of landslide and rockfall activity in Afganistan, the Surhandariya River channel was dammed causing the flooding of 400 houses. There was activisation of ancient Baipasa landslide in Tadjikistan with a total volume 5.0 millions m^3 which resulted in partial damming of Vahsh river downstream from Vahsh HPP. During the same day, in Kyrgyzstan, movements were registered on an ancient landslide located on km. 86–87 of regional Bishkek-Osh road. In 2003, during 2 days on April 20–21 there were 300 new landslides observed in the south of Kyrgyzstan, along the rim of Fergana valley (see location in Fig. 1b) – these mass movements were triggered by Hindukush earthquakes and local seismic events.

Tien-Shan Landslides Triggered by Hindukush Earthquakes

Sary-Bulak Landslide

One of the seismically triggered landslides involving liquefaction caused by Hindukush earthquake is the Sary-Bulak landslide formed in the south-east slopes of Fergana valley, in the north-west of Kok-Jangak town (Fig. 2b). First, two minor scarps with a length of 100–120 m, width up to 0.3 m and depth down to 3 m occurred in the upper part of the landslide at the end of February, 1974. There are some arguments for the idea that these scarps occurred after a seismic event with $M = 5.4$ that happened on February, 22 in Pamir-Hindukush zone at a depth 116 km. In the area below the scarps there was subsidence of 0.5–1.0 m in loess-like soil. Jurassic and Quaternary sediments are present within this landslide.

They are dipping towards the west with dipping angles varying from 20° to 40° depending on fault structure. Quaternary sediments are widespread in the target area and are basically composed of loess-like loam of diluvium and proluvium type. They are macroporous and have a significant thickness of up to 40 m (Figs. 2b and 3). Underlying Jurassic sediments are in contact with loess-like loam through an angular non-conformity and this contact, visible in scarps, is dipping to the north with an angle of 10–12°. Presence of this angular non-conformity was one of the reasons of landslide occurrence in this area.

The Sary-Bulak landslide formed in loess-like loam with an average thickness of 20 m and with higher content of rubble and boulder in the lower part of the cross-section.

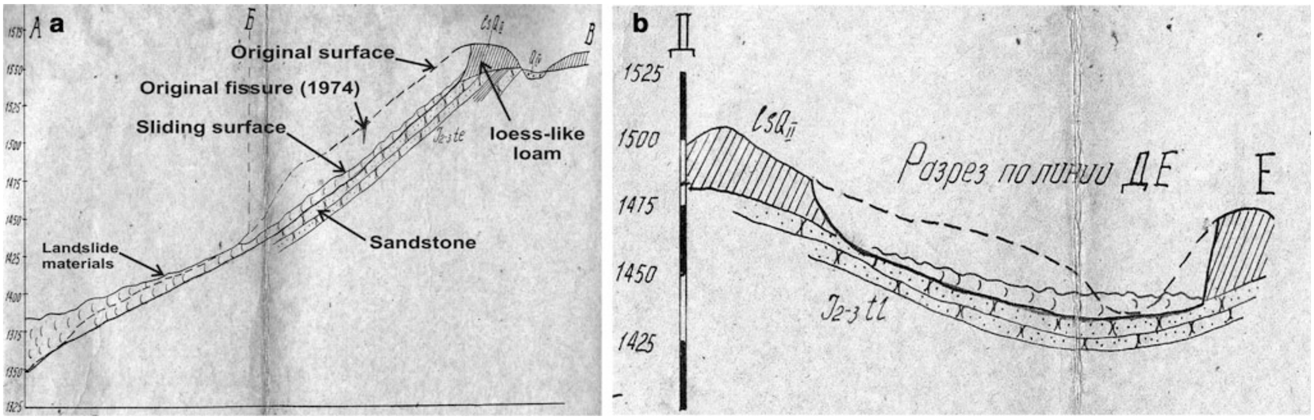

Fig. 3 Sary-Bulak landslide in the vicinity of Kok-Jangak settlement: (**a**) Cross-section; (**b**) Along-section

From a geomorphological point of view this landslide is characterized by dissected topography with slope angles ranging from 12–14° up to 30°. There are some faults in the eastern rim of the area and some of the faults hypothetically come through the landslide body.

Hydrogeologic properties of target area are mainly determined by aquifers in the Jurassic sediments. Underground water in aquifer is under pressure and groundwater flow occurs along cracks. Water discharge takes place in faults which are covered by quaternary sediments on the surface of the landslide. The discharge of springs connected with the aquifer is 0.3–2.0 l/s. The above-described angular nonconformity between Jurassic and quaternary sediments played significant role in water discharge. Water saturation along this contact leads to decrease of the strength of the sediments from both sides of the contact. Strength properties decreased significantly in some places forming a sliding surface and favouring the formation of Sary-Bulak landslide together with contact inclination and topography. So, the main reason of decreasing slope stability was the groundwater level which starting to rise in 1969.

Monitoring of landslide displacements based on geodetic reference points installed in initial cracks showed that there were not displacements in the period between 1974 and 1975, except for small (4–6 cm) movements in springtime. In spring 1976, starting from April there were displacements registered in this landslide. Generally, these displacements were small (1.7–2.0 mm/day), but sometimes increased up to 8.0–10.0 mm/day with pauses of activity from 10 to 30 days. Cumulative landslide displacement starting from April until catastrophic failure on November, 27 1976 was 0.5 m.

Most probably, this major landslide failure was initiated by a seismic event with $M = 6.1$ that happened on November, 27 1976 in the Hindukush at the depth of 190 km. There is the need to indicate that normally the most of mass movements in target area take place in springtime. The chronology of landslide failure is the following: first, there was fast and loud failure of the left part of slope with a travel distance of more than 1 km along the valley of Sary-Bulak Creek. The high speed of travel can be proved by the fact that a woman with child situated 700 m far from the scarp was not able to run away from the moving mass. The volume of the initially failed mass was 2.5 millions m^3. The second failure happened 3 h later than the first, it happened in the central part of slope below the existing scarp. Failed material rapidly travelled along the stream valley sometimes running up the slopes in turning points. All constructions within the travel distance were destructed by the moving mass. The total volume of failed material was 4.5 millions m^3 and consisted of wet, pasty soil with high viscosity. On December, 9 1976 the total value of travel distance was 4.5 km (Fig. 2b), while travel distance on the first day was 2.0 km, during the next 2 days (November, 28–29) there was another 2.0 km displacement and from November, 30 till December, 9 another 0.5 km.

During January, 1977 the most active part of the landslide was the left flank and the landslide scarp was gradually approaching the crest of the hill. Other failure with volume up to 80, 000 m^3 in the upper part of landslide took place in August, 1977. Till this time total cumulative volume of failed material reached value of 8 million m^3.

The extremely long travel distance of the failed material (more than 4.5 km) can be explained not only by the inclination of valley, but also by the liquefaction of loess-like loam along the sliding surface caused by seismic vibrations of long duration originated from the Hindukush earthquake on November, 27 1976. Liquefaction of material in sliding surface can be proved by witnesses who observed dust during main displacement and saw water fountains exactly after failure which disappeared after some time. It was noted that the upper part of landslide body had low water saturation and sometimes it was even dry. After landslide displacement the springs appeared at the toe of landslide and new water ponds formed in this part which grew in size with time.

Some geotechnical test of loess-like loam was provided in this area using samples taken from three boreholes with

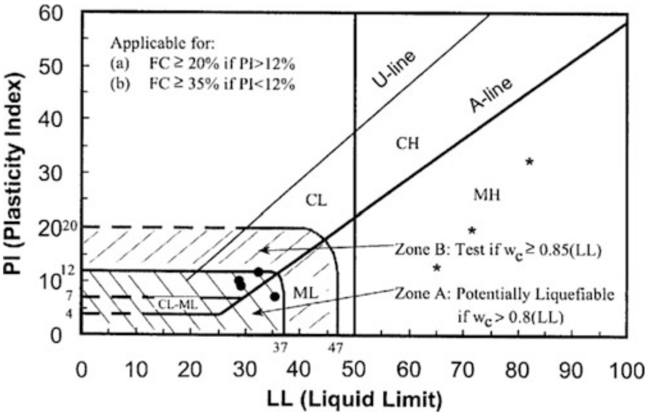

Fig. 4 Plasticity diagram for soil samples from landslides in Kok-Jangak, Taran-Bazar (●) and Mailuu-Suu (*)

a depth down to 25 m (Torgoev and Minetti 2004). Based on the grain-size distribution, the soil can be considered as dusty material with the next composition:

- Clay with grain size less than 0.005 mm – 11.3–18.1 %;
- Dust with grain size 0.005–0.05 mm – 71.9–85.7 %;
- Sand – 3.0–10.0 % with prevailing grain size 0.05–0.5 mm.

Soil density is 2.67–2.71 g/cm^3. Natural water content of loam is varying from 7.7 % in the upper part up to 30.2 % in the lower part. The plasticity limit ranges from 27.6 % up to 35.4 %, the viscosity limit is 18.8–23.9 % and the plasticity index is 8.8–16 %. Average porosity is 52 %, which contributes to its susceptibility to subsidence which appeared in 1974. The carbonate content is ranging from 20 % up to 25 %. Geotechnical tests were provided in conditions of natural wetness and with water saturation. It was found out that the effective angle of internal friction (φ') in water saturated conditions ranges from 23.3° up to 26.1°, the effective cohesion (C') is 5.0–10.0 kPa. Based on Kazagrande soil classification loess-like loam can be considered as clayey silt (CL) of non-organic origination (Fig. 4).

Taking into account the above-described conditions the subjected soils exhibit typical loess-like characteristics and can be considered as metastable material subjected to collapse under certain site conditions.

It is well known, that non plastic or slightly plastic silt and silty sand soils with no or very low clay fraction in saturated, loose state can be subjected to liquefaction upon dynamic loads induced during earthquakes. Recent studies (Seed et al. 2003) on the soils of higher plasticity and/or higher clay content behaviour during recent earthquakes occurred in Turkey and Taiwan showed that generally these soils are not susceptible to liquefaction and tend to modify the previously established criteria (Seed et al. 1983).

According to these new evidences, a "state of the art" modified plasticity chart for the assessment of liquefiable soil types has been produced. This chart is presented in Fig. 4 and confirms the fact that soils presented in target area fall within the zone of potential liquefaction (Torgoev and Minetti 2004).

It is possible to evaluate if seismically induced shear stresses, at any depth, can cause liquefaction of the soils (Prakash 1981). The procedure leading to preliminary assessment needs much more detailed field and laboratory studies confirming liquefaction potential – this approach was used in the target area and is described below.

The average-earthquakes induced shear stress (τ_{av}) was computed using the (1):

$$\tau_{av} = \frac{0.65 * \gamma * h * a_{\max}}{g * R_d}, \tag{1}$$

where h is the targeted depth, γ – total value of normal stress at the targeted depth, a_{max} – maximal expected seismic acceleration in targeted area, g – gravitational acceleration, R_d – depth dependent factor, here $R_d = 0.9$ (Prakash 1981). The next values of input parameters were chosen in our example: $\gamma = 14$ kN/m^3, $a_{max} = 0.2$g for Kok-Jangak area and $a_{max} = 0.15$ g for Taran-Bazar area.

The stresses leading to liquafaction were calculated using (2):

$$\tau_1 = \frac{\sigma'_{vo} * \sigma_{dc}}{2 * \sigma_a} * \frac{c_r * D_r}{50}, \tag{2}$$

where σ'_{vo} is the vertical effective stress; $\sigma_{dc}/2\sigma_a$is the stress ratio leading to liquefaction and depending on the earthquake magnitude through significant stress cycles (N_c) and mean grain size of targeted soil (D_{50}), for magnitude 7, N_c is 10 cycles and with $D_{50} = 0.03$ mm the stress ratio will be 0.2; D_r is the relative density of targeted soil (40 %); c_r is the correction factor for the relative density of soil, for $D_r < 50$ %, c_r is 0.57.

The results of calculations presented in Fig. 5 indicate that water saturated soil in target areas is potentially liquefiable down to depth of 10 m in case of Taran-Bazar (TB) and down to depth of 30 m in case of Kok-Jangak (K).

Landslides in the Northern Tien-Shan, Tatyr village

Landslides situated in the area of Tatyr village are considered to be seismically triggered mass movements formed and periodically activated close to seismically active faults. One of them, called Western landslide, formed at night from May, 15 to May, 16 2004. It formed at 400 m to the south-east from

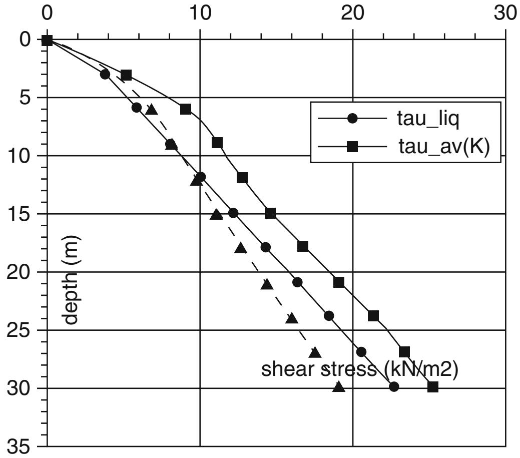

Fig. 5 Liquefaction potential for loes-like loam soil for samples taken from different depth levels for Sary-Bulak landslide (K) situated in Kok-Jangak and for Taran-Bazar landslide (TB)

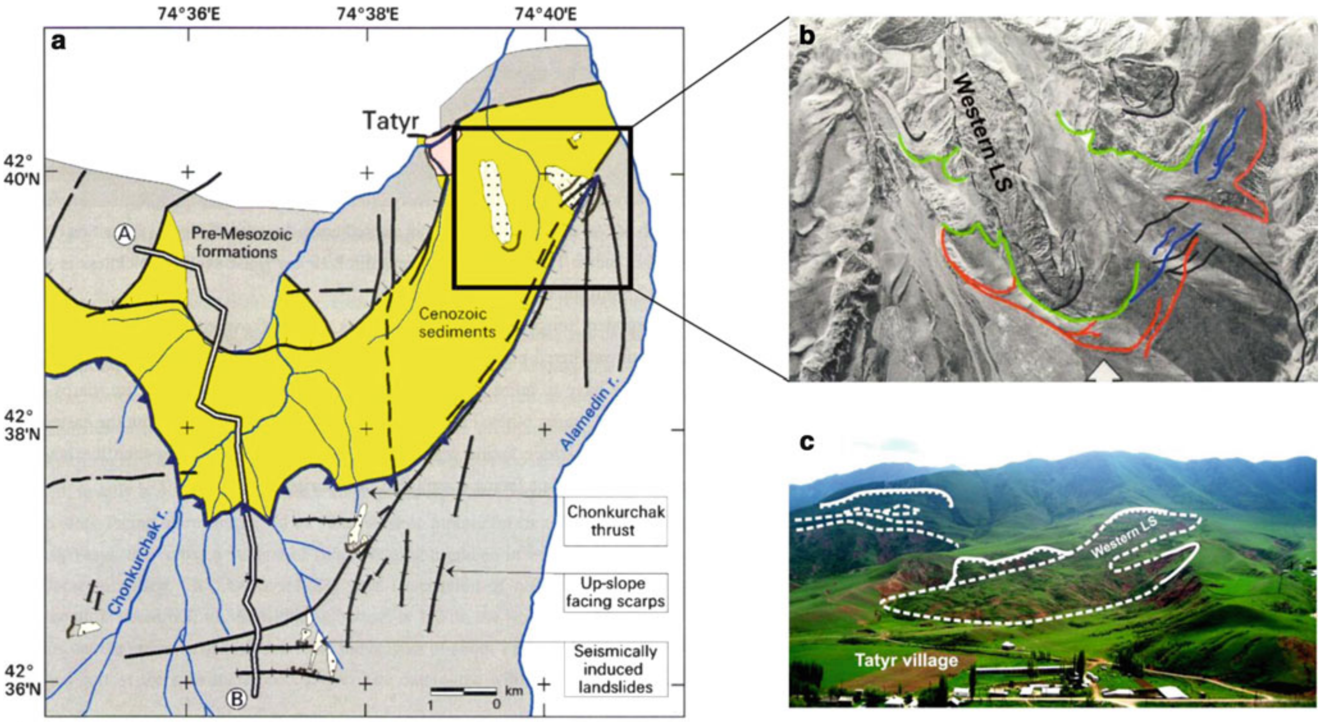

Fig. 6 Landslides triggered by earthquakes in the area of Tatyr village: (**a**) Structural and geomorphological map of seismic deformations in the Chonkurchak basin (Korjenkov et. al. (2006); (**b**) Aerial image of landslides and indicated seismic deformations; (**c**) Photo of landslides (2010)

this village on the slope with northern exposition and maximal steepness up to 30° (Fig. 6). Landslide coordinates are the next: N42°39′24.9″, E74°39′43.7″. The landslide scarp in the upper part of the landslide has a length of about 400 m and a height of 6–10 m. There are outcrops of red colour sediments of Shamsy formation (Pg_3–N_1sm). The total area of landslide is 0.43 km^2, average thickness of moving material is 6 m, total volume is around 2.6 millions m^3.

Most probably, the triggering event for the landslide displacement was a Hindukush earthquake with M = 4.8 that occurred on May, 14 at a depth of 117 km. Further a stronger seismic event with M = 5.1 happened on May, 16 – its seismic deformations could also cause landslide displacements. There is one more ancient landslide situated in the area of Chonkurchak thrust – this landslide is situated to the east from Tatyr landslide (Fig. 6a). There are several scarps situated upslope from the modern one – these scarps were created by seismic events and have different time of origination. These scarps prove the fact that target area was subjected to seismic stresses several times in the past, resulting from the continuous uplift of Tien-Shan mountains. As it can be seen from Fig. 6, the whole basin of Chonkurchak river is crossed by many faults and tectonic features. There are a lot of mass movements of different formation time resulted from intense seismic activity along Chonkurchak thrust which is contact zone between the bedrock of the Kyrgyz Ridge and Ceinosoic sediments of Chu depression.

Conclusion

The Tien Shan Mountains, Central Asia, are very prone to many types of landslides. In Kyrgyzstan and Tajikistan, every year hundreds of people are affected by mass movements. Many of the large landslides are directly or indirectly (through delays) triggered by earthquakes. During the last century, the Kemin (Ms = 8.2, 1911), the Khait (Ms = 7.4, 1949), the Gissar (M = 5.5, 1989) and the Suusamyr (Ms = 7.3, 1992) events all together triggered hundreds of rockslides and earth flows causing extensive damage and killing several thousands of people.

While the effects of regional earthquakes on local slope stability are well known, landslides and mudflows triggered by low frequency seismic vibrations (with duration of 1.5–2.5 min) originated from remote earthquakes are unexpected. Generally, for those events, neither place nor time of remote landslide failure can be reliably predicted. Such kinds of mudflows move very quickly and travel long distances. The sliding surface of these mass movements has a steep inclination, outlines and scarps do not have wavy structure, which indicate synchronous failure of the entire volume of material. Failed material usually consists of homogenous loess soil with natural moisture 0f 20–25 %, which is strongly over-smashed due to rapid movement and collision with neighbouring slopes during failure.

References

Havenith HB, Bourdeau S (2010) Earthquake induced landslide hazards in mountainous regions: a review of case histories from Central Asia. Geologica Belg J 13(3):137–152

Korjenkov AM, Michajljov W, Wetzel HU et al (2006) International training course “seismology and seismic hazard assessment”. Field Excursions Guidebook, Bishkek/Potsdam, pp 15–18

Niyazov RA, Nurtaev BS (2009) Landslides in Uzbekistan caused by earthquakes in Pamir-Hindukush zone. In: Proceedings of international conference “mitigation of natural hazards in mountainous areas”, Bishkek, 15–18 Sept 2009, pp 136–139

Prakash S (1981) Soil dynamics. McGraw-Hill, New York, 426p. ISBN 0070506582

Seed HB, Idriss IM, Arango I (1983) Evaluation of liquefaction potential using field performance data. J Geotech Eng ASCE 109(3):458–482

Seed RB et al (2003) Recent advances in soil liquefaction engineering: a unified and consistent framework, EERC-2003–06, EERI, Berkeley

Torgoev IA, Minetti L (2004) Report on the results of investigations and inspections of landslide hazardous zones in Kyrgyzstan. Ministry of Environment and Emergency Situations, Bishkek, 39p

THE SECOND
WORLD
LANDSLIDE FORUM

Inferring Seismic Response of Landslide-Prone Slopes from Microtremor Study

Vincenzo Del Gaudio, Janusz Wasowski, and Chyi-Tyi Lee

Abstract

The difficulty in identifying factors controlling the dynamic response of landslide-prone slopes to seismic shaking makes desirable the development of reconnaissance techniques to reveal site resonance conditions that can favour seismically-induced slope failures. Tests were performed to derive information on the occurrence of directional resonance by analysing the azimuthal variations of the horizontal-to-vertical spectral ratios of ambient noise (HVNR) recorded by portable seismometers. In particular, data were acquired in an area of central Italy (Caramanico Terme), affected in the past by seismically-induced landslides, and in two areas of Taiwan (Tsaoling and Jiufengershan), where the 1999 Chi-Chi earthquake triggered giant landslides. The HVNR analysis demonstrated that the presence of a pronounced directional resonance can be recognised from data acquired under different ambient conditions and with different sensors. However, measurement repetitions and uncertainty assessment are fundamental to distinguish persistent features, attributable to site effects, from transient phenomena due to variable ambient conditions.

Keywords

Seismically-induced landslides • Slope dynamic response • Microtremors • HVNR

Introduction

Several studies pointed out that site amplifications affecting marginally unstable slopes can considerably influence landslide triggering during earthquakes (e.g. Sepúlveda et al. 2005; Meunier et al. 2008; Bozzano et al. 2008). Furthermore, during a long-term accelerometric monitoring conducted in a landslide-prone area of central Italy (Caramanico Terme), evidence emerged that phenomena of directional resonance can occur on slopes along potential sliding directions, thus increasing slope susceptibility to seismic failures (Del Gaudio and Wasowski 2007, 2010).

We hypothesise that similar phenomena may have contributed to catastrophic failures observed during the 1999 Chi-Chi earthquake (Taiwan), i.e. the Tsaoling and Jiufengershan landslides (Hu et al. 2009). However, the complexity of factors controlling site effects makes difficult the assessment of conditions actually determining an increase of potential seismic landslide hazard. Thus, it is desirable to develop reconnaissance techniques for characterising relevant properties of slope dynamic response to seismic shaking.

One promising technique, based on the so-called "Nakamura method" (Nakamura 1989), consists of recording microtremors generated by ambient noise sources with portable seismometers and analysing the azimuthal variations of the spectral ratios between noise horizontal and vertical components (commonly named "HVNR"). We had previously

V. Del Gaudio (✉)
Dipartimento di Geologia e Geofisica, Universita' degli Studi "Aldo Moro", via E. Orabona 4, Bari, Italy
e-mail: delga@geo.uniba.it

J. Wasowski
Istituto di Ricerca per la Protezione Idrogeologica, Consiglio Nazionale delle Ricerche, Bari, Italy

C.-T. Lee
Institute of Applied Geology, National Central University, Jhongli, Taiwan

C. Margottini et al. (eds.), *Landslide Science and Practice*, Vol. 5,
DOI 10.1007/978-3-642-31427-8_26, © Springer-Verlag Berlin Heidelberg 2013

tested this technique at some sites of the Caramanico accelerometer network using an ultra-compact sensor (Tromino®) with velocimetric properties (Del Gaudio et al. 2008). However, an extension of observations to low frequencies (<1 Hz) is of interest to enlighten slope response to seismic waves of longer wavelength, which could be important for the triggering of large failures. Therefore, we first tested the employment of a portable broad-band sensor both at the same sites of the previous Caramanico tests and on the slopes affected by the giant Tsaoling and Jiufengershan landslides in Taiwan. Then the data obtained with different sensors and at different sites were compared and analysed also with reference to the available accelerometer recordings of seismic events, in order to evaluate the stability of the measurements. Finally, the significance of the results in terms of slope dynamic response to seismic shaking is discussed.

Method

For the new tests of HVNR measurements we used, as a microtremor recorder, a Nanometrics Trillium Compact: this is a small (~10 cm size) and light (~1 kg weight) three component broad-band sensor having a theoretically homogeneous response (with an approximation of 99 %) in the frequency interval 0.02–50 Hz. Field measurements require recording sessions of at least ½ hour. In order to reduce long period disturbance induced by temperature variations and air movements around the seismometer, during the recording sessions the sensor was insulated with a foam-lined rigid plastic cover (Fig. 1). Data acquisition was carried out with a Nanometrics Taurus Portable Seismograph, a compact data acquisition unit (15 × 26 × 6 cm, 1.8 kg) requiring at most a power consumption of 3.5 W, supplied by an external 12 V battery. This unit include a 24-bit digitiser, a data logger storing data on a Compact Flash card and a GPS receiver for location of the recording site and for accurate timing.

Following the recommendations derived from the outcome of the European research project SESAME (Site EffectS assessment using AMbient Excitations: Bard and The SESAME TEAM 2004), Fourier Transforms were calculated for at least 20 time windows of 30 s and spectra were smoothed using a triangular average on frequency intervals of ± 5 % of the central frequency. The spectral ratios were then calculated between horizontal components oriented at 10° azimuth intervals and vertical component and, finally, for each station, the average spectral ratios H/V of all the recording intervals in each direction were obtained.

For a correct evaluation of the HVNR calculation results, it is fundamental to assess uncertainty in the identification of frequency, azimuth and amplitude of HVNR values. This is needed to point out whether observed peaks are persistent features, attributable to site effects, or transient effects due to microtremor source characteristics or ambient conditions (e.g. pressure and temperature) disturbing broad-band acquisitions.


Fig. 1 Trillium Compact broad band seismometer placed on the ground (*left*) and under the insulating cover (*right*)

Data Analysis

Caramanico Test Area

The first test area is located in the municipality of Caramanico Terme, in the Abruzzi region (Central Italy), at the confluence of the Orfento and Orta Rivers (Fig. 2). The east flank of the Orta River valley is characterised in its lower part by Pliocene clay-rich formation mantled by colluvium. Here, in 1989, a few tens of meters thick colluvial deposit was mobilised by a landslide affecting the slope for a down-dip length of about 500 m, to the Orta river.

Beginning in 2002 a local accelerometer network was set up to study differences in slope dynamic response to seismic shaking under different lithologic and topographic conditions. At present this network consists of five stations named CAR$_{1–5}$. One of them (CAR$_4$), located on a nearly flat bedrock surface, was set up as reference station. The acquired accelerometer data revealed the presence of systematic directional amplifications oriented according to local topography features in two sites, one on the head of a quiescent landslide (CAR$_2$) and the other on the rim of a gorge (CAR$_3$) (Del Gaudio and Wasowski 2007). The presence of phenomena of systematic directional resonance, first observed in weak motion recordings, was confirmed by the recordings of stronger events, during the 2009 L'Aquila sequence (Del Gaudio and Wasowski 2010).

The amplification observed at CAR$_2$, on the landslide head, appears related to the impedance contrast between colluvial deposits and the underlying mudstone substratum; a similar amplification was observed also at the site CAR$_5$

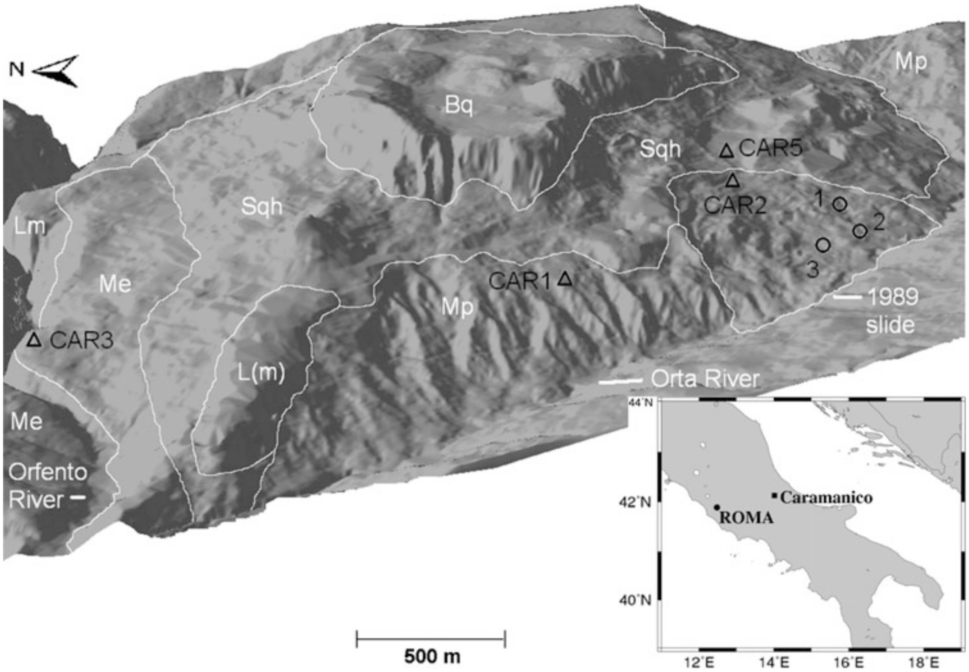

Fig. 2 Caramanico test area geographical location (inset) and DEM showing lithological units and measurement sites. White lines mark lithological contacts and the boundary of 1989 landslide: Lm/L(m) = Limestones of Miocene/uncertain Miocene age; Me = Messinian sandy-silty deposits with carbonate breccia; Mp = Pliocene mudstones; Bq = Quaternary limestone megabreccias; Sqh = Quaternary and Holocene soils (colluvium and artificial ground); $CAR_{1–5}$ mark the location of the accelerometer stations (reference station CAR_4, located 2.5 km SE of Caramanico, is not shown); HVNR measurements were carried out at $CAR_{1–5}$ and on additional three sites within the 1989 landslide (numbers 1–3)

located on the same colluvium, but 200 m upslope from the landslide crown. However, unlike at CAR_5, at CAR_2 the amplification had a clear directional character with a systematic pronounced maximum oriented along the maximum slope direction (approximately E-W). This suggested that site response directivity at CAR_2 is due to the presence of the landslide body.

Subsequent investigations demonstrated that site response directivity can be recognised from the analysis of directional variations of HVNR values obtained by recording ambient microtremors with a portable seismometer (Del Gaudio et al. 2008). For these first tests we used a Tromino, an ultra-compact velocimeter developed in Italy for noise measurements (see http://www.tromino.it). However, the reliability of the results obtained at frequencies around and below 1 Hz appeared uncertain. Thus, considering that shaking at such frequencies could be the most relevant for the mobilization of large landslides, we repeated the measurements with a Trillium Compact seismometer. The results demonstrated that sites characterised by a clear response directivity have similar response even when data are acquired under different ambient conditions and with different sensors.

As an example, HVNR values derived at CAR_2 from Tromino measurements carried out on July 2007 had shown similarly oriented directional peaks of spectral ratios larger than three at different frequencies, around a mean azimuth (N80°E) close to the maximum slope direction (Fig. 3). The new measurements carried out with Trillium on June 2010 showed a similar pattern, even though with somewhat different values of the spectral ratio peak and a slight rotation (by ~20°) of the maxima's azimuth. Since the differences between directional maximum (red curves in the bottom diagrams of Fig. 3) and orthogonal minimum (blue curves) exceed standard deviation (see in Fig. 3 bottom), they are considered significant. Trillium data show an additional pronounced maximum at a frequency of 0.6 Hz, not detected with Tromino, but at this frequency the standard deviation is larger than difference between the directional maximum and minimum, thus its attribution to a site effect is uncertain.

Comparatively, at site CAR_5, located 200 m upslope from the 1989 slide (see Fig. 2), no site response directivity was observed. HVNR values from Tromino measurements had not shown iso-orientation of peak values at different frequencies and measurements with broad-band sensor showed a different

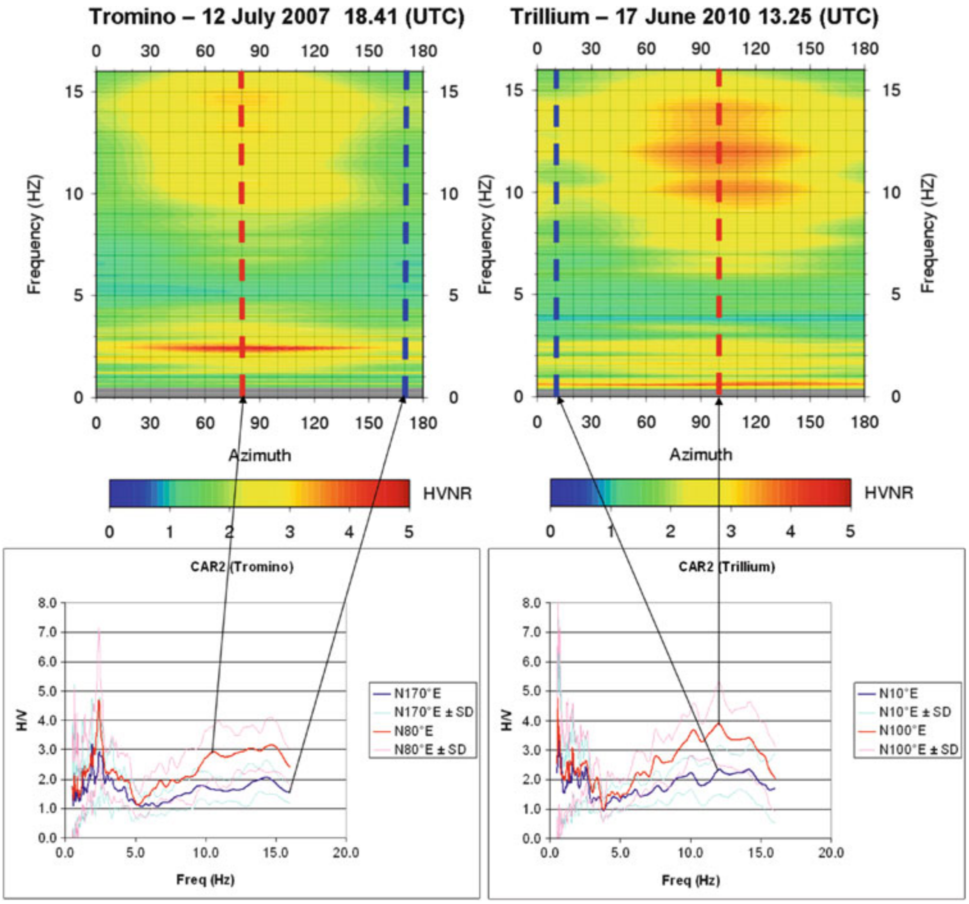

Fig. 3 Azimuthal variation of the HVNR values at site CAR2, obtained from noise recordings carried out, at different times (indicated as UTC in the headers), with Tromino (*left*) and Trillium (*right*). Amplitude of spectral ratios are represented with a colour bar scale. Azimuth where HVNR values have directional maximum and minimum are marked by *red* and *blue dashed lines*, respectively. The averages ± one standard deviation (*light colour curves*) of spectral ratios at these azimuths are shown with the same colours (*bottom diagrams*)

pattern, possibly related to temporally different polarisation of noise source (Fig. 4). Differences between directional maxima and minima are generally smaller than one standard deviation.

Taiwan Test Areas

HVNR measurements in Taiwan were carried out at the sites of two large landslides triggered by the Chi-Chi earthquake of 20 September 1999 (moment magnitude Mw = 7.6), i.e. Jiufengershan and Tsaoling. The earthquake was associated with the 85 km long rupture of the Chelungpu fault (Fig. 5).

Jufengershan Data

The Jiufengershan landslide occurred on the hanging-wall of the Chelungpu fault, about 14 km east of the surface rupture and 12 km north of the mainshock epicentre. The mass movement was a rock and soil avalanche that mobilised a 60 m thick sequence of shales and sandstones (Fig. 6), along bedding surfaces of a monoclinal structure dipping about 22°SE (Chang et al. 2005). The landslide was 1.5 km long, involved about 40×10^6 m^3 of material and caused the death of 39 persons.

Tests of HVNR measurements were carried out, using Trillium, at three sites: one on the slip surface in the landslide detachment area (site J2), and the others near the landslide crown (J1) and its left boundary (J4). At site J2 measurements repeated in two successive days (Fig. 7) showed a very strong directional variation affecting the entire investigated frequency band (0.3–16 Hz). HVNR maxima are oriented along the bedding/slip surface dip direction (N150°E), reaching peak values of 10–20 at frequencies of 0.8–1.0 Hz, with spectral ratio minima less than 1 in orthogonal direction, which suggests a possible deamplification of ground motion in this direction.

Standard deviations of HVNR values are quite large (particularly at frequencies lower than 5 Hz), which implies a strong variability of H/V spectral ratios during the recording session from one time window to the other; this is likely an effect of temporally variable properties of noise sources. However, the differences between directional maxima and minima largely exceed one standard deviation; thus the presence of directivity in ground motion is well

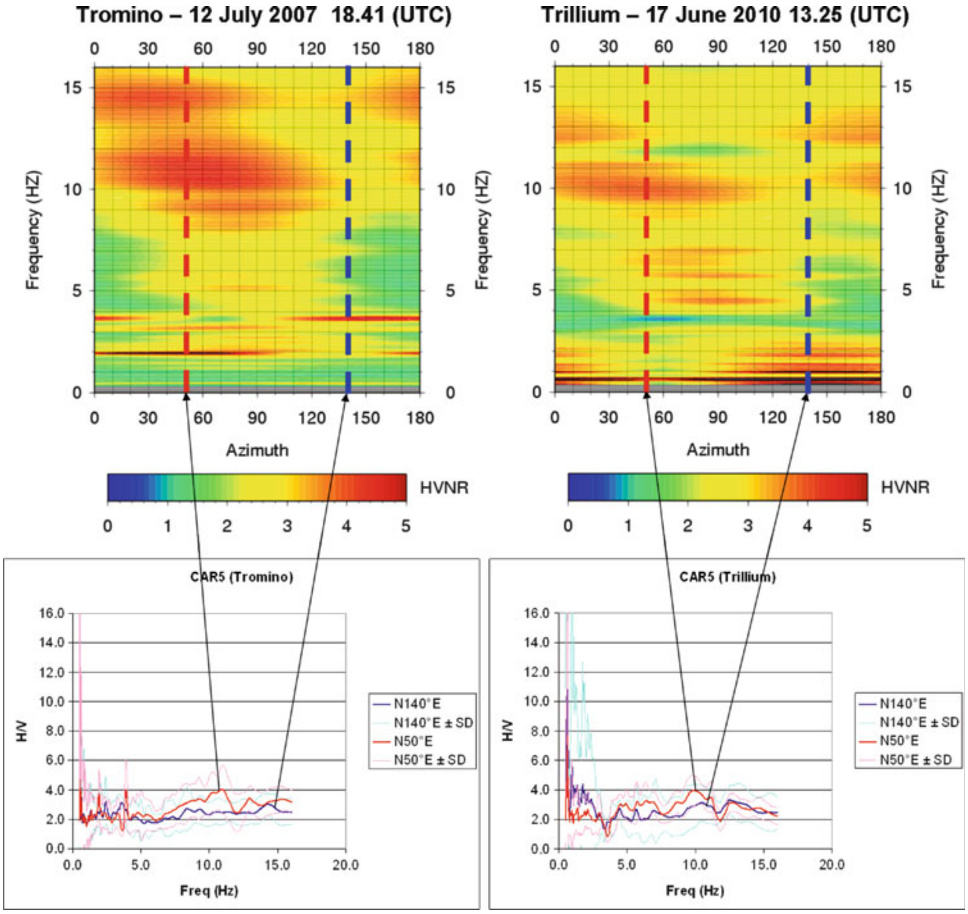

Fig. 4 Azimuthal variation of the HVNR values at site CAR$_5$, obtained from noise recordings carried out, at different times (indicated as UTC in the headers), with Tromino (*left*) and Trillium (*right*). Azimuth of the HVNR maximum significant peak (i.e. having a standard deviation smaller than the HVNR average) and of the minimum at the same frequency are marked by *red* and *blue dashed lines*, respectively. The averages ± one standard deviation of spectral ratios at these azimuths are shown with the same colours (*bottom diagrams*)

supported. In principle, this directivity could be due to noise polarisation properties, but measurements carried out in the same day at J1 and J4 sites outside the landslide (Fig. 8), did not show such directivity. Thus the directivity at J2 appears to be specific to the detachment area - slip surface site conditions.

Tsaoling Data

The Tsaoling landslide occurred about 6 km away from the southern end of the Chelungpu fault rupture (see Fig. 5) and was responsible for the death of 29 persons. The mass movement mobilised a volume of 125 × 10^6 m^3 of material of the Cholan Formation (Fig. 9), consisting of interbedded shales and sandstones. Sliding occurred along a bedding surface dipping 14°SW, covering a distance of more than 2 km and damming the Chingshui river (Hung et al. 2002).

The Mount Tsaoling slope opposite to that affected by the 1999 landslide hosts an accelerometer station (CHY080), which recorded the Chi-Chi earthquake mainshock. This recording showed that ground motion had a pronounced maximum very close to that of the sliding direction (S_{50}°W). Shaking energy, represented by Arias intensity (Ia) (Arias 1970), was three times larger in this direction than in the orthogonal direction (Fig. 10, left). The horizontal to vertical spectral ratios (HVSR) calculated for the mainshock recording (Fig. 10, right) showed a strong peak (H/V spectral ratio $\approx$ 10) at a frequency of 1.2 Hz, parallel to the Ia maximum. This suggested the possible presence of a site resonance oriented along the sliding direction.

However, extending the analysis to the recordings of other seismic events, the presence of a systematic directional amplification close to a sliding direction was not confirmed. Normalising the directional variations of Arias intensity observed in 253 seismic events recorded at CHY080, and calculating their averages in different directions, the Ia maximum turned out much less pronounced (being only 60 % larger than minimum) and HVSR values showed main peaks, between 1 and 4 Hz distributed in a relatively wide range of azimuths (Fig. 11).

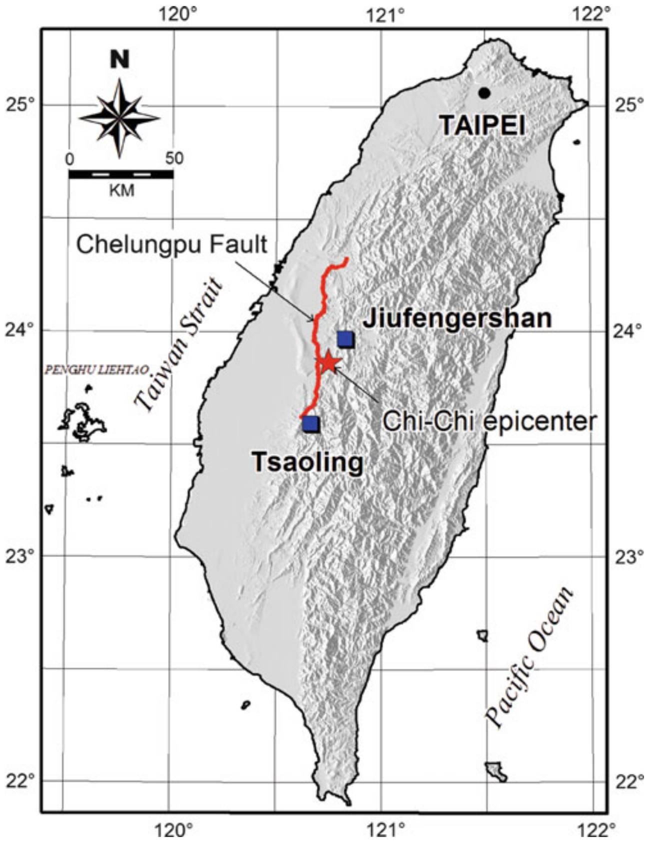

Fig. 5 Geographical location of the landslide sites in Taiwan (*blue squares*) where HVNR measurement tests were carried out. The *red* star marks the epicentre of Chi-Chi earthquake mainshock and the *red line* represents the trace of the Chelungpu fault surface rupture

This suggests that the directional maximum observed for the Chi-Chi earthquake was not a systematic feature of site response and, at least in part, may have been due to wave polarisation controlled by source properties of the 1999 event. Neither the analysis of spectral ratio of ambient noise recordings, carried out at the accelerometer station site (CHY080) with Trillium, provided evidence of site response directivity. HVNR measurements showed a maximum of ~6 at 0.9 Hz, directed due N_{110}°E, but its difference from a minimum due North was much less than one standard deviation (Fig. 12).

However, HVNR measurements carried out at site S2 located on the landslide slip surface (detachment area) showed, similarly to the case of the Jiufengershan site J2, a strong directional variation (Fig. 13). In this case the orientation of the maximum (East-West) differed from the sliding direction (S_{50}°W), but the HVNR values along the sliding direction were still very high (~15 at 0.7 Hz).

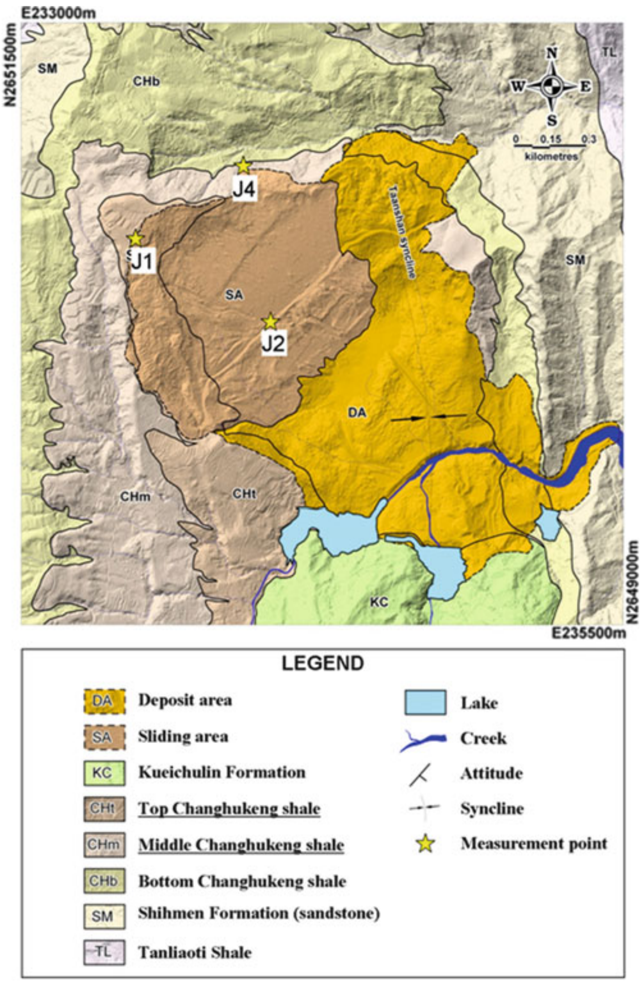

Fig. 6 Geology of the Jiufengershan landslide area. Formations involved in landsliding are *underlined*. *Yellow* stars mark the location of the HVNR measurement sites (Modified after Chang et al. (2005))

At other sites the measurements carried out in the same days did not revealed a similar pattern (see Fig. 14). Considering that especially at low frequencies the microtremors produced by the same noise sources should be observed over a large area, we conclude that the directional maxima at site S_2 are not due to noise properties. Therefore, at this site a strong amplification of ground motion seems to be present in the sliding direction. We infer that during the Chi-Chi earthquake mainshock the directivity at Tsaoling was mainly controlled by source properties, but when combined with the directional site amplification in the detachment area it resulted in the considerable enhancement of the ground motion in the sliding direction.

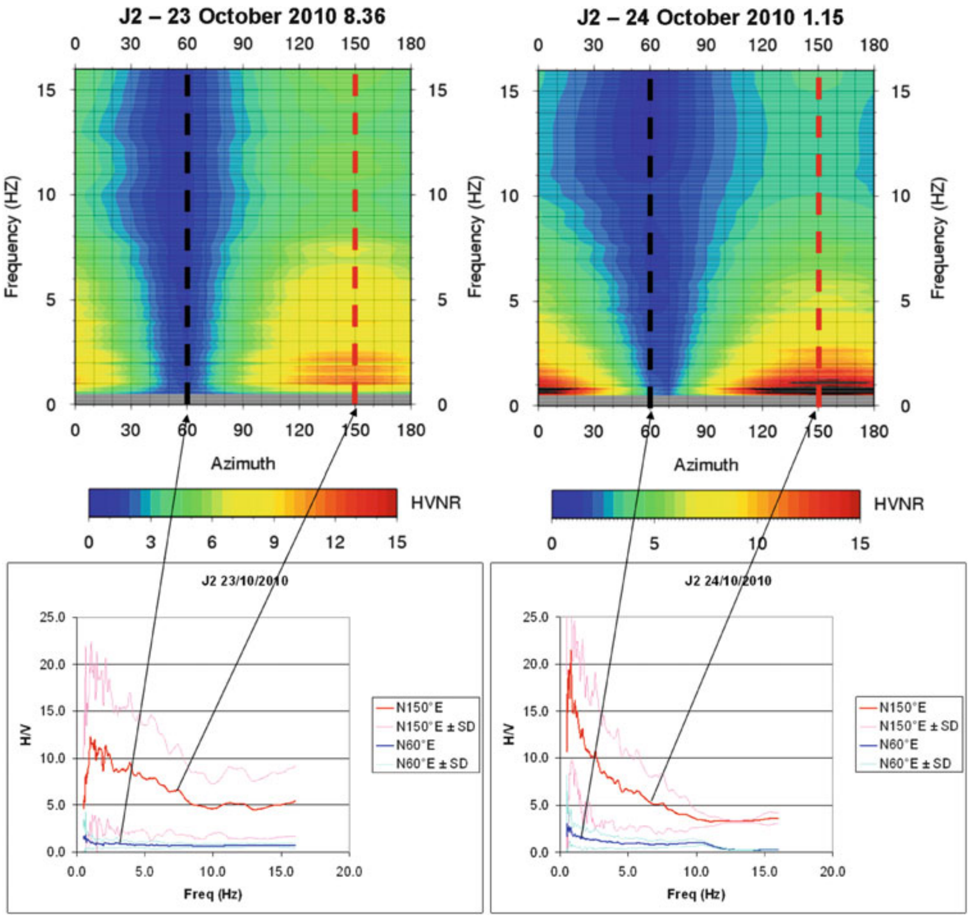

Fig. 7 Azimuthal variation of the HVNR values at site J_2 (on the Jiufengershan landslide detachment/sliding area - slip surface), obtained from noise recordings carried out in two different days (indicated in the headers with UTC time). Azimuths where HVNR values have directional maximum and minimum are marked by *red* and *blue dashed lines*, respectively. The averages ± one standard deviation of spectral ratios at these azimuths are shown with the same colours (*bottom diagrams*)

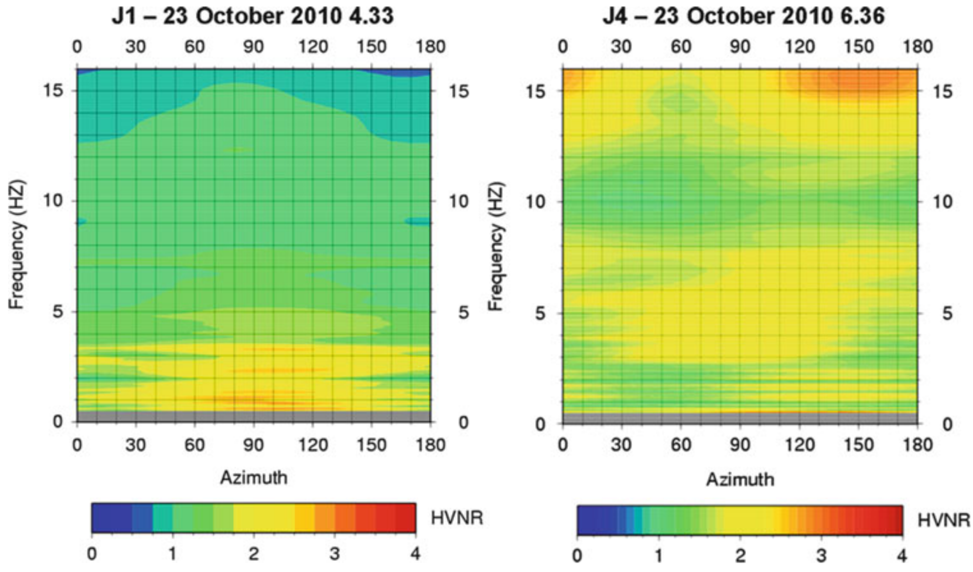

Fig. 8 Azimuthal variation of the HVNR values at sites J_1 (*left*) and J_4 (*right*), located near the border of the Jiufengershan landslide (see Fig. 6 for location), obtained from noise recordings carried out the same day as the first measurement at J_2

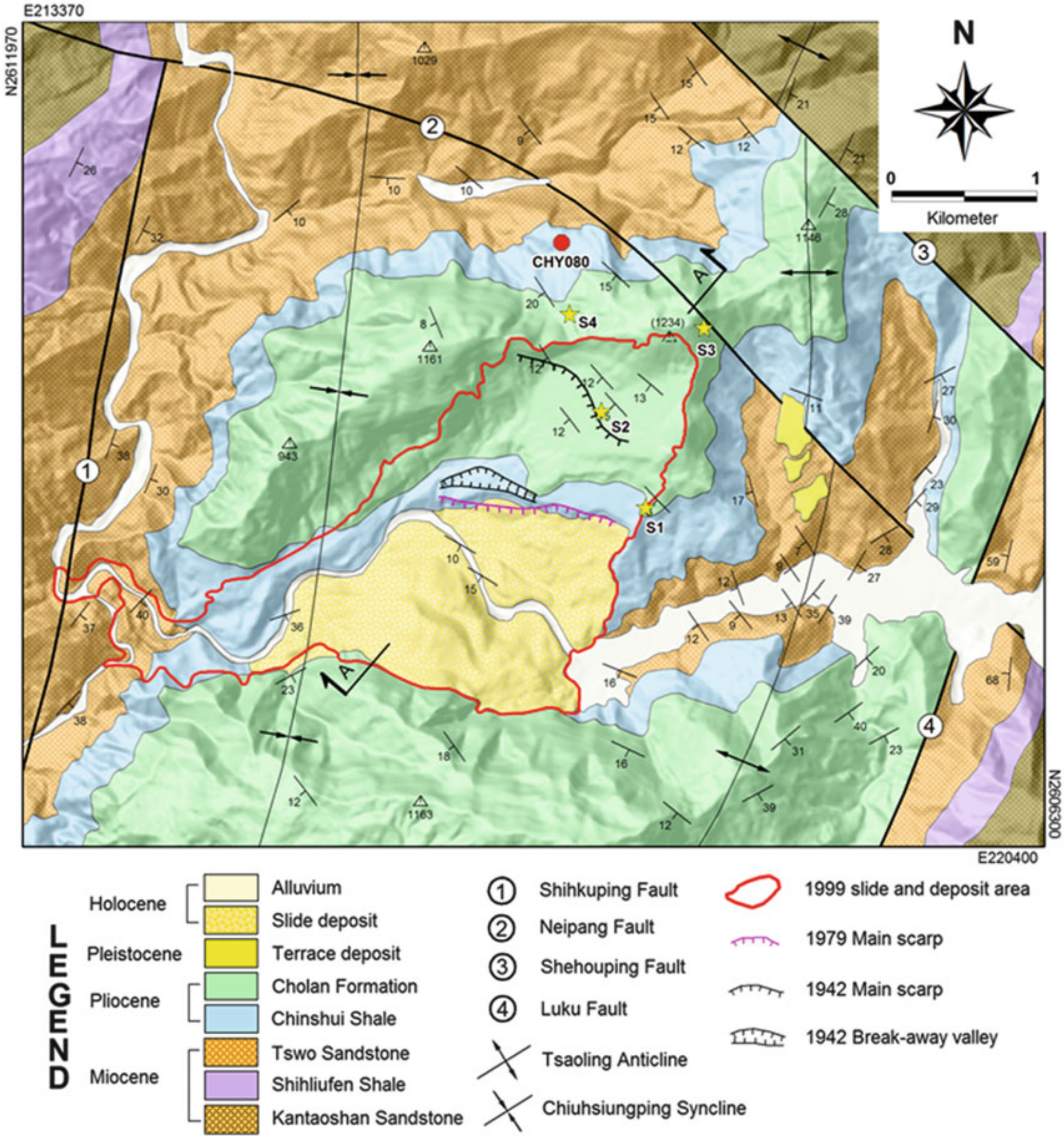

Fig. 9 Geology of the Tsaoling landslide area. *Yellow* stars mark the location of HVNR measurement sites, *red dot* that of the accelerometer station CHY080

Conclusions

The analysis of azimuthal variation of HVNR values obtained from microtremor measurements, conducted with a broad-band sensor in central Italy on the landslide-prone slopes known to show directional maxima of seismic shaking, confirmed that reliable evidence of site response directivity can also be obtained from observations extended to low frequencies (~1 Hz or even less).

Our microtremor measurements in the detachment areas (on the slip surfaces) of two catastrophic landslides triggered by the 1999 Chi-Chi earthquake (Taiwan) demonstrated that along their sliding directions the spectral ratios show a pronounced directional maximum or, at least, a very high value; this suggests the presence of conditions for strong amplification of ground motion during earthquakes. The microtremor recordings conducted elsewhere on the same slopes did not reveal similar properties. However, the representativeness and the exact significance of the HVNR data acquired on the landslide slip surfaces should be more deeply investigated repeating measurements of noise with different types of instruments at varying environmental conditions. This is needed to exclude the

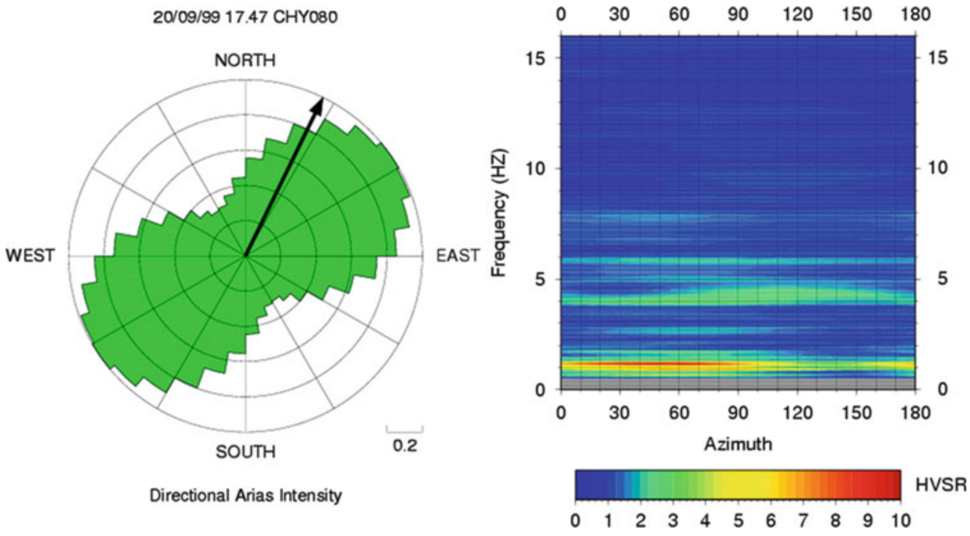

Fig. 10 Azimuthal relative variation of normalised Arias intensity measured from accelerometer recording of the Chi-Chi earthquake mainshock at station CHY080 (*left*) and horizontal-to-vertical spectral ratio (HVSR) obtained for the same event as function of ground motion direction (*right*). *Black arrow* marks the station-epicentre direction

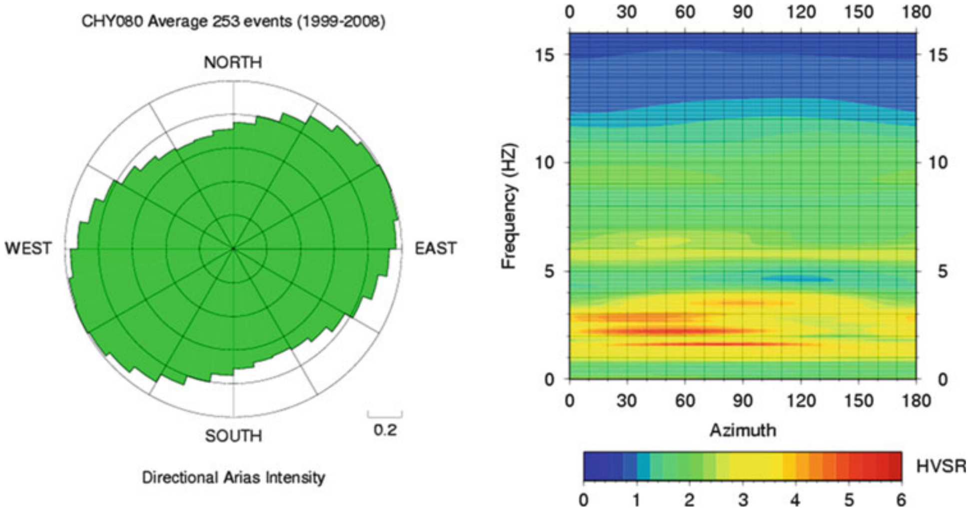

Fig. 11 Azimuthal relative variation of normalised Arias intensity values averaged for 253 events recorded by the station CHY080 (*left*) and mean horizontal-to-vertical spectral ratio (HVSR) obtained for the same events as function of ground motion direction (*right*)

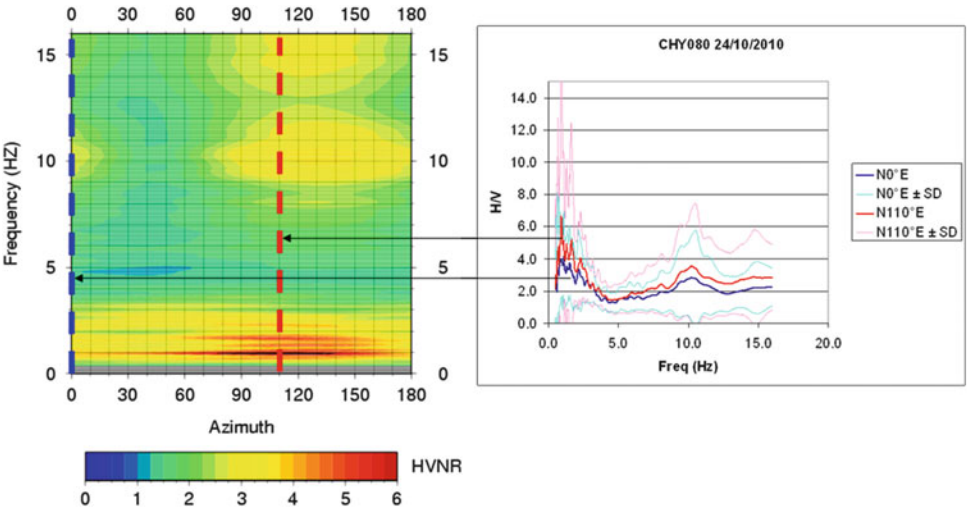

Fig. 12 (*Left*) Azimuthal variation of the HVNR values at site CHY080. Azimuths of HVNR maximum and of minimum at the same frequency are marked by *red* and *blue dashed lines*, respectively. (*Right*) The averages ± one standard deviation of spectral ratios at these azimuths are shown with the same colours

Fig. 13 (*Left*) Azimuthal variation of the HVNR values at site S_2 (on the Tsaoling landslide detachment/sliding area - slip surface). Azimuths where HVNR values have directional maximum and minimum are marked by *red* and *blue dashed lines*, respectively, whereas *green dashed line* marks the azimuth of the sliding direction. (*Right*) The averages ± one standard deviation of spectral ratios at these azimuths are shown with the same colours

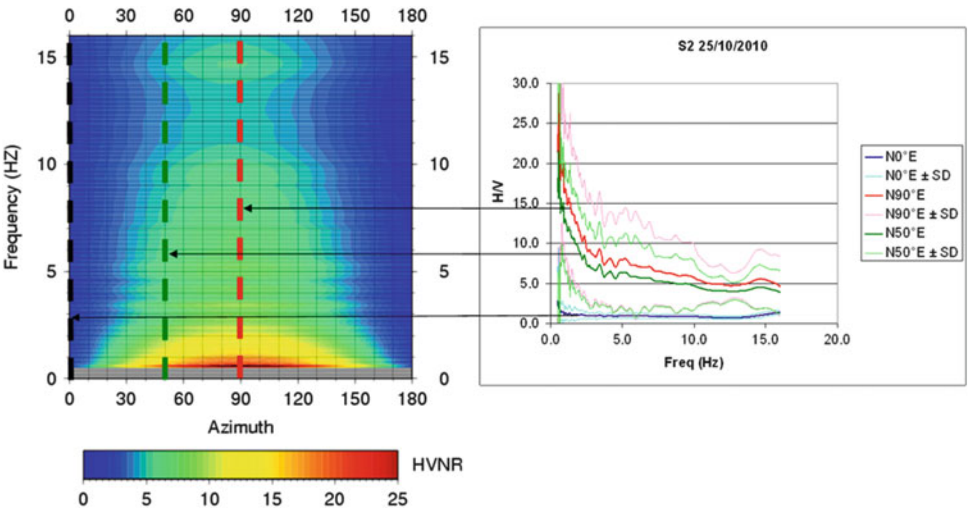

Fig. 14 Azimuthal variation of the HVNR values at site S_3 (*left*) and S_4 (*right*) near the Tsaoling landslide (see Fig. 9 for location)

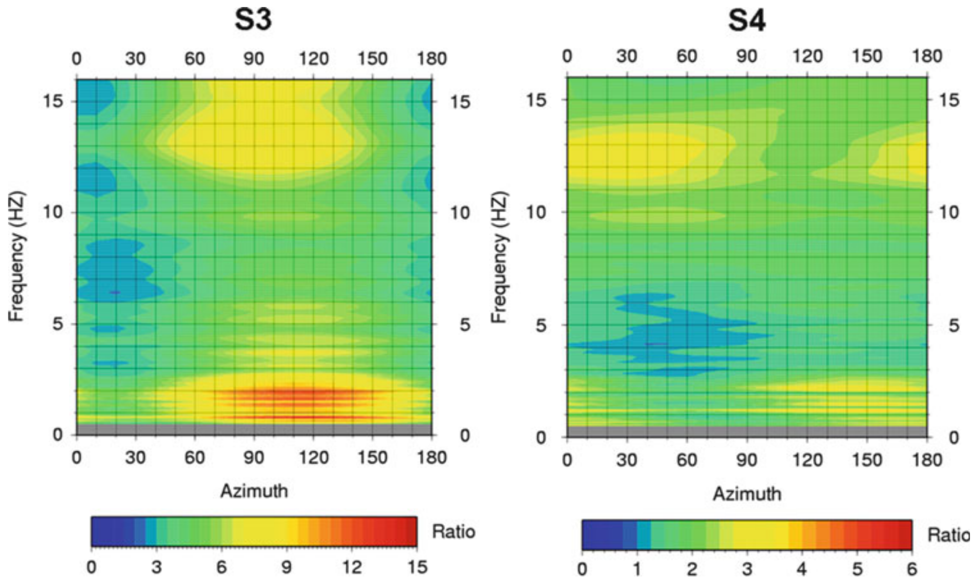

effects of anomalous acquisition conditions and thus strengthen the reliability of our inferences on the presence and significance of directivity in seismic site response at Jiufengershan and Tsaoling.

References

Arias A (1970) A measure of earthquake intensity. In: Hansen RJ (ed) Seismic design for nuclear power plants. MIT Press, Cambridge, MA, pp 438–483

Bard PY (coordinator), The SESAME TEAM (2004) Guidelines for the implementation of the H/V spectral ratio technique on ambient vibrations measurements, processing and interpretation. SESAME European research project, WP12 – Deliverable D23.12, 62p. http://sesame-fp5.obs.ujf-grenoble.fr/Papers/HV_User_Guidelines.pdf

Bozzano F, Lenti L, Martino M, Paciello A, Scarascia Mugnozza G (2008) Self-excitation process due to local seismic amplification responsible for the reactivation of the Salcito landslide (Italy) on 31 October 2002. J Geophys Res 113:B10312. doi:10.1029/2007JB005309

Chang KJ, Taboada A, Chan YC (2005) Geological and morphological study of the Jiufengershan landslide triggered by the Chi-Chi Taiwan earthquake. Geomorphology 71:293–309

Del Gaudio V, Wasowski J (2007) Directivity of slope dynamic response to seismic shaking. Geophys Res Lett 34:L12301. doi:10.1029/GL029842

Del Gaudio V, Wasowski J (2010) Advances and problems in understanding the seismic response of potentially unstable slopes. Eng Geol. doi:10.1016/j.enggeo.2010.09.007

Del Gaudio V, Coccia S, Wasowski J, Gallipoli MR, Mucciarelli M (2008) Detection of directivity in seismic site response from microtremor spectral analysis. Nat Hazard Earth Syst Sci 8:751–762

Hu JC, Tang CL, Tseng CH, Lin ML, Chan YC, Chu HT, Lee JF, Wie JY (2009) Giant landslides induced by the 1999 Chi-Chi earthquake. In: Proceedings of the conference "the next generation of research on earthquake-induced landslides", Jhongli, 21–26 Sept 2009, pp 141–147

Hung JJ, Lee CT, Lin ML (2002) Tsao-Ling rockslides, Taiwan, catastrophic landslides: effects, occurrence, and mechanisms. Geol Soc Am Rev Eng Geol 15:91–115

Meunier P, Hovius N, Haines JA (2008) Topographic site effects and the location of earthquake induced landslides. Earth Planet Sci Lett 275:221–232

Nakamura Y (1989) A method for dynamic characteristics estimation of subsurface using microtremors on the ground surface. Q Rep Railw Tech Res Inst 30:25–30

Sepúlveda SA, Murphy W, Jibson RW, Petley DN (2005) Seismically induced rock slope failures resulting from topographic amplification of strong ground motions: The case of Pacoima Canyon California. Eng Geol 80:336–348

Evaluation of the Temporal Probability of Earthquake-Induced Landslides in the Island of Lefkada, Greece

George Papathanassiou, Sotiris Valkaniotis, and Spyros Pavlides

Abstract

In the island of Lefkada, earthquakes are considered as the main causal factor of slope instabilities according to the seismic catalogues. In this study, the temporal probability was estimated as a joint probability of the exceedance probability of earthquake threshold per decade and the probability of landslide occurrence once the threshold has been exceeded. Initially, landslide inventory maps were compiled for the instrumental period of seismicity in Greece, indicating that the occurrence of landslide phenomena is mainly concentrated within the western part of the island. For this period, 21 earthquakes were recorded with magnitudes $M > 5.3$ and 6 of $M > 6.0$, while five landslide events were defined. Thus, the mean recurrence interval per decade between successive threshold exceedance was estimated at 0.48 and 1.66 for earthquake magnitudes $M = 5.3$ and $M = 6.0$, respectively. Taking into account that the probability of occurrence of landslide after the threshold has been exceeded is 0.23 and 0.83 for $M > 5.3$ and $M > 6.0$, the estimated temporal probability of earthquake-induced landslides for different time periods, from 10 to 500 years, ranges from 0.2 to 0.23 for earthquake magnitudes $M > 5.3$ and from 0.37 to 0.83 for magnitude $M > 6.0$.

Keywords

Landslide • Earthquake • Temporal probability • Lefkada • Greece

Introduction

The population growth and the expansion of settlements and life-lines over hazardous areas are increasing the impact of natural disasters both in the developed and developing world (Alexander 1995). Varnes (1978) defined landslides as the downward and outward movement of slope-forming materials composed of rocks, soils or artificial fills. Movement may take place by falling, sliding or flowing or some combination of these factors (Bell 1999). Casualties due to slope failures are larger in the developing countries, whereas economic losses are more severe in the industrialized world. The costs of landslides range from the expense of clean-up operations and repair or replacement of structures to reduced productivity and property values. Nonetheless, landslides are considered to be one of the most potentially predictable of geological hazards (Bell 1999). Nowadays, earth scientists mainly make use of GIS-based techniques in order to map the landslide susceptibility, hazard and evaluate the risk within an area.

Brabb (1984) define the landslide susceptibility as the likelihood of a landslide occurring in an area on the basis of local terrain conditions. The evaluation of susceptibility can be achieved using regional landslide predictive models that estimate "where" landslides are likely to occur over a given region on the basis of a set of environmental characteristics (Guzzetti et al. 1999). However, do not directly incorporate time and magnitude; hence, they cannot be correctly defined as hazard models (Guzzetti et al. 1999).

G. Papathanassiou (✉) • S. Valkaniotis • S. Pavlides
Department of Geology, Aristotle University of Thessaloniki, Thessaloniki, Greece
e-mail: gpapatha@auth.gr

C. Margottini et al. (eds.), *Landslide Science and Practice*, Vol. 5,
DOI 10.1007/978-3-642-31427-8_27, © Springer-Verlag Berlin Heidelberg 2013

Landslide hazard is the probability of occurrence of a potentially damaging phenomenon within a given area and in a given period of time (Varnes 1984) and incorporates the concepts of location i.e. where, and time i.e. when, or "how frequently" it will occur (Guzzetti et al. 1999).

The quantitative assessment of landslide hazard can be computed as the joint probability of the spatial probability of occurrences of landslides and of the temporal probability of occurrence of triggering event (Guzzetti et al. 2005; Jaiswal et al. 2010). In this study, the latter is evaluated using the exceedance probability of an earthquake magnitude required to trigger landslides, following the method presented by Jaiswal and vas Westen (2009) that had been used in order to determine the temporal probability for rainfall-induced landslide initiation. In our case, the parameter that was taken into account for the evaluation of temporal probability is the occurrence of earthquakes since the main triggering mechanism of slope failures within this area is the seismic activity.

Geology of the Area

The geology of the Lefkada island, which has been studied in detail by Bornovas (1964), comprises: (1) a carbonate sequence of the Ionian zone, (2) Limestone of Paxos (Apulia) zone restricted in the SW peninsula of the island, (3) few outcrops of ionian flysch (turbidites) and Miocene marls–sandstones mainly in the northern part of the island (Cushing 1985; Rondoyanni-Tsiambaou 1997). Pleistocene and especially Holocene coastal deposits are extended in the northern edge of Lefkada, where the homonym capital town is founded, in the valley of Vassiliki and in the coast Nydri (Fig. 1). The main structures are thrust faults of the Ionian limestone on to Miocene marls from NE towards SW and a system of neotectonic faults. The NE-SW to NNE-SSW trending neotectonic main faults are normal structures with a significant right-lateral component, while some minor faults NW-SE trending show left-lateral character. Typical normal dip-slip faults are oriented ENE-WSW and N-S. By using morphotectonic criteria most of them can be considered as active or possibly active structures.

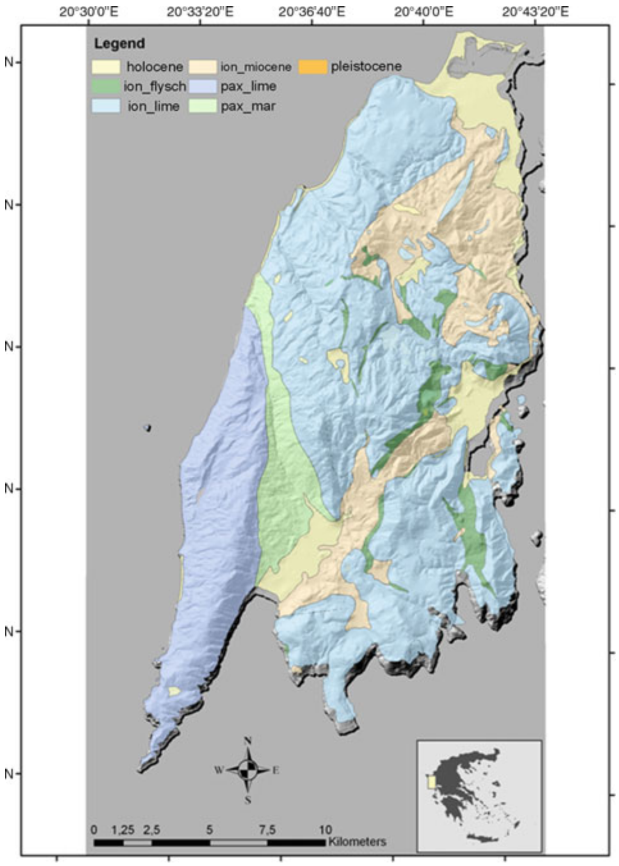

Fig. 1 Simplified geological map of Lefkada (Holocene: Holocene sediments; ion_flysch: flysch of Ionian zone; ion_lime: limestone of Ionian zone; ion_miocene: Miocene age formation of Ionian zone; pax_lime: limestone of Paxi (Apulia) zone; pax_mar: Marls of Paxi (Apulia) zone; Pleistocene: Pleistocene sediments)

Historical Seismicity and Slope Instability Phenomena in the Island of Lefkada

The area of Ionian Islands is considered as the most prone to earthquake region not only in Greece but in whole Europe. Characteristic seismic events that occurred within this area from the seventeenth century have been recorded and detailed reported. In particular, for the island of Lefkada reliable information existed for at least 23 events, since 1612, which induced ground failures. Our evaluation of historical seismicity-induced landslides is based on reports published by the Newspapers "Aeon", "Filomathon", "Eho"; Archive of Lefkada for the seismicity of the island; Barbiani, D. and Barbiani, G. (1864), Stamatelos (1870). Galanopoulos (1955). Rondoyannis (1995), Papazachos and Papazachou (1997), and Papazachos et al. (2000). A list of historical earthquakes-induced landslides/rockfalls, which occurred in Lefkada Island, is shown in Table 1. The focal parameters of the events have been collected from the seismic catalogues of Papazachos et al. (2000, 2009) except of the case EqID 3, which was collected from Galanopoulos (1981). The area that

Table 1 Historical earthquakes-induced landslides/rockfalls occurred in Lefkada Island

EqID	Date (dd/mm/yy)	Latitude	Longitude	M
1	23/03/1783	38.7	20.61	6.7
2	7/01/1825	38.7	20.6	6.5
3	14/12/1885	38.5	20.75	5.7
4	27/11/1914	38.65	20.62	6.3
5	7/08/1915	38.5	20.62	6.7
6	22/04/1948	38.68	20.57	6.5
7	30/06/1948	38.8	20.6	6.4
8	14/08/2003	38.74	20.53	6.3

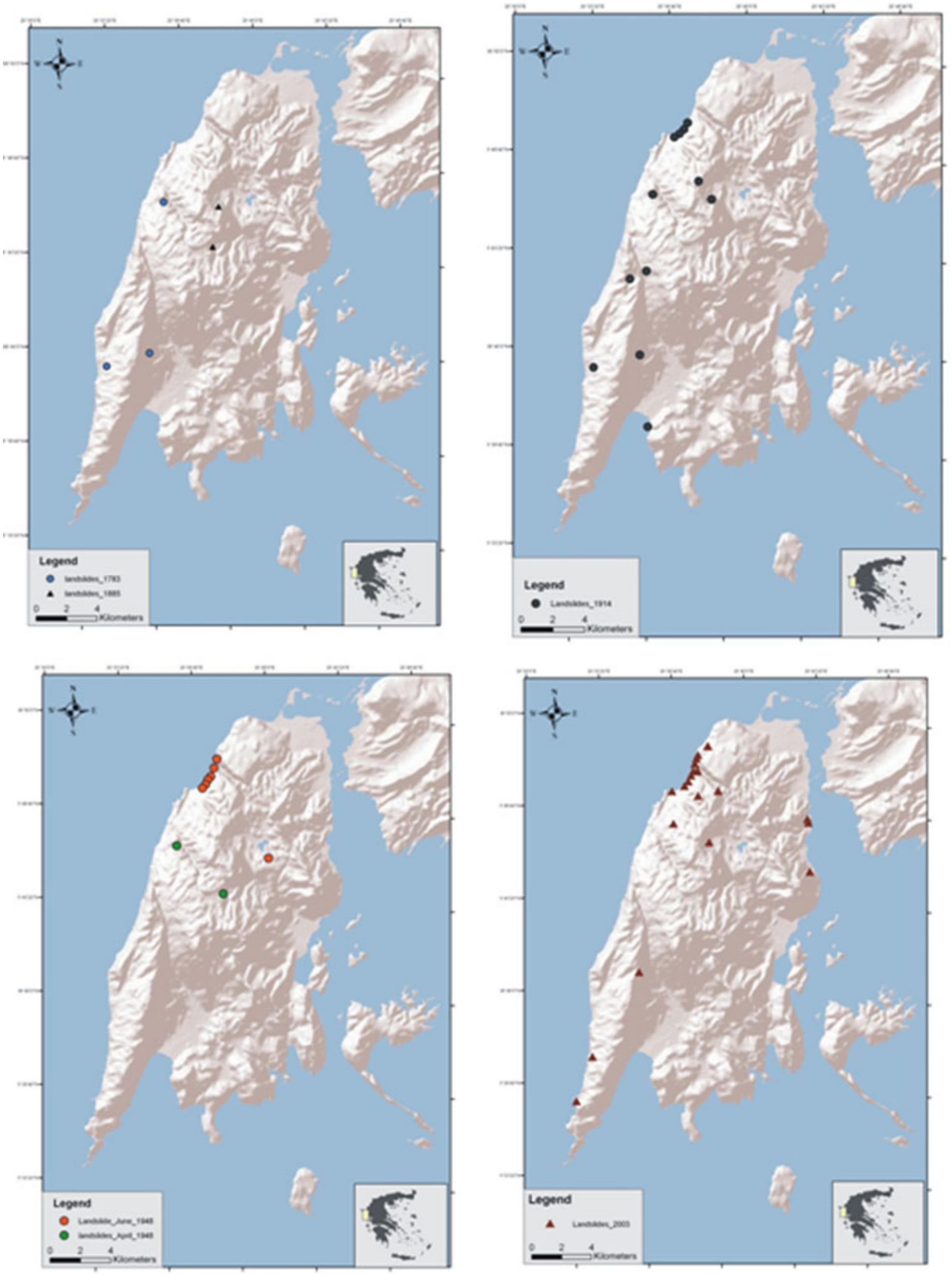

Fig. 2 Event-based inventory maps regarding the occurrence of landslides in the island of Lefkada (*up left*: landslides triggered by the 1783 and 1885 events; *up right*: landslides triggered by the 1914 event; *down left*: landslides triggered by the 1948 events and down right: landslides triggered by the 2003 event)

was mostly affected by the earthquake-induced landslides/ rockfalls is the western part of the island where steep slopes of low cohesion material is appeared.

Event-Based Inventory Maps

Detailed, comprehensive inventories of landslides triggered by earthquakes are the essential parts of seismic landslide hazard analyses. The importance of such a detailed and comprehensive landslide inventory becomes paramount when the earthquake occurs in an area in which an extensive network of strong-motion seismometers has also recorded the strong shaking from the earthquake (Harp et al. 2011). In such a case, the landslide distribution, the topography, the geology, and the ground shaking can be compared and analyzed on a Geographic Information Systems (GIS) platform to produce a probabilistic landslide hazard analysis for the affected region (Harp et al. 2011). However, when using these data, it has to be remembered that not all events will have been recorded and the quality of historical evidence is strongly dependent on recording procedures and available records (Glade et al. 2005).

In this study, earthquake-induced landslide inventory maps were compiled based on literature review. Obviously, the description of ground failures triggered by an historical event cannot be as reliable and accurate as the one related to a recent event. However, despite the fact that the quality of historical evidence is strongly dependent on recording procedures and available records, this approach provides an indication of at least the minimum level of landslide activity in an area (Glade et al. 2005). Thus, we proceeded to the compilation of event-based inventory maps (Fig. 2) taken into account the information provided by the list of Table 1.

In particular, the 23 March 1783 shock caused rockalls and landslides that induced severe damages to the villages of Athani, Dragano and Agios Petros. The 7 January 1825 event caused slope failures close to the village Kalamitsi and the 14 December 1885 earthquake was mainly induced failures in the central part of the island of Lefkada and particularly close to the villages of Eglouvi, Karia and Kalamitsi. The 27 November 1914 triggered soil slides of cohesionless materials mainly in the western part of mountain Pefkoulia and close to the villages of Athani and Komilio. Moreover, rockfalls of 1–3 m^3 volume reported on the road network of the villages Agios Petros-Hortata-Komilio and on the road Karia - city of Lefkada. Moreover, structural damages to houses were reported at the villages of Kalivata and Poros. The 7 August 1915 triggered large scale rockfalls at the mountains of Stavrotas, Vournikas and Lefkatas and the 22 April 1948 caused soil slides and rockfalls in the vicinity of villages Kalamitsi and Eglouvi while soil slides at the Pefkoulia mountain and rockfalls close to village Nikiana were generated by the 30 June 1948 earthquake.

Finally, the 14 August 2003 caused characteristic rock falls, with diameters up to 4 m that were observed along the 6 km long road of Tsoukalades-Agios Nikitas, which is very close to the epicentral area, and are accompanied by gravel, small rock and soil slides. In this region, the rock falls follow the trace of a 300-m high morphological scarp, and especially a 10–40 m high artificial slope. In most cases rock falls are directly associated with pre-existing tectonic discontinuities and steep slopes within the Ionian limestone. Although many slope failures-flows were observed, only few of them can be considered as typical landslides like those along the road to Kalamitsi and Agios Petros villages. At the center of the island, Karya village, a landslide is clearly associated to the pre-existing faults and fractures.

Table 2 Number of times of the occurrence of earthquake-induced landslides that exceed the threshold values of M = 5.3 and M = 6

Period	Threshold exceedance M > 5.3	Threshold exceedance M > 6.0	landslides event
1911–1920	7	3	2
1921–1930	2	0	–
1931–1940	2	0	–
1941–1950	5	2	2
1951–1960	0	0	–
1961–1970	0	0	–
1971–1980	1	0	–
1981–1990	0	0	–
1991–2001	2	0	–
2001–2010	2	1	1
	21	6	

Evaluating the Temporal Probability of Earthquake-Induced Landslide

It is well known that a landslide can be triggered by rainfall, earthquakes, volcanic eruption and man-made activities. The activation of slope instability depends on the magnitude of the causal factors and several efforts have been made in order to establish relative threshold values, defined as the minimum magnitude that should be exceeded for the initiation of landslides.

Furthermore, having estimated the probability of occurrence of the triggering threshold, the probability of landslide occurrence can be assumed since in this simplified model landslides always occur when magnitude M exceeds magnitude threshold Mt and never occur when the value of M is lower or equal to Mt (Jaiswal and van Westen 2009). However, the threshold may be exceeded without triggering a landslide. In order to overcome this Floris and Bozzano (2008) suggested to take into account the conditional probability of a given threshold exceedance [P{M > Mt}] and the probability of occurrence of a landslide [P{L}], given the exceedance. Thus, the probability of occurrence of both {M > Mt} and {L} is equal to the probability of {M > Mt} multiplied by the probability of occurrence of {L}, assuming that the {M > Mt} has already occurred (Jaiswal and van Westen 2009). The probability of {M > Mt} can be obtained by determining the exceedance probability of the earthquake magnitude threshold using a Poisson model and the probability of {L M > Mt} relies on the frequency of occurrence of landslides after the threshold has been exceeded (Jaiswal et al. 2010).

In this study, the temporal probability of earthquake-induced landslide was estimated using information provided by historical reports describing environmental effects triggered by earthquakes. Two threshold values have been

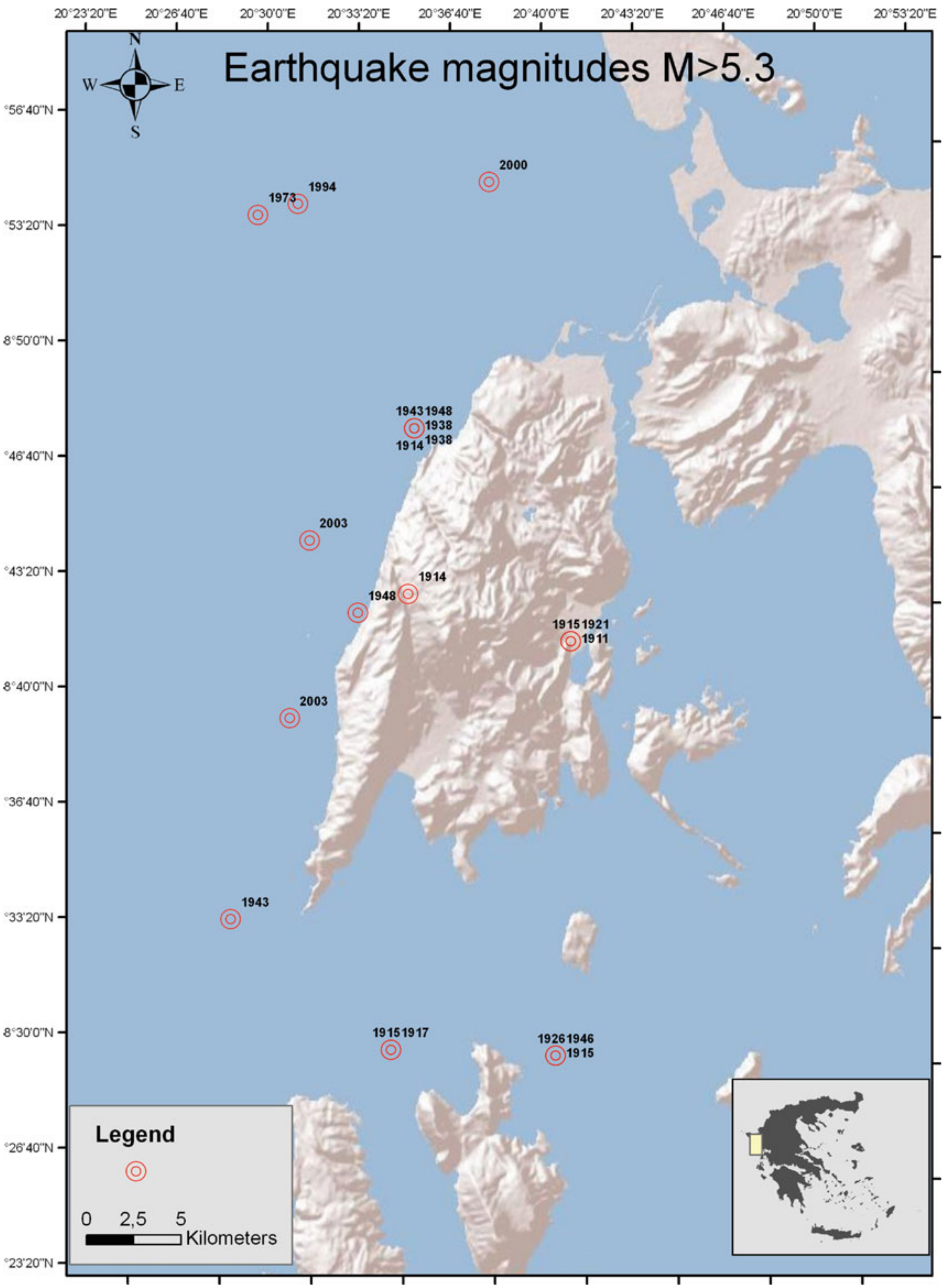

Fig. 3 Map showing the distribution of earthquake epicenters with magnitude M > 5.3 that occurred during the instrumental period of seismicity

employed in this model, M = 5.3 and M = 6.0. The former was suggested by Papadopoulos and Plessa (2000) as the lowest value of earthquake-induced slope failures in Greece and the latter was adopted by the authors of this study due to the fact that the seismic catalogues can be characterized as complete and reliable, regarding the description and report of secondary effects, for earthquake magnitude M > 6. Furthermore, in our analysis we decided to take into consideration only the events that occurred during the instrumental period of seismicity from 1911 to 2010, in order to ensure a reliable and accurate evaluation of the earthquake magnitude.

Table 3 Corresponding values of AEP and temporal probability of earthquake-induced landslides computed for a time equal to 10, 25, 50, 75, 100 and 500 years

AEP	AEP	Years	Temporal probability	
(M > 5.3)	(M > 6.0)		M > 5.3	M > 6.0
0.877	0.451	10	0.208	0.375
0.994	0.776	25	0.236	0.647
0.999	0.950	50	0.238	0.791
0.999	0.988	75	0.238	0.824
0.999	0.997	100	0.238	0.831
1	1	500	0.238	0.833

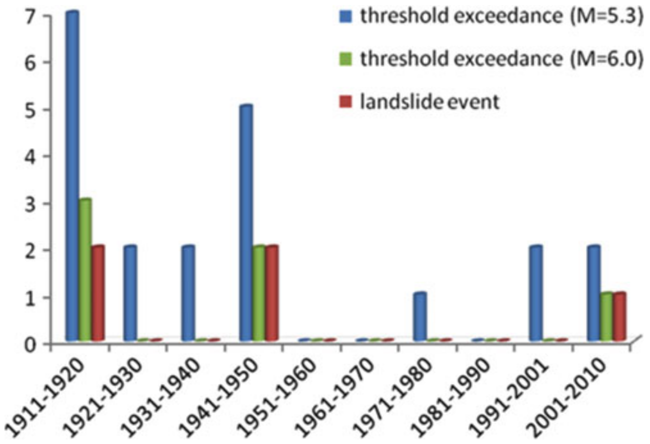

Fig. 4 Threshold exceedance per decade. Bars with *blue* and *green* indicate the frequency that the threshold M = 5.3 and M = 6, respectively, was exceeded in a decade. *Red* bars indicate the frequency of an earthquake-induced landslide occurrence

In order to estimate the temporal probability, we initially compute the "annual" exceedance probability (AEP) which is defines as the probability that an event of specific magnitude will be exceed in any given year (Fell et al. 2005). We decided to use decade instead of year as "annual" exceedance because the occurrence of earthquakes, the causal factor that was examined in this study, is described in a more rational way using this period of time. The AEP was computed based on Poisson model and using the equation

$$P[N(t) > 1] = 1 - \exp(-\frac{t}{\mu}) \qquad (1)$$

Where μ is the mean recurrence interval between successive landslides as it was resulted by the inventory data, and t is time.

The frequency of landslides events was obtained by the historical archive of the municipality of Lefkada, including newspapers and published reports. According to the seismic catalogue of Papazachos et al. (2000, 2009) for a period of 100 years, from 1911 to 2010, the thresholds M = 5.3 and M = 6.0 were exceeded 21 and 6 times, respectively (Table 2). In Fig. 3, is shown the epicenter's distribution and the date of occurrence of the selected events.

Thus, the mean recurrence interval between successive threshold exceedance per decade is equal to 0.48 for M = 5.3 and 1.6 for M = 6. Taking into account these values, the corresponding AEP were computed and listed in Table 3 for a time equal to 10, 25, 50, 75, 100 and 500 years using (1).

Afterwards, the probability of occurrence of a landslide after the threshold exceeded was estimated using the inventory-based information. According to the literature, five landslide events were reported for the instrumental period of seismicity, thus the estimated probability P(L M > Mt) is equal to 0.23 for threshold M = 5.3 and 0.83 for a threshold earthquake magnitude M = 6. Taking into account the estimated AEP values that are listed in Table 3 and the resulted probability P(L M > Mt), we computed the temporal probability of earthquake-induced landslide in the island of Lefkada for different time periods, from 10 to 500 years. As it is shown in Table 3, the maximum temporal probability (83 %) is estimated for a period of 500 years and a threshold magnitude of M = 6.0 and the minimum (20 %) for a 10 years period and a threshold equal to M = 5.3 (Fig. 4).

Conclusions

The basic aim of this study was the evaluation of the temporal probability of earthquake-induced landslides since the main triggering mechanism of slope failure in the island of Lefkada is the occurrence of earthquakes. The event-based inventory maps for the instrumental period of seismicity in Greece (1911 to 2010) that were compiled based on collected historical information, show that the most prone area to slope failures is the western part of the island where large scale rock and debris slides have been reported. The threshold earthquake magnitudes that have been taken into account in this study were M = 5.3 and M = 6.0. The former was identified by Papadopoulos and Plessa (2000) as the lowest magnitude capable to trigger landslides in Greece and the latter was introduced by the authors of this study due to the fact that in seismic catalogues detailed reports for secondary effects exists for M > 6.0. The outcome provided by this study, shows that the estimated temporal probability of earthquake-induced landslides in the island of Lefkada for different time periods, from 10 to 500 years, ranges from 0.2 to 0.23 for earthquake magnitudes M > 5.3 and from 0.37 to 0.83 for magnitude M > 6.0.

References

Alexander ED (1995) A survey of the field of natural hazards and disaster studies. In: Carrara A, Guzzetti F (eds) Geographical information systems in assessing natural hazards. Kluwer, Dordrecht, pp 1–19

Barbiani DG, Barbiani BA (1864) Memoires sur les tremblements de terre dans l'ile de Zante. Presented by A. Perrey in Academic Imperiale des Sciences, Dijon, 112p

Bell F (1999) Geological hazards, their assessment, avoidance and mitigation. E & FN Spon, London, 648p

Bornovas J (1964) Géologie de l'île de Lefkade, vol 1, 10th edn, Geological geophysique research (IGSR). Geological Geophysique Research, Athens

Brabb EE (1984) Innovative approaches to landslide hazard mapping. In: Proceedings of the 4th international symposium on landslides, vol 1, Toronto, pp 307–324

Cushing M (1985) Evoluation structurale de la marge nord-ouest hellenique dans l'ile de Lefkada et ses environs (Greece nord-occidentale), Ph.D. thesis, Univ. de Paris-Sud (XI), Centre d' Orsay, France

Fell R, Ho KKS, Lacasse S, Leroi E (2005) A framework for landslide risk assessment and management. In: Hungr O, Fell R, Eberhardt E (eds) Landslides risk management. Taylor and Francis, London, pp 3–26

Floris M, Bozzano F (2008) Evaluation of landslide reactivation: a modified rainfall threshold model based on historical records of rainfall and landslides. Geomorphology 94:40–57

Galanopoulos GA (1955) Seismic geography of Greece. Annales Géologique de Pays Helleniques 6:83–121

Galanopoulos GA (1981) The damaging shocks and the earthquake potential of Greece. Annales Géologique de Pays Helleniques 30:648–724

Glade T, Anderson M, Crozier M (2005) Landslide hazard and risk. Wiley, England, 802p. ISBN 0-471-48663-9

Guzzetti F, Carrara A, Cardinali M, Reichenbach P (1999) Landslide hazard evaluation: a review of current techniques and their application in a multi-scale study, Central Italy. Geomorphology 31: 181–216

Guzzetti F, Reichenbach P, Cardinali M, Galli M, Ardizzone F (2005) Probabilistic landslide hazard assessment at the basin scale. Geomorphology 72:272–299

Harp E, Keefer D, Sato H, Yagi H (2011) Landslide inventories: the essential part of seismic landslide hazard analyses. Eng Geol. doi:10.1016/j.enggeo.2010.06.013

Jaiswal P, van Westen C (2009) Estimating temporal probability for landslide initiation along transportation routes based on rainfall thresholds. Geomorphology 112:96–105

Jaiswal P, van Westen C, Jetten V (2010) Quantitative landslide hazard assessment along a transportation corridor in southern India. Eng Geol 116:236–250

Papadopoulos GA, Plessa A (2000) Magnitude-distance relations for earthquake-induced landslides in Greece. Eng Geol 58:377–386

Papazachos BC, Papazachou K (1997) The earthquakes of Greece. Ziti Publication, Thessaloniki, 356p

Papazachos BC, Comninakis PE, Karakaisis GF, Karakostas BG, Papaioannou ChA, Papazachos CB, Scordilis EM (2000) A catalogue of earthquakes in Greece and surrounding area for the period 550BC-1999, Publication of Geophysical Laboratory, University of Thessaloniki, Thessaloniki, 333p

Papazachos BC, Comninakis PE, Scordilis EM, Karakaisis GF, Papazachos CB (2009) A catalogue of earthquakes in the Mediterranean and surrounding area for the period 1901–Sep 2009, Publication of Geophysical Laboratory, University of Thessaloniki, Thessaloniki

Rondoyannis GP (1995) The seismicity of Lefkada (1469-1971). Society of Lefkada's studys. H. (in Greek)

Rondoyanni-Tsiambaou T (1997) Les seismes et l'environnement géologique de l'île de Lefkade, Grèce: Passe et Futur. In: Marinos P et al (eds) Engineering geology and the environment. Balkema, Rotterdam, pp 1469–1474

Stamatelos JN (1870) The thirteen mentioned destruction of Leukada, from 1612 till 1869. Efimeris of Philomathon, Athens, 24 Jan 1870, p 726 (in Greek)

Varnes DJ (1978) Slope movements: types and processes. In: Schuster RL, Krizek RJ (eds) Landslide analysis and control, vol 176, Transportation research board special report. National Academy of Sciences, Washington, pp 11–33

Varnes DJ, IAEG Commission on Landslides and other Mass-Movements (1984) Landslide hazard zonation: a review of principles and practice. The UNESCO Press, Paris, 63p

Building Vulnerability to the 2008 Ilia-Achaia Earthquake Induced Slides

Stavroula Fotopoulou, Anastasios Anastasiadis, and Kyriazis Pitilakis

Abstract

The present paper, after providing a brief description of the recently developed analytical tool for assessing vulnerability of RC (reinforced concrete) structures to earthquake triggered earth slides, focuses on the exploration of the reliability and applicability of proposed procedure through its application to a real case study. In particular, the approach is implemented to a representative RC building located near the crest of the Kato Achaia slope where most of the structural damage was concentrated in consequence of the Ilia-Achaia, Greece 2008 (Mw = 6.4) earthquake. Both the structure and slope configuration are realistically reproduced using non-linear constitutive models to estimate the vulnerability of the reference building and to assess the validity of the developed methodological framework and the corresponding fragility relationships. In terms of numerical simulations, the analysis involves two consecutive steps: (a) estimation of the differential permanent deformation at the foundation level derived through a finite difference, non-linear, slope dynamic model and (b) static application of the computed differential displacement at the building 's supports via a fibre-based finite element (static time history) analysis. The proposed probabilistic fragility curves were found to adequately capture the simulated and recorded performance of the representative RC building affected by the slope co-seismic differential displacement.

Keywords

Vulnerability • RC buildings • Fragility curves • Kato achaia slope • Co-seismic landslide displacements

Introduction

Seismically triggered landslides are recognized as one of the most destructive natural hazards associated to earthquakes as they may result to significant direct and indirect losses to the population and the build-up environment (Bird and Bommer 2004). Therefore, assessing the vulnerability of affected build structures subjected to earthquake induced landslide hazards is of major importance for design, urban planning, and for seismic and landslide risk studies.

Within the context of landslide risk assessment practice, physical (technical) vulnerability comprises a key component that still requires significant research (e.g. Van Westen et al. 2006). It may be defined as the degree of loss (in terms of percentage % of structural damage) of the affected built structures subjected to a landslide event of a given type and intensity. Physical vulnerability depends both on the structural properties of exposed elements and on the mechanism and magnitude of the landslide processes. In this respect, methodologies to assess physical vulnerability may be classified in relation to the landslide type, the element at risk and the scale of analysis. However, focusing in

---

S. Fotopoulou (✉) • A. Anastasiadis • K. Pitilakis
Department of civil Engineering, Aristotle University of Thessaloniki, P.O.B. 424, Thessaloniki 54124, Greece
e-mail: sfotopou@civil.auth.gr

C. Margottini et al. (eds.), *Landslide Science and Practice*, Vol. 5,
DOI 10.1007/978-3-642-31427-8_28, © Springer-Verlag Berlin Heidelberg 2013

particular on earth slides, it is seen that most of the existing methodologies resort to expert judgment and empirical data and they are principally applicable to studies at regional and local scales (e.g. AGSO 2001; Remondo et al. 2008; Zêzere et al. 2008; Uzielli et al. 2008, etc.). Very few models are available in the literature to quantify the vulnerability of the affected facilities impacted by earth slides using analytical relationships and numerical simulations with potential application from site specific to local scale. Among these, Fotopoulou et al. (2011) and Fotopoulou and Pitilakis (2011) have recently developed an efficient probabilistic framework based on a comprehensive set of numerical computations and statistical analysis for assessing physical vulnerability of RC structures due to seismically triggered earth slides. The final output of the analysis is given in terms of fragility curves as a function of the Peak Horizontal Ground Acceleration (PHGA) at the assumed "seismic bedrock", allowing for the quantification of various sources of uncertainty in a cost effective manner.

The present study, after providing a summary of the developed procedure, is aimed at the exploration of the reliability and applicability of the proposed fragility curves through its application to a real case history. More specifically, the approach is implemented to a reference RC building located in the vicinity of the Kato Achaia slope's ridge, where most of the building damages were observed as a result of the Ilia-Achaia, Greece 2008 (Mw = 6.4) earthquake. The ultimate goal of the analysis is to assess the validity of the developed fragility curves via comparison with recorded and simulated building damage data.

Methodology

The proposed method may be applied to assess the vulnerability of RC buildings impacted by earthquake triggered earth slides. It has been developed as part of the SAFELAND research project supported by the European Commission. Figure 1 illustrates a schematic representation of the proposed framework.

The vulnerability is defined through specific probabilistic fragility functions that are numerically estimated in terms of peak ground acceleration at the "seismic bedrock", versus the probability of exceedance of each limit state. The use of the PGA at rock conditions instead of our descriptors is decided in order to be consistent with the nominal accelerations proposed in EC8 or other seismic codes. In that way the soil and topographic amplification is directly included. In terms of numerical simulation, a two-step uncoupled analysis is performed. In the first step, the differential permanent displacements at the building's foundation level are estimated using a FLAC2D (ITASCA Consultants 2005) finite difference dynamic slope model. Different gradually increasing acceleration time histories are applied at the base of the model to cover a wide range of seismic motions in terms of the seismotectonic environment, amplitude, frequency content and significant duration. The computed permanent displacements at the foundation level were validated through comparison with simplified Newmark-type displacement methods. Then, the calculated differential displacements in the sliding slope are statically imposed to building's model at the foundation level to assess the building's response for different ground landslide displacements induced by the earthquake. The numerical (static time history) analyses of the buildings are performed through the fibre-based finite element code SEISMOSTRUCT (Seismosoft 2007). It 's worth noticing that the complex issue of combined damages on the building by ground shaking and ground failure due to landslide is not taken into account in the evaluation of the building's vulnerability, that is assessed only for effect of the permanent co-seismic displacement. Structural limit states are defined in terms of a threshold value of building's material strain based on the work of Crowley et al. (2004), Bird et al. (2006), Negulescu and Foerster (2010), and engineering judgment. Uncertainties related to the capacity of the building, the definition of the limit states and the deformation demand are considered.

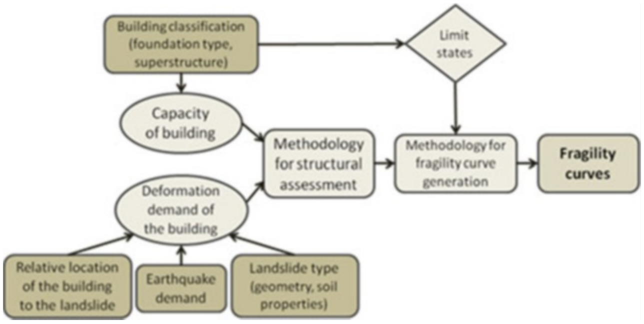

Fig. 1 Flowchart for the proposed framework of fragility analysis of RC buildings

The methodology has been applied to different soil types, slopes geometries, foundation and superstructure configurations allowing for the identification and classification of the most influential factors in assessing the structure's vulnerability. Further details regarding the developed methodological framework and the derived fragility functions are provided in Fotopoulou et al. (2011) and Fotopoulou and Pitilakis (2011).

Application to Kato Achaia Slope, Western Greece

The Earthquake of 8 June 2008 in Achaia-Ilia, Greece

On 8 June 2008, an Mw 6.4 strong earthquake occurred in the area of northwest Peloponnese, western Greece, at a distance of about 17 km southwest of the town of Patras on a dextral strike slip fault (Fig. 2). The main shock was recorded by 27 strong motion instruments at distances

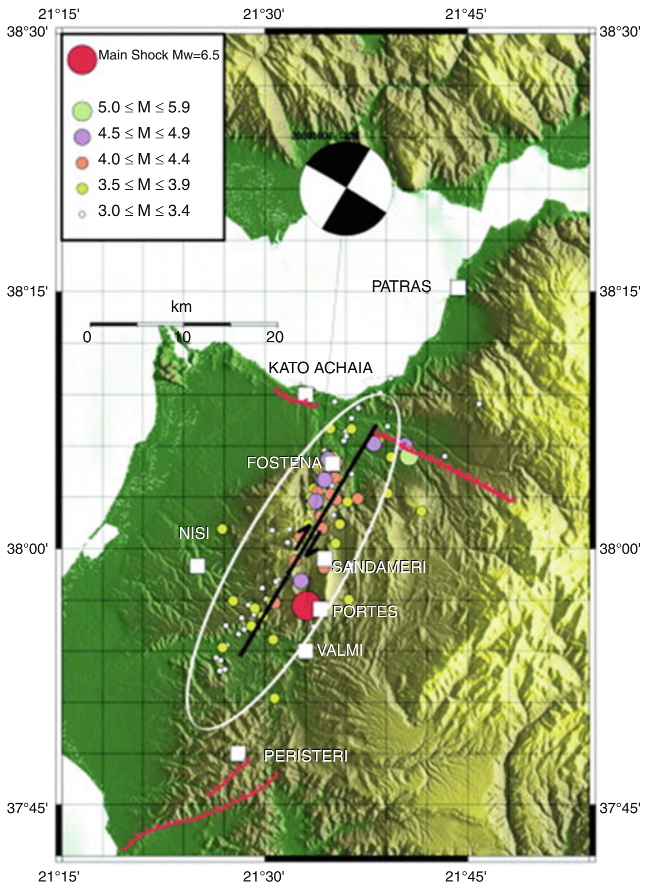

Fig. 2 Fault of the June 8, 2008 sequence (*black*) (determined by analysis of the main shock and aftershock distribution) and already mapped faults (*red*). The *red circle* denotes the epicenter of the main shock. Towns affected by the earthquake are denoted by squares (Margaris et al. 2010)

ranging approximately from 15 to 350 km from the surface projection of the fault. Of those 27 stations, six are within a relatively small region in Patras (Margaris et al. 2010). The event caused considerable structural damage to buildings and infrastructures. Ground failure was widely observed within approximately 15 km of the fault, taking the form of landslides (mostly rockfalls), liquefaction, coastal subsidence, and settlement of fills (Margaris et al. 2008).

The town of Kato Achaia is located approximately 20 km from the epicenter of the main shock and from the town of Patras (Fig. 2). The minimum distance from the surface projection of the fault is estimated as Rjb = 6 km. The site along the coast of Kato Achaia was found to suffer extensive ground deformation due to liquefaction. However, it is not our objective here to study liquefaction phenomena. Preliminary investigation on Kato Achaia area indicates peak horizontal ground acceleration values on the order of 0.3 g, quite higher than the values recorded in Patras downtown.

An important concentration of severe building damages is observed near the edge of the cliff that comprises the northern boundary of Kato Achaia town (Fig. 3). This is probably due to simple site amplification in the vicinity of the crest as it is illustrated by the amplification of the horizontal acceleration and the generation of parasitic vertical acceleration near the top of the slope (Athanasopoulos and Pefani, 2010, personal communication). However such models are not considering any effect from permanent ground displacements due to differential ground movements close to the slope and the crest. In the present we are investigating the possible presence of both phenomena.

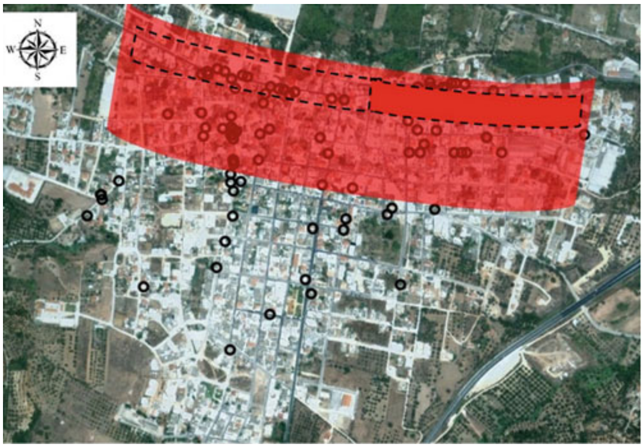

Fig. 3 Geographical distribution of the buildings (*black circles*) that suffered severe damage in Kato Achaia

Figure 3 denotes the area with the larger concentration of damaged buildings (in red), while the narrow red zone indicates the area with complete collapses of the buildings. As expected for this level of shaking, the field reconnaissance survey revealed that the earthquake did not cause the complete failure of the slope; only limited permanent deformations were observed close to the slope's crest, implying that probably the building damage occurred primarily as a result of ground shaking and its amplification due to the topographic and complex site effects and not in consequence of extensive co- seismic irreversible slope deformation. However this has to be confirmed through numerical non-linear analysis.

Slope Non-linear Dynamic Analysis

The present study aims at the investigation through numerical fully non-linear dynamic analysis of the Kato Achaia slope performance and the potential effects on the buildings located in the vicinity of the slope's crest; we examine different earthquake scenarios. The main idea is first to verify through numerical nonlinear models that for the 8 June 2008 earthquake the observed building damages occurred primary as a result of amplified ground shaking; then, for a stronger earthquake hazard scenario (e.g. with a mean return period Tm of 1,000 years), we are proposing to assess the vulnerability due to permanent co-seismic slope displacement of a reference RC building standing near the slope's crown. More specifically, the numerical methodology described in the previous section for the vulnerability assessment of RC buildings subject to earthquake induced slow moving slides is used.

In order to estimate structural vulnerability for a given earthquake triggered landslide scenario, one could directly use the fragility curves that have already derived via numerical parametric analysis (Fotopoulou et al. 2011; Fotopoulou and Pitilakis 2011). These correspond to the simplified geometrical, geological and structural settings for the slope and the structure. Nevertheless, it was decided to reproduce the numerical simulation for the real slope geometrical, hydro-geotechnical, geological and shaking characteristics to check the reliability and applicability band of the proposed simplified curves.

Figure 4 presents the topographic map (original scale 1:5,000) of the Kato Achaia area and the location of the 2 dimensional cross-section A-A' used to conduct the numerical dynamic analysis. A geotechnical and geophysical investigation has been performed by the University of Partas (Greece) Civil Engineering Department (UPatras; http://www.civil.upatras.gr/) in the broader area including geotechnical boreholes, N_{SPT} tests, Surface Waves tests (using ReMi, SASW and MASW techniques) and classical geotechnical laboratory tests on representative and undisturbed soil samples. Based on the above data provided by the University of Patras, Fig. 5 presents the simplified 2-dimensional cross-section used for the dynamic analysis together with the (two) sites of geotechnical boreholes. The water table is found to be located 30 m below the slope's crest and 1 m above the slope's toe. The geotechnical surveys reveal nine different soil layers. The geotechnical characteristics assigned to each layer are summarized in Table 1. It should be noted that the investigation of the potential for liquefaction is beyond the scope of this study.

In order to establish correlation between the earthquake demand and the permanent differential displacements for the building, dynamic non-linear analyses were performed using the computer code FLAC 5.0 (Itasca 2005). The soil materials are modeled using an elastoplastic constitutive model with the Mohr-Coulomb failure criterion, assuming a zero dilatancy non-associated flow rule. The discretization allows for a maximum frequency of at least 10 Hz to propagate through the finite difference grid without distortion. A small amount of mass- and stiffness-proportional Rayleigh damping is also applied (0.5–2 %), to account for the energy dissipation during the elastic part of the response and during wave propagation through the site. The center frequency of the installed Rayleigh damping is selected to lie between the fundamental frequencies of the input acceleration time histories and the natural modes of the system. The 2D dynamic model is 800 m wide and the elevations of ground surface vary from 160 to 195 m. The slope's height and inclination are estimated at 23 m and 28° respectively.

Fig. 4 Topographic map (original scale 1:5,000) of Kato Achaia area and position of A-A' cross section

Free field absorbing boundaries are applied along the lateral boundaries while quiet (viscous) boundaries are used along the bottom of the dynamic model to minimize the affect of reflected waves. In order to apply a compliant base along the same boundary as the dynamic input, the seismic motion is modeled as stress loads combining with the quiet (absorbing) boundary condition.

A RC building is assumed to be located 3 m from the slope's crest. At this (first) stage of the numerical analysis, the building is modeled only by its foundation with a width of 6 m (uncoupled approach). The combined effect of the soil-structure interaction and of the topographic irregularity on the dynamic response of the building (e.g. see Pitilakis 2009) is not taken into account in the analysis. A flexible foundation system (isolated footings) simulated with concentrated loads (P = 50 KN/m) at the footings' links is considered. Thus, no relative slip between foundation and subsoil is permitted.

Due to the lack of acceleration records within the slope area, two different strong motion time-histories recorded at the stations PAT3—(Patra High School) and Pat_Hosp (Patras Hospital) of the town of Patras were used in the numerical simulations. The base motions imposed in the dynamic model were obtained by deconvolution of the motion recorded in Patras and appropriate scaling for distance. The code Cyberquake (BRGM Software 1998) and the profiles of Fig. 6 were used for this purpose. Site conditions for the selected stations were made available from previous geotechnical and geophysical investigations (Athanasopoulos and Pefani, 2010, personal communication). Three different sets of G-γ-D curves proposed by Darendeli (2001), which account for soil plasticity, OCR, and overburden pressure, were used for the deconvolution

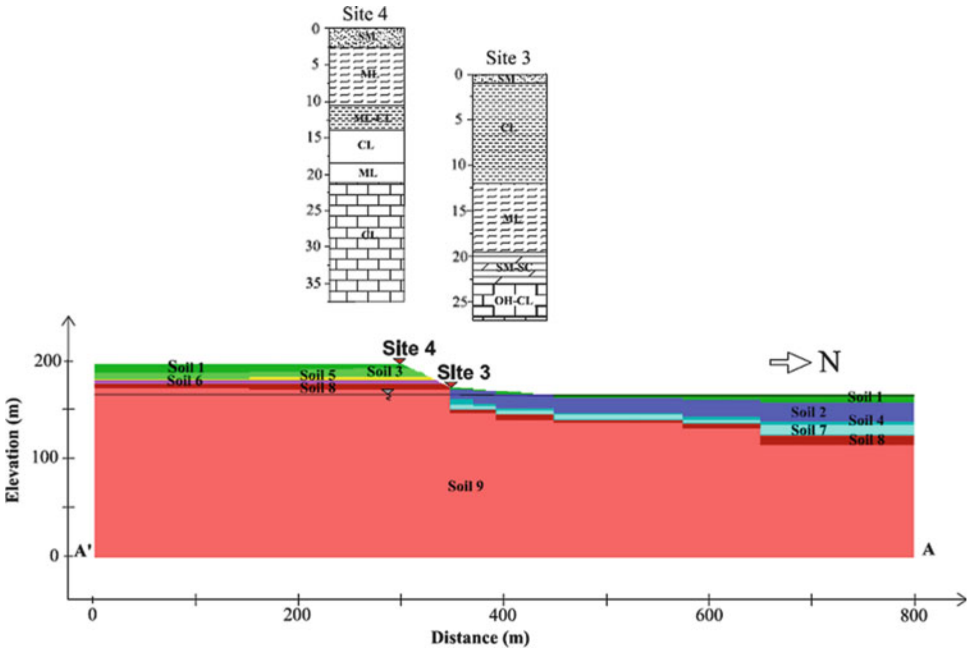

Fig. 5 Soil model used for the 2D finite difference dynamic analysis

Table 1 Soil properties used for the 2D finite difference cross-section

Material	γ_d (KN/m^3)	γ_{sat} (KN/m^3)	Poisson's ratio	Vs (m/s)	φ (o)	c (KPa)
Soil 1 (SM-CL)	18	20	0.4	150–250	27	5
Soil 2 (CL)	19	21	0.4	250–450	20	35
Soil 3 (ML)	19	21	0.4	450–550	34	5
Soil 4 (ML)	19	21	0.4	450–550	38	5
Soil 5 (CL-ML)	20	21	0.4	450–550	30	8
Soil 6 (ML)	20	21	0.4	550	24	15
Soil 7 (SM-SC)	20	21	0.4	550	40	8
Soil 8 (OL-CL-OH)	20	21	0.4	550	22	50
Soil 9 (OL-CL)	21	22	0.4	550–1,000	28	80

analysis (Fig. 7). The deconvoluted excitations which were obtained and used as seismic input are shown in Fig. 8. Before applied to our Kato Achaia 2D the model, they are subjected to appropriate correction (baseline correction and filtering) to allow for an accurate representation of wave transmission through the model.

Finally the input accelerograms are scaled for two levels of peak ground acceleration at the assumed seismic bedrock, namely $\mathrm{PGA}_{\mathrm{base}} = 0.2$ and 0.5 g. The low level of excitation is taken to be consistent with the PGA values reported at the Kato Achaia area during the 2008 Ilia Achaia earthquake (reaching PGA values on the order of 0.3 g at the free surface). The higher excitation level ($\mathrm{PGA} = 0.5$ g) is considered in order to further investigate irreversible deformation beneath the building's foundation and finally to assess the vulnerability of the assumed building due to the differential permanent ground displacement induced by the landslide. The differential horizontal ground displacements at the foundation level derived from the 2D finite difference dynamic analysis by applying the PAT3-T and Pat_hosp-N accelerograms at the assumed seismic bedrock are schematically illustrated in Fig. 9 for the two levels of excitation.

In accordance with the field observations carried out after the 2008 Achaia-Ilia earthquake, relatively small (<10 cm) total and differential deformations at the building's foundation level are anticipated when applying the outcropping horizontal accelerograms scaled at $\mathrm{PGA}_{\mathrm{base}} = 0.2$ g (Fig. 9- up). In contrast, for the stronger earthquake scenario ($\mathrm{PGA}_{\mathrm{base}} = 0.5$ g), remarkable differential permanent displacements (0.4–0.6 m) are expected (Fig. 9- down).

Fragility Analysis of the Building

The analysis of the building is conducted by means of the finite element code SeismoStruct (Seismosoft 2007), which is capable of calculating the large displacement behavior of space frames under static or dynamic loading, taking into account both geometric nonlinearities and material inelasticity. Both local (beam-column effect) and global

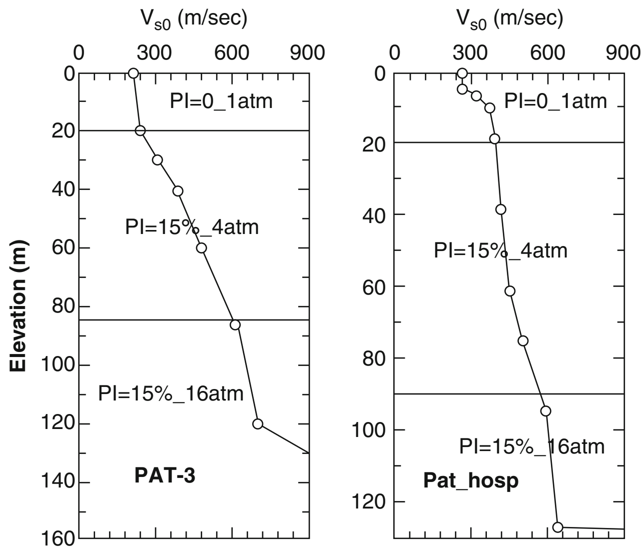

Fig. 6 Shear wave velocity variation with depth for the selected recording stations

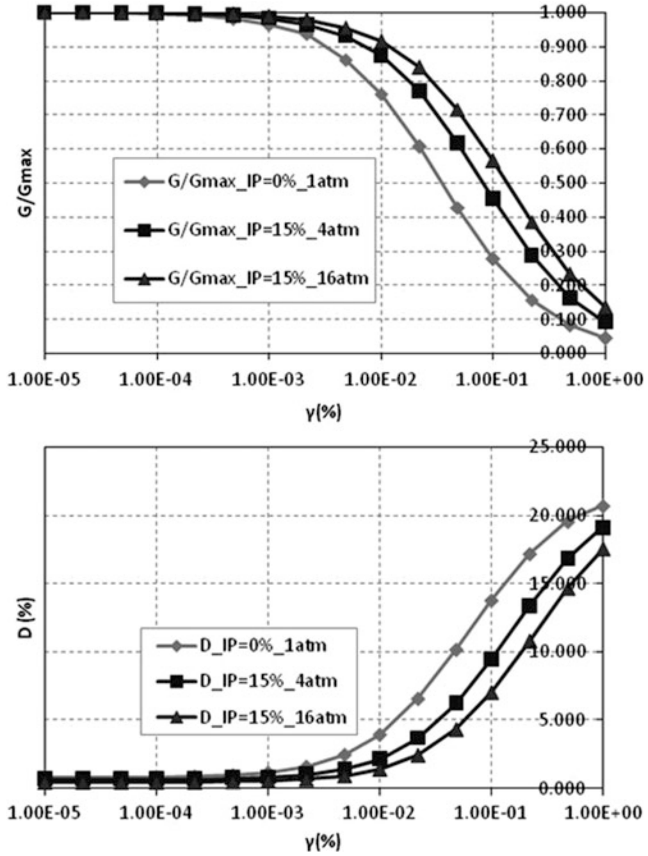

Fig. 7 Modulus reduction and damping curves of Darendeli (2001) used for the 1D deconvolution analysis

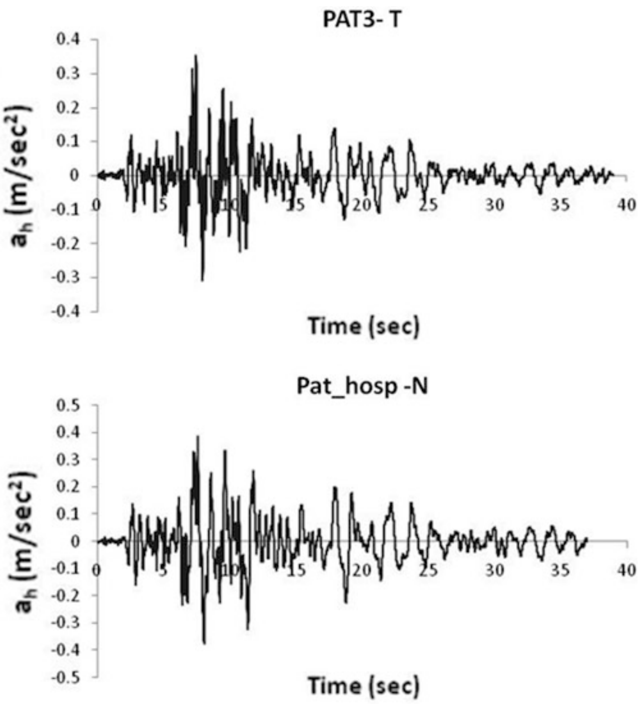

Fig. 8 Input outcropping horizontal accelerations used in the dynamic analysis

(large displacements/rotations effects) sources of geometric nonlinearity are automatically taken into account. The spread of material inelasticity along the member length and across the section area is represented through the employment of a fibre-based modeling approach, implicit in the formulation of SeismoStruct's inelastic beam-column frame elements. Nonlinear static time-history analyses are performed for all numerical simulations. In particular, the differential permanent displacement (versus time) curves (Fig. 9), directly extracted from the FLAC dynamic analysis, are statically imposed at one of the RC frame supports.

The studied building is a "low code" single bay-single storey RC bare frame structure, considering that most of the existing RC buildings found in the area are low rise, old, poorly constructed structures. The building's height and length are 3 m and 6 m respectively. A uni-axial non-linear constant confinement model is used for the concrete material (fc = 20 MPa, ft = 2.1 MPa, strain at peak stress 0.002 mm/mm, confinement factor 1.2), assuming a constant confining pressure throughout the entire stress–strain range (Mander et al 1988). For the reinforcement, a uni-axial bilinear stress–strain model with kinematic strain hardening is utilized (fy = 400 MPa, E = 200 GPa, strain hardening parameter $\mu = 0.005$). All columns and beams have rectangular cross sections (0.40×0.40 m). A low level of steel reinforcement is used (8Φ12) for all the cross sections considered.

The building structural response is obtained for the two different levels of excitation by analyzing the building capacity under the deformation demand (differential displacement time histories). In order to identify the building performance (damage) state, 4 limit states (LS1, LS2, LS3, LS4) are defined in terms of allowable values of steel reinforcement strain, based on the work of Crowley et al. (2004),

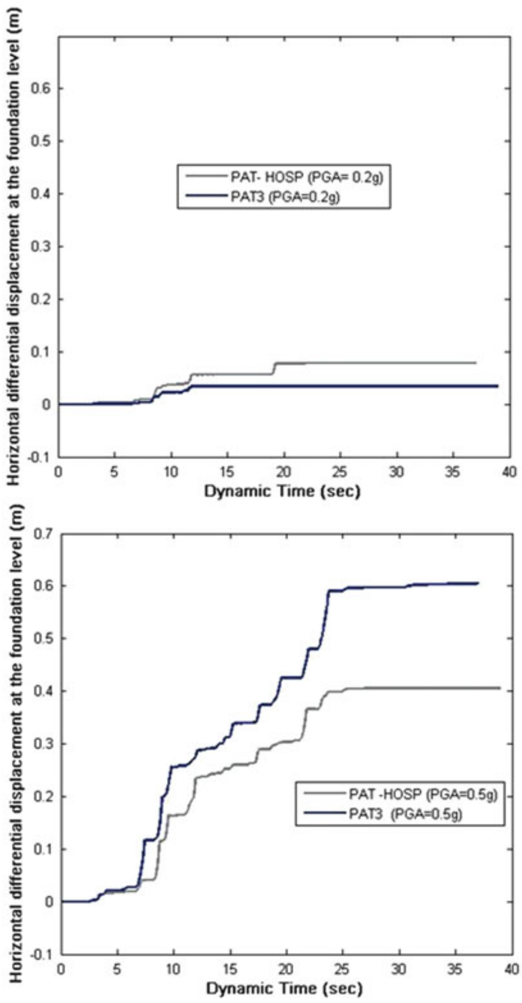

Fig. 9 Differential horizontal ground displacements at the building's foundation level for low and high excitation level

Table 2 Definition of limit states for "low code" RC buildings

Limit state	Steel strain (ε_s) –low code design
Limit state 1	Steel bar yielding
Limit state 2	0.0125
Limit state 3	0.025
Limit state 4	0.045

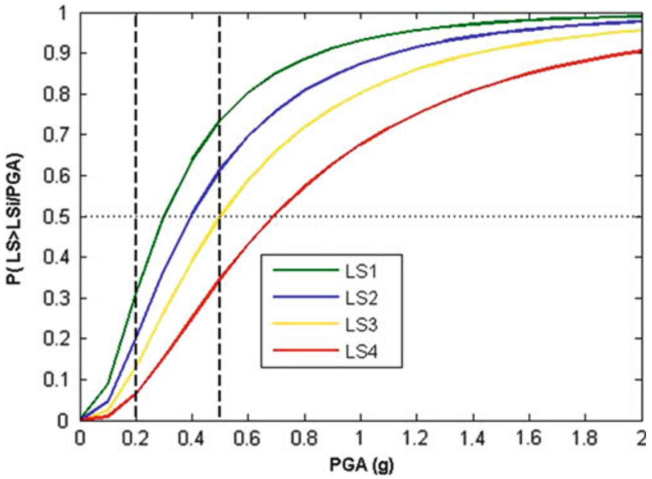

Fig. 10 Fragility curves proposed for the specific site and structural characteristics

Bird et al. (2005), Negulescu and Foerster (2010) and engineering judgment (Table 2). This concern exceedance of minor, moderate, extensive and complete damage of the "low code" designed building.

The building's damage level is finally assessed by comparing the response of the critical member of the building (in terms of maximum steel bar strain) for the given hazard level to the specified threshold values for each limit state. As expected, the building will sustain slight damage (average maximum steel strain at the critical column $\varepsilon_{s,ave} = 0.0027 > 0.002 = Es/fy$) due to permanent ground deformation (landslide) for the low level of input excitation ($PGA = 0.2$ g), which most probably happened during the earthquake under consideration. This is in line with the minor permanent slope displacement observed after the 2008 Achaia-Ilia earthquake. On the contrary, for the strong earthquake scenario ($PGA = 0.5$ g), the structure is expected to suffer complete damage (average maximum steel strain at the critical column $\varepsilon_{s,ave} = 0.0545 > 0.045$), making the repair of the building non feasible in physical or economical terms.

The fragility curves that are found to be more representative of the geotechnical, geological, geometrical and structural characteristics of the site and the building, derived via an extensive parametric analysis (Fotopoulou and Pitilakis 2011), are depicted in Fig. 10. It is observed that the proposed curves predict that the typical building studied herein would suffer extensive damage (worst probable damage state/ i.e. exceeding probability >50 %) for the high seismic hazard scenario ($PGA_{base} = 0.5$ g) and no or low damage for the low seismic hazard scenario ($PGA_{base} = 0.2$ g). These observations are in good agreement with the recorded (for the low hazard scenario) and simulated damages (for both hazard levels) of the typical building, considering also the high variability associated with the curves (standard deviation of the natural logarithm of PGA, βi, on the order of 0.8).

Conclusions

The recently developed analytical tool to quantify vulnerability of simple RC frame structures due to earthquake induced earth slides has been shortly reviewed. To assess the reliability of the aforementioned approach and the corresponding probabilistic fragility curves, the methodology has been applied to a representative RC building located next to the crown of the Kato Achaia slope where most of the structural damage was recorded as a result of the Ilia-Achaia, Greece 2008 (Mw = 6.4) earthquake. Both the slope and the structure were realistically modeled using nonlinear numerical simulations to evaluate the building vulnerability impacted by the co-seismic landslide deformation considering two different levels of dynamic excitation. The reference building is expected to sustain slight and complete damage for the low and high excitation levels respectively. The direct comparison of the simulated and recorded damage with the corresponding damage predicted by the developed fragility functions proved that the proposed fragility curves could adequately capture the performance of the representative RC building affected by the slope co-seismic landslide differential displacement. Further validation with well documented case histories is desirable to enhance their effective implementation within a probabilistic risk assessment study.

Acknowledgments The work described in this paper was supported by the project SafeLand "Living with landslide risk in Europe: Assessment, effects of global change, and risk management strategies" under Grant Agreement No. 226479 in the 7th Framework Program of the European Commission. This support is gratefully acknowledged. Furthermore, the authors would like to express their sincere thanks to Professor George Athanasopoulos and Helen Pefani (University of Partas, Civil Engineering Department) for providing most of the data used for the specific study area.

References

AGSO (2001) Natural hazards and the risk they pose to South-East Queenland. AGSO-Geoscience Australia. Digital report on CD-ROM, 389p

Bird JF, Bommer JJ (2004) Earthquake losses due to ground failure. Eng Geol 75:147–179

Bird JF, Crowley H, Pinho R, Bommer JJ (2005) Assessment of building response to liquefaction induced differential ground deformation. Bull N Z Soc Earthq Eng 38(4):215–234

Bird JF, Bommer JJ, Crowley H, Pinho R (2006) Modelling liquefaction-induced building damage in earthquake loss estimation. Soil dynamics and Earthquake Engineering 26(1):15–30

BRGM (French Geological Survey) Software (1998) Cyberquake, version 1.1. User's guide, Orleans

Crowley H, Pinho R, Bommer JJ (2004) A probabilistic displacement-based vulnerability assessment procedure for earthquake loss estimation. Bull Earthq Eng 2(2):173–219

Darendeli M (2001) Development of a new family of normalized modulus reduction and material damping curves. Ph.D. dissertation, University of Texas

Fotopoulou S, Pitilakis K (2011) An analytical approach for the vulnerability assessment of RC buildings subjected to earthquake induced ground displacements. In: Papadrakakis M, Fragiadakis M, Plevris V (eds) Proceedings of 3rd international conference on computational methods in structural dynamics and earthquake engineering, Corfu, 25–28 May 2011

Fotopoulou S, Pitilakis K, Anagnostopoulos C (2011) Vulnerability Assessment of RC buildings due to earthquake induced slow moving slides. In: Proceedings of 5th international conference on earthquake geotechnical engineering, Santiago, 10–13 Jan 2011

Itasca Consulting Group, Inc (2005) FLAC (Fast Lagrangian Analysis of Continua), version 5.0. Itasca Consulting Group, Inc, Minneapolis

Mander JB, Priestley MJN, Park R (1988) Theoretical stress–strain model for confined concrete. J Struct Eng 114(8):1804–1826

Margaris B, Papaioannou C, Theodoulidis N, Savvaidis A, Klimis N, Makra K, Karakostas C, Lekidis V, Makarios T, Salonikios T, Demosthenus M, Athanasopoulos G, Mylonakis G, Papantonopoulos C, Efthymiadou V, Kloukinas P, Ordonez I, Vlachakis V, Stewart JP (2008). Preliminary report on the principal seismological and engineering aspects of the Mw_6:5 Achaia-Ilia (Greece) earthquake on 8 June 2008, GEER Association Report No. GEER-013, http://research.eerc.berkeley.edu/projects/GEER/Post_EQ_Reports.html. Accessed Oct 2008

Margaris B, Athanasopoulos G, Mylonakis G, Papaioannou C, Klimis N, Theodoulidis N, Savvaidis A, Efthymiadou V, Stewart JP (2010) Mw = 6.4 Achaia-Elia (Greece) earthquake on 8, June 2008 source characteristics, ground motions, and ground failure. Earthq Spectra 26(2):399–424

Negulescu C, Foerster E (2010) Parametric studies and quantitative assessment of the vulnerability of a RC frame building exposed to differential settlements. Nat Hazard Earth Syst Sci 10:1781–1792

Pitilakis D (2009) Topographic irregularities and soil- foundation-structure interaction. In: Proceedings of 3rd Greece–Japan workshop: seismic design, observation, and retrofit of foundations, Santorini, 22–23 Sept 2009

Remondo J, Bonachea J, Cendrero A (2008) Quantitative landslide risk assessment and mapping on the basis of recent occurrences. Geomorphology 94:496–507

SeismoSoft (2007) SeismoStruct—a computer program for static and dynamic nonlinear analysis of framed structures, (online). www.seismosoft.com

Uzielli M, Nadim F, Lacasse S, Kaynia AM (2008) A conceptual framework for quantitative estimation of physical vulnerability to landslides. Eng Geol 102:251–256

Van Westen CJ, Van Asch TWJ, Soeters R (2006) Landslide hazard and risk zonation—why is it still so difficult? Bull Eng Geol Environ 65:167–184

Zêzere J, Garcia RAC, Oliveira SC, Reis E (2008) Probabilistic landslide risk analysis considering direct costs in the area north of Lisbon (Portugal). Geomorphology 94:467–495

THE SECOND
WORLD
LANDSLIDE FORUM

Seismic Slope Performance: Comparison of FEM Results to Displacement-Based Methods

Carolina Sigarán-Loría, Robert Hack, and Jan D. Nieuwenhuis

Abstract

Soil slopes from six types of generic soils (three sands and three clays) were modeled systematically as step-like slopes with the stress-deformation plane-strain finite element method (FEM). The models are assessed at different slope heights (5–20 m for the clay slopes and 5–40 m for the sand slopes), and monochromatic seismic loads with different frequencies (1, 2, 4, 6 Hz). At yield, the peak accelerations and slope displacements computed with the FEM are compared to the predictions from two displacement-based methods: Californian (Blake TF, Hollingsworth RA, Stewart JP (2002) Recommended procedures for implementation of DMG special publication 117: Guidelines for analyzing and mitigating landslide hazards in California. Southern California Earthquake Center, University of Southern California, California, 110p), and USGS Jibson (Eng Geol 91:209–18, 2007). For the slopes in clay, the results from the Californian method are in agreement with the FEM results for 4 and 6 Hz, while better matches between the FEM and the USGS method are obtained for 2, 4, and 6 Hz. The FEM results for the slopes in sand were compared to the Californian displacement-method only because this approach is calibrated with different types of materials and failure types while the USGS cannot be compared to these results as it is restricted to translational slip surfaces and the sands show more circular slip surfaces. The Californian predictions from the sand slopes are comparable, to the FEM results but with higher scatter. The FEM outputs provide further valuable insight among the relations from the different variables.

Keywords

Seismic slope instability • Displacement-based method • Co-seismic displacement • Finite element method (FEM) • Earthquake engineering

Introduction

Strong earthquakes can potentially trigger landslides catastrophic for human live and infrastructure (e.g. Hack et al. 2007; Huang et al. 2009). It is estimated that around 20 % of the registered landslides are triggered by earthquakes (Wen et al. 2004). Therefore, the prediction of slope instabilities triggered by strong motions is very important. Landslides can be classified according their fragmentation and deposition mechanisms (Varnes 1978) as: (1) disrupted slides and falls, (2) coherent, and (3) lateral spreads and flow slides. This paper focuses on the prediction of co-seismic slope

C. Sigarán-Loría (✉)
Faculty of Geo-Information Science and Earth Observation, University of Twente, Hengelosestraat 99, Enschede, The Netherlands

Faculty of Civil Engineering and Geosciences, Delft University of Technology, Delft, The Netherlands

Witteveen+Bos, Geotechnical Engineering Group, Deventer, The Netherlands
e-mail: sigaran@itc.nl

R. Hack
Faculty of Geo-Information Science and Earth Observation, University of Twente, Hengelosestraat 99, Enschede, The Netherlands

J.D. Nieuwenhuis
Faculty of Civil Engineering and Geosciences, Delft University of Technology, Delft, The Netherlands

C. Margottini et al. (eds.), *Landslide Science and Practice*, Vol. 5,
DOI 10.1007/978-3-642-31427-8_29,

displacements from coherent failures. There are three approaches for the evaluation of coherent slope performance during strong motions: pseudo-static, displacement-based, and stress-deformation. Jibson (2011) provides a good synthesis and comparison among them.

The pseudo-static method is applicable to planar, circular and non-circular failure surfaces. It makes use of a horizontal destabilizing seismic coefficient (k_y), based on the expected level of acceleration within the mass expected to fail. It is a very simple, conservative approach that can be applied within conventional limit equilibrium assessments. In hazards evaluations, its use is recommended as a fast "screening" to obtain the spatial susceptibility, identifying the small areas that will require a more precise evaluation (Blake et al. 2002; Stewart et al. 2003). In design, Eurocode 8 (NEN-EN 2004) allows it unless the surface topography and soil stratigraphy present very abrupt irregularities, or if substantial ground softening is likely or large pore pressures can occur.

The displacement-based methods have shown to be more accurate (e.g. Wilson and Keefer 1983). Different predictive models have been developed to estimate co-seismic slope stability from different perspectives and at different scales, depending on the application of interest. Each method requires certain parameters as predictors giving varying results with different accuracies within their conceptual boundaries. Most of these methods include within the predictors only variables that characterize the ground motion, with the assumption that the yield acceleration (a_y) or k_y coefficient represent intrinsically the site and slope. The yield component (either a_y or k_y) is derived from the relation defined by Newmark (1965) as:

$$a_y = (FS - 1) \cdot g \cdot \sin i \qquad (1)$$

Where a_y is the peak ground acceleration at yield; FS is the static factor of safety of the slope; and i the slope angle. The displacements are obtained by double-integrating this acceleration. Some attempts derived their empirical relations of co-seismic slope displacements based on data from a certain area with certain geological conditions, e.g. Jibson et al. (2000) in an area from California. Others have used specific ground types, e.g. Bray and Rathje (1998) assessed man-made solid-waste landfills with three landfill foundation conditions: rock, sand, and clay. More recently, databases of strong motions are used to develop more advanced predictions, including site conditions. For instance, Jibson (2007) used records from hard and soft rocks, stiff and soft soils, and Bray and Travasarou (2007) and Saygili and Rathje (2008) used the motions from PEER (2010) database, excluding soft soil sites. The a_y used within the displacement-based approach (1) is an approximation based on the static condition of the slope. Newmark (1965) assumed the sliding mass to be a rigid-plastic body that does not deform internally and does not suffer permanent displacements at seismic loads (e.g. accelerations) below yield. Consequently, its use is restricted to planar failures.

The stress-deformation method is not restricted to planar failures. This method can represent the state of stresses and strains in the ground at any stage of seismic loading. It is very appealing because it can be extended to two- or three-dimensions, and can comprise ground non-linearity. It gives spatial insight on deformations and stresses during the seismic loading, and the ground mass can be modeled with sophisticated constitutive models (e.g. Sigarán-Loría and Jaspers Focks 2011). However, it requires a big effort and investment to achieve high quality soil parameters from a particular site and computation timings are high. It also needs a good knowledge to select a suitable material model, define efficient dimensions to the model and elements, and adequate damping. Normally, it is only economical for site-specific evaluations (e.g. Sigarán-Loría and Jaspers Focks 2011; Chugh and Stark 2006; Sigarán-Loría and Hack 2006; Crosta et al. 2005; Havenith et al. 2002).

In this paper, two important displacement-based approaches are compared with two-dimensional stress-deformation models, executed with the finite elements method (FEM) using Plaxis (version 9). The FEM models are systematically performed for generic soils (three sands and three clays), and their displacements at yield are measured and compared to the displacements predicted with two important predictive methods, named in this paper for practicality: (1) Californian method (by Blake et al. 2002), and (2) USGS method (by Jibson 1993, 2007; Jibson et al. 2000). Other older and more recent developments (e.g. Saygili and Rathje 2008; Bray and Travasarou 2007; Yegian et al. 1991; Ambraseys and Menu 1988; Makdisi and Seed 1978) are not compared, due to the incompatibility between the variables used in the different methods, especially the use of the peak ground acceleration (PGA) among the variables. For the FEM models, PGA is equal to the a_y, as explained in the 2D FEM models section. Nevertheless, the most recent predictive models are briefly mentioned just for reference (Bray and Travasarou 2007; Saygili and Rathje 2008).

Displacement-Based Approaches

Californian Method

The Californian method is the guideline for the evaluation of seismic landslide hazard and mitigation for California, USA (Blake et al. 2002). It provides a site-specific evaluation of the permanent displacements and recommendations for design purposes. After identifying with the pseudo-static approach the areas likely unstable, the displacements the seismic load will produce are suggested to be estimated with the empirical relation from Bray and Rathje (1998):

$$u = k_{\max} D_{5-95} \cdot 10^{1.87-3.477\frac{k_y}{k_{\max}}} \quad (2)$$

Where u is the seismically induced displacement in the slope (in cm), and $D_{5\text{–}95}$ is the significant duration of shaking (in seconds), measuredas the time between the 5 % and 95 % of the normalized Arias intensity (Blake et al. 2002), k_{max} is a peak demand coefficient, defined by Bray and Rathje (1998) as $k_{max}{=}MHEA/g$, where g is the gravity load and *MHEA* the maximum horizontal equivalent acceleration, which is a function of a nonlinear response factor (*NRF*) and the peak ground acceleration at the bedrock (PHA_r): $MHEA/(PHA_r{*}NRF){=}1.0$, when the slip surfaces are not deeper than 20 m (ibid.). *NRF* can be directly measured knowing PHA_r. The predictive relation from this method (2) has a standard error of 0.35 in *log-10* units. It was developed based on 309 Newmark displacements from earthquakes with magnitudes ranging between 6.25 and 8 at four k_y/k_{max} ratios, applicable to any slip surface, but based on solid-waste landfills data with heights from 10 to 90 m. This method has been found conservative for deep-seated slide surfaces and unconservative for shallow surfaces near slope crests (Rathje and Bray 1999), and is not applicable on liquefiable materials and soft clays (Blake et al. 2002).

USGS Method

Jibson (2007) provides a set of four empirical predictive models to estimate permanent displacements meant for regional evaluations or rapid site-screening, based on the previous findings from Jibson (1993) and Jibson et al. (2000) (Jibson 2007; 1993; Jibson et al. 2000). He developed the relations from 6,632 Newmark displacements and 2,270 strong motions at four yield or critical accelerations (a_y) between 0.05 and 0.4 g, at four site types: hard and soft rock, stiff and soft soil. The variables he used and main statistical coefficients are summarized in Table 1.

Since the FEM models (section “2D FEM models” below) in this research used monochromatic artificial acceleration time histories, those histories are magnitude independent and *PGA* is equal to a_y. Consequently, only the third relation from Jibson (2007) can be used to compare the predictions of the co-seismic slope displacements:

$$\log u = 2.401 \log I_a - 3.481 \log a_y - 3.23 \pm 0.656 \quad (3)$$

Table 1 Predictors and statistical coefficients for the predictive relations from Jibson (2007)

Predictors[1]	Standard errors	R^2 (%)
a_y, *PGA*	$\pm$*log-10* $= 0.51$	84
a_y, *PGA*, *M*	$\pm$*log-10* $= 0.45$	87
a_y, I_a	$\pm$*log-10* $= 0.66$	71
a_y, *PGA*, I_a	$\pm$*log-10* $= 0.62$	75

[1] a_y yield or critical acceleration, *PGA* peak ground acceleration, *M* earthquake magnitude (moment magnitude), I_a arias intensity

Where u is the slope displacement (in cm), I_a the Arias intensity (in m/s), and a_y the yield acceleration (in g). To implement this equation with the numerical outputs the empirical relation from Travasarou et al. (2003) is used to obtain I_a, further details are in the section of Comparison among approaches below. Jibson (2007) points that his regressions are not intended for site-specific assessments but for regional-scale evaluations or as a rapid screening and mapping of hazards.

Other Recent Methods

Bray and Travasarou (2007) extended the model from Bray and Rathje (1998) for earth/waste slopes, to earth dams, earth fills, natural slopes, and solid-waste landfills (Bray and Travasarou 2007; Saygili and Rathje 2008). They used 688 records with $M{=}5.5\text{–}7.6$, and distances smaller than 100 km from site types C, D. They define the system strength with k_y (10 values from 0.02 to 0.4) and its stiffness with the fundamental site period (T_s) at 8 values: 0, 0.2, 0.3, 0.5, 0.7, 1, 1.4, and 2 s. Non-zero T_s have average shear wave velocities (v_s) between 200 and 425 m/s and H from 12 to 100 m. They use a second-order polynomial form in their prediction including as predictors: k_y, $S_a(T_s)$, T_s, M, with a standard deviation (in *ln*) of 0.66. The $S_a(T_s)$ is the spectral acceleration at a degraded period equal to 1.5 times the initial fundamental period of the slope.

Saygili and Rathje (2008) proposed a set of scalar and vector predictive relations implementing only parameters from the strong motions within the predictors. They use 2,383 motions with $M{=}5\text{–}7.9$, and distances from 0.1 to 100 km at four yield coefficients k_y between 0.05 and 0.3, resulting in 14,000 non-zero Newmark displacements. They use a fourth-order polynomial equation in their mathematical model and found that peak ground acceleration (*PGA)* is the most efficient predictor, and their best predictive model is the one that uses *PGA* and *PGV* when using two predictors, or *PGA, PGV*, I_a when combining three.

2D FEM Models

Soils Description

Six generic soils (three loose to dense sands and three soft to stiff clays) are used in systematic plane-strain dynamic analysis in FEM (Plaxis, v.9) to assess the seismic performance of coherent slopes and measure their displacements at yield. The sands are assessed at four heights: 5, 10, 20, 40 m, and the clays at three: 5, 10, 20 m. The depth of all models below the slope toe is constant: 50 m. The steepness ranges from 10° up to the slope with static factor of safety equal to one, defined with a simple strength-reduction approach.

To reduce possible sources of uncertainty simplicity is important. Thus, a simple constitutive model is implemented, one type of soil is used per slope, and for all models are assumed dry conditions. The constitutive model used was the simple linear elastic perfectly plastic Mohr Coulomb. The main reference values at the upper part of the slopes are summarized in Table 2. To approximate non-linearity some adjustments are necessary in the properties and slope geometries. For the sand slopes, strength and stiffness are increased in depth below the slope toe (Fig. 1a) and for the clays, the slopes are subdivided (Fig. 1b) and strength and stiffnesses are proportionally increased.

Seismic Loads

The dynamic loads are artificial acceleration time histories of sinusoidal functions at four frequencies (f): 1, 2, 4 and 6 Hz with a constant duration of 20 s (Fig. 2). The records are horizontally loaded along the base of the models propagating vertically, such as in-plane SV waves. Each slope is loaded with different *PGA* values until yield. At yield the critical acceleration (PHA_c) and slope displacements (u) are measured. Slope failure is assumed when the Cartesian shear strains (γ_{xy}) reach levels near 10 %, showing a uniform distribution within a potential sliding surface. The co-seismic displacements are measured at several PHA_c every 0.05 g between 0.01 and 1.25 g.

To assure appropriate wave propagation and damping, Rayleigh damping is applied within the frequencies used. The element sizes are determined in relation to the soil wavelength (λ) and shear wave velocity, satisfying the suggested size<λ/8 (Kuhlemeyer and Lysmer, 1973). The model geometries are calibrated in their length to the side boundaries to avoid any possible reflection. Many hundreds of models are executed but the results used in this analysis correspond to 240 sands and 140 clays with PHA_c ranging from 0.1 to 0.55 g.

Comparison Among FEM and Displacement-Based Approaches

Seismic Parameters Definition from FEM Outputs

The FEM values are matched to pair values of moment magnitude (M) and site-source distance (r) with the simple attenuation relationship from Campbell (1981):

$$\ln PGA = -4.141 + 0.868M - 1.09 \times \ln[r + 0.0606\exp(0.7M)] \tag{4}$$

This relation is defined for near source (≤50 km) events of magnitudes 5–7.7. 31 pairs are obtained for M: 6–7.25, and r: 3–20 km. As the FEM computations have constant duration, this parameter is also matched with the relation from Abrahamson and Silva (1996, in Blake et al. 2002) to the median duration of strong motion measured as the time across 90 % of the earthquake's energy is released ($D_{5\text{-}95}$). In this relation, duration depends solely on M and r. According to this duration estimation, the closest magnitude found to the FEM time histories is 7.25, both at $r<10$ km, and $r>10$ km.

Furthermore, k_y is obtained from the pseudo-static concept: $k_y = a_y/g$. For the Californian method, the *NRF* factor is directly obtained from the peak horizontal acceleration at bedrock (PHA_r, input load that is equal to the FEM PHA_c), and *MHEA* assuming slip surfaces not deeper than 20 m from, thus: $MHEA/(PHA_r{*}NRF) = 1.0$. Another parameter required for the Californian method is the mean period (T_m). It is approximated with the relation from Rathje et al. (1998) as function of M and r, and valid between 0.25 and 20 Hz. It ranges between 0.42 and 0.56 s. For the USGS method, the Arias intensity (I_a) is required. This parameter is estimated with the relation proposed by Travasarou et al. (2003), where I_a is function of M, r, and some soil class and mechanism of rupture coefficients. The soil coefficients are directly obtained from the soils used, but for the fault-type coefficients the three scenarios defined by Travasarou et al. (2003) are used: strike-slip, normal, and reverse, reverse-oblique ruptures. This relation is valid for motions with M: 4.7–7.6 and $r<250$ km.

Comparison Among FEM and Californian Method

After selecting the FEM outputs with $M = 7.25$ and PHA_c from 0.2 and 0.55 g, the amount of data used for this

Table 2 Main properties from the soils near surface

Parameter[1]	Sand 1	Sand 2	Sand 3	Clay 1	Clay 2	Clay 3
γ_{unsat}	17	18	20.4	16	17.5	19
G_{ref}	6.5E + 4	7.6E + 4	1.0E + 5	3.1E + 3	8.9E + 3	1.9E + 4
v_{s30}	194	204	222	162	185	211
c_{ref}	0.5	0.5	0.5	4.5	10.5	19
φ	30	32	40	0.4	0.4	0.4

[1] γ_{unsat} unit weight (in kN/m^3), G_{ref} shear modulus at reference level (in kPa), v_{s30} shear wave velocity from upper 30 m, c_{ref} cohesion at reference level (in kPa), φ friction angle (in degrees)

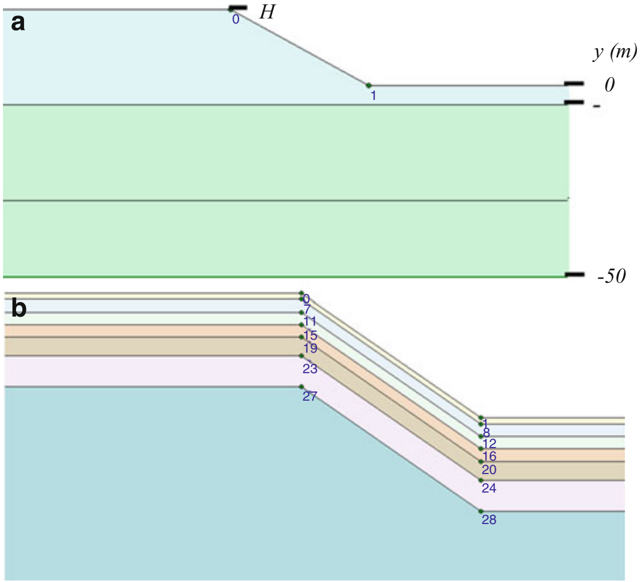

Fig. 1 Slope geometries used: (**a**) Sands, (**b**) Clays

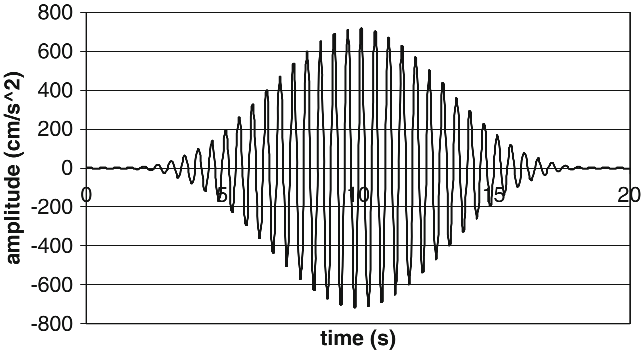

Fig. 2 Example from $f = 2$ Hz artificial time history

comparison is: 34 values from clays and 60 from sands. The co-seismic slope displacements obtained with these methods are shown in Fig. 3.

The predictions from the Californian method show a higher dispersion than the FEM measurements (Fig. 3). The FEM results from the sands are within the range of the Californian method results, but not for the clays. The FEM-clays show higher co-seismic slope displacements at lower frequencies (f=1, 2 Hz, Fig. 3). The outputs from the two approaches for the clays become alike at higher frequencies (f=4 and 6 Hz, Fig. 3). The results from the empirical method (Californian) have a high standard deviation in relation to the other approaches (Table 3).

Further is observed in terms of input frequency (f), that the co-seismic displacements from the Californian method have similar ranges at the four assessed frequencies, while the ones measured with the FEM decrease at higher frequencies, for the clays (Fig. 3). Furthermore, the softer clays have slightly smaller co-seismic slope displacements than the stiffer in the FEM output (Fig. 4). In the sands, no trend was observed in this regard and some even seem to have bigger displacements for the weaker soils. Within the clays, the stiffest clay ("C3", over-consolidated, v_{s30} = 211 m/s) could be assessed only in the lower frequencies (1 and 2 Hz). It produces the largest displacements at yield within the numerical outputs. These bigger displacements associated to the stiffest clay could be related instead to the mentioned above smaller frequencies from the seismic load.

The slope height (H) shows also a relation with the slope displacements induced by the seismic load. The results from both approaches (FEM and Californian) are consistent for the clay soils but not for the sands. The clays exhibit bigger displacements for higher slopes at lower frequencies (1 and 2 Hz). At the higher frequency (6 Hz), this relation seems inverted, e.g. the displacements become smaller for the higher slopes (Fig. 5), but data to sustain this is limited. A similar trend is observed by Bray and Rathje (1998) but they observe the invertion around 1 Hz.

Comparison Among FEM and USGS Method

The results from the modeled clays with M=7.25 and PHA_c: 0.2–0.55 g are used to compare the FEM and USGS methods. The sands are discarded because they show more circular failure planes and Newmark's approach is strictly meant for translational slip surfaces. Only one equation (3) from this method is used in the comparison as this is the only one without the predictor "PGA", not available within the FEM models (Table 1). Three scenarios are

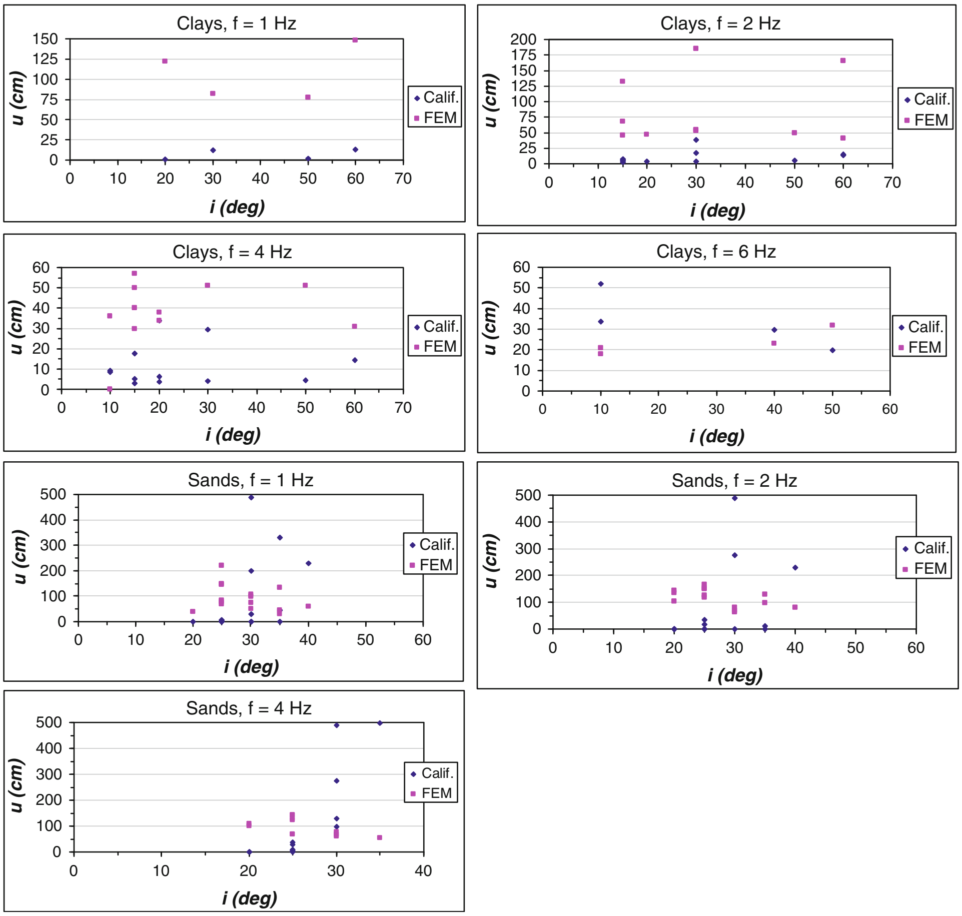

Fig. 3 Co-seismic slope displacements per slope inclination (i) and input frequency (f)

Table 3 Descriptive statistics of co-seismic displacements.

Soil group	Method	Min (cm)	Max (cm)	Mean (cm)	Std. Dev.
Clays (n = 34)	Californian	2	419	38.9	79.8
	USGS	33	49	45.2	3.6
	FEM	14	295	72.1	66.1
Sands (n = 62)	Californian	0	1139	160.2	254.8
	FEM	29	227	95.6	43.3

considered for three types of fault rupture: strike-slip, normal, and reverse, reverse-oblique slip, as defined in the relation used to estimate I_a from Travasarou et al. (2003). The co-seismic slope displacements found are illustrated in Fig. 6.

The predictions obtained with the USGS method have smaller dispersions and standard deviations than the FEM measurements (Fig. 6 and Table 3). The FEM-clays show higher co-seismic slope displacements at lower frequencies ($f=1$ and 2 Hz). At higher frequencies (above 2 Hz) the results are similar and at the highest frequency (6 Hz) the USGS prediction for the reverse fault type is larger (Fig. 6). In general, the predictions with the USGS method remain within similar ranges of displacement (u) among all frequencies. The reverse fault gives results of the USGS method that are more similar to the FEM measurements than for the other fault types. Therefore, only this one was used to further investigate the comparison between the methods.

Looking at the influence of the type of soil on the resultant displacements of the slopes during the seismic load, the outputs from the USGS did not show any differentiation depending on soil type while the FEM does, e.g. the larger displacements are in the stiffer clay (Fig. 7). Furthermore, the FEM results are larger for higher slopes at smaller frequencies (1 and 2 Hz), while at higher frequencies (4 and 6 Hz) the pattern becomes less clear but at each slope angle, the highest slope remains having the largest displacements (Fig. 8).

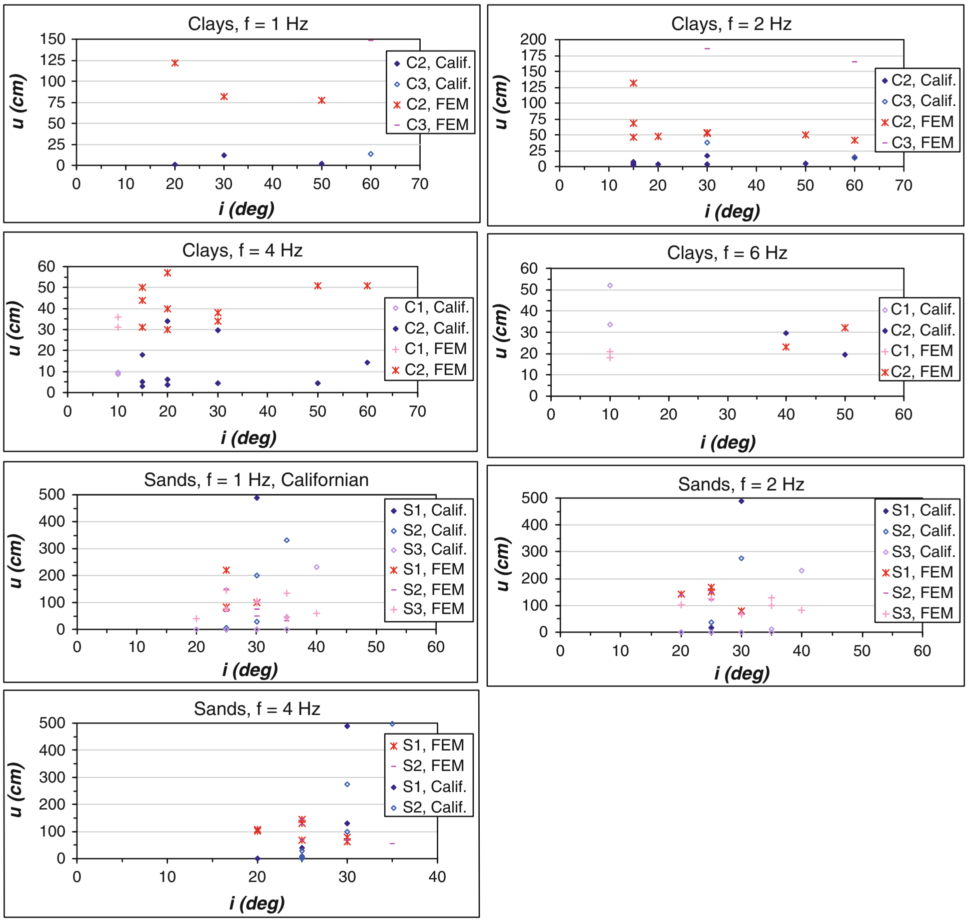

Fig. 4 Co-seismic slope displacements per input frequency (*f*) and soil type

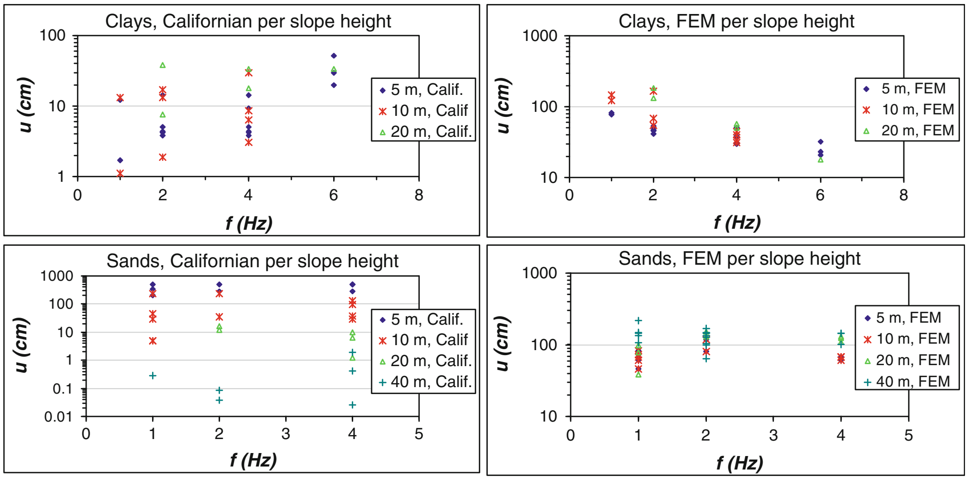

Fig. 5 Co-seismic slope displacements per input frequency (*f*) and slope height

Discussion and Conclusions

In this paper the predictions from slope displacements that result from strong motions according two popular displacement-based empirical methods are compared to plane-strain stress-deformation assessments with FEM computations. They are valid within the boundaries described in this paper. One of the empirical methods shows the largest variability in its prediction (Californian), while the other the smallest (USGS, Table 3), in comparison to the FEM. The co-seismic displacements obtained with the FEM for the

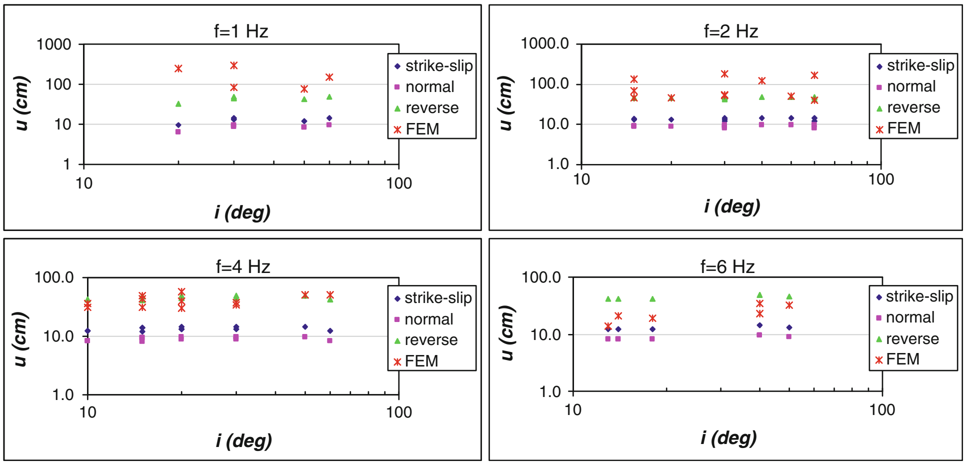

Fig. 6 Co-seismic slope displacements per slope inclination (*i*) and input frequency. Prediction from USGS method are expressed in terms of the type of rupture (strike-slip, normal, reverse)

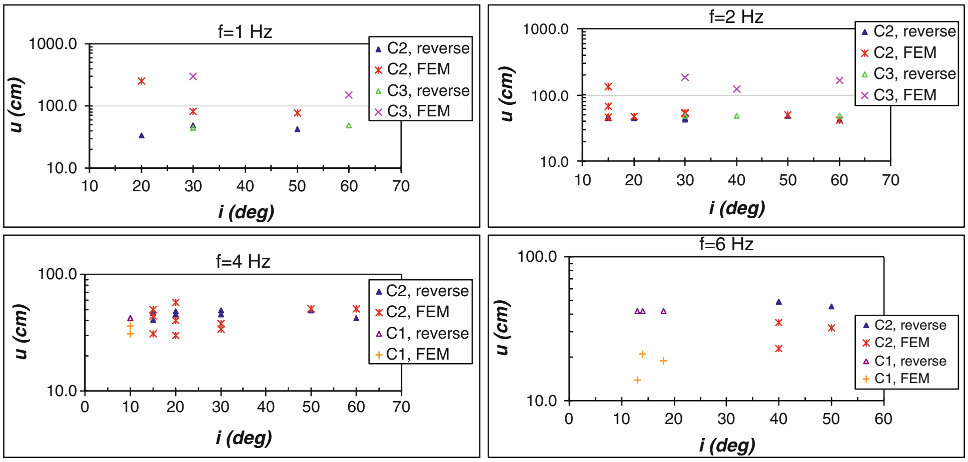

Fig. 7 Co-seismic slope displacements per slope inclination (*i*), input frequency, and soil type

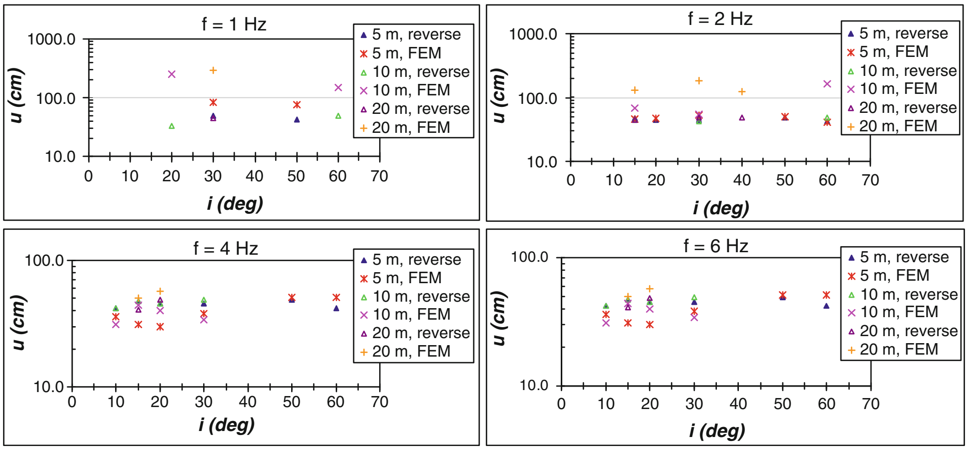

Fig. 8 Co-seismic slope displacements per slope inclination (*i*), input frequency, and slope height

clays are in accordance with the predicted ranges from the empirical methods at the higher frequencies: 4 and 6 Hz with the Californian, and 2, 4, and 6 Hz with the USGS. Towards the lower frequencies (1 and 2 Hz), the FEM co-seismic slope displacements are larger. The FEM displacements from the sands are within the range predicted by the Californian approach. For the USGS method there are three possible scenarios depending on the type of rupture from the source: reverse, strike-slip, and normal, included in the relation used to estimate I_a from Travasarou et al. 2003. The best fit of these to the FEM results is for the reverse-fault.

It is difficult to generalize trends due to the influence of the different types of variables involved in this physical phenomenon of displacements caused by strong motions. For instance, with the available results no trend is detectible among the co-seismic displacements (u) and the slope angle (i), but differentiating them per soil types, input frequencies (f), and slope heights (H) some qualitative trends can be identified. For example, lower frequencies have larger co-seismic displacements and higher slopes have associated larger displacements as well but towards the lower frequencies only, e.g. for 1 and 2 Hz in the FEM results. Bray and Rathje (1998) report this trend at f <1 Hz.

The sand-slopes could not be compared to the empirical results due to the intrinsic restrictions from each model: the Newmark approach is strictly meant to translational-slip planes and in the Californian method Bray and Rathje (1998) restrict the application of their relation to slopes with a ratio site period (T_s) to mean period (T_m): $T_s/T_m > 0.5$. The slopes in sand with $H = 5$ and 10 m have $T_s/T_m < 0.5$.

The large discrepancy found among the estimated co-seismic displacements largely depends on the assumptions and limitations from each method. For example, many of the slopes in clays have heights of 5 m, which are out of the range as prescribed in the definition of the Californian approach (by Bray and Rathje 1998). Secondly, Blake et al. (2002) state that the Californian approach is not applicable for soft clays. Regarding material types, the Californian method was developed for man-made solid-waste landfills which differ from natural soils. As shown by Miles and Keefer (2000) the predictions from the displacement-based methods vary because of the variation in the predictors used.

Existing methods differences rely on the amount of strong motions used, mathematical model applied to determine the predictive relation, and the selection of predictors. The uncertainty in the ground motion characterization is the major source of uncertainty in the predictive method, according to Bray and Travasarou (2007). Thus, for simplicity and to control sources of uncertainty artificial acceleration time histories (Fig. 2) are used in the assessments described in this paper. This also allows to evaluate the influence of the input frequency on the response of the system. Real strong motion records would add unnecessary complications for the purpose of this analysis.

The major source of variability for the FEM results is related to the different aspects involved: the different types of soil, input frequency, and slope geometries. Furthermore, the yield or critical acceleration might bias the outputs because these are to a certain extend arbitrarily.

The results obtained in this research are very important to show the strength and weaknesses of the different methods for predicting the slope performance under seismic loading. In the results from this research, the displacement-based methods show varying standard deviations, and as suggested by different authors (Miles and Keefer 2000; Jibson 2007), they provide an index and are meant for general regional assessments and screening sites, and are not intended for site evaluations. Site-specific assessments are usually recommended to be performed with stress-deformation methods (e.g. FEM), well known for their accuracy and complexity. The results from the FEM computations give valuable insight in the relations among the variables (e.g. f, soil type, H, i) but the results from the other methods do not. These results are a first attempt on assessing the capacities of FEM modeling as tool to develop predictive relations of co-seismic soil slope displacements for hazard/engineering purposes independent of the type of failure of the material.

Acknowledgments Support for this research has been given by Plaxis, the International Centre for Geohazards (ICG) and the Norwegian Geotechnical Institute (NGI), Norway.

References

Ambraseys NN, Menu JM (1988) Earthquake-induced ground displacements. Earthq Eng Struct Dyn 16:985–1006

Blake TF, Hollingsworth RA, Stewart JP (2002) Recommended procedures for implementation of DMG special publication 117: Guidelines for analyzing and mitigating landslide hazards in California. Southern California Earthquake Center, University of Southern California, California, 110p

Bray JD, Rathje EM (1998) Earthquake-induced displacements of solid-waste landfills. J Geotech Geoenviron Eng 124(3):242–253

Bray JD, Travasarou T (2007) Simplified procedure for estimating earthquake-induced deviatoric slope displacements. J Geotech Geoenviron Eng 133(4):381–392

Campbell KW (1981) Near-source attenuation of peak horizontal acceleration. Bull Seismol Soc Am 71(6):2039–2070

Chugh AK, Stark TD (2006) Permanent seismic deformation analysis of a landslide. Landslides 3:2–12

Crosta GB, Imposimato S, Roddeman D, Chiesa S, Moia F (2005) Small fast-moving flow-like landslides in volcanic deposits: The 2001 Las Colinas landslide (El Salvador). Eng Geol 79:185–214

Hack HRGK, Alkema D, Kruse G, Leenders N, Luzi L (2007) Influence of earthquakes on the stability of slopes. J Eng Geol 91:4–15

Havenith HB, Jongmans D, Faccioli E, Abdrakhmatov K, Bard PY (2002) Site effect analysis around the seismically induced Ananevo Rockslide, Kyrgyzstan. Bull Seismol Soc Am 92(8):3190–3209

Huang RQ, Qiang X, Huo JJ (2009) Mechanism and geolmechanics models of landslides triggered by “5.12” Wenchuan earthquake. In: Proceedings of international symposium and 7th Asian regional conference of the IAEG, Chengdu, 9–11 Sept 2009, pp 845–855

Jibson RW (1993) Predicting earthquake-induced landslide displacements using Newmark’s sliding block analysis. Transp Res Rec 1411:9–17

Jibson RW (2007) Regression models for estimating co-seismic landslide displacement. Eng Geol 91:209–218

Jibson RW (2011) Methods for assessing the stability of slopes during earthquakes – a retrospective. Eng Geol 122:43–50

Jibson RW, Harp EL, Michael JA (2000) A method for producing digital probabilistic seismic landslide hazard maps-an example from the Los Angeles, California, area. Eng Geol 58:271–289

Kuhlemeyer RL, Lysmer J (1973) Finite element method accuracy for wave propagation problems. J of Soil Mech Found, ASCE 99(5):421–427

Makdisi E, Seed H (1978) Simplified procedure for estimating dam and embankment earthquake-induced deformations. J Geotech Eng Div 104(7):849–867

Miles SB, Keefer DK (2000) Evaluation of seismic slope-performance models using a regional case study. Environ Eng Geosci VI(1):25–39

NEN-EN 1998-5 (2004) Eurocode 8: design of structures for earthquake resistance – Part 5: foundations, re-taining structures and geotechnical aspects. European Standard EN 1998-5. 44p

Newmark NM (1965) Effects of earthquakes on dams and embankments. Geotechnique 15(2):139–159

PEER (2010) PEER ground motion database. http://peer.berkeley.edu/peer_ground_motion_database

Rathje EM, Bray JD (1999) An examination of simplified earthquake-induced displacement procedures for earth structures. Can Geotech J 36(1):72–87

Rathje EM, Abrahamson NA, Bray JD (1998) Simplified frequency content estimates of earthquake ground motions. J Geotech Geoenviron Eng 124(2):150–159

Saygili G, Rathje EM (2008) Empirical predictive models for earthquake-induced sliding displacements of slopes. J Geotech Geoenviron Eng 134(6):790–803

Sigarán-Loría C, Jaspers Focks DJ (2011) HSS model adequacy in performance-based seismic design approach, Filyos New Port, Turkey. In: Proceedings of XV European conference on soil mechanics and geotechnical engineering, Athens, 12–15 Sept 2011, pp 1579–1586

Sigarán-Loría C, Hack HRGK(2006) Two – dimensional assessment of topographical site effects on earthquake ground response. In: Proceedings of 4th international FLAC symposium on numerical modeling in geodynamics, Madrid, 29–31 May 2006, Paper 04–08, 9p

Stewart JP, Blake TF, Hollingsworth RA (2003) A screen analysis procedure for seismic slope stability. Earthq Spectra 19(3):697–712

Travasarou T, Bray JD, Abrahamson NA (2003) Empirical attenuation relationship for Arias intensity. Earthq Eng Struct Dyn 32:1133–1155

Varnes DJ (1978) Slope movement types and processes. In: Schuster RL, Krizek RJ (eds) Landslides analysis and control, vol 176, National academy of sciences transportation research board special report. National Research Council, Washington, DC, pp 12–33

Wen B, Wang S, Wang E, Zhang J (2004) Characteristics of rapid giant landslides in China. Landslides 1(4):247–261

Wilson RC, Keefer DK (1983) Dynamic analysis of a slope failure from the 6 August, 1979 Coyote Lake, California. Seismol Soc Am Bull 73(3):863–877

Yegian MK, Marciano EA, Ghahraman VG (1991) Earthquake-induced permanent deformations: Probabilistic approach. J of Geotech Eng 117(1):35–50

Possible Vapor Lock Generation Near a Sliding Surface as a Mechanism of Huge Earthquake Landslides

Eisaku Hamasaki, Osamu Watanabe, Syuichi Hashimoto,
Shinichi Yamashina, Toyohiko Miyagi, and Norio Takeuchi

Abstract

The Iwate-Miyagi Nairiku earthquake in 2008 (M7.2) caused the Aratozawa landslide which have a huge earthquake landslide exceeding 900 m in width, 1,300 m in length and 100 m in depth. Although the average slope of the main sliding surface of this landslide was remarkably gentle (about 2°), the landslide body moved about 350 m. In addition, although the moving distance was large, the main landslide body reportedly experienced minimal damage except at the edges. The Higashi Takezawa landslide caused by the Chuetsu earthquake in 2004 (M6.8) is a similar example. In that case, although the landslide body moved about 100 m, the main moving body retained its original form for most of its part (Nakamura 2009).

In this study, we researched why the erarthquake landslides move long distances despite the gentleness of the slope and why the sliding bodies caused by the earthquake landslides minimally damaged although the moving distances were large. The research was conducted by the transdusing law of conservation of energy and the modeling by using actual mesured values of the Aratozawa earthquake landslide. We concluded that the ground water temperature near slip surface of the earthquake landslide exceeds the vaporization temperature by frictional heat of moving masses and it make the water vapor. The water and vapor near slip surface behave as shock absorber to downward pressure and the sliding energy of moving masses. As a result, landslide movement becomes easy, which can reduce the damage of the moving body. We named this phenomena "Vapor lock phenomena in earthquake landslides".

Keywords

Vapor lock • Landslides • Earthquake

Model Methodology of Analyzing

According to the law of conservation of energy, it is possible to make the hypothesis that all frictional energy can be converted into thermal energy, Q, in closed system. In this study, all frictional energy mean the work of moving masses, *W*, which slide along the direction of main sliding surface of the landslide. Thus, next three formulas can be true.

$$W = N \tan \phi \, x \tag{1}$$

$$Q = m C \varDelta T \tag{2}$$

$$W = Q \tag{3}$$

E. Hamasaki (✉)
Advantechnology Co., Ltd.,, Sendai 980-0013, Japan
e-mail: hamasaki@advantechnology.co.jp

O. Watanabe
Suimon LLC Co., Ltd., Sendai, Miyagi, 981-3134, Japan

S. Hashimoto
Touhoku Development consultant Co., Ltd., Sendai, Miyagi, 980-0804, Japan

S. Yamashina
Japan Conservation Engineering & Co., Ltd., Yamagata, Yamagata, 990-2473, Japan

T. Miyagi
Tohoku-Gakuin University, Sendai, Miyagi, 981-3193, Japan

N. Takeuchi
Hosei University, Chiyoda-ku, Tokyo, 102-8160, Japan

C. Margottini et al. (eds.), *Landslide Science and Practice*, Vol. 5,
DOI 10.1007/978-3-642-31427-8_30, © Springer-Verlag Berlin Heidelberg 2013

Equation 1 shows the work of moving masses which slide along the direction of main sliding surface of the landslide. This is the product of acting force, $N \tan\phi$, and relative displacement, x, of bedrock and moving masses of landslide. N is perpendicular stress and ϕ is an internal friction angle. m in (2) is weight of layer V, which is holding water and the water could rise in the temperature. ΔT is the amount of rise in the temperature. C is specific feet. W can transduce displacement of moving mass on a slope with Enoki's model (2007) when the bedrock got strong seismic shocks. Enoki suggests that coseismic behavior of rigid-plastic solid can be modeled by using the relationship of inertial force and continuity condition of acceleration by d'Alembert's principle. Soil is frictional material in this model (Fig. 1).

In this study, we use this model to examine the coseismic behavior of moving mass. In $N \geqq 0$, bedrock and moving masses slide together without separating or making shear layer between bedrock and moving masses. It is when absolute value of shear force T is less than maximum shear resistance, $Smax$. Moving masses slide downwards when absolute value, T, which is acting downwards is more than $Smax$. On the other hand, absolute value, T, which is acting upward is more than $Smax$ when moving masses move upward on a slope.

$$Smax = |N \tan\phi + c/\tan\theta| \tag{4}$$

In (4), c is cohesion and θ is slope gradient. Only shear force, T, transmits from bedrock to soil masses when moving masses is sliding. T is maximum frictional resistance in this time. Seismic acceleration in bedrock showsαv andαh. One in moving masses shows $\alpha' v$ and $\alpha' h$. In relative motion, we write,

$$\alpha v \neq \alpha' v, \quad \alpha h \neq \alpha' h \tag{5}$$

$\alpha' v$ and $\alpha' h$ are calculated by these continuity condition of acceleration. As a result, we can calculate how much relative acceleration, $\Delta\alpha\theta$, increase when soil masses slide downwards on a slope. In addition, moving distance, x, relating to frictional mortion can be found by integrating time, dt, twice. Therefore, amount of rise in temperature, ΔT, is given by obtaining m and C in shear layer by use of (1).

Model Examination by Using the Results of the Aratozawa Landslide Survey

The Amount of Relative Displacement, *x*, and the Work, *w*

From the results of Aratozawa landslides survey, the set values of model slope were 100 m in height, 2° in gradient and 70 m in head of water. Physical values and condition to conduct the examination are shown in Fig. 2.

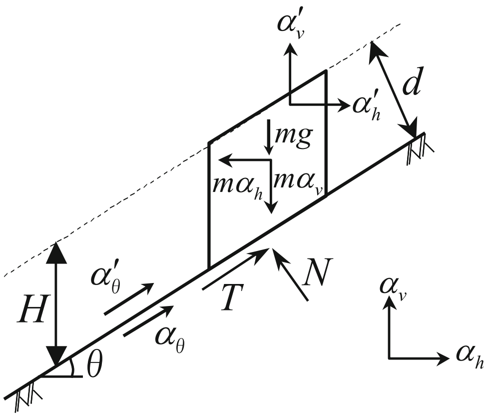

Fig. 1 Seismic response modeling of soil masses on infinitely long slope (Enoki 2007)

Data of strong motion measured by seismometers was used for analysis. The seismometers were buried in a basic bedrock inspection corridor of Aratozawa dam. In this examination, the maximum component of sliding soil masses on a slope divided into horizontal component, αh, and vertical component, αv. $\alpha\theta$ of Fig. 1 is the energy converted the traveling seismic acceleration through bedrock. Similarly, $\alpha'\theta$ of Fig. 1 is the energy converted the traveling seismic acceleration through moving masses. Both of them are upward positive power. From the results of calculations, moving masses were sliding together with bedrock until 12.65 s. However, moving masses started gradually separating from bedrock after that. The cumulative amount of relative displacement was 4 cm between 15 s and 16 s. Ultimately, the total amount of relative displacement during earthquake reached 5.1 cm. The work, W, of this displacement can be found of (1) which is the multiplication of perpendicular stress, N, and relative displacement, x. As a result of the calculation, the answer, W, was 1,589,590 J ($=\mathrm{kgf \cdot m^2/s^2}$).

Phase Transition and Heat Requirement, *Q*

In this analysis, 5 mm in depth of deformation layer, V, near slip surface, 0.1 in effective porosity, 1.7 $\mathrm{g/cm^3}$ in density of bedrock, ρ, and 0.8 J/g·°C in Specific heat of soil fraction, Cb were hypothesized as physical value. 4.178 J/g· °C was applied to the calculation as specific heat of water, Cw, when ground water temperature was 15°C. Head of water at slip surface, V, is 70 m. This was determined by the result of water level observation at field works. In this case, the saturated water vapor pressure is approximately 8 atm. Thus, boiling point of water at slip surface becomes approximately 170°C by the equation of state for international studies (IAPWS-95). In this case, the ground water near slip surface can boil when deformation layer at slip surface, V, got over 155°C in heat. It means that liquid phase can be

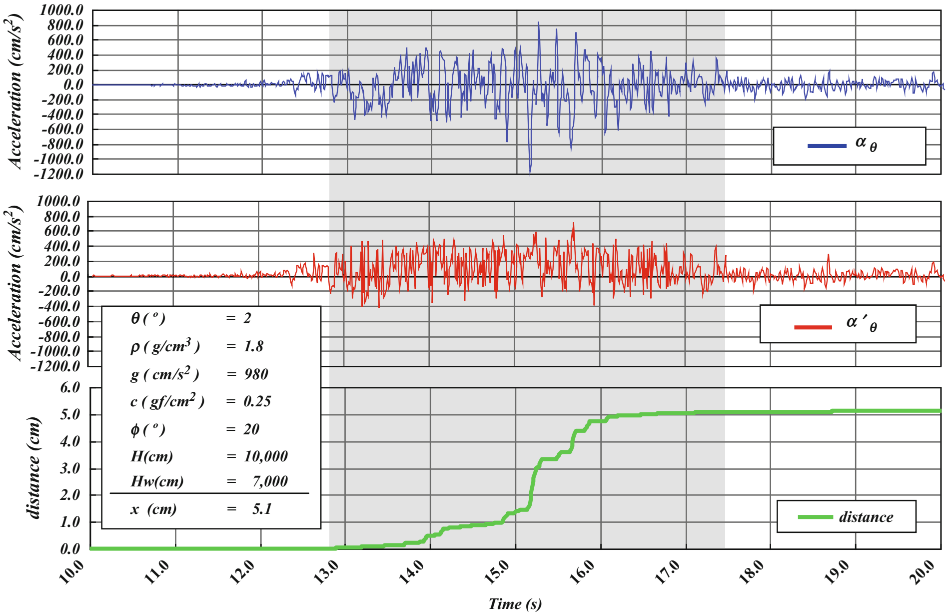

Fig. 2 Amount of relative displacement and seismic response of soil masses on slope

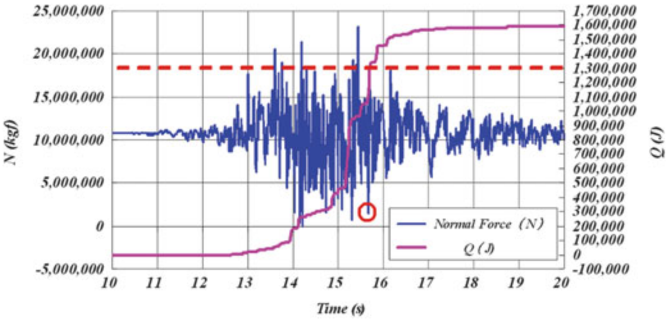

Fig. 3 Change of normal stress, *N*

changed to gas-liquid phase mixed state. In addition, heat quantity, Q, to make the ground water near slip surface vapor can be found from (2). The answer is 1,272,395 J. The ground water deformation layer V near slip surface can boil with this heat quantity, because the work, W, at Aratozawa landslides which was calculated by (1) in a previous chapter was 1,589,590 J. This value is over the heat quantity, Q, which is possible value causing vapor generation.

Vapor Lock Phenomena in Earthquake Landslides

We suggest the following possibility and hypothesis. The work that happened at the bottom of sliding soil masses by earthquake changes frictional heat. This heat energy makes the ground water temperature up and vaporize the water. In other words, the ground water temperature near slip surface exceeds the vaporization temperature by soil mass moving and it make the water vapor. Schematic diagram of this hypothesis shows Fig. 4. This phenomenon is rapid change in state within 2 s as shown in Fig. 3.

We estimate that water and vapor are mixing in the interspace between moving masses and bedrock in the early state of this phenomenon. Incidentally, the vapor lock is the phenomenon that foot brakes went out caused by the vapor generation in a hydraulic brake as a transmission when foot brakes heated up. Pressure from brake pedal transmits to a brake shoe because liquid is hardly compressed in a hydraulic brake system. However, the pressure from brake pedal can not be transmitted to a brake shoe because bobbles are easily compressed after brake fluid became liquid-bobble mixed state caused by evaporation of brake fluid in parts by heat. We hypothecate that such vapor rock phenomenon happen near slip surface of landslide. As soon as W increased over Q at layer V holding ground water near slip surface, babbles generated in layer V. As a result, the downward pressure from soil masses to bedrock is absorbed by the compaction property of bobbles. Therefore, the pressure does not transmit to bedrock easily. In addition, the product of the pressure and the volume of gas is equal by Boyle's law at isothermal condition. After friction layer near slip surface became liquid – gas mixture, it behave as shock absorber when moving masses slide on rugged slip surfaces (Fig. 4). As a result, the damage of moving masses becomes extremely small. We hypothecate that W exceed Q, the moment when downward pressure rapidly decreases by upward action of seismic acceleration to soil masses, and babbles generate

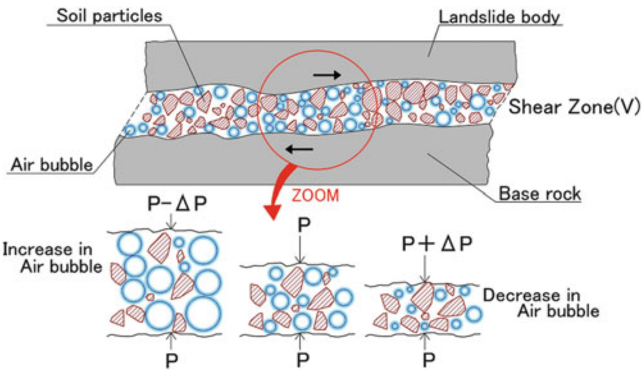

Fig. 4 Conceptual diagram of Vapour lock

(red circle on Fig. 3). At the moment, the phase transition to babble explodes and it cause that the speed of displacement acceleration increases at once. It can make moving masses sliding smoothly just like a hovercraft's sailing. In such situation, it can be possible that moving masses slide long distance at gentle slopes.

Conclusion

In this research, we examined the possibility of vapor lock generation near a sliding surface as one of the mechanisms that generate a huge earthquake landslide in which the landslide body suffers little damage. When a strong earthquake occurs, the frictional heat resulting from the relative displacement near a slip surface increases the groundwater temperature. The pressure change near a sliding surface could change the phase of the hot groundwater, resulting in a simultaneous vapor lock state. As a result, landslide movement becomes easy, which can reduce the damage of the moving body.

Further Work

It is important to verify the vapor lock phenomena in earthquake landslides.

Necessary temperature is 170°C to cause gas-liquid phase transition. If shear layer was heated to 170°C, crystallized Calcite as a geothermometer could be found near heated slip surface. The amount of calcite may be little, because landslide happens in short time. For this reason, it might be difficult to find calcite by X-ray diffraction. However, microscopic observation has possibility to find it. Furthermore, it is significant to clarify the impact of gas bubbles on shear strength.

By adding a heat-generating device in a shearing tester, it make possible to investigate what gas bubbles effect shear strength. It is valuable and necessary to test.

First of all, I would like to thank Ms rt .

Acknowledgments First of all, I would like to thank Ms Mika YAMAO for the support to writing this article.

References

Hiroyuki Nakamura (2009) Easy-to-understand SABO technique (15) Earthquake and Landslide, SABO and CHISUI 41(2), 65–69, Japanese book

Meiketsu Enoki (2007) Analyzing method of stability and transformation of soil as frictional material DENKISHOIN, pp 266, Japanese book

Xuan Binh Luong, Thanh Thuy Hoang and Meitetsu Enoki (2009) Development of generalized limit equilibrium method for the failure of retaining walls under seismic loadings. Sci J Transp, Moscow/Chengdu/Hanoi, Especial 166 Issue J Transp, Moscow/Chengdu/Hanoi, Especial 166 Issue

Statistical Analysis of Deep-Seated Landslides Induced by Recent Strong Earthquakes in Eastern Japan: An Approach Based on Pre-Existing Landslide Topography

Bateer Hasi, Kiyoteru Maruyama, Akira Nakamura, and Tomoyuki Noro

Abstract

This paper conducted logistic regression analysis for earthquake-induced landslides within pre-existing landslide topographies. We constructed logistic regression model by using landslides data set of the Chuetsu earthquake, Niigata Prefecture, 2004. The results showed that surface roughness and marginal erosion ratio are the most influential factors for the landslide occurrence. The model was validated by the part of landslides data set of the Chuetsu earthquake and the Iwate-Miyagi inland earthquake, 2008. Based on ROC curves, the AUC is larger than 0.8, showed a good prediction accuracy and suggested the method is useful.

Keywords

Landslide • Earthquake • Logistic regression • Chuetsu • Iwate-Miyagi • Japan

Introduction

In many cases, damage by earthquake-induced landslides includes the major part of the whole earthquake damage in earthquakes that occur in mountainous regions. Especially, in mountainous countries such as Japan, earthquake-induced landslides destroy infrastructures, lifelines, dam rivers, and cause serious damage. Recently, several strong earthquakes occurred in eastern Japan, such as the Chuetsu earthquake in 2004 (Chigira and Yagi 2006), and the Iwate-Miyagi inland earthquake in 2008 (Yagi et al. 2009), caused extensive damage to the affected areas. Throughout the world, large earthquakes have triggered numerous landslides and caused damage, such as the northern Pakistan earthquake in 2005 (Marui et al. 2006; Owen et al. 2008), and the 2008 Wenchuan earthquake in China. (Yin et al. 2009; Chigira et al. 2010).

For landslide susceptibility analysis, statistical analysis is an important method that has been used throughout the world. Recently, logistic regression analysis has been widely used to evaluate earthquake-induced landslides (Guzzetti et al. 1999; Ayalew and Yamagishi 2005; Chang et al. 2007; Garcia-Rodriguez et al. 2008). Discriminant analysis is another widely used multivariable analyzing method. However, in the case of earthquake-induced landslides, which are not always normally distributed, logistic regression analysis is considered as an appropriate method than discriminant analysis, because it does not require normally distributed data, while the discriminant analysis request normally distributed data (Dong et al. 2009).

In this paper, we analyze deep-seated landslides induced within pre-existing landslide topographies by the Chuetsu earthquake and the Iwate-Miyagi inland earthquake. We take three steps to construct a logistic regression model and validate the result. At first, we select part of the data of the deep-seated landslides induced by the Chuetsu earthquake and construct a logistic regression model; second, we validate the model by using the data that were not used to construct the model; finally, we validate the model by using the data of the Iwate-Miyagi inland earthquake. In this study, we only focus on deep-seated landslides within pre-existing landslide

---

B. Hasi (✉)
Snow Avalanche and Landslide Research Center, PWRI,
2-6-8 Nishiki-cho, Myoko-shi, Niigata, Japan

Now at Asia Air Survey, Co., Ltd., Manpukuji 1-2-2, Asao Dis.,
Kawasaki, Japan
e-mail: has.baator@ajiko.co.jp

K. Maruyama • A. Nakamura • T. Noro
Snow Avalanche and Landslide Research Center, PWRI,
2-6-8 Nishiki-cho, Myoko-shi, Niigata, Japan

C. Margottini et al. (eds.), *Landslide Science and Practice*, Vol. 5,
DOI 10.1007/978-3-642-31427-8_31, © Springer-Verlag Berlin Heidelberg 2013

topography. In many cases in Japan, countermeasures for deep-seated landslides are different from that for other types of landslides; and pre-existing landslide topography is easily identified and data is readily available in Japan (NIED 2011).

Regional Setting

The study areas are located in eastern Japan (Fig. 1). Study area 1 is the focal area of the Chuetsu earthquake and its surrounding area occupying about 127 km^2. Study area 2 is the focal area of the Iwate-Miyagi inland earthquake, an area of 459 km^2.

The Chuetsu earthquake occurred on October 23, 2004, in the southern part of Higashiyama, central Niigata Prefecture. The earthquake, M_{JMA}6.8 (Japan Meteorological Agency scale), directly caused 16 casualties, in which 6 were due to landslides (Niigata Prefecture 2009). The geomorphology of the region is characterized by ridgelines 300–700 m above sea level, distributed in a NNE-SSW direction. The region is mainly occupied by Neogene to Quaternary sedimentary sandstones, mudstones, siltstones and some unconsolidated materials. The geological structure of the study area is dominated by NNE-SSW directed active fold axes that are sup-parallel to each other with 1-km intervals (Yanagisawa et al. 1986; Kobayashi et al. 1991). A large number of pre-existing landslides topographies are distributed in northern Japan, especially in Niigata Prefecture (NIED 2011). The study area 1 is near the Sea of Japan, which is rainy in summer and has heavy snow in winter. The average annual rainfall is about 2,500 mm (JMA, http://www.data.jma.go).

The Iwate-Miyagi inland earthquake of M_{JMA}7.2 occurred on July 14, 2008, in the central part of the Ou Backbone Mountains. There were 17 fatalities from this earthquake and six people missing, almost all of them due to landslides and debris flows (Ushiyama and Ohta 2009). The geomorphology of the area is characterized by 400–600 m elevation ridgelines that deeply eroded by several rivers. The geology of the study area is composed of volcanic rocks, shallow-sea tuffaceous sedimentary rocks (Osawa and Takisawa 1992). According to JMA, the average annual precipitant is about 2,000 mm in the study area (JMA, http://www.data.jma.go)

Data Sources and Causative Factors

The deep-seated landslides induced by the earthquake and pre-existing landslide topographies were interpreted within the study areas 1 and 2, respectively. The interpretation was conducted by using aerial photographs before and after of the earthquakes and by field surveys. The aerial photographs and digital geological map and digital elevation models (DEM) used in this study are listed in Table 1.

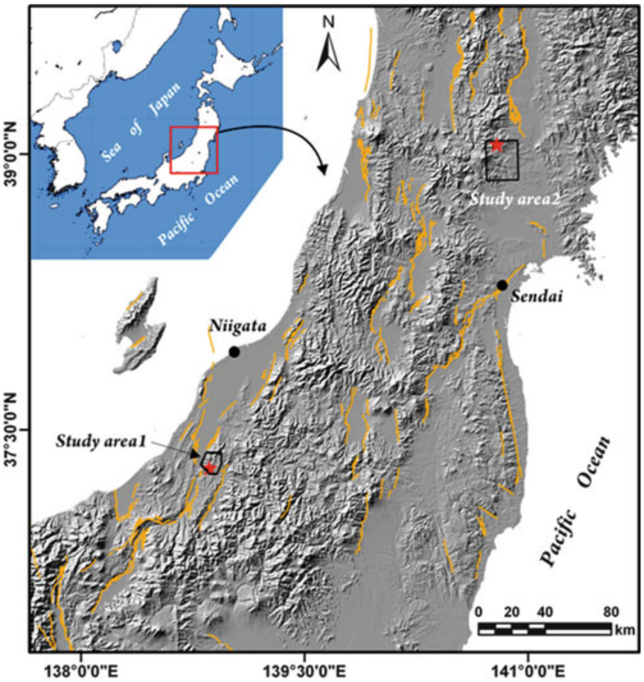

Fig. 1 Location of the study areas. *Orange solid lines* indicate active faults (AIST 2009)

In study area 1, 1,050 pre-existing landslide topographies and 96 earthquake-induced landslides were interpreted (Fig. 2a). In those 1,050 pre-existing landslide topographies, 87 contained landslides triggered by the Chuetsu earthquake. In study area 2, 973 pre-existing landslide topographies were interpreted in which 29 were re-activated by the Iwate-Miyagi inland earthquake (Fig. 2b). The pre-existing landslide topographies of study area 2 were modified from GSI (2009). In this study, we excluded shallow surface failures and debris flows, only considering deep-seated landslides. In this paper, we focused on geomorphologic factors and distance data from geological structure, ridgelines and channel lines.

1. Digital elevation model (DEM): A 10 m grid DEM (Hokkaido-Chizu Co., Ltd.) was used to calculate the ridgeline data, channel line data and surface roughness. The grid size was resized to 30 m in the calculating.
2. Surface roughness (SR): It is defined as the standard deviation of elevation values within the pre-existing landslide topography. Larger surface roughness values indicate steeper slope gradient, larger roughness of the ground surface, or larger landslide area.
3. Distance to river channel line: Defined as the shortest distance from landslide center to river channel line, which is calculated from the above DEM. A shorter distance may indicate greater erosion at landslide toe areas, indicating the instability of that landslide.
4. Distance to ridgeline: Defined as the shortest distance from a landslide center to a ridgeline calculated from

Table 1 List of data sources

Event	Data types	Scale		Year of Acquisition	Organization
Chuetsu EQ	Aerial photograph	Before EQ	1:10,000	Jul.26, 1975; Nov.2, 1976	CSI, Japan
			1:25,000	Oct.25, 1994	
		After EQ	1:10,000 ~ 12,000	Oct.24–29, 2004	
	Digital geological map	Before EQ	1:50,000		Takeuchi et al. (2004)
	DEM		10 m	1993	Hokkaido Chizu Co. Ltd, Japan.
Iwate-Miyagi inland EQ	Aerial photograph	Before EQ	1:30,000	Sept. 23, 2006	CSI, Japan
		After EQ	1:10,000	Jun.16–18, 2008	
			1:10,000	Jun.16–18, 2009	Asia Air Survey, Co., Ltd.
	DEM	Before EQ	10 m	1993	Hokkaido Chizu Co. Ltd., Japan

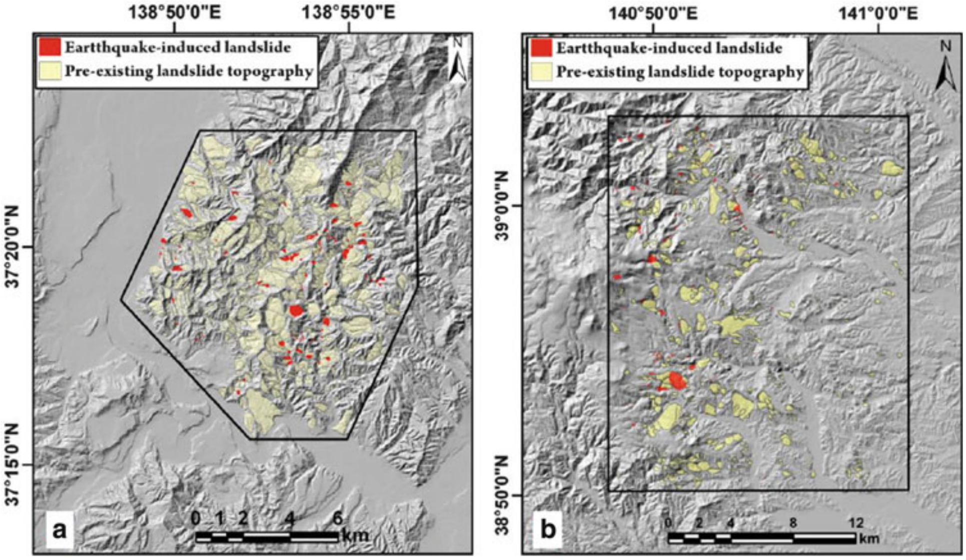

Fig. 2 Distribution of earthquake-induced landslides and pre-existing landslide topographies. (**a**)Study area 1, (**b**)Study area 2

the above DEM. Aslope, closer to a ridgeline may suffer larger shaking by an earthquake (Meunier et al. 2008), so a shorter distance may cause more landslides from earthquakes.

5. Distance to geological structures: Defined as the distance from fault and fold axes to landslide centers. Shorter distances may indicate more influence by the structure because of closely spaced fractures.
6. Marginal erosion ratio (MER): Defined as eroded length divided by whole marginal length of landslide block (Suzuki et al. 2010). It indicates the erosion condition of the slope and the instability of the slope.

Methodology-Logistic Regression

Logistic regression is a multivariate method where the dependent variable is categorical and the explanatory variables are numerical, categorical or both. This method can be used to predict a binary phenomenon such like landslides induced by an earthquake.

If the probability of one event (here the occurrence of landslides by an earthquake) is P, it could be written as

$$P = \frac{1}{1 + e^{-Y}} \qquad (1)$$

Where, P is probability, y is logit, the natural log of odds (p/1-p), could be written as

$$Y = Log[\frac{P}{1 - P}] = B_0 + B_1X_1 + B_2X_2 + \ldots + B_nX_n \qquad (2)$$

Where, B_0 is a constant. B_1, B_2,... B_n are the coefficients of the causative factors of X_1, X_2,... X_n. The value Y changes from – to +, as a linear relationship with the explanatory variables. The value of probability of P changes from 0 to 1. The coefficients, B, are estimated by the maximum likelihood method. The significance of B_n is validated by Wald validation; if the value <0.001, this indicates a significance at the 0.001 level.

In this study, we used the SPSS Statistics Ver.19 (IBM) to conduct logistic regression analysis. A forward stepwise analysis has been used. In the case of earthquake-induced landslides, the dependent variable is the occurrence of a landslide, the binary value of landslide occurrences and non-occurrences. The explanatory variables are the causative factors mentioned above.

In some literature of logistic regression analysis, while the data of occurrence and non-occurrence of landslides is different, the same number of data points were used (e.g., Dai and Lee 2002; Süzen and Doyuran 2004). In this study, the landslide occurrence is 87, non-occurrence is 963; we decided to use the same number of data for analysis. We randomly selected 87 landslide non-occurrence pre-existing landslide topographies from the whole data of 963, added to the 87 landslides occurrence data to make a sub-data set. From this sub-data set, we selected 75 % of them (occurrence 65, non-occurrence 65) to construct the logistic model, and then used 25 % of the remaining data (occurrence 22, non-occurrence 22) to validate the model.

Construction of Logistic Regression Model

After running the logistic regression analysis by using the SPSS, the explanatory variables of surface roughness and marginal erosion ratio, seemed to strongly influence the deep-seated landslide occurrence within pre-existing landslide topographies. However, the other factors were excluded from the model. The coefficients of the factors are listed in Table 2. The predicting result of the model was shown in Table 3. Here, the cut-off value is 0.50. The correctly predicted percentage for landslide occurrence is 70.8 %, for landslide non-occurrence is 78.5 % and the overall percentage is 74.6 %.

Validation

Validation 1

To validate the logistic model, we predicted the landslide occurrence of the remaining 25 % data of the sub-data set of study area 1. The predicted result is shown in Table 4. The results showed that 77.3 % of the landslides occurrence and 72.7 % of the landslide non-occurrence was correctly predicted. The correctly predicted percentage for landslide occurrence is comparably higher than that of the model construction. The result indicated that the model is good. Here, the cut-off value is 0.50.

We validated the accuracy of predicted model by using ROC (Receiver Operating Characteristic). Figure 3 is the ROC curve of the results of the probability P value of the remaining 25 % of the sub-data set of study area 1.

In Fig. 3, the sensitivity, the cumulative rate of correctly predicted landslide occurrence is plotted on the Y-axis in the ROC curve. The specificity is the probability of the landslide non-occurrence. The X-axis is 1-specificity, as the cumulative rate of incorrectly predicted landslide occurrence. In the prediction model, the area under the ROC curve (AUC) indicates the accuracy of the model prediction. In general, the larger the AUC, the more accurate the model, AUC = 0.9–1.0 is excellent, 0.8–0.9 is good and 0.7–0.8 is fair (Craig et al. 2007). In Fig. 3, the AUC is 0.804, meaning the accuracy of prediction is good.

Correction and Validation 2

Since the ratio of landslide occurrence of the model construction data and the whole data set is different, the constant of the model needs to be corrected (Takada 2007). The correction was conducted from substituting values from formula (3) into (4), achieving formula (5).

$$\frac{q_1}{q_2} = \frac{s(1-r)}{r(1-s)} \tag{3}$$

Where, r is landslide occurrence ratio of the whole data set (87/1050≒0.08), and s is the landslide occurrence ratio of data set for model construction (65/130 = 0.50)

Formula (5) is the model after correlation.

$$P = \frac{1}{1 + e^{-(Log(q1/q2) + 0.060\,SR + 0.035\,MER - 2.630)}} \tag{4}$$

$$P_c = \frac{1}{1 + e^{-(Log(0.060\,SR + 0.035\,MER - 5.320)}} \tag{5}$$

Using this corrected model, we confirmed the utility of the model by predicting the landslide occurrence of study area 2. The predicted result is shown in Table 5. The 75.9 % of landslide occurrence and 75.0 % of landslide non-occurrence is correctly predicted. Here, the cut-off value is 0.08, according to the landslide occurrence ratio of the Chuetsu earthquake. Figure 4 is ROC curve of probability of P_c for study area 2. The AUC is 0.835, indicating the result is good.

Table 2 Coefficients of explanatory variables

Explanatory variables	B	SE	Wald	df	Sig.	Exp(B)
SR	0.060	0.019	9.631	1	0.002	1.061
MER	0.035	0.010	13.336	1	0.000	1.036
Constant	−2.630	0.579	20.607	1	0.000	0.072

B constant, *SE* standard error, *Wald* Wald chi-square, *df* degree of freedom, *Sig.* significance, *Exp(B)* exponentiated coefficient

Table 3 Predicting result of model construction

		Predicted		
		Positive(predicted landslide occurrence)	Negative (predicted landslide non-occurrence)	Percentage correctly predicted
Observed	True (landslide occurred)	True Positive(TP)	False Negative(FN)	TP/(TP + FN)*100:**70.8 %**
		46	**19**	
	False (landslide not occurred)	False Positive(FP)	True Negative(TN)	TN/(FP + TN)*100:**78.5 %**
		14	**51**	
Overall percentage				(TP + TN)/(TP + FN + FP + TN) *100:**74.6 %**

Cut-off value is 0.50

Table 4 Classification summary of the validation 1

		Predicted		
		Positive(predicted landslide occurrence)	Negative (predicted non-landslide occurrence)	Percentage correctly predicted
Observed	True (landslide occurred)	True Positive(TP)	False Negative(FN)	TP/(TP + FN)*100:**77.3 %**
		17	**5**	
	False (landslide not occurred)	False Positive(FP)	True Negative(TN)	TN/(FP + TN)*100:**72.7 %**
		6	**16**	
Overall percentage				(TP + TN)/(TP + FN + FP + TN) *100:**75.0 %**

Cut-off value is 0.50

Conclusions

By using a part of earthquake-induced landslide inventories and pre-existing landslide topographies of the Chuetsu earthquake, 2004, Niigata, Japan, we constructed a logistic regression model. Geomorphological and distance data were analysed as causative factors of landslide occurring, and the surface roughness and marginal erosion ratio were selected from the model. The result was validated by the data set not used in the model. The result was also corrected and validated by the data set of the Iwate-Miyagi inland earthquake, 2008. After correction and validation, the results showed that the AUC of the model is larger than 0.80, suggesting a good accuracy of the model. The results suggested that the model is useful for predicting landslide occurrence within pre-existing landslide topography.

In Japan, main active faults have been documented and assessed (The Headquarters for Earthquake Research Promotion 2011). The above model could be used for landslide susceptibility mapping around the

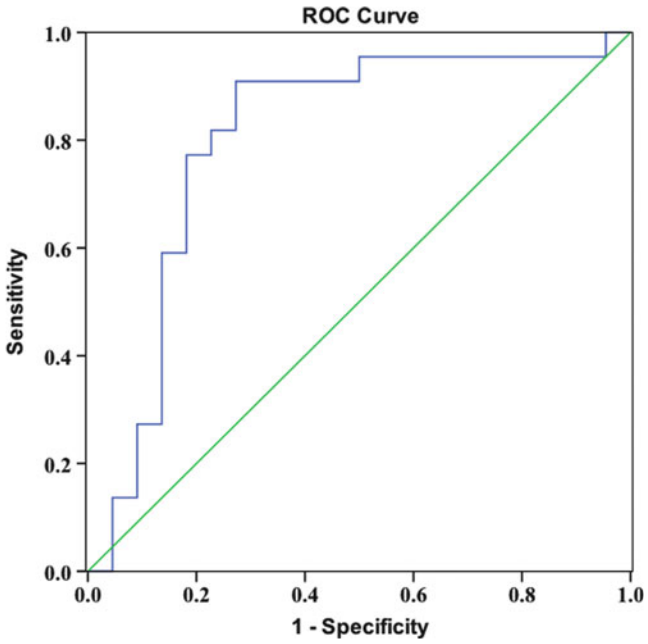

Fig. 3 ROC of validation 1

Table 5 Classification summary of the validation 2

		Predicted		
		Positive(predicted landslide occurrence)	Negative (predicted non-landslide occurrence)	Percentage correctly predicted
Observed	True (landslide occurred)	True Positive(TP)	False Negative(FN)	TP/(TP + FN)*100:**75.9 %**
		22	**7**	
	False (landslide not occurred)	False Positive(FP)	True Negative(TN)	TN/(FP + TN)*100:**75.0 %**
		236	**708**	
Overall percentage				(TP + TN)/(TP + FN + FP + TN) *100:**75.0 %**

Cut-off value is 0.08

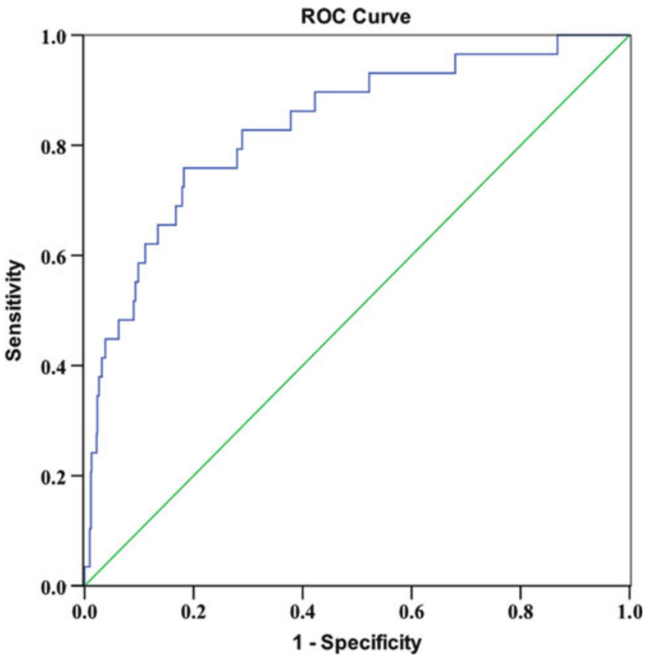

Fig. 4 ROC of validation 2

assessed active faults by using the model achieved in this study.

Acknowledgements The authors would like to express their appreciation to Dr. Edwin L. Harp for detailed review and helpful suggestions on ways to improve the paper.

References

AIST (2009) Active fault database of Japan, June 23, 2009 version, Research information database DB095. National Institute of Advanced Science and Technology, http:riodbo2.ibae.go.jp/activefault/index_e.html.

Ayalew L, Yamagishi H (2005) The application of GIS-based logistic regression for landslide susceptibility mapping in the Kakuda-Yahiko Mountains, Central Japan. Geomorphology 65:15–31

Chang KT, Chiang SH, Hsu ML (2007) Modeling typhoon-and earthquake-induced landslides in a mountainous watershed using logistic regression. Geomorphology 89:335–347

Chigira M, Yagi H (2006) Geological and geomorphological characteristics of landslides triggered by the 2004 Mid Niigata prefecture earthquake in Japan. Eng Geol 82:202–221

Chigira M, Wu XY, Inokuchi T, Wang GH (2010) Landslides induced by the 2008 Wenchuan earthquake, Sichuan, China. Geomorphology 118:225–235

Craig LA, Beech AR, Brown KD (2007) Methodological considerations when estimating actuarial sexual recidivism risk. Forensic Update 91 (2007):32–39

Dai FC, Lee CF (2002) Landslide characteristics and slope instability modeling using GIS, Lantau Island, Hong Kong. Geomorphology 42:213–228

Dong JJ, Tung YH, Chen CC, Liao JJ, Pan YW (2009) Discriminant analysis of the geomorphic characteristics and stability of landside dams. Geomorphology 110:162–171

Garcia-Rodriguez MJ, Malpica JA, Benito B, Diaz M (2008) Susceptibility assessment of earthquake-triggered landslides in El Salvador using logistic regression. Geomorphology 95:172–191

GSI (Geospatial Information Authority of Japan) (2009) 1: 25,000 detailed active fault map (active fault, geomorphological classification and deformation) of the 2008 Iwate-Miyagi inland earthquake, Technical report of Geospatial Information Authority of Japan, D.1-No.541 (in Japanese)

Guzzetti F, Carrara A, Cardinali M, Reichenbach P (1999) Landslide hazard evolution: a review of current techniques and their application in a multi-scale study, Central Italy. Geomorphology 31:181–216

Kobayashi I, Tateishi, M, Yoshida T, Shimazu M (1991) Geology of the Nagaoka district, with geological sheet map at 1:50,000, Geological Survey of Japan, 199pp (in Japanese with English abstract)

Marui H, Yagi H, Yoshimatsu H, Chigira M, Abe S (2006) Report of the field reconnaissance and inspection on landslides induced by the 2005 Northern Pakistan Earthquake. J Jpn Landslide Soc 43(2):48–51, in Japanese with English abstract

Meunier P, Hovius N, Haines J (2008) Topographic site effects and the location of earthquake induced landslides. Earth Planetary Sci Lett. doi:10.1016/j.epsl.2008.07.020

NIED (National Research Institute for Earth Science and Disaster Prevention) (2011) Landslide distribution maps, http://lsweb1.ess.bosai.go.jp/index.html. Accessed 24 April 2011

Niigata Prefecture (2009) Damages by the huge 2004 Chuetsu earthquake (last report), Niigata prefecture press report, p 4

Osawa A, Takisawa F (1992) The geological map atlas of Japan, northeastern Japan region. Asakura Publishing, Tokyo, 135p (in Japanese)

Owen LA, Kamp U, Khattak GA, Harp EL, Keefer DK, Bauer MA (2008) Landslides triggered by the 8 October 2005 Kashmir earthquake. Geomorphology 94:1–9

Süzen ML, Doyuran V (2004) A comparison of the GIS based landslide susceptibility assessment method: multivariate versus bivariate. Environ Geol 45:665–679

Suzuki S, Has B, Maruyama K, Ishii Y (2010) Risk evaluation of earthquake-induced landslide based on analysis of erosion condition on landslide marginal part. In: Chen Su-Chin (ed) Interpraevent2010-symposium proceedings, pp 898–901

Takada N (2007) New techniques for interpreting and applying the results of logistic regression analysis-an example of the credit scoring model-, IMB professional's papers, ProVISION 53/spring 2007:71–77 (in Japanese)

Takeuchi K, Yanagisawa S, Miyazaki J, Ozaki M (2004) 1:50,000 digital geological map of Chuetsu Uonuma district(Ver.1), Geological survey center research report, no. 412, AIST

The Headquarters for Earthquake Research Promotion (2011) Long term assessment for active fault. http://www.jishin.go.jp/main/choukihyoka/katsu.htm. Accessed 24 April 2011

Ushiyama M, Ohta Y (2009) Characteristicsof death or missing caused by the Iwate-Miyagi Nairiku earthquake in 2008, J.JSNDS28-1:59-66 (in Japanese with English abstract)

Yagi H, Sato G, Higaki D, Yamamoto M, Yamasaki T (2009) Distribution and characteristics of landslides induced by the Iwate-Miyagi Nairiku earthquake in 2008 in Tohoku district, northeast Japan. Landslides 6:335–344

Yanagisawa Y, Kobayashi I, Takeuchi K, Tateishi M, Chihara K (1986) Geology of the Ojiya district, with geological map sheet at 1:50,000. Geological Survey of Japan, Tsukuba-shi, 177p, in Japanese with English abstract

Yin YP, Wang FW, Sun P (2009) Landslide hazards triggered by the 2008 Wenchuan earthquake, Sichuan, China. Landslides. doi:10.1007/s10346-009-0148-

Susceptibility Mapping of Deep-Seated Landslides Around Active Fault System, a Case Study of Western Niigata, Japan

Akira Nakamura, Bateer Hasi, Tomoyuki Noro, and Kiyoteru Maruyama

Abstract

This study conducted landslide susceptibility mapping around the West margin active fault of western Niigata Prefecture, Japan using a logistic regression model. The result showed that 84.5 % of the pre-existing landslide topographies of the study area is low susceptibility, and 11.8 % of the study area is medium susceptibility, and only 3.7 % high susceptibility.

Keywords

Landslide • Earthquake • Susceptibility mapping • Japan

Introduction

Recently, a series of strong earthquakes struck eastern Japan. These earthquakes induced a large number of landslides that destroyed infrastructures, dammed rivers and caused serious damage to mountainous areas. In mountainous regions, such as Japan, to mitigate earthquake-induced landslides disasters, landslide susceptibility mapping is an important method.

Landslides susceptibility mapping has been conducted in many places of the world, by using deterministic or statistical analysis (Guzzetti et al. 1999; Ayalew and Yamagishi 2005; Chang et al. 2007; Garcia-Rodriguez et al. 2008). Most of the susceptibility mapping is based on the cell unit, using GIS (Geographical Information System) techniques. Cell-unit susceptibility mapping is easily done using a geographic information system (GIS), and can cover entire study areas. However, when focusing on countermeasures for individual landslides, the cell-unit analysis is difficult to conduct. In Japan, generally the real landslide countermeasure is accomplished using individual slope units, or block units.

Hasi et al. (2011a) has summarized the characteristics of the distribution of deep-seated landslides induced by recent strong reverse-fault earthquakes in Japan, and suggested that most of the landslides occurred on the hanging wall within 15 km from the source fault. Based on logistic regression analyses for the Chuetsu earthquake in 2004, Niigata Prefecture, Hasi et al. (2011b, this issue) constructed a logistic model for earthquake-induced deep-seated landslide evaluation around an active fault. This model only focused on topographical features of surface roughness and marginal erosion ratio (Suzuki et al. 2010), and analyzed the landslide occurrence triggered by earthquakes within pre-existing landslide topographies (geomorphologically recognized old landslides). Hasi et al. (2011b) validated the model by using a portion of the landslides data of the Chuetsu earthquake and the data of landslides induced by the Iwate-Miyagi inland earthquake in 2008, and concluded that the model is useful to evaluate landslide susceptibility around an active fault.

Based on the logistic regression model of landslide susceptibility constructed by Hasi et al. (2011b), it is possible to establish deep-seated landslides susceptibility mapping around active reverse faults in Japan. This is because, firstly the main active faults have been evaluated in Japan by the government (The Headquarters of Earthquake Research and Promotion 2011), and have shown the source faults and expected magnitude of future earthquakes; and secondly,

---

A. Nakamura (✉) • T. Noro • K. Maruyama
Snow Avalanche and Landslide Research Center, PWRI,
2-6-8 Nishiki-cho, Myoko-shi, Niigata, Japan
e-mail: a4066@n-koei.co.jp

B. Hasi
Snow Avalanche and Landslide Research Center, PWRI,
2-6-8 Nishiki-cho, Myoko-shi, Niigata, Japan

Now at Asia Air Survey, Co., Ltd., Manpukuji 1-2-2,
Asao Dis., Kawasaki, Japan

C. Margottini et al. (eds.), *Landslide Science and Practice*, Vol. 5,
DOI 10.1007/978-3-642-31427-8_32,

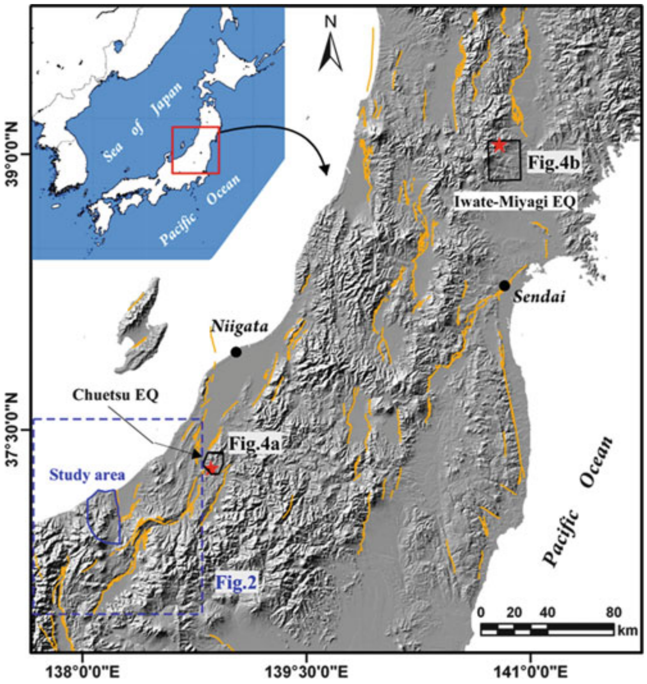

Fig. 1 Location of study area and focal area of the Chuetsu earthake and the Iwate-Miyagi earthquake. *Orange solid lines* indicate active faults (AIST 2009)

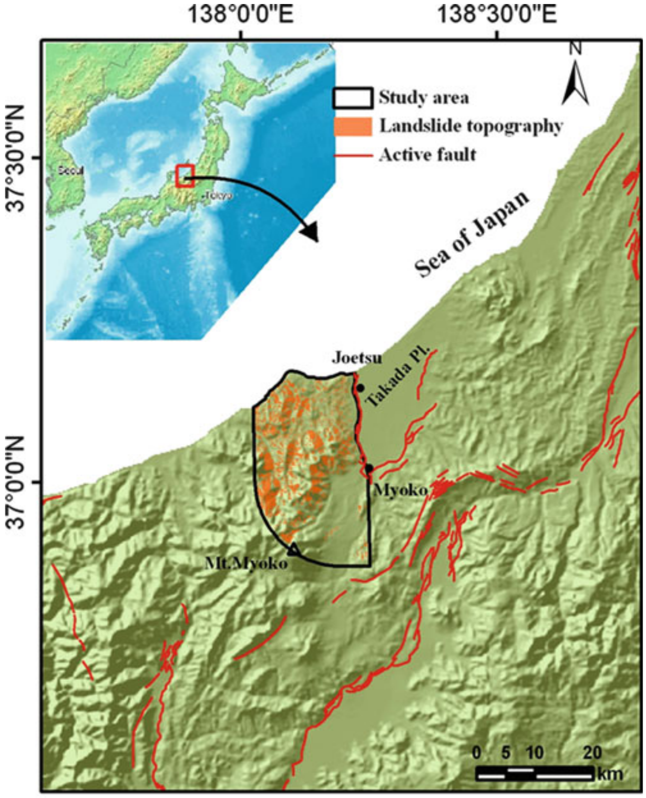

Fig. 2 Regional setting of study area

pre-existing landslide topography is easily identified and topogiaphic data is readily available in Japan (NIED 2011). Using these resource to clarify the deep-seated landslide susceptibility in the region of western side of the Takada Plain western margin fault, western Niigata Prefecture, we analyzed the landslide distribution and constructed a susceptibility map by using the model of Hasi et al. (2011b). We chose this region as a study area because it has similar characteristics of geomorphology and geologic conditions to the Chuetsu region, and is an area of densely distributed landslide topography in northern Japan.

Outline of Study Area

The study area is located in the western part of the Takada Plain, western Niigata Prefecture, Japan (Fig. 1). The study area occupies about 551 km^2 on the hanging wall of the Western Marginal Active Fault Zone of the Takada Plain (Fig. 2). The study area was selected based on Hasi et al. (2011a) and added the area between the active fault and the source fault model. According to Headquarters of Earthquake Research and Promotion (2010), the Takada Plain western fault is a reverse active fault of about 30 km length and dips to the west. According to the historical record, this fault generated a strong earthquake in 1751, named the Takada earthquake, M7.0–7.4 (Tatsuo 2001), and caused a large number of landslides (Inoue and Imamura 1999). This fault was estimated to have a maximum probable earthquake of M7.2 in the future.

The western side of the Takada Plain is the mountainous area of West Kubiki, the Sekita hill terrain and the volcanoes of Mt. Myoko and Mt. Yakiyama. The geomorphologic feature of study area is characterized by higher elevation of ridgelines in the southern part that range from 1,000 to 2,000 m, while the northern part is about 300 m. The surface roughness is large in southern part. In the study area, the Kuwatori River and the Nadachi River flow from south to north, and the Nou River and the Hayakawa River flow from southeast to northwest; all flow into the Japan Sea. Western Niigata Prefecture is a region of extensive landslides. In the study area, landslides are distributed over the whole area (NIED 2011). Figure 3 shows the geological map of the study area. Geologically, the study area is occupied by sandstone and mudstone, Miocene to Pliocene, and some dioritic dikes. The late Pleistocene to Holocene volcanic rocks and pyroclastic sediments covered the southern part of the study area. The geological structure of the study area is characterized by a series of NE-SW directed folds axes (Akahane and Kato 1989).

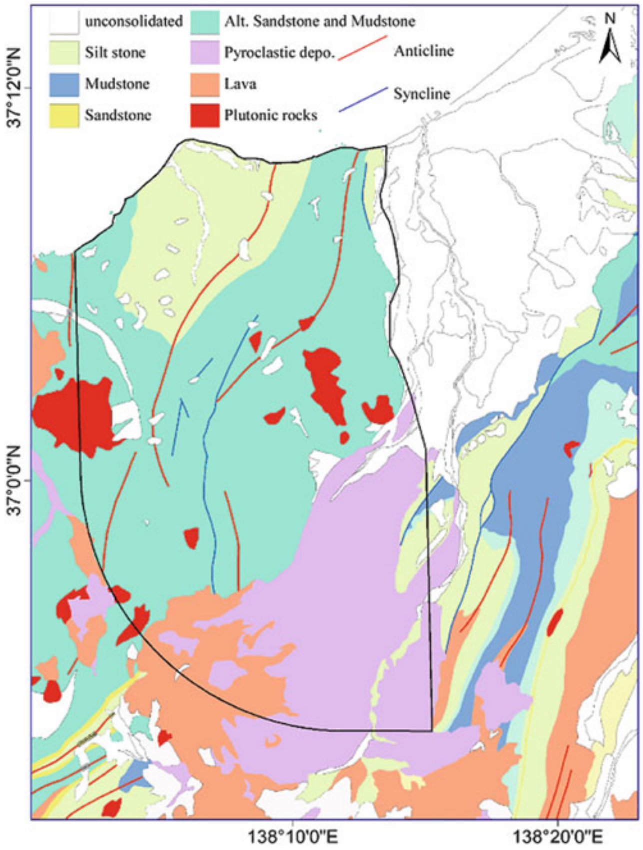

Fig. 3 Geological map of study area

Methodology, Data Source, and Causative Factors

Logistic Regression Model

In this study, we decided to use the logistic regression model of Hasi et al. (2011b) to analyze the earthquake-induced deep-seated landslide susceptibility of the study area.

The model used here was constructed by using the data set of landslides induced by the Chuetsu earthquake in 2004. In the focal area of the Chuetsu earthquake, 1,050 pre-existing landslide topographies and 96 earthquake-induced landslides were interpreted (Fig. 4a). In those 1,050 pre-existing landslide topographies, 87 contained landslides triggered by the Chuetsu earthquake. Hasi et al. (2011b) randomly selected 87 pre-existing landslide topographies where landslides were not triggered from the whole data set of 963, then selected, 87 landslide topographies where landslides were triggered to make a sub-data set and selected 75 % of them (landslide occurrence 65, landslide non-occurrence 65) to construct the logistic regression model. The model was validated by the remaining 25 % of the sub-data set (landslide occurrence 22, landslide non-occurrence 22). In addition, the model was corrected and then validated by the landslides data of the Iwate-Miyagi inland earthquake in 2008, which includes 29 landslide topographies where landslides were triggered and 944 landslide topographies

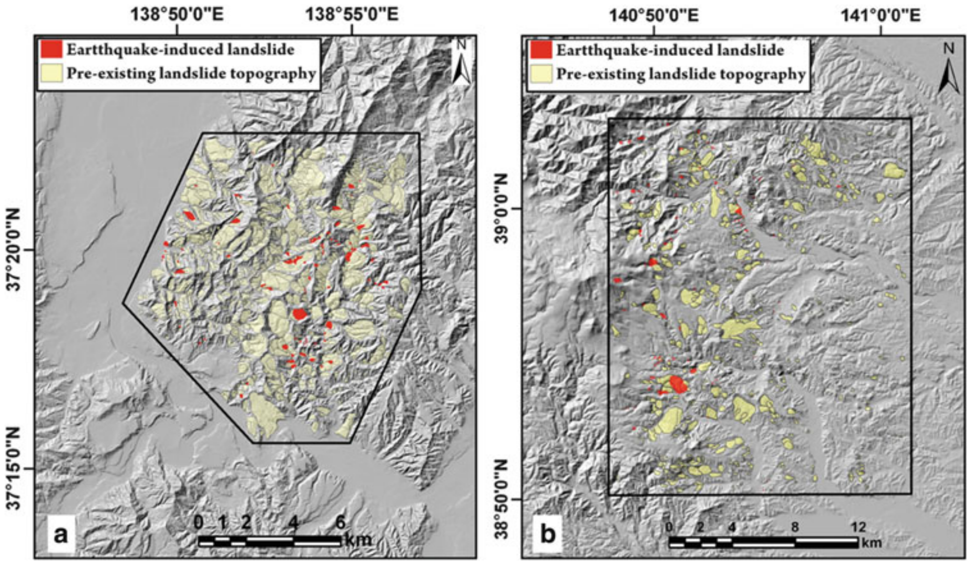

Fig. 4 Distribution of earthquake-induced landslides and pre-existing landslide topographies. (**a**)Chuetstu earthquake, (**b**)Iwate-Miyagi inland earthquake

where landslide were not triggered. We used this corrected model shown in (1).

$$P_c = \frac{1}{1 + e^{-(Log(0.060SR + 0.035MER - 5.320)}} \quad (1)$$

Where, Pc is the corrected landslide occurrence probability, which is defined as the occurrence of re-activated landslide within pre-existing landslide topography by an earthquake. In above equation, SR is surface roughness, and MER is marginal erosion ratio. For each pre-existing landslide topography (described as a landslide polygon), Pc is calculated using use its SR and MER. Here, the cut-off value is 0.08 according to landslide occurrence ratio of the Chuetsu earthquake induced landslides (Hasi et al. 2011b).

Data Source and Causative Factors

In this study, we used pre-existing landslide topographies of an NIED database (NIED 2011). We integrated small blocks of landslides topographies into a larger one.

We used aerial photographs taken in 1976 and 1999 by the Geospatial Information Authority of Japan (GSI) to check landslide topographies. Then we calculated marginal erosion ratios of the landslide topographies by using aerial photographs and topographical maps.

The digital elevation model and causative factors that were used in the model are described below.

1. Digital elevation model (DEM): A 10 m grid DEM (Geospatial Information Authority of Japan) was used to calculate surface roughness. The grid size was resized to 30 m.
2. Surface roughness (SR): The surface roughness is defined as the standard deviation of elevation values within the pre-existing landslide topography. Larger surface roughness values indicate steeper slope gradients or larger landslide areas. The surface roughness is calculated by ArcGIS within each 30 m grid cell.
3. Marginal erosion ratio (MER): This variable is defined as the eroded length of a landslide margin divided by the whole marginal length of a landslide block (Suzuki et al. 2010). It indicates the erosion condition of the slope and the instability of the slope. The marginal erosion ratio of each pre-existing topography was calculated after measuring the length of erosion according to aerial photography interpretation. The whole length of the landslide margin was calculated as the perimeter of the landslide polygon.

After calculating SR and MER, we achieved landslide occurrence probability Pc value of each landslide. Based on a susceptibility ranking derived from Pc and the landslide occurrence ratio of the Chuetsu earthquake-induced landslide, we mapped the deep-seated landslide susceptibility of the study area.

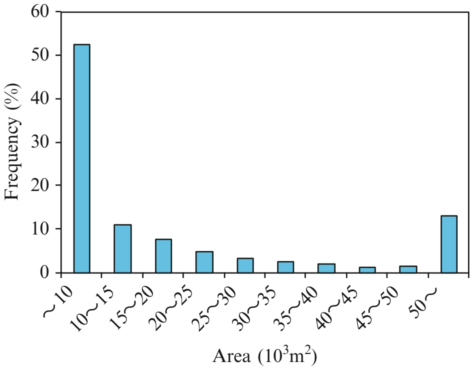

Fig. 5 Frequency of landslide area

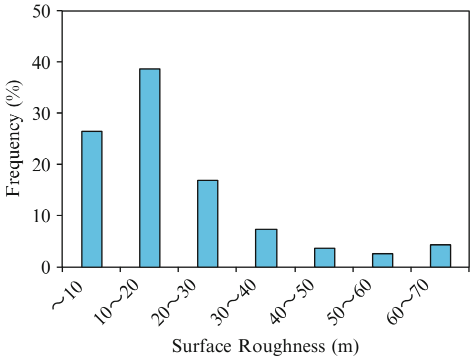

Fig. 6 Frequency of surface roughness

Results

Landslide Topographies

In the study area, a total of 3,718 landslides topographies (polygons) were tabulated (Fig. 2). The total area of landslide topographies is about 130 km^2, and occupies 23.5 % of the study area. Figure 5 shows the frequency of area of the pre-existing landslide topographies. More than half of the landslides are smaller than 10,000 m^2 (52.5 %), but 13.2 % are landslides larger than 50,000 m^2.

Frequency of Causative Factors

Figure 6 shows the frequency of surface roughness of landslide topographies in study area. The most frequent range is 10–20, which occupies 38.6 % of the landslide topographies. Most of the landslides topographies have a surface roughness of less than 30 m, which includes 82.2 % of the data.

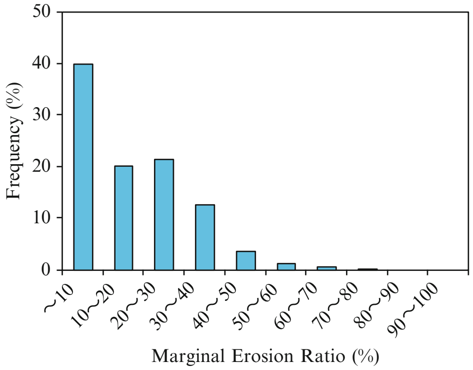

Fig. 7 Frequency of marginal erosion ratio

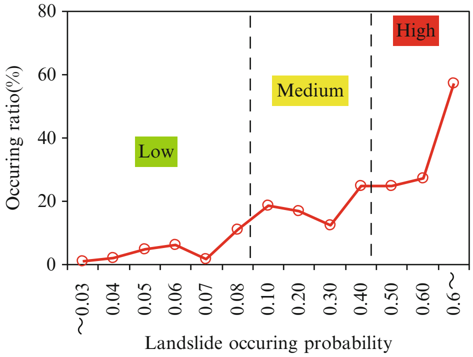

Fig. 8 Susceptibilty classification

Figure 7 shows the frequency of marginal erosion ratios of the landslide topographies of study area. The most frequent range is smaller than 10, 39.9 % of the data. Most of the landslides topographies have a MER of less than 30, 81.5 % of the data.

Susceptibility Class and Susceptibility Map

According to the data set of the Chuetsu earthquake, the landslide occurrence ratio (earthquake-induced landslide/ landslide topography) with landslide occurrence probability is shown in Fig. 8. It shows that there is a tendency of the landslide occurrence ratio to increase with the increase of landslide occurring probability. Based on this increase and a cut-off value (0.08), the susceptibility classes can be established as P < =0.08 – low susceptibility, 0.08 < P <=0.4 – medium susceptibility medium, and P >0.4 – high susceptibility.

Figure 9 shows the frequency of landslide occurring probability of landslide topographies in the study area. Most of the landslide topographies are within the class of low susceptibility.

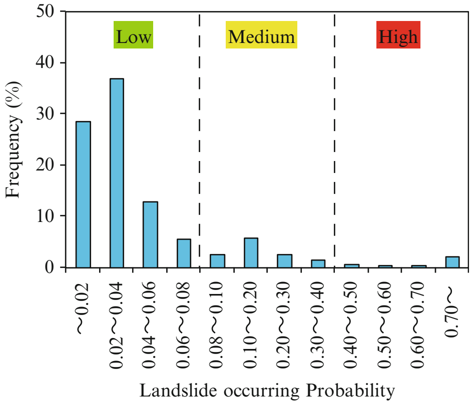

Fig. 9 Frequency of landslide occurring probability

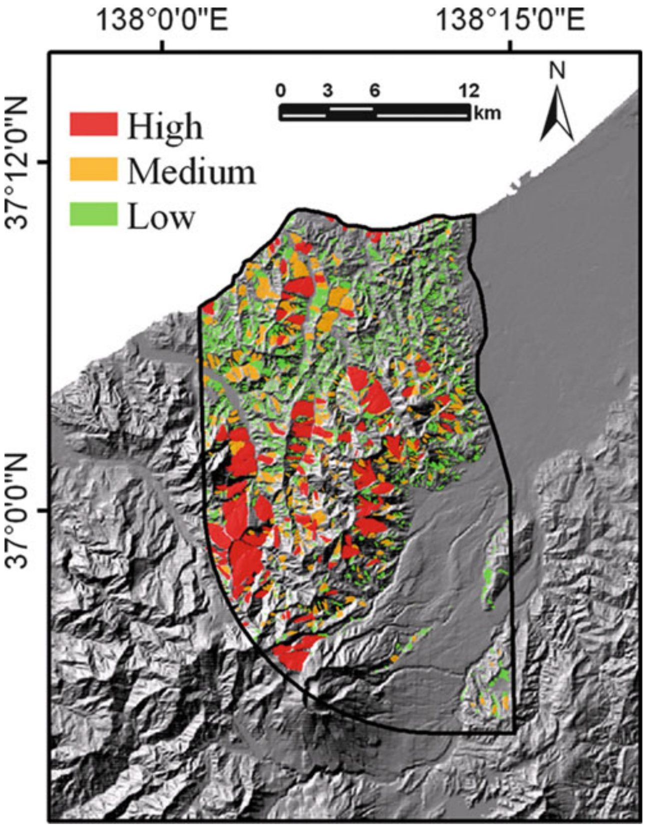

Fig. 10 Susceptibility map of study area

Figure 10 shows the susceptibility map of the study area. Most of the landslides in southern side of the study area show high susceptibility.

Table 1 lists the susceptibility class with the number and area of landslide topographies in the study area. Most of the landslide topographies, 84.5 % are low susceptibility; its mean area is 13,547.3 m^2. The medium susceptibility class a total of 438 landslides, is 11.8 % of the total. The high susceptibility class of landslide topographies includes 139

Table 1 Number of landslides and area

Susceptibility class	Number	Ratio in whole number (%)	Mean area(m^2)	Total area(m^2)	Ratio in whole area (%)
High	139	3.7	364753.8	50700781.0	39.1
Medium	438	11.8	82889.0	36305386.0	28.0
Low	3,141	84.5	13547.3	42552134.0	32.8
Total	3,718	100	461190	129558301	100

landslides, 3.7 % of the total. The mean area is 364,753.8 m^2, about 3 times larger of that of the low susceptibility class.

Discussion and Conclusion

In many cases of susceptibility mapping, digital cells are used. However when considering countermeasures of individual slopes, cell units are not applicable. In this study, we used a logistic regression model constructed achieved from an analysis of earthquake-induced landslides triggered in eastern Japan to calculate the landslide occurring probability of pre-existing landslide topographies. This method only considers pre-existing topographies. Because of some slopes that did not experience landslide activity are excluded in the susceptibility mapping. The results show that higher susceptibility classes of landslides tend to have larger mean areas. The landslide topographies of the high susceptibility class are distributed in the southern side of the study area, and may relate to the geological condition.

Using a logistic regression model, the susceptibility map of pre-existing landslide topographies was made around the West margin active fault of the Takada Plain. The result provided a primary landslides hazard map around the active fault where possible to initiate earthquakes many occur in the future.

Acknowledgements The authors would like to thank Dr. Edwin L. Harp for patient review and helpful suggestions that helpful to improve the paper.

References

AIST (2009) Active fault database of Japan, June 23, 2009 version, Research information database DB095. National Institute of Advanced Science and Technology, http://riodbo2.ibae.go.jp/activefault/index_e.html

Akahane S, Kato H (1989) Geology of the Takada-seibu district, with geological map sheet at 1:50,000, Geological Survey of Japan, 89p (in Japanese with English abstract)

Ayalew L, Yamagishi H (2005) The application of GIS-based logistic regression for landslide susceptibility mapping in the Kakuda-Yahiko Mountains, Central Japan. Geomorphology 65:15–31

Chang KT, Chiang SH, Hsu ML (2007) Modeling typhoon-and earthquake-induced landslides in a mountainous watershed using logistic regression. Geomorphology 89:335–347

Garcia-Rodriguez MJ, Malpica JA, Benito B, Diaz M (2008) Susceptibility assessment of earthquake-triggered landslides in El Salvador using logistic regression. Geomorphology 95:172–191

Guzzetti F, Carrara A, Cardinali M, Reichenbach P (1999) Landslide hazard evolution: a review of current techniques and their application in a multi-scale study, Central Italy. Geomorphology 31: 181–216

Hasi B, Ishii Y, Maruyama K, Terada H, Suzuki S, Nakamura A (2011a) Distribution and scale of landslides induced by recent reverse-fault earthquakes in Japan. J Jpn Landslide Soc 48 (1):23–38

Hasi B, Maruyama K, Nakamura A, Noro T (2011b) Statistical analysis of deep-seated landslides induced by recent strong earthquakes in eastern Japan: an approach based on pre-existing landslide topography, this issue

Inoue F, Imamura T (1999) Takada earthquake (1751) and slope disasters of Jyoetsu coast, JESE meeting of 1999, pp 290–291

NIED (2011) Landslide topography data base. http://lsweb1.ess.bosai.go.jp/index.html. Accessed 24 April 2011

Suzuki S, Has B, Maruyama K, Ishii Y (2010) Risk evaluation of earthquake-induced landslide based on analysis of erosion condition on landslide marginal part. In: Chen Su-Chin (ed) Interpraevent2010-symposium proceedings, pp 898–901

Tatsuo U (2001) Materials for comprehensive list of destructive earthquakes in Japan, latest edition. University of Tokyo Press, Tokyo, 416p

The Headquarters for Earthquake Research Promotion (2010) Long term assessment for Takada Plain active faults. http://www.jishin.go.jp/main/chousa/katsudansou_pdf/102_takada-heiya.pdf

The Headquarters of Earthquake Research and Promotion (2011) Long-term evaluation of active faults. http://www.jishin.go.jp/main/p_hyoka02_danso.htm#102

Effect of the Thickness of Geological Strata on Seismically-Induced Slope Failure in IMN Earthquake, 2008 in Japan

Shiho Asano

Abstract

Many landslides have been caused by large-scale earthquakes in volcanic mountain areas. The Iwate-Miyagi Nairiku Earthquake (IMN Earthquake) of 2008 is one such example. To constrain the effect of volcanic deposits on large earthquake-induced accelerations that trigger landslides, an earthquake response analysis that considered a range of geological conditions was carried out. The results show that the thickness and position of soft rock, such as a layer of weakly welded tuff, affected the intensity and amplification of seismic acceleration on the slope.

Keywords

Earthquake • Volcanic deposits • Numerical analysis

Introduction

A large number of landslides can occur when a large earthquake strikes in a hilly region. An example of this is the 2008 IMN Earthquake in Japan. The landslides that occurred during this event resulted in significant mass wasting and serious local damage to infrastructure. The technology behind estimates of the risk of landslides that are triggered by earthquakes requires improvement in order to reduce such landslide disasters. This is addressed by examining the seismically-induced motion that affects slope stability as an external force. For example, landslide displacement has been shown to depend on the seismic acceleration (Newmark 1965). A clarification of the distribution characteristics of the seismic acceleration on mountain slopes is needed to estimate the risk of landslide occurrence.

Many landslides occur on the steep upper slopes of mountains, near ridgelines (Harp and Jibson 1996; Tang and Grunert 1999). The amplification of earthquake acceleration by topographical effects is considered to be one of the reasons for landslide occurrences (Harp et al. 1981; Murphy 1995). The distribution of earthquake accelerations over a mountain slope has been numerically modeled in terms of its relation with the topography of the mountain (Ochiai et al. 1995). At the same time, the geological structure of the mountain is bound to affect the distribution of earthquake motion. In a volcanic area, the deposition of the volcanic sediments is complicated because of the nature of repeated volcanic activity. The IMN Earthquake of 2008 was a large-scale event that produced many landslides in a mountainous region in which there was a wide and complicated distribution of volcanic sediment.

In this study, in order to characterize the effect of geological structures on the seismically-induced motion that results in large-scale landslides, an earthquake response analysis using a mountain model that incorporates the geological structure of the mountain was used.

Study Area

The large-scale IMN M 7.2 Earthquake of 2008 occurred in northeastern Japan. Many landslides were triggered by the earthquake on the mountain slopes in the area. This study investigates an area of high landslide density

---

S. Asano (✉)
Kyushu Research Centre, Forestry and Forest Products Research Institute, Kumamoto, Kurokami 4-11-16, Kumamoto 860-0862, Japan
e-mail: shiho03@ffpri.affrc.go.jp

C. Margottini et al. (eds.), *Landslide Science and Practice*, Vol. 5,
DOI 10.1007/978-3-642-31427-8_33, © Springer-Verlag Berlin Heidelberg 2013

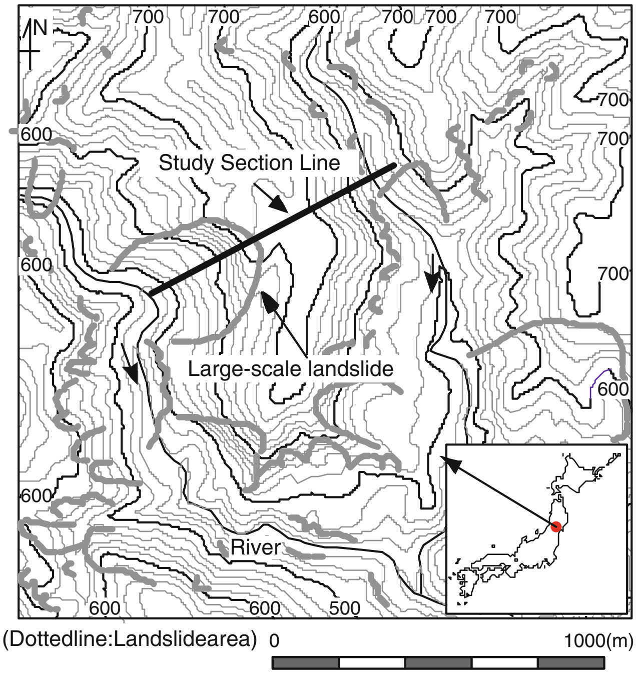

Fig. 1 Topographical map of the study area

Photo 1 Large-scale landslide in the study area

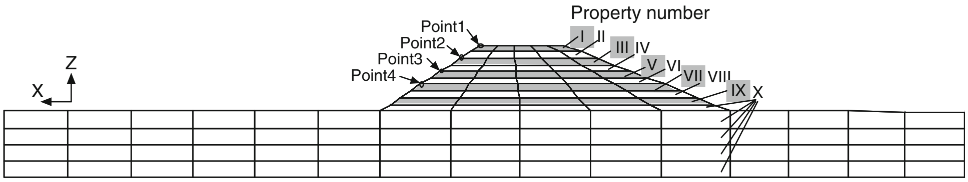

Fig. 2 Analysis model and element properties

(Fig. 1). This hilly area is located about 7 km south-southwest of Kurikoma volcano. In this area, thick volcanic sediments have accumulated and river erosion has produced a wide distribution of mountain ridges and tablelands.

In this study area, the mountains have accumulated layers of welded tuff, pumice tuff and andesite lava. The welded tuff layers are found in field investigations to consist of alternating weakly and strongly welded units.

Surface wave prospecting has been carried out at a near-by study site that has characterized the hardness of each rock stratum. The seismic wave velocity of the weakly welded tuff layer is higher than that of the strongly welded tuff layer. A large number of landslides is distributed on steep valley side slopes, and some large-scale landslides occurred from the tops of slopes. Also, many landslides on steep slopes are seen to occur in the welded tuff layer.

Method

The earthquake response analysis was carried out using a typical model that considered the geological strata of the study site in order to examine the characteristics of earthquake motion. In this analysis, the distribution of acceleration responses was calculated for various thicknesses of the geological strata.

For the earthquake response analysis, a dynamic elasto-plastic finite-element analysis was carried out to investigate the characteristics and distribution of the seismically-induced accelerations on the mountain slopes. The mountain ridges generally consist of a hard rock mass and a soft surface soil layer. Therefore, the rock mass was considered to deform elastically and the surface soil to deform elasto-plastically. Elasto-plastic analysis employed an elasto-perfect plasticity model based on the nonlinear Mohr–Coulomb failure criterion, with the plasticity following the associated flow rule.

The analysis model was constructed from a cross-section of a mountain on which a large-scale landslide had occurred (Photo 1). The geological structure of the mountain was based on a geological map of the area (Yamada et al. 1986) and a field investigation. All strata are assumed to have been vertically accumulated on the sides of the mountain.

The analysis model was a typical three-dimensional model (Fig. 2). The thickness of the model was 1 m. The width of the mountain model was 1,050 m at the base and 250 m at the top and the altitude was 500 m at the

Table 1 Material property for analysis

	Unit weight (kN/m^3)	Modulus of elasticity (kN/m^2)	Poison's rate	Cohesion (kN/m^2)	Angle of shear resistance (degree)
Surface soil (sand)	17.7	$2.02 * 10^4$	0.40	0	38
Welded tuff (Strongly welded)	22.6	$2.74 * 10^6$	0.47	3118	48
Welded tuff (Weakly welded)	20.6	$1.79 * 10^6$	0.43	3118	48
Pumice tuff	17.7	$1.88 * 10^6$	0.45	3118	48
Andesite lava	24.5	$1.07 * 10^7$	0.38	3118	48

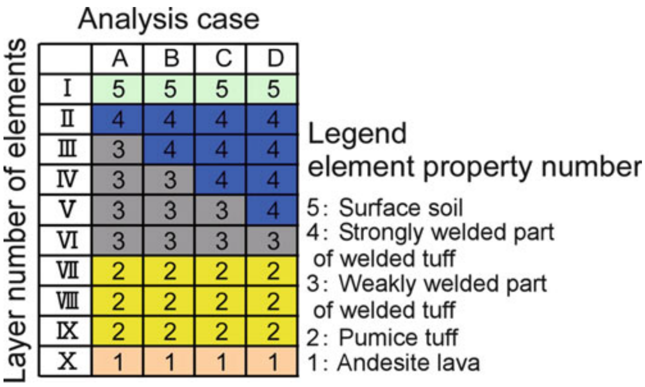
Analysis case

Layer number of elements

	A	B	C	D
I	5	5	5	5
II	4	4	4	4
III	3	4	4	4
IV	3	3	4	4
V	3	3	3	4
VI	3	3	3	3
VII	2	2	2	2
VIII	2	2	2	2
IX	2	2	2	2
X	1	1	1	1

Legend
element property number
5: Surface soil
4: Strongly welded part of welded tuff
3: Weakly welded part of welded tuff
2: Pumice tuff
1: Andesite lava

Fig. 3 Element properties for modeled cases

base and 700 m at the top. The bedrock under the mountain was also part of the model. The altitude of base of bedrock part of the model was arbitrarily set at 300 m. The analysis model was then divided into eight-node isoparametric finite elements. The model used consisted of 110 elements and 280 nodes. The elements of the top layer of the mountain were assumed to represent the surface soil. All other elements were assumed to be rock. As a boundary condition for analysis, the displacement in the direction normal to the bottom, the thickness faces and the side faces of the model were all set to zero. As an initial condition, gravitational acceleration was assigned for all elements.

The material property parameter was assumed to be as follows even though there was no well data for control (Table 1). The density of rock was determined from a sample test. The coefficient of deformation of the rock was determined from the velocities of P and S waves, which in turn were estimated from seismic exploration results collected near the study area and seismic wave velocities measured at the MYGH02 earthquake observation well of KIK-NET by NIED in Japan. The shear strength of the surface soil was taken as the strength of sand determined in a previous study (Asano and Ochiai 2008). The difference in the hardness of the weakly and strongly welded tuff layers was assumed by surface wave prospecting near the study site. The damping parameter and dependency of the hardness on the strain were assumed by the reproduction of the analysis of observed accelerations at MYGH02.

For the earthquake response analysis, the seismic acceleration was determined for all nodes at the bottom, and then the response acceleration and displacement of each node was calculated. The seismic acceleration input consisted of the east–west oriented component of the acceleration observed 200 m underground at the MYGH02 well of KiK-net. The acceleration data were provided for a period of 2.5 s. The time step frequency in the analysis was 500 Hz and the recording frequency was 50 Hz.

Results and Discussion

A mixture of weakly welded zones and strongly welded zones are found in the welded tuff strata. Also, the S-wave velocity of the weakly welded zone is higher than in the strongly welded zone. Some large-scale landslides occurred across the weakly and strongly welded zones in the welded tuff layer. So, to examine the effect of these zones on earthquake distribution, this study examines four scenarios by using the model to vary the thickness of the welded zone. The thicknesses of welded zone used in each case are shown in Fig. 3.

The distribution of maximum response accelerations for each case is shown in Fig. 4. A positive value indicates that acceleration in the x direction. The large-scale landslide that occurred on the modeled mountain during the IMN Earthquake is seen on the left side slopes. The seismic motion transmitted from the bottom of the model to the ground surface was amplified at each depth. A large acceleration response appeared at the top of mountain and along the surface of the steep slope. The distribution of accelerations in each case was slightly different.

In order to examine the effect of layer thickness, the acceleration characteristics were obtained for the case in which a single pumice tuff layer was assumed to cover the entire mountain component of the model. The distribution of acceleration increments for each case was obtained (Fig. 5). This shows the effect of a welded tuff layer on the amplification of seismic acceleration.

The thickness and height of the strongly and weakly welded parts of the welded layer were observed to affect the position of the maximum acceleration response. The weakly welded part of the welded layer was thick in case A, whereas the strongly welded part was thick for case D. The acceleration response was amplified in the weakly welded part of the welded layer, although the amplified area in case D appears at a lower altitude than in case A. Also, the acceleration was

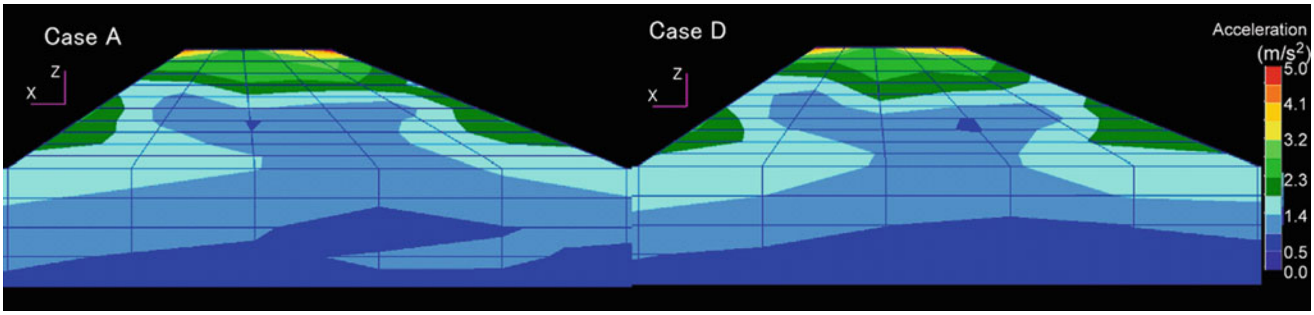

Fig. 4 Maximum acceleration response in the *x* direction for the mountain in cases A and D

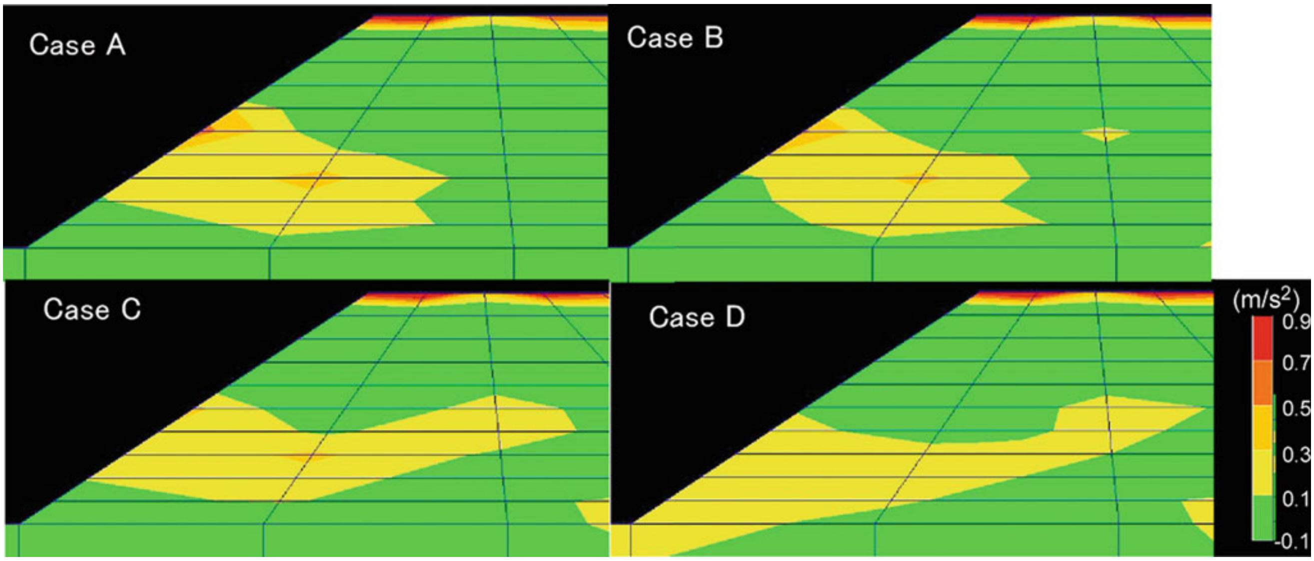

Fig. 5 Amplification of maximum acceleration by the distribution of the welded tuff layer

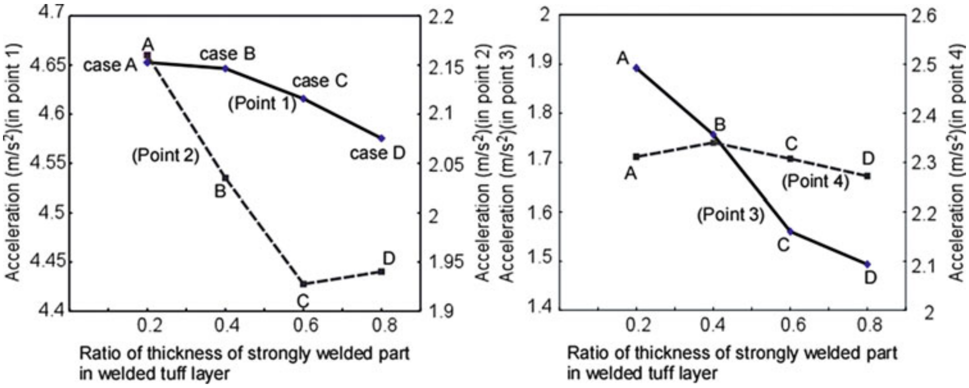

Fig. 6 Relationship of maximum acceleration and thickness of welded tuff layer at points on the slope

amplified around the boundary with the weakly and strongly welded parts of the layer, with the amplification being much higher in case A as compared with case D.

The relationship between the intensity of the acceleration response and the thickness of the weakly welded part of the welded tuff layer is calculated at various points along the surface of the mountain slope (Fig. 6). The acceleration response at the top of the slope (e.g., points 1 and 2) was greater than at the base. The acceleration at the top of slope was more greatly amplified for the case in which the weakly welded layer was thick. The effect of geological structure on the distribution of the earthquake accelerations is therefore considered to have an effect on the position of landslides that occur.

Conclusion

In this study, the distribution and amplification of earthquake-induced accelerations that resulted in mountain-slope landslides were examined by an earthquake response analysis technique. The analysis was carried out using a mountain model based on an actual large-scale landslide for which seismically-induced motion was observed during the IMN earthquake. The effect of the thickness of a welded tuff layer on the distribution of maximum earthquake accelerations was investigated.

The response acceleration was more greatly amplified in the weakly welded part of the welded tuff layer. Furthermore, the greater acceleration tended to occur around the boundary area between the weakly and strongly welded parts of the welded layer. Earthquake-induced accelerations on the upper slope, which triggered a large- scale landslide, were affected by the thickness and position of the weakly welded part of the welded tuff layer.

Acknowledgments Field investigations were carried out with the cooperation of the Forest Agency of Japan and Forestry and Forest Products Research Institute. Seismic observation data were obtained from KiK-net of the National Research Institute for Earth Science and Disaster Prevention (NIED).

References

Asano S, Ochiai H (2008) Influences of earthquake motion on slopes in a hilly area during the Mid-Niigata Prefecture Earthquake 2004. Landslides and Engineered Slopes, pp 1375–1379

Harp EL, Jibson RW (1996) Landslides triggered by the 1994 Northridge, California, earthquake. Bull Seismol Soc Am 86(1B): S319–S332

Harp EL, Wilson RC, Wieczorek GF (1981) Landslides from the February 4, 1976, Guatemala earthquake, vol 1204A, Professional paper. United States Geological Survey, Washington, DC

Murphy W (1995) The geomorphological controls on seismically triggered landslides during the 1908 Straits of Messina earthquake, southern Italy. Q J Eng Geol Hydrog 28(1):61–74

Newmark NM (1965) Effects of earthquakes on dams and embankments. Geotechnique 15(2):139–159

Ochiai H, Kitahara H, Sammori T, Abe K, (1995) Earthquake-induced landslides and earthquake response analysis. Research report of landslides and slope failures triggered the Hyogoken-Nanbu Earthquake, Japan landslide society, Japan. pp 119–132

Tang C, Grunert J (1999) Inventory of landslides triggered by the 1996 Lijiang Earthquake, Yunnan Province, China. Trans Jpn Geomorph Union Jpn 20(3):335–349

Yamada E, Sakaguchi K, Takashima I, Abe K, Hiruma T, Komazawa M, Suda Y, Murata Y (1986) Geological map of Kurikoma geothermal area, vol 21-3, Miscellaneous map series. Geological survey of Japan, Ibaraki-Ken

Landslides Induced by the 1908 Southern Calabria: Messina Earthquake (Southern Italy)

Valerio Comerci, Anna Maria Blumetti, Elisa Brustia, Pio Di Manna,
Luca Guerrieri, Mauro Lucarini, and Eutizio Vittori

Abstract

Five hundred and two different testimonies of coseismic environmental effects of the 1908 Southern Calabria-Messina earthquake have been identified and catalogued, based on a careful screening of contemporary documents, i.e. technical and photographic reports, newspapers and other archive material. Out of the 348 independent occurrences, landslides are the most represented category with 150 cases (43 % of the whole set of effects). The area, which is prone to slope instability even without seismic triggering, due to its lithological characters and rugged topography, undergoes now a much higher seismic risk because of the unconcerned strong urban development of recent decades. So, the obtained scenario of landslides distribution triggered by the 1908 earthquake helps to evaluate the impact on this region of a 1908-like future event.

Keywords

1908 earthquake • Induced landslides • Hazard evaluation

The Earthquake Environmental Effects database

The December 28, 1908, Southern Calabria - Messina earthquake (Intensity MCS XI, Mw 7.24) has been the strongest seismic event to hit Italy during the twentieth century and the most devastating, with a death toll of at least 80,000 (Boschi et al. 1995; Gruppo di lavoro CPTI 2004). The impact of the earthquake was particularly catastrophic along the coastlines facing the Messina Straits, mostly because of building collapses and tsunami waves. The macroseismic epicentre is located close to Reggio Calabria town (Guidoboni and Mariotti 2008). The estimated hypocentral depth was between 5 and 15 km (Pino et al. 2000).

We collected 502 contemporary testimonies related to 348 earthquake environmental effects, that were found in newspapers, the Official Gazette and tens of reports, several of them compiled by true authorities of that time on this subject, such as Mercalli, Baratta, etc. Our basic geological and geophysical documental sources were Baratta (1909, 1910), Cortese (1923), Crema (1909, 1921), Di Stefano (1909), Franchi (1909), Galli (1910), Luiggi (1909), Gor'kji-Meyer (1909), Martinelli (1909), Marzolo (1909), Mercalli (1909), Novarese (1909), Occhiuto (1909), Oddone (1909), Oldham (1909), Omori (1909), Platania (1909), Ricciardi (1909, 1910), Riccò (1909), Rizzo (1909), Taramelli (1909), Sabatini (1909) and Società Fotografica Italiana (1909). Once pertinent descriptions of effects were found in the original sources, they were classified in one of 12 categories (based on the ESI - Environmental Seismic Intensity - scale, Michetti et al. 2007): slope movement, ground crack, ground lowering and uplift, differential lowering, coastline retreat, sinkhole, liquefaction, hydrological anomaly, gas emission, light and rumble. In Fig. 1, the

---

V. Comerci (✉)
ISPRA, Italian Institute for Environmental Protection and Research, Geological Survey of Italy, Via Curtatone 3, Rome 00185, Italy
e-mail: valerio.comerci@isprambiente.it

A.M. Blumetti • E. Brustia • P. Di Manna • L. Guerrieri • M. Lucarini • E. Vittori
ISPRA, Italian Institute for Environmental Protection and Research, Geological Survey of Italy, Rome, Italy

C. Margottini et al. (eds.), *Landslide Science and Practice*, Vol. 5,
DOI 10.1007/978-3-642-31427-8_34,

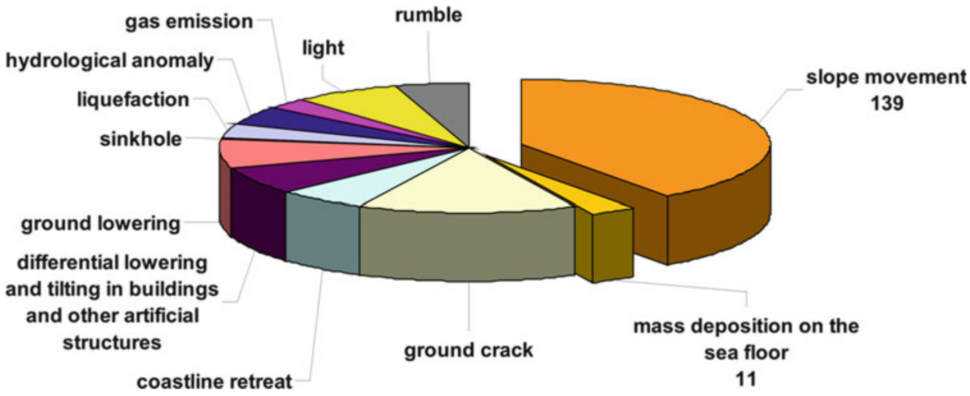

Fig. 1 Distribution by type of the 348 collected effects induced by the 1908 earthquake

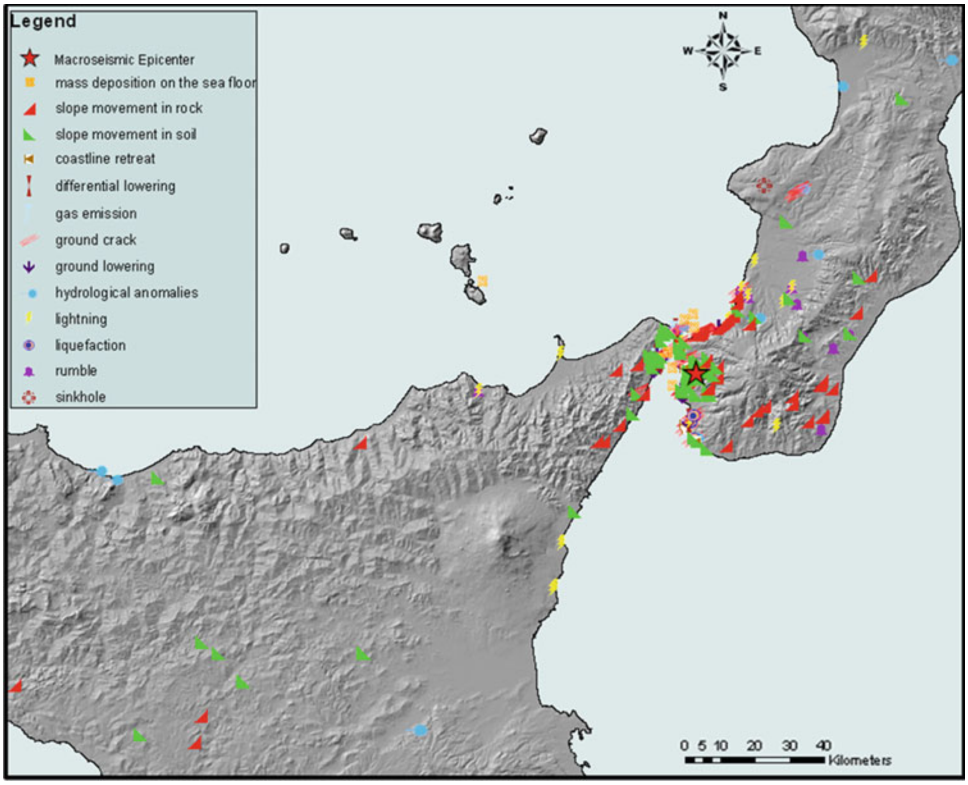

Fig. 2 The 348 effects on the environment described by the contemporary sources. Their geographical distribution is uneven, because the territory was mostly investigated in inhabited and most accessible areas. At this scale many of the symbols overlap

percentage distribution of landslides (150), compared to the other 198 collected effects is reported.

Geo-referenced and placed on a map, some of the 348 collected effects overlap (Fig. 2) and in general, their geographical distribution is strongly uneven. The latter could be directly caused by the irregular pattern of investigation conducted then on the territory by the surveyors: they concentrated their efforts in the towns and villages and roads along the coastal area, which were much more accessible than the inner mountain region.

Out of the 348 effects, 140 are located in Calabria, 197 in Sicily, and 11 at sea (mass depositions on the sea floor). The locality with the largest number of effects (123) is Messina. If we exclude the effects collected at Messina and Reggio Calabria (40), the number of effects in Calabria (100) is larger than that in Sicily (74).

Landslides Induced by the 1908 Earthquake

Slope movements represent the largest part of the reported effects: 150 (43 % of the total). Of them, 52 occurred in Sicily (35 %), 87 in Calabria (58 %) and 11 at sea (7 %). In fact, bathymetric measurements, taken soon after the earthquake in the Straits area, detected reductions of depth of the

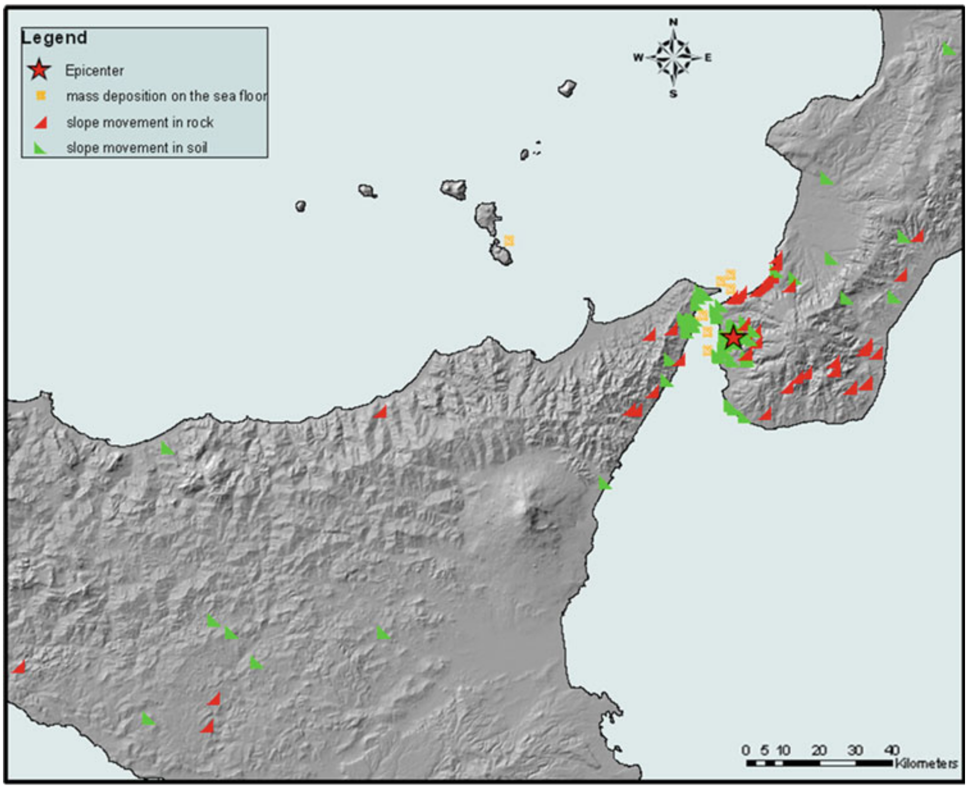

Fig. 3 The 1908 earthquake triggered many landslides inland and also underwater. We collected the description of 59 slope movements in rock, 80 slope movements in soil and 11 mass deposition on the sea floor

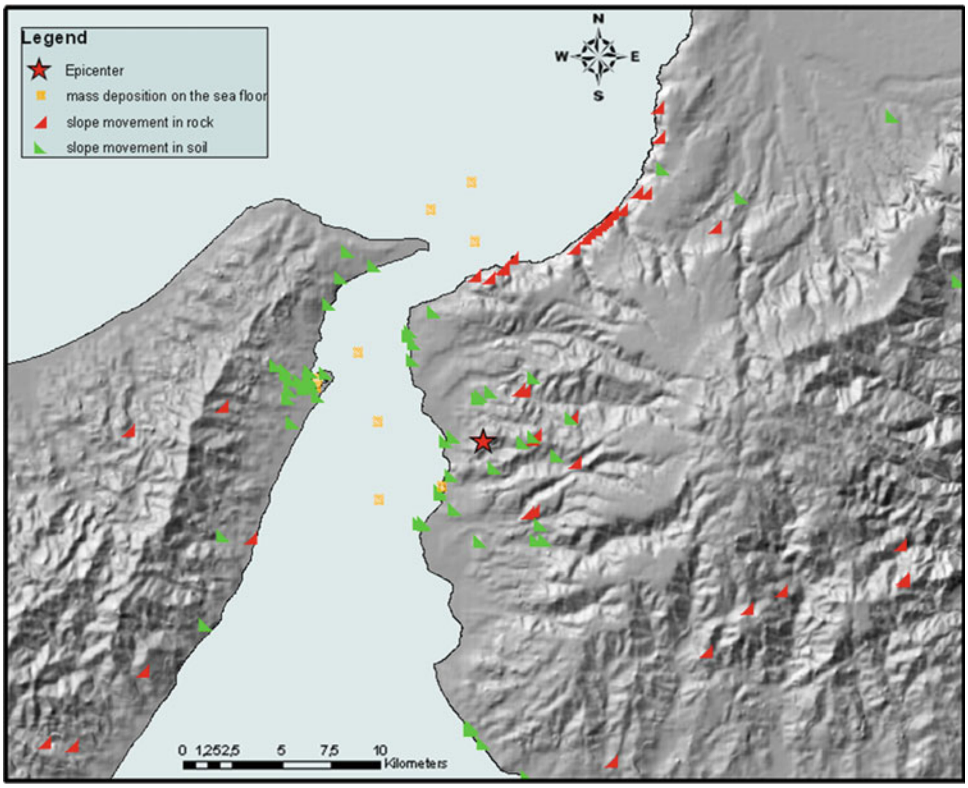

Fig. 4 Landslides triggered by the 1908 earthquake: close-up of the epicentral area

Fig. 5 Rockslides and rockfalls occurred along the railway line in Favazzina (Società Fotografica Italiana 1909)

Fig. 6 Rockfalls along the railway line in Favazzina (Società Fotografica Italiana 1909)

sea floor at eight sites, where underwater mass depositions of sediments very likely occurred. Moreover, the interruptions (burial or severing) of communication cables laid on the sea floor between Milazzo and Lipari, Gazzi and Gallico, and Malta and Zante, are attributed to underwater landslides or turbidity currents (Ryan and Hezen 1965).

Inland, the landslides are distributed on different lithologies and many of them are reactivations of pre-existing slope movements. We differentiated them into two main categories, on the basis of the competence of the affected lithology: slope movement in rock (coherent and stiff lithology) and slope movement in soil (sand, clay and loose material in general). The lithologies were obtained from the Calabrian and Sicilian sheets of the Geological map of Italy at the scales 1:50,000 and 1:100,000 (http://www.isprambiente.gov.it/site/en-GB/Cartography/Geological_and_geothematic_maps/default.html). Figures 3 and 4 show the location of all the slope movements, 59 were in rock, 80 in soil and 11 underwater, probably in loose sediments.

Unfortunately, most of the descriptions do not allow recognition of the type of slope movement. In addition there are few cases well documented and also photographed by the contemporary authors. In many sites between Bagnara and Favazzina, altered gneiss slid down along the steep slopes, interrupting the railway line (Figs. 5 and 6). At Cannitello a considerable landslide was photographed by Mercalli, as well as the rock fall that damaged the small village of Orti Superiore, near Reggio Calabria (Fig. 7). Also a rockslide occurred and was photographed (Fig. 8) on the mule track between Cataforio and S. Salvatore (East of Reggio Calabria): it killed three muleteers with their animals (Taramelli 1909).

The Coseismic Effects in Messina

We collected many accounts (123) of environmental effects in Messina: ground cracks, ground lowering, slope movements, tsunami waves (that in this area reached 3 m of run-up), etc. (Fig. 9). The wharf area was severely damaged and a large part of it collapsed, because of the combined action of seismic shaking and tsunami.

Moreover, several reporters described a generalised ground movement toward the sea. In fact, the recent loose alluvial deposits forming the coastal area as well as the sands and gravels constituting the Pleistocene terraces could have been affected by slope movements toward the sea, triggered by the earthquake. Therefore, many of the described effects (ground cracks, ground settlements, ground uplifts, ground deformations, etc.) could be interpreted as a consequence of slope movements involving a large part of the Messina seacoast. Tectonic slip along the faults bordering the coastal area might have also contributed to coastal subsidence (Franchi 1909).

Landslides Area Versus Magnitude

The area affected by landslides (ca. 20,000 km^2) was determined by drawing a polygon around the mapped landslide localities. If we plot this value in the graph drawn by Keefer (1984), which relates the area affected by landslides with earthquake magnitudes (Fig. 10), the resulting magnitude matches exactly the one estimated for the 1908 earthquake. Therefore, the area distribution of the collected accounts of landslides is in good agreement with the Keefer's database.

Moreover, the distance (216 km) of the farthest landslide (in south-western Sicily) from the 1908 epicentre results in good agreement with the plot of Keefer (1984) of maximum distance of landslides from epicentre versus magnitude (Fig. 11). Because we do not know if the farthest landslide

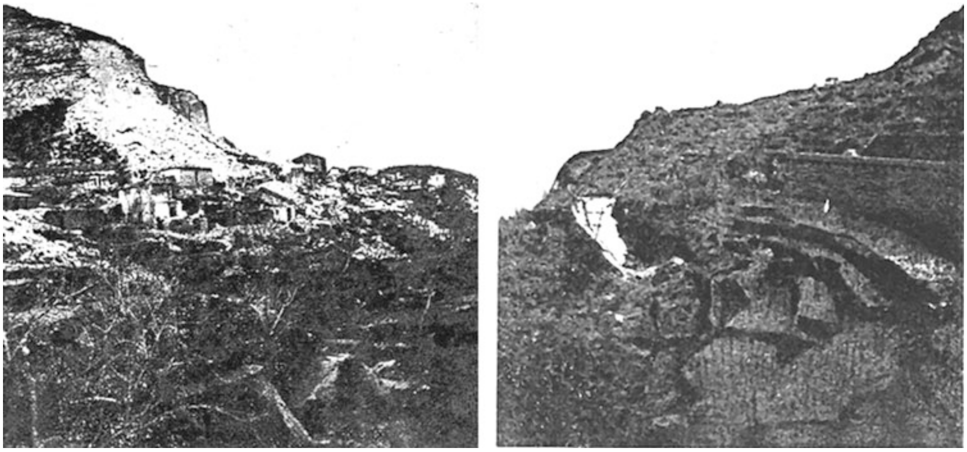

Fig. 7 (*left*) The village of Ortì Superiore damaged by a rockfall; (*right*) A considerable landslide disrupted the road between Scilla and Cannitello (These photographs were taken by Mercalli in April 1909 (Mercalli 1909))

Fig. 8 The rock fall on the mule track between Cataforio and S. Salvatore (East of Reggio Calabria), that killed three muleteers (Taramelli 1909)

was a disrupted fall or slide, or a coherent slide, the magnitude value in Fig. 11 is bracketed between 7 and 7.2, which is consistent with the uncertainty affecting the estimation of the magnitude of the 1908 earthquake.

The distribution of slope movements, as commonly observed (Esposito et al. this volume), rarefies moving outward from the epicentre. The area significantly affected has a radius of ca. 40 km: 129 out of the 150 collected events (86 %) fall within this distance. This spatial distribution is consistent with a crustal seismic event such as the 1908 event; in fact, for deeper earthquakes, with focal depths ≥ 30 km, generally landslides extend over much larger areas (Keefer 1984).

Discussion and Conclusions

Despite the fact that a large portion of the mesoseismal area falls at sea, the areal distribution of the 1908 induced landslides scales well (see also Esposito et al. 2011, in this volume) with the areal distribution of landslides triggered by other seismic events along the Apennines (e.g. 1980, 1997, 2009) and can be used as a diagnostic element for intensity assessment by means of the ESI scale (Michetti et al. 2007). The envelop of all the compiled seismically induced landslides gives a total area of at least 20,000 km^2, corresponding to intensity XI (ESI), in agreement with the MCS estimated maximum intensity (Guidoboni et al. 2007).

Secondary effects induced by earthquakes can highly contribute to increase the seismic damage, e.g., by direct impact on buildings or interrupting/threatening crucial lifelines, consequently, they have to be considered in order to define a realistic seismic hazard scenario. The picture here presented of the landslide distribution caused by the 1908 earthquake offers a valid tool to estimate the potential impact of a 1908-like event on the Straits area, which is already prone to slope instability even without seismic triggering, and has seen an unconcerned broad urban and infrastructural development in the last decades.

The detailed knowledge of the environmental effects occurred in 1908 e.g. at Messina (where damages were described carefully) offers the possibility to (1) carry out appropriate surveys targeted to test the susceptibility of the territory to the same phenomena (landslides, liquefaction, inundation, etc.); and (2) improve our preparedness to face the land changes that a strong seismic event commonly produces.

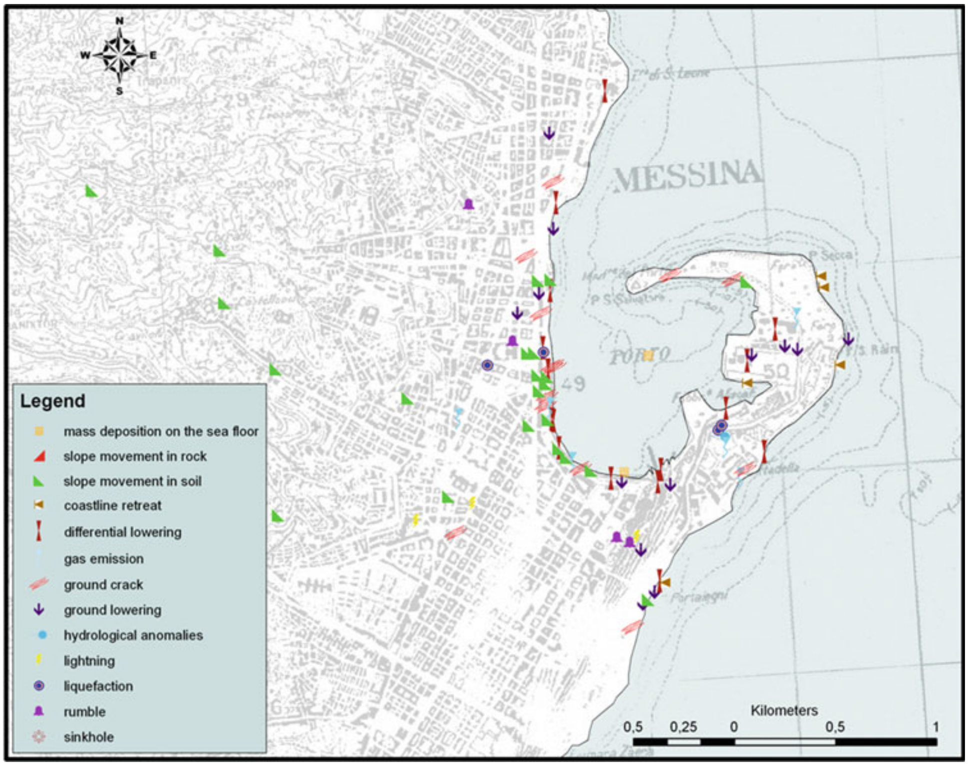

Fig. 9 The environmental effects occurred in Messina. Many of them are related to slope movements that involved a large part of the town's seacoast

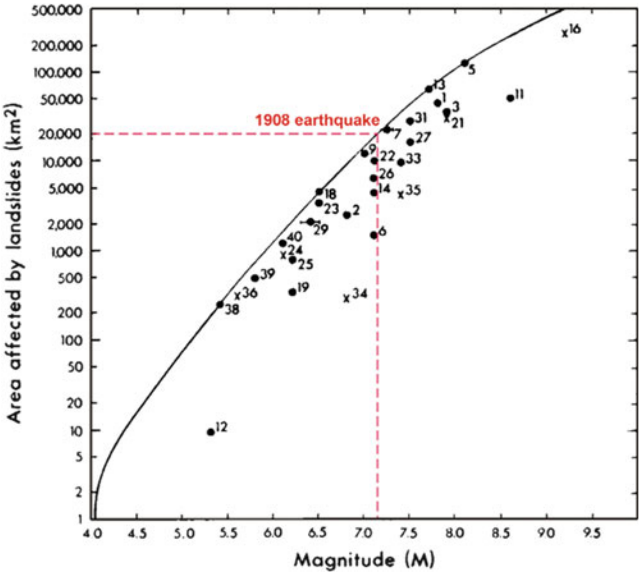

Fig. 10 Area affected by landslides versus earthquake magnitude (After Keefer 1984), with the plot of the 1908 affected area

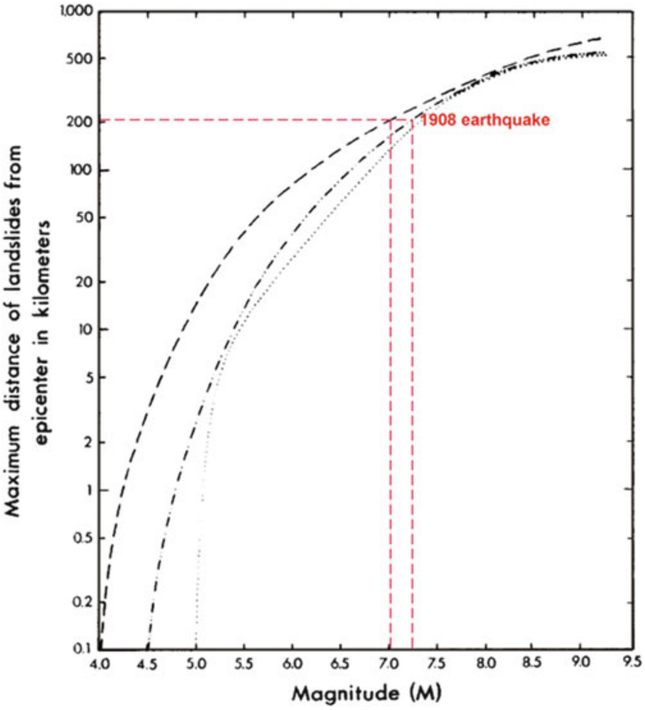

Fig. 11 Maximum distance from epicentre of landslides versus earthquake magnitude (After Keefer 1984), with the plot of the 1908 landslide farthest from the epicentre. *Dashed line* is the upper boundary for disrupted falls and slides, *dash-double-dot line* is the upper boundary for coherent slides

References

Baratta M (1909) Alcuni risultati ottenuti dallo studio del terremoto calabro-messinese del 28 dicembre 1908. Relazione preliminare. Boll. Soc. Geogr. Ital., Roma. Serie IV, X: 1218–1224

Baratta M (1910) La catastrofe sismica calabro-messinese. 28 Dicembre 1908. Societa' Geografica Italiana, Roma. 2 vols, 426p

Boschi E, Ferrari G, Gasperini P, Guidoboni E, Smriglio G, Valensise G (1995) Catalogo dei Forti Terremoti in Italia dal 461 a.C. al 1980, ING, SGA Bologna, 973p

Cortese E (1923) Sulle rive dello Stretto di Messina. Boll della Società Geologica Ital 42:226–234

Gruppo di lavoro CPTI (2004) Catalogo Parametrico dei Terremoti Italiani, versione 2004 (CPTI04), INGV, Bologna. http://emidius.mi.ingv.it/CPTI04/

Crema C (1909) Riunione annuale della Società Geologica Italiana in Sicilia. Bollettino del Regio Comitato Geologico d'Italia, series IV. 40: 346–354

Crema C (1921) Le frane di Girifalco (Catanzaro). Bollettino del Regio Comitato Geologico d'Italia 48(5):1–10

Di Stefano G (1909) Osservazioni sulle comunicazioni verbali del Prof. Ricciardi. Resoconto dell'Adunanza Generale invernale (Rendiconti). Bollettino della Società Geologica Italiana 28: XXX–XXXIV

Esposito E, Guerrieri L, Porfido S, Vittori E, Blumetti AM, Comerci V, Michetti AM, Serva L (2011) Landslides induced by historical and recent earthquakes in Central – Southern Apennines (Italy): a tool for intensity assessment and seismic hazard. The Second World Landslide Forum, Roma, 3–9 Oct 2011

Franchi S (1909) Il terremoto del 28 dicembre 1908 a Messina in rapporto alla natura del terreno ed alla riedificazione della città. Boll. R. Comitato Geologico, Roma, Serie IV. X:111–157

Galli I (1910) Raccolta e classificazione di fenomeni luminosi osservati nei terremoti. Bollettino della Società Sismologica Italiana. XIV:221–448

Gor'kij M, Meyer MW (1909) Zemletrjasenie v Kalabrii i Sicilii 12/28 Dekabrja 1908. Znanie, Sankt Peterburg

Guidoboni E, Mariotti D (2008) Il terremoto e il maremoto del 1908: effetti e parametri sismici. Bertolaso G, Boschi E, Guidoboni E, Valensise G (eds) Il terremoto e il maremoto del 28 dicembre 1908: analisi sismologica, impatto, prospettive, INGV-DPC. pp 17–136

Guidoboni E, Ferrari G, Mariotti D, Comastri A, Tarabusi G, Valensise G (2007) CFTI4Med. Catalogue of Strong Earthquakes in Italy 461 B.C. – 1997 and Mediterranean Area 760 B.C. – 1500. An Advanced Laboratory of Historical Seismology. http://storing.ingv.it/cfti4med/ Accessed July 2011

Keefer DK (1984) Landslides caused by earthquakes. Geol Soc Am Bull 95:406–421

Luiggi L (1909) Quel che ho veduto all'alba del terremoto calabro-siculo del 1908. Nuova Antologia di Lettere, Scienze e Arti, series 5. 141 (maggio-giugno): 297–317

Martinelli G (1909) Osservazioni preliminari sul terremoto calabro-messinese del mattino del 28 dicembre 1908. Boll. Bimensuale della Soc. Meteor. Ital., Torino, Serie III. XXVIII

Marzolo P (1909) Relazione sui risultati degli scandagli eseguiti nello Stretto di Messina da alcune R. Navi e Torpediniere nel primo trimestre 1909. In: Blaserna P (ed), Relazione della Commissione Reale incaricata di designare le zone più adatte per la ricostruzione degli abitati colpiti dal terremoto del 28 dicembre 1908 o da altri precedenti. Tipografia della R. Accademia dei Lincei, Roma

Mercalli G (1909) Contributo allo studio del terremoto calabro-messinese del 28 dicembre 1908. Reale Istituto d'Incoraggiamento di Napoli. Cooperativa Tipografica, Napoli

Michetti AM, Esposito E, Guerrieri L, Porfido S, Serva L, Tatevossian R, Vittori E, Audemard F, Azuma T, Clague J, Comerci V, Gurpinar A, Mc Calpin J, Mohammadioun B, Morner NA, Ota Y, Roghozin E (2007) Intensity Scale ESI 2007. Memorie Descrittive Carta Geologica d'Italia. Guerrieri L and Vittori E (eds) APAT, Servizio Geologico d'Italia, Roma. 74, 53p

Novarese V (1909) Il terremoto del 28 dicembre in Reggio Calabria e provincia. Boll. Regio Comitato Geologico d'Italia, Roma. 4: 424–496

Occhiuto B (1909) Effetti della scossa principale. Bollettino Sismologico dell'Osservatorio Morabito nel seminario di Mileto (Calabria). Anno I, num. 11 e 12. Supplemento al Bollettino di Decembre 1908

Oddone E (1909) Appunti fisici per lo studio del terremoto di Sicilia e Calabria. Annali della Soc. degli Ing. ed Arch. Ital., fasc. VII. Roma

Oldham R D (1909) The Italian earthquake of December 28, 1908. Geographical Journal, 8, issue 2

Omori F (1909) Preliminary report on the Messina-Reggio earthquake of Dec. 28, 1908. Bull Imp Earth Invest Comm 3(2):37–46

Pino NA, Giardini D, Boschi E (2000) The December 28, 1908, Messina Straits, southern Italy, earthquake: Waveform modelling of regional seismograms. J Geoph Res 105:25473–25492

Platania G (1909) Il maremoto dello Stretto di Messina del 28 dicembre 1908. Bollettino Società Sismologica Italiana, Modena. 13

Ricciardi L (1909) Il vulcanismo nel terremoto calabro-siculo del 28 dicembre 1908. Bollettino della Società dei Naturalisti in Napoli 23:65–120

Ricciardi L (1910) Su le Relazioni delle Reali Accademie di Scienze di Napoli e dei Lincei di Roma sui terremoti calabro-siculi del 1783 e 1908. Bollettino della Società dei Naturalisti in Napoli 24:23–75

Riccò A (1909) Terremoto del Messinese e della Calabria al 28 Dicembre 1908. Boll. Accad. Gioenia di Sc. Nat., Catania. Serie II, fasc. VI

Rizzo GB (1909) Relazione sul terremoto di Messina e della Calabria nel 28 dicembre 1908. Blaserna P (ed), Relazione della Commissione Reale incaricata di designare le zone più adatte per la ricostruzione degli abitati colpiti dal terremoto del 28 dicembre 1908 o da altri precedenti. Tipografia della R. Accademia dei Lincei, Roma

Ryan WBF, Hezen BC (1965) Ionian sea submarine canyons and the 1908 Messina turbidity current. Geol Soc Am Bull 76:915–932

Sabatini V (1909) Contribuzione allo studio dei terremoti calabresi. Boll. del R. Comitato Geologico d'Italia. Serie IV. X, fasc. 3

Società Fotografica Italiana (1909) Messina e Reggio prima e dopo il terremoto del 28 dicembre 1908. Firenze

Taramelli T (1909) Relazione sull'operato della sottocommissione incaricata di visitare i luoghi del terremoto Calabro-Siculo del 28 dicembre 1908. In: Blaserna (ed) Relazione della Commissione Reale incaricata di designare le zone più adatte per la ricostruzione degli abitati colpiti dal terremoto del 28 dicembre 1908 o da altri precedenti. Tipografia della R. Accademia dei Lincei, Roma, pp 89–112

Earthquake Damage Zone GIS Modelling: A Modulation Between Co-Seismic Deformation and Landslide Susceptibility

Jian Guo Liu, Philippa J. Mason, Eric Yu, Meng-Che Wu,
Tang Chuan, Huang Runqiu, and Liu Hanhu

Abstract

In mountainous regions, earthquake events are typical of naturally-occurring multiple hazards and are frequently the trigger for cascade effects which range from the destruction of the initial shock, to extensive and complex slope failures in the immediate, short and very long-term. The conventional seismic intensity zonation method cannot adequately characterise both the current damage level and long-term geohazards, while detailed information is critical in guiding post-disaster mitigation and regional development. In studying the most severely damaged Beichuan area by the Mw7.9 Wenchuan earthquake, we proceeded with a qualitative numerical method for earthquake damage zone mapping which is novel in its integration of the multi-variable GIS modelling of geohazard susceptibility with co-seismic deformation via a modulation. This new model, we call it *earthquake damage*, characterise not only the destruction immediately after an earthquake but also the potential for future damage as the consequences of the earthquake.

Keywords

Earth quake damage zone • Landslide • GIS modelling • Satellite remote sensing • DEM • DInSAR

Introduction

A devastating Mw 7.9 earthquake occurred on 12th May 2008 in Wenchuan County near the western edge of the Chengdu basin in Sichuan Province, China. This caused tremendous ground damage and loss of human life, and a total economic loss of over 110 billion USD (Xie et al. 2009). These effects were induced both by direct earthquake shaking and by large earthquake-triggered geohazards. The most common forms of the earthquake induced geohazards in the region are landslides and mudflows (Chigira et al. 2010; Dai et al. 2011) which account for 15 % of deaths (Wang et al. 2009). The Beichuan county town is a typical example. It is situated in the main rupture zone along the Yingxiu-Beichuan fault (Cui et al. 2011), and in a deeply incised valley surrounded by very steep mountainous slopes. The town was completely destroyed by the strong earthquake and the ensuing massive landslides which involved entire mountain slope collapse.

Seismic intensity is widely used to assess damage levels induced by an earthquake. Unlike the earthquake magnitude scales, which express the seismic energy released by an earthquake, seismic intensity denotes how severely an earthquake affects a specific place. The China Seismic Intensity Scale (CSIS) is a national standard and is called '*Liedu*' in Chinese. Established by China Earthquake Administration (CEA) in 1980, Liedu is similar to European Macroseismic Scale 1998 (Grünthal 1998) that categories seismic impacts into 12 degrees of intensity (Chen et al. 1999). Seismic intensity is largely descriptive of either predicted or occurred end results of destruction but lack any direct link to the actual various factors that cause the destruction. The Wenchuan

---

J.G. Liu (✉) • P.J. Mason • E. Yu • M.-C. Wu
Department of Earth Science and Engineering, Imperial College London, London SW7 2AZ, UK
e-mail: j.g.liu@imperial.ac.uk

T. Chuan • H. Runqiu • L. Hanhu
State Key Laboratory of Geohazard Prevention, Chengdu University of Technology, Chengdu, Sichuan 610059, China

C. Margottini et al. (eds.), *Landslide Science and Practice*, Vol. 5,
DOI 10.1007/978-3-642-31427-8_35, © Springer-Verlag Berlin Heidelberg 2013

Fig. 1 The location of the Wenchuan earthquake and the major aftershocks along the Longmenshan fault zone. The study area is indicted by the *red box* (Adapted from Ouimet (2010) and Xu et al. (2009))

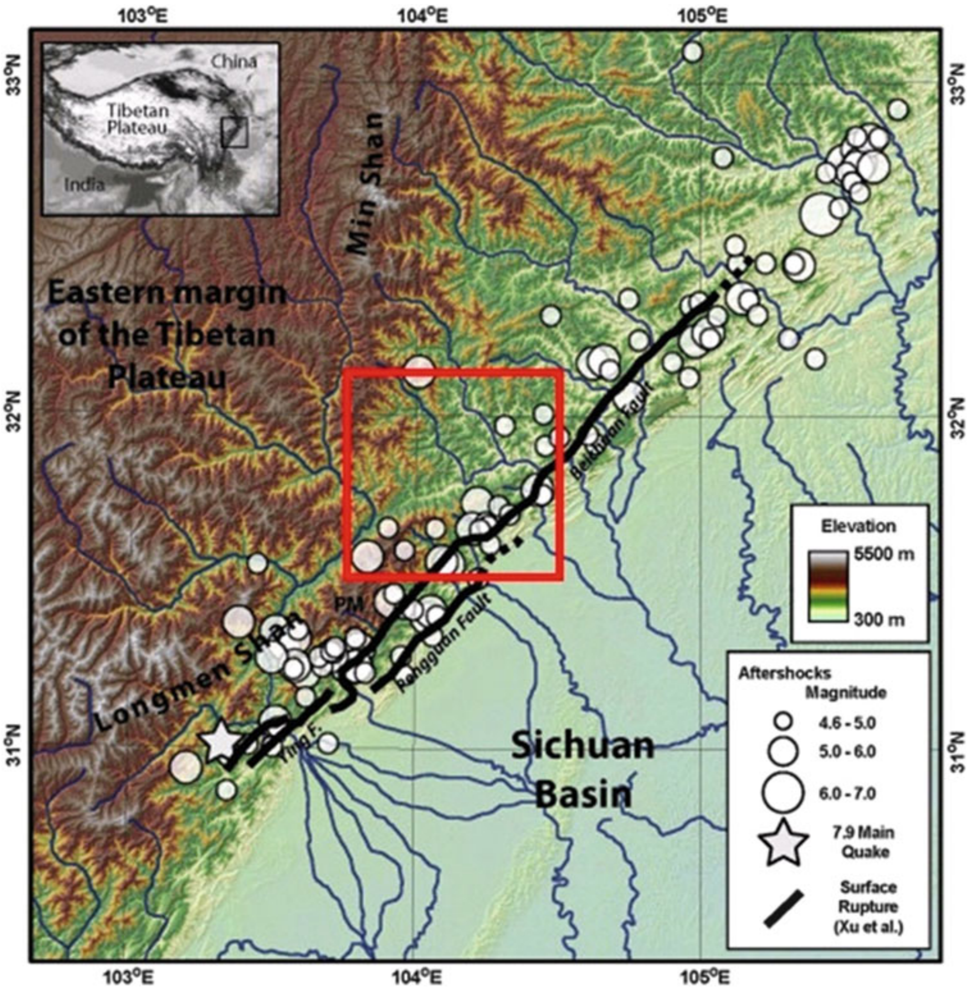

earthquake region was largely categorised as VI ~ VIII Liedu before and then up scaled to VIII ~ XI after the earthquake this matches our field observations in Beichuan county town. However the particular devastation in Beichuan town was a combined result of destructive shake and massive landslides triggered by the earthquake. Our field investigations have shown that many areas along the Yingxiu-Beichuan fault were subject to the same level of earthquake shock but experienced far less significant damage because their locations were not independently prone to geohazards. For effective hazard management and prevention of earthquake-induced damages, the lesson to be learnt is that the seismic intensity zonation system should be enhanced to be able to characterise localised variation of damage level that an earthquake may produce.

In this paper we present a study of the GIS based modelling of earthquake damage zones, using the Beichuan area of the Wenchuan earthquake zone as an example (Fig. 1). The novel idea shown here is the combination of earthquake deformation, as derived from differential interferometric SAR (DInSAR) data, with environmental factors (such as slope, lithology, drainage and fracturing) derived from broad-band multi-spectral satellite imagery and DEM data. While the DInSAR data derived from cross-event ALOS (Advanced Land Observation Satellite) PALSAR (Phased Array type L-band Synthetic Aperture Radar) image pairs provide broad-scale co-seismic deformation zones relating to seismic intensity, far more detailed damage levels within each deformation zone can be mapped using local environmental factors via a multi-criteria GIS model. By incorporating measurable variables of co-seismic deformation and environmental factors, within a GIS model, the resultant map characterises not only the destruction immediately after an earthquake but also the future potential of damage caused by an earthquake; this result no longer represents a conventional measure of seismic intensity, and we thus call it *earthquake damage*.

The Models

Many studies, as well as our own field investigations, indicate mass wasting (mainly landslides and debris-flows) are the dominant but not exclusive forms of geohazard in the region triggered by the Wenchuan earthquake (Chigira et al. 2010; Dai et al. 2011; Tang et al. 2009). In this paper we use the word 'geohazard' as a general term to denote all forms of catastrophic slope failure, to emphasize the hazard aspect of this otherwise nature process of surface geology.

The GIS-based modelling of susceptibility to geohazards and the modelling of current damage levels are two separate but closely linked issues. Given various environmental conditions relating to geohazards, an earthquake will intensify the overall susceptibility to those geohazards. We therefore consider that the GIS modelling of susceptibility to earthquake related geohazards is a conventional geohazard susceptibility model modulated by seismicity, hence:

$$E_{\mathrm{gh}} = G \times S \tag{1}$$

Here E_{gh} represents the earthquake related geohazard susceptibility, G and S are the geohazard susceptibility model and seismicity respectively. The modulation relationship between G and S represents the fact that the two co-exist all the time and intensify each other.

The *earthquake damage* zonation model should consider both geohazards already induced by the earthquake and any future geohazard potential, defined by (1), and is therefore given as:

$$E_{\mathrm{dz}} = H \times E_{\mathrm{gh}} = H \times G \times S \tag{2}$$

Here E_{dz} is the earthquake damage zonation and H mapped geohazard induced specifically by the earthquake. A map produced using (2) not only reflects the current status of earthquake damage but also indicates the future damage potential.

The choice of geological/topographical variables relating to slope instability geohazards and their relative importance are decided on the basis of field observations and in reference to our previous work (Liu et al. 2004; Fourniadis et al. 2007). Accordingly, the most important variables chosen are rock competence (Rc), slope (Sp), drainage (Dr) and faults/fractures (Ff). We thus propose a geohazard susceptibility model based on four variables:

$$G = Rc \times Sp + Dr + Ff \tag{3}$$

This formula involves both intra-variable modulation (multiplication) and linear combination (summation). The multiplication is used to modulate the key variables, slope angle with rock competence. The relationship between these two is a modulation because any slope must be composed of a lithology. This ensures a representative lithology/slope classification but does not duplicate their effects. For instance, the same slope angle is regarded significantly less stable in soft rock with a competence rank of 3, than in a hard rock with a competence rank of 1, in case of debris-flows. Secondly, drainage and faults/fractures often overlap, especially when river channels follow weak deformation zones but they do not necessarily coexist or interact with one another. Their contributions to geohazard susceptibility can also be quite different; whilst faults and fractures provide planar discontinuities on which rock-slides may develop, drainage channels often form the confining pathways for debris-flows. We therefore consider Dr and Ff as individual 'add-on' variables in linear combination with the rock competence modulated slopes. However, to minimise the duplication effect of Dr and Ff when they do coexist and to reflect different relationships between rock competence and drainage channels and fault/fracture, Dr and Ff are assigned quite different ranks for rock-slides and debris-flows, as shown later, to characterise the different effects when these two variables interact with rock competence.

Replacing (3) in (1) and (2), we have

$$E_{\mathrm{gh}} = S \times (Rc \times Sp + Dr + Ff) \tag{4}$$

$$E_{\mathrm{dz}} = S \times (Rc \times Sp + Dr + Ff) \times H \tag{5}$$

There are no weights specified for any of the additive items in the above formulae. As a numerical qualitative (not quantitative) modelling process, each variable is assigned a sequence of ranks, the range of which determines the relative contribution of the variable to the model and so effectively acts as a weighting scheme.

The major types of geohazards, rock-slides and debris-flows, have different mechanical characteristics, and so the environmental variables influencing the model will be different for each type; for instance, debris-flows often occur in rocks of low competence, and/or in unconsolidated sediments, whilst rock-slides are more likely to happen in competent lithologies which are well bedded and fractured (especially if the fractures were caused or reactivated by earthquake shock). The two types of geohazard are therefore modelled separately, using the same input variables, but with different ranking schemes. Since the relationship between the two types is one of coexistence but not overlap and is accumulative, the final earthquake related geohazard susceptibility map is a weighted linear combination of the likelihoods of rock-slide and debris-flow occurrence. Field evidences strongly indicates that rock-slides are the more frequent geohazards triggered by the earthquake; they are of massive scale and extent. Debris-flows tend to be of a much smaller extent than rock-slides but they are very widely spread. To reflect this basic observation, the weighting for rock-slides (E_{ghr}) is empirically assigned twice that of debris-flows (E_{ghd})

$$E_{\mathrm{gh}} = 2E_{\mathrm{ghr}} + E_{\mathrm{ghd}} \tag{6}$$

Table 1 Datasets used in this study, the dates they were acquired and their sources (Courtesy to all data sources)

Satellites	Sensor/data types	Imaging dates		Data source
		Before	After	
ALOS	AVNIR-2: 4 VNIR bands (B, G, R, NIR), 10 m resolution.	31/03/07	04/06/08	JAXA
	PALSAR: L-band (23 cm wavelength). SLC, 5 m pixel size	05/03–17/02/08	05/06–19/05/08	
Landsat-5	TM: 6 VNIR & SWIR bands, 30 m resolution and 1 thermal band, 120 m resolution.	p129r3801/05/1988 p130r3826/06/1994		GLCF, NASA/University of Maryland
Terra-1	ASTER GDEM: 30 m resolution Global DEM	Multiple		NASA/JPL

The model described here cannot include all conceivable factors influencing geohazard susceptibility. Instead our idea is to keep the model simple, and therefore appropriate for regional assessment, using the most significant factors derivable from satellite remote sensing data and conducted independently of detailed field investigation that is often logistically difficult and/or restricted. As a result, important variables which are heavily dependent on field work, such as the relationship between slope azimuth (aspect) and the dip-direction of sedimentary rock formations, must be omitted.

Derivation of Input Variables

Imagery and DEM Data

Source data for this study are from JAXA's ALOS, Landsat TM (Thematic Mapper) and ASTER (Advanced Spaceborne Thermal Emission and Reflection Radiometer) Global DEM as listed in Table 1. For the GIS modelling, all the chosen variables are derived from satellite imagery data and DEM as raster layers.

Rock Competence

Lithology has a background control on geohazard susceptibility. The mechanical properties of rocks are far more influential here than any specific rock type. The rock competence mapping is largely based on TM image interpretation in reference to field observation and publications (e.g. Dai et al. 2011). The study area is mapped into four classes of rock competence. High competence: thick layers of limestone, sandstone and metamorphic rocks. High-medium competence: folded, inter-bedded limestone and sandstone. Medium-low competence: highly fractured and weathered rocks. Low competence: Tertiary sandstone and unconsolidated Quaternary sediments

Rock competence has varying influence on different types of geohazards and causes rocks to respond differently to earthquake shock. In general, rock-slides tend to be more common in lithologies of above medium competency, where failures occur along bedding planes and fractures. Conversely, slopes composed of low competence materials are more prone to debris-flows. Rock competence is therefore ranked differently for these two types, as shown Table 2.

Table 2 Rank values for rock-slides and debris-flows in each rock competence class

Rock competence	Ranking	
	Rock-slide	Debris-flow
Low	0	3
Low-medium	1	2
High-medium	3	1
High	2	0

Table 3 Rank values for slope angle classes

Slope Angle (deg)	Ranking
0–10	0
11–30	1.5
31–40	3
>40	4.5

Slope

Slope is the single most important variable controlling the mass wasting process. As the gradient of elevation, a slope layer can be easily derived from a DEM, using a 3 × 3 slope angle kernel, based on the formula:

$$\theta = \tan^{-1}\sqrt{(\partial z/\partial x)^2 + (\partial z/\partial y)^2} \tag{7}$$

Here z is elevation at position (x,y) in the DEM data.

An image of slope angles of the study area was generated from the ASTER GDEM. It was then divided into four classes by thresholding based on natural breaks in the distribution of the slope image histogram. To reflect its relative importance, slope is given a rank range of 0–4.5 with an increment of 1.5 based on empirical assessment of the modelling results (Table 3).

Proximity to Drainage

Proximity to drainage has an indirect influence on slope instability since river undercutting at the toes of slopes is a

Table 4 Rank values for rock-slides and debris-flows in each drainage buffer zone

Drainage order	Buffer width (m)	Ranking	
		Rock slide	Debris flow
None	–	0	0
3	100	0.5	1
4–5	200	1	2
6–7	400	1.5	3
8–9	800	2	4

common trigger of debris-flows. Here the area affected by fluvial erosion is decided by the magnitude of the river channels and water flow capacity which is in turn controlled by rainfall intensity. Considering the average annual precipitation in the region (~800–900 mm) and the highest recorded rainfall in a 24-h period (*ca* 334.7 mm), we generated a drainage network buffer map from the GDEM with varying buffer widths corresponding to four stream-order levels which are given different rank values for rock-slide and debris-flow as listed in Table 4.

Fracture Density

In the context of seismically triggered geohazards, the proximity of a fault is highly relevant. Field evidence indicates that faults/fractures have direct impact on surface damage.

The TM image was used for visual interpretation of structural lineaments, with maps in relevant publications (Chen and Wilson 1996; Lin et al. 2009; Xu et al. 2009) used as reference to produce a lineament map. Uncertainty and subjectivity are unavoidable in mapping faults and fractures either from images or from field observation. Coupled with the concept that faults and fractures may deform and destabilize a much wider region than the immediate area of fault displacement, it was deemed more relevant to consider the density of fracturing rather than the positions of each fracture. A fracture density map was then generated in several steps. First the lineament map was encoded such that structural lineaments of different magnitude were assigned a series of weights, as defined in Table 5.

Table 5 Structural lineament weights

Lineament magnitude	Weights
Regional	4
Major	3
Sub-major	2
Local	1

Density (D) is calculated as a value representing the total lineament length of each rank within a circular search radius of 3 km, multiplied by the weight value for each rank, and divided by the area of the search radius:

$$D = \sum_{n} wL/A_{\mathrm{SR}} \tag{8}$$

Where L represents feature length, w the weight, and A_{SR} the area of the search radius. The resultant density values are in the range of 0–3.2 (km/km^2). Finally, the fracture density map was simplified into four broad density levels based on its histogram (Table 6).

Table 6 Fracture density ranking

Fracture density	Ranking	
	Rock-slide	Debris-flow
None	0	0
Low	1	0.5
Medium	2	1
High	3	1.5
Very high	4	2

Co-Seismic Deformation

The strong tremors of the Mw 7.9 Wenchuan earthquake weakened the entire body of the mountain belt along the Longmenshan fault zone. New faults and fractures, as well as those reactivated by the earthquake, have destabilised many otherwise stable slopes making the whole region more vulnerable to geohazards than ever before, and for many years to come. The impact upon a model of the susceptibility to earthquake related geohazards can be considered directly proportional to the co-seismic deformation as a modulation to the geohazard susceptibility without the earthquake. The JAXA’s ALOS provided speedy coverage of PALSAR data in a short period after the main shock and then released cross event interferometric PALSAR data that in combination with ASTER GDEM have enabled us to generate differential SAR interferograms of the region. The DInSAR data have been widely used for investigation of co-seismic deformation along the Longmenshan fault zone but rather little for studying earthquake induced geohazards. As shown in Fig. 2a, the co-seismic deformation is mapped by 2π wrapped interferometric fringe patterns. Each fringe represents a ground displacement of a half wavelength of the L-band PALSAR (118 mm) in the SAR look direction. In the central part of the seismic fault zone within near vicinity of earthquake raptures, the deformation is so great and chaotic that the cross-event SAR signals have lost coherence, leaving no clear fringe patterns to quantify the deformation. The unwrapped interferogram in Fig. 2b presents the magnitude of the deformation only in the areas with adequate coherence.

The density of fringes in the interferogram corresponds to the gradient of the unwrapped interferogram or the

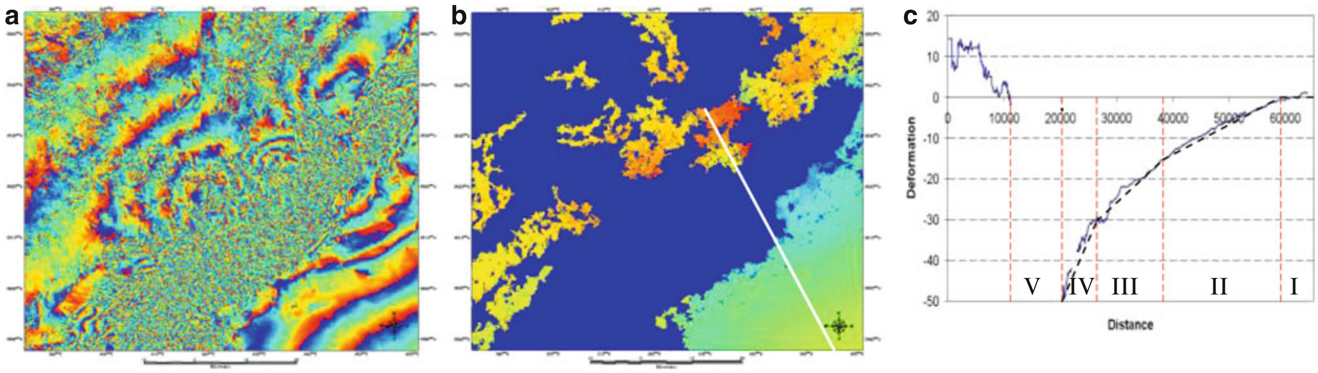

Fig. 2 (**a**) ALOS PAL SAR differential interferogram of the study area; (**b**) Unwrapped differential interferogram; and (**c**) Deformation profiles (in metres) plotted from the unwrapped interferogram along the white line in (**b**)

Fig. 3 Co-seismic deformation zones and mapped earthqauke induced geohazards

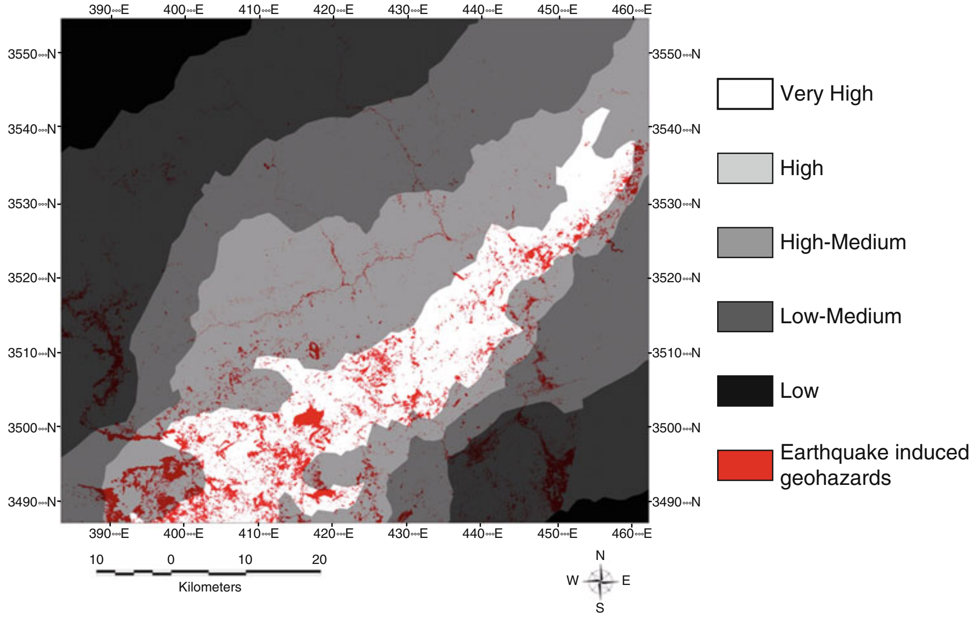

deformation gradient that is considered a more effective measurement relating to seismic intensity than the deformation magnitude. The unwrapped interferogram is too noisy to reliably calculate pixel-wise gradient but for the earthquake damage modelling presented here, simply quantified zones of different deformation levels are adequate. This zonal definition is achieved by plotting deformation profiles from the unwrapped interferogram, perpendicular to the fault zone and then locating sections of different deformation gradient. As illustrated in Fig. 2c, where the vertical red dashed lines define different co-seismic deformation zones I-V, from low to very high, on the foot-wall of the Yingxiu-Beichuan fault zone, and the oblique black dashed lines indicate the average deformation slope in each zone, except zone V, where deformation is not measurable because of decoherence. Obviously, the deformation slope increases step by step and becomes progressively more significant from low to high deformation zones.

Table 7 Rank values for co-seismic deformation zones

Co-seismic deformation	Ranking
Low	1
Low-medium	2
High-medium	3
High	4
Very high	6

Using the deformation slopes as control, in combination with the observed fringe densities in the interferogram (Fig. 2a), a co-seismic deformation map with five deformation levels was generated (Fig. 3). The highest deformation level is assigned to the decoherence zone. Although the actual deformation is unknown in the decoherence zone, faintly detectable fringes can be observed. which are much denser than the sparse patterns outside the zone. This highest deformation class is therefore assigned two levels higher rank than the class immediately below it (Table 7).

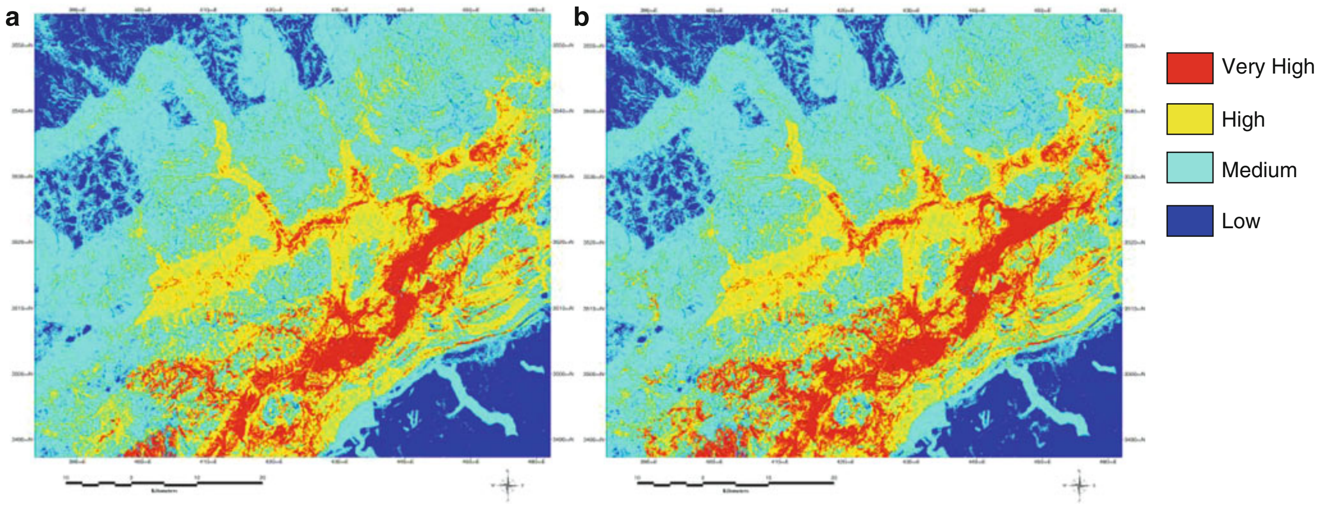

Fig. 4 (**a**) Susceptibility map of earthquake related geohazards. (**b**) Map of earthquake damage zones

Mapping the Earthquake Induced Geohazards

In this heavily vegetated region, the earthquake induced landslide geohazards are typically characterised by broken ground which is stripped of vegetation, in the AVNIR-2 images taken shortly after the earthquake and therefore can be quite accurately mapped using Normalised Differential Vegetation Index (NDVI). We used an Inverse NDVI (INDVI) with a threshold (T):

$$INDVI_{ALOS} = (B3 - B4)/(B3 + B4) > T \tag{9}$$

Here $B3$ and $B4$ represent AVNIR-2 band 3 (Red) and band 4 (NIR).

Because of the cloudy and rainy weather conditions during the period immediately after the Wenchuan earthquake, the AVNIR-2 image is degraded by haze and partially covered by clouds. Thresholds decided based on spectral analysis were then applied to eliminated clouds and cloud shadows and formula (9) is then modified as:

If B1 > 220 then NULL else If B4 < 25 then NULL else
If (B3-B4)/(B3 + B4) > 0.2 then (B3-B4)/(B3 + B4)
else NULL

The mapped geohazards (Fig. 3) are assigned a value of 2, with 1 representing the background when applied to the earthquake damage zone model defined by formula (5). As a modulation factor, the value 2 doubles the susceptibility scores of the pixels representing geohazards, whilst the value 1 keeps the scores of other, non-geohazard pixels unchanged in the final map of earthquake damage zones.

Earthquake Damage Zone Modelling

With all the input variables prepared, the earthquake damage zone modelling comprises two steps, as defined in formulae (4) and (5): (1) mapping the susceptibility of earthquake related geohazard and (2) final map of earthquake damage zones.

Susceptibility Mapping of Earthquake Related Geohazards

Applying all the variables, except the layer of mapped earthquake induced geohazards, with different variable rankings for rock-slides and debris–flows to formula (4), two susceptibility layers were derived. These were then combined using formula (6). The resulting layer was classified into four susceptibility levels based on the natural breaks points in the image histogram to finally produce the susceptibility map of the earthquake related geohazards (Fig. 4a). This map shows that the very high susceptibility class forms a belt along the Yingxiu-Beichuan fault zone and is coincident with the very high co-seismic deformation zone on the hanging wall of the seismic fault. The model defined by formula (4) imposes a strong effect of the co-seismic deformation on the result. High mountains characterised by competent rock formations, which would not otherwise be particularly susceptible to geohazards, become highly vulnerable during and after the earthquake. This agrees with reality.

Mapping the Earthquake Damage Zones

An earthquake damage zone map should present both the current damage caused by the earthquake, the seismic intensity, and the future potential damage from geohazards under the changed environmental conditions caused by a major earthquake. We therefore proposed to model earthquake damage zones by modulating the geohazard susceptibility with the mapped earthquake induced geohazards as defined in formula (5). The final map of earthquake damage zones is shown in Fig. 4b. Considering that this *earthquake damage* map is different from the earthquake related geohazard susceptibility map (Fig. 4a) only in areas of mapped geohazards, where the score is doubled, the same thresholds were applied to classify the earthquake damage into four levels: Low, Medium, High and Very High. This assures that the mapped geohazards in the areas of highest susceptibility level are saturated at the same level whereas those at lower susceptibility levels are raised to higher levels.

The two maps in Fig. 4 are very similar because most damage caused by the earthquake does indeed occur in the areas of very high susceptibility to earthquake related geohazards. The map of earthquake damage zones in Fig. 4b clearly illustrates that the very high damage zones form a belt along the Yingxiu-Beichuan fault zone and mainly on the hanging wall, which is subject to very high co-seismic deformation, and it is characterised by rock formations of medium-high and high competency. The destroyed Beichuan county town and most of the large landslides triggered by the Wenchuan earthquake are concentrated in this belt. Rock-sliding is the dominant failure mechanism.

In comparison with the new Liedu map of the region produced by the CEA after the earthquake, the four earthquake damage zones in Fig. 4b roughly correspond to Leidu VIII to XI from the western margin of the Chengdu Plain to the most intensively damaged zone along the Yingxiu-Beichuan fault. While the Liedu map is rather crude, the earthquake damage zone map in Fig. 4b details the spatial variations of earthquake damage zones, which can be used to guide regional and local management for recovery from the earthquake disaster.

Conclusions

In this paper, we have presented a multi-variable modelling procedure for the mapping of susceptibility to earthquake related geohazards and of earthquake damage zones, based on the case study of the Beichuan area where the most of the devastation and destruction was triggered by the Mw 7.9 Wenchuan earthquake event.

The proposed GIS model for earthquake damage zone mapping is novel in its combination of geohazard susceptibility factors with co-seismic deformation derived from DInSAR data. In developing this new model, we stepped further from the conventional descriptive approach of seismic intensity, aiming to characterise not only the destruction immediately after an earthquake but also the future potential for damage as a consequence of the earthquake. The result from such a GIS model no longer strictly refers to seismic intensity though highly relevant and we call it *earthquake damage*.

Our study indicates that under the circumstance of a strong earthquake, co-seismic deformation takes the first order regional control in causing earthquake induced geohazards and susceptibility to future geohazards, whilst other variables can be used effectively to categorise local hazard levels. The final map of earthquake damage zones fairly accurately reflects the ground reality and matches the geohazards inventory data. The four relative levels of earthquake damage zones correspond to the regional Liedu scale zones of VIII to XI, but with great local variation from the simple Liedu pattern. The importance of the map is not only to show what has already happened but also to indicate where geohazards are most likely to happen in future, as a long term impact of the Wenchuan earthquake in the Beichuan region.

References

Chen SF, Wilson CJL (1996) Emplacement of the Longmen Shan Thrust-Nappe belt along the eastern margin of the Tibetan plateau. J Struct Geol 18:413–430

Chen D, Shi Z, Xu Z, Gao G, Nian J, Xiao C, Feng Y (1999) “China seismic intensity scale” (in Chinese). http://www.csi.ac.cn/ymd/flfg/fd007.htm. Accessed 10 June 2011

Chigira M, Wu X, Inokuchi T, Wang G (2010) Landslides induced by the 2008 Wenchuan earthquake, Sichuan, China. Geomorphology 118:225–238

Cui P, Chen X, Zhu Y, Su F, Wei F, Han Y, Liu H, Zhuang J (2011) The Wenchuan Earthquake (May 12, 2008), Sichuan Province, China, and resulting geohazards. Nat Hazard 56:19–36

Dai FC, Xu C, Yao X, Xu L, Tu XB, Gong QM (2011) Spatial distribution of landslides triggered by the 2008 Mw 7.9 Wenchuan earthquake, China. J Asian Earth Sci 40:883–895

Fourniadis IG, Liu JG, Mason PJ (2007) Landslide hazard assessment in the Three Gorges area, China, using ASTER imagery: Wushan-Badong. Geomorphology 84(1–2):126–144

Grünthal G (ed) (1998). European Macroseismic Scale 1998 (EMS-98). Cahiers du Centre Européen de Géodynamique et de Séismologie 15, Centre Européen de Géodynamique et de Séismologie, Luxembourg, 99p

Lin AM, Ren ZK, Jia D, Wu XJ (2009) Co-seismic thrusting rupture and slip distribution produced by the 2008 M-w 7.9 Wenchuan earthquake, China. Tectonophysics 471:203–215

Liu JG, Mason PJ, Clerici N, Chen S, Davis A, Miao F, Deng H, Liang L (2004) Landslide hazard assessment in the three Gorges area of the Yangtze river using ASTER imagery: Zigui-Badong. Geomorphology 61:171–187

Ouimet WB (2010) Landslides associated with the May 12, 2008 Wenchuan earthquake: Implications for the erosion and tectonic evolution of the Longmen Shan. Tectonophysics 491:244–252

Tang C, Zhu J, Liang J (2009) Emergency assessment of seismic landslide susceptibility: a case study of the 2008 Wenchuan earthquake affected area. Earthq Eng Eng Vib 8:207–217

Wang FW, Cheng QG, Highland L, Miyajima M, Wang HB, YAN CG (2009) Preliminary investigation of some large landslides triggered by the 2008 Wenchuan earthquake, Sichuan Province, China. Landslides 6:47–54

Xie FR, Wang ZM, Du Y, Zhang XL (2009) Preliminary observations of the faulting and damage pattern of Mw 7.9 Wenchuan, China, earthquake. Prof Geol 46:3–6

Xu X, Wen X, Yu G, Chen G, Klinger Y, Hubbard J, Shaw J (2009) Coseismic reverse- and oblique-slip surface faulting generated by the 2008 Mw 7.9 Wenchuan earthquake, China. Geology 37:515–518

THE SECOND
WORLD
LANDSLIDE FORUM

Spatial Distribution of Landslide Dams Triggered by the 2008 Wenchuan Earthquake

Xuanmei Fan, Cees J. van Westen, Qiang Xu, Tolga Gorum, Fuchu Dai, Gonghui Wang, and Runqiu Huang

Abstract

Landslide dams are a common type of river disturbance in tectonically active mountain belts with narrow and steep valleys. Here we present an unprecedented inventory of 828 landslide dams triggered by the 2008 Wenchuan earthquake, China. Of the 828 landslide dams, 501 completely dammed the rivers, while the others only caused partial damming. The spatial distribution of landslide dams was similar to that of the total landslide distribution, with landslide dams being most abundant in the steep watersheds of the hanging wall of the Yingxiu-Beichuan Thrust Fault, and in the northeastern part of the strike-slip fault near Qingchuan. We analyzed the relation between landslide dam distribution and a series of seismic, topographic, geological, and hydrological factors.

Keywords

Landslide • Landslide dam • Wenchuan earthquake • Spatial distribution

Introduction

Landslide dams are a common type of river disturbance in tectonically active mountain belts with narrow and steep valleys (Costa and Schuster 1988; Chai et al. 1995; Hewitt 1998). Besides a number of landslide-dam inventories (Costa and Schuster 1988, 1991; Chai et al. 1995; Casagli and Ermini 1999; Korup 2004), there are also many case studies (e.g. Dunning et al. 2005; Harp and Crone 2006; Nash et al. 2008; Duman 2009; Schneider 2009). Most studies use a geomorphic approach to analyze the characteristics of the landslides, dams, rivers and impounded lakes (e.g. Ermini and Casagli 2003; Korup 2004; Dong et al. 2009). Research on landslide dams has been reviewed by Korup (2002). However, there is hardly any work specifically on earthquake-induced landslide dams (Adams 1981; Hancox et al. 1997), due to the scarcity of well-documented inventories.

The devastating Wenchuan earthquake (Mw 7.9) with a focal depth of ~14 km to 19 km occurred on the NE-trending Longmenshan thrust fault zone, which separates the Sichuan basin from the eastern margin of the Tibetan Plateau. This fault zone consists of three major subparallel faults: the Wenchuan-Maowen, Yingxiu-Beichuan and Pengguan faults

---

X. Fan (✉)
Faculty of Geo-Information Science and Earth Observation (ITC), University of Twente, P.O. Box 217, Enschede 7500 AE, The Netherlands

The State Key Laboratory of Geohazards Prevention and Geoenvironment Protection, Chengdu University of Technology, Chengdu, Sichuan, China
e-mail: fan21676@itc.nl

C.J. van Westen • T. Gorum • R. Huang
Faculty of Geo-Information Science and Earth Observation (ITC), University of Twente, P.O. Box 217, Enschede 7500 AE, The Netherlands

Q. Xu
The State Key Laboratory of Geohazards Prevention and Geoenvironment Protection, Chengdu University of Technology, Chengdu, Sichuan, China

F. Dai
Institute of Geology and Geophysics, Chinese Academy of Sciences, Beijing, China

G. Wang
Disaster Prevent Research Institute, Kyoto University, Uji, Kyoto, Japan

C. Margottini et al. (eds.), *Landslide Science and Practice*, Vol. 5,
DOI 10.1007/978-3-642-31427-8_36,

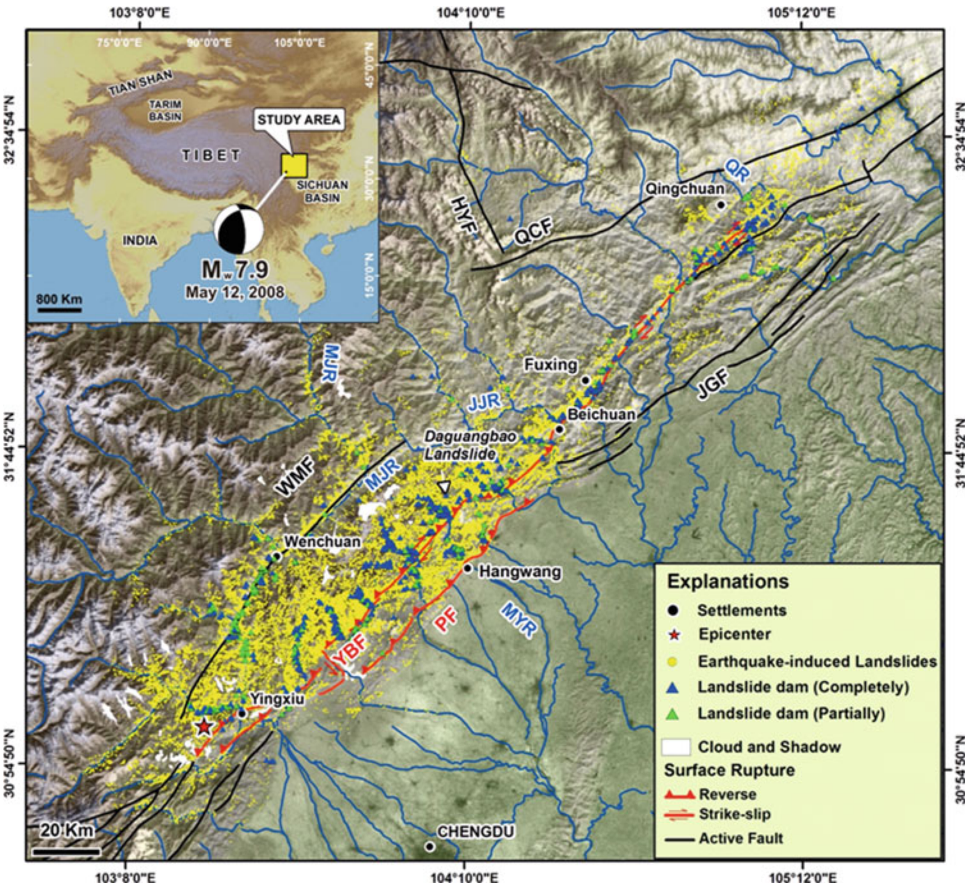

Fig. 1 Distribution map of landslides and landslide dams triggered by the Wenchuan earthquake. The Danguangbao landslide is indicated with a triangle. The white areas are unmapped due to the presence of clouds and shadows in the post-earthquake images. The following faults are indicated: *WMF* Wenchuan-Maowen fault, *YBF* Yingxiu-Beichuan fault, *PF* Pengguan fault, *JGF* Jiangyou-Guanxian fault, *QCF* Qingchuan fault, *HYF* Huya fault, *MJF* Minjiang fault (After Xu et al. 2009). The rivers indicated in the figures are *MJR* Minjiang River, *MYR* Mianyuan River, *JJR* Jianjiang River, *QR* Qingzhu River. The epicenter location is from (USGS 2008)

(Fig. 1). The coseismic rupture initiated near Yingxiu town (31.0610N, 103.3330E) and propagated unilaterally towards the northeast, generating a 240-km long surface rupture along the Yingxiu Beichuan fault, and a 72-km long rupture along the Pengguan fault (Xu et al. 2009; Lin et al. 2009; Shen et al. 2009). GPS and InSAR data helped quantify the variability of fault geometry and slip rate distribution (Yarai et al. 2008; Hao et al. 2009), showing that in the southwest (from Yingxiu to Beichuan) the fault plane dips moderately to the northwest, becoming nearly vertical in the northeast (from Beichuan to Qingchuan region), associated with a change from predominantly thrusting to strike-slip motion. The fault zone runs through a mountain range with elevations ranging from 500 m in the Sichuan Basin to over 5,000 m over a distance of ~50 km. Slope gradients within in the deeply dissected fault zone are steep, commonly > 300.

The Wenchuan earthquake provides a unique opportunity to study the co-seismic landslide dams, since several hundreds of landslide dams and over 60,000 landslides were triggered (Gorum et al. 2011). This study aims to present an unprecedented inventory and analyse the spatial distribution of landslide dams triggered by the Wenchuan earthquake, derived from detailed remote sensing interpretation and fieldwork. We focus on the relation between landslide dam distribution and a series of seismic, topographic, geological, and hydrological factors, aiming to create a landslide dam susceptibility model by the multivariate statistical method in future.

Event-Based Mapping of Landslide Dams

Event-based landslide mapping is usually carried out after single landslide triggering events, such as an earthquake, an intense rainfall event or a serious snowmelt event. It is a mandatory step for analyzing the landslide distribution (Harp and Jibson 1996; van Westen et al. 2008).

Source Data for Landslide Dam Mapping

In a previous study Gorum et al. (2011) presented the method for mapping all landslides in the earthquake affected region using 52 pre- and post earthquake satellite images. The same data was used in this study for mapping the landslide dams, including pre- and post- earthquake ASTER (15 m), ALOS AVNIR-2 (10 m) and PRISM (2.5 m), Indian Cartosat-1 (2.5 m), SPOT-5 (2.5 m), IKONOS (2.5 m), as well as a number of aerial photos (0.3 m). In addition, a pre-earthquake DEM was used, which was generated from

1:50,000 scale digital topographical maps. Unfortunately insufficient data was available for generating a post-earthquake DEM, so that volume analysis was not possible.

Mapping and Interpretation Method

Landslide dams were mapped through visual interpretation by comparing pre- and post-earthquake images, assisted by field checks in accessible areas. The "fresh" landslides are clearly recognizable change detection of the monoscopic images also allowed to achieve good results by making optimal use of image characteristics such as tone, texture, pattern and shape.

Landslides were identified which blocked the rivers completely or partially, and for these the initiation and runout areas were mapped as polygons, as well as the associated barrier lakes. The polygon mapping was done first using medium resolution images (ASTER and ALOS AVNIR-2), and was refined for those areas where also high resolution images were available (ALOS PRISM, Cartosat-1, SPOT-5, IKONOS an Airphotos). Figure 1 shows the distribution of the landslide dams, plotted on a map with the overall landslide distribution made by Gorum et al. (2011). Figure 2 gives an example of the use of medium and high resolution imagery for landslide dam mapping. On the medium resolution images, the landslide initiation and runout areas cannot be mapped as separate polygons (Fig. 2 a, c), whereas this is possible using high resolution images (Fig. 2 b, d).

Landslide dams can be easily identified by a number of diagnostic features. They have a higher reflectance rate compared to the surrounding areas with vegetation cover, and often show clear geomorphological characteristics, such as scarps, rock fall talus, flow lobes, hummocky and asymmetric deposits, transverse depression and an elongated shape downslope. A very important characteristic is the disruption of surface drainage, by partially or completely blocking the river below. The presence of a barrier lake is certainly the most important characteristic, although this was not the case for many of the identified landslide dams as the damming had been partially, or the dam had already broken.

In total, 828 landslide dams were mapped. Of them, 501 completely dammed the rivers with a total area of 23.7 km^2, while the others only caused partial damming.

Analysis of Landslide Dam Spatial Distribution

Gorum et al. (2011) concluded that the distribution pattern of landslides triggered by the Wenchuan earthquake is primarily controlled by the coseismic slip rate distribution, the fault geometry and characteristics. We found that landslide distribution in the section of the fault that had mainly a thrust component with a low angle fault plane was much higher than the sections that had steeper fault angles and a major strike slip component. Figure 1 shows that areas with a high landslide density in the vicinity of rivers are prone to produce a high density of landslide dams. There are relatively many landslide dams along the deeply-incised Minjiang River, of which most are partially damming due to the high discharge and erosive capacity. The landslide dams are distributed in a relative wider region with comparatively higher density in the SW from the epicenter to Beichuan town and around the end of the main fault in Qingchuan. Around 70 % of landslide dams concentrated in the Pengguan Massif along the fault thrust component, mainly due to two reasons: (1) this region has a high landslide density; (2) the traverse rivers in the Pengguan Massif has smaller catchment area than the Minjiang river and Jianjiang river, thus, the smaller discharge and river width (Kirby and Whipple 2003).

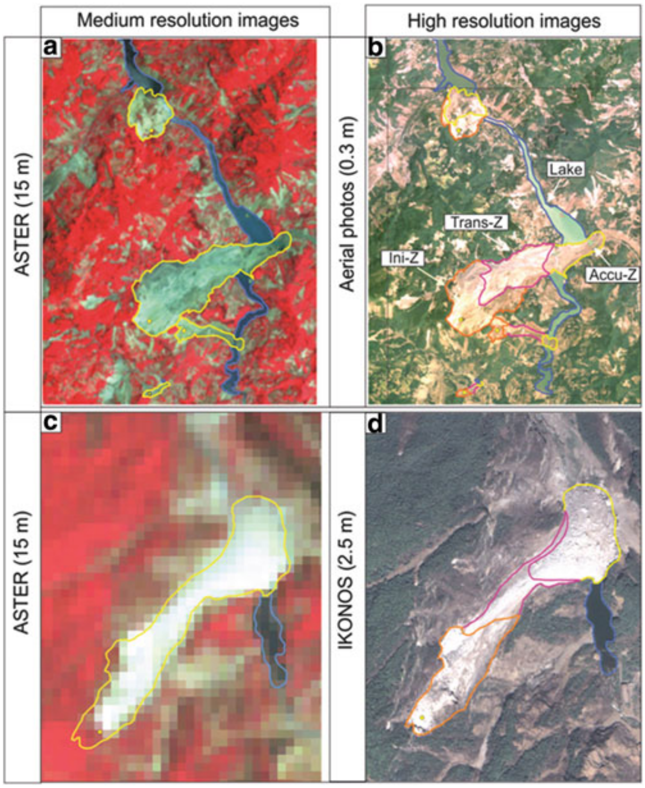

Fig. 2 Examples of medium (*left*) and high (*right*) resolution images showing landslide dam polygon mapping. Detailed mapping allowed delineating the initiation (Ini-Z), transportation (Trans-Z) and accumulation (Accu-Z) parts of damming landslides, whereas the landslides can only be mapped as single polygons using medium resolution images

The spatial distribution of landslide dams is controlled by several seismic and geo-environmental factors (Keefer 2000). We will analyze the variation of landslide dam distribution with aforementioned factors to statistically evaluate the impacts of these factors on landslide dam distribution.

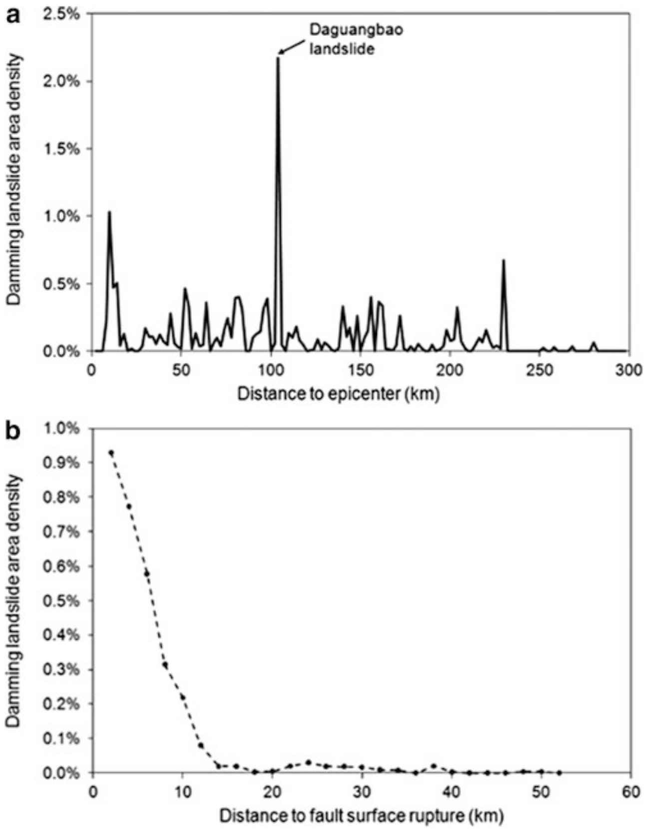

Fig. 3 (**a**) Damming landslide area density versus Distance to epicentre; (**b**) Damming landslide area density versus Distance to fault surface rupture

Variation of Damming Landslide Occurrence with Seismic Factors

We selected two most commonly used factors, the distance to epicenter and to the fault surface rupture to analyze the relation of landslide dam occurrence with seismic factors. The damming landslide area density (LDAD) was determined for a sequence of concentric bands 2 km wide extending outward from the seismic source in ArcGIS. Figure 3a shows the variation of LDAD with epicentre distance. A obvious peak with the LDAD value of 2.17 % was caused by the largest landslide, the Daguangbao landslide in the study area. The Daguangbao landslide has an area of 7.1 km^2 and an estimated volume of 7.5 × 10^8 m^3 (Huang et al. 2011) to 8.4 × 10^8 m^3 (Chigira et al 2010). The damming landslide area density (LDAD) didn't show a clear decay relationship with the distance to epicenter. It means that the distance to epicenter is not a control factor for landslide dam generation. Differently, with the increase of distance to the fault surface rupture, the LDAD decreased significantly, from 0.93 % at 2 km distance to 0.004 % at 50 km, but the decay rate become slight after 12 km (Fig. 3b).

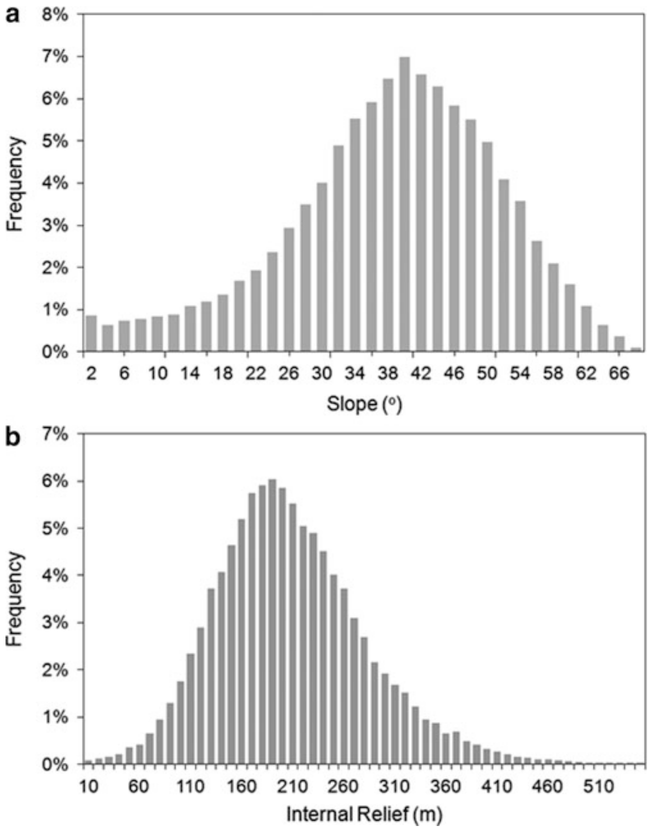

Fig. 4 (**a**) Frequency distribution of slope gradient and damming landslide ratio; (**b**) Frequency distribution of internal relief and damming landslide ratio

Variation of Damming Landslide Occurrence with Terrain Factors

We considered the slope gradient, internal relief, altitude, slope aspect, profile curvature and plan curvature as the main terrain factors, which can be extracted from 25-m DEM. The slope gradient and internal relief seems to be more important than others (Fig. 4). In the study area, the mean altitude value is calculated as 2,361 m, on the grid cells with landslides the average value is obtained as ~1,900 m (Gorum et al. 2011). The damming landslides are most abundant between altitude 700 m and 1,700 m, which are lower than the mean altitude of landslides, because damming landslides more densely distributed in the hill slopes in the vicinity of rivers. There is no preferential aspect for damming landslides, since it might more depend on the river direction. The rest of factors, such as the plan and profile curvature do not show clear relationship with landslide dam occurrence. The frequency distribution of slope gradient and internal relief was plotted in Fig. 4 a, b, which indicates that most abundant damming landslides with the slope gradient of ~40° and the internal relief of ~180 m.

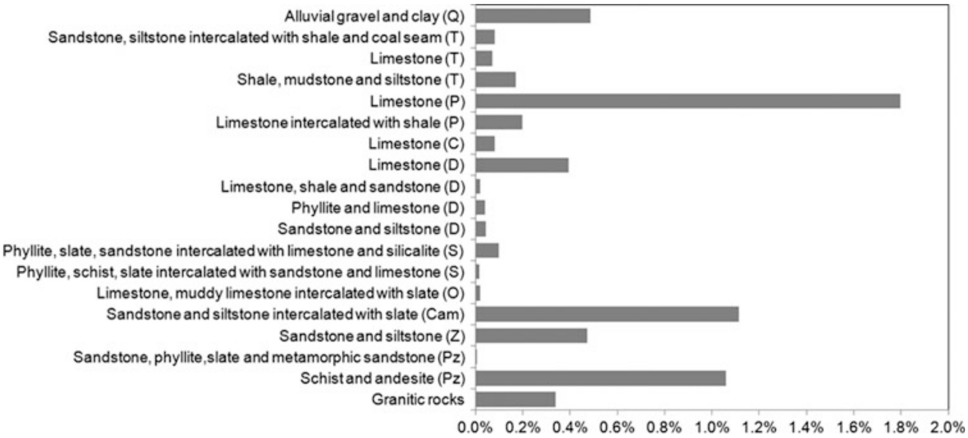

Fig. 5 Damming landslide point and area densities for lithologic units

Variation of Damming Landslide Occurrence with Lithology

Lithology is considered the most important geological factor. In this study, a geological map was compiled from ten 1: 200,000 scale standard geological maps. The landslide dam area density (LDAD) was determined for each lithologic unit (Fig. 5). The lithology of damming landslides varies from Quaternary alluvial gravel and clay to Pre-Sinian rocks. A peak of LDAD value of 1.8 % appears in the Permian limestone, due to the contribution of the aforementioned Daguangbao landslide. The results show that the Cambrian sandstone and siltstone intercalated with shale, as well as the Pre-sinian schist and andesite have the relatively high damming landslide area density. The same rock types also produced high density of coseismic landslides, according to Dai et al. (2010). Field investigation also revealed that the Pre-sinian schist is very weak and fractured, producing a large amount of landslides. The shale intercalated in sandstone and siltstone of the Cambrian age largely affects the integrity and strength of the slopes, resulting in the high density of landslides and landslide dams. Limestone and limestone intercalated with shale are generally well stratified and densely jointed, generating both deep-seated rockslides on cataclinal slopes and shallow rockslides or rock falls on anaclinal slopes. Chigira et al (2010) found that many of the sliding surfaces in carbonate rocks had rough surfaces with dimple-like depressions by dissolution. Large rock avalanches were mostly observed in the intensely cracked granitic rock masses as well as sandstones and siltstones.

Variation of Damming Landslide Occurrence with Hydrological Factors

Hydrological factors play important roles in landslide dam formation, such as the distance to streams, stream order, upper catchment area, stream power index etc. Here, we focus on the distance to streams and stream order. Figure 6 shows that generally with the increase of landslide distance to streams, the damming landslide number decreases. Over 80 % of damming landslides concentrated within 400 m distance to the streams. Besides, the average area of damming landslides shows an increasing trend with the increase of the distance to streams. It implies that the farther away from the river, the larger the landslide is required to block a river and form a dam.

The stream order was calculated by the method proposed by Strahler (1957) using SAGA software (System for Automated Geoscientific Analyses). Figure 7 depicts that ~90 % of damming landslides occur along the rivers with stream order varying from 1 to 3. The stream order reflects the stream power of a river. The higher the stream order, the more powerful the river is. Therefore, the damming landslide frequency decreased significantly, when the stream order increased from 2 to 6. However, few damming landslides occurred along the river with stream order of 1, because those low stream order rivers are the small tributaries at the initial (upper) part of catchments, thus, with very low discharge and incision. The area range of damming landslides with each stream order was represented by box plot in Fig. 7, which indicates a general trend that the higher the stream order, the larger the landslide is required to block a river. However, this trend is not so pronounced when the stream order varies from 1 to 3, as it does from 4 to 6.

Conclusions

Temporary or permanent blockage of stream by landslides is a serious secondary hazard in mountainous areas that are affected by strong earthquakes or major rainfall events. They may pose a large risk to downstream areas as a result of catastrophic lake outbreak flooding. This phenomenon has gradually received more attention in literature, although several issues are still poorly

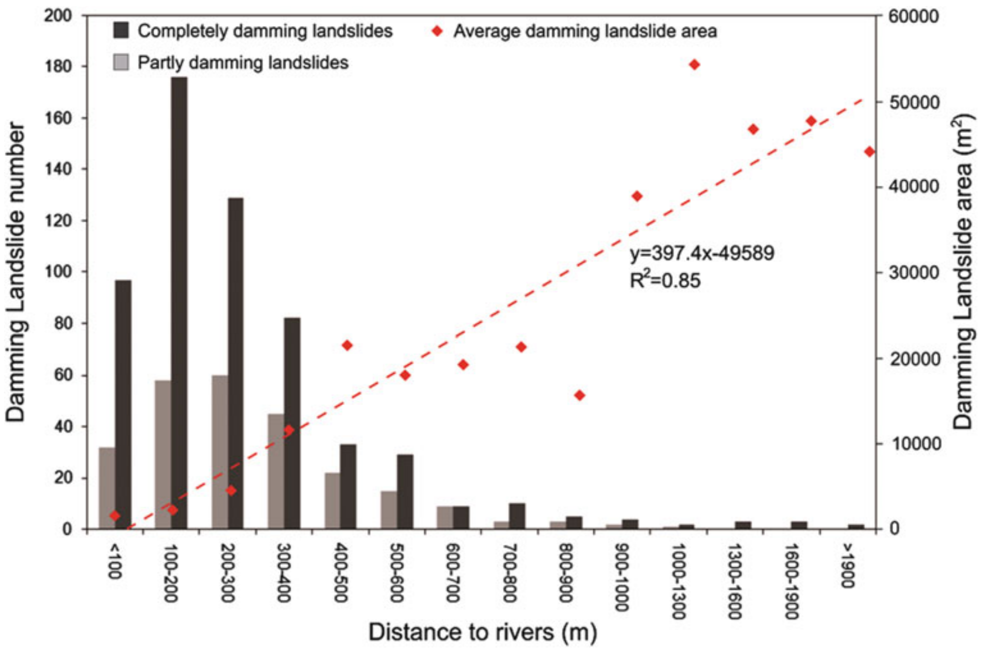

Fig. 6 Relationship between damming landslide number, average area and distance to rivers

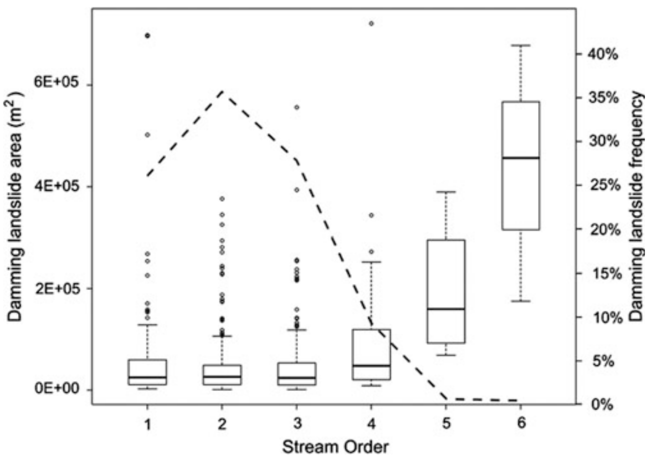

Fig. 7 Relationship between damming landslide frequency (represented by the *dash line*), area and stream order. The boxes and whiskers show ranges of damming landslide area for each stream order. *Black circles* are the outliers. *Horizontal line* defines the median

understood, such as the landslide dam formation conditions, dam classification, and in particular landslide dam susceptibility and hazard assessment. To understand these aspects better research on individual datasets of landslide dams caused by the same triggering event is important.

The Wenchuan earthquake provided the opportunity to generate an event-based landslide dam inventory of 828 individual landslide dams, of which 501 caused the complete blockage of the drainage. In this study, efforts were paid to create an almost complete landslide dam database for a single triggering event, and use it to analyze the spatial distribution of landslide dams and the related controlling factors, including the seismic, terrain, lithologic and hydrological parameters. Next site-specific details such as the valley geomorphometry and stream discharge should also be taken into account. The ultimate aim is to combine this with earthquake acceleration modelling and landslide hazard assessment in order to provide a probabilistic landslide dam hazard assessment.

Acknowledgments This research was carried out under the collaboration agreement between the State Key Laboratory on Geohazards Prevention (Chengdu University of Technology) and the United Nations University – ITC School for Disaster Geo-Information Management, University of Twente, the Netherlands. It was financially supported by the National Basic Research Program “973” Project of the Ministry of Science and Technology of the People’s Republic of China (2008CB425801). The authors acknowledge Dr. Oliver Korup for his valuable suggestions. We appreciate that the Japan Aerospace Exploration Agency (JAXA), GeoEye foundation, and Indian Space Research Organisation (ISRO) for providing the data for this research.

References

Adams J (1981) Earthquake-dammed lakes in New Zealand. Geol Soc Am Geol 9:215–219

Casagli N, Ermini L (1999) Geomorphic analysis of landslide dams in the Northern Apennine. Trans Jpn Geomorphol Union 20:219–249

Chai HJ, Liu HC, Zhang ZY (1995) The catalog of Chinese landslide dam events. J Geol Hazard Environ Preserv 6(4):1–9, In Chinese

Chigira M, Xu XY, Inokuchi T, Wang GH (2010) Landslides induced by the 2008 Wenchuan earthquake, Sichuan, China. Geomorphology 118(3–4):225–238

Costa JE, Schuster RL (1988) The formation and failure of natural dams. Geol Soc Am Bull 100:1054–1068

Costa JE, Schuster RL (1991) Documented historical landslide dams from around the world, vol 91–239, U.S. geological survey open-file report. U.S. Geological Survey, Vancouver, 486p

Dai FC, Xu C, Yao X, Xu L, Tu XB, Gong QM (2010) Spatial distribution of landslides triggered by the 2008 Ms 8.0 Wenchuan earthquake, China. J Asian Earth Sci. doi:10.1016/j.jseaes.2010.04.010

Dong JJ, Tung YH, Chen CC, Liao JJ, Pan YW (2009) Discriminant analysis of the geomorphic characteristics and stability of landslide dams. Geomorphology 110:162–171

Duman TY (2009) The largest landslide dam in Turkey: Tortum landslide. Eng Geol 104:66–79

Dunning SA, Petley DN, Rosser NJ (2005) The morphology and sendimentology of valley confined rock-avalanche deposits and their effect on potential dam hazard. In: Hungr O, Fell R, Couture R, Eberhardt E (eds) Landslide risk management. Taylor & Francis, London. ISBN 04 1538 043X

Ermini L, Casagli N (2003) Prediction of the behavior of landslide dams using a geomorphological dimensionless index. Earth Surf Process Landf 28:31–47

Gorum T, Fan XM, van Westen CJ, Huang RQ, Xu Q, Tang C, Wang GH (2011) Distribution Pattern of Earthquake-induced Landslides Triggered by the 12 May 2008 Wenchuan Earthquake. Geomorphology. doi:10.1016/j.geomorph.2010.12.028

Hancox GT, Perrin ND, Dellow GD (1997) Earthquake-induced landsliding in New Zealand and implications for MM intensity and seismic hazard assessment. Institute of Geological and Nuclear Sciences Client Report 43601B prepared for Earthquake Commission Research Foundation, Lower Hutt, p 85

Hao KX, Si H, Fujiwara H, Ozawa T (2009) Coseismic surface-ruptures and crustal deformations of the 2008 Wenchuan earthquake Mw 7.9, China. Geophys Res Lett 36(11):2–6

Harp EL, Crone AJ (2006) Landslides triggered by the October 8, 2005, Pakistan earthquake and associated landslide-dammed reservoirs, vol 2006–1052, U.S. geological survey open-file report. U.S. Geological Survey, Reston, 13p

Harp EL, Jibson RW (1996) Landslides triggered by the 1994 Northridge, California earthquake. Bull Seismol Soc Am 86:319–332

Hewitt K (1998) Catastrophic landslides and their effects on the upper Indus streams, Karakoram Himalaya, northern Pakistan. Geomorphology 26:47–80

Huang RQ, Pei XJ, Fan XM, Zhang WF, Li SG, Li BL (2011) The characteristics and failure mechanism of the largest landslide triggered by the Wenchuan earthquake, May 12, 2008, China. Landslides. doi:10.1007/s10346-011-0276-6

Keefer DK (2000) Statistical analysis of an earthquake-induced landslide distribution-the 1989 Loma Prieta, California event. Eng Geol 58:231–249

Kirby E, Whipple KX (2003) Distribution of active rock uplift along the eastern margin of Tibetan Plateau: Inferences from bedrock channel longitudinal profiles. J Geophys Res 108:1–24

Korup O (2002) Recent research on landslide dams-a literature review with special attention to New Zealand. Prog Phys Geogr 26:206–235

Korup O (2004) Geomorphometric characteristics of New Zealand landslide dams. Eng Geol 73:13–35

Lin A, Ren Z, Jia D, Wu X (2009) Co-seismic thrusting rupture and slip distribution produced by the 2008 Mw 7.9 Wenchuan earthquake, China. Tectonophysics. doi:10.1016/j.tecto.2009.02.014

Nash T, Bell D, Davies T, Nathan S (2008) Analysis of the formation and failure of Ram Creek landslide dam, South Island, New Zealand. N Z J Geol Geophys 51:187–193

Schneider JF (2009) Seismically reactivated Hattian slide in Kashmir, Northern Pakistan. J Seismol 13(3):387–398

Shen Z, Sun J, Zhang P, Wan Y, Wang M, Bürgmann R, Zeng Y, Gan W, Liao H, Wang Q (2009) Slip maxima at fault junctions and rupturing of barriers during the 2008 Wenchuan earthquake. Nat Geosci 2:718–724. doi:10.1028/NGEO636

Strahler AN (1957) Quantitative analysis of watershed geomorphology. Trans Am Geophys Un 38:913–920

U.S. Geological Survey (2008) Magnitude 7.9 – Eastern Sichuan, China, 2008 May 12 06:28:01UTC. http://earthquake.usgs.gov/earthquakes/eqinthenews/2008/us2008ryan/

van Westen CJ, Castellanos E, Kuriakose SL (2008) Spatial data for landslide susceptibility, hazard, and vulnerability assessment: an overview. Eng Geol 102:112–131

Xu X, Wen X, Yu G, Chen G, Klinger Y, Hubbard J, Shaw J (2009) Coseismic reverse- and oblique-slip surface faulting generated by the 2008 Mw 7.9 Wenchuan earthquake, China. Geology 37:515–518

Yarai H, Nishimura T, Tobita M, Amagai T, Suzuki A, Suito H, Ozawa S, Imakiire T, Masaharu H (2008) A fault model of the 2008 Wenchuan earthquake estimated from SAR measurements. In: 7th Academic surgical congress meeting, X2-040, Reykjavik

THE SECOND
WORLD
LANDSLIDE FORUM

Geological and Structural Control of Earthquake-Induced Landslides in El Salvador

Ignacio García-Flórez and Meaza Tsige

Abstract

El Salvador is located at one of the most seismically active areas in Central America. It has suffered several destructive earthquakes during the past 100 year, which have caused severe damage and great loss of life, mainly due to the earthquake-triggered landslides. The triggered landslides are of different types, ranging from relatively shallow falls and slides in rock and debris landslides to large deep-seated landslides, being the latter the most damaging. A detailed analysis of historical and recent coseismic-landslides (failure mechanism, distribution and concentration), together with geological and geotechnical aspects of materials and location of main geological structures, has been carried out. The study shows that there is a great concentration of landslides in the central part of the country, especially near to the El Salvador Fault Zone (ESFZ) independent to the distance and origin of the earthquake. Despite the possible lithological and topographical amplification which are associated mainly to the unconsolidated pyroclastic deposits and the volcanic cones with steep slopes, here it seems that there has been a great ground motion independently to the origin of the earthquake and focal distance, due to local seismic wave deviation or guiding and seismic energy liberation along the fault zone.

Keywords

El Salvador • Landslides triggered by earthquakes • El Salvador fault zone • Seismic wave guiding

Introduction

El Salvador, due to its geodynamic setting –close to the Cocos-Caribbean segment of the Middle American subduction zone, where the plates converge-, is affected by a great number of earthquakes of large and moderate magnitudes. One of the secondary effects associated with these events, which contributes to a large extent to increase the destruction and loss of life, are the landslides. During the last decades El Salvador has suffered many earthquakes of large and moderate magnitude that have caused severe damage and great social alarm, fundamentally because of the associated geological process (landslides, liquefaction, etc.) (Bommer et al. 2002; White and Harlow 1993). Some authors (Keefer 1984) (Rodríguez et al. 1999) have shown that the number of landslides triggered by earthquakes in Central America is disproportionally high in comparison with other places that suffer earthquakes of similar magnitude. The impact that these phenomena can have was demonstrated with the two 2001 earthquakes, that produced and reactivated a great number of landslides across the whole country. During these two events nearly 1,200 people died, from which around 500 casualties were directly related with the induced landslides (CEPAL 2001). Most of the instabilities during the 2001 earthquakes were superficial (<10 m). Rock falls

---

I. García-Flórez (✉) • M. Tsige
Facultad de Ciencias Geológicas, Madrid, University Complutense de Madrid, C/José Antonio Novais, 12, Ciudad Universitaria, Madrid 28040, Spain
e-mail: igarciaf@geo.ucm.es

C. Margottini et al. (eds.), *Landslide Science and Practice*, Vol. 5,
DOI 10.1007/978-3-642-31427-8_37, © Springer-Verlag Berlin Heidelberg 2013

and rock slides were common in the volcanoes slopes, being its occurrence related to the very steep slopes of these areas. This factor also had a definitive role in the road cuts opened in the materials characterized by discontinuities. There also occurred numerous large deep-seated landslides most of them located at a distance more than 50 km away from the epicenters. These last are not associated to a specific geological material and steep slopes. They occur near or at structural discontinuities like the El Salvador Fault Zone (ESFZ).

Investigations of seismically-induced paleo- and recent landslides have shown that a number of earthquakes have triggered widespread damaging landslides in many parts of El Salvador, with a great concentration in the central part of the country, some times at a very important epicentral distances.

Apart from the possible lithological amplification, associated to some specific lithologies (Bommer et al. 1998a; Bourdeau 2006; Lotti and Hydro 2001; and Crosta et al. 2005), and the topographical amplification (García Rodríguez 2008), that contribute to the generation of landslides, here it seems that there has been a great ground motion independently of the origin of the earthquake and the focal distance.

Geodynamic Setting

Tectonics and Seismicity

El Salvador is framed within the Central America geodynamic setting, characterized by the interaction between the tectonic plates of Caribbean and Cocos, the latter sliding beneath the Caribbean plate along the Middle American Trench, in SW-NE direction (Fig. 1). The high rate of convergence (DeMets 2001) induces a very high seismic activity (Fig. 2).

According to the origin and location, two different seismic sources affecting the country are recognized. The first one is the Middle American Trench. It generates the largest earthquakes ($M_W > 7$) at intermediate depths (40–200 km) through two mechanisms: thrust faulting in the Benioff-Wadati zone, and normal faulting due to the extensional forces originated as a consequence of the sliding plate bending. The second seismic source is the strike-slip faults that run from east to west across the volcanic arc, constituting the El Salvador Fault Zone (Martínez-Díaz et al. 2004). Even when they produce smaller earthquakes ($5.5 < Mw < 6.8$), they tend to cause ruptures in the upper crust (<20 km), (White 1991) making havoc in densely populated areas close to the event, thus contributing greatly to the destruction of the country throughout its history (White and Harlow 1993).

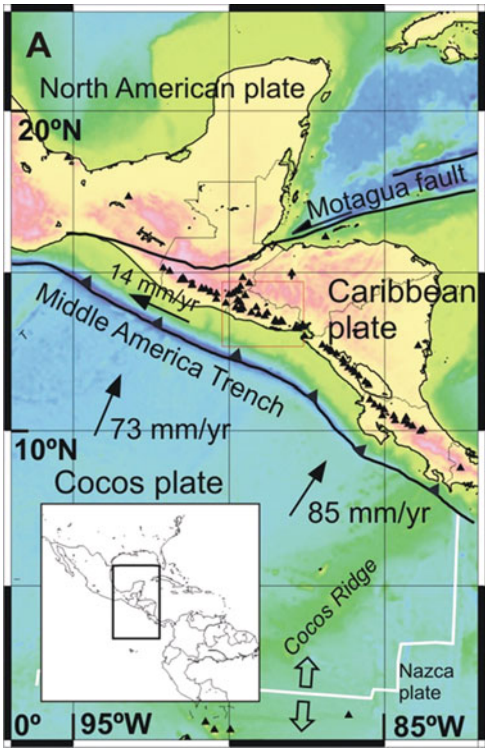

Fig. 1 Geodynamic setting (DeMets 2001)

Regional Geology and Geomorphology

From the geological point of view, El Salvador is a relatively young country, where most of the territory is occupied by recent materials of Plio-Quaternary age and volcanic origin. These are effusive rocks, as well as pyroclastic materials (Bosse et al. 1978). There are also intrusive igneous rocks. The oldest materials are Mesozoic (Jurassic-Cretaceous) and of sedimentary origin. They comprise limestones, quartz conglomerates, and sandstones. The most recent deposits are composed by non-consolidated volcanic ashes, lapilli, pyroclastics flows deposits, and breccias. In many parts of El Salvador outcrop volcanosedimentary levels of little extension pertaining to old pyroclastic deposits, reworked and sedimentated in fluvial and lacustrian environments, as well as diatomite and lignite rocks.

Geomorphologically El Salvador is divided in four units with a marked tectonic origin, for their development is conditioned by the geodynamic setting in which the country is immerse: high subduction rate responsible of the intense fracturation, and high seismic and volcanic activity. Each one of these units forms a band with an E-W orientation that runs parallel to the coast (Weyl 1980). The northernmost unit is called Montaña Fronteriza. To the south of these mountains is the Fosa Central unit. Is a depression limited

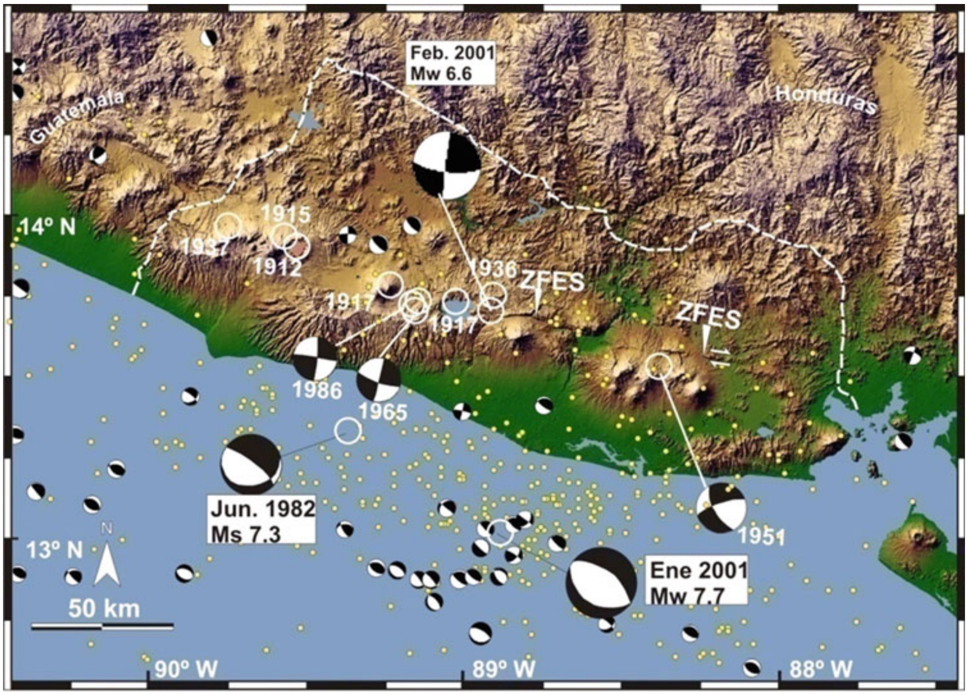

Fig. 2 Radar–Shuttle Radar Topography Mission image (courtesy of Jet Propulsion Laboratory) with historical destructive earthquakes (*white circles*) and instrumental epicentres (M_S >2.5, period 1977–2001) from U.S. Geological Survey–National Earthquake Information Center (USGS-NEIC) catalogue (*small dots*) (Martínez-Díaz et al. 2004)

by faults originated during a transtensive regime. Its relief is characterized by slopes with 30–50 % of inclination. Further to the south the Quaternary volcanoes rise crossing the country from east to west. To the south of this volcanic range are three coastal mountain ranges. Between the Coastal Ranges are two Coastal Plains that represents a fifth geomorphological unit.

Landslides in El Salvador

Earthquakes in Central America are accompanied by large landslides that increase the destruction and the resulting damages (Bommer and Rodríguez 2002). Keefer (1984) and Rodríguez et al. (1999), point out that in Central America the number of landslides triggered by earthquakes is higher than in other places of the world when considering earthquakes of similar magnitudes.

Besides this, from the analysis done in this work it also has been seen an anomalous concentration and distribution of earthquake-triggered landslides which seems to be independent from a specific lithology, origin and distance of earthquake epicenter (Tsige et al. 2008). This urges us to study which are the factors that determine this reality for El Salvador, where the areas affected by earthquake-induced landslides are much bigger than in any other location (Bommer and Rodríguez 2002) (Rodríguez et al. 1999) and why they are concentrated in the central part of the country.

As already said, throughout El Salvador history many earthquakes have occurred. Most of them have triggered widespread damaging landslides in many parts of the El Salvador, (Fig. 3). Table 1 collects the characteristics of some of the main earthquakes that have taken place during recent history, and information about the landslides induced by them. This table is composed mainly by the information collected previously by other authors which is available in the scientific literature. Nevertheless, we have carried out a search and revision work in order to extend and complete the existing information. There is no complete information about the distribution of the triggered landslides for all of them, except for the recent ones. The most complete available data is from the two 2001 earthquakes, from which there is a good landslide inventory with information regarding location, distance, size, involved lithology, slope angle, and failure mechanism. Considering that these two

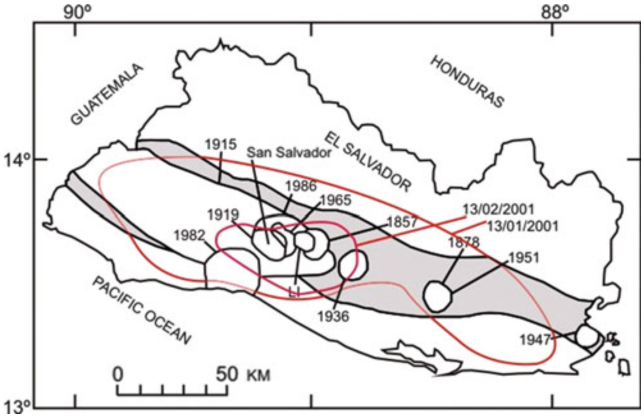

Fig. 3 Areas affected by landslides triggered by historical earthquakes (Rymer and White 1989). In *grey*, the areas that have experienced MM VII intensities. In *red*, the areas of concentration of landslides triggered during the 2001 earthquakes

Table 1 Characteristics of the earthquakes occurred in El Salvador and the landslides induced by them

No	Date	Focal depht[a] (km)	Origin[b]	Magnitude[c]	Failure mechanism[d]
1	23-V-1576				GC, UI
2	6-III-1719		sub	M_W 7.1*	GC
3	IV-1765			M_L 5.7	UI
4	22-III-1839			M_L 6.2	GC, UI
5	16-IV-1854		v.c.	M_W 6.6*	GC
6	18-VI-1854				SluR
7	6-XI-1857		u.c.	M_L 6.25	UI
8	8-XII-1859		sub	M_W 7.4*	GC
9	3-XII-1860			M_L 7.1	UI
10	19-III-1873			M_L 7.1	UI
11	2-X-1878		u.c.	M_L 6.5	UI
12	20-XII-1879				RSf, UI, Li
13	7-IX-1915	60	sub	M_W 7.8*	RF, UD, SB, GC, UI, Slu
14	28-IV-1919	s	u.c.	M_W 6.1*	UD
15	20-XII-1936	s	u.c.	M_W 6.2*	DS, GC
16	6-V-1951	s	u.c.	M_W 6.1*	RF, SB, UD, RS, DS, GC
17	6-V-1951	s	u.c.	M_W 6.2*	UD
18	3-V-1965	18	u.c.	M_W 6.2*	UD, SLs, Li
19	19-VI-1982	80	sub	M_W 7.3	UD
20	10-X-1986	10	u.c.	M_W 5.7	RF, SF, UD, RS, RSf, GC, Slu
21	13-I-2001	40	sub	M_W 7.7	RF, SF, RB, SB, RS, DS, SLs, RSf, Li, Rslu, Sslu
22	13-II-2001	14	u.c.	M_W 6.6	RF, SF, RB, SB, RS, DS, SLs, RSf, Li, Rslu, Sslu

References: Ambraseys and Adams (1996), Bommer and Rodríguez (2002), Bommer et al. (1998b), Lardé (1960), Meyer-Abich (1952), Martínez (1980), own data; Rymer and White (1989), SNET- Servicio Nacional de Estudios Territoriales, El Salvador; USGS- National Earthquake Information Center; White and Harlow (1993)

[a] Focal depth: *s* shallow events with focus in upper crust

[b] Origin: assumed tectonic origin of the earthquake based on the hypocentral location: *v.c.* volcanic chain, *u.c.* upper crust (<10 km), *sub* subduction

[c] Magnitudes: values marked with * are M_S converted to M_W using the empirical relationship of Ambraseys and Adams (1996); *mb* body-wave magnitude, M_L Richter magnitude, M_S surface-wave magnitude, M_W moment magnitude

[d] Failure mechanism: *RF* Rock Fall, *SF* Soil Fall, *UD* Undetermined Disrupted Slide, *RB* Rock Block Slide, *SB* Soil Block Slide, *RS* Rock Slide, *DS* Disrupted soil Slide, *SuS* Subaqueous landslide, *SLs* Soil Lateral Spreads, *RSf* Rapid Soil Flow, *GC* Ground Cracks, *UI* Undetermined Instabilities, *Li* Liquefaction, *Rslu* Rock Slump, *Sslu* Soil Slump

earthquakes have similar characteristics to the historical ones (origin, magnitude, rupture mechanism and depth), it is possible to think that past events could have triggered the same landslide typologies and distributed over areas of similar extension. It is for this, even when the Table 1 is incomplete regarding the landslides induced information, that the table is still proving useful for studying these phenomena over time in El Salvador. Figure 4 shows the numerous paleo-landslides together with one of the largest landslide (Jiboa) triggered by the 13 February 2001, (M_W 6.7) earthquake.

As it is mentioned above, the 13 January 2001 earthquake (M_W 7.7) off the coast El Salvador and the 13 February 2001 earthquake (M_W 6.7) triggered widespread damaging landslides in many parts of the country. Nevertheless, in both cases there was a great concentration in the central part of the country (Fig. 5). Most of the triggered landslides were relatively shallow falls and soil slides and occurred in the soft, weak, pyroclastic deposits locally known as Tierra Blanca, and rock falls in the lava flow belonging to the El Bálsamo Formation. These earthquakes also triggered deep large-scale landslides in addition to the usual shallow failures independently of the lithology. More surprisingly, they triggered instabilities at epicentral distances of more than 50 km and on slopes less than 20°. Having these last ones caused greater damage. These tended to be highly disrupted masses of rock and soil. The coherent slides, both in rock and in soil (block slides) transformed to rapid soil flows, travelling long distances due to an anomalous post-rupture (fluid like) behavior causing severe economic damage together with numerous fatalities.

The detailed analysis of triggered landslides caused by ancient and recent (2001) earthquakes, which comprised the study of the landslides typologies and their geometries, the distribution, together with an study of the geological materials involved, the topography and pre-existing discontinuities, has led us to think that the anomalous concentration of seismic triggered landslides, independently of

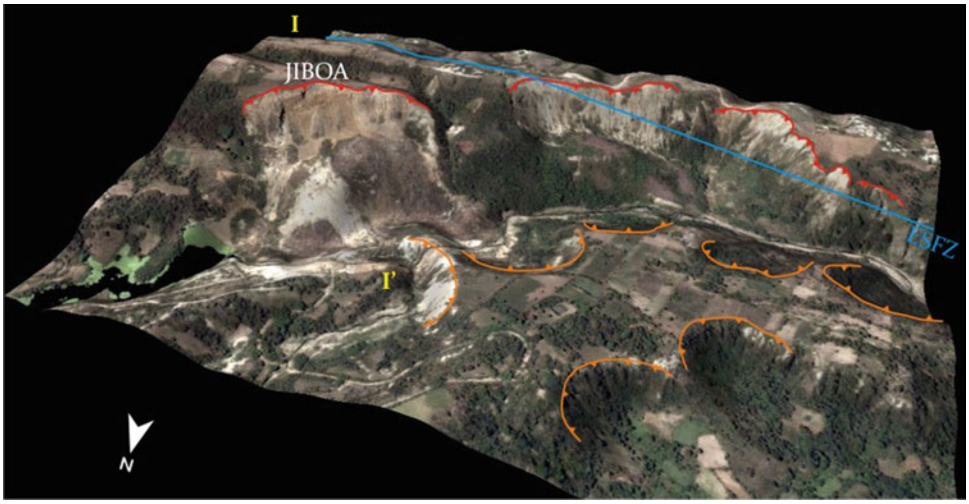

Fig. 4 3D model of part of the area of maximum landslides concentration during the 2001 earthquakes. In *red* are the active landslides; in *orange*, paleo-landslides; in *blue*, the assumed El Salvador Fault Zone main fault trace

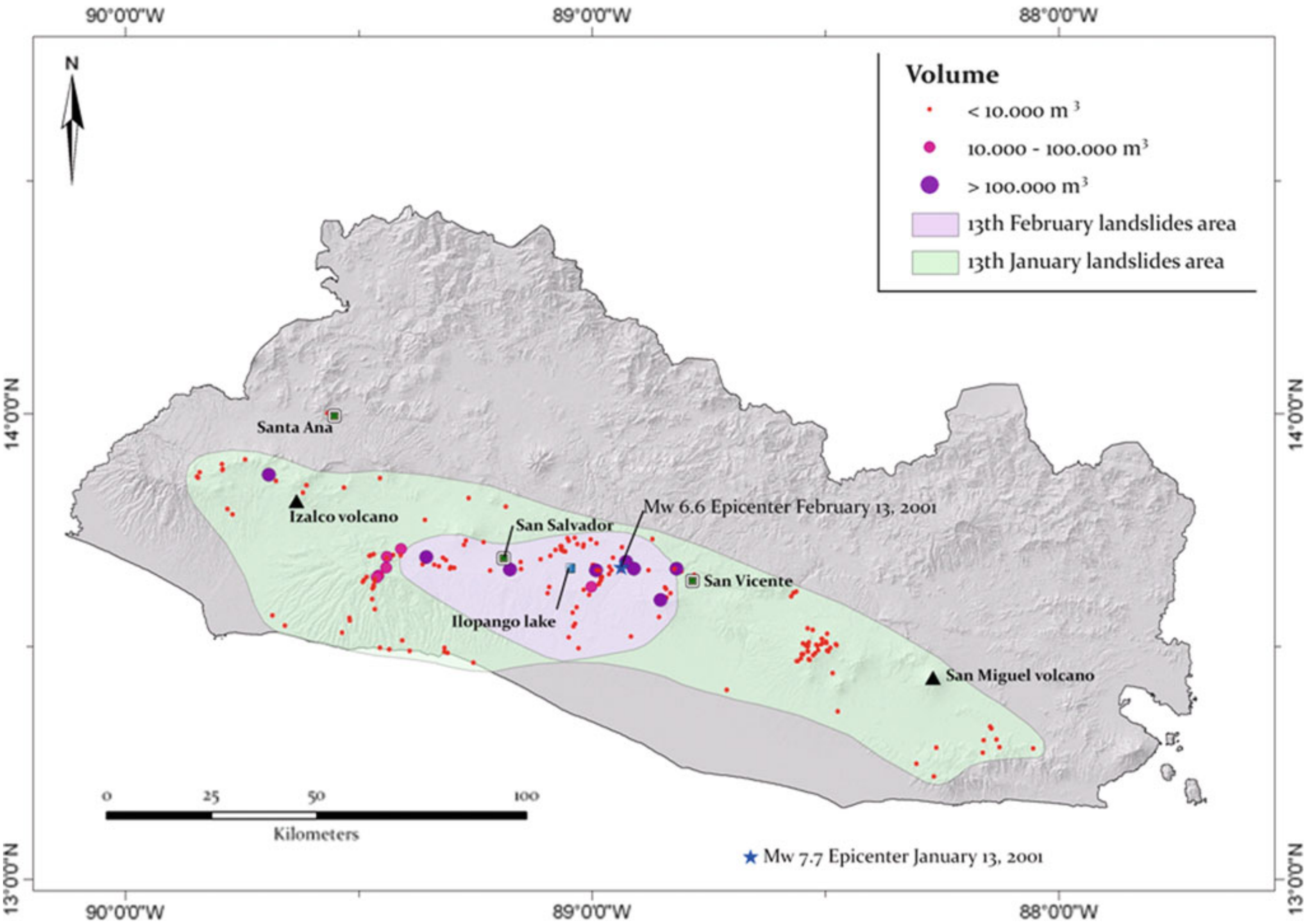

Fig. 5 Areas affected by the coseismic landslides during the 2001 earthquakes (elaborated using the landslides inventory collected by the SNET). The size of the landslides is proportional to the volume of material remobilized

the origin and focal distance, have occurred in situations in which aggravating factors (site effects, topographic effects, geomorphological features and soil type) and specific ray paths due to preexisting structural discontinuities are involved. This site effects produce different type of instabilities depending on the location.

The majority of shallow landslides triggered by earthquakes in El Salvador are located along the volcanic chain, concentrating mainly in the materials composed by volcanic ashes (lapilli and tuffs), locally known as Tierra Blanca and Tobas Color Café, both belonging to the San Salvador formation that overlies a hard basaltic flow, and most of them are related to the greatest reliefs of the territory, volcanoes and road cuts opened artificially.

The peculiar meta-stable microstructure and the low dynamic strength of these unconsolidated and weak recent volcanic soils (Tierra Blanca) provide a series of elements that are known to play an important role in site effects and might enhance the level of ground motion which in some locations it has been estimated at up to 6 times factor of amplification. The strong ground motion 1.2 g, of these soils recorded in Santa Tecla (Las Colinas landslide located more than 100 km away from the epicenter) during the January 2001 earthquake indicates that the Tierra Blanca formation could be responsible for ground accelerations higher than expected. (Bourdeau 2006).

On the other hand, the rock falls and debris-avalanches are originated commonly in the indurate lava flow and most of them are associated to steep slopes. They consisted primarily of boulders up to several tens of cubic meters in volume that were shaken loose from steep outcrops and then bounced and rolled down steep slopes. The important topographic relief observed on volcanic cones at the volcanic chain area certainly accounts for topographic effects (Geli et al. 1988). For these reasons, the topographic effects can be held responsible for the high number of superficial debris avalanche type failures observed at the upper part of the hills. Zaslawski and Shapira (1998) showed that the topographical amplification in the frequency range 1.2–2.0 Hz varies in between a factor of 2 and 4, depending on the orientation of the topographic relief relative to the seismic source. Here it has not been seen a clear relationship between seismic origin and relief orientation. García-Rodríguez et al. (2008) indicate that in the case of the January 2001 (M_W 7.7) earthquake, topography roughness has major importance than relief orientation.

In the case of large deep seated landslide their concentration along the country is suggested to be controlled by several factors; amongst them the most important seems to be the preexisting discontinuities and fault zones where a dispersion pattern of seismic energy occurred influenced by the main ESFZ, (Tsige et al. 2008) (Fig. 5). These landslides occurred in different types of materials, rhyolitic tephra, pyroclastic debris of Cuscatlán formation, volcanic breccia of coarse boulder (Balsamo formation) and thick pyroclastic lapillis. Most of these materials are cemented and behave like hard rock, which after failure have anomalous mechanical behavior producing a large internal deformation during seismic shaking. Some of them were very deep (more than 170 m) and have an estimated large volume of 1.5 million m^3 (El Desagüe landslide), 12 million m^3 (Jiboa landslide), (Baum et al. 2001). These landslides were the most damaging ones producing large river dams (Desagüe and Jiboa), road blockage (Curva la Leona), which produced a significant threat to people (Baum et al. 2001), and produce numerous fatalities.

After having studied the distribution, concentration, and failure mechanism of these large landslides it is possible to conclude that they are neither bound to a particular lithology nor has the topography played any influence, as some of them have occurred in a 20° slope, such as the Jiboa landslide. Nonetheless, there seems to exist a sort of control by the pre-existing discontinuities. Besides that the fault zones serve as a weakened zone where the major landslides can initiate not in the traditional way acting as weak planes through which masses of soils or rocks slide, but as channels that guide the released seismic energy, trapping it and consequently provoking high peak ground accelerations (Imposa et al. 2004), as it has been registered in the closest stations (0.439 g in the vertical component during the January 13th event, registered in Zacatecoluca station; 0.262 g in the vertical component during the February 13th event, registered in the San Pedro Nonualco station, (Bommer et al. 2002)). These high values would be the ones responsible for the deep seated landslides within the El Salvador Fault Zone.

Conclusions

The information contained in the bibliography regarding typologies and areas affected by landslides induced by earthquakes in El Salvador is either scarce or absent for the majority of the events occurred in this country. Nevertheless, we consider that the latest events of 2001, both for their origin and for their magnitude, are sufficiently characteristic to conform an idea of the landslides that similar historical earthquakes could have triggered, both in terms of typology and areas of concentration.

The majority of seismic triggered landslides by earthquakes in El Salvador are located preferably in the central part of the country, independently of the origin, type and focal distance of the earthquake.

These anomalous distribution and concentration of triggered landslides in El Salvador, is controlled by three important site effect elements; lithological and topographical aspects, that controls the superficial soil and rocks slides and debris avalanches; and high level seismic energy liberation due to seismic wave guiding along the major structural discontinuities in the region (ESFZ) that controls the large deep seated landslides.

References

Ambraseys NN, Adams RD (1996) Large-magnitude Central American earthquakes, 1898–1994. Geophys J Int 127:665–692

Baum RL, Crone AJ, Escobar D, Harp EL, Major JJ, Martinez M, Pullinger C, Smith ME (2001) Assessment of Landslide Hazards Resulting from the February 13, 2001, El Salvador Earthquake; a report to the government of El Salvador and the U.S. Agency for International Development, U. S. Geological Survey, R., VA, United States (USA). U.S. Geological Survey, Reston, p 20

Bommer JJ, Rodríguez CE (2002) Earthquake-induced landslides in Central America. Eng Geol 63:189–220

Bommer J, Reinaldo R, Méndez P (1998a) Propiedades Mecánicas de la Tierra Blanca y la Inestabilidad de Taludes, ASIA, vol 129, San Salvador

Bommer J, Salazar W, Samayoa R (1998b) Riesgo Sísmico en la Región Metropolitana de San Salvador, PRISMA, San Salvador

Bommer JJ, Benito MB, Ciudad-Real M, Lemoine A, López-Menjívar MA, Madariaga R, Mankelow J, Méndez de Hasbun P, Murphy W, Nieto-Lovo M, Rodríguez-Pineda CE, Rosa H (2002) The El Salvador earthquakes of January and February 2001: context, characteristics and implications for seismic risk. Soil Dyn Earthq Eng 22:389–418

Bosse HR, Lorenz W, Merino A, Mihm A, Rode K, Schimdt-Thomé M, Wiesemann G, Weber HS (1978) Geological map of El Salvador Republic. Bundesanstalt für Geowissenschaften und Rohstoffe, Hannover

Bourdeau C (2006) Site effects study in the Las Colinas slope (El Salvador, 2001). In Hart R, Varona P (eds) 4th International FLAC symposium on numerical modeling in geomechanics−2006, Vol 04–09, Minneapolis

CEPAL (2001) El Salvador: Evaluación del terremoto del martes 13 de febrero de 2001. In: S.S.e.M (ed) Addendum al documento de evaluación del terremoto del 13 de enero, in Comisión Económica para América Latina y El Caribe (CEPAL). Naciones Unidas, México, p 63

Crosta GB, Imposimato S, Roddeman D, Chiesa S, Moia F (2005) Small fast-moving flow-like landslides in volcanic deposits: the 2001 Las Colinas landslide (El Salvador). Eng Geol 79:185–214

DeMets C (2001) A new estimate for present-day Cocos-Caribbean plate motion: implications for slip along Central America volcanic arc. Geophys Res Lett 28:4043–4046

García Rodríguez MJ (2008) Metodología para la evaluación de peligrosidad de los deslizamientos inducidos por terremotos. Doctoral thesis, Universidad de Alcalá, Madrid

García-Rodríguez MJ, Malpica JA, Benito B, Díaz M (2008) Susceptibility assessment of earthquake-triggered landslides in El Salvador using logistic regression. Geomorphology 95:172–191

Geli L, Bard P-Y, Julien B (1988) The effect of topography on earthquake ground motion: a review and new results. Bull seism Soc Am 78:42–63

Imposa S, Coco G, Corrao M (2004) Site effects close to structural lineaments in eastern Sicily (Italy). Eng Geol 72:331–341

Keefer DK (1984) Landslides caused by earthquakes. Geol Soc Am Bull 95:406–421

Lardé J (1960) Historia sísmica y erupciones volcánicas de El Salvador, Documentación histórica, critica y conclusiones: Obras completas, Tomo I. Min Cultura, Depto. Ed. El Salvador, vol. 1, p 441–576

Lotti C, Hydro A-E (2001) Informe final. Investigación geotécnica integral en la cordillera El Bálsamo, al Sur de Santa Tecla, entre Las Colinas, Las Delicias y Las Colinas, p 1–30

Martínez MA (1980) Cronología sísmica y eruptiva de la república de El Salvador a partir de 1520. Centro de Investigaciones Geotécnicas, Ministerio de obras Públicas, San Salvador. http://www.snet.gob.sv/ver/sismologia/registro/estadisticas/

Martínez-Díaz JJ, Álvarez-Gómez JA, Benito B, Hernandez D (2004) Triggering of destructive earthquakes in El Salvador. Geology 32:65–68

Meyer-Abich H (1952) Terremoto de Jucuapa en El Salvador (America Central), 6–7 de Mayo de 1951: Comunicaciones del Instituto Tropical de Investigaciones Científicas, Universidad de El Salvador, El Salvador

Rodríguez CE, Bommer JJ, Chandler RJ (1999) Earthquake-induced landslides: 1980–1997. Soil Dyn Earthq Eng 18:325–346

Rymer MJ, White RA (1989) Hazards in El Salvador from earthquake-induced landslides. In: Brabb EE, Harrod BL (eds) Landslides: extent and economic significance. A. A. Balkema, Rotterdam, pp 105–109

Tsige M, García-Flórez I, Mateos R (2008) Large earthquake induced landslides in El Salvador: Lithological and structural controls, II European conference of international association for engineering geology: Escuela Universitaria de Ingeniería Técnica de Obras Públicas de la Universidad Politécnica de Madrid, Madrid

USGS-NEIC (2003) United States Geological Survey-National Earthquake Information Center. http://earthquake.usgs.gov/earthquakes/eqarchives/epic/epic_global.php

Weyl R (1980) Geology of Central America. In: Bender F, Jacobshagen V, de Jong JD, Luettig G (eds) Beitraege zur regionalen Geologie der Erde. Federal Republic of Germany Gebrueder Borntraeger, Berlin

White RA (1991) Tectonic implications of upper-crustal seismicity in Central America. In: Slemmons DB, Engdahl ER, Zoback MD, Blackwell DD (eds) Neotectonics of North America, vol 1, Volume decade map. Geological Society of America, Boulder, pp 323–328

White RA, Harlow DH (1993) Destructive uppercrustal earthquakes of Central America since 1900. Seismol Soc Am Bull 83:1115–1142

Zaslawski Y, Shapira A (1998) The influence of topographical effects on seismic ground motion, XXVI General Assembly of the European Seismological Commission, Tel Aviv, Israel, Aug 23–28, Papers Vol. 241–245

Landslides Induced by Historical and Recent Earthquakes in Central-Southern Apennines (Italy): A Tool for Intensity Assessment and Seismic Hazard

Eliana Esposito, Luca Guerrieri, Sabina Porfido, Eutizio Vittori,
Anna Maria Blumetti, Valerio Comerci, Alessandro M. Michetti,
and Leonello Serva

Abstract

Analysis of distribution of landslides (rock falls and coherent slides), induced by 12 moderate to strong earthquakes occurred in the last three centuries in Central–Southern Apennines, has permitted to investigate the relationship of their maximum distance versus magnitude and ESI epicentral intensity.

For coherent slides, the correlation of magnitude or ESI intensity versus distance is fairly good and consistent with global datasets. Instead, rock falls show a less evident correlation with distance. We stress here the usefulness of such relationships to define the expected scenario of earthquake-induced landslides. However, the data base needs to be improved and enlarged to allow more robust estimates.

Keywords

Earthquake-induced landslides • Intensity scales • Central-Southern apennines

Introduction

The inner sector of Central–Southern Apennines is the most seismic sector of the Italian territory (Fig. 1), characterized in historical times by a number of earthquakes with magnitude around 7 and frequent moderate earthquakes (magnitude around 6).

Events of M ≥ 6 typically cause environmental effects (surface faulting, landslides, liquefactions, ground cracks, hydrological anomalies, etc.) that are a significant independent source of seismic hazard in addition to damages due to ground acceleration.

Many historical documents detail the effects of earthquakes in the Apennines, especially the strong events occurred in the last three centuries, reporting lots of data also on the characteristics of the effects on the natural environment. This extraordinary wealth of information has allowed (1) to identify the most vulnerable regions, i.e., the most prone to hazardous Environmental Effects of Earthquakes (i.e. the effects produced by an earthquake on the natural environment or EEEs) and (2) to evaluate the earthquake intensity (epicentral and local) by means of the ESI intensity scale (Michetti et al. 2007), a recently developed intensity scale only based on EEEs.

This study aims at relating the spatial distribution of seismically-induced landslides with magnitude and with the intensity of the event resulting from the application of the ESI scale.

E. Esposito • S. Porfido
Istituto per l'Ambiente Marino e Costiero, CNR, Calata Porta di Massa, Naples 80133, Italy

L. Guerrieri (✉) • E. Vittori • A.M. Blumetti • V. Comerci • L. Serva
Dipartimento Difesa del Suolo, Servizio Geologico d'Italia, ISPRA, Via V. Brancati 48, Rome 00144, Italy
e-mail: luca.guerrieri@isprambiente.it

A.M. Michetti
Dipartimento di Scienze Chimiche e Ambientali, Università dell'Insubria, Via Valleggio, 11, Como 22100, Italy

C. Margottini et al. (eds.), *Landslide Science and Practice*, Vol. 5,
DOI 10.1007/978-3-642-31427-8_38,

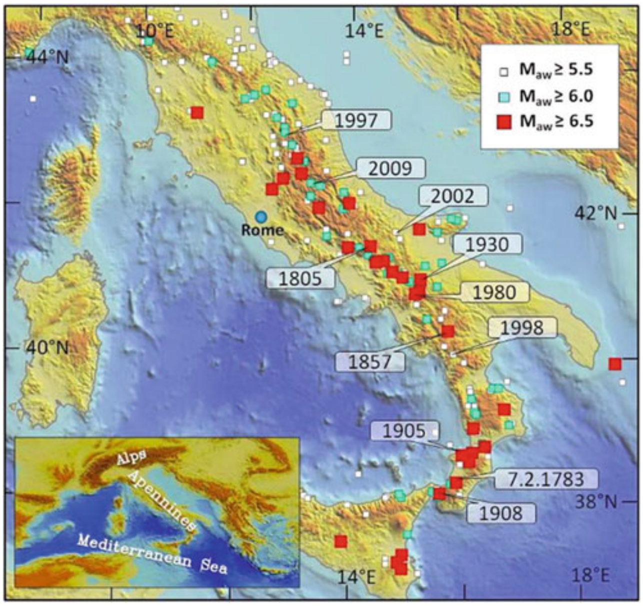

Fig. 1 Historical seismicity of Central–Southern Apennines (CPTI 2004). Labels locate the epicentres of the seismic events considered in this study

Background

Seismotectonic Framework of the Apennines

The present tectonic structure of the Apennines is the result of Upper Miocene–Lower Pliocene northeast-verging thrust tectonics (Patacca et al. 1990) overprinted by Late Pliocene to Quaternary northeast–southwest crustal extension, migrating in time and space from west to east; the latter is still active now, as demonstrated by seismic (including palaeoseismic) and morphotectonic evidence (Demangeot 1965; Blumetti et al. 1993; Roberts and Michetti 2004). Geodetic data provide velocities (with respect to stable Eurasia) that imply extension rates of 4–5 mm/year across the Apennines (D'Agostino et al. 2008; Devoti et al. 2008).

Historical catalogues (CPTI 2004; Guidoboni et al. 2007) summarize all available information for several moderate to strong earthquakes affecting Central-Southern Apennines in a time window larger than two millennia, but with good completeness only for the last 500 years.

Seismic hazard maps based on historical seismicity and integrated with paleoseismic evidence locate the areas with highest expected magnitudes (even more than 7) in the inner sector of the Central-Southern Apennines.

Magnitude Versus Landslide Distance: State of the Art

Empirical relationships between earthquake-triggered landslide distribution and magnitude based on a global database (about 40 events in the period 1811–1980) have been proposed by Keefer (1984). These relations were refined by Rodriguez et al. (1999) and Bommer and Rodriguez (2002) using a similar approach based on a larger dataset (almost 80 earthquakes). The last papers also discuss the potential relation between landslides distribution and MM intensity degrees. The best fit of data is given by polynomial curves of second degree.

Other relationships between magnitude and landslide distance were published for regional areas (e.g. Papadopoulos and Plessa 2000, for Greece).

In Italy, Prestininzi and Romeo (2000) related the maximum distance of ground failures collected in the CEDIT database (that includes landslides, fractures, liquefaction, topographic changes) with MCS epicentral intensities. Other empirical relationships were pointed out in previous papers of the Authors of this note (e.g. Porfido et al. 2002, 2007), where the distribution of the number of landslides with distance appears to follow a negative exponential trend (e.g. 1805 and 1980 earthquakes). A similar trend has been highlighted for the 2009 earthquake (Guzzetti et al. 2009; Vittori et al. in prep.).

ESI 2007 Intensity Scale

The ESI 2007 intensity scale (Michetti et al. 2007) classifies earthquake intensity based only on Earthquake Environmental Effects (EEE)., either directly linked to the earthquake source or triggered by the ground shaking. EEEs include surface faulting, regional uplift and subsidence, tsunamis, liquefaction, ground resonance, landslides, rock falls and ground cracks.

The definition of the ESI intensity degrees has been the result of a revision conducted by an International Working Group made of geologists, seismologists and engineers. It has been ratified by INQUA (International Union for Quaternary Research) in 2007.

The use of the ESI 2007 intensity scale, alone or integrated with the other traditional scales affords a better picture of the earthquake scenario, because only environmental effects allow suitable comparison of the earthquake intensity both:

- *In time*: effects on the natural environment are comparable for a time-window (recent, historic and palaeo seismic events) much larger than the period of instrumental record (last century), and
- *In different geographic areas*: environmental effects do not depend on peculiar socio-economic conditions or different building practices.

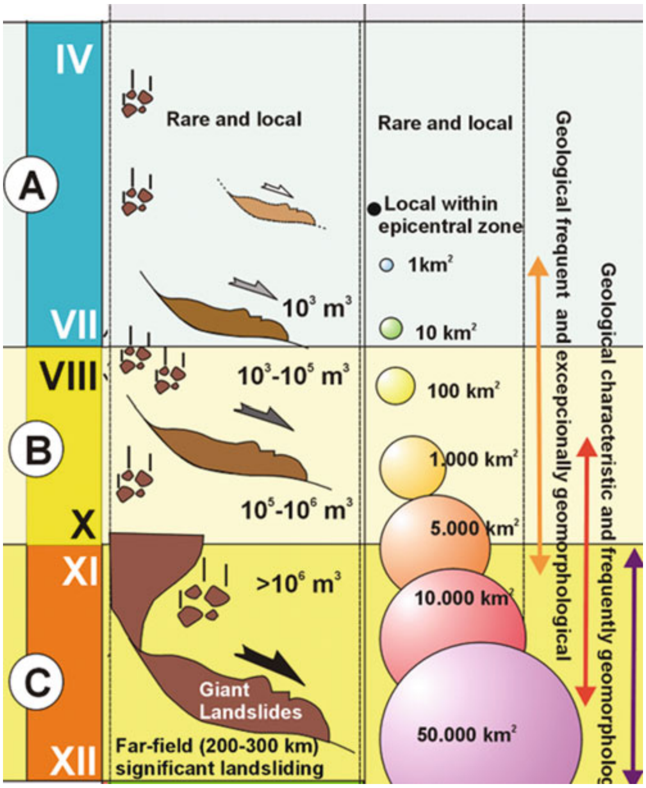

Fig. 2 Schematic picture of the typical landslide size and spatial distribution for ESI intensity degrees ranging from IV to XII (Michetti et al. (2007); Silva et al. (2008))

Thus, the new scale aims at integrating traditional seismic scales:

- For earthquake intensity degree larger or equal to X, when damage-based assessments are extremely difficult (because of tendency to saturation), while environmental effects are still diagnostic;
- In sparsely populated areas, where the effects on man-made structures are lacking and therefore intensity assessments have to be based on the environmental effects, which are the only available diagnostic elements.

The occurrence of landslides is expected from intensity IV ESI. The spatial distribution area of secondary effects (including landslides) allow to estimate the ESI epicentral intensity up to XII (Fig. 2). Furthermore, the growing size (volume, area) of slope movements are considered diagnostic elements for the assessment of the ESI local intensity in the range IV to X.

Landslides Versus Intensity in the Apennines

Landslides Triggered by Selected Earthquakes

We have taken into account 12 earthquakes occurred in the last three centuries, many of which studied in detail by the Authors for macroseismic purposes, with specific focus on the characterization of Earthquake Environmental Effects (Comerci et al. 2009; Esposito et al. 1998, 2000a, 2009; Esposito and Porfido 2010; Guerrieri et al. 2007, 2009; Porfido et al. 2002, 2007, 2011; Serva et al. 2007; Vittori et al. 2000, 2011).

Fig. 3 A landslide triggered by the 1783 Calabrian seismic sequence damned the S. Cristina narrow valleu and formed a temporary lake (Sarconi 1784)

The **1783 Calabrian seismic sequence** (Ms = 6.9; I_o = XI MCS; I_o = X-XI ESI) was characterized by a 3 years long sequence and five main shocks generated by individual fault segments of regional WNW-ESE trends. The 1783 multiple event started at the beginning of February and went on until the end of March, reaching a release of energy on March 28 with assessed macroseismic magnitude M = 6.9. More than 30,000 lives were lost and 200 localities were completely destroyed by the February 5 main shock. The epicentral area was located on the Gioia Tauro plain, at the western foot of the northern Aspromonte mountain.

The shock produced spectacular ground effects, both primary and secondary, such as tectonic deformations, ground fractures, liquefactions phenomena, tsunamis, hydrological changes and diffuse landslides of large size, which in most cases dammed the rivers creating more than 200 new temporary lakes (Porfido et al. 2011). A great density of mass movements occurred in the area bounded by Santa Cristina d'Aspromonte (Fig. 3), Molochio-Cittanova and Palmi (Cotecchia et al. 1986). The most common landslides were earth-block type, translational and rotational movement affecting the Plio-Pleistocene deposits of Gioia Tauro Plain (Cotecchia et al. 1986). Nevertheless, a reliable dataset of rock fall distribution is not available.

The **1805 July 26 Molise** earthquake (Ms = 6.6; I_o = X MCS; I_o = X ESI) affected mostly the Molise region, where at least 30 municipalities, located in the Bojano plain and the eastern foot of the Matese massif, were nearly totally destroyed (Esposito et al. 1987).

About one hundred seismically induced environmental effects are known for the 1805 earthquake mostly in the near-field area although some were reported as far as 70 km from the epicentre (Esposito et al. 1987; Porfido et al. 2002, 2007; Serva et al. 2007).

The earthquake triggered at least 26 slides: mainly rock falls, topples, slumps, earth flows and slumpearth flows. Among the largest of them were the earth flow of San Giorgio la Molara (Benevento), which affected the course of the Tammaro River, the earth flow of Acquaviva di Isernia, the rotational slide at San Bartolomeo in Galdo (Benevento), and a rotational slide-flow at Calitri (Avellino) (Esposito et al. 1987, 1998).

The **1857 December 16 Basilicata** earthquake (Ms = 7.0; I_o = X-XI MCS scale; I_o = X–XI ESI) caused extensive damage over an exceptional large area; high values of intensities, X and XI MCS, were observed over an area of 900 km^2, killing about 13,000 people and causing severe damages to man-made works and to the environment.

This event was characterized by multiple main shocks; the second shock, felt two minutes after the first one, with higher energy (Branno et al. 1985). Earthquake-induced environmental effects were recorded over a large area extending from the Vallo di Diano (Campania) to the Val d'Agri (Basilicata).

Primary and secondary geological effects were recognized both in the near and far field. Forty-three landslides phenomena have been localized and classified. The most common slides were rock fall (Atena Lucana, Teggiano, Montesano sulla Marcellana, Grumento Nova, Marsico Vetere) and topless and subordinately rotational slides (Viggiano, Polla), earth flows (Pignola), and slump earth flows (Bella, Muro Lucano), Mallet (1862), Esposito et al. (1998), Porfido et al. (2002).

On **1905 September 8,** a large earthquake (Ms = 7.1; I_o = XI MCS; I_o = X-XI ESI) occurred in the Southern part of the Calabria region. It extensively ruined several villages located in the northern part of the Capo Vaticano peninsula within an area that suffered a MCS intensity greater than IX, causing the death of 557 people. The earthquake was characterized by different epicenters both inland, near to Vibo Valentia, and offshore not far from the coastline, suggesting as capable faults the Vibo and Capo Vaticano normal fault segments (Catalano et al. 2008).

The event induced a great number of effects on the environment in a wide area: large landslides, accompanied by several cracks and fractures and liquefaction features occurred in several places within the epicentral area, hydrological variation (changes in flow and in the temperature of springs and rivers) were also observed over the entire Calabria region both in the near and far field. This event also generated a tsunami that inundated the whole northern coast of the peninsula from Vibo to Tropea with an estimated height of waves of about 1–2 m.

The earthquake triggered at least 40 slides: mainly slump earth flows (Belmonte Calabro, Caraffa di Catanzaro, Cessaniti, Gizzeria, Martirano, Piscopio, Mileto ecc.) and subordinately rock falls (Aiello Calabro, Caulonia, Conidoni, San Leo, Tiriolo, Zungri) (Chiodo and Sorriso-Valvo 2006; Tertulliani and Cucci 2008; Porfido et al. 2011).

The **1908 December 28 Southern Calabria-Messina** earthquake (Ms = 7.2; I_o = XI MCS; I_o = X-XI ESI) is one of the strongest seismic events that struck Italy during the XXth century and the most ruinous in terms of casualties (at least 80,000). The epicenter was located at sea in the Messina Straits. The location of seismogenic fault is still an open issue (Valensise et al. 2008; Aloisi et al. 2009) and therefore the corresponding distance was not evaluated.

The impact of the earthquake was particularly catastrophic in Reggio Calabria and Messina cities, damages have been more intense and widespread along the Calabrian coast, between south of Reggio Calabria and south-west of Scilla (Comerci et al. 2009; Porfido et al. 2011). In Sicily the most damaged area was the coast from its easternmost tip to south of Messina. Some minutes after the earthquake, a destructive tsunami inundated both sides of the Strait, with a run up that rose above 10–13 m.

More than 400 environmental effects were catalogued (Caciagli 2008; Comerci et al. 2009). Among them, particularly relevant were the changes in elevation along both sides of the Strait, partly due to the settlement of loose sediments and artificial filling (e.g., Messina and Reggio Calabria harbor areas), and partly ascribed to landslides and tectonic slip. Portions of the coast were lost, especially on the Calabrian side, most of them eroded by the tsunami. Landslides and rockfalls occurred in many Sicilian and Calabrian localities (especially between Reggio C. and Bagnara C.). A submarine telephone cable between Gallico (Calabria) and Gazzi (Sicily) was cut likely by a slide.

The **1930 July 23 Irpinia** earthquake (Ms = 6.7; I_o = X MCS; I_o = IX-X ESI) occurred in the most seismic part of the Southern Apennines. The earthquake affected a wide area of 36,000 km^2, comprising the regions of Campania, Puglia and Basilicata. The studies of seismically-induced ground effects benefited from numerous historical and scientific sources, and allowed recognition of primary effects (surface faulting), secondary effects (fractures, landslides, settlements, hydrological changes, variations in the chemical and physical activity related to the volcanic and/or thermal zones).

The earthquake caused many sliding phenomena, which mainly affected the rural area and, to a lesser extent, the towns around the epicentral area. At least, 26 landslides were triggered by the earthquake. Large landslides struck Aquilonia (Avellino) and San Giorgio la Molara (Benevento). The former was a reactivation of a slump-earth flow, along the north side of the Rione San Pietro, that forced the abandonment of the entire village (Esposito et al. 2000a). The latter was a 1 km wide and 3 km slump within the Argille Varicolori formation, on the left bank of the Tammaro River, that dammed a short section of the river. Other noteworthy landslides occurred at Ariano Irpino, Vallata, Montecalvo Irpino, Lacedonia, Rocchetta S. Antonio and Acerenza (Esposito et al. 1998; Porfido et al. 2002).

The **1980 November 23** Campania–Basilicata earthquake ($Ms = 6.9$; $I_o = X$ MCS; $I_o = X$ ESI) affected 800 localities over a large area of the Southern Apennines, killing 3,000 people. This event was felt nearly everywhere in the Italian peninsula, from Sicily to Emilia Romagna and Liguria (Postpischl et al. 1985).

The review of more than 100 technical and scientific publications has allowed to locate and classify 200 landslides over a total area of 22,000 km^2. About 47 % of the landslides were rock falls/toppling, 20 % rotational slides, 20 % slump-earthflows, 3 % rapid earth flows, 9 % left undefined (Cotecchia 1986; Esposito et al. 1998; Porfido et al. 2002, 2007). The largest rock falls occurred mostly in the epicentral area, with volumes ranged from 1,000 to 10,000 m^3 as well as slump-earth flow that affected some historical centre in the Apennines. The largest one (23 million m^3) affected Calitri (Avellino) and its recent urban expansion. Even larger were the mudflows at Buoninventre(30 million m^3), near Caposele and Serra d'Acquara, Senerchia (28 million m^3).

The **September–October 1997 Colfiorito** seismic sequence ($Mw = 6.0$; I_o o = VIII-IX MCS; I_o = VIII-IX ESI) struck the Umbria and Marche regions (Central Italy). Three main events occurred on 26 September at 00:33 and 09:40 GMT, and 14 October with magnitude *M*w equal to 5.8, 6.0 and 5.4, respectively; furthermore hundreds of minor but significant events were also recorded. Primary and secondary effects were observed, including surface faulting phenomena, landslides, ground fractures, compaction and various hydrological phenomena.

Landslides, which were the most recurrent among the phenomena induced, consisted mainly of rock falls (Stravignano Bagni, Sorifa, Val Nerina), and subordinately of rotational (Afrile, Foligno, Acciano, Monte d'Annifo), which were generally mobilised by the inertia forces during the seismic motion (Esposito et al. 2000a; Guerrieri et al. 2009; Guzzetti et al. 2009).

On **1998 September 9,** a moderate earthquake ($Mw = 5.7$; I_o = VII MCS; I_o = VIII ESI) hit the Southern Apennines at the NW margin of the Pollino Massif, between Basilicata and Calabria regions. Historical towns, such as Lagonegro, Lauria and Castelluccio suffered significant damage (I = VIII MCS). Several ground effects followed the shock, and a rock fall, far from the epicenter, on the road between Cersuta and Acquafredda claimed one life.

Landslide phenomena consisting in rock fall, toppling, rotational slides and earth slumps were observed in Castelluccio Inferiore and Superiore, Fardella, Lauria, Maratea, Monte Alpi, Nemoli, Noepoli, Rivello, Rotonda, Tortora. Trecchina and Viggianello territories (Michetti et al. 2000).

The **2002 October 31, San Giuliano di Puglia,** earthquake ($Mw = 5.8$; I_o = VII-VIII MCS; I_o = VIII ESI) caused relevant damages to some villages in Southern Molise (San Giuliano di Puglia, Bonefro, Colletorto), including the tragic collapse of a school at San Giuliano that killed 27 children.

Environmental effects (Vittori et al. 2003) included mainly ground cracks, but also slope movements and hydrological anomalies. Seismically induced landslides consisted mainly in rotational slides (e.g. Castellino sul Biferno) but also translational slides even at significant distance from the epicenter (e.g., Salcito). Rock falls were not surveyed in a systematic way.

The **2009 April 6 L'Aquila** earthquake ($Mw = 6.3$; MCS I_o = IX; ESI I_o = IX), which rocked the Abruzzo region, in Central Apennines is part of a seismic sequence active from December 2008 to October 2009. The epicenter for the main shock was located near L'Aquila. Two $M > 5$ aftershocks followed on 7 April (ML 5.3, Mw 5.6, epicenter about 10 km southeast of L'Aquila) and on 9 April (ML 5.1, Mw 5.4, epicenter near Lake Campotosto).

Damages were concentrated on the historical town of L'Aquila which, together with many villages in the surrounding area. The death toll reached 308.

The earthquake produced a widespread set of geological effects on the natural environment. Clear evidence of surface faulting was found along the Paganica fault (Guerrieri et al. 2010; Vittori et al. 2011), and secondary effects have been mapped over an area of about 1000 km^2, mostly gravitational movements and ground fissures, and secondarily liquefactions and hydrological anomalies (Blumetti et al. 2009).

Regarding slope movements, rock falls in calcareous slopes (Fig. 4) and artificial cuts have been the most common type of effect Sliding phenomena have also occurred, threatening in some cases the viability of important roads. The scenario includes also some local peculiar effects, like the ground failures along the shores of the Lake Sinizzo.

Empirical Relationships

Similarly to Keefer (1984), we have measured for each earthquake the maximum distance of coseismic slides and rock falls from either the causative fault and the epicentre (Table 1).

Then, such distances have been plotted versus magnitude and versus ESI epicentral intensity (Figs. 5 and 6) with the aim to find a potential correlation.

Fig. 4 Two rock falls triggered by the 2009 L'Aquila earthquake at San Demetrio ne' Vestini (*above*) and Fossa (*below*)

Table 1 Maximum distances of coseismic rock falls and slides from epicentre and from the fault plane for the 12 earthquakes considered in this study. M_{aw} are from CPTI04

			Rock falls		Slides	
Earthquake	M_{aw}	ESI I_o	Epic	Fault	Epic	Fault
1783.02.05	6,9	X–XI	–	–	13	16
1783.03.28	6,6	X	–	–	70	70
1805.07.26	6,6	X	80	60	100	82
1857.12.16	7	X–XI	86	48	66	30
1905.09.08	7,1	X–XI	49	51	116	115
1908.12.28	7,2	X–XI	36	–	180	–
1930.07.23	6,7	IX–X	15	23	77	52
1980.11.23	6,9	X	50	43	118	97
1997.09.26	6	VIII–IX	25	20	19	15
1998.09.09	5,7	VIII	23	26	16	18
2002.10.31	5,8	VIII	–	–	36	35
2009.04.06	6,3	IX	45	37	46	38

Concerning coherent slides (Fig. 5), a quite good correlation is evident with either magnitude and ESI intensity ($R^2 > 0.8$). In general, these data are quite consistent with the Keefer's envelope (black dashed line in Fig. 5 above), which is based on a global data base. However, substantial deviations (above Keefer's envelope) do exist for some earthquakes (e.g., 1805, 1908, 2002 events).

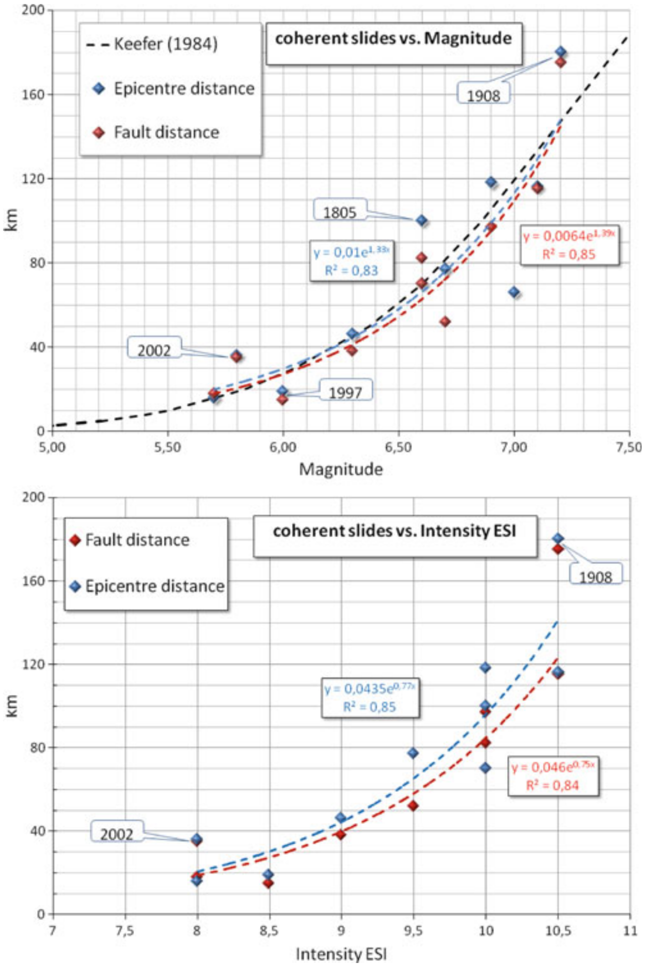

Fig. 5 Relationships between maximum fault distance (in *red*) and epicentral distance (in *blue*) of coseismic coherent slides versus magnitude (*above*) and ESI epicentral intensity (*below*). *Black bold dashed line* in the upper graph is the envelope curve of Keefer (1984)

Instead, rock fall data only show a weak trend (Fig. 6). In our opinion, this is due to the very diverse susceptibility to coseismic rock fall/collapse, which is controlled by precise lithological and morphological factors. Moreover, maximum distances for rock falls are always lower than those typically expected for similar magnitudes (see envelope line of Keefer 1984 in Fig. 6 above). Such evidence points out the incompleteness of collected data, especially for historical earthquakes.

Conclusions

Analysis of distribution of landslides (rock falls and coherent slides), induced by 12 moderate to strong earthquakes occurred in the last three centuries in Central–Southern Apennines, has permitted to investigate the relationship of their maximum distance versus magnitude and ESI epicentral intensity.

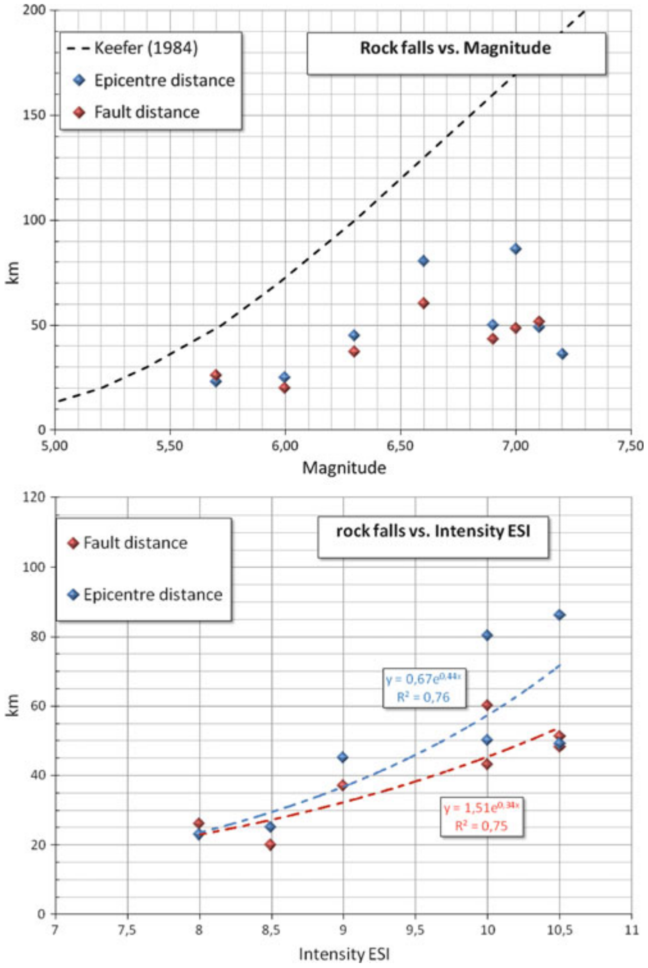

Fig. 6 Maximum fault distance (in *red*) and epicentral distance (in *blue*) of rock falls versus magnitude (*above*) and versus ESI epicentral intensity (*below*). *Bold dashed line* in the upper graph is the envelope curve of Keefer (1984). The point distribution is too scattered here to assess reliable trend lines

For coherent slides, the correlation of magnitude versus distance is fairly good and consistent with global datasets (e.g. Keefer 1984; Rodriguez et al. 1999).

For rock falls, maximum distances increase with magnitude, as expected and commonly observed in earthquakes. However, the correlation is much less evident, most likely influenced by local lithological and morphological factors as well as by the incompleteness of data base.

Moreover, although ESI intensity values are actually discrete categories (not numbers), based on the correlation already established between intensities and magnitudes (e.g., CPTI 2004), we have explored their correlation with maximum distance of rock falls and coherent slides. Resulting correlations seem to be reasonably good, for either coherent slides and rock falls.

Being based only on the effects of earthquakes on the natural environment and independent from seismological parameters or damage-based intensity assessments, we stress here the usefulness of such a tool to define the expected scenario of earthquake-induced landslides, especially in sparsely populated areas or where seismic hazard assessment is based only on pre-instrumental seismicity. However, the data base needs to be improved and enlarged to allow more robust estimates.

References

Aloisi M, Ferranti L, Mattia M, Monaco C (2009) A new analitical approach to the modelling of the 1908 earthquake source (Messina Straits) from the inversion of the 1897/1906-1909 levelling data: comparison with geological data. Riassunti estesi della Sessione 1.1, GNGTS

Blumetti AM, Dramis F, Michetti AM (1993) Fault generated mountain fronts in the Central Apennines (Central Italy): geomorphological features and seismotectonic implications. Earth Surf Process Landf 18:203–223

Blumetti AM, Comerci V, Di Manna P, Guerrieri L, Vittori E (2009) Geological effects induced by the L'Aquila earthquake (6 April 2009; ML_5:8) on the natural environment, Preliminary Report, 38p. http://www.apat.gov.it/site/_files/Inqua/2009_abruzzo_earthquake_report.pdf

Bommer JJ, Rodriguez CE (2002) Earthquake-induced landslides in Central America. Eng Geol 63(3–4):189–220

Branno A, Esposito E, Ferrari G, Maturano A, Porfido S, Rinaldis V, Stucchi M (1985) The Irpinia earthquake of November 23, 1980. In: Postpischl D (ed) Atlas of isoseismal maps of Italian earthquakes, vol 114 (2A), Quaderni de la Ricerca scientifica. Consiglio nazionale delle ricerche, Progetto finalizzato geodinamica, Bologna, pp 152–157

Caciagli M (2008) Le tracce del terremoto del 1908 nell'ambiente naturale. In: Bertolaso G, Boschi E, Guidoboni E, Valensise G (eds) Il terremoto e il maremoto del 28 dicembre 1908: analisi sismologica, impatto, prospettive. DPC – INGV, Roma, pp 197–214

Catalano S, De Guidi C, Monaco C, Tortorici G, Tortorici L (2008) Active faulting and seismicity along the Siculo-Calabrian Rift Zone (Southern Italy). Tectonophysics 453:177–195

Chiodo G, Sorriso-Valvo M (2006) Frane sismo-indotte: casistica e fenomeni innescati dal terremoto dell'8 settembre 1905. In: Guerra I (ed) 8 settembre 1905 – Terremoto in Calabria, Deputazione di Storia Patria della Calabria, Università della Calabria, Regione Calabria, pp 207–224

Comerci V, Blumetti AM, Brustia E, Di Manna P, Esposito E, Fiorenza D, Guerrieri L, Porfido S, Serva L, Vittori E (2009) One century after the 1908 Southern Calabria – Messina earthquake (southern Italy): a review of the geological effects. In: European Geophysical Society (ed) Geophysical Research Abstracts, vol 10, EGU2008-A-00000, 2008. European Geophysical Society, Katlenburg-Lindau

Cotecchia V (1986) Ground deformation and slope instability produced by the earthquake of novembre 1980 in Campani and Basilicata. In: IAEG proceedings international symposium, problems seismic areas, vol 5, Bari, pp 31–100

Cotecchia V, Guerricchio A, Melidoro G (1986) The Geomorphogenetic crisis triggered by the 1783 earthquake in Calabria (Southern Italy). In: Estratto da Proceedings of the international symposium on engineering geology problems in seismic areas, vol 6, Bari

CPTI (2004) Catalogo Parametrico dei Terremoti Italiani Gruppo di Lavoro CPTI. Bologna, http://emidius.mi.ingv.it/CPTI99

D'Agostino, N., A. Avallone, D. Cheloni, E. D'Anastasio, S. Mantenuto, and G. Selvaggi (2008). Active tectonics of the Adriatic region from

GPS and earthquake slip vectors, J. Geophys. Res. 113, no. B12413, doi 10.1029/2008JB005860.

Demangeot, J. (1965). Géomorphologie des Abruzzes Adriatiques. Mémoires et documents, Editions du Center National de la Recherche Scientifique, Paris, 403pp

Devoti R, Riguzzi F, Cuffaro M, Doglioni C (2008) New GPS constraints on the kinematics of the Apennines subduction, Earth Planet. Sci Lett 273:163–174. doi:10.1016/j.epsl.2008.06.031

Esposito E, Porfido S (2010) Gli effetti cosismici sull'ambiente fisico per la valutazione della vulnerabilità del territorio. In: Gizzi FT, Masini N (eds) Dalle Fonti all'Evento. Percorsi strumenti e metodi per l'analisi del terremoto del 23 luglio 1930 nell'area del Vulture. EESI, Napoli, pp 129–142. ISBN 978-88-495-2050-7

Esposito E, Luongo G, Marturano A, Porfido S (1987) Il Terremoto di S. Anna del 26 luglio 1805. Mem Soc Geol It 37:171–191

Esposito E, Gargiulo A, Iaccarino G, Porfido S (1998) Distribuzione dei fenomeni franosi riattivati dai terremoti dell'Appennino meridionale. Censimento delle frane del terremoto del 1980. In: Proceedings conversion international prevention of hydrogeological hazards: the role of scientific research, Alba, vol. 1, CNR-IRPI, pp 409–429

Esposito E, Porfido S, Simonelli AL, Mastrolorenzo G, Iaccarino G (2000a) Landslides and other surface effects induced by the 1997 Umbria-Marche seismic sequence. Eng Geol 58:353–376

Esposito E, Porfido S, Iaccarino G, Tranfaglia G (2000) Terremoti e centri storici dell'Irpinia: gli effetti del terremoto del 1930. In: Proceedings GeoBen 2000, CNR-GNDCI 2133, Torino, pp 477–484

Esposito E, Pece R, Porfido S, Tranfaglia G (2001) Hydrological anomalies connected to earthquakes in Southern Apennines (Italy). Nat Hazard Earth Syst Sci, EGS 1:137–144

Esposito E, Pece R, Porfido S, Tranfaglia G (2009) Ground effects and hydrological changes in the Southern Apennines (Italy) in response to the 23 July 1930 earthquake (MS=6.7). Nat Hazard Earth Syst Sci 9:539–550

Guerrieri L, Tatevossian R, Vittori E, Comerci V, Esposito E, Michetti AM, Porfido S, Serva L (2007) Earthquake environmental effects (EEE) and intensity assessment: the inqua scale project. Boll Soc Geol Italiana 126:375–386

Guerrieri L, Blumetti AM, Esposito E, Michetti AM, Porfido S, Serva L, Tondi E, Vittori E (2009) Capable faulting, environmental effects and seismic landscape in the area affected by the Umbria-Marche (Central Italy) seismic sequence. Tectonophysics. doi:10.1016/j.tecto.2008.10.034

Guerrieri L, Baer G, Hamiel Y, Amit R, Blumetti AM, Comerci V, di Manna P, Michetti AM, Salamon A, Mushkin A, Sileo G, Vittori E (2010) InSAR data as a field guide for mapping minor earthquake surface ruptures: Ground displacements along the Paganica Fault during the 6 April 2009 L'Aquila earthquake. J Geophys Res 115: B12331. doi:10.1029/2010JB007579

Guidoboni E, Ferrari G, Mariotti D, Comastri A, Tarabusi G, Valensise G (2007) CFTI4Med, catalogue of strong earthquakes in Italy (461 B.C.–1997) and Mediterranean area (760 B.C.–1500). http://storing.ingv.it/cfti4med/

Guzzetti F, Esposito E, Balducci V, Porfido S, Cardinali M, Violante C, Fiorucci F, Sacchi M, Ardizzone F, Mondini A, Reichenbach P, Rossi M (2009) Central Italy seismic sequence-induced landsliding: 1997–1998 Umbria-Marche and 2008–2009 L'Aquila Cases. In: Proceedings of the next generation of research on earthquake-induced landslides: an international conference in Commemoration of 10th anniversary of the Chi-Chi earthquake, Taiwan, pp 52–61

Keefer DK (1984) Landslides caused by earthquakes. Bull Geol Soc Am 95:406–421

Mallet R. (1862) Great Neapolitan earthquake of 1857. The first principles of observational seismology, Chapman and Hall, London, 1862, 2 vols

Michetti AM, Ferreli L, Esposito E, Porfido S, Blumetti AM, Vittori E, Serva L, Roberts GP (2000) Ground effects during the 9 September 1998, Mw = 5.6 Lauria earthquake and the seismic potential of the "Aseismic" Pollino region in Southern Italy. Seismol Res Lett 71:31–46

Michetti AM, Esposito E, Guerrieri L, Porfido S, Serva L, Tatevossian R, Vittori E, Audemard F, Azuma T, Clague J, Comerci V, Gurpinar A, McCalpin J, Mohammadioun B, Morner NA, Ota Y, Roghozin E (2007) Intensity scale ESI 2007. In: Guerrieri L, Vittori E (eds) Memorie descrittive carta geologica d'Italia, vol 74. APAT, Servizio Geologico d'Italia–Dipartimento Difesa del Suolo, Roma, p 53

Papadopoulos GA, Plessa A (2000) Magnitude–distance relations for earthquake-induced landslides in Greece. Eng Geol 58(3–4):377–386

Patacca E, Sartori R, Scandone P (1990) Tyrrhenian basin and Apenninic arcs. Kinematic relations since late Tortonian times. Mem Soc Geol Italiana 45:425–451

Porfido S, Esposito E, Vittori E, Tranfaglia G, Michetti AM, BlumettI AM, Ferreli L, GuerrierI L, Serva L (2002) Areal distribution of ground effects induced by strong earthquakes in the southern Apennines (Italy). Surv Geophys 23:529–562

Porfido S, Esposito E, Vittori E, Tranfaglia G, Guerrieri L, Pece R (2007) Seismically induced ground effects of the 1805, 1930 and 1980 earthquakes in the Southern Apennines (Italy). Boll Soc Geol Italy (Italy J Geosci) 126(2):333–346

Porfido S, Esposito E, Molisso F, Sacchi M, Violante C (2011) Earthquake-induced environmental effects in coastal area : some example in Calabria and Sicily (Southern Italy). Marine reSEArch@CNR.it (in press)

Postpischl D, Branno A, Esposito E, Ferrari G, Maturano A, Porfido S, Rinaldis V, Stucchi M (1985) The Irpinia earthquake of November 23, 1980. In: Postpischi D (ed) Atlas of isoseismal maps of Italian earthquakes, vol 114 (2A). CNR-PFG, Bologna, pp 152–157

Prestininzi A, Romeo R (2000) Earthquake-induced ground failures in Italy. Eng Geol 58(3–4):387–397

Roberts GP, Michetti AM (2004) Spatial and temporal variations in growth rates along active normal fault systems: an example from the Lazio-Abruzzo Apennines, central Italy. J Struct Geol 26:339–376. doi:10.1016/S0191-8141(03)00103-2

Rodriguez CE, Bommer JJ, Chandler RJ (1999) Earthquake induced landslides: 1980–1997. Soil Dyn Earthq Eng 18(1999):325–346

Sarconi M (1784) Istoria dè fenomeni del tremoto avvenuto nelle Calabrie, e nel Valdemone nell'anno 1783 posta in luce dalla Reale Accademia delle Scienze, e delle Belle Lettere di Napoli – G. Campo, Napoli. Ristampa anastatica presso M. Giuditta Editore, Catanzaro, 1983

Serva L, Esposito E, Guerrieri L, Porfido S, Vittori E, Comerci V (2007) Environmental effects from five hystorical earthquakes in Southern Apennines (Italy) and macroseismic intensity assessment: contribution to INQUA EEE scale project. Q Int 173–17:30–44

Silva PG, Rodríguez Pascua MA, Pérez-López R, Bardaji T, Lario J, Alfaro P, Martínez-Díaz JJ, Reicherter K, Giménez García J, Giner J, Azañón JM, Goy JL, Zazo C (2008) Catalogacion de los efectos geologicos y ambientales de los terremotos en Espana en la Escala ESI 2007 y su aplicacion a los estudions paleosismologicos. Geotemas 6:1063–1066

Tertulliani A, Cucci L (2008) Fenomeni associati al terremoto della Calabria dell'8 settembre 1905. Quaderni di Geofisica 60:4–17

Valensise G, Basili R, Burrato P (2008) La sorgente del terremoto del 1908 nel quadro sismo tettonico dello Stretto di Messina. In: Bertolaso G, Boschi E, Guidoboni E, Valensise G (eds) Il terremoto e il maremoto del 28 dicembre 1908: analisi sismologica, impatto, prospettive. INGV-DPC, Roma, pp 161–182

Vittori E, Deiana G, Esposito E, Ferreli L, Marchegiani G, Mastrolorenzo G, Michetti AM, Porfido S, Serva L, Simonelli AL, Tondi E (2000) Ground effects and surface faulting in the September-October 1997 Umbria-Marche (Central-Italy) seismic sequence. J Geodyn 29:535–564

Vittori E, Comerci V, Guarneri E, Guerrieri L, Ligato D (2003) I terremoti del 31 ottobre e 1 novembre 2002 nel Molise orientale. In: Le attività APAT a seguito di emergenze alluvionali e sismiche (Settembre 2002- Gennaio 2003). APAT, Serie Rapporti 35/2003, 180pp

Vittori E, Di Manna P, Blumetti AM, Comerci V, Guerrieri L, Esposito E, Michetti AM, Porfido S, Piccardi L, Roberts GP, Berlusconi A, Livio F, Sileo G, Wilkinson M, McCaffrey K, Phillips RJ, Cowie PA (2011) Surface Faulting of the 6 April 2009 Mw 6.3 L'Aquila Earthquake in Central Italy. Bull Seismol Soc Am 101(4). doi:10.1785/0120100140

Slope Stability of Continental Megalandslides

Nguyen Anh Tuan, José Darrozes, Jean-Claude Soula, Marianne Saillard,
Frédéric Christophoul, Nicole Guerrero, and Pierre Courjeault-Radé

Abstract

Continental megalandslides, although rare, are found in various morphological settings including mountain fronts and valley sides with steep ($> 30°$) to shallow ($<3°$) slopes, under climates varying from high-precipitation temperate to hyperarid, and are associated with poorly active tectonics as well as hyper-active tectonics with frequent and very high-magnitude ($\geq$ Mw 8) earthquakes. All but one (Mayunmarca, 25 April 1974) are pre-historic with ages ranging from 3.5 Ma to 9 ky BP.

Static and dynamic slope stability analyses show that in all cases the slope will remain stable when using values of effective cohesion and angle of internal friction for hard rocks. It appears that the studied megalandslides could not have formed without the presence of accurately oriented pre-existing discontinuities, including bedding, tectonic fractures, foliation and intrusive contacts. With such discontinuities being present, steep-sloping megalandslides may have formed with no help of seismic shaking. In any case, three of the four studied shallow-sloping megalandslides require high to very high magnitude earthquakes.

The large discrepancies between the Arias intensities predicted by the different attenuations relationships established when passing from moderate/high magnitude domains to very high magnitude domains show that megalandslides could hardly be used as paleomagnitude indicators.

Keywords

Megalandslides stability analyses earthquakes paleo magnitude

Introduction

The largest non-volcanic sub-aerial landslide observed by eye witnesses is the 25-4-1974 Mayunmarca event involving a rock volume of 1 km^3 (Kojan and Hutchinson 1978). The greatest of the non-volcanic continental megalandslides is the early Pleistocene Baga Bogd (60 km^3, Philip and Ritz 1999). Only 12 of the yet known megalandslides (e.g. Hayashi and Self 1992, their table 1, and refs in Table 1) (see location in Fig. 1) have been studied in detail (Table 1). These include (1) steep-sloping megalandslides formed on steep-sloping (20–35°) valley sides or valley heads and affecting silicic rocks (augengneisses, migmatites, granitoids, and hard sandstones); (2) Shallow-sloping megalandslides formed on shallow-sloping ($<8°$) mountain fronts or valley sides made up of ductile but cohesive rocks (more or less altered ignimbrites, poorly cemented clastic rocks); (3) Megalandslides with intermediate slope (10–25°) formed on slopes of a valley side or on the flank of an ancient volcano.

N.A. Tuan (✉) • J. Darrozes • J.-C. Soula • F. Christophoul •
N. Guerrero • P. Courjeault-Radé
Géosciences, environnement, Toulouse (OMP, CNRS, UPS),
14 avenue Edouard Belin, 31400 Toulouse, France
e-mail: Nguyen@lmtg.obs-mip.fr

M. Saillard
Université Nice Sophia Antipolis, 28, avenue Valrose, B.P. 2135,
06103 Nice Cédex 2, France

C. Margottini et al. (eds.), *Landslide Science and Practice*, Vol. 5,
DOI 10.1007/978-3-642-31427-8_39, © Springer-Verlag Berlin Heidelberg 2013

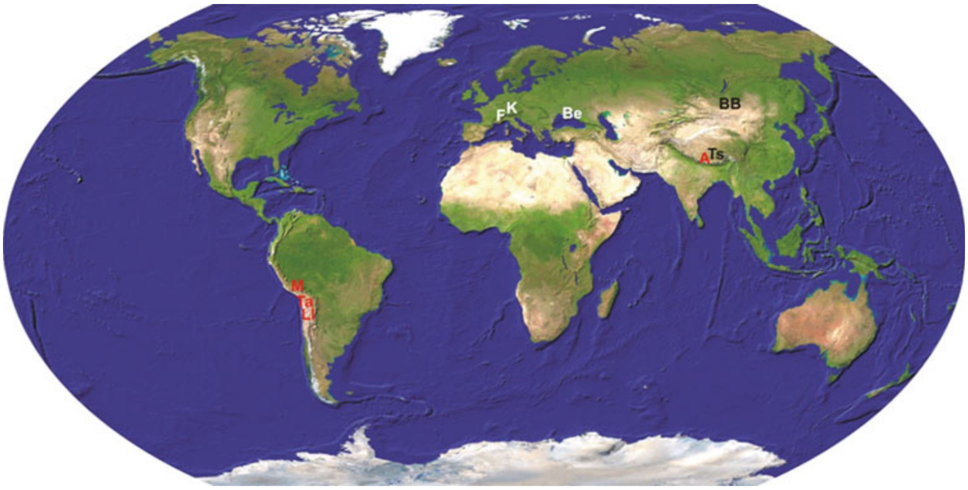

Fig. 1 Location of the studied megalandslides. A: Anapurnas (Braga, Dukhur Pokhari, Kalopani, Latamrang); BB: Baba Bogd; Be: Belbek; F: Flims; K: Köfels; Ll: Lluta; M: Mayunmarca; Ta: Tarapaca; Ts: Tsergo Ri

These landslides will be investigated by means of static and dynamic slope-stability analyses using mechanical parameters (effective cohesion and angle of internal friction) for hard (non-fractured) rocks and those for pre-existing discontinuities likely present in the rock mass (Table 1). Dynamic stability analyses include back calculations of threshold shaking intensities to establish a lower bound magnitude to the triggering earthquake. These calculations involve empirical or semi-empirical attenuations relationships for predicting Arias intensity as a function of earthquake magnitude, distance to source (and eventually focal depth), sites conditions and style of faulting (Wilson and Keefer 1985; Campbell 1989; Sabetta and Pugliese 1996; Del Gaudio et al. 2003; Travasarou et al. 2003; Stafford et al. 2009). The present study is also aimed at checking the pertinence of extending landslide hazard prediction methods based on those attenuation relationships established in moderate/high magnitude domains to isolated events in very high magnitude domains.

Static Slope-Stability Analysis

Practically all the studied megalandslides (except Thames Township and Belbek) can be analyzed using the simplest model of an infinite slope (planar slip surface parallel to the slope). The assumption of infinite slope failure is valid if (1) the landslide mass is thin compared to its length; (2) the failure surface is parallel to the ground surface; (3) failure occurs as basal sliding. In these conditions, the static factor of safety can be expressed as:

$$FS = \frac{c'}{\gamma H \cos\alpha \; \sin\alpha} + \left(1 - m\frac{\gamma_w}{\gamma}\right)\frac{\tan\varphi'}{\tan\alpha} \qquad (1)$$

where c' is the effective cohesion, φ' is the effective angle of internal friction, γ is the material unit weight, γ_w is the unit weight of water, α is the angle of the slope from the horizontal, H is the vertical depth of the failure surface and m is a ratio of H indicating the height of the ground water table. Water pressure is expressed as the relative height of the ground water table m which in general varies from 0 to 1. The slope is stable for FS > 1.5; unstable for $1 >$ FS ≥ 1.5; and sliding occurs for FS ≤ 1.

Dynamic Slope-Stability Analyses in Case of Earthquake Shaking

Dynamic slope-stability analysis can be used to estimate the minimum shaking conditions required to cause failure. When the earthquake acceleration time-history is unknown as for the paleo-landslides, back calculations of threshold shaking intensities can be used to establish a lower bound magnitude to the triggering earthquake (Jibson and Keefer 1993; Del Gaudio et al. 2003; Del Gaudio and Wasowski 2004; Jibson 1993; Jibson et al. 1998; Romeo 2000). In the popular Newmark's (1965) approach the slope-parallel critical acceleration required to overcome the shear resistance (a_{cN}) of the block has been defined as a simple function of the static factor of safety and the landslide geometry. In Inglès et al.'s (2005) generalized approach, the ratio of vertical to horizontal components of seismic acceleration $k_I = a_{\mathrm{Sv}}/a_{\mathrm{Sh}}$ depends on the seismic situation of the selected slope. These calculations involve attenuation relationships for Arias intensity.

Attenuation Relationships for Arias Intensity

Several empirical or semi-empirical attenuations relationships for predicting Arias intensity in terms of magnitude, source-distance, sites conditions and style of faulting have been developed (Wilson and Keefer 1985; Campbell 1989; Sabetta and Pugliese 1996; Del Gaudio et al. 2003; Travasarou et al. 2003; Stafford et al. 2009). If the critical

Table 1-a Static and dynamic slope-stability analyses of the megalandslides. Landslides characteristics after: 1: Brückl 2001; 2: Brückl and Parotidis 2005; 3: Darrozes et al. 2002, 2007; 4 : Fort 2000; 6: Hermanns et al. 2006; 7: Hewitt 1998; 8: Ibetsberger 1996; 9: Ivy-Ochs et al. 1998; 10: Ivy-Ochs et al., 2009b; 11: Kojan and Hutchinson 1978; 12: Moon and Simpson 2002; 13; Pánek et al. 2008; 14: Philip and Ritz 1999; 15: Pollet 2004; 16: Pollet et al. 2005; 17: Poschinger et al. 2006; 18: Schramm et al. 1998; 19: Sörensen and Bauer 2003; 20: Stässer and Schlunegger 2005; 21: Weidinger 2006; 22: Weidinger et al. 1996. Mechanical parameters: (23) Hoek and Bray 1981; (24) Barton 1973; (25) FE simulation, Brückl and Parotidis 2005; (26) Voight 1978

Landslide	Vol (km^3)	Rock type	H (m)	slope (°)	ϕ' (°) €	c' (kPa)	m	FS	D_c (cm)	a_{Shc}	M at 20 km			
											D G I	DG	W&K	WKI
Steep-sloping megalandslides														
Kalopani, Anapurnas (21, 4)	3	Hard rocks (23, 24)	1,000	17	35	35,000	1	6,22	5	1	8,72	9	8,4	8,19
							0,5	6,66		1,1	8,77	9	8,5	8,23
GNEISSES					45	55,000	1	9,58		1,3	8,91	9,3	8,7	8,35
Translational rockslide and rock avalanche							0,5	10,2		1,4	8,96	9,4	8,7	8,39
Failure parallel to foliation		Clay filled faults (23,24)			24	0	1	0,9	10	−0	0	0	0	0
							0,5	1,18		0	6,6	6,7	6,5	6,4
							0,25	1,32		0,1	7	7,1	6,8	6,7
		Shear zones in granite (23, 24)			45	240	1	2,05	10	0,2	7,5	7,9	7,5	7,1
							0,5	2,67		0,3	7,8	8,2	7,8	7,4
Braga, Anapurnas (21)	~5		200	20	35	20,000	1	13,2	5	2,8	9,4	9,6	9	8,8
		Hard rocks(23)			45		1	13,7		2,3	9,3	9,7	9	8,7
		Hard rocks (24)			25		1	12,8		3,4	9,5	9,6	9	8,9
		Clay filling (23, 24)			13,5	100	1	0,47	5	−0				
							0,5	0,59		−0				
LIMESTONES							0,25	0,66		−0				
Translational rockslide		Thin clay filling (23, 24)			19	50	1	0,61		−0				
							0,25	0,88		−0				
						200	1	0,7		−0				
							0,25	0,97		−0				
		Marlaceous joints (23, 24)			25	0	1	0,79	10	−0				
							0,25	1,16	10	0,1	6,8	7	6,7	6,6
Dukhur Pokhari	1	Hard rocks (24)	500	26,5	35	20,000	1	4,59	5	1,2	8,8	9	8,5	8,3
Anapurnas (21)					45		1	4,97	5	1	8,7	9,1	8,5	8,2
					25		1	4,29	5	1,4	8,9	9	8,4	8,4
LIMESTONES		Clay filling (23,24)			13,5	100	0,25	0,45	10	−0				
AND SCHISTS		Thin clay filling (g = 25)			19	50	0,25	0,63		−0				
		(23,24)				200		0,66		−0				
		Marlaceous joints (23,24)			25	0	0,25	0,85		−0				
Latamrang, Anapurnas (21)	~5	Hard rocks (23)	700	26	35	35,000	1	5,6	5	1,5	9	9,2	8,6	8,4
					45			5,99		1,3	8,9	9,2	8,6	8,3
		Shear zones in granites (23,24)				240	0,25	1,89	5	0,2	7,7	8,1	7,6	7,3
GNEISSES, QUARTZITES							0,5	1,7		0,2	7,5	7,9	7,5	7,2
Rockslide and rock avalanche							0,75	1,51		0,1	7,3	7,7	7,3	7
							1	1,32		0,1	7	7,4	7	6,7
				Sliding			Unstable				Stable		Irremovable	

Table 1-b Static and dynamic slope-stability analyses of the megalandslides

Landslide	Vol (km^3)	Rock type	H (m)	slope (°)	ϕ' (°) €	c' (kPa)	m	FS	D_c (cm)	a_{Shc}	M at 20 km			
											D G I	DG	W&K	WKI
Tsergo Ri Himalayas (8,18,22)	10	Hard rocks (23)	750	26	35	35,000	1	5,29	5	1,4	8,9	9,1	8,6	8,4
LEUCOGRANITES Rapid rock block slide Failure filled with weathered or deposits		Shear zones in granites (23)			45	240	1	1,32		1,2	7	7,4	7	6,7
					24		1	0,6		−0				
					45	0	1	1,29		0,1	6,9	7,3	6,9	6,6
							0,25	1,86		0,2	7,7	8	7,6	7,3
					24		0,5	0,74		−0				
							0,25	0,82		−0				
Flims,Swiss Alps (15, 16, 17, 10)	12	Hard rocks (23, 24)	500	13	35	20,000	1	4,66	5	1,1	8,8	9	8,5	8,2
		Clay filling (23, 24)			13,5	100	0,25	0,97		−0				
LIMESTONES		Thin clay filling (g = 25) (23, 24)			19	50		1,37		0,1	7	7,1	6,8	6,7
Rapid block slide						200		1,42		0,1	7	7,2	6,8	6,7
Rock slolution along bedding		Marlaceous joints (23, 24)			25	0		1,83		0,1	7,4	7,6	7,2	7,1
							1	1,24		0	6,6	6,8	6,5	6,4
Köfels, Austrian Alps (19, 15, 6)	3	Shear zones in granites (23)	500	26	45	240	1	1,31		0,1	7	7,4	7	6,7
GNEISSES							0,5	1,71		0,2	7,5	7,9	7,5	7,2
Rapid block slide					25		0,5	0,82		−0				
Shear planes parallel to foliation							0,25	0,91		−0				
					35		0,25	1,34		0,1	7,2	7,5	7,1	6,9
							0,5	1,21		0,1	6,9	7,1	6,8	6,6
							1	0,93		−0				
					45	0	0,25	1,86		0,2	7,7	8	7,6	7,3
					25			0,87		−0				
Köfels, Austrian Alps	3	*Brückl and Parotidis* 2005 *(simulation)*			*28*	*2,100*	1	1,08		0	6,39	6,5	6,3	6,2
GNEISSES (1, 2)							0,5	1,29		0,1	7,2	7,3	7	6,9
Penetrative creep					*35*		0,5	1,6		0,2	7,6	7,8	7,4	7,2
Mayunmarca	1	Hard rocks (26)	1,900	22?	35	15,000	1	1,94	10	0,2	7,9	8,2	7,8	7,6
					45		1	2,4		0,3	8	8,5	8	7,7
Peruvian Andes (11)					45		0,5	2,87		0,4	8,2	8,6	8,2	7,8
HARD SANDSTONES		Thick clay filling in schists and quartzites	1,900	22	32	80	1	0,96	10	−0				
Rockslide/débris flow							0,7	1,13		0	6,7	6,9	6,7	6,5

Sit/clay interbeds		Bedding thin clay (23, 24)			41	740	1	1,37		0,1	7,2	7,6	7,2	7
							0,7	1,62		0,1	7,6	7,9	7,5	7,2
							0,5	1,78		0,2	7,7	8,1	7,7	7,4
		Bedding thick clay (23, 24)			31	380	1	0,94		−0				
							0,7	1,11		0	6,6	6,8	6,6	6,4
							0,5	1,22		0,1	7,1	7,2	7	6,8
							0,25	1,37		0,1	7,4	7,6	7,2	7,1
Shallow-sloping megalandslides														
Belbek	12	Various clays (23)	90	7	8	0	1	0,7		−0				
Crimean Mountains (13)							0,7	0,84		−0				
							0,5	0,92		−0				
CLAYS							0,25	1,03		0	5,2	5,3	5,3	5,2
Soil/rock spreading and multiple slumps					19	270	1	2,68		0,2	7,7	7,8	7,5	7,3
							0,7	3		0,2	7,8	8	7,6	7,4
							0,5	3,22		0,2	7,9	8	7,6	7,5
Baga Bogd, Altai, Mongolia (14)	60	Soft sedimentary rocks (23)	400	3	25	1,000	0,5	9,03		0,3	8,1	8,3	7,9	7,7
						150	0,5	7,46		0,2	7,9	8,2	7,8	7,6
SANDSTONES AND SILTS					35	1,000	0,5	12,6		0,4	8,2	8,6	8,1	7,8
Soil block slide Basal evaporite layer		Mixed-grained glacial tills (23)			25	250		7,65		0,2	7,9	8,2	7,8	7,6
						150		7,46		0,2	7,9	8,2	7,8	7,6
TarapacaN Chile (3)	4		200	7,5	25	30	0,5	2,91		0,2	7,7	8	7,6	7,4
“IGNIMBRITES” Soil block slide Basal altered layer					50			7,36		0,4	8,2	8,8	8,3	7,8
					25	100		3,01		0,2	7,8	8	7,6	7,4
					50			7,46		0,4	8,2	8,8	8,3	7,8
Lluta, SW Peru (20)	26		600	3	25	30	0,5	7,22		0,2	7,9	8,1	7,7	7,5
VOLCANICLASTICS Soil block slide Basal altered layer			300					7,26		0,2	7,9	8,1	7,7	7,5
				Sliding			Unstable			Stable			Irremovable	

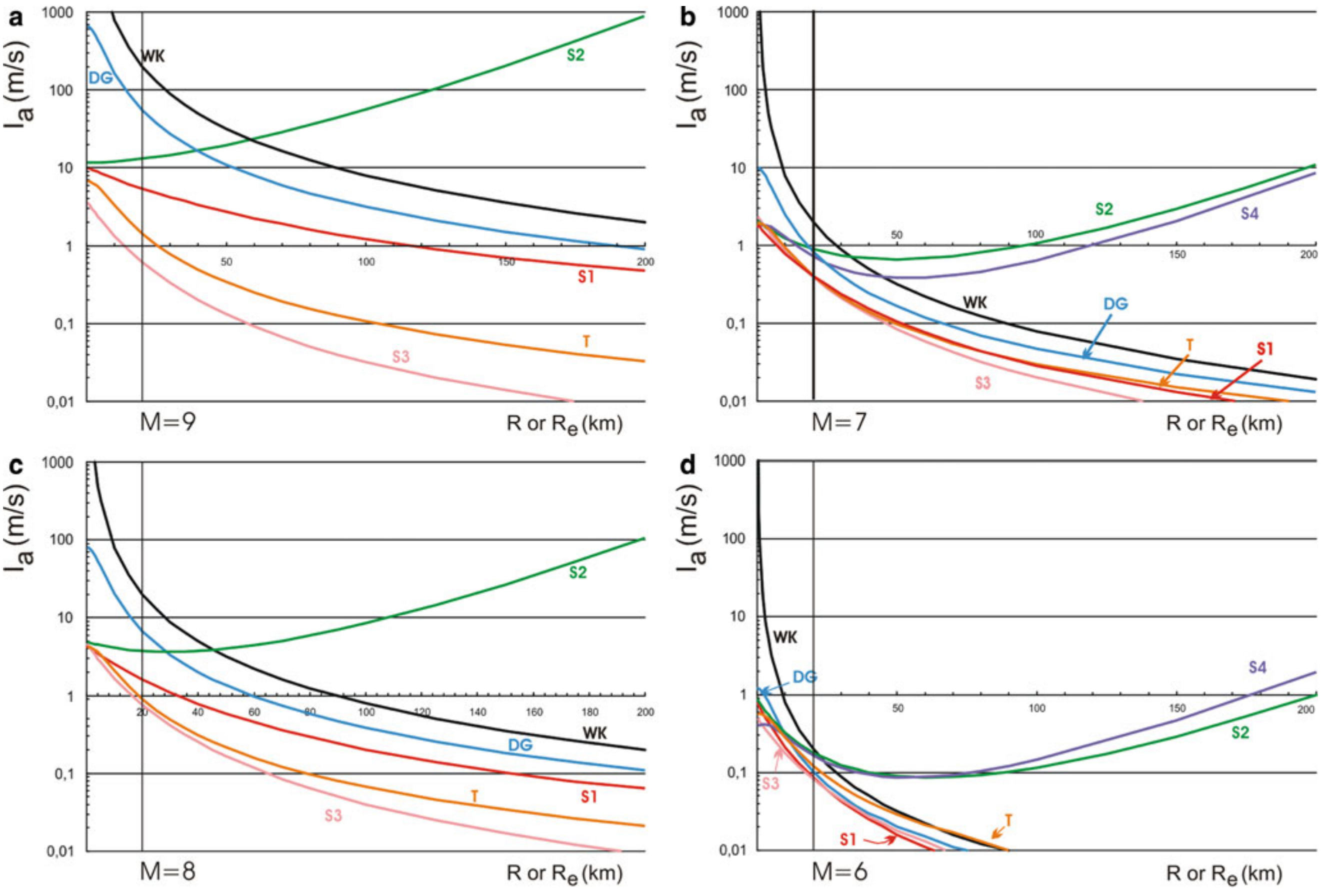

Fig. 2 Arias intensity as a function of distance-to-source (R) or epicentral distance (R_e). DG: Del Gaudio et al. (2003); S1, S2; S3; S4: Stafford et al.'s (2009) models 1, 2, 3, 4; T: Travasarou et al. (2003); WK: Wilson and Keefer (1985)

acceleration can be determined and a critical displacement estimated (Wieczorek et al. 1985; Jibson and Keefer 1993), these relations could be used to estimate the threshold Arias intensity required to initiate failure.

Using these relations for paleo-megalandslides leads to outpace the ranges of magnitude and focal depths of the datasets used to establish these models. Figure 2 shows that I_a-R and R_e curves given by most of the models are rather consistent for magnitudes *M6* and *M7*, but considerable differences appear for magnitudes *M8* and *M9* even in the ranges of focal depths ($Z < 20$) and source to site distance ($R < 250$ km) envisaged by the authors. A special difficulty arises with Stafford and al.'s models 2 and 4 which show I_a increasing with increasing R to values greater that those near the source (Fig. 2a, b, c).

Case Studies of Megalandslides

The characteristics of the megalandslides yet studied are shown in table 1 with references to publications dealing with them. Except the Thames Township landslide for which a best fit circular large-radius and shallow basal surface has been calculated, all the megalandslides studied in detail obey Skempton and Hutchinson's (1969) criterion of translational sliding (ratio thickness/length <0.15). In all the regions where the megalandslides occurred, the precipitations are presently moderate (650–1,000 mm yr^{-1}) to hyper arid. For Tarapaca and Lluta, and probably Baga Bogd the climate remained arid to hyper arid all along the late Cenozoic (Alpers and Brimhall 1988; Gregory-Wodzicki 2000). In contrast, the climate had varied during the Pleistocene and the Holocene when the other megalandslides formed (see e.g. van Husen 1997; Ivy-Ochs et al. 1998, 2009a, b; Magny et al. 2001; Vollweiler et al. 2006). Only 4 of the megalandslides have been dated: Belbeck at 15 ^{14}C kyr BP (~18.5–18.1 cal kyr BP, Pánek et al. 2008), Köfels at 9800 cal years BP (Kubik et al. 1998), Flims at 8,900 cal years BP (Poschinger et al. 2006; Ivy-Ochs et al. 2009a, b), Braga at ~5.4 cal yr BP (Weidinger 2006) and can be shown to have formed in various conditions of temperature and precipitations. It is in any case impossible to know if they formed or not during unusual high precipitations, or unusually long periods of precipitation. The unique example actually observed, the Mayunmarca megalandslide, formed under no particular precipitation conditions. Several *m* values were thus checked in each case (Table 1).

Static Slope Stability Analyses

The principal results of these analyses are the following:

1. In all cases the slope will remain stable when using values for hard (non-fractured) rocks. Among the shallow-sloping megalandslides, only Belbek may be unstable in non-seismic conditions and this only if assuming no cohesion.
2. Steep-sloping megalandslides are unstable if assuming the presence of through-going pre-existing discontinuities (tectonic fractures, bedding, foliation) with low or no cohesion.
3. Increasing the factor *m* (relative height of the water table) reduces the stability but even for steep-sloping megalandslides generates instability only when discontinuities are present.

Seismic Shaking

In Table 1, possible seismic shaking was evaluated on the bases of Jibson et al.'s (1998) and Wilson and Keefer's (1985), and Del Gaudio et al.'s (2003) expressions for critical displacement and attenuation relationship. In either case, the equation for the cumulative displacement was modified using Inglès et al.'s (2005) horizontal critical acceleration a_{Shc} instead of Newmark's critical acceleration a_{cN} . Earthquake magnitude M was estimated for a source distance R or R_e of 20 km. M at 20 km vanishes where static slope-stability analysis predicts sliding (FS and thus a_c or $a_{Shc} \leq 0$) and takes very high values where static slope-stability analysis predicts stability. More surprisingly, values of M at 20 km are rather high where static slope-stability analysis predicts instability.

Discussion and Conclusion

In the Altai Mountains (Baga Bogd) or the western Andes (Tarapaca, Lluta), values of M 7.7 to M 8.8 would be required to trigger sliding. In these areas, such values are not unreasonable as $M > 8$ events were recorded in the recent past (Pritchard et al. 2002; Florensov and Solonenko, 1963 in Philip and Ritz 1999; Okal 1976; Kanamori 1977).

In the case of hard-rock steep-sloping Himalayan and Alpine megalandslides, the analyses predict high or very high M values if c' and φ' values for non-fractured hard rocks are used. These predicted M values are much higher than those recorded in the area. The presence of low cohesion discontinuities or deep-penetrating alteration (e.g. Thames township, Moon and Simpson 2002) is thus needed for landsliding to occur (Table 1). These discontinuities might be bedding (e.g. silt-clay interbeds at Mayunmarca, Kojan and Hutchinson 1978; fine-grained interbeds at Flims, Pollet 2004; Pollet et al. 2005; Poschinger et al. 2006), foliation-parallel shear planes at Köfels (Pollet 2004), Braga (Fort 2000; Weidinger 2006) and Tsergo Ri (Weidinger et al. 1996), magmatic contact marked by altered sulfidic ore deposits at Tsergo Ri (Weidinger et al. 1996; Schramm et al. 1998). Low cohesion along fractures or bedding may be due to tectonic crushing (low temperature cataclasites) facilitating subsequent water penetration (seepage) with alteration of feldspars and ferro-magnesian minerals and sulfidic mineralization in magmatic rocks, and decarbonatation in limestones. According to the rock type, sliding can be localized along a single surface (basal failure in most cases) or distributed in the whole rock mass (e.g. Flims, Pollet et al. 2005)

In shallow-sloping megalandslides, a ductile layer (evaporites at Baga Bogd, altered ignimbrite at Tarapaca and Lluta, thick clay bed at Belbek) is present at the base of the slide mass. This layer was able to store water even in the arid or hyper arid environment in which these landslides formed.

In another ground, our study emphasizes the large discrepancies between Arias intensities in very high magnitude domains (Fig. 2a, b). This problem of extending regional landslide hazard prediction methods established – and successfully applied – in moderate to high magnitude domains to isolated events in very high magnitude domains is also underlined by the high values of M at 20 km where static slope stability analysis predicts instability.

Applied to megalandslides back calculations of a lower bound magnitude to the triggering earthquake can be used to establish whether a high or very high magnitude earthquake is required but not to estimate accurately this magnitude.

References

Alpers CN, Brimhall GH (1988) Middle Miocene climatic change in the Atacama Desert, northern Chile: evidence from supergene mineralization at La Escondida. Geol Soc Am Bull 100:1640–1656

Barton N (1973) A review of the shear strength of filled discontinuities in rocks. Fjellspregningsteknikk, Bergmekanikk, Oslo, Tapir Press, Trondheim, pp 19.1–19.38

Brückl EP (2001) Cause-effect models of large landslides. Nat Hazards 23:291–314

Brückl E, Parotidis M (2005) Prediction of slope instabilities due to deep-seated gravitational creep. Nat Hazards Earth Syst Sci 5:155–172

Campbell KW (1989) Empirical prediction of near-source ground motion for the Diablo Canyon power plant site, San Luis Obispo

County, California. US Geological survey, open-file report. pp 89–484

Darrozes J, Pinto L, Inglès J, Soula JC, Maire E, Courjault-Radé P, Hérail G (2002) Origin of the paleolandslide of Tarapaca (North Chile, Andean belt). Geophysical research abstract (Abstract EGS02-A-03 136)

Darrozes J, Soula JC, Inglès J, Riquelme R (2007) From paleo to possible present-day large-scale landslide. A generalized Newmark approach of the Tarapaca Landslide (northern Chile). 4th International conference on earthquake geotechnical engineering. Paper n° 1427

Del Gaudio V, Wasowski J (2004) Time probabilistic evaluation of seismically induced landslide hazard in Irpinia (southern Italy). Soil Dyn Earthq Eng 24:915–928

Del Gaudio V, Pierri P, Wasowski J (2003) An approach to time-probabilistic evaluation of seismically induced landslide hazard. Bull Seismol Soc Am 93:557–569

Florensov NA, Solonenko VP (ed) (1963) The Gobi-Altai earthquake. Akademiya Nauk USSR, Moscow, 391 p [in Russian] (English translation by Israel Program for Scientific Translation) Jerusalem 1965, 424 p

Fort M (2000) Glaciers and mass wasting processes: their influence on the shaping of the Kali Gandaki valley (higher Himalaya of Nepal). Quatern Int 65/66:101–119

Gregory-Wodzicki KM (2000) Uplift history of Central and Northern Andes: A review. Geol Soc Am Bull 112:1091–1105

Hayashi JN, Self S (1992) A comparison of pyroclastic flow and debris avalanche mobility. J Geophys Res 97:9063–9071

Hermanns RL, Blikra LH, Naumann M, Nilsen B, Panthi KK, Stromeyer D, Longva O (2006) Examples of multiple rock-slope collapses from Köfels (Ötz valley, Austria) and western Norway. Eng Geol 83:94–108

Hewitt K (1998) Catastrophic landslides and their effect on the Upper Indus streams, Karakoram Himalaya, northern Pakistan. Geomorphology 26:47–80

Hoek E, Bray JW (1981) Rock slope engineering. Institution of Mining and Metallurgy, London, p 358

van Husen D (1997) LGM and late-glacial fluctuations in the eastern Alps. Quatern Int 38/39:109–118

Ibetsberger HJ (1996) The Tsergo Ri landslide: an uncommon area of high morphology activity in the Langthang valley Nepal. Tectonophysics 260:85–93

Inglès J, Darrozes J, Soula J-C (2005) Effects of vertical component of ground shaking on earthquake-induced landslides displacements using generalized Newmark's analysis. Eng Geol 86:134–147

Ivy-Ochs S, Heuberger H, Kubik PW, Kerschner H, Bonani G, Frank M, Schlüchter C (1998) The age of the Köfels event: relative, ^{14}C and cosmogenic isotope dating of an early Holocene landslide in the central Alps (Tyrol, Austria). Z . Gletsch. kd. Glazialgeol. 34/1: 57–68

Ivy-Ochs S, Kerschner H, Maisch M, Christl M, Kubik PW, Schlüchter C (2009a) Latest Pleistocene and Holocene glacier variations in the European Alps. Quatern Sci Rev 28:2137–2149

Ivy-Ochs S, Poschinger AV, Synal H-A, Maisch M (2009b) Surface exposure dating of the Flims landslide, Graubünden Switzerland. Geomorphology 103:104–112

Jibson RW, Keefer DK (1993) Analysis of the seismic origin of landslides – Examples of the New Madrid seismic zone. Geol Soc Am Bull 105:421–436

Jibson RW (1993) Predicting earthquake-induced landslide displacement using Newmark's sliding block analysis. Transport Res Rec 1411:9–17

Jibson RW, Harp EL, Michael JA (1998) A method for producing digital probabilistic seismic landslide hazard map: an example from the Los Ageles, California, area. US Geological survey open file report. pp 98–113

Kanamori H (1977) The energy release in great erthquakes. J Geophys Res 82:2981–2987

Kojan E, Hutchinson JN (1978) Mayunmarca rockslide and debris flow, Peru. In: Voight B (ed) Rockslides and avalanches, 1. Natural phenomena. Elsevier, Amsterdam, Oxford, New York, pp 315–361

Kubik PW, Ivy-Ochs S, Masarik J, Frank M, Schlüchter C (1998) ^{10}Be and ^{26}Al production rates deduced from an instantaneous event within the dendro-calibration curve, the landslide of Köfels, Ötz Valley Austria. Earth Planet Sci Lett 161:231–141

Magny M, Guiot J, Schoellammer P (2001) Qualitative reconstruction of Younger Dryas to Mid-Holocene paleoclimates at Le Locle, Swiss Jura, using pollen and lake-level data. Quatern Res 56:170–180

Moon V, Simpson CJ (2002) Large-scale mass wasting in ancient volcanic material. Eng Geol 64:41–64

Newmark NM (1965) Effects of earthquakes on dams and embankments. Geotechnique 15:139–159

Okal EA (1976) A surface-wave investigation of the rupture mechanism of the Gobi-Altai (December 4, 1957) earthquake. Phys Earth Plan Interiors 12:319–328

Pánek T, Hradecký J, Smolková V, Šilhán K (2008) Gigantic low-gradient landslides in the northern periphery of the Crimean Mountains (Ukraine). Geomorphology 95:449–473

Philip H, Ritz JF (1999) Gigantic paleolandslide associated with active faulting along the Bogd fault (Gobi-Altay, Mongolia). Geology 27:211–214

Pollet N (2004) Mouvements gravitaires rapides des grandes masses rocheuses : apport des observations de terrain à la compréhension des processus de propagation et de dépôt. Application aux cas de la Madeleine (Savoie, France), Flims (Grisons, Suisse) et Köfels (Tyrol, Autriche). Thèse, Ecole nationale des Ponts et Chaussées, Paris. http://pastel.paristech.org/bib/archive/00000820/

Pollet N, Cojean R, Couture R, Schneider J-L, Strom AL, Voirin C, Wassmer P (2005) A slab-on-slab model for the flims rockslide (Swiss Alps). Canadian Geotech J 42:587–600

Poschinger AV, Wassmer P, Maisch M (2006) The flims rockslide: history of interpretation and new insight. In: Evans SG (ed) Landslides from massive rock slope failure. Springer, Dordrecht, pp 239–356

Pritchard, Simons M, Rogen PA, Hensley S, Webb FH (2002) Coseismic slip from the July 30, 1995, Mw = 8.1 Antofagasta, Chile earthquake as constrained by InSAR and GPS observations. Geophys J Int 150:362–376

Romeo R (2000) Seismically induced landslide displacements: a predictive model. Eng Geol 58:337–351

Sabetta F, Pugliese A (1996) Estimation of response spectra and simulation of non stationary earthquake ground motion. Bull Seismol Soc Am 86:337–352

Schramm JM, Weidinger JT, Ibetsberger HJ (1998) Petrologic and structural control on geomorphology of prehistoric Tsergo Ri slope failure, Lanthang Himal Nepal. Geomorphology 26:107–121

Skempton AV, Hutchinson JN (1969) Stability of natural slopes and embankment foundations. State of art report, 7th Conference Soil Mechanics and Foundation Engineering. Mexico, pp 291–335

Sörensen S-A, Bauer B (2003) On the dynamics of the Köfels sturzstrom. Geomorphology 54:11–19

Stafford PJ, Berill JB, Pettinga JR (2009) New predictive equations for Arias intensity from crustal earthquakes in New Zealand. J Seismol 13:31–52

Stässer M, Schlunegger F (2005) Erosional processes, topographic length-scale and geomorphic evolution in arid climatic environments: the 'Lluta collapse', northern Chile. Int J Earth Sci 94:433–446

Travasarou T, Bray JD, Abrahamson NA (2003) Empirical attenuation relationship for Arias Intensity. Earthq Eng Struct Dyn 32:1133–1155

Voight B (ed) (1978) Rockslides and avalanches. I. Natural phenomena. Elsevier, Amsterdam-Oxford-New York, p 833

Vollweiler N, Scholz D, Mühlinghaus C, Mangini A, Spötl C (2006) A precisely dated climate record for the last 9kyr from three high alpine stalagmites, Spannagel Cave Austria. Geophys Res Lett 33:L20703

Weidinger JT (2006) Predesign, failure and displacement mechanisms of large rockslides in the Anapurnas Himalayas Nepal. Eng Geol 83:201–216

Weidinger JT, Schramm JM, Surenian R (1996) On preparatory causal factors initiating the prehistoric Tsergo Ri landslide (Langthang Himal, Nepal). Tectonophysics 260:95–107

Wieczorek GF, Wilson RC, Harp EL (1985) Map showing slope sability during earthquakes of San Mateo County, California. U.S. Geological survey miscellaneous geologic investigation map I-1257E, scale 1.62,500

Wilson RC, Keefer DK (1985) Predicting areal limits of earthquake-induced landsliding. In: Ziony JI (ed), Evaluating earthquake Hazards in the Los Angeles region – An Earth-science perspective. US Geological survey professional paper 1360, 316–345

Seismically Induced Landslides in Abruzzo (Central Italy): Morphostructural Control

Enrico Miccadei, Tommaso Piacentini, Nicola Sciarra, and Rosamaria Di Michele

Abstract

Recent earthquakes show that damages due to collateral effects could, in some cases exceed the economic and social losses directly connected to the seismic shaking. Among the effects induced by the seismic energy release, landslides are one of the most significant in terms of hazard and related risk, owing to the occurrence of exposed elements.

This work analyzes the geomorphological effects, and particularly the rock falls, which occurred in the L'Aquila area during and immediately after the April 2009 earthquake. The analysis is focused mainly on the rock fall distribution related to the local morphostructural setting. As regards the rock falls, on the base of geomorphological and morphostructural analysis, the >60 cases surveyed are referable to three main morphostructural settings:

1. Calcareous faulted homoclinal ridges;
2. Calcareous rock slopes of karst landforms;
3. Structural scarps on conglomerates and breccias of Quaternary continental deposits.

These elements provide useful indications both at local scale, for seismic microzonation studies and seismic risk prevention, and at regional scale, for updating studies and inventory of landslides.

Keywords

Seismically induced landslides • L'Aquila 2009 Earthquake • Morphostructural setting

Introduction

Recent earthquakes showed that damages due to collateral effects could in some cases exceed the economic and social losses directly connected to the seismic shaking. Among the effects induced by the seismic energy release, landslides are one of the most significant in terms of hazard and related risk, owing to the occurrence of exposed public building, private houses, infrastructures, etc. (Keefer 1984; Keefer et al. 2006). Therefore a complete study for the evaluation of the seismic hazard should necessarily include the component of triggering or reactivation of landslides. Different types of landslides can be triggered by seismic shaking, depending on earthquake magnitude and the morphostructural setting of the area involved in the event, although the most frequent types are rock falls, toppling and debris flows (Keefer 1984, 2003; Prestininzi and Romeo 2000; Capolongo et al. 2002; Bozzano et al. 2004; Keefer et al. 2006).

This work analyzes the geomorphological effects, and particularly the rock falls, which occurred in the L'Aquila area during and immediately after the April 2009 earthquake that involved an area more than 30 km long, between L'Aquila and the Aterno River valley (MI Richter 5,8; hypocentre 8,8 km deep, extensional movement along NW-SE fault planes with SW-NE extension, Chiarabba et al. 2009; data available online at www.ingv.it; http://earthquake.usgs.gov/). The earthquake heavily damaged urban areas and villages and induced several coesismic

---

E. Miccadei • T. Piacentini (✉) • N. Sciarra • R. Di Michele
Dipartimento di Geotecnologie per l'Ambiente ed il Territorio, Università degli Studi "G. D'Annunzio" Chieti-Pescara, Via dei Vestini 31, Chieti scalo (CH), Italy
e-mail: tpiacentini@unich.it

C. Margottini et al. (eds.), *Landslide Science and Practice*, Vol. 5,
DOI 10.1007/978-3-642-31427-8_40,

deformations and geomorphologic effects, including different types of instability such as: rock falls, debris falls, ground collapses, liquefaction, etc. Previous studies in the near post-earthquake time period have analyzed types and pattern of the coseismic fractures and the occurrence of vertical displacement, as related to the surface propagation of the seismogenic fault (Anzidei et al. 2009; Falcucci et al. 2009; Boncio et al. 2010, and references therein) and have been focused on seismic microzonation and paleoseismologic investigation (Gruppo di lavoro Microzonazione sismica area aquilana 2010; Boncio et al. 2011), whereas only a few preliminary studies have dealt with distribution and features of the surface geomorphological effects (Boscaino et al. 2009; Blumetti et al. 2009; Farabollini et al. 2009; Emergeo 2009; Miccadei et al. 2010).

In this work we analyze the morphostructural features of the rock falls that occurred during and immediately after the April 6th 2009 earthquake. The distribution of landslides around the epicenter area is analyzed concerning the magnitude/distance from the epicenter ratio of the triggered rockfall, according to Keefer (1984) and Del Prete et al. (1992).

L'Aquila Area and Abruzzi Region Geomorphologic Setting

The Abruzzi region is located in the Central Apennines in the eastern part of Central Italy. The geomorphologic evolution of the region is related to a complex geological and structural framework developed since the Late Miocene, due to the formation of the Apennine thrust belt, but mostly to the following uplift process and extensional tectonics. The whole region is characterized by active geomorphologic processes, caused by the drainage network evolution and slope processes. Evidences of karst and glacial processes are also present.

The L'Aquila area is a wide NW-SE depression and comprises a series of adjacent and partly coalescent basins and plains, with elevation ranging from 500 to 900 m, mostly SE-striking and up to 10 km wide. The basins are surrounded by NW-SE ridges, with elevation ranging from 1,000 m to more than 2,000 m, up to the elevation of the Gran Sasso toward NE (Corno Grande, 2,912 m), to Mt. Ocre (2,204 m) and Mt. Sirente (2,348 m) toward the SW. In some cases, small elevations separate adjacent plains and basins, defining a well articulated physiography. The whole L'Aquila depression is longitudinally crossed by the Aterno River, from NW to SE, and belongs to the Aterno-Pescara drainage basin, the major feature of the Abruzzo region. Moreover, several endoreic basins are located both within and around the main basin, linked to tectonic and karst processes.

Detailed geomorphologic studies on landslides performed at local and regional scale (Buccolini and Sciarra 1989; Nicoletti et al. 1993; Cinti et al. 2000; Paolucci et al. 2001; D'Alessandro et al. 2003a; Scarascia Mugnozza et al. 2006) and within the Italian inventory of landslides (D'Alessandro et al. 2007) show that mechanism, types, and dimensions are irregular and inhomogeneous, and are controlled by lithostratigraphic units and structural settings of the different morphostructural domains: Apennine chain, piedmont area, and coastal area (D'Alessandro et al. 2003a, b).

Seismically Induced Landslides

After the April 6th 2009 earthquake, in the area of the epicentre, the occurrence of geomorphologic effects has been surveyed (by the authors and other working groups, Boscaino et al. 2009; Blumetti et al. 2009; Farabollini et al. 2009; Emergeo 2009). The effects include rock falls, debris slides and falls, small landslide reactivations, fluvial embankment falls, soil liquefaction, and even small snow avalanches (Figs. 1 and 2). The distribution shows a moderate directional trend that is SE-elongated parallel to the L'Aquila basin and the related main faults, as indicated by the ellipse in Fig. 1. Most of the landslides occurred during and immediately after the main shocks, but many occurred several days later, involving already mobilized blocks and triggered by aftershocks or by heavy rainfall.

Rock falls are one of the most frequent seismically induced geomorphological effects that occurred in the L'Aquila area, as well as during many earthquakes in mountainous areas in Italy and worldwide (Harp and Wilson 1995; Bozzano et al. 1997; Keefer 1984, 2003; Keefer et al. 2006). More than 60 rock falls have been analyzed, that involved slopes with variable gradient (from more than 100 % to vertical) over a wide area up to 50 km from the epicentre area. As well as for the total geomorphological effects, the rock falls show an anomalous distribution with distance from the epicentre (Fig. 2).

Rock falls occurred mostly on calcareous bedrock slopes or on scarps developed on conglomerates and breccias of Quaternary continental deposits. Geological and geomorphological surveys have outlined different types of rock falls on different morpho-structural settings, which can be summarized as follow:

1. Rock falls on calcareous faulted homoclinal ridges;
2. Rock falls on calcareous rock slopes of karst landforms;
3. Rock falls on structural scarps on conglomerates and breccias of Quaternary continental deposits.

Rock falls on calcareous faulted homoclinal ridges (Fig. 3a). These landslides occurred in the L'Aquila area, both on SW-facing slopes and on NE-facing slopes of the major calcareous homoclinal ridges such as in the Assergi area (NE of L'Aquila), in the Stiffe area (SE of L'Aquila) and in the Aterno gorges area (SE of L'Aquila) (Fig. 4a, b). In the case of Assergi the rock falls detached from the step-like slope of a calcareous faulted homoclinal ridge

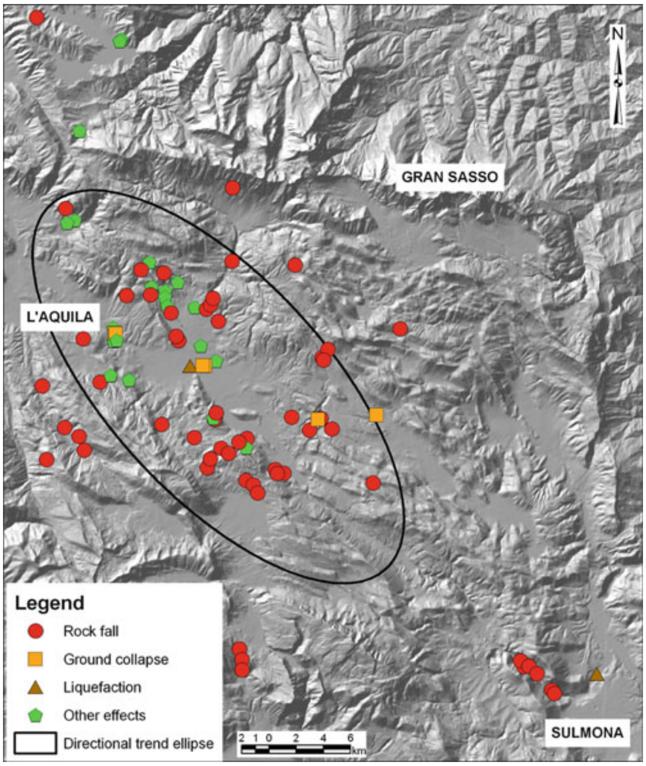

Fig. 1 Distribution of the main geomorphological effects of the 2009 L'Aquila earthquake and ellipse indicating the SE-striking structural trend (Modified from Boscaino et al. (2009); Blumetti et al. (2009); Farabollini et al. (2009); Emergeo (2009); Miccadei et al. (2010))

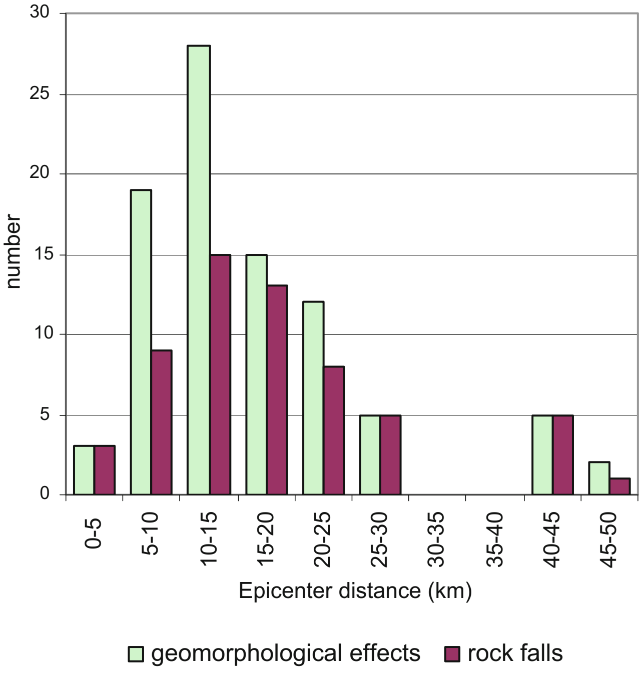

Fig. 2 Frequency histogram of geomorphological effects rock falls versus distance from the epicentral area

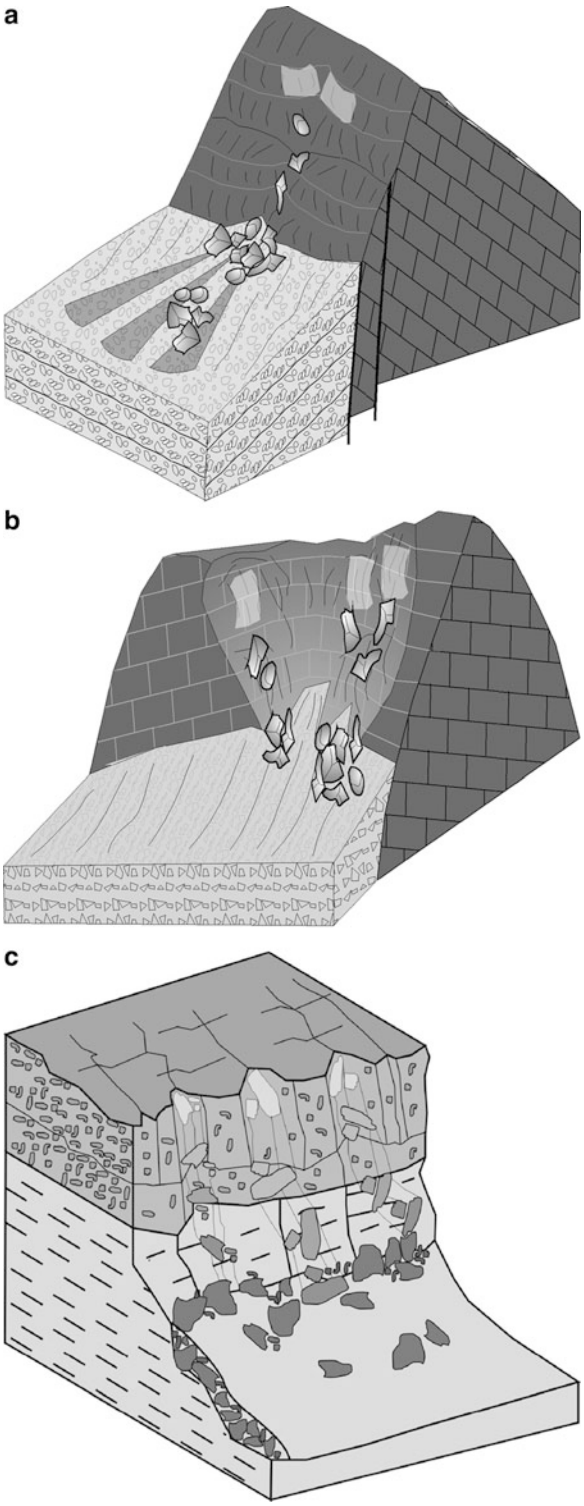

Fig. 3 Morphostructural scheme of rock falls: (**a**) on calcareous faulted homoclinal ridges, (**b**) on calcareous rock slopes of karst landforms, and (**c**) on structural scarps of conglomerates and breccias of Quaternary continental deposits

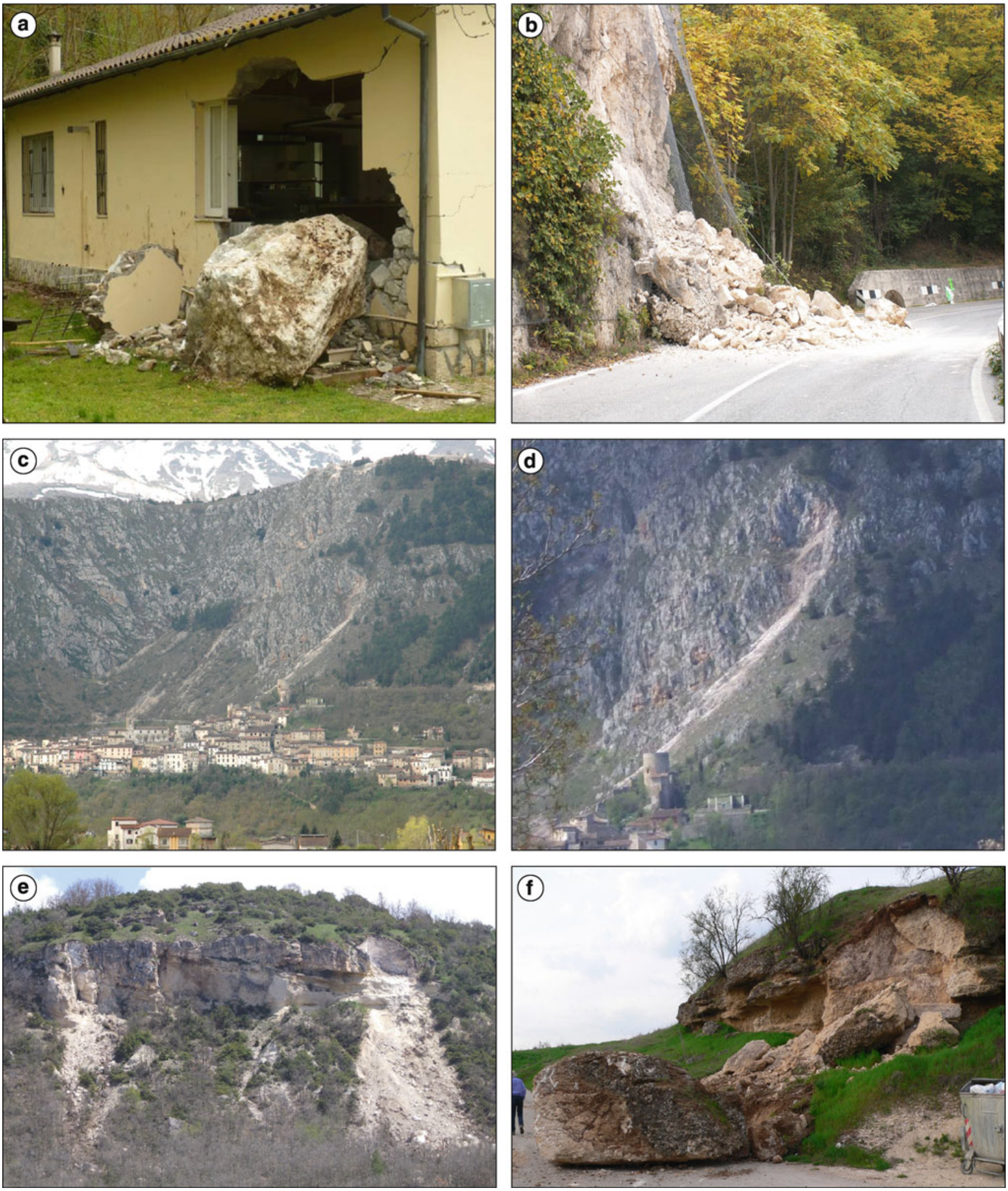

Fig. 4 Examples of rock falls triggered by the L'Aquila earthquake. (**a**) Rock mass fallen from Stiffe's gorges fault homoclinal ridge (near Fossa town); (**b**) rock fall along the scarp of the Aterno gorges faulted homoclinal ridge; (**c**) Fossa village located at the base of a half doline, relict landform preserved by erosion and tectonic processes; (**d**) rock falls along the calcareous rock scarp of the Fossa village doline; (**e**) rock falsl occurred in the structural scarp surrounding the Sinizzo Lake on conglomerates affected by vertical joints, parallel and perpendicular to the main scarp; (**f**) rock topple and fall along a structural scarp on alluvial fan conglomerates (San Demetrio village)

ESE-striking. The detachment zone is a scarp with a gradient more than 100 %, on well stratified carbonate rocks with several metres thick lenses and banks of calcarenites and calcirudites. These rocks belong to the Meso-Cenozoic carbonate slope and basin succession of the Gran Sasso area. The lower part of the slope is on Quaternary continental superficial deposits made up of slopes debris and breccias. These deposits onlap a major ESE-striking fault that displaces the homocline (Ghisetti and Vezzani 1986; Boncio et al. 2010). The homoclinal ridge is characterized by a large step-like slope with the main scarps along the thick banks and lenses of the calcareous sequence. The middle part of the slope is marked by a clear fault scarp. Several incisions carve the upper part of the slope, due to debris avalanches and snow avalanches, forming coalescent fans in the lower part.

The rock falls are made up of several blocks of a few metres in size, detached from the step-like scarps. The blocks passed through incised gullies, and reached the lower part of the slope where the gradient is <30 % on which the debris accumulated. In many cases, the blocks were stopped by natural and artificial obstacles, such as trees and roads running perpendicular to the slope.

Rock falls on calcareous rock slopes of karst landforms (Fig. 3b). Calcareous ridges surrounding the L'Aquila area are affected by widespread karst landforms (solution and collapse dolines, sink-holes, dry valleys, etc.; Burri et al. 1995). Rock falls occurred mostly on slopes and scarps of dolines, wide and, in some cases, deep karst depressions. In some cases, these types of rock falls involved and damaged villages and houses, as in the Stiffe area or in the Fossa village.

Here, moreover, two casualties occurred in the village, due to rock falls.

In the case of Fossa, the village is located at the base of a wide and deep doline on a faulted calcareous homoclinal ridge, a NW-striking feature with horizontal to SW-dipping strata. Only half of the doline is now preserved, and this indicates an origin by ancient karst processes and subsequent erosion by other geomorphological processes. The doline has slopes up to 200 m high and an average steepness of up to >130 %. On the slopes several rock scarps are present (Fig. 4c). The carbonate rocks of slopes and scarps are tectonically fractured and intensely weathered by karst processes with micro and mesolandforms such as lapiez, karren, small caves etc.

Rock fall detachment zones are located in the upper part of the slopes on some of the main rock scarps. Several blocks moved down slope of >100 m relief and stopped at the base of the slope on the houses of the upper part of the village (Fig. 4d). The detachment was due both to high, steep slopes and to intense weathering of the rocks.

Rock falls on structural scarps on conglomerates and breccias of Quaternary continental deposits (Fig. 3c). These landslides locally occurred in the lower part of the L'Aquila basin, particularly in the SE portion of the area. The Quaternary deposits include calcareous siltstone Early-Middle Pleistocene in age, overlain by several units of alluvial fan gravel and sands, from loose to highly cemented, Middle Pleistocene to Late Pleistocene in age (Bertini and Bosi 1993; SGI 2006; Galli et al. 2010; Boncio et al. 2011). These units are faulted mostly along SE-striking elements, affected by mostly vertical joints spaced from few decimetres to a few metres, and deeply incised by fluvial and karst processes. The present morphostructural setting is characterized by widespread steep structural scarps, on highly cemented conglomerates overlying erodible siltstone. The scarps are from few metres up to more than 100 m high with slopes >100 %. They are mostly SE-striking, along the main faults, or SW-striking, formed by fluvial incision, or locally subcircular related to karst landforms.

Rock falls occurred on these scarps, in some cases along with topples, led to the detachment of highly cemented conglomerate blocks of prismatic or sub-rounded shapes up to several metres in diameter, partially fragmented and rounded during the fall process (Fig. 4e, f).

The block detachments are along the joints affecting the conglomerate rock masses, particularly along tension joints parallel to the main scarps (Fig. 4e).

During the earthquake, the seismic shaking induced the detachment of conglomerate blocks, which were already in poor stability conditions, caused by open joints parallel to the scarp and to the high energy relief on the scarp.

Conclusion

The geomorphologic surveys carried out in the L'Aquila area after the April 2009 earthquake were compared to previous studies on landslides in the Abruzzi Region. The analysis was focused mainly on the general spatial distribution of geomorphological effects and on the rock fall distribution related to the local morphostructural setting.

The distribution of rock falls vs. distance from the epicentre area shows a peculiar pattern with few landslides in the 0–5 km interval and a maximum in the 10–15 km interval (Fig. 2). It suggests a strong control of local topographic and geomorphologic setting on the rock fall distribution. The occurrence of no rock fall between 30 and 40 km and several in the 40–50 km interval provides a further confirmation of topographic and geomorphic control. The remote effects are due to a strong local topographic relief along the Aterno River gorges located close to the outlet of the river into the Sulmona basin.

Based on geomorphological and morphostructural analysis, the ~60 rock falls surveyed are grouped into three main morphostructural categories summarized in Fig. 3:

1. Rock falls on calcareous faulted homoclinal ridges;
2. Rock falls on calcareous rock slopes of karst landforms;
3. Rock falls on structural scarps on conglomerates and breccias of Quaternary continental deposits.

These elements provide useful indications both at local scale, within the studies of seismic microzonation and seismic risk prevention, and at regional scale, for integration and detailing studies and inventory of landslides.

References

Anzidei M, Boschi E, Cannelli V, Devoti R, Esposito A, Galvani A, Melini D, Pietrantonio G, Riguzzi F, Sepe V, Serpelloniet E (2009) Coseismic deformation of the destructive April 6, 2009 L'Aquila earthquake (central Italy) from GPS data. Geophys Res Lett 36: L17307

Bertini T, Bosi C (1993) La tettonica quaternaria della conca di Fossa (L'Aquila). Il Quat 6(2):293–314

Blumetti AM, Comerci V, Di Manna P, Guerrieri L, Vittori E (2009) Geological effects induced by the L'Aquila earthquake (6 April 2009, ml = 5.8) on the natural environment. Preliminary report. Dipartimento Difesa del Suolo Servizio Geologico d'Italia. http://www.apat.gov.it/site/_files/Inqua/2009_abruzzo_earthquake_report.pdf. April 2009

Boncio P, Pizzi A, Brozzetti F, Pomposo G, Lavecchia G, Di Naccio D, Ferrarini F (2010) Coseismic ground deformation of the April 6th 2009 L'Aquila earthquake (central Italy, Mw 6.3). Geophys Res Lett 37:1–6

Boncio P, Pizzi A, Cavuoto G, Mancini M, Piacentini T, Miccadei E, Cavinato GP, Piscitelli S, Giocoli A, Ferretti G, De Ferrari R, Gallipoli R, Mucciarelli M, Di Fiore V, Naso G, Working Group Macroarea 3 (2011) Geological and geophysical characterization of the Paganica-San Gregorio area after the April 6, 2009 L'Aquila earthquake (Mw 6.3, central Italy): implications for site response. Boll di Geofisica Teorica e Applicata 52(3). doi:10.4430/bgta/0014

Boscaino G, Pipponzi G, D'Eramo A (2009) Coseismic landslides of the April 2009 L'Aquila earthquake : considerations on the PAI (Piani per l'Assetto Idrogeologico). Geoitalia 2009, Rimini, 9–11 Settembre 2009. Epitome, 3, 2009. p 175

Bozzano F, Scarascia Mugnozza G, Valentini G (1997) Frane indotte da terremoti: un confronto tra gli eventi dell'Irpinia (1980) e di Kobe (1995). Atti dei Convegni Lincei 134:119–124

Bozzano F, Martino S, Naso G, Prestininzi A, Romeo RW, Scarascia Mugnozza G (2004) The large Salcito landslide triggered by the 2002 Molise, Italy, earthquake. Earthq Spectra 20(S1):95–105

Buccolini M, Sciarra N (1989) Conoscenze geologico tecniche e distribuzione dei fenomeni franosi nella provincia di Pescara. Studi Geologici Camerti 11:23–35

Burri E, Agostini S, Celico P, Iacovone D, Romano B (1995) Unità morfocarsiche della Regione Abruzzo, scala 1:200,000, Regione Abruzzo, Società Geografica Italiana, Società Speleologica Italiana, SELCA, Firenze

Capolongo D, Refice A, Mankelow J (2002) Evaluating earthquake-triggered landslide hazard at the basin scale through GIS in the Upper Sele river Valley. Surv Geophy 23(6):595–625

Chiarabba C, Amato A, Anselmi M, Baccheschi P, Bianchi I, Cattaneo M, Cecere G, Chiaraluce L, Ciaccio MG, De Gori P, De Luca G, Di Bona M, Di Stefano R, Faenza L, Covoni A, Improta L, Lucente FP, Marchetti A, Margheriti L, Mele F, Nichelini A, Monachesi G, Moretti M, Pastori M, Piana Agostinetti N, Piccinini D, Roselli P, Seccia D, Valoroso L (2009) The 2009 L'Aquila (Central Italy) MW6.3 earthquake: main shock and aftershocks. Geophy Res Lett 36:L18308

Cinti G, Donati A, Fumanti F, Scarascia-Mugnozza G (2000) La grande frana di M. Arezzo (Abruzzo). Mem Soc Geol Ital 56:41–51

D'Alessandro L, Berti D, Buccolini M, Miccadei E, Piacentini T, Urbani A (2003a) Relationships between the geological-structural framework and landslide types in Abruzzi (Central Apennine). Atti 1° Congresso Nazionale AIGA, Chieti, 19–20 Febbraio 2003. Rendina Editori, Roma, pp 255–275

D'Alessandro L, Miccadei E, Piacentini T (2003b) Morphostructural elements of central-eastern Abruzzi: contributions to the study of the role of tectonics on the morphogenesis of the Apennine chain. Quat Int 101–102:115–124

D'Alessandro L, Del Sordo L, Buccolini M, Miccadei E, Piacentini T, Urbani A (2007) Regione Abruzzo (Chap. 18). In: Rapporto sulle frane in Italia. Il Progetto IFFI, Rapporti APAT 78/2007. elaborazioni, e rapporti regionali, Risultati, pp 464–497

Del Prete M, Giaccari E, Trisorio-Liuzzi G (1992) Rischio da frane intermittenti a cinematica lenta nelle aree montuose e collinari urbanizzate della Basilicata. Università della Basilicata, G.N.D.C.I., Rapporto U.O. 2.37

Emergeo Working Group (2009) Evidence for surface rupture associated with the Mw 6.3 L'Aquila earthquake sequence of April 2009 (central Italy). Terra Nova 22:43–51

Falcucci E, Gori S, Peronace E, Fubelli G, Moro M, Saroli M, Giaccio B, Messina P, Naso G, Scardia G, Sposato A, Voltaggio M, Galli P, Galadini F (2009) The Paganica fault and surface coseismic ruptures due to the April 6, 2009 earthquake (L'Aquila, Central Italy). Seismic Res Lett 80(6):940–950

Farabollini P, Miccadei E, Piacentini T, De Pari P, Scalella G (2009) The contribution of geomorphology and Quaternary geology to the seismic prevention: examples from 2009 Abruzzi earthquake. Geoitalia 2009, Rimini 9–11 Settembre 2009. Epitome 3. p 171

Galli P, Giaccio B, Messina P (2010) The 2009 central italy earthquake seen through 0.5 myr-long tectonic history of the l'Aquila faults system. Quater Sci Rev 29:3768–3789

Ghisetti F, Vezzani L (1986) Carta geologica del Gruppo M. Siella-M. Camicia-M. Prena- M. Brancastello (Gran Sasso d'Italia, Abruzzo). Scale 1: 15,000, S.EL.CA., Firenze

Gruppo di lavoro Microzonazione sismica area aquilana (2010) Microzonazione sismica per la ricostruzione dell'area aquilana. Dipartimento della Protezione Civile, Rome

Harp EL, Wilson RC (1995) Shaking intensity thresholds for rock falls and slides: evidence from 1987 Whittier Narrows and Superstition Hills earthquake strong-motion records. Bull SeismolSoc Am 85:1739–1757

Keefer DK (1984) Landslide caused by earthquakes. Geol Soc Am Bull 95:406–407

Keefer DK (2003) Investigating landslides caused by earthquakes. a historical review. Surv Geophy 23(6):473–510

Keefer DK, Wasowski J, Del Gaudio V (eds) (2006) Special issue from the European geosciences union symposium on landslides induced by earthquake and volcanic activity. Eng Geol 86(2–3):85–250

Miccadei E, Piacentini T, Sciarra N (2010) Seismically induced landslides caused by the earthquake of 6 April 2009 in Abruzzo Region (Central Italy). In: Williams et al (eds) Geologically active, proceedings of 11th IAEG congress, Auckland, pp 127–141. Taylor Francis, London

Nicoletti P, Parise M, Miccadei E (1993) The Scanno rock avalanche (Abruzzi, south-central Italy). Boll Soc Geol Ital 112:523–535

Paolucci G, Pizzi R, Scarascia-Mugnozza G (2001) Analisi preliminare della frana di Lettopalena (Abruzzo). Mem Soc Geol Ital 56:131–137

Prestininzi A, Romeo R (2000) Earthquakes-induced ground failures in Italy. Eng Geol 58:387–397

Scarascia Mugnozza G, Petitta M, Bianchi Fasani G, Esposito C, Barbieri M, Cardarelli E (2006) The importance of geological model to understand and predict the life span of rockslide dams: the Scanno lake case study, Central Italy. Ital J Eng Geol Environ 1:127–132

SGI Servizio Geologico d'Italia, ISPRA (2006) Carta geologica d'Italia, scala 1:50000, Foglio 359 L'Aquila. Istituto Poligrafico Zecca dello Stato, Roma

Semi-Empirical Assessment of Road Vulnerability to Seismically Induced Slides

Sotiris Argyroudis, Stavroula Fotopoulou, and Kyriazis Pitilakis

Abstract

The present paper aims at the proposition and quantification of a semi-empirical methodology to estimate physical vulnerability of roads subjected to earthquake induced landslide hazards. It is based on a modification of the existing engineering judgmental HAZUS fragility curves using an empirical model that relates the seismic permanent ground displacement (PGD) with the peak ground acceleration (PGA) for the Newmark rigid sliding block case. In this regard, it is possible to account for the specific characteristics of soil and local topography within the estimation of road vulnerability. Various sets of fragility curves can be constructed as a function of peak ground acceleration (PGA), considering the characteristics of the slope (i.e. yield coefficient, k_y) and the earthquake magnitude. A preliminary application of the proposed methodology is performed with the aid of GIS tool to the roadway system of city of Grevena in NW Greece for three different earthquake scenarios. It is observed that the level of damage predicted using the aforementioned methodology is less severe compared to the corresponding level of damage anticipated using the HAZUS methodology.

Keywords

Vulnerability • Roadway system • Earthquake induced landslide hazard • Fragility curves

Introduction

Landslides triggered by earthquakes may have a significant impact on the transportation infrastructures resulting to both direct and indirect losses in the affected area. A typical example is the 2008, Wenchuan earthquake in China that triggered more than 15,000 landslides of various types covering an area of 50,000 km^2, causing a large number of fatalities and economic losses. The extensive damage to highways, bridges and other infrastructure resulted to isolation of many towns and hindrance of the rescue and relief efforts (Tang et al 2011). Hence, the estimation of road vulnerability due to seismically induced landslides is of major importance for the seismic risk analysis of the transportation network and the efficient risk management and emergency planning.

Vulnerability of a roadway system to earthquake induced landslide may be attributed both to the partial or complete blockage of the road as well as to the structural damage to the road pavement and it is associated to the serviceability level of the road. For debris flows, the volume of material deposited on a road may be considered the most appropriate intensity parameter while for earth slides the permanent ground displacement and/or peak ground acceleration at the road surface comprise the most adequate intensity measures. Information regarding the type and classification (e.g. highway, main road, unpaved road, railroad), geometry (e.g. width or number of lanes), and traffic volume (for different times of the day) is also important to assess the vulnerability and risk of transportation infrastructure to various landslide hazards.

Research regarding the quantitative estimation of vulnerability of roads due to landslides is limited and in process. The available methodologies are primarily empirical and mainly

---

S. Argyroudis • S. Fotopoulou (✉) • K. Pitilakis
Department of Civil Engineering, Aristotle University of Thessaloniki, P.O.B. 424, Thessaloniki 54124, Greece
e-mail: sfotopou@civil.auth.gr

C. Margottini et al. (eds.), *Landslide Science and Practice*, Vol. 5,
DOI 10.1007/978-3-642-31427-8_41, © Springer-Verlag Berlin Heidelberg 2013

refer to rainfall triggered landslide processes. In addition, the specific characteristics of the potential precarious slopes have not been explicitly considered in any vulnerability assessment methodology. An overview of the available methodologies found in the literature is provided in the following.

Leone et al. (1996) introduced vulnerability matrices that correlate, in terms of vulnerability, the exposed elements to the characteristics of landslides using empirical data and judgment. Few years later, AGSO (2001) proposed fixed vulnerability values for roads subjected to landslides. Similarly, Michael-Leiba et al. (2003) suggested fixed vulnerability values for roads exposed to debris flows. More recently, Zêzere et al. (2008) estimated the vulnerability of roads in regional/local scale under different landslide hazards based on the empirical or historic data, in conjunction with available data regarding the road type (motorway, national, county, and rural road). Remondo et al. (2008) performed a detailed inventory of exposed transportation infrastructure in the study area of northern Spain to assess landslide vulnerability. Vulnerability values (0–1) were obtained by comparing damages experienced in the past by each type of road with its actual monetary value. The derived vulnerability values express the degree of potential monetary loss with respect to the total value of the element. Pitilakis et al. (2010) developed a methodology within the framework of SAFELAND research project to estimate physical vulnerability of roads to debris-earth flows, based on engineering judgment. An appropriate questionnaire has been prepared and widely distributed to experts on debris flows and road vulnerability. Various sets of fragility curves were derived as a function of the volume of the landslide deposit for each road type and damage state, based on the statistical exploitation of the results of the questionnaire.

HAZUS multi-hazard methodology (NIBS 2004) is the only available tool known by the authors to tackle the problem of estimating road vulnerability subjected to earthquake triggered landslides, by providing fragility curves based on expert judgement and empirical data. Different fragility functions have been proposed depending on the level of damage and the roadway typology.

The present study, as an effort to improve the available background, is focused on the proposition and quantification of a semi-empirical methodology, taking into account the geometrical and strength characteristics of the potential unstable slope (through its yield coefficient) and the magnitude of the earthquake ground motion within the framework of road vulnerability estimation. An application of the proposed approach to the roadway system of Grevena city in Greece is also provided.

Proposed Methodology

The existing HAZUS (NIBS 2004) fragility functions for roads provide the conditional probability of reaching or exceeding a certain damage state, under a range of ground failure events of given type and intensity. They result from a combination of expert judgmental and empirical models based on statistical analysis of damage data from previous events (Giovinazzi and King 2009). They are defined with respect to road classification and permanent ground displacement (PGD) due to landslides, liquefaction and fault rupture.

Given the applied permanent ground displacement PGD at the road level, the probability of exceeding a given limit state, SLi, is modeled as:

$$f(PGD) = \Phi\left[\frac{1}{\beta_i}\ln\left(\frac{PGD}{\overline{PGD_i}}\right)\right] \qquad (1)$$

Where:

- Φ is the standard normal cumulative distribution function,
- $\overline{PGD_i}$ is the median value of permanent ground displacement at which the road reaches the limit state, i (Table 2),
- β_i is the standard deviation of the natural logarithm of permanent ground displacement for limit state, i (Table 2).

The median values of permanent ground displacement are defined as the values that correspond to the 50 % probability of exceeding each damage state. The standard deviation values [β] describe the total variability associated with each fragility curve. Two different types of lognormally distributed curves are given, for roads with two traffic lanes (urban roads) and roads with four or more lanes (major/highway roads) (Fig. 1). Five damage states are defined; a qualitative description of these is given in Table 1. The parameters of fragility functions in quantitative terms for each damage state and road typology are presented in Table 2.

The aforementioned curves have shown to give in most cases a realistic assessment of the expected damage level (Azevedo et al. 2010). However, they comprise a generalized approach that does not take into account the specific characteristics of soil and local topography. In the framework of this study, it is attempted to propose fragility curves for roads in case of earthquake triggered slides as a function of peak ground acceleration (PGA) considering the characteristics of the slope (i.e. yield coefficient k_y). In this respect, the existing HAZUS curves are modified using the Bray and Travasarou displacement (2007) model that captures the primary influence of the system's yield coefficient (k_y), its initial fundamental period (Ts), and the ground motion's spectral acceleration at a degraded period equal to

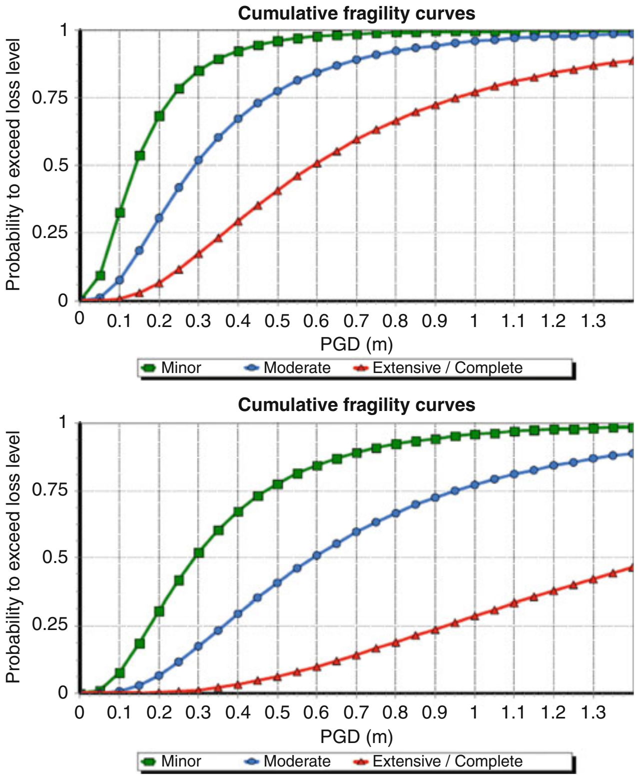

Fig. 1 Fragility curves at various damage states for Highways and Urban roads (NIBS 2004)

Table 1 Damage state definition for roads in HAZUS

Damage States	Description
ds1. None	–
ds2. Slight/minor damage	Slight settlement (few cm) or off set of the ground
ds3. Moderate damage	Moderate settlement (several cm) or offset of the ground
ds4. Extensive damage	Major settlement of the ground (few m)
ds5. Complete damage	Major settlement of the ground (i.e., same as ds4).

Table 2 Damage algorithms for roadways (From HAZUS, NIBS 2004)

Permanent ground deformation			
Components	Damage states	Median (m)	Dispersionβ
Major road	Slight/minor	0.30	0.70
	Moderate	0.60	0.70
	Extensive/complete	1.50	0.70
Urban road	Slight/minor	0.15	0.70
	Moderate	0.30	0.70
	Extensive/complete	0.60	0.70

1.5Ts. Assuming that the potential landslide mass behaves as a rigid block ($Ts = 0$), the seismic permanent ground displacement PGD can be related to the PGA (peak ground acceleration of the ground motion, i.e. $S_a(Ts = 0)$) using the following equation:

$$\begin{aligned}\ln(\mathrm{PGD}) = & -0.22 - 2.83\ln(k_y) - 0.333(\ln(k_y))^2 \\ & + 0.566\ln(k_y)\ln(\mathrm{PGA}) + 3.04\ln(\mathrm{PGA}) \\ & - 0.244(\ln(\mathrm{PGA}))^2 + 0.278(M - 7) \pm \varepsilon\end{aligned} \quad (2)$$

Where:

- ky is the yield coefficient (i.e., the seismic coefficient that brings the slope to a factor of safety of one in a pseudostatic analysis)
- M is the earthquake moment magnitude,
- ε is the normally distributed random variable with zero mean and standard deviation $\sigma = 0.67$

It 's worth noting that the Newmark rigid block assumption is appropriate for analyzing relatively thin landslides in stiff or brittle materials, but it introduces significant errors as landslides become thicker and material becomes softer (Jibson 2010). Using the fragility curves provided by HAZUS, the exceedance probabilities of each damage state are calculated for the corresponding PGD values that are derived for a range of PGA values based on the aforementioned relationship. Then a lognormal distribution is fitted on each curve and the median and standard deviation parameters (β) are estimated. Different sets of fragility curves can be generated for different values of k_y (e.g. for $Ky = 0.05$, 0.1, 0.2, 0.3) and earthquake moment magnitude for both urban and highway roads. An example is given in the next paragraph. It is pointed out that road vulnerability is highly reduced with increasing values of k_y. Thus, the yield coefficient of a slope, which comprises the threshold base acceleration required to overcome the shear resistance of the slope and initiate failure, represents a crucial parameter in estimating road vulnerability to seismically induced landslides.

Case Study

Application to the Roadway System of Grevena City, Greece

Grevena is a town and municipality in Greece, capital of the Grevena Prefecture located on the NW part of Greece (Fig. 2). The city is surrounded by mountains, while is situated by the river Greveniotikos, which itself flows into the main river Aliakmon. Consequently the landslide risk during a strong earthquake may be quite important. The seismic vulnerability of the roadway system of Grevena has been investigated in previous project using the HAZUS (NIBS 2004) multi-hazard methodology. The results revealed that most of the expected damages are attributed to the occurrence of permanent ground deformations due to landsliding and not to the effect of ground shaking (Pitilakis et al. 2009, 2011). The total length of the urban road network under study is approximately 20 km.

Fig. 2 Location of the city of Grevena in Greece

Table 3 Fragility parameters for urban roads on slope for M = 6.3

		Peak ground acceleration							
Components		$k_y = 0.05$		$k_y = 0.1$		$k_y = 0.2$		$k_y = 0.3$	
	Damage states	Median (g)	β	Median (g)	β	Median (g)	β	Median (g)	β
Major road	Slight/minor	0.30	0.40	0.55	0.40	0.97	0.35	1.36	0.30
	Moderate	0.60		0.78		1.36		1.88	
	Extensive/complete	1.50		1.34		2.22		2.90	
Urban road	Slight/minor	0.15	0.40	0.40	0.35	0.71	0.35	1.00	0.30
	Moderate	0.30		0.55		0.97		1.36	
	Extensive/complete	0.60		0.78		1.36		1.88	

Critical accelerations for landsliding were estimated as a function of local soil and groundwater conditions and topography using the HAZUS simplified methodology. They were found to vary from 0.1 to 0.3 g for slope angles between 5° and 90° (see Figs. 4a and 5a). The expected PGA values at the free ground surface were derived from the results of the microzonation study of the area for three seismic scenarios that refer to earthquakes with mean return periods of 100, 500 and 1,000 years (Pitilakis et al. 2009, 2011) (see Figs. 4b and 5b for the 500 and 1,000 years seismic scenarios).

Based on the deaggregation of seismic hazard, the most likely earthquake moment magnitude and source-site distance for three mean return periods ($T_m = 100$, 500 and 1,000 years), and two soil conditions (B and C according to EC8) were estimated. For example, the 500 years scenario corresponds to a Mw = 6.3 earthquake with R = 14km for soil type B and R = 13km for soil type C.

For the vulnerability assessment of the roadway system of Grevena, the fragility curves are estimated based on the parameters that are provided in Table 2 and the empirical equation (2), following the procedure that is described in the previous section. The estimated parameters (medians and dispersion) for each damage state and yield coefficient are presented in Table 3, where a common dispersion is assigned in each road class based on the best fitting of the lognormal distribution. The graphs of the fragility curves for urban roads, which are used in the present application, are illustrated in Fig. 3. Table 4 describes the percentage of the roads of the

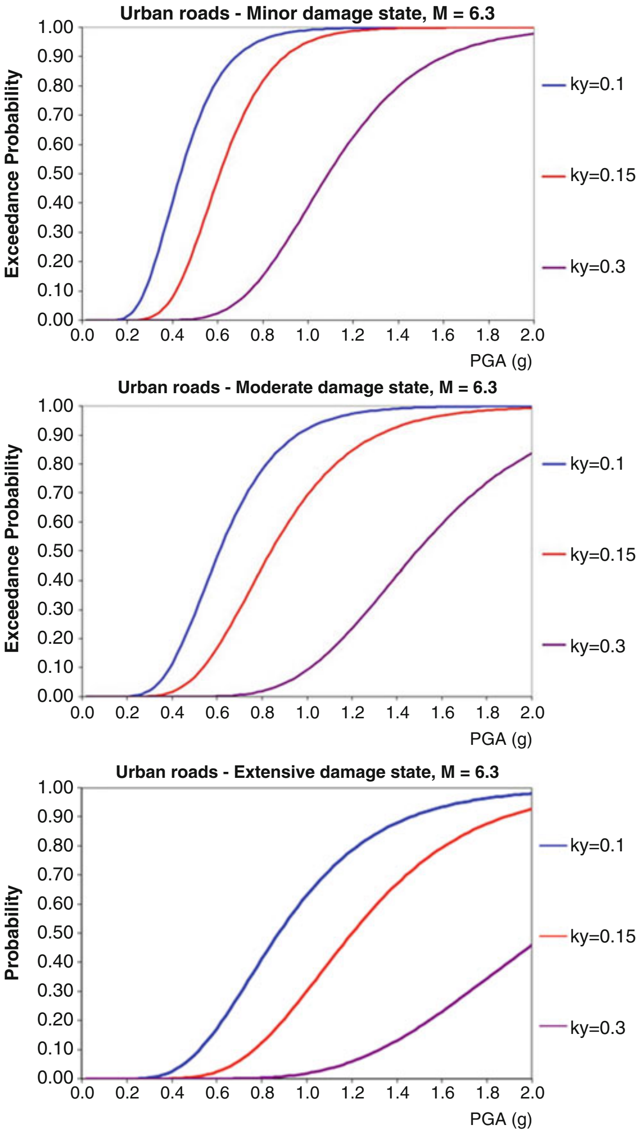

Fig. 3 Fragility curves at various damage states and different yield coefficients (ky) for urban roads on slope for Mw = 6.3

Table 4 Percentage (%) of the roads of the network that is expected to sustain damages for each damage state and scenario

		Seismic scenario		
		100 years	500 years	1,000 years
Percentage (%)	Slight/ minor	0.00	2.30	10.10
	Moderate	0.00	0.00	0.80
	Extensive/ complete	0.00	0.00	0.00

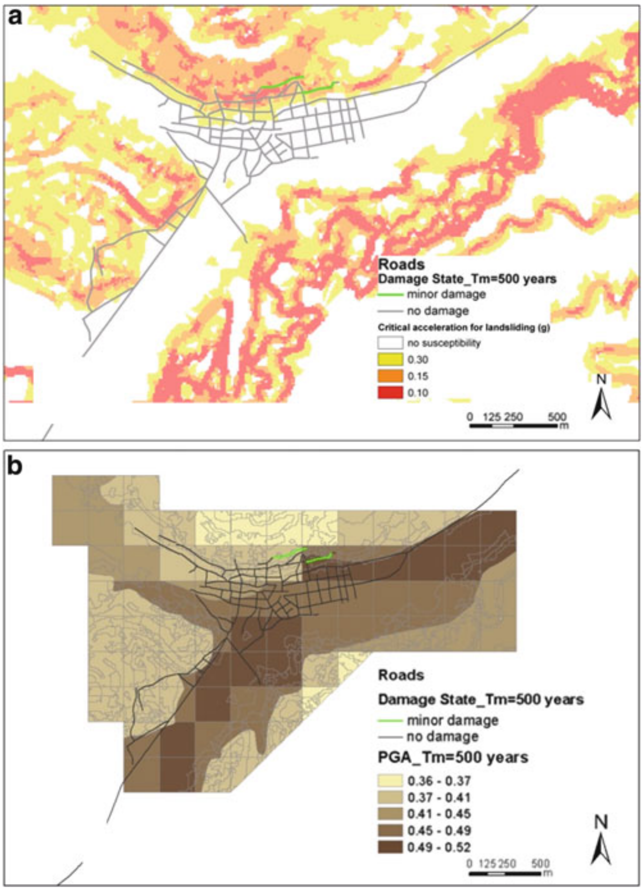

Fig. 4 Vulnerability assessment of the roadway system of Grevena due to landsliding for the 500 years seismic scenario. The spatial distribution of critical acceleration (**a**) and PGA (**b**) values is also shown

network that is expected to sustain damage (worst probable damage state/i.e. exceeding probability >50 %) for each damage state and scenario. The spatial distribution of the damages for the 500 and 1,000 years seismic scenario is illustrated in Figs. 4 and 5 respectively.

Discussion-Results

According to the results of the above application, the roadway system of Grevena is expected to sustain no damages for the 100 years scenario. For the 500 years scenario, 2.3 % of the network is expected to sustain slight damages, while for the 1,000 years scenario, 10.1 % of the network would suffer slight damages and 0.80 % moderate damages. As it was expected the damages are observed in the steep slope

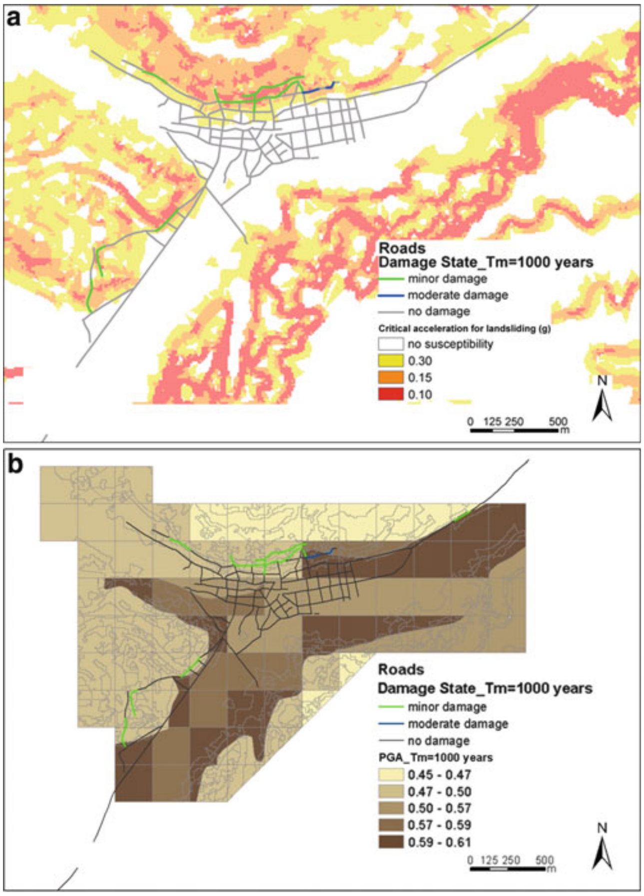

Fig. 5 Vulnerability assessment of the roadway system of Grevena due to landsliding for the 1,000 years seismic scenario. The spatial distribution of critical acceleration (**a**) and PGA (**b**) values is also shown

regions of the city. For the 1,000 years scenario the rate of damages is increased and more road segments are estimated to suffer important damages. It is worth noting that the level of damage estimated using the aforementioned methodology is less severe compared to the corresponding level of damage anticipated using the HAZUS methodology (Pitilakis et al. 2009).

Conclusions

A semi-empirical methodology to quantify vulnerability of roads due to earthquake induced earth slides has been presented. The method incorporates the characteristics of the slope (geometry, material properties) and the magnitude of the scenario earthquake within the probabilistic methodological framework. Several sets of fragility curves in terms of PGA can be constructed depending on the value of the yield coefficient of the potential landslide mass and the moment magnitude of the expected earthquake scenario.

The proposed approach is applied with the aid of GIS tool to assess the vulnerability of the roadway system of city of Grevena in NW Greece for three different earthquake scenarios. The proposed fragility curves predict less damage compared to the corresponding, generally conservative, HAZUS curves.

Acknowledgments The work described in this paper was supported by the project SafeLand "Living with landslide risk in Europe: Assessment, effects of global change, and risk management strategies" under Grant Agreement No. 226479 in the 7th Framework Program of the European Commission. This support is gratefully acknowledged.

References

AGSO (2001) Natural hazards and the risk they pose to South-East Queenland. AGSO-Geoscience Australia. Digital report on CD-ROM, Queenland, 389pp

Azevedo J, Guerreiro L, Bento R, Lopes M, Proença J (2010) Seismic vulnerability of lifelines in the greater Lisbon area. Bull Earthq Eng 8:157–180

Bray JD, Travasarou F (2007) Simplified procedure for estimating earthquake-induced Deviatoric slope displacements. J Geotech Geoenviron Eng 133(4):381–392

Giovinazzi S, King A (2009) Estimating seismic impacts on lifelines: an international review for riskscape. In: Proceedings of 2009 NZSEE conference New Zealand, Christchurch, April 2009

Jibson RW (2010) Methods for assessing the stability of slopes during earthquakes – a retrospective. Eng Geol. doi:10.1016/j.enggeo.2010.09.017

Leone F, Aste JP, Leroi E (1996) L'évaluation de la vulnerabilité aux mouvements de terrain. Rev Géographie Alpine 84(1):35–46

Michael-Leiba M, Baynes F, Scott G, Granger K (2003) Regional landslide risk to the cairns community. Nat Hazard 30:233–249

National Institute of Building Sciences (NIBS) (2004) Earthquake loss estimation methodology HAZUS 2004, technical manual. FEMA, Washington, DC

Pitilakis et al (2009) SRM-DGC: Development and proposition for implementation of an efficient methodology and appropriate local instruments for the management, prevention and reduction of seismic risk in Düzce – Turkey, Grevena – Greece and Catania – Italy. Final Report, Part A (2009), Final report for the city of Grevena (WP: 1-5), Laboratory of Soil Mechanics, Foundations & Geotechnical Earthquake Engineering, Department of Civil Engineering, Aristotle University of Thessaloniki, Thessaloniki

Pitilakis K et al (2010) Physical vulnerability of elements at risk to landslides: Methodology for evaluation, fragility curves and damage states for buildings and lifelines. Deliverable 2.5 in EU FP7 research project No 226479 SafeLand – living with landslide risk in Europe: Assessment, effects of global change, and risk management strategies

Pitilakis K, Anastasiadis A, Kakderi K, Manakou M, Manou D, Alexoudi M, Fotopoulou S, Argyroudis S, Senetakis K (2011) Development of comprehensive earthquake loss scenarios for a Greek and a Turkish city: Seismic hazard, Geotechnical and Lifeline Aspects. Earthquakes and Structures (accepted for publication)

Remondo J, Bonachea J, Cendrero A (2008) Quantitative landslide risk assessment and mapping on the basis of recent occurrences. Geomorphology 94:496–507

Tang C, Zhu J, Qi X (2011) Landslide hazard assessment of the 2008 Wenchuan earthquake: a case study in Beichuan. Can Geotech J 48:128–145

Zêzere JL, Garcia RAC, Oliveira SC, Reis E (2008) Probabilistic landslide risk analysis considering direct costs in the area north of Lisbon (Portugal). Geomorphology 94(3–4):467–495

THE SECOND
WORLD
LANDSLIDE FORUM

Earthquake Related Landslides in the Indian Himalaya: Experiences from the Past and Implications for the Future

Surya Parkash

Abstract

Most parts of the Indian Himalaya fall in seismic zone V and IV, indicating a high degree of susceptibility to earthquakes. Although numerous studies on earthquake risk assessment have been done by different researchers yet very few of these studies and reports have focused on landslides related to earthquakes. It has been observed globally that many casualties during an earthquake in a hilly terrain are attributed to the incidences of landslides triggered by the earthquake and the response actions are also hurdled by the rockfalls/landslides along the highways. Field observations have indicated that such landslides are often associated with earthquakes of magnitude 4 or more. About 20–25 % losses during earthquakes in hilly terrains have been attributed to landslides. The earthquake triggered landslides have affected even the structures and buildings which were well constructed but adversely located in the ground. However, a perusal of seismic zonation studies indicate that landslides have not received due attention. Similarly most of the landslides hazard zonation studies do not consider the impacts of earthquakes in generating numerous and large landslides. Hence, the present paper emphasizes the significance of earthquake related landslides in the hilly terrains through experiences from the past incidences of landslides during earthquakes along with their impact and proposes its consideration in future earthquake risk management programmes as well as in landslides hazard zonation studies for effective risk reduction strategies. The significant earthquakes that affected the Himalayan terrain include Assam (1897), Kangra (1905), Bihar-Nepal (1934), Shillong (1950), Bihar-Nepal (1988), Uttarkashi (1991), Chamoli (1999), Kashmir (2005) etc., that caused heavy damages/losses as well as casualties which were found partly related to the ground and slope failures during these earthquakes. A study of landslides associated with earthquakes has lead to identification of morphological, lithological, tectonic, hydrological and landuse conditions that govern the occurrence of such landslides. For example, most of earthquake triggered landslides/rockfalls happened on convex slopes whereas rain-induced landslides are more common on concave slopes. The concentration of landslides and their size has also been found proportional to the magnitude of the earthquake to some extent. An attempt has also been made to differentiate freshly triggered and reactivated co-seismic landslides in earthquake affected areas as well as post-seismic landslides.

Keywords

Earthquake • Landslide • Himalaya • Risk

S. Parkash (✉)
Geohazards Division, National Institute of Disaster Management, 5B,
I.P. Estate, M.G. Road, New Delhi 110002, India
e-mail: suryanidm@gmail.com

C. Margottini et al. (eds.), *Landslide Science and Practice*, Vol. 5,
DOI 10.1007/978-3-642-31427-8_42, © Springer-Verlag Berlin Heidelberg 2013

Introduction

Globally several earthquakes took place in different hilly regions like Bam earthquake (26 December 2003, Ms-6.5), Wenchuan earthquake (12 May 2008, Ms-8.0), Pak earthquake (8 October 2005, Mw-7.6), Elazig earthquake (8 March 2010, Mw-6.1) and resulted in heavy damages/losses due to landslides related to these earthquakes. Similarly the Indian territory has also faced significant earthquakes like Shillong (12 June 1897, M-8.7), Kangra (4 April1905, M-8.0), Bihar-Nepal (15 January 1934, M-8.3), Assam (15 August 1950, M-8.6), Bihar-Nepal (20 August 1988, M-6.6), Uttarkashi (20 October 1991, M-6.4), Chamoli (29 March 1999, M-6.6), Bhuj (26 January 2001, M-7.7), Indian Ocean (26 December 2004, M-9.3), Kashmir (8 October 2005, M-7.6), Sikkim (14 February 2006, M-5.7) etc., that caused heavy damages/losses as well as casualties which were found partly related to the ground and slope failures during the earthquakes.

The paper will briefly discuss the broad topography, seismicity and landslides along with the observations made by former researchers in the study area and also relate them with other parts of the world. Finally, it will try to assess the impacts of earthquake related landslides and implication in future strategies for earthquake risk reduction.

Topography, Seismicity and Landslides in Himalaya

Topography is one of the most important parameter in earthquake related landslides in the hilly terrains. Therefore, it is desirable to briefly discuss about the topography of the area under study. The Indian Himalaya constitutes large variations in relief from low lying valleys (close to mean sea level) to high altitude mountainous areas (ranging >20,000 ft) as well as plateau regions. Thus, the likelihood of earthquake related landslides are very high. Further the region receives heavy rainfall (sometime >5,000 mm per year) during the monsoons and also due to orographic phenomenon resulting into cloudburst/thunderstorms. Intense & frequent rainfalls, particularly during the monsoons, have a marked impact on the spatial distribution of landslides. The antecedent precipitation before the earthquake events also makes the slopes more susceptible to landsliding. Similarly post event precipitation results into seepage of water into the slopes through the fissures and cracks developed during the earthquake causing post-earthquake landslides.

Seismically, the continuous tectonic activities have produced several catastrophic events in the past, as indicated through the seismic zonation map of India, where this area falls in seismic zone V and IV. It indicates that earthquakes of seismic intensity VIII or IX are possible in this region; with peak ground acceleration (PGA) as high as 0.4 g and 0.25 g, respectively for a return period of 500 years. It is quite possible that these levels of accelerations can generate landslides in hillslopes. However, large epicentral distances where landslides have been reported seem to be controlled by slope susceptibility rather than seismic load as can be seen by low values of minimum accelerations related to farthest landslides.

Landslides – Rock falls have commonly occurred in road and river cut slopes usually causing traffic disruption whereas translational landslides are commonly found along discontinuities dipping out of the slope face. These landslides are sometimes responsible for damming river or its channels and at times breaching of the dams/reservoirs, resulting in flash floods on downstream side. Lateral spreads are commonly found in sands or silts that liquefy due to building of dynamic pore water pressure. These slides initiates in very gentle slopes in the alluvial, deltaic or lacustrine deposits.

Review of Literature

A review of literature has been made to find out the major observations and suggestions from the past earthquake in the Indian Himalaya. The following section describes these earthquake events with particular reference to landslides.

During the Shillong earthquake (12 June 1897, M-8.7), landslips were caused on an enormous scale and deserved a special notice, both as to their origin and distribution. The landslips were produced by displacement of weathered surface layer that seldom extended deep into the hill. Besides these, the high sandstone scarps of the southern edge of Khasi and Garo Hills exhibited landslides due to throwing off of a greater or less width of solid sandstone on a large scale. In case of both these forms of landslips, the part of the hill which is left standing is always scarred with deep fissures, extending more or less parallel to the free face of the fall, and due to partial detachment of the material between them and the edge of the actual slip.

Bihar-Nepal Earthquake (15 January 1934, M-8.3): Landslides occurred in the mountain areas near Kathmandu, Udaipur, Garhi and in eastern Nepal. Most of these landslides in Kathmandu area were falls in metamorphic and crystalline rocks (phyllites, quartzites, granite-pegmatites) that formed part of the ridge in this valley. The hillsides in Udaipur Garhi were widely scarred with rock fall in gneisses and schists where vegetation was scanty. The falls were observed in the Siwalik Sandstones near Muksar which blocked the local channel and created lakes. Two of these lakes emptied after several weeks. The larger of the remaining lakes was about 600 ft long with a probable maximum depth of 25 ft. In Dharan, Dhankuta, one landslide caused 30 deaths while the other one resulted in 13 deaths.

These landslides weighing thousands of tons, occurred in gneisses, mica-schists and shattered quartzites. In Taplejung, two large pre-existing landslides were also reactivated. One of these landslides originated in 1927 and the other started in 1924. However, the Happy Valley Landslip Area did not move, evidently due to precautions taken in the previous years proved effective.

Bihar-Nepal earthquake (20 August 1988, M-6.6): The report of the Geological Survey of India on Bihar – Nepal Earthquake (20 August 1988) indicates that while many of the slides were attributed to the combined effects of earthquake and rainfall, the rockslides at Tindharia in Darjeeling district have directly been triggered by the earthquake. At Bansoi in North Sikkim, major landslides have occurred as a result of earthquake vibrations. However, as the ground vibrations did not penetrate deep into the slope, landslides on extra-ordinary scale did not occur.

In addition to the review of literature, the author would like to mention about some experiences gained from Uttarkashi earthquake (20 October 1991, M-6.4), Chamoli earthquake (29 March 1999, M-6.6) and Elazig earthquake (8 March 2010, M-6.0). The author observed an intimate relationship between seismic vibrations and landslides that either directly generated co-seismic landslides or destabilized the slope mass through volume expansion, fissures, cracks and deformations which subsequently caused post-seismic landslides. The size and distribution of these landslides appeared to be a function of the earthquake magnitude, depth, epicentral distance, and location on the fault plane. However, the occurrence of these landslides was subjected to various factors controlling landslide susceptibility, climatic and anthropogenic interventions. Sometimes these landslides appear to be very deceptive in nature making it difficult to identify them in the field.

Mechanism of Failure for Earthquake Related Landslides

Basically two major types of failures can be distinguished for earthquake related landslides. These are (1) Co-seismic landslides which occur during the earthquake event. These can be freshly triggered landslides or re-activated existing/ancient landslides. (2) Post-seismic landslides which occur after the earthquake event has passed but owes its origin to fissures, cracks, deformations induced by the earthquake event. The following section discusses the mechanism of failures for co-seismic and post-seismic landslides.

Co-seismic Landslides

According to Oldham (1899), when the rock of hill is set into elastic vibration by the earthquake wave, the superficial portion will, at one period or the other of the shock, be set in movement outwards, and this movement will be communicated to the soil cap. In the next semi-phase of the wave, the movement of the surface of the rock will be inwards, but the inertia of the overlying soil cap will prevent this following at once, and the effect will be a more or less complete reduction of the pressure of the soil cap on the rock. This reduction of pressure means a reduction of the friction, which alone prevents the soil cap from sliding down the hill, and so a landslip is formed where the reduction of resistance and the slope of the hill are sufficient to allow it.

In cases, where the adhesion of the subsoil to the underlying rock is great, where its thickness is small, or where the violence of the shock is not great enough, the slippage of the surface layer does not amount to a landslip, and in these cases the hillsides are found to be scarred with fissures. At the other extreme, the momentum imparted to the surface layer may be so great that an actual outward pull is set up, sufficient to overcome the resistance of both gravity and adhesion of the subsoil to the rock, and then we have not merely a landslide but the whole face of hill shot bodily off. The conditions that allow this appear to be rare, but they certainly did occur in some of the high scarps of the Khasi and Garo Hills.

In case of both these forms of landslips, the part of the hill which is left standing is always scarred with deep fissures, extending more or less parallel to the free face of the fall, and due to a partial detachment of the material between them and the edge of the actual slip.

It is only under very exceptional circumstances that a wave of low velocity, or acceleration, of wave particle could give rise to landslips. Given a sufficiently violent earthquake, the other factor that comes into play is the natural tendency of the hill to slip. This obviously varies with the slope; a gentle slope being much less liable to slip than a steep one and the nearer the slope reaches that critical angle at which the soil cap should slip away at its own accord, the less the impulse required to set it in motion. During earthquakes, slope materials behave in an undrained manner because excess pore pressures induced by dynamic deformation of the soil column can not dissipate during the brief duration of seismic shaking.

There is, however, another factor which appears to be of almost equal importance with the angle of the slope that is the height from base to crest. Steep slopes and scarps of low height, had remained uninjured, while gentle slopes that formed part of a hill rising to several hundred feet had been scarred with landslips. Where the hills are high and cut by deep valleys, landslips are common. But where the height of the hills above the valleys is much smaller, landslips are almost unknown though the earthquake was on the average equally severe.

The explanation of the connection between the height of the slope and the degree to which they have been scarred by landslips is doubtless the greater swing which was imparted to higher hills. This is due to the fact that an equal angular motion would result in greater linear movement at the top of a high hill than of a low one. But mainly it is due to the greater elastic play of the high hill, especially when steep sided; just as the end of a long switch jerked to and fro describes a larger area than that of a short one.

There is yet another factor in generating landslips, i.e. mineral constitution of the hill. When the hill is composed of crystalline rocks, the surface layer of disintegrated and weathered material is either thin or it passes down into the unweathered rock in a gradual manner. In the former case, the thin skin may not acquire sufficient momentum to cause it to be detached from the underlying rock. In the latter, the gradual increase in the cohesion of the surface layer, adhesion to the underlying rock is proportionate to the increase of strain applied, and the surface layer will be much less liable to come away than if there was a more or less well defined plane of weakness.

In the case of sedimentary rocks, the boundary between the weathered soil cap and the underlying rock is generally more abrupt and the surface layer readily separates from the rock below. These rocks (sandstones) have much lower cohesive strength than the crystallines and metamorphic rocks and when such rocks form high scarps, portions of solid rock itself may be thrown off.

Thus, besides the energy of earthquake waves, the production of landslips is controlled by the petrological composition of the hill, slope angle and height of the hill including size and form. Attributing the whole effects to only one of the operating causes may not be appropriate.

It is difficult to detect any relation between the size and frequency of the landslips and the direction of the slope, direction of the travel of earthquake wave as the geological and orographical conditions control the highest and steepest slopes.

Post-seismic Landslides

The observations on landslides that occurred after some time of the main earthquake has provided the following information.

A part of the effects noticed was due to the action of heavy rains following the earthquake and partly to the aftershocks of the main earthquake. Many of these were themselves violent enough to cause landslips, the more so as many hillsides, which had not come down in the main shock, had been badly shattered and weakened, and were more easily broken down than otherwise would have been the case.

The heavy rains which followed the earthquake probably had even a greater effect than the aftershocks in bringing down the hill sides, which had been fissured and weakened by the earthquake. It was not found possible to distinguish the direct effects of earthquake from its indirect effects or those of after-shocks. However, the larger number of landslides occurred during the earthquake and the subsequent additions to the size and number were only a fraction of what could be seen immediately after the main shock.

Bhandari (2006) laid down the following observations for cases of earthquake induced landslides.

- No slope mass with a static factor of safety of 1.7 or greater has failed in an earthquake, no matter how large in magnitude
- Steep sided bedrock ridges are generally subjected to more intense level of ground shaking than adjacent valleys are in the near field area, close to the source of shaking. An exception of this may come because of the amplification of the strong motion due to alluvium cover on the valley bottom.
- The response of a large ancient landslide to seismic forces is significantly modulated by number of strong motion cycles (duration of shaking) rather than by short-lived peak ground acceleration. With each cycle, more and more of seismic energy gets trapped into the body of the slope, thereby robbing of its elastic response, eventually causing local slippages, or a full fledged landslide.
- When a slope fails as a rigid body, the acceleration is assumed to be constant over the entire slope, and usually it refers to the horizontal component of the slope surface acceleration.
- Ground surface acceleration alone is a poor measure of the effect of shaking on slope stability, intensity even more so. Ground velocity, the experiences during the occurrence of past large magnitude earthquakes, and the duration of the shaking are considered to be better indicators of landslide susceptibility under seismic conditions.
- Ground cracks generated by earthquakes serve as conduits for rain water and become source for weak ground in the long run.
- The limiting threshold for an earthquake induced landslide is earthquakes of magnitude 4 or more on the Richter scale.
- Area within which landsliding is generated tend to increase with the magnitude of earthquake shock, from $<100\ \text{km}^2$ at magnitude 4, rising to about 500,000 km^2 at magnitude 9.2 (Keefer 1984). The influence zone gets modified by external factors such as ridges, convex slopes and escarpments.

Observations Made by Other Researchers

- Where landslides can be triggered by typhoons (tropical cyclones) and earthquakes, a rain-induced model is insufficient because it provides only a partial explanation of landslide occurrence and overlooks the potential effect of earthquake on typhoon triggered landslides (Chang et al. 2007). Thus, there is a need to develop models for earthquake induced landslides as well as typhoon induced landslides. Typhoon triggered landslides tend to be near stream channels and earthquake triggered landslides were more likely to be near ridge lines.

- Most of the loess landslides triggered by the Haiyuan earthquake (China 1920) occurred on concave slopes gentler than 15° with long run-out distance, showing very small equivalent friction angle (Zhang and Wang 2007)
- Landslide moving directions showed preferred orientations normal to the fault ruptures, indicating the effect of the directivity of the seismic wave (Chigira et al. 2010). Slow and fast moving landslides as well as factors affecting their occurrence are also very important for estimation of landslide impacts.
- ANOVA (Analysis of Variance) technique has been used to determine how the occurrence of landslides correlates with distance from the earthquake source, slope steepness, and rock types. The landslide concentration (defined as the number of landslide sources per unit area) has a strong inverse correlation with distance from the earthquake source and a strong positive correlation with slope steepness. The landslide concentration differs substantially among the various geologic units in the area. The difference correlated to some degree with differences in lithology and degree of induration, but this correlation is less clear, suggesting a more complex relationship between landslide occurrence and rock properties (Keefer 2000)
- The number of landslides is disproportionate for the size of the earthquake. There are also important differences in the characteristic type of landslides in different geological terrains. For example, soil falls and slides in steep slopes in volcanic soils predominated in Guatemala and El Salvador, whereas extensive translational slides in lateritic soils on large slopes are the principal hazards in Costa Rica and Panama (Bommer and Rodriguez 2002).
- Rodriguez (2006) studied the relationship between earthquake magnitude and landslide characteristics in Colombia. It was found that residual and volcanic soils are more susceptible to landslides by earthquakes. The influence of precedent climatic conditions was observed in reducing the seismic load required to induce landslides.
- Over 10,000 landslides were triggered by the September 21, 1999 Chi-Chi earthquake. The most abundant landslides were shallow, disaggregated rock and soil slides. Landslides occurred primarily in Tertiary sedimentary rocks, which are well known for their susceptibility to landsliding in many parts of the world. Landslide concentration values diminish beyond epicentral distance of 40 and 70 km from the epicenter and the surface projection of the fault plane respectively (Khazai and Sitar 2004).
- In the epicentral areas of major recent earthquakes, landslide density scales with PGA. Topographic site effects on seismic waves are known to cause important gradients in ground acceleration in individual mountain areas. Earthquake triggered landslides clustered ner ridge crests, where the susceptibility to landsliding was greatest. Secondary landslide clusters were found in colluvial slope toes (Meunier et al. 2008).
- Nepop and Agatova 2008 attempted to derive the magnitude of pre-historic earthquakes on southeastern Gomy Altai from the size of the largest landslides that triggered using an empirical correlation between the earthquake magnitude and the volume of associated landslides.
- Northridge, California Earthquake (17 January 1994, Mw-6.7) triggered thousands of landslides over a broad area. Landslides occurred primarily in young (Late Miocene through Pliocene) uncemented or weakly cemented sediments that has been repeatedly folded, faulted and uplifted in the past 1.5 million years. The most common types of landslides triggered by the earthquake were highly disrupted, shallow falls and slides of rock and debris. Far less numerous were deeper, more coherent slumps and block slides, primarily occurring in more cohesive and competent materials. To quantify and rank the relative susceptibility of each geologic unit to seismic landsliding, susceptibility index and frequency index have been used. Susceptibility Index is ratio (given as a percentage) of the area covered by landslide sources within a geologic unit to the total outcrop area of that unit and Frequency Index (given in landslides per square kilometer) is the total number of landslides within each geologic unit divided by the outcrop area of that unit. Susceptibility categories include very high (>2.5 % landslide area or >30 ls/km^2), high (1–2.5 % landslide area or 10–30 ls/km^2), moderate (0.5–1 % landslide area or 3–10 ls/km^2) and low (<0.5 % landslide area or <3 ls/km^2) as reported by Parise and Jibson (2000)
- A total of 4,134 landslides covering 19.7 km^2 that accounted for 6.4 % of the study area were reported from Anxian to Beichuan after the Wenchuan earthquake (12 May 2008, Ms-8.0). The number of landslides with areas less than 5,000 m^2 is upto 85.22 %. The smallest landslide is 6 sq.m and the largest is 1515,000 m^2. The number of landslides which have occurred is 1.6 times more prevalent in hanging walls as opposed to foot walls. Also the relationship between the number of landslides and distance to an earthquake rupture at a hanging wall is linear but exponential at a footwall. This indicates that landslide activity is more severe at hanging walls than at foot walls. (Yin et al. 2009)
- In the near field of causative faults, landslides tend to have the initial sliding direction similar to the movement of causative fault. It is indicated that landslide incidences vary in different slopes with different structure, and consequent slopes and obsequent slopes have a higher landslide incidences than the layered slopes (Qi et al. 2010)

- 2004 Mid Niigta prefecture earthquake (Mjma-6.8) triggered more than one thousand landslides in the Miocene to Quaternary sedimentary rocks in Japan. The most common landslides were shallow disrupted landslides on steep slopes. The earthquake triggered more than one hundred deep landslides. Reactivation of existing landslides and undercutting of slopes are the most important factors for deep landslides. In addition, planar sliding surfaces seem to be essential for the generation of catastrophic landslides. Planar bedding – parallel sliding surfaces were formed at the boundary between overlying permeable sandstone and underlying siltstone or along the bedding planes of alternating beds of sandstone and siltstone (Chigira and Yagi 2006).
- The Kashmir earthquake (8 October 2005, Mw-7.6) destabilized numerous slopes by creating a large number of tension cracks which may lead, together with the monsoonal climatic conditions, to increased landslide activity. The landslide inventory showed that 158 landslides were triggered along Balakot – Bagh fault. The most abundant type of active landslide was translational, which was mainly concentrated along the fault line in the Muzaffarabad Formation (Saba et al. 2010). Kamp et al. (2008) mapped 2,252 landslides after the Kashmir earthquake using satellite imagery. A multi-criterion evaluation was applied to determine the significance of event-controlling parameters in triggering landslides. The parameters included lithology, faults, slope gradient, aspect, elevation, landcover, rivers and roads. It indicated that lithology had the strongest influence on landsliding particularly when the rock is highly fractured. Moreover, the proximity of the landslides to faults, rivers and roads was also an important factor to initiate failure. Owen et al. (2008) reported that most of these landslides were mainly rock-falls and debris-falls, although translational rock and debris slides also occurred. In addition, a sturzstrom (debris avalanche) comprising ~80 million m^3 buried four villages and blocked streams to create 2 lakes. Although landslides occurred throughout the region, covering an area of >7,500 km^2, the failures were highly concentrated, associated with six geomorphic-geologic-anthropogic settings, including natural failures in (1) highly fractured carbonate rocks comprising the lowest beds in the hanging wall of the likely earthquake fault; (2) Tertiary siliciclastic rocks along antecedent drainages that traverse Hazara – Kashmir syntaxis; (3) Steep slopes (>50°) comprising Precambrian and Lower Paleozoic rocks; (4) very steep (>>50°) lower slopes of fluvially undercut Quaternary valley fills; (5) Ridges and spur crests and (6) Roads.
- The Avaj, Iran earthquake (22 June 2002, Mw-6.5) triggered landslides that include 47 falls and topple zones, 9 slides and 3 lateral spreads. The density of landslides decreases away from the fault zone in a manner that is asymmetric with respect to direction. Although several slides and lateral spreads were seen, the most common types of triggered landslides are falls and topples (Mahadavifar et al. 2006)
- Over 56,000 landslides were triggered by Wenchuan earthquake (12 May 2008, Ms-8), with a total area of 811 km^2. The spatial distribution of these landslides was analysed using Landslide Point Density (defined as the number of landslides per sq km) and the Landslides Area Density (the percentage of area affected by landslides) by Dai et al. (2011).

Impacts of Landslides

Primary impacts of earthquake landslides include

- Loss of human lives and livestock due to burial; Injuries to people being hit by landslides
- Loss of land, its productivity (in case of agricultural or farm lands) and revenue
- Loss of livelihood, living places, belongings, business, commercial and social activities
- Damage to building, structures, infra-structure and utilities located on failed slope
- Loss of trees in forest lands and damage to natural environment
- Clogging of damming of river channels (by debris, boulders and uprooted trees) forming landslide dammed lakes which burst and bring flash-floods on downstream side
- Sedimentation and inundation of reservoirs

Secondary impacts of the landslips are

- Modification in the forms of water courses. The dislodgement of large bodies of weathered rocks, and to no less an extent the consequent exposure of hill sides previously protected by forest, caused enormous volumes of sand to be cast into the streams. Thus, landslides not only change the morphology of the terrain but also an effective factor in sediment production. There still large quantities of sand not yet removed from the landslips and the bare faces of the hills will be the source of fresh supplies of sand as they are scoured by the rain, until such time as vegetation once more resumes its away. Often the channels are encumbered by innumerable landslips, forming a mass of boulders, gravels, sand and trunks of trees, carried down stream sometimes within and beyond the limits of hills.
- The burden of sand cast on to the streams was far greater than they could carry along their old gradients, and everywhere the beds have been raised, changing the whole character of the river channel in the process. Ordinarily, the beds of these rivers, which are raging torrents when in

floods, consist of succession of deep pools separated by rocky rapids. It was found that the pools had been filled up, and the rapids obliterated by a great deposit of sand, over which the rivers flowed in a broad and shallow stream. The remaining level of the river beds are raised due to debris brought down by the rain water. A remarkable instance was that of landslips near Sinya (1897 earthquake), to the east of Rambrai, which dammed up the drainage of a large area for nearly 3 months and gave the destructive flood.

Implications in Future Strategies and Programmes

The results of the above study can be applied in future strategies and programmes for development and disaster risk reduction in the following ways:

- Compile Inventory/Database of Earthquake Induced Landslides from the historical records of past earthquakes. This inventory will be used to improve the understanding of earthquake induced landslides and the casual relation between landslides and geo-environmental and triggering factors. The inventory should also include cascading hazards like landslide dams and flash-floods due to breaching of dams by landsliding. Identify the most common of types of slopes failures due to earthquakes.
- Assessment of the relationship between earthquakes and landslide characteristics, volume, velocity, frequency and spatial distribution. Establish relationship between number, type and size of landslide to the seismic parameters (earthquake magnitude, depth, distance from epicenter etc.)
- Landslide characteristics and their relationship between predetermined and predisposing factors should be evaluated.
- Landslides Relations with distance from focus/epicentre of earthquake, location on the fault plane (foot-wall and hanging wall), tectonic plane, slope aspect and form (concave and convex), location on slope (ridge or toe), degree of consolidation, extent of weathering, drainage, thickness of over-burden etc. to understand the seismic landslide susceptibility. The relationship of the interface between the overburden and bedrock (as well as different rock types) and depth of sliding is also important.
- Siting Guidelines for buildings, structures, Infra-structure and Utilities in Earthquake Prone Areas Susceptible to Landsliding (with main concern on landslides and slope stability under seismic action)
- Monitoring and assessment of landslide hazards in earthquake prone areas is an important task for decision making and policy planning in landslide prone areas.
- Disaster Management and Development programmes to include concerns for earthquake induced landslides in hilly terrains.
- Landslide micro-zonation studies to consider the impacts of earthquake and seismic micro-zonation studies to include the impacts of landslides. Identify the possible types of landslides, their characteristics and consequences.
- The influence of the precedent climatic conditions and effects of climate changes on landslide risks in earthquake prone areas should also be considered.
- Any new construction or rehabilitation or resettlement should consider slope stability and susceptibility to landslides in seismic hazard zones.
- Infrastructure development practice in the mountainous terrains prone to earthquakes, need extensive care on slopemass, morphology and aspects to reduce landslide risks.
- Existing zonation methods of earthquake induced landslides must be reviewed and compared with historical data information in order to define the most important triggering and susceptibility factors and to establish a method to assess them to be applied in an improved zonation methodology. At present, no such standard or code of practice exists in India.
- Establish relationship between seismic parameters and number of landslides, area affected by landslides and landslide characteristics including seismic shaking thresholds for triggering landslides

Conclusion

It may be concluded from the present study that there is an urgent need to systematically compile the database of earthquake induced landslides from the past earthquake and assess the relationships between earthquakes and landslides characteristics, volume, velocity, frequency and spatial distribution. There is a need to study the relation between magnitude of earthquakes and terrain characteristics like topography, geology, morphology, landuse and landcover conditions etc.

Scientific studies involving mapping of co-seismic and post-seismic landslides along with factors affecting their occurrence in terms of magnitude and impacts are very important to develop an appropriate understanding as well as strategy for earthquake risk mitigation and preparedness. The neglect of this field in the earthquake risk management of hilly terrains has proved quite costly in terms of lives lost and damages to the structures, infrastructure and services.

The lessons learnt from the past earthquake related landslide events clearly indicate that a pro-active mitigation and response strategy is needed to manage the consequences of any major earthquake in the hilly terrains of north east India. A proper documentation of the historical database of earthquake induced landslides would help in delineating the probable susceptible zones that may fail in future earthquakes. Most sensitive or susceptible conditions for earthquake related landslides have been found to be among the younger, unconsolidated or less consolidated fragile/fractured/laminated materials located in a high topography towards the ridges with steeper convex slopes and unfavorable orientations.

Based on these studies, the disaster management authorities and all other concerned department/organizations can plan the developmental activities and prepare strategies to reduce the impending risks.

In general, topographical, geological, tectonic, seismic and climatic conditions, besides the uncontrolled anthropogenic interventions, are the common causes of earthquake related landslides that have large socio-economic and environmental impacts. The emerging issues related to climate change induced precipitation changes should also be considering in simulating scenarios for earthquake related landslides for future risk mitigation strategies and programmes. Development of siting guidelines for earthquake prone areas in hilly terrains which are susceptible to landslides, is essential for effectively reducing the envisaged risks.

References

Bhandari RK (2006) “Importance of earthquake induced landslides in landslide hazard mapping” keynote address at first India disaster management congress, New Delhi, 29–30 Nov 2006

Bommer Julian J, Rodriguez Carlos E (2002) Earthquake induced landslides in Central America. Eng Geol 63(3–4):189–220

Chang K-T, Chiang S-H, Hsu M-L (2007) Modeling typhoon and earthquake induced landslides in a mountainous watershed using logistic regression. Geomorphology 89:335–347

Chigira M, Yagi H (2006) Geological and geomorphological characteristics of landslides triggered by the 2004 Mid Niigta prefecture earthquake in Japan. Eng Geol 82(4):202–221

Chigira M, Wu X, Inokuchi T, Wang G (2010) Landslides induced by the 2008 Wenchuan earthquake, Sichuan, China. Geomorphology 118(3–4):225–238

Dai FC, Xu C, Yao X, Xu L, Tu XB, Gong QM (2011) Spatial distribution of landslides triggered by the 2008 Ms.8.0 Wenchuan earthquake, China. J Asian Earth Sci 40(4):883–895

Kamp U, Growley BJ, Khattak GA, Owen A (2008) GIS-based landslide susceptibility mapping for the 2005 Kashmir earthquake region. Geomorphology 101(4):631–642

Keefer DK (1984) Landslides caused by earthquakes. Bull Geol Soc Am 95:406–421

Keefer DK (2000) Statistical analysis of an earthquake-induced landslide distribution – the 1989 Loma Prieta, California event. Eng Geol 58(3–4):231–249

Khazai B, Sitar N (2004) Evaluation of factors controlling earthquake-induced landslides caused by Chi-Chi earthquake and comparison with the Northridge and Loma Prieta events. Eng Geol 71:79–95

Mahadavifar MR, Solyamani S, Jafari MK (2006) Landslides triggered by the Avaj, Iran earthquake of June 22, 2002. Eng Geol 86 (2–3):166–182

Meunier P, Hovius N, Haines JA (2008) Topographic site effects and the location of earthquake induced landslides. Earth Planetary Sci Lett 275(3–4):221–232

Nepop RK, Agatova AR (2008) Estimating magnitudes of prehistoric earthquakes from landslide data: first experience in southeastern Altai. Russ Geol Geophys 49(2):144–151

Oldham RD (1899) Report on the great earthquake of 12th June 1897, vol 29, Memoirs of the geological survey of India. Office of the Geological Survey, Calcutta, p 379

Owen LA, Kamp U, Khattak GA, Harp EL, Keefer DA, Bauer MA (2008) Landslides triggered by the 8 October 2005 Kashmir earthquake. Geomorphology 94(1–2):1–9

Parise M, Jibson RW (2000) A seismic landslide susceptibility rating of geologic units based on analysis of characteristics of landslides triggered by the 17 January, 1994 Northridge, California earthquake. Eng Geol 58:251–270

Qi S, Xu Q, Lan H, Zhang B, Liu J (2010) Spatial distribution analysis of landslides triggered by 2008.5.12 Wenchuan Earthquake, China. Eng Geol 116(1–2):95–108

Rodriguez CE (2006) Earthquake induced landslides in Colombia. ECI conference on Geohazards, Norway

Saba SB, Meijde M, Werff H (2010) Spatio-temporal landslide detection for the 2005 Kashmir earthquake region. Geomorphology 124 (1–2):17–25

Yin YP, Wang FW, Sun P (2009) Landslide hazards triggered by the 2008 Wenchuan earthquake, Sichuan, China. Landslides 6:139–152

Zhang D, Wang G (2007) Study of the 1920 Haiyuan earthquake induced landslides in loess (China), Enginerring Geology, 94(1–2):76–88

THE SECOND
WORLD
LANDSLIDE FORUM

Relationships Between Slope Instabilities, Active Tectonics and Drainage Systems: The Dúdar Landslide Case (Granada, Southern Spain)

Martín Jesús Rodríguez-Peces, José Vicente Pérez-Peña,
José Miguel Azañón, and Alicia Jiménez-Gutierrez

Abstract

A geomorphologic description of the Dúdar landslide (Granada, S Spain) has been carried out using a high-resolution digital elevation model derived from LIDAR (Light Detection and Ranging) data. We have analysed the significant changes that the landslide caused in the drainage system of the Aguas Blancas and Darro rivers, which in turn are the consequence of the tectonic activity of the north-eastern border of the Granada Basin. These modifications comprise river diversions and active incision within the body of the landslide, making it susceptible to future reactivations. A stability back-analysis of the landslide has been performed to identify the mechanism of failure and the most-likely triggering factors. This analysis shows that a low-to-moderate magnitude earthquake (M_w 5.0–6.5) related to the active faults in the Granada Basin seems to be the main triggering factor of the Dúdar landslide.

Keywords

Active tectonic • Betic Cordillera • Drainage system • Dúdar • Landslide • Newmark • Seismicity

Introduction

Large and giant landslides (>5 hm^3 according to Fell 1994) develop typically in active mountain belts, in areas with high local relief (Weidinger 2006; Korup et al. 2007; Prager et al. 2008). These slope movements act as active geomorphic agents, modifying the landscape and disturbing drainage networks (Turnbull and Davies 2006; Korup et al. 2007). Nevertheless, there are examples of extremely large landslides developed in areas with medium to low landscape gradients (Philip and Ritz 1999; Strasser and Schlunegger 2005; Davies et al. 2006; Van Den Eeckhaut et al. 2007; Pánek et al. 2007, 2010). In such areas, those giant slope instabilities can be considered as rare, and normally they are controlled by specific geomorphologic and tectonic settings.

In this paper, we have carried out a geomorphologic description of the Dúdar landslide. This large fossil landslide was developed in an area with medium landscape gradient as is the Granada Basin (Betic Cordillera, SE Spain). In the NE border of this basin, the landscape evolution during the Quaternary is the consequence of its active tectonic configuration (Rodríguez-Fernández and Sanz de Galdeano 2006). We analyzed the landslide geomorphic features with the aid of a high-resolution digital elevation model (DEM) derived from LIDAR (Light Detection and Ranging) data. We studied the significant changes that the landslide caused in the drainage system of the Aguas Blancas and Darro rivers.

M.J. Rodríguez-Peces (✉)
Department of Geodynamics, University Complutense of Madrid,
Ciudad Universitaria s/n, Madrid 28040, Spain
e-mail: martinjr@geo.ucm.es

J.V. Pérez-Peña • A. Jiménez-Gutierrez
Department of Geodynamics, University of Granada, Campus de
Fuentenueva s/n, 18071 Granada, Spain

J.M. Azañón
Department of Geodynamics, University of Granada, Campus de
Fuentenueva s/n, 18071 Granada, Spain

Instituto Andaluz de Ciencias de la Tierra (UGR-CSIC), Granada,
Spain

C. Margottini et al. (eds.), *Landslide Science and Practice*, Vol. 5,
DOI 10.1007/978-3-642-31427-8_43, © Springer-Verlag Berlin Heidelberg 2013

Finally, a stability back-analysis of the Dúdar landslide has been performed to identify the mechanism of failure and the most-likely triggering factors. By means of this analysis we realized if the presence of water could be the main controlling factor required to trigger the landslide, and the seismic activity related to the active faults located in the Granada Basin could be regarded as the main cause of the occurrence of this landslide.

Geological and Seismotectonic Context of the Dúdar Landslide

The Dúdar landslide is located in the eastern border of the Granada Basin (South Spain), which is one of the largest Neogene basins of the central Betic Cordillera (Fig. 1). The Dúdar landslide, with an extension of around 380 ha, is one of the largest landslides developed in this part of the Cordillera. The landslide mass comprises deposits from the sedimentary infilling of the Granada Basin. The sedimentary sequence within the landslide area comprises from bottom to top: (a) calcarenites, sandstones and marls (Lower Tortonian); (b) grey conglomerates, sandstones and marls (Upper Tortonian); (c) reddish conglomerates (Uppermost Tortonian); (d) reddish clays, sands and conglomerates (Lower Pleistocene to Upper Pliocene). The sedimentary units (a) and (b) were deposited in a marine environment related to a shallow coastal platform and fan deltas (García-García et al. 1999). The reddish conglomerates are related with alluvial fans, marking the change to continental conditions in the Granada Basin. The reddish clays, sand and conglomerates are related with a glacis residual surface developed at the end of the sedimentary record (Fernández et al. 1996). The contacts between these sedimentary units, in spite of being discordant, are mainly sub-horizontals.

One of the most important determinant factors for the Dúdar landslide development was the altitude difference between the Aguas Blancas and Arroyo de Belen Creek (tributary of the Darro River, Fig. 2). These two rivers, in despite of running parallel and separated by less than 2 km of distance, have an average altitude difference of around 200 m. This geomorphic configuration is the consequence of the tectonic activity in the NE border of the Granada Basin. This tectonic activity comprises NW-SE striking normal faults and roughly N70E directed-folds. Moreover, the Aguas Blancas River flows in this area through a synclinal hinge and the Darro drainage basin is located in the SE dipping flank of the fold. As a consequence of this tectonic configuration, the northwest margin of the Aguas Blancas River is highly unstable and presents a number of small landslides.

The most-likely triggering factor for the Dúdar landslide seems to be a great earthquake, as for other large landslides located in the Granada Basin such as the Güevéjar landslide (Rodríguez-Peces et al. 2011). Nevertheless, there are not historical data for such event but probably occurred prior to 1400, which is the date of the first historical records of the Dúdar village, located in one side of the landslide. In addition, the active normal faults of this part of the Granada Basin can potentially generate earthquakes with magnitudes greater than M_w 6.0 (Sanz de Galdeano et al. 2003).

Geotechnical Investigations

The main failure surface of the Dúdar landslide was estimated based on the field observations. This critical surface can be related to a translational movement developed successively in the grey conglomerates, sandstones and marls.

The main shear strength parameters corresponding to the sedimentary units involved in the landslide have been derived from some geotechnical tests developed in prior studies in similar Neogene marly and silty soils in the Granada Basin (El Amrani Paaza et al. 1998, 2000; Oteo 2001; Azañón et al. 2006, 2010, 2011; Rodríguez-Peces 2010; Rodríguez-Peces et al. 2011). The average values of these parameters (Table 1) have been used in the back-analysis of the Dúdar landslide, reported later.

Geomorphological Features of the Landslide

The Dúdar landslide covers an area of about 343 ha, with a maximum length of 2.9 km and maximum width of 1.9 km (Fig. 2). The complete geometry of the Dúdar landslide is described in Table 2, following the nomenclature for landslides suggested by the IAEG Commission on landslides (1990). Assuming an average depth of the failure surface of approximately 111 m (66–156 m), the mean volume of the landslide may then be roughly estimated at 379 hm^3 (226–533 hm^3).

The volume of landslides can also be estimated by means of empirical equations relating the landslide volume to geometrical features, mainly the landslide area. Recently, Guzzetti et al. (2009) have developed an area versus volume empirical relationship from a worldwide catalogue of landslides. These authors consider that the relationship is largely geometric, and not significantly influenced by geomorphological or mechanical properties of the failed soils or rocks, or the type of landslide. For this reason, this area-volume relationship has been used to obtain an additional estimation of the Dúdar landslide volume. The obtained mean volume is 286 hm^3

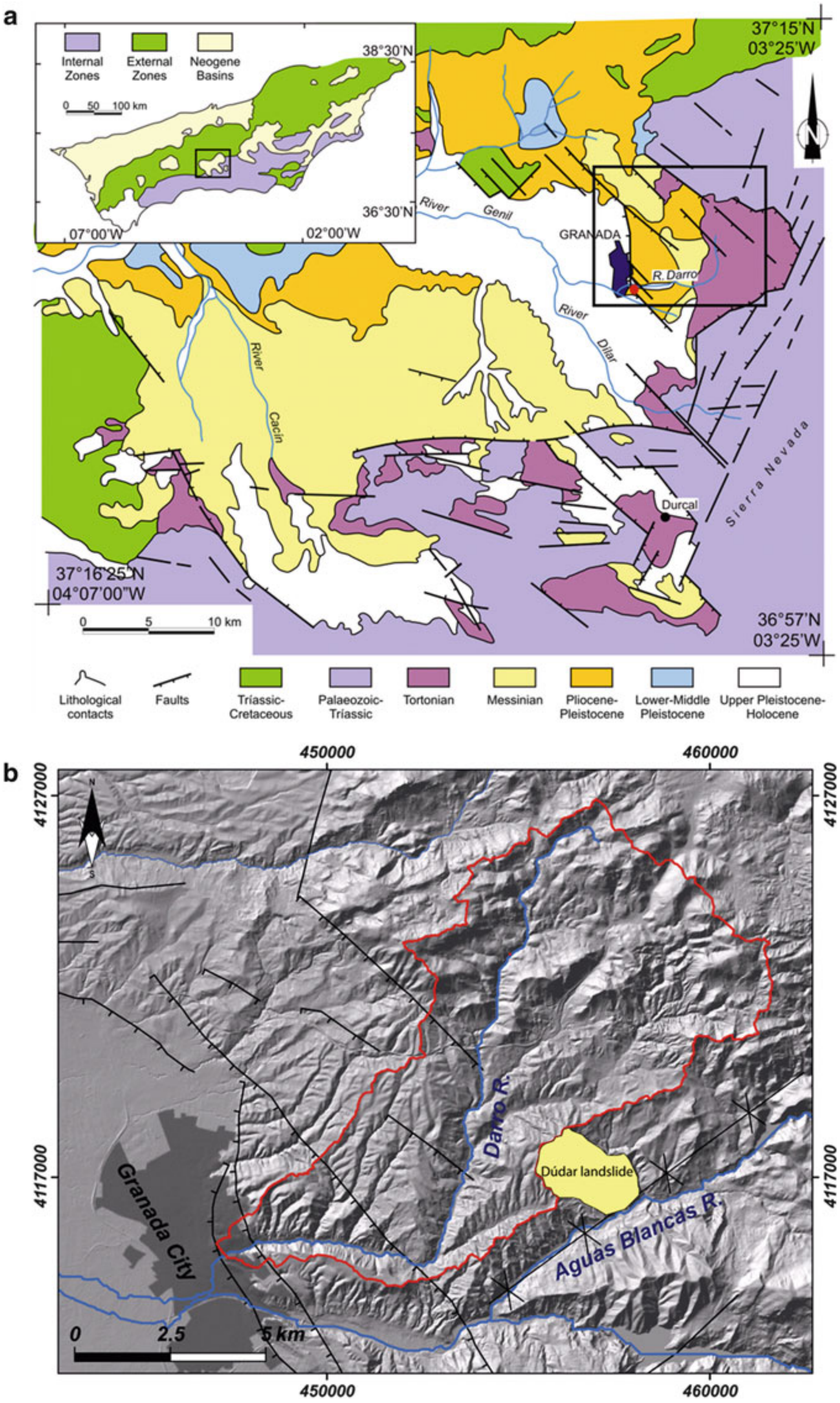

Fig. 1 (**a**) Simplified geological sketch of the central part of the Betic Cordillera (South Spain). The location of the Dúdar landslide area is marked with a *black* rectangle. (**b**) Digital elevation model (DEM) showing the location of the Darro and Aguas Blancas rivers. The location of the Dúdar landslide and the main tectonic structures are depicted

(251–326 hm^3). This mean value is slightly smaller than the one estimated above, but the minimum volumes estimated using this two different methods are of the same order of magnitude.

From field observations, the landslide body can be divided into three different parts: the head, the intermediate and the toe zones (Fig. 3). The head area corresponds to a large hill of about 110 m thick with an average slope gradient of 55°. These values are related to the main scarp of the landslide. The intermediate part of the landslide is related to the erosion of the landslide body by a river incision. The incision is particularly stronger in the landslide body since the sediments have been weakened as a consequence of the landslide

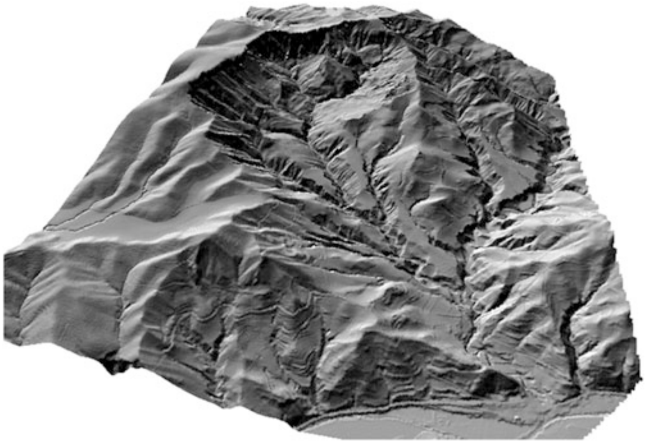

Fig. 2 High-resolution digital elevation model (DEM) of the Dúdar landslide derived from LIDAR (light detection and ranging) data

Table 1 Summary of the main geotechnical properties of the lithological units found in the Dúdar landslide. γ, unsaturated unit weight; γ_{sat}, saturated unit weight; c_r, residual cohesion; Φ_r, residual friction angle

Lithological unit	γ (kN/m^3)	γ_{sat} (kN/m^3)	c_r (kPa)	Φ_r (°)
Reddish conglomerates	21.53	23.16	81.90	38
Grey conglomerates, sandstones and marls	21.90	15.40	10.70	20
Calcarenites, sandstones and marls	23.76	24.53	30.41	29

movement. At the toe sector the thickness of the landslide mass is greater, but it was eroded by the Aguas Blancas River at the most distal sector, between the Dúdar and Quéntar villages.

Drainage System Changes

The Dúdar landslide caused significant changes in the drainage system of the Aguas Blancas and Darro rivers (Fig. 4). These modifications comprise river diversions and active incision within the body of the landslide, making it susceptible to future reactivations The Arroyo de Belen Creek (tributary of the Darro River) ends abruptly when it reaches the landslide, and the Darro main watershed makes an anomalous turn in that point (Fig. 4). The creek that flows at present-day to the Aguas Blancas River matches perfectly in shape with the Arroyo de Belen Creek, indicating that it should be part of the same watershed. The altitude difference between the Arroyo de Belen Creek and the Aguas Blancas is around 200 m. The Dúdar landslide altered the drainage, capturing part of the Darro Basin (i.e. the upper part of the Arroyo de Belen watershed). This capture had as a consequence a lowering in the base level and a prominent incision within the landslide mass (Fig. 3). Even though the landslide is now inactive, the river incision caused by this base-level lowering could reactivate the landslide in some points, making it a natural hazard to take into account.

Table 2 Summary of the main geomorphologic parameters of the Dúdar landslide following the nomenclature suggested by the IAEG Commission on landslides (1990)

Total length	L = 2,893 m
Length of the displaced mass	L_d = 2,758 m
Length of the rupture surface	L_r = 2,343 m
Width of the displaced mass	W_d = 1,880 m
Width of the rupture surface	W_r = 1,493 m
Depth of the displaced mass (maximum)	D_d = 202 m
Depth of the rupture surface (maximum)	D_r = 202 m
Total height (height from the crown to the tip of toe)	ΔH = 358 m
Perimeter	P = 8,319 m
Total area	A = 3,427,062 m^2

Stability Back-Analysis of the Dúdar Landslide

The first step in performing the stability back-analysis was the reconstruction of the topography of the slope before the sliding based on a high-resolution digital elevation model (DEM) of the Dúdar landslide area. This DEM was derived by means of a LIDAR survey resulting in a model with a grid size of 3 × 3 m. Pre-sliding topography was reconstructed subtracting the contour lines of the total landslide area, interpolating a new DEM by means of a geographic information system (GIS) and moving the displaced mass to its original location.

The back-analyses of the Dúdar landslide have been made using Slide (Rocscience Inc 2003), a 2D slope stability software which calculates safety factors (SF) for circular and non-circular slope failure surfaces based on a number of widely used limit equilibrium methods. The Morgenstern-Price method was used as it is considered the most appropriate for slope ruptures developed in soils and is valid for circular and non-circular failure surfaces. In general, to evaluate the stability of a slope the Slide program calculates a significant number of possible circular slip surfaces in order to find the location of the most critical one with the minimum safety factor value.

The slope profile was derived from the high-resolution DEM (3 × 3 m) obtained of the LIDAR survey cited above. This cross-section represents the observed main path of the landslide. The geometry and location of the potential failure surfaces were particularly fixed by means of different control points and analysing the slope surface geometry (Fig. 5). The main scarp and toe location have been set based on field observations. Hence, the possible slip surfaces were obtained fitting their location to these control points.

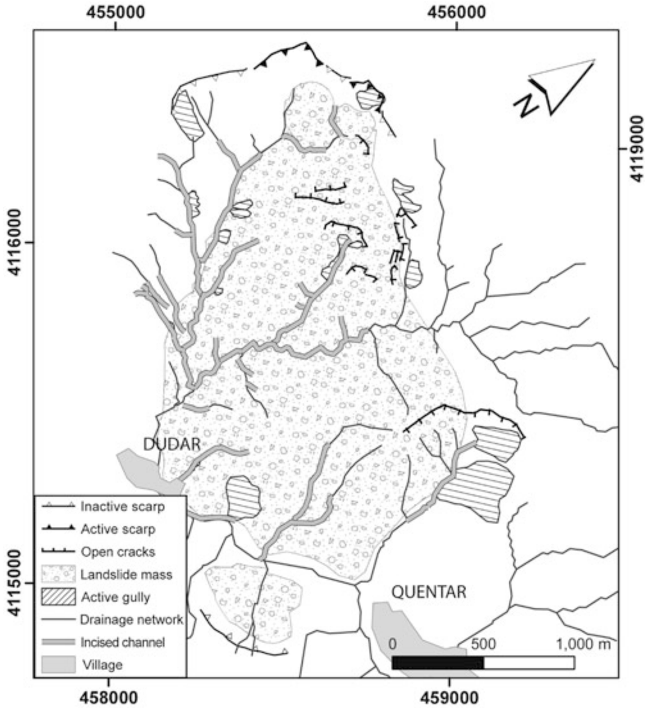

Fig. 3 Geomorphologic map of the Dúdar landslide showing the location of the main scarp, active gullies, incised channels, and the main displaced mass of the landslide

We have considered two main potential triggering factors in the back-analysis: water saturation and seismicity. The presence of water is a major factor controlling the triggering of landslides. This condition is very common in the south of Spain as a consequence of the typical Mediterranean heavy rainfall regime. To model this situation, we have considered a complete saturation of the sedimentary materials involved in the landslide.

Furthermore, the seismic activity related to the active faults located in the Granada Basin can be regarded as an additional cause of the occurrence of landslides. In this case, we have considered the horizontal peak ground acceleration (PGA) as a representative seismic parameter to model the seismic motion in the landslide. The minimum seismic acceleration required for overcoming the shear resistance and initiating the displacement of the landslide (i.e. the critical acceleration) was evaluated fitting the PGA value by iteration until the safety factor obtained was equal to one (stability condition). However, the critical acceleration related to a circular approximation of the failure surface was also obtained by means of the equation (Newmark 1965):

$$a_c = (SF - 1) g \sin \alpha \qquad (1)$$

where a_c is the critical seismic acceleration (in gravity units, $1\ g = 9.81\ m/s^2$), g is the gravity acceleration, SF is the static safety factor and α is the thrust angle. For rotational movement, Newmark (1965) showed that the thrust angle is the angle between the vertical and a line segment connecting the centre of gravity of the landslide mass and the centre of the slip circle. Then, the static safety factor prior to the earthquake has been obtained removing the seismic acceleration value.

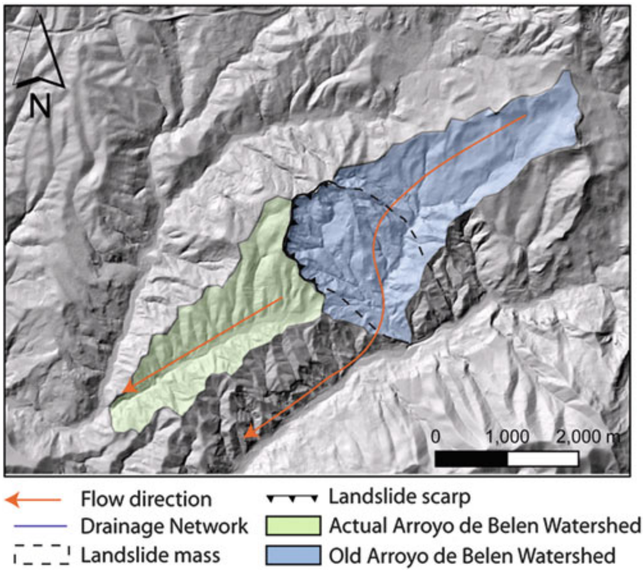

Fig. 4 Significant changes caused by the Dúdar landslide in the drainage system of the Aguas Blancas and Darro rivers

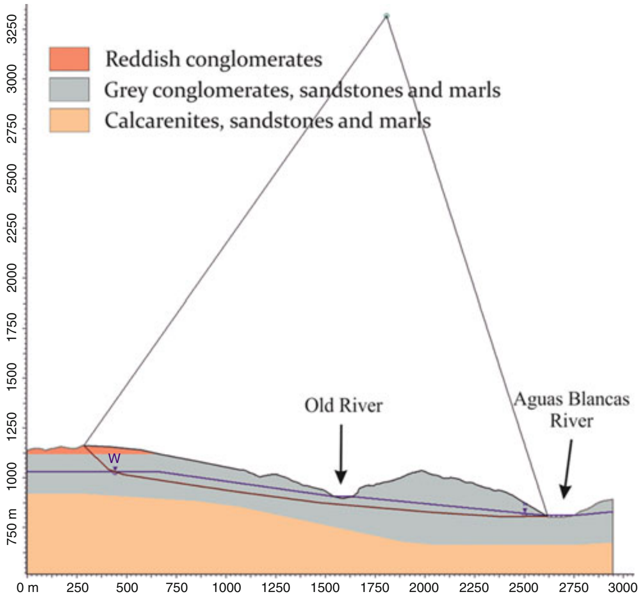

Fig. 5 Longitudinal cross-section of the Dúdar area prior to the landslide considering a shallow water table (*blue line*) and residual shear strength parameters. Failure surface is shown by a *red line*

Finally, we have estimated the most likely magnitude-distance pairs of the potential earthquake which PGA could exceed the critical acceleration and, thus, triggered the

Table 3 Most likely magnitude-distance pairs of potential earthquakes which might exceed the critical acceleration in the Dúdar landslide. M_w: moment magnitude; R_{ep}: epicentral distance to landslide (km)

M_w	5.0	5.5	6.0	6.5
R_{ep}	≤ 1	≤ 7	≤ 11	≤ 16

Dúdar landslide. The magnitude and epicentral values have been obtained using a number of ground motion prediction equations (GMPEs) selected from the literature (Skarlatoudis et al. 2003; Ambraseys et al. 2005; Akkar and Bommer 2007; Bindi et al. 2010).

The Dúdar Landslide Considering the Presence of Water as the Main Triggering Factor

The slope stability analysis indicated the Dúdar slope was stable before the occurrence of the landslide. We have obtained a high safety factor (SF = 2.51), assuming a relative shallow water table. From the analysis, the slope would remain stable even after considering a complete saturation of the slope. In this case the minimum safety factor is still high (SF = 1.71).

The Dúdar Landslide Considering the Seismicity as the Main Triggering Factor

The critical acceleration estimated for the Dúdar landslide is 0.19 g. In addition, a thrust angle of 8° and a critical acceleration of 0.21 g have been estimated assuming a circular approximation of the failure surface by means of (1). This critical acceleration is slightly greater than the value obtained using the Slide software (0.19 g), which is a more accurate estimation.

The most likely magnitude-distance pairs of potential earthquakes which have been able to overcome this critical acceleration value have been obtained using the different GMPEs selected (Table 3). This analysis indicates the Dúdar landslide could be triggered by an earthquake of $M_w = 5.0–6.5$, provided that it takes place within < 16 km of the landslide.

The magnitude values must be considered as the minimum ones, so the occurrence of an earthquake with a larger magnitude than the estimated ones for each magnitude-distance pair could trigger also the Dúdar landslide. Besides, all the estimated earthquakes would very likely be associated with the rupture of one of the active faults present in the Granada Basin, which can potentially generate earthquakes with magnitudes greater than $M_w = 6.0$ (Sanz de Galdeano et al. 2003) and are located very close to the Dúdar landslide.

Discussion and Conclusions

The Dúdar landslide is one of the largest landslides of the Betic Cordillera. Despite of being located in an area of medium-low relief, can be considered as a giant landslide on the basis of its dimensions.

Giant landslides are rare in such areas with low-to-medium relief gradients, and normally they respond to specific tectonic or lithologic configurations. In the case of the NE border of the Granada Basin, the active tectonic played an important role in the genesis of the Dúdar landslide. The altitude difference of the Arroyo de Belen Creek (tributary of the Darro River) and the Aguas Blancas River is one of the most important determinant factors for this landslide. This elevation difference is, in part, due to the location of both sub-basins. The Aguas Blancas River flows through an N70E synclinal axe, whereas the Belen Creek is located in the south-eastern dipping flank.

The Dúdar landslide acted as a geomorphological agent, changing the landscape and diverting the head of the Arroyo de Belen to the Aguas Blancas River. This river diversion caused, in turn, a lowering in the base level, resulting in a increase of the river incision. Despite the Dúdar landslide can be considered as a fossil landslide, the river incision in the landslide mass could be a risk due to future partial reactivations.

The paper also reports a stability back-analysis of the Dúdar landslide, in particular looking at the role played by the main potential triggering factors: water saturation and seismicity. We have found that the presence of water can be not regarded as the triggering factor of the Dúdar landslide. By the contrary, our calculations indicate the Dúdar landslide could be triggered by a low-to-moderate magnitude earthquake (M_w 5.0–6.5), which could very likely be associated with the rupture of one of the active faults present in the Granada Basin, located very close to the landslide.

Acknowledgments This study was supported by research projects CGL2008-03249/BTE, TOPOIBERIA CONSOLIDER-INGENIO2010 CSD2006-00041.

References

Akkar S, Bommer JJ (2007) Empirical prediction equations for peak ground velocity derived from strong-motion records from Europe and the Middle East. Bull Seismol Soc Am 97:511–530

Ambraseys NN, Douglas J, Sarma SK, Smit PM (2005) Equations for the estimation of strong ground motions from shallow crustal earthquakes using data from Europe and the Middle East: horizontal peak ground acceleration and spectral acceleration. Bull Earthq Eng 37:1–53

Azañón JM, Azor A, Cardenal Escarcena JF, Delgado García J, Delgado Marchal J, Gómez-Molina A, López-Chicano M, López-Sánchez JM, Mallorqui-Franquet JJ, Martín W, Mata de Castro E, Mateos RM, Nieto F, Peña-Ruano JA, Pérez-García JL, Puerma-Castillo M, Rodríguez-Fernández J, Teixidó-Ullod T, Tomás-Jover R, Tsige M, Yesares J (2006) Estudio sobre la predicción y mitigación de movimientos de ladera en vías de comunicación estratégicas de la Junta de Andalucía. IACT, CSIC-UGR (ed), Granada, 380p

Azañón JM, Azor A, Yesares J, Tsige M, Mateos RM, Nieto F, Delgado J, López-Chicano M, Martín W, Rodríguez-Fernández J (2010) Regional-scale high-plasticity clay-bearing formation as controlling factor on landslides in Southeast Spain. Geomorphology 120 (1–2):26–37

Azañón JM, Rodríguez-Peces MJ, García-Mayordomo J, de Justo-Alpañés JL (2011) Fallas activas y sismicidad en las partes altas de la ciudad de Granada: comportamiento dinámico de la Formación Alhambra. In: Proceedings of 4° Congreso Nacional de Ingeniería Sísmica, Granada, 18–20 May 2011, 7p

Bindi D, Luzi L, Massa M, Pacor F (2010) Horizontal and vertical ground motion prediction equations derived from the Italian accelerometric archive (ITACA). Bull Earthq Eng 8:1209–1230

Davies TR, McSaveney MJ, Beetham RD (2006) Rapid block glides: slide-surface fragmentation in New Zealand's Waikaremoana landslide. Q J Eng Geol Hydrog 39:115–129

El Amrani Paaza N, Lamas F, Irigaray C, Chacón J (1998) Engineering geological characterization of Neogene marls in the Southeastern Granada Basin, Spain. Eng Geol 50:165–175

El Amrani Paaza N, Lamas F, Irigaray C, Chacón J, Oteo C (2000) The residual shear strength of Neogene marly soils in the Granada and Guadix basins, southeastern Spain. B Eng Geol Environ 58:99–105

Fell R (1994) Landslide risk assesment and acceptable risk. Can Geotech J 31(2):261–272

Fernández J, Viseras C, Soria J (1996) Pliocene-Pleistocene infilling of the Granada and Guadix Basins (Betic Cordillera, Spain): the influence of allocyclic and autocyclic processes on the resulting stratigraphic organization. In: Friend PF, Dabrio CJ (eds) Tertiary basins of Spain. Cambridge University Press, Cambridge, pp 366–371

García García F, Viseras C, Fernández J (1999) Organización secuencial de abanicos deltaicos controlados por la tectónica (Tortoniense superior, Cuenca de Granada, Cordillera Bética). Rev Soc Geol España 12(2):199–208

Guzzetti F, Ardizzone F, Cardinali M, Rossi M, Valigi D (2009) Landslide volumes and landslide mobilization rates in Umbria, central Italy. Earth Planet Sci Lett 279:222–229

IAEG Commission on Landslides (1990) Suggested nomenclature for landslides. Bull Eng Geol Environ 41:13–16

Korup O, Clague JJ, Hermanns RL, Hewitt K, Strom AL, Weidinger JT (2007) Giant landslides, topography, and erosion. Earth Planet Sci Lett 261(3–4):578–589

Newmark NM (1965) Effects of earthquakes on dams and embankments. Geotechnique 15:139–160

Oteo Mazo C (2001) Informe sobre el deslizamiento de Diezma (A-92) y las soluciones para estabilizarlo. Consejería de Obras Públicas y Urbanismo de la Junta de Andalucía, 60p

Pánek T, Smolková V, Hradecký J, Kirchner K (2007) Landslide dams in the northern part of Czech Flysch Carpathians: geomorphic evidence and imprints. Stud Geomorphol Carpatho-Balc 41:77–96

Pánek T, Hradecky J, Smolkova V, Silhan K, Minar J, Zernitskaya V (2010) The largest prehistoric landslide in northwestern Slovakia: chronological constraints of the Kykula long-runout landslide and related dammed lakes. Geomorphology 120(3–4):233–247

Philip H, Ritz JF (1999) Gigantic paleolandslide associated with active faulting along the Bogd fault (Gobi-Altay, Mongolia). Geology 27 (3):211–214

Prager C, Zangerl C, Patzelt G, Brandner R (2008) Age distribution of fossil landslides in the Tyrol (Austria) and its surrounding areas. Nat Hazard Earth Syst 8(2):377–407

Rocscience Inc (2003) Slide 5.0 user's guide. Part I, Toronto, 199p

Rodríguez-Fernández J, Sanz de Galdeano C (2006) Late orogenic intramontane basin development: the Granada basin, Betics (southern Spain). Basin Res 18:85–102

Rodríguez-Peces MJ (2010) Analysis of earthquake-triggered landslides in the South of Iberia: Testing the use of the Newmark's method at different scales. Ph.D. thesis, University of Granada, Spain, 254 pp.

Rodríguez-Peces MJ, García-Mayordomo J, Azañón JM, Insua Arévalo JM, Jiménez Pintor J (2011) Constraining pre-instrumental earthquake parameters from slope stability back-analysis: palaeoseismic reconstruction of the Güevéjar landslide during the 1st November 1755 Lisbon and 25th December 1884 Arenas del Rey earthquakes. Quater Int (in press). doi: 10.1016/j.quaint.2010.11.027

Sanz de Galdeano C, Peláez Montilla JA, López Casado C (2003) Seismic potential of the main active faults in the Granada basin (Southern Spain). Pure Appl Geophys 160:1537–1556

Skarlatoudis AA, Papazachos BN, Margaris N, Theodulidis C, Papaioannou I, Kalogeras EM, Scordilis EM, Karakostas V (2003) Empirical peak ground-motion predictive relations for shallow earthquakes in Greece. Bull Seismol Soc Am 93(6):2591–2603

Strasser M, Schlunegger F (2005) Erosional processes, topographic length-scales and geomorphic evolution in arid climatic environments: the 'Lluta collapse', northern Chile. Int J Earth Sci 94(3):433–446

Turnbull JM, Davies TRH (2006) A mass movement origin for cirques. Earth Surf Proc Land 31(9):1129–1148

Van Den Eeckhaut M, Poesen J, Verstraeten G, Vanacker V, Nyssen J, Moeyersons J, van Beek LPH, Vandekerckhove L (2007) Use of LIDAR-derived images for mapping old landslides under forest. Earth Surf Proc Land 32(5):754–769

Weidinger JT (2006) Predesign, failure and displacement mechanisms of large rockslides in the Annapurna Himalayas, Nepal. Eng Geol 83(1–3):201–216

THE SECOND WORLD LANDSLIDE FORUM

Modern Seismogenic Landslides Caused by the Pamir-Hindu Kush Earthquakes and Their Consequences in Central Asia

Rustam Niyazov and Bakhtiar Nurtaev

Abstract

When studying the effect of seismic events the development of landslides and mud flows in Central Asia, special attention has to be spent to the influence of deep earthquakes from the Pamir-Hindu Kush zone. A preliminary comparative analysis of the synchronicity in time of Pamir-Hindu Kush earthquakes and the dates of formation of large landslides during the period from 1969 to 2011 showed that more than 100 cases of landslides in the south of Kyrgyzstan, Uzbekistan and Tajikistan could be attributed to effects of those deep and far earthquakes. These earthquakes in Central Asia caused low-frequency (1–5 Hz) prolonged (2–3 min) ground motions able to trigger processes of compaction, liquefaction and displacement of loess soils on moist slopes in spring time. Several examples of the combined effect of two spatial factors – precipitation and earthquakes on the time, place and mechanism of landslides, which occurred in last years in Central Asia, are presented in this paper.

Keywords

Large-scale landslides • Earthquakes • Triggering mechanism • Case study

Introduction

In the past landslide research has been focused on where they have occurred but today, more emphasis is placed on the timing of landslides. Many authors consider short, intense rainfall as main triggering factor (Wieczorek and Glade 2005), often associated with a certain quantity of rainfalls before the event. Most authors agree that these techniques are valid in a specific geological, geomorphological and climatic context and cannot be applied directly to other situations. The combined effect of two external spatial factors (atmospheric) rainfall and earthquakes on the time and place of formation of landslides is very complex. It is due to the fact that seasonal conditions of moist slopes can increase its susceptibility to seismic vibrations for the orders (Keefer 1984).

This paper examines modern seismogenic landslides in loess and sandy-clayey deposits. We consider different types of failures such as lateral spreading, tilting, liquefaction and debris flows that formed at a considerable distance (250–600 km) from the epicenter of the deep (180–220 km) Pamir-Hindu Kush earthquakes (Afghanistan). These earthquakes in Central Asia caused low-frequency (1–5 Hz) prolonged (2–3 min) ground motions able to trigger processes of compaction, liquefaction and displacement of loess soils on moist slopes in spring time. The stability of the deforming rock mass reaches a critical threshold, beyond which even small ground motion events may trigger catastrophic failure. For a better understanding of these large-scale landslides in Central Asia, some typical ones that were rarely reported are introduced, and their formation processes are briefly analyzed in this paper.

R. Niyazov
Engineering Geology, Institute Hydroingeo, Olimlar 64, Tashkent 100041, Uzbekistan

B. Nurtaev (✉)
Department of Geophysics, Institute of Geology and Geophysics, Olimlar 49, Tashkent 100041, Uzbekistan
e-mail: nurtaevb@gmail.com

C. Margottini et al. (eds.), *Landslide Science and Practice*, Vol. 5,
DOI 10.1007/978-3-642-31427-8_44, © Springer-Verlag Berlin Heidelberg 2013

Pamir-Hindu Kush Zone of Deep Earthquakes

For the Central Asian region, the largest center of seismic activity is the zone of Pamir-Hindu Kush deep-earthquakes. Every year in this area occur about 200 M >4.5 earthquakes at depths of 180–250 km and 35–40 % of it occurs in the spring (Lukk and Nersesov 1970). Some events are reaching M-7 and in the Central Asia territory, they produce ground motions of 3–4 MSK units of intensity.

The comparative analysis of time synchrony of Pamir-Hindu Kush earthquakes and the formation of large landslides in the period from 1969 to 2011 showed that more than 200 cases of landslides in South Kyrghystan, Uzbekistan and Tajikistan could be partly related to these deep and far earthquakes.

Three groups of landslides were considered. The first – massive landslides in wet years with frequent earthquakes. The second – mass manifestation of landslides in wet years, but with the lack of strong earthquakes. The third one – activation of major landslides related to anthropogenic effects and earthquake vibrations.

Landslides in Wet Years with Frequent Earthquakes

In the first group were considered 20 cases of landslides which formed in 1969. During this year, a great amount of precipitation (1,640 mm/year) was registered and in the Hindu Kush from March 5 to June 10 occurred 14 earthquakes of magnitudes from 4.5 to 5.9. During this year mostly mudslides in loess were formed. They were widely distributed and were extremely dangerous due to the suddenness of motions which in few minutes reached a high speed and a large runout (up to 4.5 km), presenting greatest threat to human life. The mechanism of displacement of landslides during the earthquake is characterized by the formation of almost simultaneous deformation of rocks throughout the landslide area. Liquefaction of soils occurs in thin layers inside the massif or within the entire mass with a simultaneous appearance of a large amount of water over the area of the landslide.

On March 5, 1969, in the Hindu Kush occurred an earthquake of M-5.9 and a landslide formed in the village Tally. According to eyewitnesses, at first, the flow of springs sharply increased and a sinkhole with diameter 2 m formed in the middle of the slope. This hole then reached 60 m. The movement started above and below the clay rocks of Cretaceous age. The sinkhole has been completely filled and the amount of displaced mass was equal to 0.4 million m^3, the length was 550 m and the width between 70 and 150 m. The landslide was moving slowly with fragmentation of the surface. In the final stage there was "emerging" ground in the tongue part of the flow, which is connected with soil liquefaction.

This earthquake also caused landslide Suffa with a volume of 0.4 million m^3, which was formed on the right side of the river Igrisu (Kashkadarya). In the morning of March 6, in the middle of the slope in the upper part of the village appeared springs producing 0.1–0.2 l/s. The initial displacement of soil started on March 7 with the appearance of swelling knobs around the hill. A few hours later appeared cracks, and the entire mass has begun to move. Landslide movement was slow and continued during 4 days. The length of displacement was 500 m, the width at the top was 300 m and at the toe 80–120 m, the depth was 5–6 m. The landslide destroyed 11 farms.

The third landslide flow occurred during the night from March 5 to 6 close to the 120.3 km section of highway Tashkent-Kokand. A mudflow moved over 270 m and completely blocked a highway with a width of 30 m and a height of 1.7–1.9 m (Niyazov 1974).

On March, 10, an earthquake occurred in the Hindu Kush with M-5.1. As a result, the block landslide Dumalak formed in Bostanlik zone, with a volume of 2.5 million m^3. The biggest displacement this day occurred in the south of Kyrgyzstan in the basin of river Karaungur. The Beshbulak landslide with volume of 5 million m^3 was of liquefaction type; the loess mass with a width of 1,300 m and thickness of 40 m was displaced over up to 4.0 km.

The largest landslide of block type occurred in the site Laisu with volume 2.5 million m^3 on the left side of river Kyzylsu, which may be caused by the earthquake of May 4. According to eyewitnesses, the mass displacement of landslide began in the morning of May 5, when on the top of the landslide new fractures had formed. After a few hours the process increased, and between 16 and17 h was accompanied by main displacement. The total length of landslide was 633 m, the width at the top was 440 m, 280 m in middle, and the depth of failure of loess, clay, sandstone was nearly 40–50 m.

On May 19 an earthquake caused a landslide with a volume of 1.1 million m^3 on the left slope of the valley Karaungur at the site Achi. Soil displacement occurred in sandy strata of Cretaceous age, covered by loess loam with a thickness 10–20 m in the ancient landslide circus.

The formation of Chimgan landslide – flow with a volume of 0.24 million m^3 was associated with the May 21 earthquake with M –5.0. One day before there was no indication of progress of the landslide. Liquefied loess with a thickness 15 m was displaced at the contact of clay and silt of the Paleogene-Neogene sediments. The flow reached distance of 250 m with catastrophic speed, destroying the buildings of the recreation area. In addition, at the same time were formed two mud flows at the site of Sary-Cheku and Tanga-Topty of highway Tashkent-Osh, destroying the highway bridge (Niyazov 1974).

Thus, the year 1969 was a year marked by slope failures in March, April and May simultaneously affected by two factors – precipitation and seismic ground motions. Many landslides were caused by liquefaction (Niyazov and Nurtaev 2010).

Landslides in Wet Years Without Earthquakes

The second group includes landslides, which appeared during the year 1994 marked by large precipitation but small number of earthquakes during spring time. This year was very tragic for the Central Asian republics.

In Kyrgyzstan, from 9 to 24 March five landslides had formed which destroyed residential buildings and killed 103 people (village Tatosh, Mailysuu, Alma-Bura, Komsomolabad, Suzak). In Uzbekistan, in the basin of river Gushsay six landslides occurred between March 14 and April 3; they killed 10 people (see one example in Fig. 1).

In Tajikistan, in April, three large landslides occurred on – April 11, Shurak (Kizilsu) landslide with a volume of 0.7 million m^3, on April 18 – Buvak (Haragon) landslide with a volume of 1.0 million m^3 and on April 19 – Beshbulak (Yavansu) landslide with a volume 15 million m^3. Eleven landslides occurred within 20 days in March 1994. Most occurred on five different sites on March 17–18 when no earthquake motions were registered. However, there was another important factor, in all these areas, there were large cracks in the top of the slope before the landslide. The formation of the cracks in the higher parts of the slopes in the watershed area may be associated with four $6 < M < 7$ earthquakes which occurred in August and September 1993. These cracks were at the origin of the landslides due to the intense snowmelt in spring 1994. The formation of large cracks in loess does not begin with packing of the grains, but with reduction of the structural links between the particles. This deformation is susceptible to long-term and low frequency effects of seismic ground motions, which cause the expulsion of water and the compacting of the soil. Landslide process initiation is determined by the frequency, amplitude and duration of the vibrations as well as by the, mechanical strength and thickness of the rock mass.

Two landslides at site Tokberdy were directly triggered by earthquakes. The first landslide with a volume of 0.07 million m^3 initiated in April 23, 1994 after an earthquake of $M = 4.4$. The second of a volume 0.2 million m^3 occurred 10 years later, after a $M = 4.7$ earthquake on April 23, 2004 (Fig. 2).

Thus, as a result of deep-focus earthquakes of the Pamir-Hindu Kush zone which occurred in the autumn-winter period, can form large cracks in of loess rocks at high linear slopes in the watershed area, which in the following years may pass into the landslide process.

Fig. 1 Photo of landslide Gushsay, 1994

Fig. 2 Landslide flow in loess soils at site Tokberdy

Man-Made Landslides Activation at Earthquakes

The third group includes impact of seismic waves to the large-scale mining areas under the influence of groundwater. Over the past 60 years more than 2 billion m^3 of rock were extracted in the coal mine Angren to a depth of 300 m. As a result, 15 landslides had formed with volume from 0.4 million m^3 to 800 million m^3 (Niyazov 2009). The last major landslide "Central" was formed in April 1985 close to the western limit of the coal mining area of Angren. The first crack in the loess soils with an extent of 300 m was formed at a distance of 250–280 m from the top edge of the section under the Baksuk debris storage dam. Since 1974, extensive studies have been made to analyze the trigger mechanisms and movement dynamics of the masses. On the basis of complex measures have been developed to manage the landslide risk and to stabilize the biggest landslide without interrupting the mining activity (Niyazov 2009). Geodetic observations have been carried out for 36 years and are still continuing.

In March 1987, the upper part of the open pit mine has been moved close to the crack over a distance of 50–150 m and its length has increased up to 1,300 m. The total volume of the landslide was equal to 58 million m^3 (Fig. 3). The height of the moving part of the landslide is 145 m, the dip angle is 17o°; the sliding surface is confined to the Paleogene clay, with a dip of 3–40°.

Since then, the landslide Central has continued to move for 22 years (1987–2009) and the total amount of displacement was more than 140 m (Fig. 4). All these years, coal mining was carried out providing conditions when volume of rock excavated from the upper prism was 1.5–2 times more than volume, excavated from the lower terrace.

This technology of mining made it possible to restrain landslide displacement rate at the level of 20–24 mm/day. As a result, its length was reduced from 750 m in 1990 to 320 m in 2002. The maximum thickness of 105 m was reduced to 30 m, from the previous volume 20 % or 8–10 million m^3 were left.

However, in May 1993, on the site “Old substation,” a series of cracks formed with a length of 100–500 m, covering the upper ledge of the working board. So, there appeared the threat of the connection of fracturing process at the site “Old Substation” with the head wall of landslide Central.

The first reactivation of landslide Central occurred on April 6, 2004, due to the seismic impact of Hindu Kush earthquake of M-6, 6. In Angren city, at the distance 530 km from the hypocenter, it was felt with an intensity MSK of 2–3 units and the duration of vibration was over 2 min. The rate of displacement of the landslide has risen from 31.4 mm/day to 117.3 mm/day in April to 261 mm/day in May and to 287 mm/day in July, i.e. increased within 4 months over 10 times (Fig. 4).

In subsequent years (2005–2010), the rate of horizontal displacement of the landslide decreased to 5–24 mm/day and the vertical movement to 1.6–2.4 mm/day. At the site of old substation in 2003–2004 the unloading of upper terrace was carried out, and the deformation of the thick loess deposits decreased to 0.07–0.14 mm/day. The horizontal displacement over a 3-year period (2005–2008) was equal to 60–66 mm. The activation of the landslide was observed in October, November and December 13.4–18.7 mm/day and in February to 23.6 mm/day, with average values 0.6–3.8 mm/day. Maybe it was due to two Hindu Kush earthquakes which occurred on September 17, 2010 with M-6, 3 and on January 24, 2011 with M-6.1, because the maximum displacement (on reper 6) occurring between October 13, 2010 and March 5, 2011 was in total 1.8 m on the horizontal component, with a rate of 13 mm/day and on the vertical component of 2.9 m with a rate 21 mm/day, i.e. it increased within 5 months to 10 times (Fig. 4).

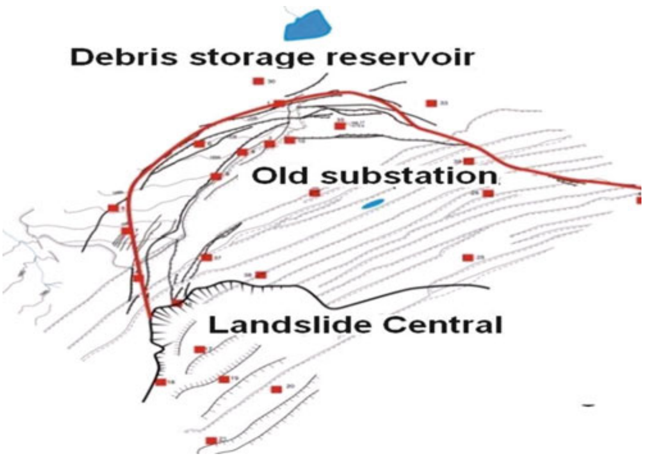

Fig. 3 Plan of landslide Central and Old substation

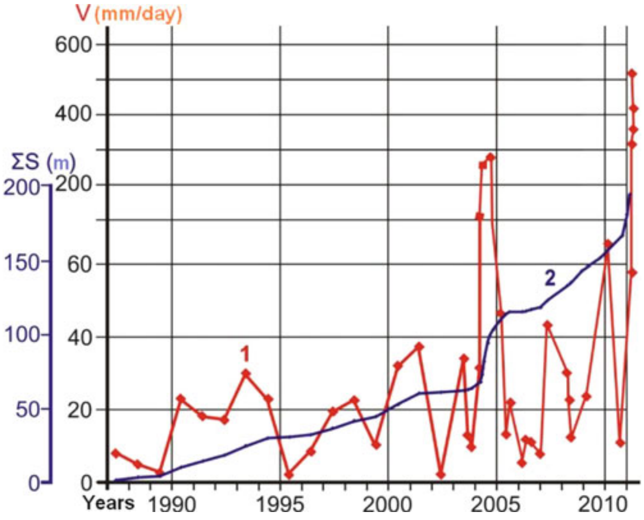

Fig. 4 Graph of change of speed (*1*) and value of horizontal displacement (*2*) of landslide Central

At the same time on the left side of the bottom of the prism two block landslides formed in limestone with a thickness of up to 15–20 m and a volume of 1 million m^3. The right flank above the landslide was broken by a series of longitudinal cracks with a length of 40–60 m and with amplitudes of 0.5–2.0 m. Fractures were connected with the vertical cross graben like depressions. As a result, a large single circus landslide formed with a width of 1,400 m, a length of 900 m and a thickness of 100 m. The volume of the landslide was equal to 120–130 million m^3 (Fig. 5).

The separation wall of the landslide was confined to the altitude of 1,100 m, and the output of sliding surface to 905 m, i.e. the difference of elevation was 200 m.

The geology of the landslide is composed of Quaternary loess with the inclusion of boulder-pebble deposits with a

Fig. 5 Down warping of upper part of landslide Old substation

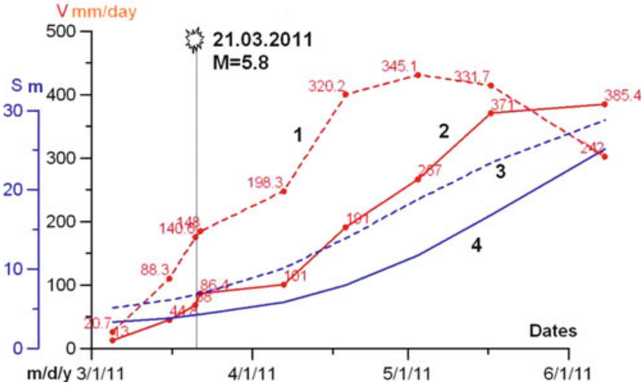

Fig. 6 Graph of change of speed of horizontal (*1*) and vertical (*2*) displacements and value of horizontal (*3*) and vertical (*4*) displacements (marker 6) for the period from March to June 2011

thickness 65–70 m at the top and 15–20 m in the central areas of pit wall. The thickness of interbedded Neogenic siltstones, sandstones is 30–35 m. In the lower ledges of the mining pit the Quaternary and Neogene deposits are absent, because they had been excavated. They are mainly represented by Paleogene strata of interbedded sandstone, mudstone, fractured limestone and shale with total thickness of up to 40 m that are overlying Cretaceous and Jurassic shale and carbonaceous sediments. The displacement of rocks of about 3–4 m is localized in the zone of contact between Alai limestone interbedded with fine-grained sands and greenish clays of Paleogene.

On March 21, 2011, a M = 5.8 earthquake occurred in the Hindu Kush , which was felt in Angren as 2–3 MSK intensity units; the duration of vibration was 1.5 min. As a result, the groundwater flow sharply increased by 4–5 times within 7–8 h, and on the top ledge a lake formed with a length of 20–25 m, a width of 15 m and a depth of 1.0 m. The rate of displacement of rocks in the central zone increased from 19 to 74 cm/day (Fig. 6). During the 78 days after the earthquake the horizontal movement in the central zone reached 46 m and in marginal boundaries up to 29 m. The vertical displacements of the separation wall for the time being reached 25 m and in the lower zone the embankment cone rose by 8.9 m.

On May 14, 2011 an earthquake with M-6.0 occurred in the Hindu Kush, which increased the ground water discharge in the area of the landslide and formed small lakes. Currently, on June 8 2011, the rate of displacement in the central zone decreased from 75 cm/day down to 64 cm/day.

Thus, five cases of Hindu Kush earthquakes in 2004 and 2010–2011 with M −5.8–6.6 caused the increase of displacement rate of landslides from 10 to 100 times. The duration of active movement of landslides took place from March 21 to June 8, or within 75–78 days, when the total value of horizontal displacement was 40–46 m.

Conclusion

Landslides in Central Asia occur regularly in spring, presenting social and economic damage in the foothill areas, where most settlements and the Quaternary loess fertile lands are located. A common type of damage is the destruction of residential and commercial buildings, as well as recreational areas. In 1969, in the Central Asian republics by landslides more than 1,000 housings have been destroyed or damaged. In wet years, there are 20–60 cases of temporary interruption of mountain roads by landslides. Often there were deformation of power lines, water pipes breaks, fall of ground in the sidewalls of channels and pits. Each year there is temporary damming of gully beds, etc.

Fifty six cases of landslides were revealed to initiated due to the impact of long-term, low-frequency distant Pamir-Hindu Kush earthquakes. The complex combined effects of two spatial factors – precipitation and earthquake ground motions on the spatio-temporal distribution of slope failures and their mechanisms were shown through several examples. Risk of landslides and mud flows caused by the Pamir-Hindu Kush earthquakes, is related to the suddenness and almost unpredictable location of their formation. As a result, it is suggested that agencies devote more attention and resources to early detection, warning, and loss prevention of landslide hazards associated with Pamir-Hindu Kush earthquakes

References

Keefer DK (1984) Landslides caused by earthquakes. Bull Geol Soc Am 95:406–421

Lukk AA, Nersesov IL (1970) Deep Pamir-Hindu Kush earthquakes. In: Nauka M (ed) Earthquakes in the USSR in 1966. Nauka Publishing House, Moscow, pp 118–137

Niyazov RA (1974) Landslides in loess soils in south eastern part of Uzbekistan. FAN, Tashkent, 148p

Niyazov RA (2009) Landslides in Uzbekistan. FAN, Tashkent, 207 p

Niyazov RA, Nurtaev BS (2010) Landslides of liquefaction, caused by the joint influence of rainfall and long distant earthquakes. In: Problems of seismology in Uzbekistan, vol II. FAN, Tashkent, pp 29–54

Wieczorek GF, Glade T (2005) Climatic factors influencing occurrence of debris flow. In: Jacob H (ed) Debris flow hazard and related phenomena. Springer, Berlin, pp 325–352

THE SECOND
WORLD
LANDSLIDE FORUM

Hazard and Risk Scenarios of Landslides Triggered by Earthquakes

Roberto W. Romeo, Milena Mari, Giulio Pappafico, Pierpaolo Tiberi,
Umberto Gori, Francesco Veneri, Gianluigi Tonelli, and Carmela Paletta

Abstract

This study shows, for a landslide prone area, the assessment of the slopes capacity to withstand earthquakes and how triggered mass movements can threaten potentially exposed structures and facilities. As a result a set of spatial representations (i.e., scenarios) of slope performances in a variety of seismic and climatic conditions is given and how they can induce damages or interruptions of public services such as rescue activities, communication roads, or the disruption of lifelines and urban settlements is presented.

Keywords

Landslides • Earthquakes • Rainfall • Scenarios

Introduction

Rainfall or earthquakes of significant intensity can lead to the reactivation of landslide bodies apparently stable under ordinary physical conditions, as well as trigger first-time activation of new landslides. It is equally true that in the event of natural disasters, the mobilization of mass movements poses a serious drawback to the operations of civil protection, besides being a direct cause of damage to people and properties.

Simplified seismic analyses are performed to evaluate the behaviour of slopes during and after seismic shaking. They take into account the different hydraulic conditions that can arise due to the relationships between precipitation, saturation and seepage into the landslide bodies. Specific matrices [shaking] [seepage] define the different seismic and climatic conditions that can occur under which different landslide scenarios may arise.

These analyses represent a tool for the local government: (1) to apply prevention planning policies; (2) to adopt real-time decisions during an emergency to minimize losses. Finally, since triggering events are natural events that occur at specified recurrence intervals, an assessment of the overall hazard is further provided.

Hereinafter the adopted methodology and the first results of a research study carried out in a training area (the Cesano River basin, in Central Italy) are shown.

Methodology and Data

The Model

The procedure adopted to assess the response of slopes against seismic forces is a seismo-geotechnical model, namely, a model based on the assessment of the landslide capability to withstand seismic forces (resistance) whose capacity (of resistance) is given by the following expression:

$$A_c = (FS - 1)g\ \tan(\beta) \tag{1}$$

where A_c is the horizontal acceleration (here termed as critical acceleration) required to bring the safety factor to the limit state condition (FS = 1), whose equation is:

R.W. Romeo (✉) • M. Mari • G. Pappafico • U. Gori • F. Veneri •
G. Tonelli • C. Paletta
Department of Earth Sciences Life and Environment, University of
Urbino Carlo Bo, Scientific Campus, 61029 Urbino, Italy
e-mail: gislab@uniurb.it

P. Tiberi
Department of Civil Protection, Marche Regional Government,
Ancona, Italy

C. Margottini et al. (eds.), *Landslide Science and Practice*, Vol. 5,
DOI 10.1007/978-3-642-31427-8_45,

Table 1 Geomechanical properties of lithological units shown in Fig. 1 (U.W. is the saturated unit weight)

Lithology	U.W. kN/m^3	Friction angle (°)	Cohesion kPa	k m/s	χ (%)
RM massive rocks	26.5	–	–	–	70
					100
RS layered rocks	19.8	28	10	10 E-3	50
	21.0	32	20	10 E-5	80
ACM alternating limestones marlstones	18.0	24	10	10 E-6	20
	19.0	26	24	10 E-9	30
AAM alternating sandstones marlstones	18.6	24	10	10 E-5	20
	20.2	32	20	10 E-9	30
AMC alternating marlstones limestones	18.6	20	20	10 E-8	5
	19.6	25	40	10 E-9	15
RTA weak sandstones	19.4	32	15	10 E-5	20
	20.6	33	18	10 E-9	30
RTP weak pelitic rocks	19.6	23	10	10 E-8	5
	20.6	27	25	10 E-9	10
DG coarse debris	22.6	33	0	10 E-2	60
	24.5	38		10 E-3	80

$$FS = \frac{c}{\gamma\, h\ \sin(\beta)} + \frac{\tan(\varphi)}{\tan(\beta)} \left(1 - \frac{\gamma_w}{\gamma} \left\{ \frac{i}{k} \frac{\chi}{\tan(\beta)} \leq 1 \right\} \right) \quad (2)$$

which has been written so that the first right-hand member is the adimensional contribution to resistance of cohesion respect to the shear stress and the second member is the adimensional frictional resistance by the reduction factor taking into account seepage (the argument of brackets). The slope angle β accounts for slope-parallel movements (infinite slope model) for both shallow and deep slides accounted, in turn, by the slope-normal thickness h of the sliding mass and taken equal to 2.5 and 9.0 m, respectively.

The argument of braces (truncated at the upper limit of 1) is the proportion of the saturated soil's thickness (h_w/h) that contributes to seepage (from Montgomery and Dietrich 1994; reformulated), which is made of two ratios: the first ratio represents the adimensional contribution to infiltration, namely the ratio of the effective average hourly intensity rainfall (i, m/h) to the soil's permeability (i.e., hydraulic conductivity, k in m/h); the second ratio is the adimensional contribution to the outflow, namely the ratio of the potential infiltration coefficient χ (depending on the lithology and the vegetation cover) to the slope gradient tan(β). Rainfall intensity is taken as the net of the evapotranspiration (effective rainfall) averaged over the time-span of the scenario. Effective rainfall is computed by means of geospatial analyses of rainfall and temperature distributions (ordinary kriging).

Once the seismic resistance (i.e., critical acceleration A_c) has been computed, the comparison with the seismic demand (i.e., effective ground acceleration) gives a measure of the slope susceptibility to withstand earthquakes, here termed as seismic safety factor, FD.

Geomechanical Properties

At a basin scale a lot of geologic units outcrop, which may differ more or less from each other. The identification of some relevant common features may help to reduce them to few lithological units, where the main difference is in the mechanical properties. Features that most contribute to the identification of lithological units are joints (bedding and fractures as well), particle size distribution (coarse or fine) and the results of in situ and laboratory geomechanical tests.

Following this procedure we identified three macroscopic units: massive versus layered rocks; rocks of alternating lithology, such as limestone and or sandstone and marl; soils (weak rocks) mainly coarse (sands) or fine (clays).

This led to the identification of seven different lithological units whose relevant mechanical properties are unit weight (dry and saturated), cohesion and angle of internal friction (peak and residual) and undrained shear resistance. An additional unit called coarse debris have been further identified mainly composed of loose and weakly cemented rocks outcropping along the slopes or at their toes.

In Table 1 the geomechanical properties of lithological units are shown, whose spatial distribution is displayed in Fig. 1. The geomechanical properties shown in Table 1 refer to the weathered soil's cover and are in terms of peak effective stresses. Only for the stability analyses of shallow

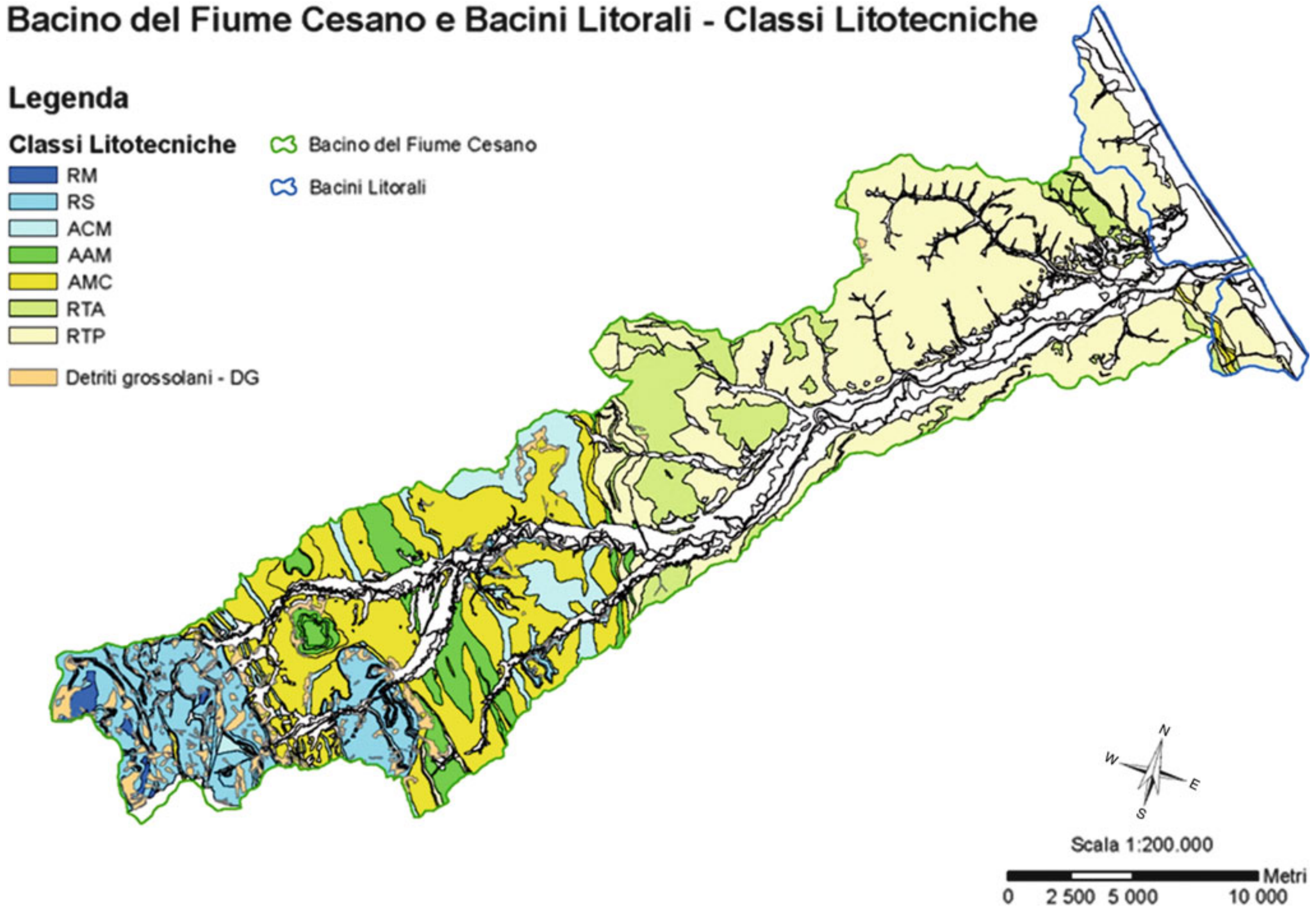

Fig. 1 Lithological units (see Table 1 for the meaning of lithological abbreviations). White polygons are alluvial and beach deposits

Table 2 Seismotectonic model. Provinces refer to different seismic regimes (outer compressional and inner extensional). Active faults belonging to each tectonic province are parameterized by their characteristic magnitude derived from the Wells and Coppersmith's (1994) relationships. The shortest distance between each fault area and the barycenter of the basin is reported. Average return period (in years) of characteristic M_w earthquakes and the last ones historically known that occurred on each fault are also reported in the last columns

Tectonic province	Active fault	M_w	Dist. km	Return period	Last eqk.
Outer apennine	Fano-Ardizio	6.1	22	1,667	1000 A.D.
	Marotta-Mondolfo	5.6	20	556	1924
	Senigallia	5.9	27	1,111	1930
Inner apennine	Cagli	6.2	37	500	1781
	Fabriano	6.2	27	550	1741

slides ($h = 2.5$ m) or existing landslides, residual shear strengths were used with zero cohesion.

Seismic Actions

Seismic actions are determined according to the seismotectonic framework of the region. The Marche Region is characterized by two different seismic regimes: compressional on the outer side of the Apennine chain (parallel to the Adriatic Sea coastline) and extensional on the inner side. According to this distinction, two sets of active faults are identified, whose relevant parameters for the seismic hazard of the basin are shown in Table 2.

The two provinces provide the rationale for far-strong (inner Apennine) and near-moderate (outer Apennine) ground motion scenarios.

An ad-hoc attenuation relationship has been derived from the strong motion records available for the Marche Region. The records span a magnitude range between 5 and 6.5 and distances within 100 km from the epicenters. The attenuation relationship for peak ground acceleration (in gal) is:

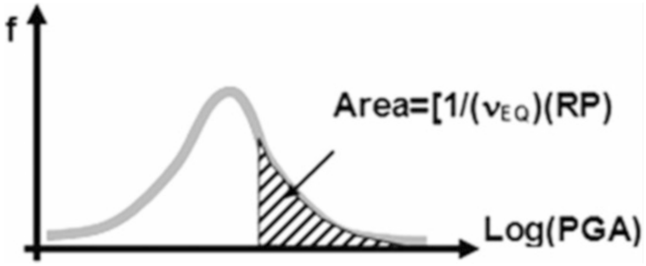

Fig. 2 Sketch of the computation of standard error in the attenuation equation. Symbols explanation: ν_{EQ} is the earthquake yearly frequency, the inverse of the average return period; RP is the reference period (see text below); PGA is the peak ground acceleration labelled as A in (3)

$$\begin{aligned}\mathrm{Log}(A) = 2 + 0.2M_w - \log\left[\sqrt{(R^2+6^2)}\right] + 0.15S_{B,C} \\ + 0.3S_{D,E} \pm 0.3\varepsilon\end{aligned} \quad (3)$$

where R is the Joyner-Boore (1981) distance, namely the shortest distance from the surface projection of the fault rupture; $S_{B,C}$ is a flag whose value is 1 when soil category is B or C according to Eurocode 8, zero otherwise; $S_{D,E}$ is a flag whose value is 1 when soil category is D or E according to EC8, zero otherwise; ε is the standard error (a random variable with zero mean and unity standard deviation).

The distance coefficient (-1) is equal to the former Sabetta and Pugliese's (1987) attenuation equation for the whole country, while the standard error is relatively higher (about twice) due to the summation of inter- and intra-events uncertainty.

The lithological units shown in Fig. 1 have been divided into three soil category classes, according to EC8, based on an expert judgement about soils' rigidity (V_S and/or G-modulus) integrated by some geophysical survey. The seismic classes are: A (bedrock-like) which encompasses massive and layered rocks and alternations (abbreviations RM, RS, ACM, AAM, AMC); B-C (stiff soils), which encompasses soils (fine and coarse as well, abbreviations RTA, RTP); D-E (loose soils, abbreviation DG plus alluvial and beach deposits). Loose soils show the highest amplification (twice that of bedrock), whereas stiff soils amplify the bedrock motion by a factor of 2.

Seismic shaking for each scenario has been computed according to a probabilistically-based deterministic hazard. In practice, each ground motion scenario (far-strong and near-moderate) is given by the largest ground motion values computed for each province (inner and outer Apennines, respectively), independently from the activated fault. This is made in a consistent manner taking into account the earthquake occurrence on each fault (Table 2) and computing the corresponding peak ground accelerations (3) expected with a 2 % conditional probability in 50 years as shown in Fig. 2.

As an example we consider the Cagli active fault (see Table 2) whose average return period of the characteristic M_w 6.2 earthquake is 500 years ($\nu_{EQ} = 0.002$). The reference period (RP) for a 2 % exceedance probability within 50 years is 2,475 years approximated to 2,500 years for the sake of simplicity.

Therefore the dashed area in Fig. 2 is 20% which corresponds to 0.84ε (the value 0.84 comes from the inverse of the complementary cumulative standard normal distribution for an exceedance probability of 0.2). Thus, applying (3) the acceleration for a bedrock-like outcrop in the barycentre of the basin will be 83 gal, versus 43 gal for the median and 93 gal for the mean plus one standard deviation adopting the standard deterministic seismic hazard approach. This procedure allows computing deterministic ground motion values from individual seismic sources each one at the same occurrence probability.

In Fig. 3 the peak ground accelerations computed for the near-moderate earthquake scenario (outer Apennine, whose seismic sources are located NE parallel to the Adriatic sea coastline) are shown. Peak ground accelerations range between 50 and 700 gals, clearly showing the amplification due to stiff soils in the middle and lower part of the basin and to soft soils along river valleys and the beach strip, with respect to bedrock which mainly outcrops in the upper part of the basin.

Given the seismic shaking shown in Fig. 3 and the critical acceleration computed through (1), a seismic safety factor is defined as:

$$FD = \frac{3\,A_c}{A} \quad (4)$$

Equation (4) allows taking into account effective acceleration rather than peak acceleration, that means the acceleration acting as a static action during the earthquake shaking. The approximate relation comes from a relationship found by Paciello et al. (2000) who regressed root mean square acceleration versus PGA and found a linear relationship with a coefficient of 0.33.

First Results

Landslide Hazard

Static and seismic safety factors are computed dividing the basin into cells 10 × 10 m wide. Each landslide shows therefore a distribution of safety factors depending on the local slope, mechanical and hydraulic properties and ground accelerations, for which a failure probability is computed applying the first-order second-moment reliability method:

$$P_f = \int_{-\infty}^{1} f\left(F_{S,D}\right) dF = \Phi\left(-\frac{\mu_F - 1}{\sigma_F}\right) \quad (5)$$

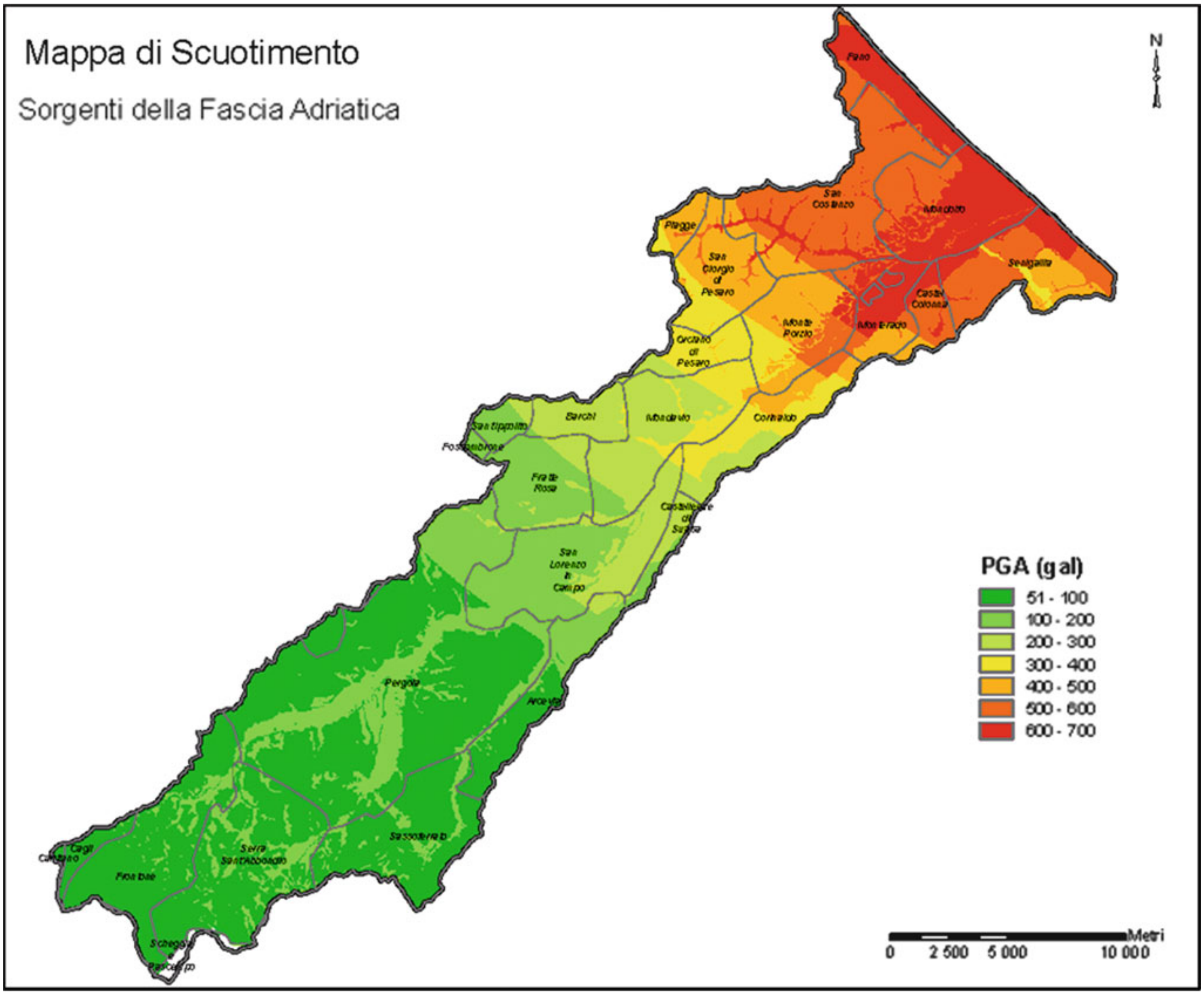

Fig. 3 Shakemap for the outer Apennine seismic sources (near-moderate earthquake scenario). Ground accelerations (in gal) expected to have a 2 % chance to be exceeded in 50 years. Active faults are elongated parallel to the coastline, at the northeast end of the basin. The ground motion takes into account the amplification effects due to local geology (soils' amplification factors: see text)

Fig. 4 Average seismic safety factor (*left*) and failure probability (*right*) distributions of seismically triggered shallow and deep landslides (thickness 2.5 and 9.0 m, respectively)

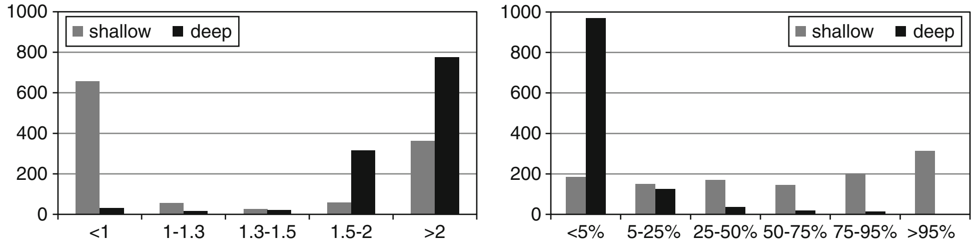

where μ_F and σ_F are, respectively, the mean and standard deviation of the safety factor (both in static and seismic conditions) of each landslide and Φ is the cumulative standard normal distribution whose argument is said 'reliability index'.

In Fig. 4-left the distribution of the average seismic safety factors computed for shallow (2.5 m thick) and deep (9.0 m thick) landslides potentially triggered by the near-moderate earthquake scenario are shown. Clearly, shallow landslides in dry conditions are more susceptible to slide than deep landslides. Nevertheless, whilst the average safety factor gives only an idea of the central moment of the landslide behaviour (i.e., the overall mean seismic safety condition), failure probability allows a better discretization of the potential landslide behaviour under the seismic shaking.

In fact, failure probabilities can be used to rank the landslide susceptibility since it depends both on the mean and standard deviation of the seismic safety factor and failure probability increases as the standard deviation increase in turn or if the mean-FD decreases. Fig. 4-right is an example of the failure probability distribution using quartiles as well as 5 % and 95 % confidence levels.

Conclusions

Preliminary results of a work still in progress regarding the formulation of seismically-induced landslide scenarios have been shown.

The work refers to scenarios at a basin scale, where morphological and climatic conditions can be considered to vary gradually and therefore geospatial analyses to distribute environmental effects such as vibratory ground motions and rainfall can be applied.

Earthquake scenarios are determined according to the local seismotectonics, which implies two different seismic regimes (compressional and extensional). More specifically they refer to two typical seismic conditions that can be easily observed in several active regions: near-moderate earthquakes ($M < 6$ at distances of some kilometres) and far-strong earthquakes ($M > 6$ at distances of some tens kilometres). Here a procedure called probabilistically-based deterministic seismic hazard scenario has been adopted, where the scenario ground motion has been computed according to a selected reference period taking into account the average activity rate of each individual seismic source.

Hydraulic conditions are then taken according to the average rainfall conditions that can be determined on a yearly basis: they refer to wet and dry conditions that are determined on the basis of a hydrologic balance between the effective rainfall and the potential infiltration.

Finally, landslide susceptibility is determined according to failure probabilities in each earthquake-hydraulic scenario based on the distribution of seismic safety factors computed for each landslide. Nevertheless, we anticipate that undergoing researches are focusing on the potential for coseismic displacements (Romeo 2000) that may threaten exposed assets for the assessment of the seismic landslide risk as a whole.

Acknowledgments The Authors acknowledge the anonymous reviewer who provided valuable comments and suggestions.

References

Joyner WB, Boore DM (1981) Peak horizontal acceleration and velocity from strong-motion records including records from the 1979 Imperial Valley, California, earthquake. Bull Seismol Soc Am 71:2011–2038

Montgomery DR, Dietrich WE (1994) A physically based model for the topographic control on shallow landsliding. Water Resour Res 30 (4):1153–1171

Paciello A, Rinaldis D, Romeo RW (2000) Incorporating ground motion parameters related to earthquake damage into seismic hazard analysis. In: Proceedings VI international conference on seismic zonation, 12–15 Nov. Palm Spring

Romeo RW (2000) Seismically-induced landslide displacements: a predictive model. Eng Geol 58(3–4):337–351

Sabetta F, Pugliese A (1987) Attenuation of peak horizontal acceleration and velocity from Italian strong motion records. Bull Seismol Soc Am 77(5):1491–1513

Wells DL, Coppersmith KJ (1994) New Empirical Relationships among Magnitude, Rupture Length, Rupture Width, Rupture Area, and Surface Displacement. Bull Seismol Soc Am 84 (4):974–1002